12-15-2014

# Behavior of Piezoelectric Wafer Active Sensor in Various Media

Tuncay Kamas
*University of South Carolina - Columbia*

# BEHAVIOR OF PIEZOELECTRIC WAFER ACTIVE SENSOR IN VARIOUS MEDIA

by

Tuncay Kamas

Bachelor of Science
Selcuk University, 2006

Master of Science
Clemson University, 2009

---

Submitted in Partial Fulfillment of the Requirements

For the Degree of Doctor of Philosophy in

Mechanical Engineering

College of Engineering and Computing

University of South Carolina

2014

Accepted by:

Victor Giurgiutiu, Major Professor

Lingyu Yu, Committee Member

Guiren Wang, Committee Member

Bin Lin, Committee Member

Paul Ziehl, Committee Member

Lacy Ford, Vice Provost and Dean of Graduate Studies

# ACKNOWLEDGMENTS

I cannot express my gratefulness enough to God for guiding me and prompting me to apply and work in this highly valued and respected research group in Laboratory for Active Material and Smart Structures (LAMSS). I would like to express my sincere gratitude to my academic advisor, Dr. Victor Giurgiutiu, for his strong support and seasoned guidance. His passionate attitude toward science and enlightening instruction has helped me overcome many difficulties, and will exist as life-time encouragement in my future career. I would also like to thank Dr. Guiren Wang, Dr. Paul Ziehl, Dr. Lingyu Yu and Dr. Bin Lin for being part of my Committee and for their invaluable guidance. I want to thank my dear colleagues for their friendship and accompany during this arduous journey, especially Dr. Jingjing Bao and Dr. Bin Lin for their help in my research, Zhenhua Tian for his help in the experiments, and my dear friends Yanfeng Shen, Banibrata Poddar, Catalin Roman, Abdelrahman Ayman, and Erik Frankforter. I would like to thank my understanding and supportive family: my wife, Sevda Kamas for her understanding and patience; my parents, Nazmi Kamas and Zehra Kamas for their understanding and encouragement.

The following funding supports are thankfully acknowledged: National Science Foundation Grant # CMS-0925466; Office of Naval Research # N00014-11-1-0271, Dr. Ignacio Perez, Technical Representative; Air Force Office of Scientific Research

#FA9550-11-1-0133, Dr. David Stargel, Program Manager; Nuclear Energy University Program Grant # DE-NE0000726, Kenny Osborne, Project Manager.

# ABSTRACT

The dissertation addresses structural health monitoring (SHM) techniques using ultrasonic waves generated by piezoelectric wafer active sensors (PWAS) with an emphasis on the development of theoretical models of standing harmonic waves and guided waves. The focal objective of the research is to extend the theoretical study of electro-mechanical coupled PWAS as a resonator/transducer that interacts with standing and traveling waves in various media through electro-mechanical impedance spectroscopy (EMIS) method and guided wave propagation. The analytical models are developed and the coupled field finite element analysis (CF-FEA) models are simulated and verified with experiments. The dissertation is divided into two parts with respect to the developments in EMIS methods and GWP methods.

In the first part, analytical and finite element models have been developed for the simulation of PWAS-EMIS in in-plane (longitudinal) and out-of-plane (thickness) mode. Temperature effects on free PWAS-EMIS are also discussed with respect to the in-plane mode. Piezoelectric material degradation on certain electrical and mechanical properties as the temperature increases is simulated by our analytical model for in-plane circular PWAS-EMIS that agrees well with the sets of experiments.

Then the thickness mode PWAS-EMIS model was further developed for a PWAS resonator bonded on a plate-like structure. The latter analytical model was to determine the resonance frequencies for the normal mode expansion method through the global

matrix method by considering PWAS-substrate and proof mass-PWAS-substrate models. The proof mass concept was adapted to shift the systems resonance frequencies in thickness mode.

PWAS in contact with liquid medium on one of its surface has been analytically modeled and simulated the electro-mechanical response of PWAS with various liquids with different material properties such as the density and the viscosity.

The second part discusses the guided wave propagation in elastic structures. The feature guided waves in thick structures and in high frequency range are discussed considering weld guided quasi-Rayleigh waves. Furthermore, the weld guided quasi Rayleigh waves and their interaction with damages in thick plates and thick walled pipes are examined by the finite element models and experiments. The dissertation finishes with a summary of contributions followed by conclusions, and suggestions for future work.

# TABLE OF CONTENTS


ACKNOWLEDGMENTS .................................................................................... ii

ABSTRACT.................................................................................................... iv

LIST OF TABLES ........................................................................................ ix

LIST OF FIGURES ...................................................................................... xi

CHAPTER 1 INTRODUCTION ........................................................................ 1

1.1 Motivation ................................................................................................ 1

1.2 Research Goal, Scope, and Objectives .................................................... 8

1.3 Organization of The Dissertation ............................................................. 9

CHAPTER 2 LITERATURE REVIEW ........................................................... 11

2.1 Ultrasonic Waves in Solid Medium ......................................................... 11

2.2 Ultrasonic Waves in Fluid Medium ......................................................... 20

2.3 Piezoelectric Transducers........................................................................ 35

CHAPTER 3 FREE PWAS E/M IMPEDANCE SPECTROSCOPY ............................. 51

3.1 State of The Art for Electromechanical Impedance Spectroscopy..................... 51

3.2 Analytical In-Plane Mode EMIS Model Under Constant $D_3$ Assumption......... 59

3.3 Analytical Thickness Mode EMIS Model under Constant $D_3$ Assumption....... 68

3.4 Analytical Thickness Mode EMIS Model under Constant $E_3$ Assumption ....... 73

3.5 Case Studies for Free PWAS EMIS .......................................................... 82

3.6 Summary and Conclusions ....................................................................... 89

CHAPTER 4 BEHAVIOR OF FREE PWAS AT ELEVATED TEMPERATURE ........ 91
4.1 State of The Art ........ 91
4.2 1-D Analytical EMIS Simulations for PWAS at Elevated Temperatures ........ 98
4.3 2-D Analytical EMIS Simulations for PWAS at Elevated Temperatures ........ 102
4.4 Experimental Work ........ 105
4.5 Summary and Conclusions ........ 121
CHAPTER 5 IN PLANE EMIS OF CONSTRAINED PWAS USING GMM ........ 123
5.1 State of The Art for Constrained PWAS-EMIS ........ 124
5.2 Global Matrix Method (GMM) in Multilayered Structures ........ 125
5.3 In-Plane Mode of PWAS Constrained from One Side ........ 127
5.4 In-Plane Mode of PWAS Constrained from Both Sides ........ 140
CHAPTER 6 THICKNESS MODE EMIS OF CONSTRAINED PWAS ........ 159
6.1 Thickness Mode of Constrained PWAS ........ 159
6.2 Thickness Mode of PWAS Constrained from One Side ........ 163
6.3 Thickness Mode of PWAS Constrained from Both Sides ........ 176
CHAPTER 7 PROOF-MASS PIEZOELECTRIC WAFER ACTIVE SENSOR ........ 182
7.1 State of The Art for Proof-Mass PWAS ........ 183
7.2 Analytical EMIS Analysis for PM-PWAS ........ 186
7.3 Coupled Field Finite Element Analysis of PMPWAS EMIS ........ 195
7.4 Experimental EMIS Study for PM-PWAS ........ 208
CHAPTER 8 BEHAVIOR OF PWAS IN FLUID MEDIUM ........ 246
8.1 State of The Art for Health Monitoring with Biomedical Sensor ........ 246
8.2 1-D Analysis Piezo-Wafer Resonator in Contact with Liquid Layer ........ 248

8.3 Mechanical Response: .......... 254

8.4 Electrical Response: .......... 261

8.5 Experimental Analysis of a PWAS Interacting with Viscous Liquid .......... 274

CHAPTER 9 PWAS GENERATED ULTRASONIC WAVES IN SOLID MEDIA .......... 278

9.1 Introduction .......... 278

9.2 Tuning Curves for Lamb Wave Modes in Thin Plate .......... 281

9.3 Tuning Curves for Quasi-Rayleigh Wave in Thick Structures .......... 287

CHAPTER 10 WELD GUIDED WAVES IN THICK STRUCTURES .......... 306

10.1 Introduction .......... 306

10.2 Weld Guided Quasi-Rayleigh Waves (QRW) .......... 308

10.3 Finite Element Model of Butt-Welded Thick Steel Plate .......... 309

10.4 Experimental Analysis for Tuning of Weld Guided QRW .......... 312

10.5 Summary and Conclusions .......... 319

CHAPTER 11 SUMMARY AND CONCLUSIONS .......... 321

11.1 Research Conclusions .......... 325

11.2 Major Contributions .......... 329

11.3 Recommendation for Future work .......... 331

REFERENCES .......... 333

LIST OF TABLES

Table 3.1 Properties of APC 850 piezoelectric ceramic (www.americanpiezo.com). ..... 67

Table 5.1 Geometric sizes and material properties of two-bar resonator. ...................... 131

Table 5.2 Orthogonality matrix that validates the mode shape solution and that gives the modal participation factors. ................................................................................ 132

Table 5.3 Normalized mode shapes and resonant frequencies. ...................................... 133

Table 5.4 Mode numbers, normalized mode shapes, and resonant frequencies ............. 149

Table 6.1 Orthogonality matrix that validates the mode shape solution and that gives the modal participation factors. ................................................................................ 169

Table 6.2 Normalized mode shapes for the first two modes PWAS at the height of 0.5 mm and length of 7 mm. ....................................................................................... 174

Table 6.3 Normalized mode shapes for the first two modes PWAS at the height of 0.2 mm and length of 7 mm. ....................................................................................... 175

Table 6.4 Three bar resonator mode shapes, resonant frequencies and amplitude differences at different modes............................................................................ 178

Table 7.1 Analytical and finite element analysis results for the thickness mode resonance frequencies of three configuration of PM-PWAS system ................................ 198

Table 7.2 E/M impedance frequencies as the proof-masses incline from no mass up to 0.15mm PM height202Table 7.3 E/M impedance frequencies as the proof-masses incline from no mass up to 0.15mm PM height ................................... 204

Table 7.4 E/M impedance frequencies in the first four thickness modes as the proof-masses incline from no mass up to 0.15mm PM height ................................... 214

Table 7.5 Geometrical sizes of the washers bonded on the first specimen..................... 223

Table 7.6 Anayltical and experimental resonance frequencies of steel PM-PWAS constrained on an aluminum plate with the proof-mass in height of 1mm....... 235

Table 7.7 Anayltical and experimental resonance frequencies of steel PM-PWAS constrained on an aluminum plate with the proof-mass in height of 2mm....... 235

Table 7.8 Comparison between analytical and experimental resonance frequencies for aluminum square PM-PWAS with proof-mass height of 1.5mm ..................... 239

Table 9.1 Free Capacitance for 7mm round PWAS with 0.2mm and 0.5mm thickness 281

Table 9.2 Material properties of SM 412 piezo- electric wafer active sensor ................ 282

LIST OF FIGURES

Figure 1.1 (a) Pipelines for energy transportation; (b) pressure vessel for pressurized gas; (c) ships and offshore structures. ........................................................................ 1

Figure 1.2: Active and passive sensing methods for in-situ SHM through PWAS generating propagating and standing Lamb waves in substrate structure to detect damage (Giurgiutiu, 2008a). ................................................................................ 2

Figure 1.3 Illustration of free PWAS transducers in different types and sizes (Giurgiutiu, 2008). ........................................................................................................ 3

Figure 1.4 Illustration of (a) PWAS sensors installed on an aircraft panel and of (b) principles of active structural health monitoring with PWAS transducers near a crack. .......................................................................................................... 4

Figure 1.5: A dry cask storage system for spent nuclear fuel. ........................................... 7

Figure 2.1: (a) Wave speed dispersion curve; (b) wavenumber dispersion curve (Shen, 2014). ........................................................................................................ 14

Figure 2.2: Simulation of Rayleigh wave propagation in a semi-infinite medium http://www.exploratorium.edu/faultline/activezone/slides/rlwaves-slide.html. . 16

Figure 2.3: Coordinate definition and particle motion of SH plate waves (Giurgiutiu 2008). ........................................................................................................ 17

Figure 2.4: (a) SH plate wave-speed dispersion curves; (b) symmetric mode shapes; (c) antisymmetric mode shapes (Giurgiutiu 2008).17Figure 2.5: Discretization of the cross sections in SAFE: (a) square rod; (b) circular pipe; (c) rail track (Hayashi et al. 2004). ........................................................................ 19

Figure 2.6 Schematic of the fluid loaded beam excited by a harmonic point force.......... 21

Figure 2.7: Schematic illustration of the BG wave problem and the coordinate system.. 23

Figure 2.8 Scholte surface-wave velocity relative variations to the shear-wave velocity, $V_{S2}$, as a function of frequency f and fluid layer thickness. The parameters $V_{P1}$, $V_{P2}$, $V_{S1}$, $\rho_1$, and $\rho_2$ [$V_{P1}$ = 1.5 km/s, $V_{P2}$ = 2.0 km/s, $V_{S1}$ = 0 km/s, $\rho_1$ = 1.0 g/cc, and $\rho_2$ = 2.0 g/cc] are common to all the three curves. ...................................... 24

Figure 2.9 Phase velocity dispersion of the quasi-Scholte mode on a steel plate surrounded by water. ........................................................................................ 26

Figure 2.10 Schematic illustration of different solid-liquid structure configurations and corresponding waves traveling along the interfaces. ........................................ 27

Figure 2.11 Schematic of the propagation of a Shear horizontal (SH) wave along the interface between a piezoelectric substrate and a liquid layer. .......................... 31

Figure 2.12 Plane transverse wave traveling between the surface and the liquid with the wavelength of the surface shear wave and the wavelength of the bulk shear wave penetrating to liquid medium. ........................................................................... 33

Figure 2.13: Illustration of differently rotated cuts such as singly and doubly rotated. (Basic Technology of Quartz Crystal Resonators, 2012). ................................. 36

Figure 2.14 Basic induced-strain responses of piezoelectric materials: (a) direct strains; thickness $\varepsilon_3 = d_{33}E_3$ and in-plane $\varepsilon_1 = d_{31}E_3$, $\varepsilon_2 = d_{32}E_3$ (b) shear strain $\varepsilon_5 = d_{15}E_1$ (c) shear strain $\varepsilon_5 = d_{35}E_3$ (Victor Giurgiutiu, 2008d). ............................................. 38

Figure 2.15 (a) Thickness-shear resonator. (b) Length-shear resonator. The shaded areas are the electrodes and the dashed arrows represent the direction of displacement at given points. The polarization direction is indicated by an arrow on the front face of the sample. ........................................................................................ 40

Figure 2.16 Solid lines represent non-deformed shape and dashed lines depict deformed shape (a) Shear horizontal (SH) deformation $T_4 = T_{23}$, (b) Shear horizontal (SH) deformation $T_5 = T_{13}$, (c) Shear vertical (SV) deformation $T_6 = T_{12}$. ................ 42

Figure 2.17 Straight crested axial vibration in a plate. .................................................... 42

Figure 2.18 Straight crested flexural vibration of a plate. ............................................... 43

Figure 2.19 PWAS interaction with Lamb waves in a plate; (a) S0 Lamb wave mode , (b) A0 Lamb wave mode. ........................................................................................ 43

Figure 2.20 Constrained thickness mode transducer. ...................................................... 45

Figure 2.21 Two port illustration of a piezoelectric transducer system. The electrical and mechanical parameters at the ports are correlated by the ABCD matrix. ...... 47

Figure 2.22 Diagram of a pitch-catch setup being used to detect a damaged region (Giurgiutiu, 2008). ........................................................................................... 49

Figure 2.23 Diagram of a pulse-echo setup being used to detect a damaged region (Giurgiutiu, 2008). ........................................................................................... 50

Figure 3.1 Piezoelectric wafer active sensor constrained by the structural stiffness (Zagrai, 2002). ........................................................................................ 53

Figure 3.2 Schematic of a piezoelectric wafer active sensor polarized in thickness direction. ........................................................................................ 54

Figure 3.3 Simulated frequency response of admittance and impedance of a PWAS (including internal damping effects of $\delta = \eta = 0.01$). ........................................ 60

Figure 3.4 Flow chart of the 1-D analytical thickness mode EMIS for free PWAS........ 72

Figure 3.5 Real part of the impedance and the admittance for 0.2mm thick and 7mm diameter PWAS in out of plane (thickness) mode............................................ 73

Figure 3.6 Schematic of thickness mode of a piezoelectric wafer active sensor and infinitesimal axial element.................................................................... 74

Figure 3.7 Electrical displacement change along the thickness of a square PWAS at frequency of 1 MHz.......................................................................... 79

Figure 3.8 Real part of the impedance and the admittance for 0.2mm thick and 7mm diameter PWAS in out of plane (thickness) mode............................................ 82

Figure 3.9 Comparison between analytical and experimental thickness mode impedance results.................................................................................................. 83

Figure 3.10 Illustration of schema and picture of square PWAS and admittance-impedance results for the free square PWAS. ................................................... 84

Figure 3.11 Analytical impedance and admittance simulation results for 7x7 mm$^2$ square 0.2 mm thick PWAS. ............................................................................ 85

Figure 3.12 Impedance comparison for two 1-D analytical models regarding in-plane mode of PWAS resonator and 2-D finite element model for a 7 mm square 0.2 mm thick PWAS. .............................................................................. 86

Figure 3.13 Impedance comparison for two models regarding in-plane mode of PWAS resonator and impedance measurement for a 7 mm square 0.2 mm thick PWAS under stress-free boundary condition................................................................ 87

Figure 3.14 The comparison of the real part of the impedance and admittance results for both thickness mode analytical models for a 0.2 thick and 7 mm round PWAS resonator. ........................................................................................ 88

Figure 3.15 Experimental results of the impedance for 0.2 thick APC-850 PWAS resonator. ........................................................................................ 89

Figure 4.1 X-cut GaPO4 PWAS wafers comprised of a single crystal disks of 7mm diameter and 0.2mm thickness single crystal discs. .......................................... 92

Figure 4.2 Low temperature elastic compliance coefficient ($s_{11}^{E}$) plotted as a function of temperature for several tetragonal and rhombohedral PZT compositions.......... 94

Figure 4.3 $-d_{31}$ of Pt/PZT/Pt stack plotted as a function of temperature for 2 μm Pt: Platinum electrode. ............................................................................................ 94

Figure 4.4 Variation of Young's modulus and $d_{31}xg_{31}$. Average thermal expansion for PZT-5A $\alpha_{PZT\text{-}5A}$=2.5μm/m-ºC. ............................................................................ 95

Figure 4.5 $-d_{31}$ and $d_{33}$ of three different PZT materials plotted as a function of temperature ......................................................................................................... 96

Figure 4.6 the effective E/M coupling coefficient and thermal expansion plotted as a function of temperature.......................................................................................... 96

Figure 4.7 The piezoelectric voltage constant, $g_{31}$ and piezoelectric charge constant, $d_{31}$ with temperature increasing.................................................................................... 97

Figure 4.8 The stiffness change influence on both anti-resonance (impedance) and resonance frequency (admittance) in-plane EMIS of 7mmx0.2mm PWAS....... 99

Figure 4.9 The piezoelectric charge constant $d_{31}$ change influence on both anti-resonance (impedance) and resonance frequency (admittance) in-plane EMIS of 7mmx0.2mm PWAS.......................................................................................... 100

Figure 4.10 The stiffness and the piezoelectric charge constant $d_{31}$ change influence on both anti-resonance (impedance) and resonance frequency (admittance) in-plane EMIS of 7mmx0.2mm PWAS.......................................................................... 101

Figure 4.11 Schema of circular PWAS in cylindrical coordinate system....................... 102

Figure 4.12 Flow-chart of the analytical modeling of 2-D in-plane EMIS of circular PWAS. ................................................................................................................ 103

Figure 4.13 Stiffness coefficient $c_{11}$, piezoelectric coefficient $d_{31}$ , and capacitance $C_0$ influence on admittance....................................................................................... 104

Figure 4.14 Stiffness coefficient $c_{11}$, piezoelectric coefficient $d_{31}$ , and capacitance $C_0$ influence on impedance. ..................................................................................... 105

Figure 4.15 High temperature PWAS testing by (a) impedance analyzer, (b) PID temperature controller (c) oven. ....................................................................... 105

Figure 4.16 a) Fixture in the oven (b) fixture, thermistor, and thermocouple (c) PWAS in the fixture.......................................................................................................... 107

Figure 4.17 Static capacitance results for PWAS 1R (7mmx0.2mm PWAS) at elevated temperatures and room temperatures in each temperature cycle. .................... 109

Figure 4.18 Static capacitance results for all of the circular PWAS resonators (7mmx0.2mm) at only elevated temperatures. ............................................. 109

Figure 4.19 Averaged static capacitance results for all of the circular PWAS resonators (7mmx0.2mm) at room temperature and elevated temperatures. .................... 110

Figure 4.20 Impedance signature of PWAS-1R (7mmx0.2mm PWAS) at elevated temperatures and room temperatures in each temperature cycle. .................... 112

Figure 4.21 Impedance signature of PWAS-1R (7mmx0.2mm PWAS) at (a) elevated temperatures and (b) room temperatures in each temperature cycle. ............... 113

Figure 4.22 Impedance (anti-resonance) frequency of PWAS-1R (7mmx0.2mm PWAS) during temperature cycle. ................................................................... 114

Figure 4.23 Impedance (anti-resonance) amplitude of PWAS-1R (7mmx0.2mm PWAS) during temperature cycle. ................................................................... 115

Figure 4.24 Averaged impedance (a) frequency and (b) ampllitde shift against elevated temperature. ..................................................................................... 116

Figure 4.25 Averaged impedance (a) frequency and (b) ampllitde shift of PWAS-1R (7mmx0.2mm PWAS) at room temperature. .............................................. 117

Figure 4.26 Impedance (anti-resonance) amplitude of PWAS-2L (7mmx0.2mm PWAS) during temperature cycle. ................................................................... 118

Figure 4.27 Impedance (anti-resonance) frequency of PWAS-2L (7mmx0.2mm PWAS) during temperature cycle. ................................................................... 118

Figure 4.28 3D contour plots for admittance spectra at elevated temperatures. ............ 119

Figure 4.29 Admittance peak amplitude at the first in-plane resonance frequency of circular PWAS at elevated temperatures. ...................................................... 120

Figure 4.30 Admittance frequency at the first in-plane resonance frequency of circular PWAS at elevated temperatures. .................................................................. 121

Figure 5.1 Schematic of a multi-layered structure for using Global Matrix Method (GMM) (Lowe, 1995). ........................................................................... 125

Figure 5.2 Generation of dispersion curves showing Lamb wave modes for 1mm thick sheet of titanium (Lowe, 1995). ........................................................... 126

Figure 5.3 Illustration of a two bar resonator model with perfectly bonded PWAS on side of a bar. ................................................................................................ 127

Figure 5.4 Schematic of two bar resonator excited by electrodes depo- sited on PWAS surfaces. ........................................................................................................ 134

Figure 5.5 Frequency response function of two-bar PWAS resonator. .......................... 139

Figure 5.6 Frequency response function for two-bar resonator. Height is 0.2 mm and length of aluminum 30 mm and length of PWAS is 40 mm. ........................... 140

Figure 5.7 Illustration of a three bar resonator model with perfectly bonded PWAS on sides of two bars. ............................................................................................ 140

Figure 5.8 Geometric sizes and material properties of proof-mass PWAS resonator. ... 147

Figure 5.9 Schematic of three-bar resonator with excited PWAS through a harmonic electrical field induced by the elecrodes deposited on PWAS ........................ 149

Figure 5.10 Frequency response function for three-bar PWAS resonator...................... 157

Figure 6.1 PWAS constrained by structural stiffness. ................................................... 160

Figure 6.2 Illustration of a schema and picture of constrained PWAS. .......................... 163

Figure 6.3 Constrained PWAS undergoing axial vibration under the excitation of an externally applied time-depen dent axial force per unit length. ....................... 166

Figure 6.4 Flow chart of the one dimensional analytical thickness mode EMIS for constrained PWAS. .......................................................................................... 171

Figure 6.5 Schematic of PWAS bonded on bar and geometric and material properties. 172

Figure 6.6 Frequency response function for two-bar resonator. Height of aluminum is 1mm and height of PWAS is 0.5mm and length is 7mm. ................................ 173

Figure 6.7 Frequency response function for two-bar resonator. Height of aluminum is 1 mm and height of PWAS is 0.2 mm and length is 7 mm. ................................ 175

Figure 6.8 Illustration of a PM-PWAS transducer bonded on a substrate material and its mode shapes at fundamental and overtone resonant frequencies. .................... 176

Figure 6.9 Illustration of the real and imaginary parts of the Frequency Response Function (FRF). ............................................................................................... 177

Figure 6.10 Illustration of the effect of Proof-Mass size change on mode shapes in relation with frequency response function amplitudes at resonance frequencies (Kamas, Giurgiutiu, & Lin, 2013). ................................................................... 179

Figure 6.11 Effect of proof-mass height on resonance frequencies at multiple modes. 180

Figure 7.1 Illustration of constrained PWAS model including adhesive bonding layer. 186

Figure 7.2 (a) Frequency response function whose amplitude is plotted in logarithmic scale; (b) experimental and analytical real part of the E/M impedance results for PWAS installed on 1mm thick aluminum 7mm x 7mm square plate-like aluminum substrate. ........................................................................... 192

Figure 7.3 Illustration of constrained PM-PWAS model including two adhesive bonding layers. ...................................................................................................... 193

Figure 7.4 Comparison of analytical and experimental (a) EMIS of PM-PWAS on aluminum substrate neglecting adhesive bonding layers (b) EMIS of PM-PWAS on aluminum substrate including two adhesive bonding layers ....................... 195

Figure 7.5 Interaction between PWAS and structure..................................................... 196

Figure 7.6 (a) three configurations of PM-PWAS in different thickness; (b) real part of the admittance spectra in regards with the corresponding configurations of PM-PWAS system ........................................................................................ 197

Figure 7.7 Illustration of proof-mass effect on PWAS-EMIS results............................ 199

Figure 7.8 Thickness mode PM-PWAS EMIS simulations by 1-D analytical and 2-D FEA-models. ........................................................................................... 201

Figure 7.9 Four different configurations designed for CF-FEA to analyze the effect of proof-mass length on PWAS resonator ........................................................... 201

Figure 7.10 Resonance frequency changes as proof-mass height increases calculated by 1-D analytical and 2-D FEA models ............................................................... 203

Figure 7.11 FEA and analytical PM-PWAS impedance spectra at first four thickness modes .......................................................................................................... 206

Figure 7.12 Resonance frequency changes as proof-mass height increases calculated by 1-D analytical and 2-D FEA models ............................................................... 207

Figure 7.13 (a) Frequency response function; (b) experimental and analytical real part of the E/M impedance results for PWAS installed on 1mm thick aluminum square plate-like aluminum substrate. ........................................................... 211

Figure 7.14 (a) Illustration of a schema and picture of constrained PWAS and (b) experimental admittance result of one of the constrained PWAS specimens .. 212

Figure 7.15 Comparison between analytical and experimental a-) resonance frequency b-) impedance results of a constrained PWAS on an aluminum substrate in thickness of 1mm and in length of 7mm and in width of 5mm....................................... 213

Figure 7.16 Schematic illustration of bonded PWAS on an aluminum substrate........... 213

Figure 7.17 EMIS measurement result for a circular PWAS in diameter of 7mm and in thickness of 0.2mm is bonded on a circular aluminum plate in diameter of 100mm and in thickness of 0.8mm .................................................................. 214

Figure 7.18 EMIS results from a) 2-D CF-FEA b) 1-D analytical models for PWAS perfectly bonded in the center of an aluminum plate with 100mm length and 0.8mm thickness ........................................................................................ 215

Figure 7.19 Second experimental setup for constrained PWAS-EMIS measure- ment: large aluminum plate in thickness of 2.1mm and PWAS in 7x7mm$^2$ ............. 216

Figure 7.20 Constrained PWAS-EMIS measurement to indicate thickness mode impedance spectra.......................................................................................... 216

Figure 7.21 1-D analytical constrained PWAS-EMIS prediction to indicate thickness mode impedance spectra................................................................................. 217

Figure 7.22 Schematic illustration of bonded PWAS on an aluminum substrate........... 217

Figure 7.23 EMIS measurement result for a circular PWAS in diameter of 7mm and in thickness of 0.2mm is bonded on a circular aluminum plate in diameter of 100mm and in thickness of 1mm...................................................................... 217

Figure 7.24 EMIS results from a) 2-D CF-FEA b) 1-D analytical models for PWAS perfectly bonded in the center of an aluminum plate with 100mm length and 0.8mm thickness ........................................................................................ 218

Figure 7.25 Schematic illustration of bonded two PWAS on two surfaces of aluminum substrate .................................................................................................... 218

Figure 7.26 EMIS measurement result for a circular PWAS in diameter of 7mm and in thickness of 0.2mm is bonded on a circular aluminum plate in diameter of 100mm and in thickness of 1mm...................................................................... 218

Figure 7.27 EMIS results from a) 2-D CF-FEA b) 1-D analytical models for PWAS perfectly bonded in the center of an aluminum plate with 100mm length and 0.8mm thickness ........................................................................................ 219

Figure 7.28 Illustration of free circular PWAS in diameter of 25mm and in thickness of 0.2mm and admittance and impedance plots .................................................. 220

Figure 7.29 Illustration of the schema and picture of the bonded PWAS on an aluminum plate........................................................................................................... 221

Figure 7.30 Illustration of admittance and impedance results of the bonded PWAS in 25mm diameter on Al plate in 100 mm diameter ............................................ 222

Figure 7.31 Illustration of schema and picture of the washer proof-mass PWAS.......... 222

Figure 7.32 Admittance and impedance results for the PM-PWAS with three washers 224

Figure 7.33 Experimental admittance peak illustration PM PWAS with no washer, one, two, and three washers installed ........................................................................ 225

Figure 7.34 Illustration of schema and pictures of a-) free PWAS b-) constrained PWAS on steel substrate c-) steel proof-mass PWAS constrained on steel disc.......... 226

Figure 7.35 Experimental admittance results for a-) free PWAS b-) constrained PWAS on steel discs with different height ........................................................................ 227

Figure 7.36 Experimental impedance results for constrained PWAS on steel discs with different height........................................................................................ 227

Figure 7.37 Experimental impedance results for constrained PM-PWAS .................... 228

Figure 7.38 Experimental admittance and impedance results for a-) free PWAS and b-) constrained PWAS on an aluminum plate in thickness of 1mm and diameter of 100mm ........................................................................................................ 229

Figure 7.39 Illustration of schema and pictures of PM-PWAS resonators with different height which are constrained on aluminum plate ............................................ 230

Figure 7.40 Experimental admittance and impedance results for PM-PWAS with different PM height........................................................................................................ 231

Figure 7.41 Illustration of the schema and picture of a constrained square PWAS and admittance/impedance results for the constrained PWAS................................ 232

Figure 7.42 Comparison between the analytical model and the experimental results for impedance of constrained PWAS ...................................................................... 233

Figure 7.43 Schematic illustration of PM-PWAS constrained on an aluminum plate and experimental admittance and impedance results for PM-PWAS different steel proof-mass height ........................................................................................ 234

Figure 7.44 Illustration of the experimental setup and the impedance results for the geometric parameters; $H_{sub} = 0.95mm, H_{PWAS} = 0.2mm, H_{PM} = 0.95mm$ and for the material properties $E_{AL} = 60GPa,\ \rho_{AL} = 1800kg/m^3$ ............................... 236

Figure 7.45 a-) Comparison between experimental and analytical resonance frequencies and b-) impedance results .................................................................................. 237

Figure 7.46 Illustration of a-) free PWAS, b-) one-side constrained PWAS c-)two-side constrained PWAS by proof-mass and substrate materials ............................. 238

Figure 7.47 Comparison between analytical and experimental admittance and impedance results for aluminum square PM-PWAS with proof-mass height of 1.5mm.... 240

Figure 7.48 Comparison between analytical and experimental a-) resonance frequencies b-) impedance results for aluminum square PM-PWAS with proof-mass height of 2mm, 2.5mm, and 3mm.................................................................... 241

Figure 7.49 Sweep (chirp) signal is transmitted through 0.2mm thick 7x7 mm$^2$ square PWAS and received by PWAS in the same sizes on an 2.1mm thick aluminum plate. The start frequency, $f_0 = 500kHz$ and the stop frequency, $f_1 = 1MHz$ ... 243

Figure 7.50 Illustration of the signal received by 0.2mm thick 7x7 mm$^2$ square receiver PWAS and the signal transmitted as a chirp signal through 0.2mm thick 7x7 mm$^2$ square PWAS in the same sizes on an 2.1mm thick aluminum plate. The start frequency $f_0 = 500kHz$ and the stop frequency, $f_1 = 1MHz$ ...................... 243

Figure 7.51 Illustration of the signal received by 0.2mm thick 7x7 mm$^2$ square receiver PWAS and the signal transmitted as a chirp signal through the same size PWAS in 10mm distance on 2.1mm thick aluminum plate. The start frequency is 1MHz and the stop frequency is 3MHz ...................................................................... 244

Figure 7.52 Measurement results of the real part of *in-plane* mode impedance for a 0.2mm thick 7x7 mm2 square PWAS on a 2.1 mm thick aluminum plate ...... 245

Figure 8.1 X-ray of bio-PWAS implanted in a rat and the impedance reading from bio-PWAS after implementation and 2 days later.................................................. 247

Figure 8.2 Schema of piezo-wafer resonator deformed in shear horizontal $d_{13}$ mode by induced $T_5 = T_{13}$ shear stress ................................................................. 248

Figure 8.3 Schema of infinitesimal chunk of solid in which the shear stress is induced249

Figure 8.4 Schema of piezo-wafer resonator in contact with a liquid layer and both PWAS and liquid layer deformed in shear horizontal $d_{13}$ mode by induced $T_5 = T_{13}$ shear stress ......................................................................................... 254

Figure 8.5 Particle velocity of PWAS along its thickness in contact with water, the particle velocity at the interface is 1315 µm/sec at electric field amplitude of 20 kV/m PWAS sizes 15mmx15mmx1mm......................................................... 259

Figure 8.6 Particle velocity of PWAS along its thickness in contact with honey, PWAS sizes 15mmx15mmx1mm.................................................................... 260

Figure 8.7 Liquid particle velocity change in the vicinity of PWAS-liquid interface at the first resonance frequency of 850.4kHz (a) for water with the density of 1000kg/m and the dynamic viscosity of 0.001 Pa.s (b) for honey with the density of 1350kg/m and the dynamic viscosity of 10 Pa.s. PWAS sizes 15mmx15mmx1mm............................................................................. 260

Figure 8.8 Admittance of PWAS resonator in 7mm of length, 7mm of width, and 0.2mm of thickness in contact with water in density is 1000 kg/m3 and dynamic viscosity is 1.002x10-3 Pa.sec at temperature of 20˚C.................................... 265

Figure 8.9 Impedance of PWAS resonator in 7mm of length, 7mm of width, and 0.2mm of thickness in contact with water in density is 1000 $kg/m^3$ and dynamic viscosity is $1.002x10^{-3}$ Pa.sec at temperature of 20˚C..................................... 265

Figure 8.10 Admittance of PWAS resonator in 7mm of length, 7mm of width, and 0.2mm of thickness in free condition; in contact with water in density of 1000 $kg/m^3$ and dynamic viscosity of $1.002x10^{-3}$ Pa.sec; and in contact with honey in density of 1000 $kg/m^3$ and dynamic viscosity is $10x10^{-3}$ Pa.sec at temperature of 20˚C.. 266

Figure 8.11 Impedance of PWAS resonator in 7mm of length, 7mm of width, and 0.2mm of thickness in free condition; in contact with water in density of 1000 $kg/m^3$ and dynamic viscosity of $1.002x10^{-3}$ Pa.sec; and in contact with another liquid in density of 1000 $kg/m^3$ and dynamic viscosity is $10x10^{-3}$ Pa.sec ...................... 267

Figure 8.12 First admittance peak of PWAS resonator in 7mm of length, 7mm of width, and 0.2mm of thickness in free condition and in contact with liquids in different density and same dynamic viscosity is 1.0 Pa.sec ........................................... 268

Figure 8.13 First impedance peak of PWAS resonator in 7mm of length, 7mm of width, and 0.2mm of thickness in free condition and in contact with liquids in different density and same dynamic viscosity is 1.0 Pa.sec ........................................... 268

Figure 8.14 First admittance of the admittance spectra of PWAS resonator in 7mm of length, 7mm of width, and 0.2mm of thickness in free condition; in contact with water in density of 1000 $kg/m^3$ and dynamic viscosity of $1.002x10^{-3}$ Pa.sec; and in contact with another liquid in density of 1000 $kg/m^3$ and dynamic viscosity is $10x10^{-3}$ Pa.sec ........................................................................................ 269

Figure 8.15 First impedance peak of the impedance spectra of PWAS resonator in 7mm of length, 7mm of width, and 0.2mm of thickness in free condition; in contact with water in density of 1000 $kg/m^3$ and dynamic viscosity of $1.002x10^{-3}$ Pa.sec; and in contact with another liquid in density of 1000 $kg/m^3$ and dynamic viscosity is $10x10^{-3}$ Pa.sec .................................................................. 270

Figure 8.16 Real part of admittance spectra of PWAS resonator in 15mm of length, 15mm of width, and 1mm of thickness in free condition and in contact with liquids in different density and same dynamic viscosity is 1.0 Pa.sec ............. 271

Figure 8.17 Real part of impedance spectra of PWAS resonator in 15mm of length, 15mm of width, and 1mm of thickness in free condition and in contact with liquids in different density and same dynamic viscosity is 1.0 Pa.sec ............. 271

Figure 8.18 First admittance peak of admittance spectra for PWAS resonator in 15mm of length, 15mm of width, and 1mm of thickness in free condition and in contact with liquid with different dynamic viscosities and both densities are assumed to be 1000 kg/$m^3$ ........................................................................................ 272

Figure 8.19 First impedance peak of impedance spectra for PWAS resonator in 15mm of length, 15mm of width, and 1mm of thickness in free condition and in contact with liquid with different dynamic viscosities and both densities are assumed to be 1000 kg/$m^3$ ........................................................................................ 272

Figure 8.20 First peak of admittance for PWAS resonator in 15mm of length, 15mm of width, and 1mm of thickness in free condition and in contact with liquid with different densities and both liquid viscosities are assumed to be 1.0 Pa.s........ 273

Figure 8.21 First peak of impedance for PWAS resonator in 15mm of length, 15mm of width, and 1mm of thickness in free condition and in contact with liquid with different densities and both liquid viscosities are assumed to be 1.0 Pa.s........ 274

Figure 8.22 Free PWAS, PWAS with silicone oil and PWAS with honey .................... 275

Figure 8.23 Real and imaginary impedance measurements for free PWAS; PWAS with silicone; and PWAS with honey ....................................................................... 275

Figure 8.24 Real and imaginary admittance measurements for free PWAS; PWAS with silicone; and PWAS with honey ....................................................................... 276

Figure 8.25 Thickness mode E/M impedance/admittance measurements ...................... 277

Figure 9.1 Schematic of a PWAS pitch-catch setup on a bar. ........................................ 281

Figure 9.2 a-) Transmitter non-harmonic excitation signal b-) Receiver voltage response under a 3-count 100 kHz tone-burst excitation................................................. 283

Figure 9.3 Schematic of the panel specimen and PWAS configuration ......................... 283

Figure 9.4 Experimental setup for assessing the difference between new (thicker) PWAS and conventional PWAS ...................................................................... 284

Figure 9.5 The wave propagation experiment instruments a-) Function generator (Hewlett Packard 33120 A 15 MHz function/ arbitrary wave- form generator) b-) Digital oscilloscope (Tektronix TDS5034B Digital Phosphor Oscilloscope 350 MHz 5GS/s) ........................................................................................ 284

Figure 9.6 Tuning curves obtained by using pitch-catch method generating and sensing Lamb wave propagation with a-) a transmitter and a receiver both having the same diameter of 8.7mm and thickness of 0.5mm b-) a transmitter and a receiver whose diameter 7mm and thickness 0.2mm ..................................................... 285

Figure 9.7 Tuning curves obtained by using pitch-catch method generating and sensing Lamb wave propagation with a-) a transmitter having the diameter of 8.7mm and thickness of 0.5mm a receiver having the diameter of 7mm and thickness of 0.2mm b-) a transmitter having the diameter of 7mm and thickness of 0.2mm a receiver having the diameter of 8.7mm and thickness of 0.5m ........................ 285

Figure 9.8. Phase velocity dispersion curves of Lamb wave modes in a steel plate where $c_s$=3062.9 m/s indi- cating the quasi-Rayleigh wave approximation of fun- damental Lamb wave modes in high f.d product............................................ 288

Figure 9.9. (a) Displacement vectors in 14 mm thick steel plate at central frequency of 450 kHz in the form of the first symmetric Lamb wave mode and (b) the mode shape through thickness ..................................................................... 289

Figure 9.10. (a) Displacement vectors in 14 mm thick steel plate at central frequency of 450 kHz in the form of the first antisymmetric Lamb wave mode and (b) the mode shape through thickness ......................................................................... 289

Figure 9.11. Analytical tuning curve of Rayleigh wave in steel plate ........................... 290

Figure 9.12 (a) Schema of PWAS transducer ideally bonded on aluminum plate and (b) high frequency modal analysis results considering the standing waves in thickness mode for PWAS bonded on aluminum plate: plate thickness=2.1 mm, PWAS thickness=0.2mm. ................................................................... 292

Figure 9.13 Schema of PWAS transducer ideally bonded on aluminum plate.............. 292

Figure 9.14 High frequency modal analysis results considering the guided waves in thickness mode for PWAS bonded on aluminum plate: plate thickness = 2.1 mm, PWAS-thickness=0.2mm.................................................................... 293

Figure 9.15 Schema of pitch-catch sensing method (Giurgiutiu, 2008) ......................... 294

Figure 9.16 (a) ¼” thick, 4” width, 3’ length high strength 2024 aluminum plate (b) A pristine steel rail I-beam ½” thick..................................................................... 294

Figure 9.17 Autotuning2011 Graphical user interface (GUI),La- boratory for Active Materials and Smart Structures (LAMSS)...................................................... 295

Figure 9.18 Received signals from 7x7 mm2 PWAS on ¼” thick aluminum plate at different frequencies ........................................................................... 298

Figure 9.19 Analytical and experimental Rayleigh wave tuning curves for $7mm \times 7mm \times 0.2mm$ SM412 PWAS on 6.35 mm thick Aluminum-2024 plate with the elastic modulus of 72.4GPa, the density of 2780kg/m$^3$ and the Pois- son’s ratio of 0.33........................................................................................ 299

Figure 9.20 Rayleigh wave phase velocity and time of flight analytical and experimental results for the distance of 910mm between T-PWAS and R-PWAS on ¼” thick aluminum plate ........................................................................................ 300

Figure 9.21 Received signals from 7x7 $mm^2$ PWAS on 1/2" thick steel rail I-beam at different frequencies ........ 300

Figure 9.22 Analytical and experimental Rayleigh wave tuning curves for $7mm \times 7mm \times 0.2mm$ SM412 PWAS on 12.7 mm thick steel rail I-beam with the elastic modulus of 200GPa, the density of 7850kg/$m^3$ and the Poisson's ratio of 0.29 ........ 301

Figure 9.23 Rayleigh wave phase velocity and time of flight analytical and experimental results for the distance of 910mm between T-PWAS and R-PWAS on 12.7 mm thick steel rail I-beam ........ 302

Figure 9.24 A pristine steel 13.75mm thick ........ 303

Figure 9.25 Quasi-Rayleigh wave tuning curve prediction for pro- pagating wave in a distance of 460 mm in a thick steel plate in thickness of 13.75 mm ........ 303

Figure 9.26 Quasi-Rayleigh wave tuning curve from pitch-catch test ac- ross the weld bead on a thick steel plate in thickness of 13.75 mm ........ 304

Figure 9.27 Quasi-Rayleigh wave tuning curve from pitch-catch test in direction of the weld bead on a thick steel plate in thickness of 13.75 mm ........ 305

Figure 10.1. Schematic of feature-guided wave propagation on a welded plate ........ 307

Figure 10.2. Finite element model of butt-welded plate including non-reflecting boundaries on two sides of the steel plate ........ 309

Figure 10.3. Group velocity dispersion curves of (a) Lamb wave modes and (b) shear horizontal (SH) wave modes in steel plate ........ 310

Figure 10.4. Snapshots of weld guided wave simulations on (a) pristine and (b) damaged thick plates. The pin-point force is excited at 300 kHz ........ 310

Figure 10.5. Overlapped plots of the received signals from pristine and damaged (a) plain plate and (b) welded plate ........ 311

Figure 10.6 Schematic illustration of the experimental setup for the pitch-catch tests. . 312

Figure 10.7 Square PWAS in 0.2mm thickness bonded on a pristine aluminum plate in 2.1mm thickness. ........ 313

Figure 10.8 Two square PWAS transducers in 0.2mm thickness are bonded on a pristine aluminum plate in ¼" thickness. ........ 314

Figure 10.9. (a) Multi-channel Acoustic Measurement System (MAS) (b) a LabVIEW graphical user interface, CANWare (c) stainless steel plates in thickness of 14mm jointed with butt weld instrumented by 7mm x 7mm x 0.2mm PWAS 315

Figure 10.10. Experimental setup layout as stainless steel plates in thickness of 14mm jointed with butt weld instrumented by 7mm x 7mm x 0.2mm PWAS on and off the weld bead on two ends.................................................................... 316

Figure 10.11. Experimental received wave signals at different central frequency from (a) path 1 on weld and (b) path 2 on plate.............................................................. 317

Figure 10.12. Experimental tuning curves of quasi-Rayleigh waves obtained from (a) path 1 on weld and from (b) path2 on plate...................................................... 318

Figure 10.13. Outline of the transmitter and receiver PWAS on the butt-welded stainless steel plate specimen ............................................................................. 319

Figure 10.14. (a) Experimental received wave signals at different central frequency (b) Experimental tuning curves of quasi-Rayleigh waves obtained....................... 319

# CHAPTER 1

# INTRODUCTION

This chapter presents an introduction to the overall dissertation manuscript by addressing the motivation and importance of conducting the research, discussing research goal, scope, and objectives will be discussed, and introducing the organization of the dissertation.

## 1.1 MOTIVATION


Figure 1.1 (a) Pipelines for energy transportation; (b) pressure vessel for pressurized gas; (c) ships and offshore structures.

Ultrasonic techniques are commonly used for validation of thick structures in many in-situ monitoring applications such as in nuclear industry, in pressure vessel industry, in pipelines, and in a range of naval applications.

Structural Health Monitoring (SHM) is a fast-growing multi-disciplinary field which aims at lowering the fatal costs due to catastrophic failures by detection in early stages of a structural damage and providing diagnosis/prognosis of structural health status in a real-time or with as needed maintenance. Exploring and inventing new SHM technologies enables the industry to reduce also the maintenance cost, shorten the machine service down time, and improve the safety and reliability of engineering structures. SHM methods have improved the management in both the health monitoring of aging structures by predicting the remaining life of the structure and the development of novel self-sensing smart structures by inclusion of sensors.

SHM also enables condition based maintenance (CBM) that is in place of scheduled maintenance by placing SHM sensors along with the monitoring systems, which is provisioned that this extends the life-cycle and likely to greatly lower the life-cycle costs as well.

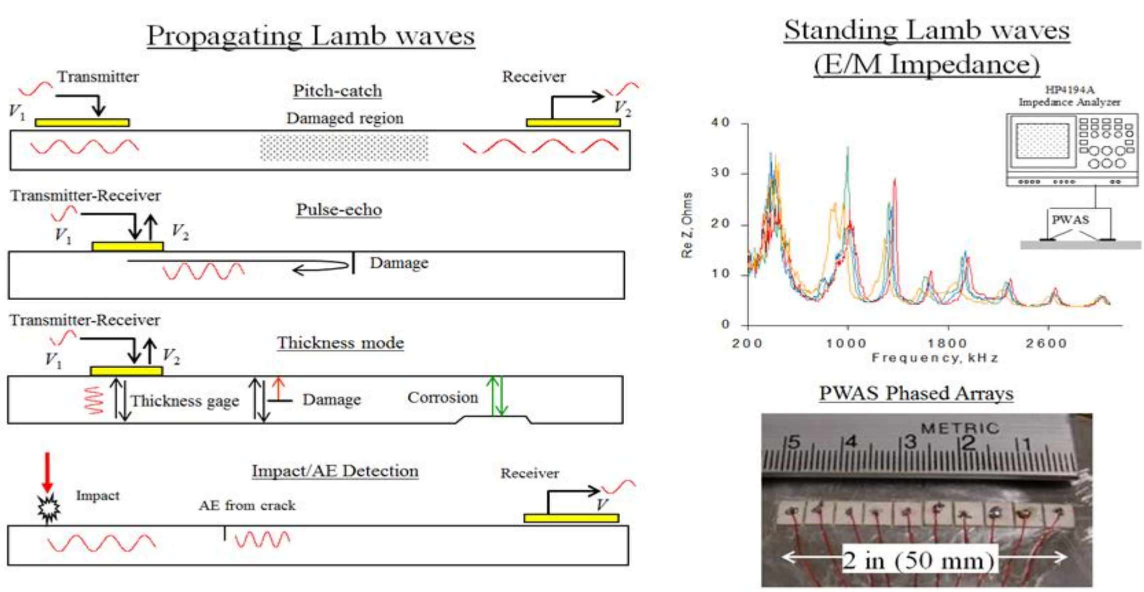


Figure 1.2: Active and passive sensing methods for in-situ SHM through PWAS generating propagating and standing Lamb waves in substrate structure to detect damage (Giurgiutiu, 2008a).

The development of SHM sensors assists to dynamically interrogate the structural variations in material of a medium where the sensors are embedded. Nonetheless, the data acquired from the sensing system should be properly interpreted based on the theoretical phenomena. Practical applications have imposed three main requirements on development on which the sensor technology lays for prediction of structural dynamic changes in the coupled sensor-medium system. The SHM sensors that are capable of active interrogation are called piezo-ceramic wafer active sensors (PWAS). They are widely employed as in-situ ultrasonic health monitoring transducers. They are used as resonators that generate standing waves as well as transducers that produce traveling waves in the embedding medium. Figure 1.2 shows a few examples for SHM active and passive sensing in near-field and far-field interrogation through PWAS that generates propagating and standing Lamb waves in substrate structure to detect damages e.g. crack or corrosion interrogating the structure with certain tuned wave modes

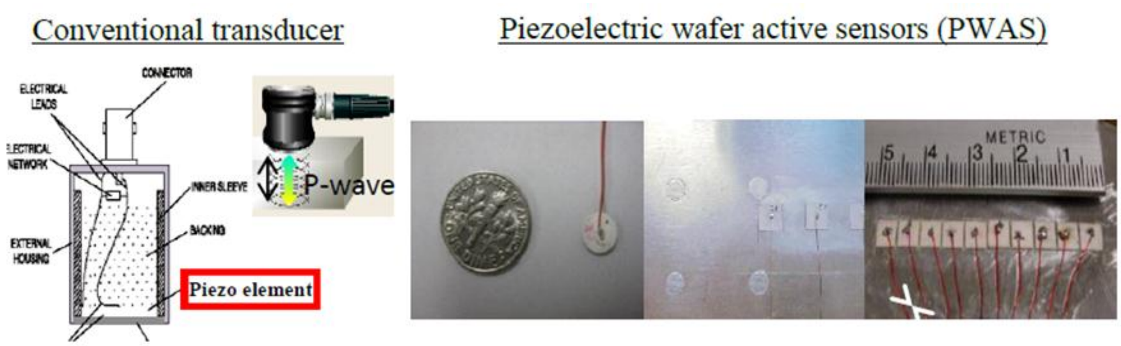


Figure 1.3 Illustration of free PWAS transducers in different types and sizes (Giurgiutiu, 2008).

Piezoelectric wafer active sensors (PWAS) that are shown in Figure 1.3 are made of piezo-ceramics (e.g. lead zirconate titanate, a.k.a. PZT) and can be utilized as both an actuator and a sensor to monitor and deliver structural health information. Most of the methods used in conventional NDE, such as pitch-catch, pulse-echo, and phased arrays, have also been demonstrated experimentally with PWAS. These successful experiments have positioned PWAS as an enabling technology for the development and implementation of active SHM systems. Figure 1.4(a) shows an array of 7 mm square PWAS mounted on an aircraft panel and Figure 1.4(b) shows principles of SHM techniques such as pitch-catch technique placed on top and pulse-echo technique placed on bottom. PWAS is light-weighted, inexpensive, minimally intrusive sensor requiring low-power. PWAS is much lighter, smaller and more inexpensive in contrast a conventional ultrasonic transducer as shown in Figure 1.3. PWAS transducers are used in SHM applications and are able to detect structural damage using Lamb waves. They achieve direct transduction between electric and elastic wave energies. PWAS transducers are essential elements in Lamb-wave SHM with pitch-catch, pulse-echo, phased array, and electro-mechanical impedance methods.

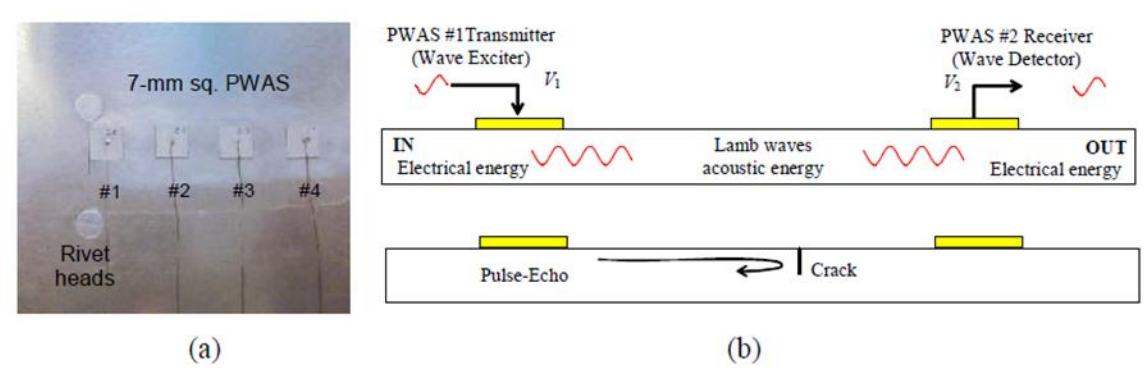


Figure 1.4 Illustration of (a) PWAS sensors installed on an aircraft panel and of (b) principles of active structural health monitoring with PWAS transducers near a crack.

Electro-mechanical impedance spectroscopy (EMIS) is one of the SHM techniques that employ PWAS as a piezo-ceramic resonator. EMIS has been widely used to determine the dynamic characteristics of a free PWAS and bonded PWAS for in-situ ultrasonics (Zagrai & Giurgiutiu, 2001) such as for high frequency local modal sensing EMIS method in the work presented by Liang et-al (1994).

PWAS itself requires a characteristic description prior its installation on a structure or embedment in a medium. The intrinsic electromechanical impedance/admittance of PWAS is an important dynamic descriptor. The frequency response of a sensor to the electrical excitation defines its dynamic properties. Electromechanical impedance spectroscopy (EMIS) method applies standing waves generated by piezoelectric wafer resonator as the resonator is embedded into a medium so that E/M impedance indicates the response of the coupled medium-resonator in frequency domain in terms of anti-resonance spectra. It is substantial to extend the theoretical development to accurately and quantitatively predict the local dynamic characteristics of PWAS in different environmental conditions and in various embedding media. The development of analytical and numerical models under simplifying assumptions is paramount importance to perform simulation of response of PWAS-EMIS and constrained PWAS-EMIS in wide range of applications.

For selective actuation and receipt of ultrasonic wave modes, the sizes of PWAS transducers, size of the structure and the excitation frequency of the input waveform should be tuned. The proof-mass concept has received considerable attention recently. Proof-masses shift the system resonance toward optimal frequency points. Therefore, proof-mass concept is adopted to develop a new method for tuning ultrasonic wave modes. The theoretical work on proof mass actuator is developed as a mass bonded to the piezoelectric actuator. The model is used to build the basis for a proof-mass piezoelectric wafer active sensor (PM-PWAS). Then, the PM-PWAS transducer model is studied by

PM analysis to investigate desired control objectives using the correlation between a PM-PWAS and structural dynamic properties in the substrate structure. Analytical and numerical models are implemented for the PM-PWAS transducer attached to an isotropic elastic plate.

Piezoelectric transducer and liquid domain interaction has been commonly investigated through theoretical analysis of resonance spectra in frequency domain using certain types of standing wave modes; shear horizontal waves and thickness shear waves by using different techniques. The electrical excitation of a PWAS can be converted into the mechanical vibration as regards to the stress and the strain waves. This piezoelectricity property of the material of PWAS has been used in literature to develop a micro-acoustic sensor to measure chemical, physical, and biological properties of a liquid medium located in the vicinity or possessing an interface with the sensor. The mechanical properties of the liquid medium such as the viscosity and the density affect the energy transduction of sensor as well as the electrical properties of the medium concerning the sensitivity of the wave mode. The detection of changes in mechanical properties and electrical conductivity of the biomedical implants by bio-PWAS enables to capture the protein or solution concentration (pH) changes that influence the conductivity, the ultrasonic wave modes and electro-mechanical impedance readings.

Rayleigh waves have been widely used in non-destructive testing (NDT), SHM applications as well as in seismology. Rayleigh waves i.e. surface acoustic waves (SAW) are a high frequency approximation of the first symmetric (S0) and anti-symmetric (A0) modes of Lamb waves as the frequency becomes relatively high. S0 and A0 wave speeds coalesce and both have the same value. This value is exactly Rayleigh wave speed. They become non-dispersive wave, i.e. constant wave speed along the frequency. Rayleigh wave can only travel along a flat surface of a semi-infinite medium, which is hardly possible to generate in reality however for the plate thickness d >> $\lambda_R$ , the measurements should be acceptable. The wave mode is then called quasi-Rayleigh wave having Rayleigh wave speed. The weld guided and tuned quasi-Rayleigh wave mode is essential for the applications in the in-situ inspection of relatively thick structures with butt weld such as naval offshore structures (Figure 1.1)c and dry cask storage system for spent nuclear fuel (Figure 1.5).

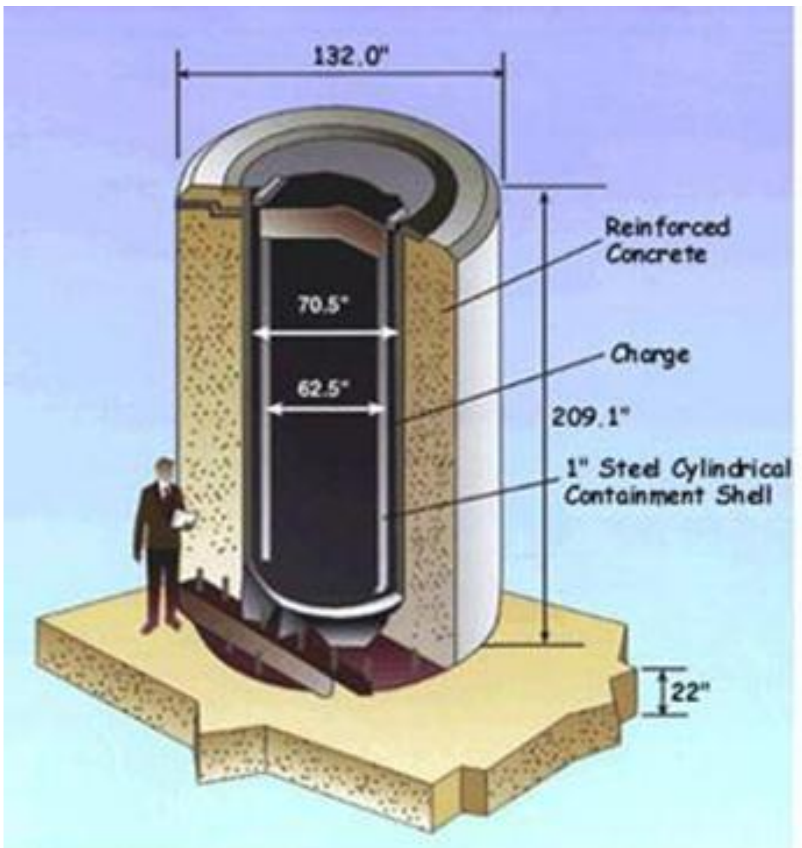


Figure 1.5: A dry cask storage system for spent nuclear fuel.

## 1.2 RESEARCH GOAL, SCOPE, AND OBJECTIVES

The research goal of the PhD work presented in this dissertation is to develop accurate and efficient theoretical models for standing and propagating waves and tuning of certain wave modes. The scope of this research covers the analytical modeling, finite element simulation, and experiments for the development of SHM concepts. The modeling techniques were advanced in both near-field and far-field interrogation. The objectives of the work presented in this dissertation are as follows:

- To construct a 1-D analytical framework which can describe standing harmonic wave in thickness mode, including frequency response function, electromechanical admittance and impedance and linear higher harmonic overtones in relatively high frequency range of MHz.
- To extend the concept developed in the thickness mode free PWAS case to the thickness mode constrained PWAS on its one surface and both surfaces i.e. two-layers and three layers.
- To construct a proof-mass PWAS actuator to tune the standing wave mode by shifting the resonance frequency of the system by adding a proof-mass and changing the size or material of a proof-mass on the piezo-ceramic actuator.
- To develop an analytical model of the electromechanical response of PWAS with various liquids with different material properties.
- To carry out an analytical simulation of 2-D circular PWAS-EMIS at elevated temperature in order to study the piezoelectric material degradation and compensation at high temperature environment.

- To carry out theoretical and experimental study on weld guided waves and the weld guided wave interaction with damages in thick structures in high frequency range.

## 1.3 ORGANIZATION OF THE DISSERTATION

To achieve the objectives set forth in the preceding section, the dissertation is organized in eleven chapters. The focus and contents of each chapter is introduced in Chapter 1.

In Chapter 2, literature is reviewed with respect to the ultrasonic waves in solid medium and the ultrasonic waves in fluid medium. In addition, the piezoelectric transducers is reviewed regarding the vibration modes, standing waves and wave propagation methods that employs piezoelectric wafer active sensors (PWAS).

In Chapter 3, after the state of the art reviewed with respect to the electromechanical impedance spectroscopy (EMIS) method, the analytical and numerical work for free PWAS-EMIS models are derived in in-plane and thickness modes.

In Chapter 4, the analytical 1-D free PWAS-EMIS and 2-D circular PWAS-EMIS simulations are presented to show the piezoelectric material degradation as the temperature increases. In addition, sets of experiments are conducted and the results are discussed in order to show thermal effects.

In Chapter 5, the global matrix method (GMM) is first reviewed for multi-layered structures, and then the analytical model procedure is presented for the constrained PWAS-EMIS from one-side and two-sides in in-plane mode using the GMM.

In Chapter 6, the similar procedure as in Chapter 5 is followed for thickness mode PWAS-EMIS in solid medium as PWAS constrained on an isotropic elastic material is presented considering two-layer and three-layer models through normal mode expansion and global matrix methods.

In Chapter 7, based on the progressive theoretical development in the preceding two chapters, proof-mass piezoelectric wafer active sensor (PM-PWAS) is introduced along with the state of the art regarding the proof-mass concept. Analytical, numerical, and experimental studies are conducted for PM-PWAS. In addition, some special case studies are presented for different materials and geometries.

In Chapter 8, the electromechanical signature of PWAS behavior in contact with liquid medium is presented in terms of analytical E/M impedance and admittance simulations as a basis of biomedical sensor development.

In Chapter 9, in general, the tuning of guided waves in thin and thick structures is discussed with different sets of experiments.

In chapter 10, in particular, the weld guided quasi-Rayleigh wave in welded thick structures is introduced and accordingly the experimental results and finite element simulations are presented.

In Chapter 11, concluding remarks are presented along with the suggested future work

# CHAPTER 2

# LITERATURE REVIEW

This chapter first introduces fundamentals of the ultrasonic waves in solid medium and in fluid medium reviewed by types, including Lamb waves, Rayleigh waves, shear horizontal (SH) plate waves. Then piezoelectric transducers are introduced and the vibration modes and standing wave modes that can be transduced by piezoelectric transducers are discussed. The concept of standing waves is introduced, and the correspondence between standing waves and structural vibration is established. Finally, the wave propagation methods using ultrasonic waves based SHM concepts and techniques are introduced.

## 2.1 ULTRASONIC WAVES IN SOLID MEDIUM

This section presents a review of ultrasonic elastic waves in elastic solid media. SHM methods based on elastic waves propagation are very diverse, and a number of approaches exist. The basic principles shall be held to understand basic principles that lay at the foundation of wave generation and propagation in solid media.

### 2.1.1 GUIDED WAVES IN PLATES

Guided waves (e.g., Lamb waves in plates) are elastic perturbations that can propagate for long distances in thin-wall structures with very little amplitude loss. In Lamb-wave NDE, the number of sensors required to monitor a structure can be significantly reduced. The potential also exist of using phased array techniques that use Lamb waves to scan large areas of the structure from a single location.

Rayleigh waves, a.k.a., surface acoustic waves (SAW) are found in solids that contain a free surface. The Rayleigh waves travel close to the free surface with very little penetration in the depth of the solid. For this reason, Rayleigh waves are also known as surface-guided waves.

In flat plates, ultrasonic-guided waves travel as Lamb waves and as shear horizontal (SH) waves. Lamb waves are vertically polarized, whereas SH waves are horizontally polarized. A simple form of guided plate waves are the SH waves. The particle motion of SH waves is polarized parallel to the plate surface and perpendicular to the direction of wave propagation. The SH waves can be symmetric and anti-symmetric. With the exception of the very fundamental mode, the SH wave modes are all dispersive. Lamb waves are more complicated guided plate waves. Lamb waves are of two basic varieties, symmetric Lamb-waves modes (S0, S1, S2,…) and anti-symmetric Lamb-waves modes (A0, A1, A2,…). Both Lamb wave types are quite dispersive. At any given value of the frequency–thickness product, $fd$, a multitude of symmetric and anti-symmetric Lamb waves may exist. The higher the $fd$ value, the larger the number of Lamb-wave modes that can simultaneously exist. For relatively small values of the $fd$ product, only the basic symmetric and anti-symmetric Lamb-wave modes (S0 and A0) exist. As the $fd$ product approaches zero, the S0 and A0 modes degenerate in the basic axial and flexural plate modes. At the other extreme, as $fd \to \infty$, the S0 and A0 Lamb-wave modes degenerate into Rayleigh waves confined to the plate surface.

## Lamb Waves

Lamb waves are a type of ultrasonic waves that are guided between two parallel free surfaces, such as the upper and lower surfaces of a plate. Lamb waves can exist in two basic types, symmetric and antisymmetric. Figure 2.19 shows the particle motion of symmetric and antisymmetric Lamb waves. The Lamb wave motion has asymptotic behavior at low frequency and high frequency. At low frequency, the symmetric mode resembles axial waves, while the antisymmetric mode resembles flexural waves. At high frequency, both symmetric and antisymmetric wave approaches Rayleigh waves, because the particle motion is strong at the surfaces and decays rapidly across the thickness. The axial wave and flexural wave, by their nature, are only low frequency approximations of Lamb waves. The plate structure cannot really sustain pure axial and flexural motion at large frequency-thickness product values.

The straight crested Lamb wave equations are derived under z-invariant assumptions using pressure wave and shear vertical wave (P+SV) waves in a plate. Through multiple reflections on the plate's lower and upper surfaces, and through constructive and destructive interference, the pressure waves and shear vertical waves give rise to the Lamb–waves, which consist of a pattern of standing waves in the thickness y–direction (Lamb–wave modes) behaving like traveling waves in the x–direction. The derivation finally reaches the Rayleigh-Lamb equation:

$$\frac{\tan \eta_S d}{\tan \eta_P d} = \left[ \frac{-4\eta_P \eta_S \xi^2}{\left(\xi^2 - \eta_S^2\right)^2} \right]^{\pm 1} \tag{2.1}$$

where +1 exponent corresponds to symmetric Lamb wave modes and -1 exponent corresponds to antisymmetric Lamb wave modes. $d$ is the half plate thickness, and $\xi$ is the frequency dependent wavenumber. $\eta_P$ and $\eta_S$ are given in Eq. (2.2). $\lambda$ and $\mu$ are Lame's constants of the material, and $\rho$ is the material density.

$$\eta_P^2 = \frac{\omega^2}{c_p^2} - \xi^2; \quad \eta_S^2 = \frac{\omega^2}{c_s^2} - \xi^2; \quad c_p = \sqrt{\frac{\lambda + 2\mu}{\rho}}; \quad c_s = \sqrt{\frac{\mu}{\rho}}; \tag{2.2}$$

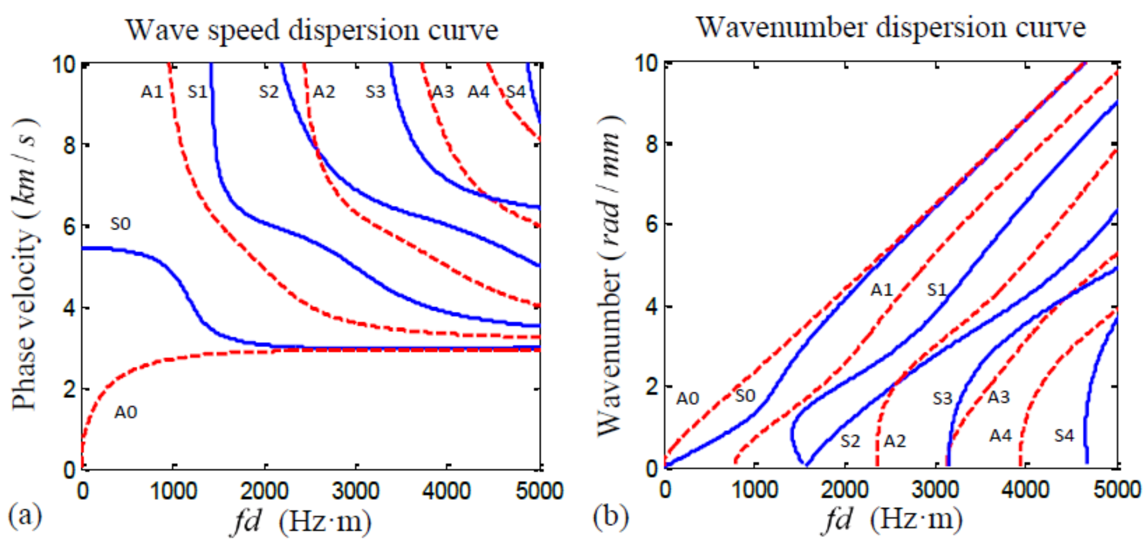


Figure 2.1: (a) Wave speed dispersion curve; (b) wavenumber dispersion curve (Shen, 2014).

Figure 2.1 shows the dispersion curves of aluminum plates calculated from the Rayleigh-Lamb equations. It can be noticed at least two wave modes (the fundamental symmetric mode: S0; the fundamental antisymmetric mode: A0) exist simultaneously. Beyond the corresponding cut-off frequencies, higher Lamb modes will participate in the propagation. At small frequency-thickness product values, the S0 mode is less dispersive than A0 mode, and all the Lamb wave modes converge to non-dispersive Rayleigh waves at large frequency-thickness product values. The dispersive and multi-mode nature of

Lamb waves adds complexity in both Lamb wave propagation modeling and SHM application.

### *Rayleigh Waves*

Rayleigh waves, known as the surface wave, propagate close to the body surface, with the motion amplitude decreasing rapidly with depth. The polarization of Rayleigh wave lies in a plane perpendicular to the surface. The effective depth of penetration is less than a wavelength.

One benefit of using Rayleigh waves for structural health monitoring lies in that Rayleigh wave is not dispersive, i.e. the wave speed is constant. It is found that the Rayleigh wave speed, $c_R$, depends on the shear wave speed, $c_S$, and the Poisson ratio, $\nu$. A common approximation of the wave speed of Rayleigh wave is given as

$$c_R(\nu) = c_S\left(\frac{0.87+1.12\nu}{1+\nu}\right) \tag{2.3}$$

For common Poisson ratio values, the Rayleigh wave speed takes values close to and just below the shear wave speed (Giurgiutiu 2008). The particle motion or the mode shape of the Rayleigh waves across the thickness direction, $y$, is given by

$$\begin{aligned} \hat{u}_x(y) &= Ai\left(\xi e^{-\alpha y} - \frac{\beta^2+\xi^2}{2\xi}e^{-\beta y}\right) \\ \hat{u}_y(y) &= A\left(-\alpha e^{-\alpha y} + \frac{\beta^2+\xi^2}{2\beta}e^{-\beta y}\right) \end{aligned} \tag{2.4}$$

where $A$ is the wave amplitude factor, $\xi = \omega/c_R$ is the wavenumber of Rayleigh surface waves, $\alpha$ and $\beta$ are coefficients given in Eq. (2.5). Figure 2.2 shows the Rayleigh wave in a semi-infinite medium.

$$\alpha^2 = \xi^2\left(1-\frac{c^2}{c_P^2}\right); \quad \beta^2 = \xi^2\left(1-\frac{c^2}{c_S^2}\right) \tag{2.5}$$

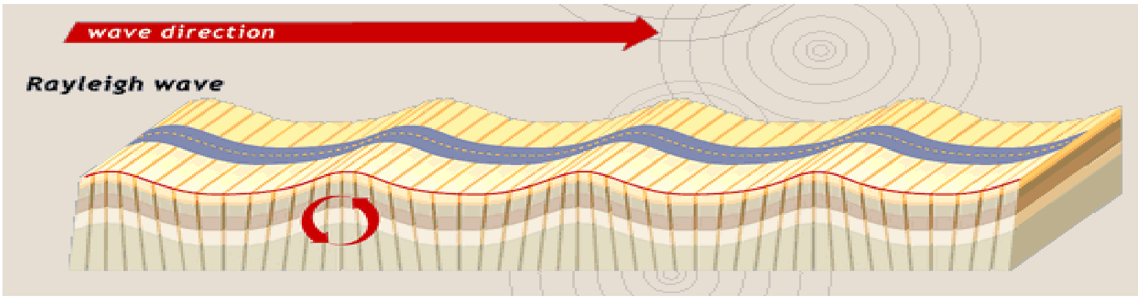


Figure 2.2: Simulation of Rayleigh wave propagation in a semi-infinite medium http://www.exploratorium.edu/faultline/activezone/slides/rlwaves-slide.html.

*Shear Horizontal Plate Waves*

Shear horizontal (SH) plate waves have a shear-type particle motion contained in the horizontal plane. Figure 2.3 shows the coordinate definition and particle motion of SH plate waves. According to the coordinate defined, an SH wave has the particle motion along the $z$ axis, whereas the wave propagation takes place along the $x$ axis. The particle motion has only the $u_z$ component. Unlike Rayleigh wave which is non-dispersive, SH plate waves are dispersive and may travel with different modes.

The phase velocity dispersion curve of the SH plate wave can be calculated as

$$c(\omega) = \frac{c_S}{\sqrt{1-(\eta d)^2\left(\frac{c_S}{\omega d}\right)^2}} \tag{2.6}$$

where $\eta$ is given in Eq. (2.7) and $d$ is the half plate thickness.

$$\eta^2 = \frac{\omega^2}{c_S^2} - \frac{\omega^2}{c^2} \tag{2.7}$$

By substituting the appropriate eigenvalue, one gets an analytical expression for the wave-speed dispersion curve of each SH wave mode. For detailed expressions, the readers are referred to Giurgiutiu (2007).

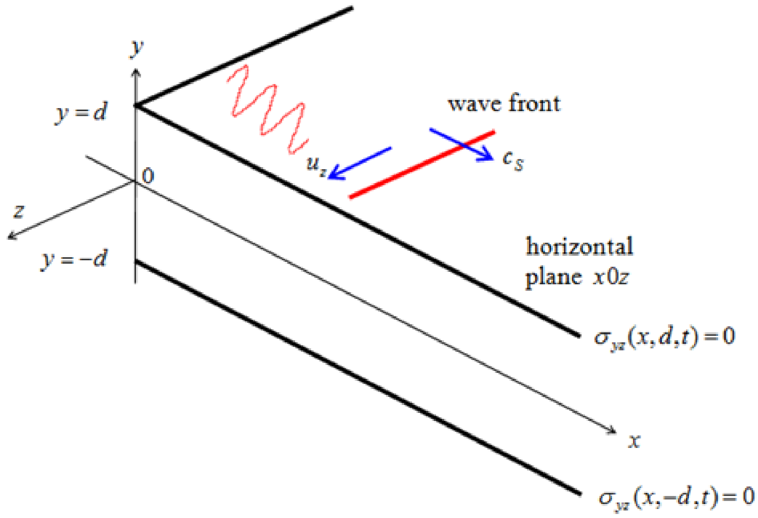


Figure 2.3: Coordinate definition and particle motion of SH plate waves (Giurgiutiu 2008).

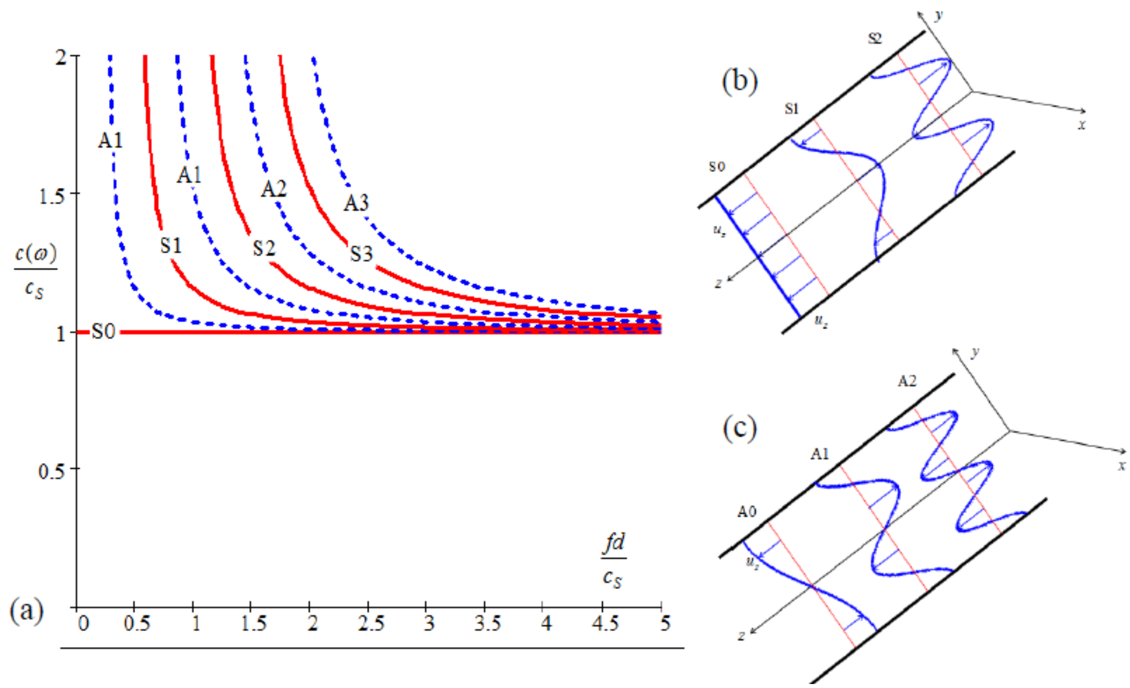


Figure 2.4: (a) SH plate wave-speed dispersion curves; (b) symmetric mode shapes; (c) antisymmetric mode shapes (Giurgiutiu 2008).

Figure 2.4 shows the wave-speed dispersion curve of SH plate waves and the mode shapes. It can be noticed that the fundamental symmetric mode (S0) wave is non-dispersive and always exists starting from low frequency-thickness product values. This nice property makes it a good candidate as the interrogating waves in SHM systems. Recently, considerable research has been carried out on the transmission and reception of SH plate wave for SHM (Kamal et al. 2013; Zhou et al. 2014). Higher wave modes only appear beyond the corresponding cut-off frequencies, showing dispersive characteristics, i.e., their phase velocity changes with frequency. For dispersive waves, group velocity is usually used to evaluate the propagation of wave packets. The definition of group velocity is given in Eq. (2.8).

$$c_g = \frac{d\omega}{d\xi} \tag{2.8}$$

### 2.1.2 Guided Waves in Rods, Pipes, and Arbitrary Cross-Section Waveguides

The guided waves in rods, pipes, and arbitrary cross section waveguides (Figure 2.5) also find great potential in nondestructive evaluation (NDE) and SHM for truss structures, pipelines, and rail tracks. Analytical solutions exist for simple geometry rods and pipes. However, for waveguides with arbitrary cross sections, the semi-analytical finite element (SAFE) method is usually adopted to obtain the numerical solutions of wave propagation problems.

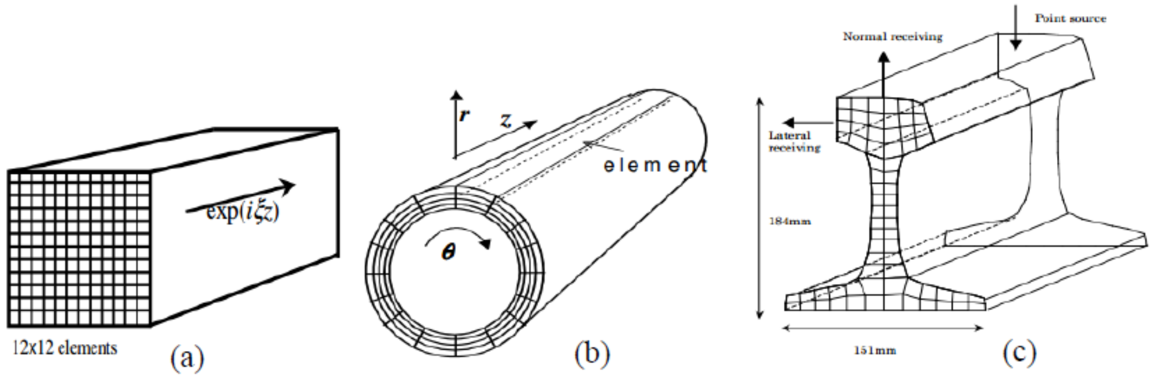


Figure 2.5: Discretization of the cross sections in SAFE: (a) square rod; (b) circular pipe; (c) rail track (Hayashi et al. 2004).

Several investigators have considered the propagation of waves in solid and hollow cylinders. Love in his fourth edition of the book published in 1944 studied wave propagation in an isotropic solid cylinder and showed that three types of solutions are possible: (1) longitudinal; (2) flexural; and (3) torsional. Comprehensive work on wave propagation in hollow circular cylinders was done by Gazis in 1959. At high frequencies, each of these solutions is multimodal and dispersive. Meitzler in 1961 showed that, under certain conditions, mode coupling could exist between various wave types propagating in solid cylinders such as wires. Extensive numerical simulation and experimental testing of these phenomena was done by Zemanek in 1972. A comprehensive analytical investigation was complemented by numerical studies. The nonlinear algebraic equations and the corresponding numerical solutions of the wave–speed dispersion curves were obtained. These results found important applications in the ultrasonic NDE of tubing and pipes. Silk & Bainton in 1979 found equivalences between the ultrasonic in hollow cylinders and the Lamb waves in flat plates and used them to detect cracks in heat exchanger tubing. Rose et-al in 1994 used guided pipe waves to find cracks in nuclear steam generator tubing. Alleyne in 2000 used guided waves to detect cracks and corrosion in chemical plant pipe work.

## 2.2 ULTRASONIC WAVES IN FLUID MEDIUM

This section presents a review of ultrasonic elastic waves in fluid media. Some of the non-destructive testing (NDT) and SHM techniques are presented along with some theories developed in the literature regarding the fluid loaded beams and the interaction between the piezoelectric transducers and liquid media. The guided interface waves and acoustic waves generated by piezoelectric transducers are reviewed as well.

### 2.2.1 ULTRASONIC IMMERSION TECHNIQUE

The propagating waves generated using a transducer can be used to test and object by coupling the sound waves with water. Two techniques exist for this testing: 1. Using water gun where the sound waves are guided through a jet of water or 2. Immersing the transducer and test object in a tank of water. In immersion testing, the transducer is placed in the water, above the test object, and a guided wave is projected.

The graph of peaks using the immersion method is slightly different. Between the initial pulse and the back wall peaks there will be an additional peak caused by the sound wave going from the water to the test material. This additional peak is called the front wall peak. The ultrasonic tester can be adjusted to ignore the initial pulse peak, so the first peak it will show is the front wall peak. Some energy loss occurs when the waves collide with the test material, so the front wall peak is slightly lower than the peak of the initial pulse.

This ultrasonic test technique can be used to interrogate components and structures to detect internal and surface breaking defects, and measures wall thickness on hard (typically metallic or ceramic) components and structures. It operates on the principle of injecting a very short pulse of ultrasound (typically between 0.1 MHz and 100 MHz) into a component or structure, and then receiving and analyzing any reflected sound pulses.

Typical detection limits for fine grained steel structures or components (hand scanning) are single millimeter sized defects. Smaller defects can be detected by immersion testing and a programmed scan pattern with higher frequency ultrasound (slower testing). Detection limits are in the order of 0.1 to 0.2 mm, although smaller defects (typically 0.04mm diameter) can be detected under laboratory conditions.

### 2.2.2 FLUID LOADED BEAM

Cheng & Wang (1998) and Zhang et-al (2003) considered a finite thick plate that has an interface with an acoustic medium on top and with vacuum on bottom side. The plate is excited by a harmonic point force as shown in Figure 2.6

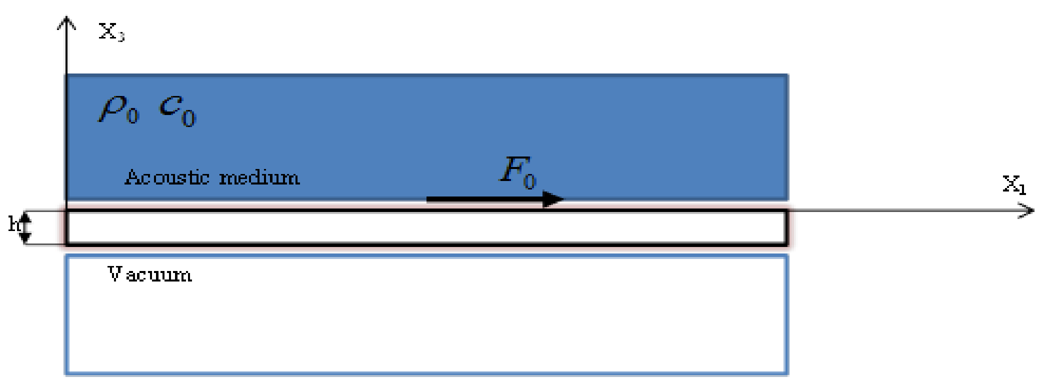


Figure 2.6 Schematic of the fluid loaded beam excited by a harmonic point force.

$$EIv''''-\omega^2\rho Av=\frac{h}{2}\left[F_0\,\delta(x-x_0)+P_a(x,0)\right] \tag{2.9}$$

where $v$ is the beam displacement, $F_0$ is the amplitude of a harmonic point force, $P_a$ is the fluid loading (acoustic) pressure on the beam, and $\delta$ is the Dirac delta function.

$$\frac{\partial^2 P_a}{\partial X_1{}^2}+\frac{\partial^2 P_a}{\partial X_3{}^2}+\xi_0{}^2 P_a=0 \tag{2.10}$$

where $\xi_0$ is the acoustic wave number. On the interface, i.e. $x_3=0$;

$$\frac{\partial P_a}{\partial X_3}=-\rho_0\omega^2 v\left(X_1\right) \tag{2.11}$$

Modal expansion method also implies

$$P_a(X_1,0)=\sum_{n=1}^{\infty}P_n\phi_n(X_1) \tag{2.12}$$

where $P_n$ is the modal expansion coefficient of sound pressure and $\phi_n$ is the eigenfunctions of the beam. The sound pressure and beam displacement in wave number domain;

$$\begin{aligned}\tilde{P}_a(\xi,x_3)&=\int_{-\infty}^{\infty}P_a(x_1,x_3)e^{-i\xi x}dx\\ \tilde{v}(\xi)&=\int_{-\infty}^{\infty}v(x_1)e^{-i\xi x}dx\end{aligned} \tag{2.13}$$

Imposing the boundary conditions in wave number, $\xi$, domain and applying inverse fast Fourier transform (IFFT), the sound pressure takes this form:

$$P_a(x_1,0)=\frac{-i\rho_0\omega^2}{2\pi}\int_{-\infty}^{\infty}\frac{\tilde{v}(\xi)}{\sqrt{\xi_0^2-\xi^2}}e^{-i\xi x}d\xi \tag{2.14}$$

### 2.2.3 GUIDED WAVES: INTERFACE WAVES

#### Bleustein-Gulyaev Waves

First, Bleustein in 1968 explored the surface wave which was later to be named Bleustein-Gulyaev (BG) wave and developed the theory for the wave. Furthermore, (Zhang et-al. 2001; Guo et-al., 2006; Guo & Sun, 2008) also theoretically analyzed the BG waves for the model employing the hexagonal 6mm class of piezoelectric which occupied semi-infinite space and overlying half-space viscous and non-conductive liquid medium.

Bleustein-Gulyaev (B-G) wave is a shear type surface acoustic wave (SH wave). B-G wave does not radiate energy into the adjacent liquid. It is sensitive to changes in both mechanical and electrical properties of the surrounding environment. B-G wave is a good candidate for liquid sensing applications (Guo & Sun, 2008).

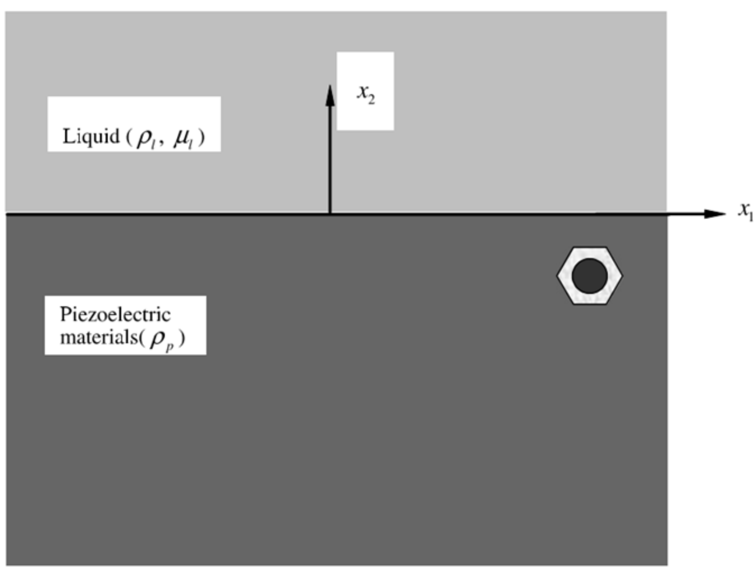


Figure 2.7: Schematic illustration of the BG wave problem and the coordinate system.

Navier-Stokes equation which is the governing equation for liquid was simplified neglecting the inertial term and the pressure gradient since the particle motion was induced only by wave propagation and only shear deformation occurs during the wave propagation so that the liquid particle velocity in transverse direction in plane was assumed to satisfy the following governing equation

$$\frac{\partial v_3}{\partial t} - \frac{\mu_l}{\rho_l} \nabla^2 v_3 \tag{2.15}$$

where $\rho_l$ and $\mu_l$ were defined to be the liquid mass density and the dynamic viscosity, respectively. Using the piezoelectric constitutive equations and Navier–Stokes equations, the dispersion relation for both the open circuit and metalized surface conditions were derived by an elaborate analytical procedure.

The Scholte Waves

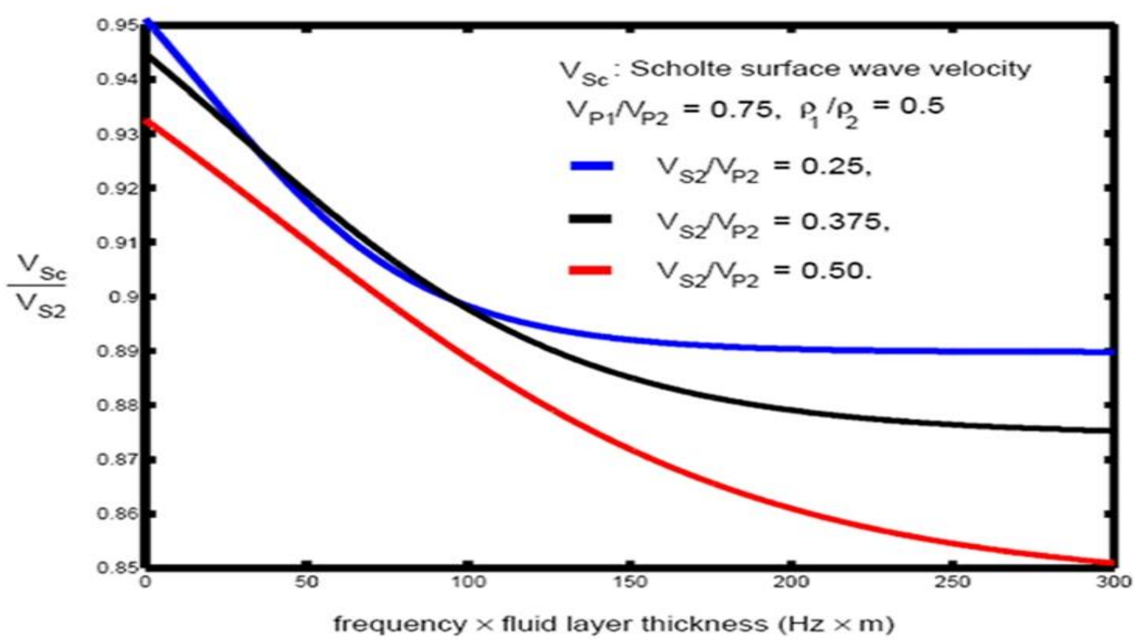


Figure 2.8 Scholte surface-wave velocity relative variations to the shear-wave velocity, $V_{S2}$, as a function of frequency f and fluid layer thickness. The parameters $V_{P1}$, $V_{P2}$, $V_{S1}$,

$\rho_1$, and $\rho_2$ [$V_{P1}$ = 1.5 km/s, $V_{P2}$ = 2.0 km/s, $V_{S1}$ = 0 km/s, $\rho_1$ = 1.0 g/cc, and $\rho_2$ = 2.0 g/cc] are common to all the three curves.

The general dispersion relation for the Scholte wave shows that for a fluid layer of finite thickness, the trapped wave is dispersive. Its velocity is always less than the shear-wave velocity. Figure 2.8 shows an example of how the Scholte surface-wave velocity varies relative to the shear-wave velocity, $V_{S2}$, as a function of frequency f and fluid layer thickness $z_1$.

The model we have looked at for the Scholte wave is a fluid layer above a solid half-space. The sea floor in most situations can be considered to represent a water-sediment interface, with a P-wave sediment velocity somewhat higher than the velocity of sound in water. For soft marine sediments consisting of clay and silt, the S-wave velocity is much smaller than the water sound velocity but shows very large gradients close to the sea floor. The interface wave then becomes highly dispersive, although recognizably of the Scholte type. Recall that the source should be close to the sea floor to excite the Scholte interface wave.

Scholte waves and quasi-scholte waves have been analyzed for liquid sensing applications subjected to various boundary conditions. Scholte waves are non-dispersive and propagates along a half space liquid-half space solid interface whereas quasi-Scholte waves are dispersive and propagates on a finite plate-liquid interface in similar fashion to the A0 mode in a free plate. The quasi-Scholte mode become asymptotic to Scholte wave at high frequencies being similar to the A0 and S0 modes becoming asymptotic to the Rayleigh wave solution (Cegla, Cawley, & Lowe, 2005).

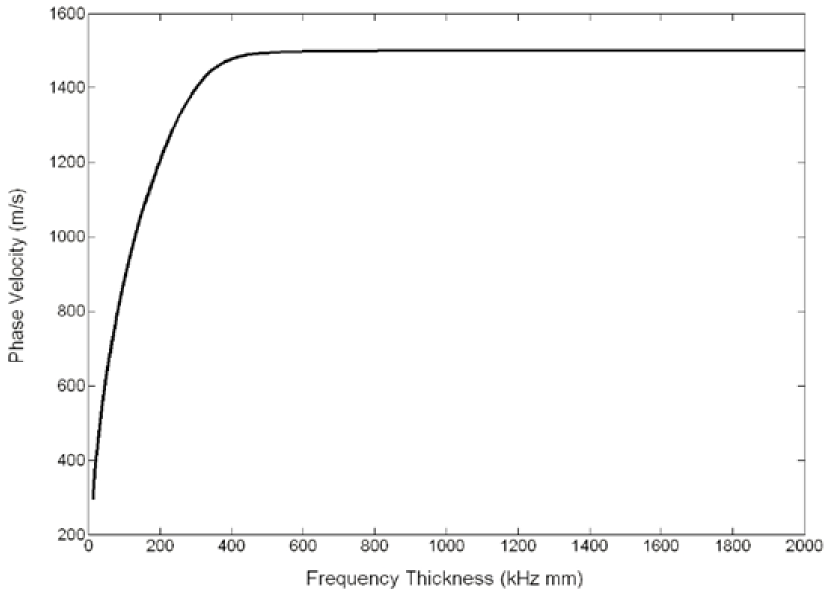


Figure 2.9 Phase velocity dispersion of the quasi-Scholte mode on a steel plate surrounded by water.

## The Leaky Lamb Waves

Mindlin in 1960 determined the pressure (P), shear vertical (SV), and shear horizontal (SH) waves and vibrations at different angle of incidence in isotropic plates with variety of boundary conditions such as traction-free (unconstrained) and strain-free (constrained) conditions on the boundaries.

For the wave propagation method, Lamb waves (Lamb, 1917) and leaky Lamb waves are of substantial and paramount importance in the group of guided elastic waves and have been widely used to develop liquid sensing technology. The propagation of Lamb waves in solid plate with traction free boundaries and leaky Lamb waves in solid-liquid structures (Wu & Zhu, 1992) have been investigated by many researchers for inviscid (Chen et-al. 2006) or viscous liquids (Nayfeh & Nagy, 1997; Zhu & Wu, 1995) and dielectric or conductive liquids (Lee & Kuo, 2006). Lamb waves are considered to be propagating in an elastic plate with a finite thickness otherwise when the waves propagate in an infinite half-space solid medium, they are considered to be Rayleigh waves. Leaky Lamb waves are variant of the Lamb waves which propagate on plate-liquid interface leaking part of the energy into adjacent liquid and therefore attenuate along its propagating direction. The similar feature of energy loss can be observed with the Rayleigh waves if a solid-liquid interface exist in the structure and in that instance, the Rayleigh wave can be also named leaky-Rayleigh waves due to the energy leakage into the liquid layer.

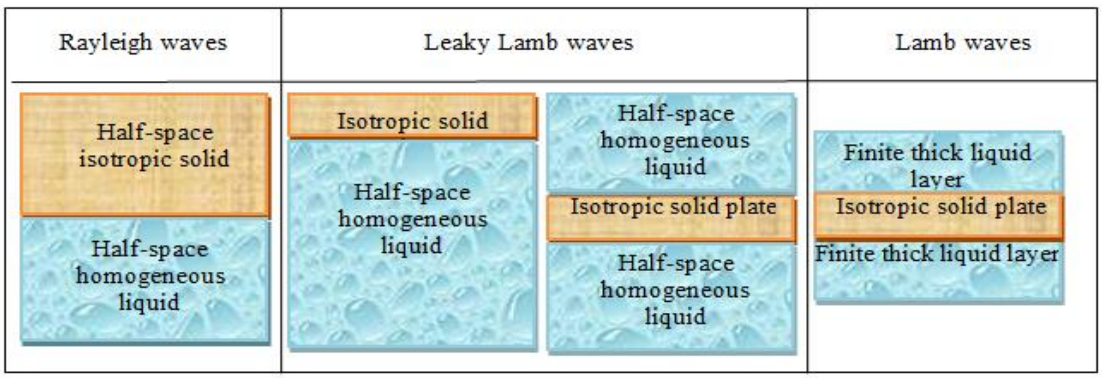


Figure 2.10 Schematic illustration of different solid-liquid structure configurations and corresponding waves traveling along the interfaces.

Guided waves are widely used as interrogating field for damage detection, because they can travel long distances without much energy loss, with the wave energy confined and guided within the structures. Besides, guides waves can travel inside curved walls, and across component joints. These aspects make them suitable for inspection of large areas of complicated structures. Ultrasonic guided waves are sensitive to changes in the propagating medium, such as plastic zone, fatigue zone, cracks, and delamination. This sensitivity exists for both surface damage and cross thickness/interior damage, because guided waves have various mode shapes throughout the cross section of the waveguides.

### 2.2.4 PIEZOELECTRIC TRANSDUCERS GENERATED WAVES IN FLUID MEDIUM

Piezoelectric transducer and liquid domain interaction has been commonly investigated through theoretical analysis of resonance spectra in frequency domain using certain types of standing wave modes; thickness shear waves and shear horizontal waves by using different techniques as discussed in the following sections.

#### Thickness Shear Waves

Nwankwo & Durning in 1998 have investigated the mechanical and impedance response of thickness shear mode quartz crystal resonators to linear viscoelastic fluid media in thickness-shear mode. It was observed that the relaxation time of viscoelastic fluid (condensed polymeric liquids) results in a lower frequency than a viscous Newtonian fluid with identical density and viscosity due to reduced viscous dissipation and smaller inertial load on the crystal surface. The analysis of the momentum transfer from the crystal to the fluid reservoir was required to interpret the frequency shifts based on contact with fluids. The momentum transfer analysis resembled to that of Kanazawa & Gordon (1985) however the analysis in addition considered a complex amplitudes in mechanical response functions for both crystal and liquid parts of the problem as well as the fluid’s complex viscosity and its complex modulus which in turn concluded a correction term for the effect of a finite relaxation time in the fluid at the observed frequency shift.

Piezoelectric wafer active sensors (PWAS) (Giurgiutiu, 2008) have been widely employed as in-situ ultrasonic health monitoring transducers. PWAS transducers are capable of active interrogation of dynamic characteristics of an embedding material in which they may be bonded. Also PWAS transducers are small, light-weighted, inexpensive, unobtrusive, which enable them to be implanted into a biological tissue. Recently, in a joint effort between the University of South Carolina (USC) Department of Mechanical Engineering and School of Medicine, PWAS have been modified and investigated as biomedical sensors (bio-PWAS) (Giurgiutiu et al.; Xu, Giurgiutiu & Crachiolo, 2006).

The electrical excitation of a bio-PWAS can be converted into the mechanical vibration as regards to the stress and the strain waves. This piezoelectricity property of the material of PWAS has been used in literature to develop a micro-acoustic sensor to measure chemical, physical, and biological properties of a medium located in the vicinity or possessing an interface with the sensor. The mechanical properties of medium such as the viscosity and the density affect the energy transduction of sensor as well as the electrical properties of the medium concerning the sensitivity of the wave mode. The detection of changes in mechanical properties and electrical conductivity of the biomedical implants by bio-PWAS enables to capture the protein or solution concentration (pH) changes that influence the conductivity, the ultrasonic wave modes and electro-mechanical impedance readings.

Impedance analysis and ultrasonic guided wave propagation are mainly employed methods to investigate behavior of different piezoelectric acoustic resonators used in structural health monitoring in various types of media. The electro-mechanical impedance spectroscopy (EMIS) of bio-PWAS implanted can transmit the status of implantation in frequency domain. EMIS method applies standing waves to a piezoelectric resonator and utilizes the resonator as both a transmitter and a receiver of the generated waves traveling in a surrounding medium. This technique can indicate the coupled response of the medium-bio-PWAS structure in terms of the electro-mechanical impedance spectrum in frequency domain. The impedance spectrum in frequency domain showed electro-mechanical changes over time associated with the short term immune response (Bender et al., 2006). The response in high frequency range (up to 15 MHz) can be analyzed in varying modes such as the longitudinal (in-plane) mode (Zagrai & Giurgiutiu, 2001), the thickness (out-of-plane) mode (Tiersten, 1963), and thickness shear mode (TSM) (Bandey, Martin, Cernosek, & Hillman, 1999; Bund & Schwitzgebel, 1998; Schneider & Martin, 1995).

Shear Horizontal Surface Waves

Kanazawa & Gordon in 1985 proposed an analytical definition of the resonance frequency shift by purely mechanical analysis which coupled the standing shear wave in the quartz to a damped propagating shear wave in Newtonian fluid i.e. $\Delta f = -f_o^{3/2}\sqrt{\eta_L \rho_L / \pi \mu_q \rho_q}$ and verified by the experimental results in terms of the changes in resonance frequency of the quartz resonator whose one surface is in contact with water that owned varying concentration of glucose and ethanol. In the paper, the boundary layer was identified as the characteristic length of exponentially decaying viscous effects of the liquid on the resonance frequency because the displacement exponentially dies out in the liquid. The approach has been applied for quartz crystal resonators with overlying viscous liquids, thin elastic films and viscoelastic layers (Josse & Shana, 1988; Nwankwo & Durning, 1998; Martin et al., 2000; Suh & Kim, 2010). However the theoretical method derived by Kanazawa & Gordon is only valid for overlying viscous fluid of infinite extent therefore the method analyzes bulk acoustic waves (BAW) which remains the sensor sensitivity low. The sensors utilizing surface acoustic waves (SAW) are superior to the conventional BAW devices in liquid sensor applications since SAW devices can operate at much higher frequencies and more mass sensitive since SAW possesses large attenuation and energy loss due to a mode conversion in the liquid and dissipates due to the viscous effects (Josse & Shana, 1988). Other alternative to the SAW presented was the shear horizontal (SH) surface wave as seen in Figure 2.6.

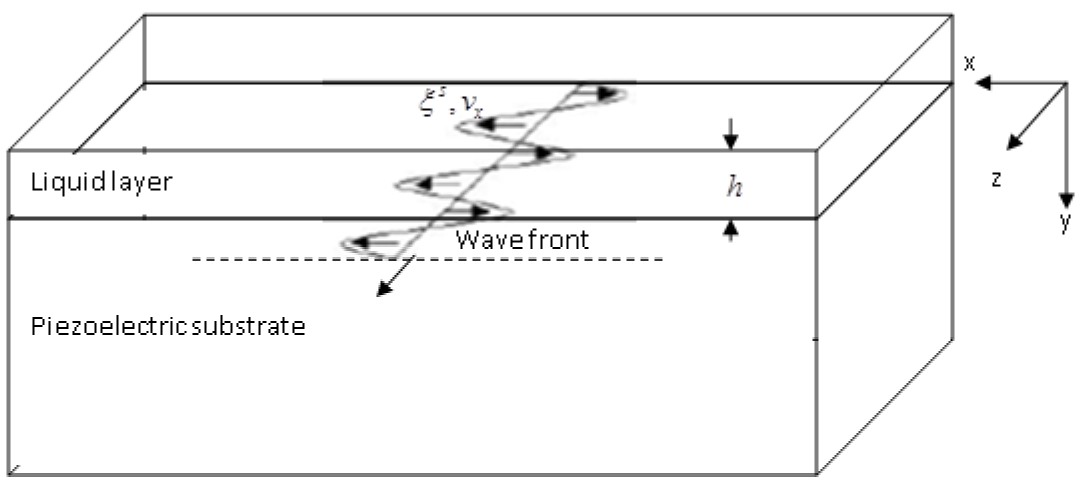


Figure 2.11 Schematic of the propagation of a Shear horizontal (SH) wave along the interface between a piezoelectric substrate and a liquid layer.

The propagation of surface shear waves on an interface (Figure 2.12) were theoretically defined by Feijter in 1979. The interface represented as a plane which has zero thickness and the mass was neglected. The surface shear wave equations in planar and circular surfaces were derived for surface of incompressible liquid which occupies infinite space beginning from introducing the complex surface shear modulus and then imposing the continuity of the stress boundary condition relating the particle displacement, $u_y$, with the liquid particle velocity, $v_x$, the shear modulus, $\mu_s$, and the viscosity $\eta$; shear force gradient with respect to y direction exerted on the interface equals to the shear force gradient with respect to the normal direction due to the presence of the viscous liquid attached to the surface i.e.,

$$\left(\frac{\delta\sigma_{yx}}{\delta y}\right)dxdy = \eta\left(\frac{\delta v_x}{\delta z}\right)_{z=0} dxdy \tag{2.16}$$

The stress-strain constitutive equation simply identifies the relation as

$$\sigma_{yx} = \mu_s S \tag{2.17}$$

$$\mu_s\left(\frac{\delta S}{\delta y}\right) = \mu_s\left(\frac{\delta^2 u_y}{\delta y^2}\right) = \eta\left(\frac{\delta v_x}{\delta z}\right)_{z=0} \tag{2.18}$$

At this point, the complex shear modulus was introduced

$$\mu_s = \mu_s' + \mu_s'' = |\mu_s|\left(\cos\Phi + i\sin\Phi\right) \tag{2.19}$$

This relation indicated that eventhough the shear waves propagated in x direction, the strain has a gradient in transverse direction and the displacement is no longer linear function of y. The Navier Stokes equation reduction occurred due to the consideration of only x component of the velocity which was defined as the time-gradient of the displacement.

$$\rho\left(\frac{\partial v_x}{\partial t}\right) = \eta\left(\frac{\partial^2 v_x}{\partial y^2} + \frac{\partial^2 v_x}{\partial z^2}\right) \tag{2.20}$$

where $\rho$ is the density of the liquid, and $v_x$ is the velocity component of the liquid in $x$ direction and defined as the temporal gradient of the $x$ component of the displacement

$$v_x = \frac{\partial u_x}{\partial t} \tag{2.21}$$

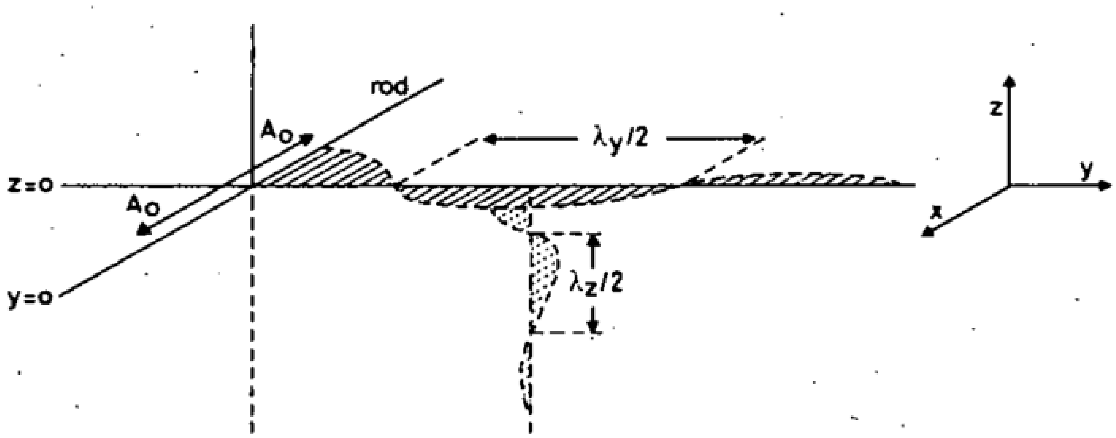


Figure 2.12 Plane transverse wave traveling between the surface and the liquid with the wavelength of the surface shear wave and the wavelength of the bulk shear wave penetrating to liquid medium.

The continuity equation for incompressible liquid is

$$\text{Div}\,\vec{v} = 0 \tag{2.22}$$

The z invariant condition ($\frac{\partial v_z}{\partial z} = 0$) and the constant velocity in y direction simplifies further the continuity equation to

$$\frac{\partial v_x}{\partial x} = 0 \tag{2.23}$$

and the stress boundary condition at the surface, Eq(2.18), can be rewritten as

$$\eta\left(\frac{\partial v_x}{\partial z}\right)_{z=0} = \eta\left(\frac{\partial^2 u_x}{\partial z \partial t}\right)_{z=0} = \mu_s\left(\frac{\partial^2 u_y}{\partial y^2}\right) \tag{2.24}$$

The harmonic displacement function $u(y,z,t) = f(y,z)e^{i\omega t}$ which defines the liquid particle motion and the surface particle motion can be introduced as a general solution to the bulk wave equation imposing the boundary conditions of no-slip and continuity of stress; therefore substituting the displacement function into equations (2.20) (N.S.

equations) and (2.24) (boundary conditions). The term, $\partial^2 v_x / \partial y^2$, in the N.S. equation can be small as negligible when the surface shear modulus is sufficiently great, $\mu_s$ thus N.S. equation is simplified and further simplified by no-slip condition.

$$i\omega\rho f(y,z) = \eta \frac{\partial^2 f(y,z)}{\partial z^2} \tag{2.25}$$

and the solution of the differential equation (2.25) was obtained as

$$f(y,z) = g(y)e^{\pm(i+1)\sqrt{\omega\rho/2\eta}z} = g(y)e^{(i+1)az} \tag{2.26}$$

where $g(y)$ was defined as an exponential function in terms of the wave dispersion ($k_s$)

$$g(y) = A_0 e^{-ik_s y} \tag{2.27}$$

The wave dispersion equation that is the complex wave number was determined by the real wave number ($\kappa_s$) and the damping coefficient ($\beta_s$) i.e. $k_s = \kappa_s - i\beta_s$. The wave equation defining the surface shear motion was revised as a combination of a complex spatial and temporal exponential function including the dispersion equation terms.

$$u(y,z,t) = A_0 e^{az} e^{-\beta_s y} \cos\left(\omega t + az - \kappa_s y\right) \tag{2.28}$$

Josse & Shana theoretically analyzed shear horizontal wave propagation at the boundary of a piezoelectric substrate with viscous fluid to develop a liquid sensor. The attenuation was observed due to the liquid viscosity and density. The theoretical analysis that they developed is applicable to both Bluestein-Gulyaev (BG) wave and surface skimming bulk wave (SSBW) which were generated using piezoelectric crystal resonator performing in liquid environment. It was quantitatively found that BG wave attenuation due to the viscosity was significantly less in comparison to that of Rayleigh SAW. The hexagonal (6mm) crystal class which generates the BG waves and the SSBW was used for the analysis. The referred paper adopted Christoffel equations (Auld, 1973) and solved the equations in three different medium; piezoelectric substrate, viscous fluid medium, and air satisfying the dispersion relations defined for each medium with the assumptions of x-invariant wave, incompressible dielectric viscous fluid, no-slip on the interface, and no-pressure, no gravity in the media. The model employed was a finite thick fluid layer overlying on the piezoelectric crystal of Cadmium Sulfide (CdS). The following boundary conditions were imposed. The electrical boundary conditions: 1-Continuity of the electrical potential at y=0 and y=h, 2-continuity of the electrical displacement at y=h; the mechanical boundary conditions: 1-continuity of normal stress, 2-continuity of the velocity particle displacement, 3-Traction-free at y=h.

## 2.3 PIEZOELECTRIC TRANSDUCERS

Piezo-electric material is a material that has a relation between a mechanical stress and an electrical voltage. As mechanical stress is applied, voltage can be generated and voltage can inversely be applied to morph the shape of material in small amount. These materials can be used as both actuators and sensors.

In the literature, researchers have employed piezo-crystal resonators (Cassiède et-al, 2011; Nwankwo & Durning, 1999) with different cut polarizations (IEEE Ultrasonics, 1987) as well as piezo-ceramic resonators (Giurgiutiu, 2005) to carry out structural monitoring. IEEE Standard on Piezoelectricity explains the crystallography which applies to piezoelectric crystals categorizing in 32 classes of 7 crystal systems (triclinic, monoclinic, orthorhombic, tetragonal, trigonal, hexagonal, and cubic) depending on their degrees of symmetry. The crystal plates are oriented in two rotations such as single rotation and double rotation to produce certain excitation modes. AT-cut (singly rotated) and SC (stress compensated) cut (doubly rotated) crystal plates are the most commonly used ones as resonators. Properly oriented electrodes generate the required excitation modes. Both types of resonators are used to generate thickness shear mode excitations and generally named Thickness Shear Mode (TSM) crystal resonators. Thickness shear mode (out-of-plane) is one of two subdivisions of shear modes whereas the other is the shear horizontal (in-plane) mode.

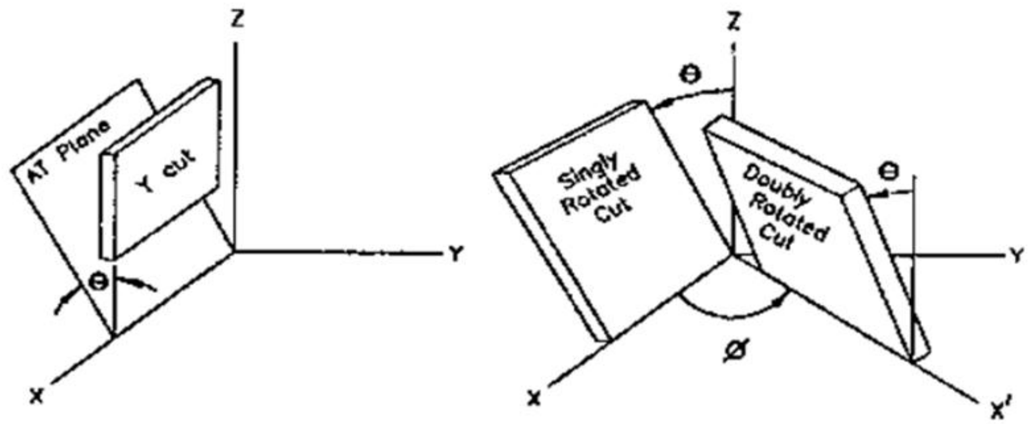


Figure 2.13: Illustration of differently rotated cuts such as singly and doubly rotated. (Basic Technology of Quartz Crystal Resonators, 2012).

Piezoceramic sensors have also been widely employed in structural health monitoring (SHM) and non-destructive evaluations (NDT) society. Piezoceramics are typically made of simple perovskites (calcium titanium oxide minerals with the chemical formula $CaTiO_3$) and solid solution perovskite alloys. Mechanical compression or tension on a poled piezoelectric ceramic element changes the dipole moment, creating a voltage. Compression along the direction of polarization or tension perpendicular to the direction of polarization generates voltage of the same polarity as the poling voltage.

In recent years, piezoelectric wafers permanently attached to the structure have been used for the guided waves generation and detection. PWAS operated on the piezoelectric principle that couples the electrical and mechanical variables in the material (mechanical strain, $S_{ij}$, mechanical stress, $T_{kl}$, electrical field, $E_k$, and electrical displacement $D_j$ in the form:

$$S_{ij} = s^{E}_{ijkl}T_{kl} + d_{kij}E_k \tag{2.29}$$

$$D_j = d_{jkl}T_{kl} + \varepsilon^{T}_{jk}E_k \tag{2.30}$$

where $s^{E}_{ijkl}$ is the mechanical compliance of the material measured at zero electric field ($E = 0$), $\varepsilon^{T}_{jk}$ is the dielectric permittivity measured at zero mechanical stress ($T = 0$), and $d_{kij}$ represents the piezoelectric coupling effect.

### 2.3.1 VIBRATION MODES OF PIEZO-WAFER RESONATORS:

Piezoelectricity describes the phenomenon of generating an electric field when the material is subjected to a mechanical stress (direct effect), or, conversely, generating a mechanical strain in response to an applied electric field. The *direct piezoelectric effect* predicts how much electric field is generated by a given mechanical stress. This *sensing effect* is utilized in the development of piezoelectric sensors. The *converse piezoelectric effect* predicts how much mechanical strain is generated by a given electric field. This *actuation effect* is utilized in the development of piezoelectric induced-strain actuators.

In-plane mode, thickness mode, shear mode

In practical applications, many of the piezoelectric coefficients, $d_{ji}$, have negligible values as the piezoelectric materials respond preferentially along certain directions depending on their intrinsic spontaneous) polarization. For example, consider the situation of piezoelectric wafer as depicted in Figure 2.14a. To illustrate the $d_{33}$ and $d_{31}$ effects, assume that the applied electric field, $E_3$, is parallel to the spontaneous polarization, $P_s$, is aligned with the $x_3$ axis, then such a situation can be achieved by creating a vertical electric field, $E_3$, through the application of a voltage $V$ between the bottom and top electrodes illustrated by the shaded surfaces in Figure 2.14a. The application of such an electric field that is parallel to the direction of spontaneous polarization $(E_3 \parallel P_s)$ results in a vertical (thickness-wise) expansion $\varepsilon_3 = d_{33}E_3$ and lateral (in-plane) extensions and contractions $\varepsilon_1 = d_{31}E_3$ and $\varepsilon_2 = d_{32}E_3$ (the lateral strains are contracted as the coefficient $d_{31}$ and $d_{32}$ have opposite sign to $d_{33}$). So far, the strains experienced by the piezoelectric wafer have been direct strains. Such an arrangement can be used to produce thickness-wise and in-plane vibrations of the wafer.

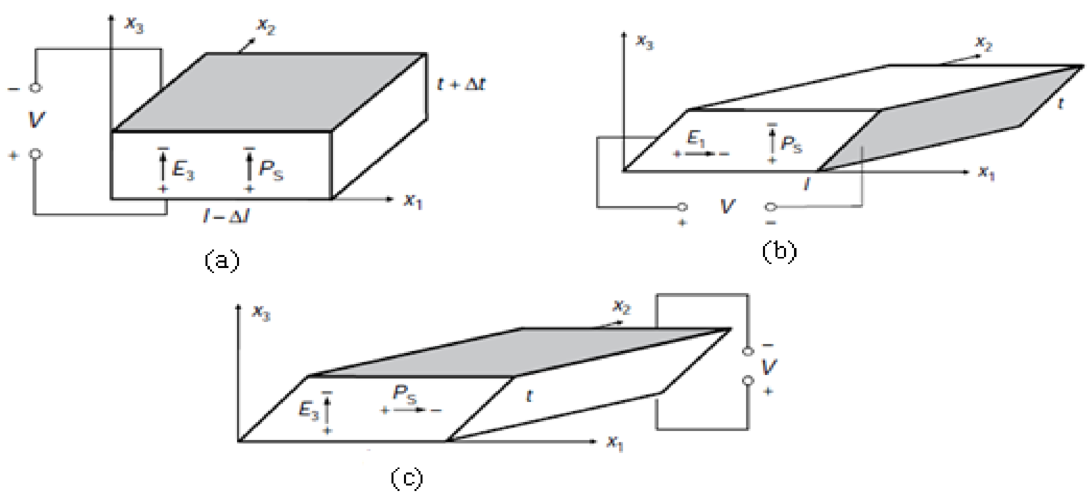


Figure 2.14 Basic induced-strain responses of piezoelectric materials: (a) direct strains; thickness $\varepsilon_3 = d_{33}E_3$ and in-plane $\varepsilon_1 = d_{31}E_3$, $\varepsilon_2 = d_{32}E_3$ (b) shear strain $\varepsilon_5 = d_{15}E_1$ (c) shear strain $\varepsilon_5 = d_{35}E_3$ (Victor Giurgiutiu, 2008d).

However, if the electric field is applied perpendicular to the direction of spontaneous polarization, then the resulting strain will be shear. This can be obtained by depositing electrodes on the lateral faces of the piezoelectric wafer. The application of a voltage to the lateral electrodes shown in Figure 2.14b results in an in-plane electric field $E_1$ that is perpendicular to the spontaneous polarization, $\left(E_1 \perp P_s\right)$. This produces an induced shear strain $\varepsilon_5 = d_{15}E_1$. Similarly, if the electrodes were applied to the front and back faces, the resulting electric field would be $E_2$ and the resulting strain would be $\varepsilon_4 = d_{24}E_2$. The shear-strain arrangements discussed here can be used to induce shear vibrations in the piezoelectric wafer. The use of lateral electrodes may not be feasible in the case of a thin wafer. In this case, top and bottom electrodes can be used again, but the spontaneous polarization of the wafer must be aligned with an in-plane direction. This latter situation is depicted in Figure 2.14c, where the spontaneous polarization is shown in the $x_1$ direction whereas the electric field is applied in the $x_3$ direction. The shear strain induced by this arrangement would be $\varepsilon_5 = d_{35}E_3$. For piezoelectric materials with transverse isotropy, $d_{32} = d_{31}$, $d_{24} = d_{15}$, $\varepsilon_{22} = \varepsilon_{11}$.

For both thickness extensional and thickness shear modes, there are relevant material constants; and elastic constant $c^E$, a piezoelectric constant $e$, a dielectric constant $\varepsilon^s$. The E/M coupling factor $\kappa$ is given in terms of these constants by (IEEE Ultrasonics, 1987)

$$\frac{\kappa^2}{1-\kappa^2} = \frac{e^2}{\varepsilon^s c^E} \tag{2.31}$$

In piezo-ceramics such as lead zirconate-titanate (PZT), the shear coupling coefficient $\kappa_{15}$ can be related to the following material constants

$$\kappa_{15}^2 = \frac{d_{15}^2}{\varepsilon_{11}^T s_{55}^E}$$
$$c_{55}^E = c_{55}^D \left(1 - \kappa_{15}^2\right) \quad (2.32)$$
$$\varepsilon_{11}^E = \varepsilon_{11}^D \left(1 - \kappa_{15}^2\right)$$

where $\varepsilon_{11}^S$ and $\varepsilon_{11}^T$ are the clamped and free dielectric permittivities perpendicular to the poling direction, respectively. $d_{15}$ is the shear piezoelectric constant, $c_{55}^E$ and $c_{55}^D$ are shear elastic stiffness constants under constant electric field and constant electric displacement, respectively (Cao, Zhu, Jiang, & Introduction, 1998).

Shear horizontal (thickness shear, length shear) modes, shear vertical mode

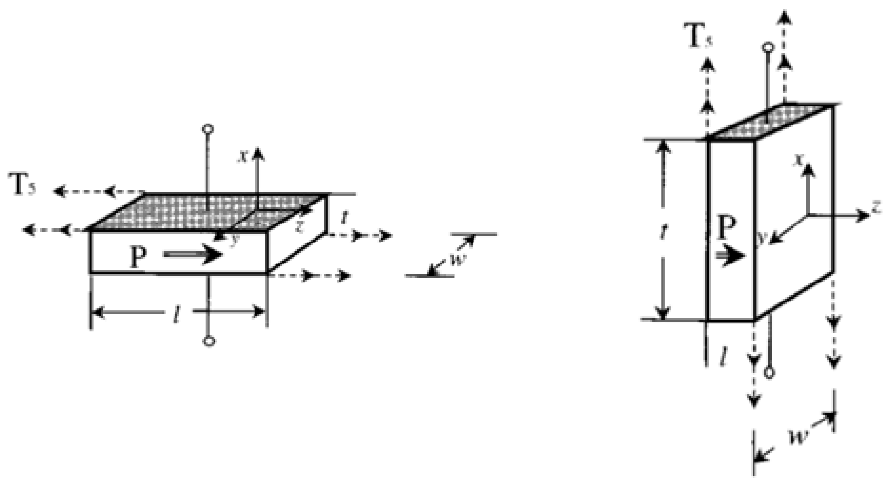


Figure 2.15 (a) Thickness-shear resonator. (b) Length-shear resonator. The shaded areas are the electrodes and the dashed arrows represent the direction of displacement at given points. The polarization direction is indicated by an arrow on the front face of the sample.

In Figure 2.15, the polarization direction is shown with respect to the geometric orientation of the two resonators. The both intrinsic polarizations are in horizontal axis however the left one is along the longest edge and the right one is along the shortest edge.

Moreover, in both resonators, the intrinsic polarizations are perpendicular to the electric field polarizations and the electrodes are deposited on the surfaces across the thicknesses of both resonators. In the left resonator, the shear stress $T_5$ applies on the surfaces lying on the yz plane and has the gradient in x axis so that this resonator is called thickness-shear resonator and other one has the shear stress $T_5$ applies on the surfaces lying on the xy plane and has the gradient in z axis so that is called length-shear resonator. The shear mode that a thickness shear resonator generates is called $d_{15}$ mode and the shear mode that length generates is also called $d_{35}$ mode eventhough both are actually shear horizontal modes whose electric field polarization directions only differ; one in $x_1$ axis and other one is in $x_3$, respectively as can also be seen in Figure 2.14.

As the polarization direction is along thickness of a piezo-wafer so that electric field is polarized in thickness direction, $E_3$ and since all stress components are zero except $T_5$, the vibration mode is $d_{35}$ mode that excites shear horizontal wave mode whose E/M coupling can be defined under constant electric field assumption as

$$\kappa_{35}^2 = \frac{d_{35}^2}{\varepsilon_{33}^T s_{55}^E} \tag{2.33}$$

and defined under constant electric displacement $D_3$ assumption as

$$\kappa_{35}^2 = \frac{e_{35}^2}{\varepsilon_{33}^S c_{55}^D} \tag{2.34}$$

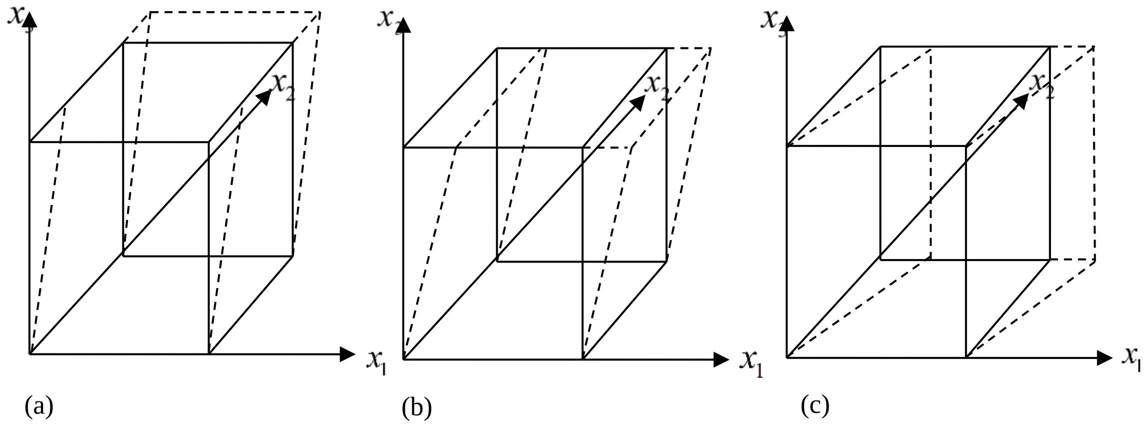


Figure 2.16 Solid lines represent non-deformed shape and dashed lines depict deformed shape (a) Shear horizontal (SH) deformation $T_4 = T_{23}$, (b) Shear horizontal (SH) deformation $T_5 = T_{13}$, (c) Shear vertical (SV) deformation $T_6 = T_{12}$.

### 2.3.2 STANDING WAVES

The concept of standing waves bridges the gap between wave analysis and vibration analysis. The particle motion can simply be considered self-similar along any line parallel to the y-axis. If plate vibration is seen as a system of standing waves in the plate, then this case can be considered as a system of standing straight-crested axial waves with the wave crest along the y-axis (Figure 2.17).

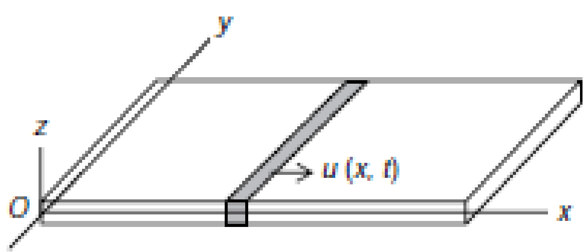


Figure 2.17 Straight crested axial vibration in a plate.

To consider straight-crested flexural plate vibrations, plate vibration is seen as system of standing waves in the plate, and then this case can be considered a system of standing straight-crested flexural waves with the wave crest along the y-axis. Taking the y-axis along the wave crest yields a y-invariant problem that depends only on x

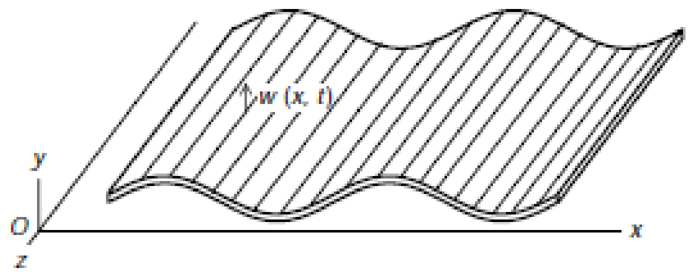


Figure 2.18 Straight crested flexural vibration of a plate.

*<u>In-plane mode piezoelectric transducer constrained by elastic media</u>*

For embedded NDE applications, PWAS resonators couple their in-plane motion, excited by the applied oscillatory voltage through the piezoelectric effect, with the Lamb-waves particle motion on the material surface. Lamb waves can be either quasi-axial ( $S_0, S_1, S_2 ...$), or quasi-flexural ( $A_0, A_1, A_2 ...$). Figure 2.19 shows the interaction between surface mounted PWAS and $S_0$ and $A_0$ guided Lamb waves.

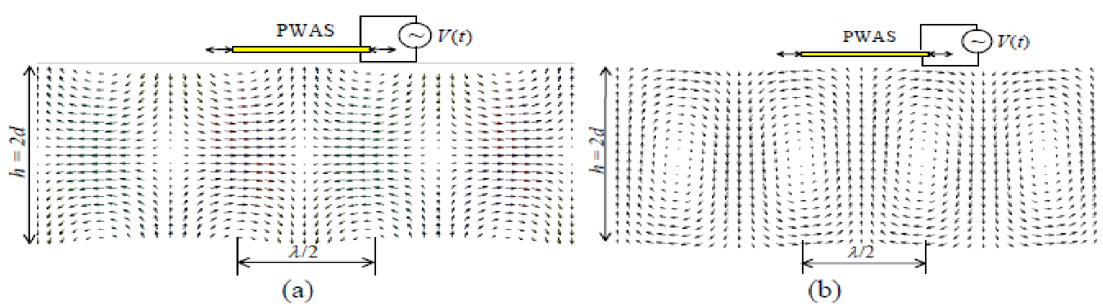


Figure 2.19 PWAS interaction with Lamb waves in a plate; (a) S0 Lamb wave mode , (b) A0 Lamb wave mode.

Zagrai in 2002 worked on standing waves to determine an analytical expression for PWAS admittance on a 1-D structure undergoing axial and flexural vibrations.

$$Y = \frac{I}{V} = i\omega C_0 \left[ 1 - \kappa_{31}^2 \left( 1 - \frac{1}{\varphi \cot \varphi + r} \right) \right] \tag{2.35}$$

where $\varphi = 1/2\gamma L$, $\gamma = \omega / c_{PWAS}$, and $c_{PWAS}$ is the sound speed in the PWAS material. The quantity $r = k_{str}(\omega)/k_{PWAS}$ is the stiffness ratio. The structural stiffness using conventional axial and flexural vibration modes of a 1-D beam was determined as

$$k_{str}(\omega) = \rho A \left\{ \sum_{n_u} \frac{\left[ U_{n_u}(x_a + l_a) - U_{n_u}(x_a) \right]^2}{\omega_{n_u}{}^2 + 2i\zeta_{n_u} - \omega^2} + \left( \frac{h}{2} \right)^2 \sum_{n_u} \frac{\left[ W'_{n_w}(x_a + l_a) - W'_{n_w}(x_a) \right]^2}{\omega_{n_w}{}^2 + 2i\zeta_{n_w} - \omega^2} \right\}^{-1} \tag{2.36}$$

where $\omega_n$ and $\zeta_n$ are the modal frequencies and damping ratios, while u and w signify axial and flexural displacements, respectively.

Zagrai & Giurgiutiu in 2001 also performed 2D analysis of PWAS immittance (impedance/admittance) for circular-crested Lamb waves in cylindrical coordinates using the Bessel functions formulation. They also determined analytical expressions for the admittance and impedance of a PWAS mounted on a 2-D structure undergoing axisymmetric radial and flexural vibrations (Figure 3.1).

*Thickness mode piezoelectric transducer constrained by elastic media*

Transducers usually interact with another medium attached over one or both surfaces and the boundary conditions change accordingly. The mechanical boundary conditions on the interfaces for the waves traveling in both directions are presented in Figure 2.20

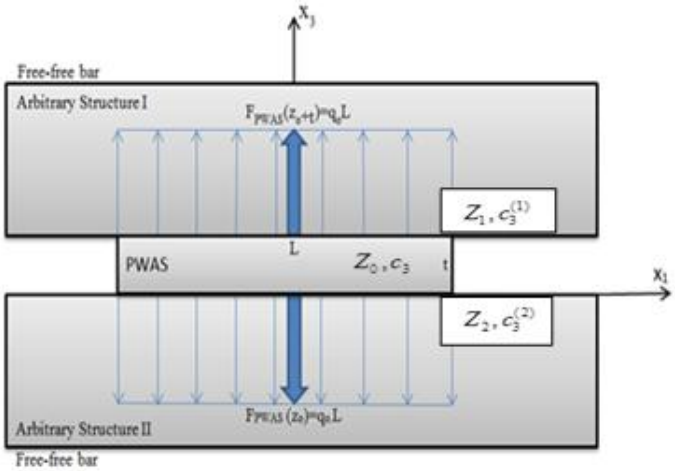


Figure 2.20 Constrained thickness mode transducer.

We can define the waves in each layer of the multilayered structure for the piezoelectric transducer, the general solution of in terms of the displacement and the force for the first elastic layer respectively are

$$\hat{u}_3^{(1)} = \left(C_1^{(1)}e^{-ikz} + C_2^{(1)}e^{ikz}\right) \tag{2.37}$$

$$\hat{F}_3^{(1)} = i\omega Z_1\left(-C_1^{(1)}e^{-ikz} + C_2^{(1)}e^{ikz}\right) \tag{2.38}$$

and for the second elastic layer

$$\hat{u}_3^{(2)} = \left(C_1^{(2)}e^{-ikz} + C_2^{(2)}e^{ikz}\right) \tag{2.39}$$

$$\hat{F}_3^{(2)} = i\omega Z_2\left(-C_1^{(2)}e^{-ikz} + C_2^{(2)}e^{ikz}\right) \tag{2.40}$$

The elastic structures are assumed to be semi-infinite half space media therefore the mechanical signal and the force exerted on the transducer by the medium 1 is represented by $C_1^{(1)}$ (incident wave amplitude) in Eqs (2.37) and (2.38) whereas the reflected wave is represented by $C_2^{(1)}$. The coefficients can be therefore determined by the nature of the applied signal whether harmonic, sine, or cosine input signal function.

Herein the velocities of the waves in the elastic media extending over large distances in the lateral directions can be calculated by using Lame constants, $\lambda$ and $\mu$, i.e. $c = \sqrt{(\lambda + 2\mu)/\rho}$ and if extending over small area using the elastic modulus, $c = \sqrt{E/\rho}$ when open circuit condition is applied, the total current flow becomes zero, i.e.,

$$\hat{I} = i\omega\hat{Q} = 0 \tag{2.41}$$

As an analogy, the mechanical force can be considered as the analog of the electrical potential and the particle velocity as the analog of the electrical current. The electro-mechanical impedance matrix establishes the relations between the mechanical forces and the particle velocities and the electrical voltage and the electrical current which present at the mechanical and electrical ports. The matrix can be functionally considered as a composition of three components such as the first 2x2 sub-matrix which includes the equations of a mechanical transmission line of thickness of the piezoelectric transducer, the characteristic acoustic impedance, and the wave speed; the piezoelectric constant, $h_{33} = e_{33}/\varepsilon_{33}^S$, terms related to the electromechanical coupling factor ( $\kappa_{33}^2 = e_{33}^2 / c_{33}^D \varepsilon_{33}^S$) by the reciprocal of the stiffened elastic coefficient or the compliance coefficient ( $s_{33}^D = 1/c_{33}^D$);the last matrix element is the pure electrical impedance of the piezoelectric transducer capacitance.

All the equivalent circuits can be represented by the 3x3 electromechanical transfer matrix. The transfer matrix of circuit theory with the parameters at the electrical and acoustic ports can be implemented to analyze the transducer performance whether a transmitter or a receiver under the short or open circuit conditions.

$$\begin{pmatrix} V_1 = V \\ I_1 = I \end{pmatrix} = \begin{pmatrix} A & B \\ C & D \end{pmatrix} \begin{pmatrix} V_2 = F_t \\ I_2 = -(u_3)_t \end{pmatrix} \tag{2.42}$$

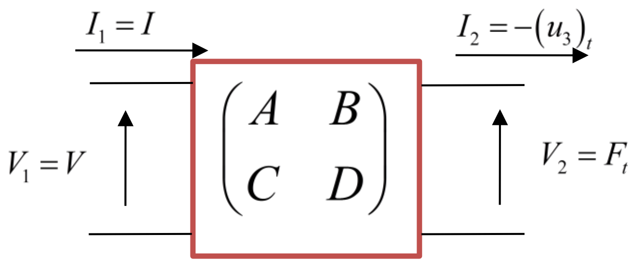


Figure 2.21 Two port illustration of a piezoelectric transducer system. The electrical and mechanical parameters at the ports are correlated by the ABCD matrix.

$F_0$, $F_t$, $(\dot{u}_3)_0$, and $(\dot{u}_3)_t$ are the forces and the particle velocities on the transducer surfaces. In the circuit, the secondary of the ideal transformer is connected to the external shield of the transmission line; however, the shield does not possess inductance therefore the transmission line model cannot be directly simulated on SPICE simulation software due to the necessity for a shield with no inductance.

The analysis and the simulation of both acoustic and electrical piezoelectric transducer elements can be easily implemented through SPICE analysis programs for modeling one dimensional multilayered structure with a stack of piezoelectric and non-piezoelectric layers and for analyzing the behavior with respect to the variations on the transducer elements by taking the acoustic losses into account (Puttmer et-al, 1997). In the active piezoelectric plates, the length and width to thickness ratios are sufficiently large so that one-dimensional models are good approximations to predict the properties of the transducer (Emeterio & Ramos, 2008).

### 2.3.3 WAVE PROPAGATION METHODS

A piezoelectric active sensor can fulfill both duties, actuating a structure and sensing the elastic waves, which it generates, being propagated into a structure and traveled back to the source (pulse-echo method). Another method can employ two piezoelectric active sensors such that one can be used as an actuator and the other as a sensor (pitch-catch method) to generate and sense the wave propagation into a structure, respectively. PWAS can be also used as a resonator generating standing waves into the structures to help identify the local dynamics of the structure via PWAS permanently mounted on the structure in order to determine occurrence and location of a defect (Yu, 2006).

Pitch-catch Method

One PWAS can be used as an actuator whereas another PWAS as a receiver and both are mounted on the same structure and then the generated wave propagates off the actuator and can be received by the other PZT active sensor and the received wave signals can be read (Figure 2.22). The wave signals recorded for the pristine form of the same sort of structure can be used as a baseline to determine whether any damage occurs in the structure. The wave signal analysis by comparing the phase and amplitude differences even provides the information about the size and the location of the defect in the material. After series of tests, the data sets can be evaluated by a statistical damage index (DI) method based on the root-mean square values.

$$RMSD\ DI = \sqrt{\frac{\sum_{j=0}^{N}\left[s_i(j)-s_0(j)\right]^2}{\sum_{j=0}^{N-1} s_0^2(j)}} \tag{2.43}$$

Lamb wave change as it travels through a damaged area. It can become more dispersed or even change speed. The pitch-catch method can detect delamination, cracks, disbond in joint or impact damage (Roman, 2012).

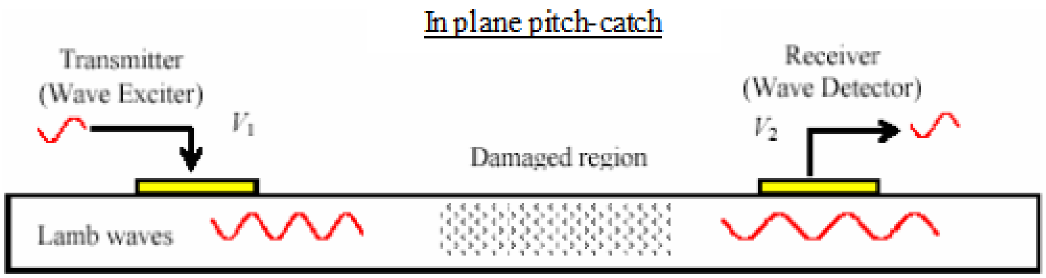


Figure 2.22 Diagram of a pitch-catch setup being used to detect a damaged region (Giurgiutiu, 2008).

Pulse-echo Method

A piezoelectric transducer can be used as both actuators and sensors since piezoelectric material has reversible material property. This material property is a relation between mechanical stress and electrical voltage. As mechanical stress is applied, voltage can be generated and inversely voltage can be applied to morph the shape of the material in small amount. These materials can be used as both actuators and sensors as seen in Figure 2.23. The piezoelectric transducer can fulfill both duties, actuating a structure and sensing the elastic wave that was generated by the transducer, being propagated into a structure and traveled back to the source.

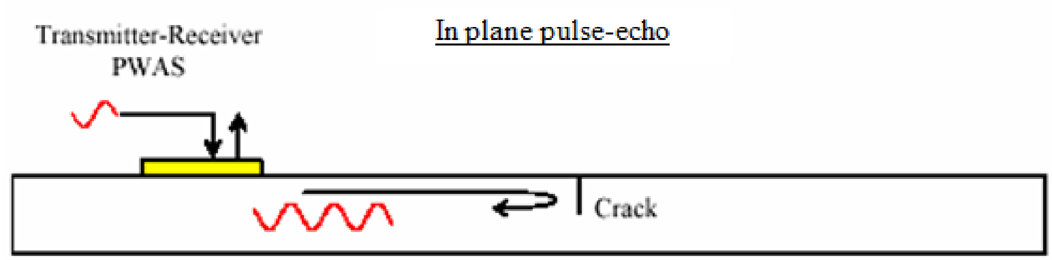


Figure 2.23 Diagram of a pulse-echo setup being used to detect a damaged region (Giurgiutiu, 2008).

When the propagating wave impinges on a defect, a part of the wave is reflected back from the defect and can be captured by the PWAS. The collected signals from damaged structure can be compared to the signal from pristine structure and the difference in the received signal in terms of phase or amplitude difference can help determine the existence, the type, and even the location of the damage. In order for the pulse-echo method to be successful, part of the incidence wave should be reflected from the damage, not be damped by the damaged zone or not be fully transmitted through the damaged zone. Different types of damage reflect the Lamb wave differently. Damage through the thickness will reflect the largest percentage of the transmitted wave. The pulse-echo method is successful at detecting cracks but not very successful to detect delamination (Roman, 2012).

# CHAPTER 3

# FREE PWAS E/M IMPEDANCE SPECTROSCOPY

This chapter presents the theory and an analytical framework for simulating in-plane and out-of-plane (thickness) modes of E/M impedance spectroscopy (EMIS) of 1-D free PWAS. Two main electrical assumptions will be applied for both PWAS-EMIS modes. These assumptions are 1- constant electrical field assumption and 2- constant electrical displacement assumption. The analytical simulations under these two assumptions will be carried out and verified by corresponding finite element simulations as well as experimental measurements.

## 3.1 STATE OF THE ART FOR ELECTROMECHANICAL IMPEDANCE SPECTROSCOPY

The intrinsic EMIS of PWAS is an important dynamic descriptor for characterizing the sensor prior to its installation on a structure. The frequency response of a sensor to the electrical excitation defines its dynamic structural properties. EMIS method has been widely used to determine the dynamic characteristic of a free PWAS and bonded PWAS for in-situ ultrasonics. For example, Sun, Liang, & Rogers (1994) Kamas, Lin, & Giurgiutiu (2013) utilized the EMIS method for high frequency local modal sensing. The analytical in-plane PWAS-EMIS model under constant electrical field assumption was developed by Zagrai in 2002.

EMIS method applies standing waves to a piezoelectric resonator and utilizes the resonator as both a transmitter and a receiver of the generated waves traveling in a medium so that this technique can indicate the response of the coupled medium-resonator in terms of the E/M impedance spectrum in frequency domain. The response in frequency domain can be  in varying modes such as the longitudinal (in-plane) mode (Giurgiutiu, 2005; Giurgiutiu & Zagrai, 2000; Zagrai & Giurgiutiu, 2001), the thickness (out-of-plane) mode (Ballato, 1977; Chen et-al, 2008; Lee, Liu, & Ballato, 2004; Meeker, 1972; Sherrit, Leary, Dolgin, & Bar-Cohen, 1999; Tiersten, 1963; Yamada & Niizeki, 1970), thickness shear mode (TSM) (Bandey et-al, 1999; Bund & Schwitzgebel, 1998; Schneider & Martin, 1995). In order to theoretically analyze the thickness and thickness shear modes of the impedance spectra of the resonators in a media, two techniques have been used in resonator theory. One technique have employed the governing differential equations and constitutive equations imposing the relevant boundary conditions and the second technique has mostly used delay line transducer theory to derive an equivalent circuit model to describe the impedance and the transfer function of the transducer (Martin et al., 2000; Nwankwo & Durning, 1999; Sherrit et al., 1999). Two equivalent circuits widely used are Mason's and KLM (Krimholtz et-al, 1970) circuits to approximate the analytical solutions for the impedance in thickness mode (Ballato, 2001).

The analytical study for thickness mode of EMIS of piezoelectric ceramic resonator has not been fully performed yet. Therefore, the constant electric displacement assumption used in the literature was adopted and the piezoelectric constitutive equations are solved for the 1-D PWAS-EMIS in thickness mode. Coupled-field finite element method (CF-FEM) was used to model and simulate free PWAS-EMIS. In addition, a set of experiments was conducted using free-rectangular PWAS. The results from the two analytical models with two different assumptions are validated by the corresponding numerical models and the experimental measurements. The comparison between theoretical prediction, simulation, and experimental data are illustrated and discussed.

### 3.1.1 IN-PLANE MODE E/M IMPEDANCE SPECTROSCOPY

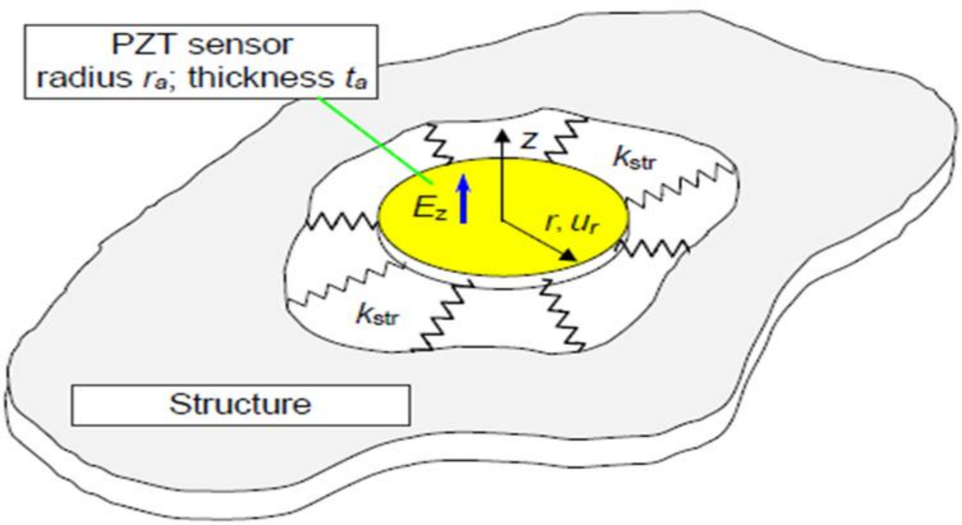


Figure 3.1 Piezoelectric wafer active sensor constrained by the structural stiffness (Zagrai, 2002).

The analytical in-plane impedance for piezoelectric ceramic transducers such as PWAS has been developed by Zagrai & Giurgiutiu (2001). One and two dimensional in-plane E/M impedance models for free PWAS and constrained PWAS (Figure 3.1) were derived to model the dynamics of PWAS and substrate structure in terms of EMIS. They assumed the constant electric field, $E_3$, to derive the in-plane EMIS.

Zagrai & Giurgiutiu (2001) assumed harmonic excitation $E_3(x_1,t)=\hat{E}_3 e^{i\omega t}$ and considering the 1-D equation of motion, the free PWAS impedance can be described as

$$Y=\frac{I}{V}=i\omega C_0\left[1-\kappa_{31}^2\left(1-\frac{1}{\varphi\cot\varphi}\right)\right] \tag{3.1}$$

where the electro mechanical coupling coefficient , $\kappa_{31}$, defined as $\kappa_{31}^2=d_{31}^2/s_{11}^E\varepsilon_{33}^T$ and the capacitance of the material $C_0=bL/t\beta_{33}^S$ and $\varphi=1/2\gamma L$ (IEEE Ultrasonics, 1987).

### 3.1.2 THICKNESS MODE E/M IMPEDANCE SPECTROSCOPY MODELS

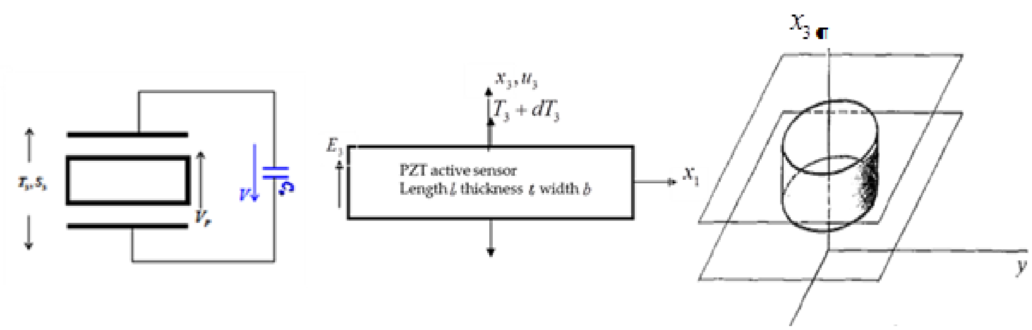


Figure 3.2 Schematic of a piezoelectric wafer active sensor polarized in thickness direction.

Many rigorous researches on the thickness (out-of-plane) mode (Figure 3.2) theory have been conducted for piezoelectric crystal and ceramic resonators. Tiersten (1963) presented a pioneering work to develop the analytical solution for the thickness vibration of an anisotropic piezoelectric plate. He used the resonator theory with traction-free $T=0$ boundary conditions at surfaces of a plate. Thickness vibration in an infinite piezoelectric plate was explored based on lossless ideal linear theory. He assumed a medium that is perfectly elastic and perfectly insulating to electric current so that the coupling of mechanical field and electric field is omitted. Meeker (1972) adopted Tiersten's basic equations to develop general impedance equations with arbitrary boundary conditions. He used a matrix method to analyze the parallel and perpendicular electrical field excitation of piezoelectric plates in thickness direction. The resonant and anti-resonant frequencies and the coupling factors were determined by solving transcendental equations. (Yamada & Niizeki, 1970; Yamada, 1970) extended the thickness mode solution for both thickness and lateral excitation. (Mason, 1948) further developed the equivalent electrical circuit theory to predict the impedance of the simple thickness mode piezoelectric transducer. These previous analytical solutions have been focused on piezoelectric crystal transducers.

Mindlin (1951) obtained the frequency equation which prompts to define the frequency spectrum of resonances by thickness shear vibration of rectangular quartz plate fully electroded (Berlincourt et-al., 1958). The shear deformation was observed to be present in flexural motion so that the forcing shear deformation generated by a piezoelectric transducer excites the flexural resonance at the resonant frequencies of flexure therefore the resonances could be designated as thickness-shear modes in a bounded plate. He improved the classical plate theory in three dimension applying to high frequency flexural modes and the accompanying thickness-shear motion. He retained the shear and rotatory inertia terms which accommodated the higher thickness-shear overtones. He neglected the width of the plate assuming the independency of resonant frequencies of z-direction and derived the solution of two-dimensional anisotropic version of Timoshenko's beam equation. Mindlin & Deresiewicz (1953) later on derived the governing equations in two dimensions for the coupled shear and flexural vibrations of isotropic, elastic circular plates by using Bessel's function and obtained the results in terms of the resonant frequencies, in thickness-shear mode, resembling to those excited in an AT-cut quartz circular disk.

Thickness vibration in an infinite, piezoelectric plate was explored by Tiersten, 1963 based on lossless ideal linear theory which assumed a medium to be perfectly elastic and perfectly insulating to electric current that result in omitting the coupling of mechanical field with electric field. He investigated the steady state thickness vibrations in an infinite -plate with infinite plated electrodes on both surfaces. Lawson's solution (Lawson, 1942) was improved in the mean of satisfying the proper boundary conditions. The analysis was applied (satisfying high electromechanical coupling) to a ferroelectric ceramic in both thickness and in-plane direction also applied to Y-cut quartz plate. The boundary conditions are traction-free and harmonic electric potential lying on both surfaces. Since neither boundaries nor the applied voltage is dependent on the lateral directions, the solution was independent of $x_2$ and $x_3$. However, the solution proposed is only valid for resonators due to the traction free conditions and invalid for the delay line transducers. Researches have been conducted by manipulating the thickness mode theory for different configurations of piezoelectric crystal and ceramic resonators.

The thickness mode theories that had been developed were synthesized by Meeker (1972) then Tiersten's basic equations was adopted to develop the theory of the simple thickness mode to obtain general impedance equations for the piezoelectric transducer for arbitrary boundary conditions. The restrictions applied to the model was to avoid the lateral excitation modes, to remain in low frequency range, and to assume no energy leakage to the surrounding media therefore considering the impedance as a pure reactance that depends on frequency, geometry and the material.

Yamada & Niizeki, (1970) analyzed the parallel and perpendicular electrical field excitation of piezoelectric plates in thickness direction by means of a matrix method and obtained the admittance of the plate with electrodes coated. The resonant and anti-resonant frequencies and the coupling factors for three vibration modes (one longitudinal and two transversal) were determined by solving transcendental equations derived and the results were verified by experiments with lithium tantalite single crystal.

The electric field was considered as parallel field to the plate surfaces which results in the anti-resonant frequencies as solutions to a transcendental equation unlike the perpendicular field case from which one can come up with the resonant frequencies (reciprocal relation) because of the assumptions made although the obtained results were in close agreement. Yamada's simple thickness mode analysis was adopted by Ballato, 1977 for the admittance of doubly rotated thickness mode plate vibrators uncoated Eq(3.2) and coated with electrodes Eq(3.3).

$$Y = i\omega C_0 \frac{1}{1 - \sum_m k_m^2 \frac{\tan X^{(m)}}{X^{(m)}}} \tag{3.2}$$

$$Y = i\omega C_0 \frac{1}{1 - \sum_m \frac{k_m^2}{1 - \mu X^{(m)} \tan X^{(m)}} \frac{\tan X^{(m)}}{X^{(m)}}} \tag{3.3}$$

where $\mu$ was defined as the reduced mass loading of the metallic electrodes and $X^{(m)}$ was the product of wave number that depends on the frequency by the plate thickness, $k_m^2$ was the electro-mechanical coupling coefficient that differs for each mode, and $C_0$ is the static shunt capacitance. In the open circuit condition, the traction-free condition was assumed and each uncoupled frequencies were determined from the roots of $\mu X^{(m)} \tan X^{(m)} = 1$ and not harmonically related however otherwise, i.e. metalized (short) circuit condition, the coupled resonance frequencies were determined from

$$\sum_m \frac{k_m^2}{1 - \mu X^{(m)} \tan X^{(m)}} \frac{\tan X^{(m)}}{X^{(m)}} = 1 \tag{3.4}$$

Ballato in 2000 extended Christoffel-Benchmann (C-B) method further to determine the solution for lateral field excitation moreover to simplify the solution of the thickness mode problem which was produced by Tiersten and extended by Yamada and Niizeki for both thickness and lateral excitation. Ballato obviated, by using C-B method, the unnecessary computation raised from the material properties tensors rotated from the crystallographic axes to the axes of the plate. The C-B method assisted to obtain the solution for an arbitrary direction of propagation, which had been fairly correct prior to the publications by Tiersten and Yamada and Niizeki nevertheless, the C-B procedure was computationally more efficient since no rotation of the material coefficients between crystallographic and crystal plate axes was taken into account.

The thickness mode has been modeled by also facilitating the network theory in the means of the simplifying electro-mechanical analogy using electrical equivalent circuits associated with somewhat complicated analytical solutions for traction-free or different loading conditions. The pioneer equivalent circuit was developed by Mason in 1948, Redwood in 1961 proposed the modified version of the Mason's equivalent circuit model and the alternative equivalent circuit called KLM was proposed by Krimholtz et al. in 1970. The equivalent circuits which are composed of mechanical, electrical ports, acoustic layer ports (if any exists), and the transmission line have been widely employed for the thickness mode transducer simulation, design, and optimization.

Damping in an anisotropic or piezoelectric plate could be involved using viscoelastic models. One of the recent investigations (Lee et al., 2004) included the dissipation of energy concerning higher operating frequency and smaller sizes of the resonators in more realistic modeling as those used in micro-sensor applications considering both piezoelectric crystal and piezoelectric ceramic resonators. The most general three-dimensional investigation was performed for the plane harmonic wave propagation and for the forced thickness vibrations in an arbitrary direction of an infinite piezoelectric plate including losses due to the acoustic viscosity and electric conductivity. The frequency dependent admittance was determined and the resonance spectrum in thickness mode was depicted in frequency domain. The real and imaginary parts of the mode shapes and potentials across the thickness of the piezoelectric plate excited in thickness mode were demonstrated. The predicted viscosity term values were eventually listed for different piezoelectric plates.

## 3.2 ANALYTICAL IN-PLANE MODE EMIS MODEL UNDER CONSTANT $D_3$ ASSUMPTION

The following assumptions for PWAS were used for the in-plane EMIS model (Giurgiutiu, 2008). The PWAS of length $l$, width $b$, and thickness $h$, undergoing piezoelectric expansion induced by the thickness polarization electric field, $E_3$. The electric field is generated by harmonic voltage $V(t)=\hat{V}e^{i\omega t}$ between the top and bottom surface electrodes. $E_3$ is assumed to be uniform over the piezoelectric wafer. Thus, its derivative with respect to $x_3$ is zero i.e. $\partial E_3 / \partial x_3 = 0$. The voltage excitation is harmonic so that the electric field $E_3 = \hat{E}_3 e^{i\omega t}$ and the mechanical response in terms of particle displacement are also harmonic, i.e. $u(x,t) = \hat{u}(x) e^{i\omega t}$ where $\hat{u}(x)$ is the $x$ dependent complex amplitude that incorporates any phase difference between the excitation and response.

Giurgiutiu & Zagrai (2000) obtained the following frequency dependent impedance equation that can be used to predict the frequency response of PWAS excited at anti-resonance frequencies. The electro-mechanical impedance follows the electrical impedance function, $1/i\omega C_0$ where $C_0$ is the capacitance of the sensor. To this purpose, we note that the term $\varphi$ is a function of frequency and wave speed, i.e. $\varphi = \frac{1}{2}\omega l / c$ and the electro-mechanical coupling is denoted by $\kappa_{31}^2$ term.

$$Z = \frac{1}{i\omega C_0}\left[1 - \kappa_{31}^2\left(1 - \frac{1}{\varphi \cot \varphi}\right)\right]^{-1} \tag{3.5}$$

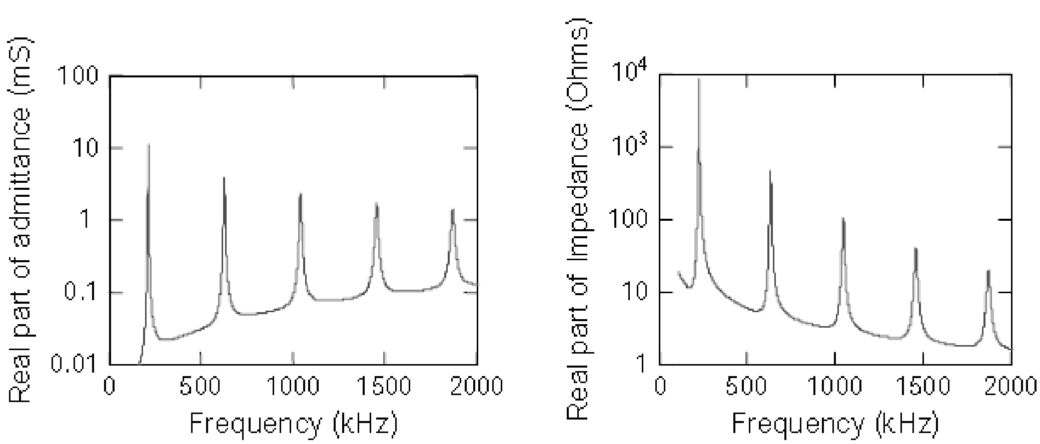


Figure 3.3 Simulated frequency response of admittance and impedance of a PWAS (including internal damping effects of $\delta = \eta = 0.01$).

Frequency plots of admittance $\left(Y=1/Z\right)$ and impedance shows the graphical determination of the resonance and anti-resonance frequencies. Figure 3.3 presents the numerical simulation of admittance and impedance response for a piezoelectric active sensor ($l=7\text{mm}$, $b=1.68\text{mm}$, $h=0.2\text{mm}$, APC-850 piezo-ceramic).

The general constitutive equations expressing the linear relation between stress-strain and stress-electric displacement in in-plane mode are

$$\begin{aligned}&\text{a-) } T_1 = c_{11}^D S_1 - h_{31} D_3\\&\text{b-) } E_3 = -h_{31} S_1 + \beta_{33}^S D_3\end{aligned}\tag{3.6}$$

The relations of the four piezoelectric constants to each other are in in-plane mode as follows (Berlincourt et al., 1958):

$$\begin{aligned}d_{31} &= \varepsilon_{33}^T g_{31} = e_{31} s_{11}^E\\g_{31} &= \beta_{33}^T d_{31} = h_{31} s_{11}^D\\e_{31} &= \varepsilon_{33}^S h_{31} = d_{31} c_{11}^E\\h_{31} &= \beta_{33}^S e_{31} = g_{31} c_{11}^D\end{aligned}\tag{3.7}$$

(IEEE Ultrasonics, 1987) standard on piezoelectricity provides other relations to alternate the forms of the constitutive equations. The relations adopted for the 31 mode are

$$\begin{array}{ll}c_{11}^E s_{11}^E = \delta_{11} & c_{11}^D s_{11}^D = \delta_{11}\\\beta_{33}^S \varepsilon_{33}^S = \delta_{33} & \beta_{33}^T \varepsilon_{33}^T = \delta_{33}\\c_{11}^D = c_{11}^E + e_{31} h_{31} & s_{11}^D = s_{11}^E - d_{31} g_{31}\\\varepsilon_{33}^T = \varepsilon_{33}^S + D_{31} e_{31} & \beta_{33}^T = \beta_{33}^S - g_{31} h_{31}\\e_{31} = d_{31} c_{11}^E & d_{31} = \varepsilon_{33}^T g_{31}\\g_{31} = \beta_{33}^T d_{31} & h_{31} = g_{31} c_{11}^D\end{array}\tag{3.8}$$

### 3.2.1 MECHANICAL RESPONSE IN IN-PLANE MODE

Under 1-D assumption, the in-plane mode wave equation can be expressed

$$\frac{\partial^2 u_1}{\partial t^2} = \frac{c_{31}^D}{\rho} \frac{\partial^2 u_1}{\partial x_1^2} \tag{3.9}$$

Introducing the wave speed in direction of $x_1$ axis, $c = \sqrt{\frac{c_{31}^D}{\rho}}$, and the wave number in 31 mode, $\gamma = \frac{\omega}{c_1}$; the particle displacement $u_1$ is given by

$$u_1(x_1, t) = \hat{u}_1(x_1) e^{i\omega t} \tag{3.10}$$

where the general solution of the wave equation in terms of the in-plane displacement amplitude

$$\hat{u}_1(x_1) = C_1 \sin \gamma x_1 + C_2 \cos \gamma x_1 \tag{3.11}$$

The coefficients $C_1$ and $C_2$ are to be determined from the boundary conditions, i.e.

$$\begin{aligned} &\text{a-) } T_1(x_1 = L/2) = 0 \\ &\text{b-) } T_1(x_1 = -L/2) = 0 \end{aligned} \tag{3.12}$$

Note the strain-displacement relation, $S_1 = \frac{\partial u_1}{\partial x_1} = u_1'$, and substitute the general solution in Eq. (3.11) into the piezoelectric constitutive equation in Eq. (3.6)a to obtain

$$T_1 = c_{11}^D \gamma \left( C_1 \cos \gamma x_1 - C_2 \sin \gamma x_1 \right) - h_{31} D_3 \tag{3.13}$$

Impose the boundary conditions to obtain the following system of equations

$$T_1(x_1 = \frac{L}{2}) = c_{11}^D \gamma \left( C_1 \cos \frac{1}{2} \gamma L - C_2 \sin \frac{1}{2} \gamma L \right) - h_{31} D_3 = 0 \tag{3.14}$$

$$T_1(x_1 = -\frac{L}{2}) = c_{11}^D \gamma \left( C_1 \cos \frac{1}{2} \gamma L + C_2 \sin \frac{1}{2} \gamma L \right) - h_{31} D_3 = 0 \tag{3.15}$$

Addition of Eq. (3.14) and Eq. (3.15) will result in

$$C_1 = \frac{h_{31}D_3}{\gamma c_{11}^D \cos\frac{1}{2}\gamma L} \tag{3.16}$$

and $C_2 = 0$ since $\sin\frac{1}{2}\gamma L$ is assumed to be non-trivial term. Recall the particle displacement $u_1$ to get the solution in terms of the displacement amplitude

$$\hat{u}_1(x_1) = \frac{h_{31}D_3}{\gamma c_{11}^D \cos\gamma\frac{L}{2}} \sin\gamma x_1 \tag{3.17}$$

and the strain amplitude

$$\hat{S}_1 = \hat{u}_1{}' = \frac{h_{31}D_3}{c_{11}^D \cos\gamma\frac{L}{2}} \cos\gamma x_1 \tag{3.18}$$

### 3.2.2 ELECTRICAL RESPONSE UNDER CONSTANT ELECTRIC DISPLACEMENT ASSUMPTION

The electrical impedance can be expressed as division of the voltage by the current; $Z = \frac{V}{I}$ and the voltage and the current are respectively

$$\begin{aligned} &\text{a-) } V = \int_0^t E_3 dx_3 \\ &\text{b-) } I = \frac{d}{dt}\int_A D_3 dA = i\omega D_3 bL \end{aligned} \tag{3.19}$$

Recall the second constitutive equation and substitute Eq. (3.17) into the equation to get the expression for the electric field

$$E_3 = -\frac{h_{31}^2 D_3}{c_{11}^D \cos\gamma\frac{L}{2}} \cos\gamma x_1 + \beta_{33}^S D_3 \tag{3.20}$$

From the relations provided in Eq. (3.7) and Eq. (3.8), one can come up with the expression, ${h_{31}}^2 = \left( \frac{\beta_{33}^S d_{31}}{s_{11}^D} \right)^2$, and plug it into Eq. (3.20) noting that $c_{31}^D = 1/s_{31}^D$ and introduce the electro mechanical coupling coefficient , $\kappa_{31}$, defined as $\kappa_{31}^2 = \frac{d_{31}^2}{s_{11}^E \varepsilon_{33}^T}$ (IEEE standard pg 39). Note that the superscripts of the parameters in the denominator of $\kappa_{31}$ are not the same as those superscripts of the parameters of $h_{31}$ therefore they should be equated to replace $h_{31}$ term with $\kappa_{31}$ in Eq. (3.20). Thus taking the relations in Eq. (3.8),

$$\kappa_{31}^2 = \frac{d_{31}^2}{s_{11}^E \varepsilon_{33}^T} = \frac{d_{31}^2 \beta_{33}^S}{s_{11}^D} \left( \frac{1 - g_{31} e_{31}}{1 + d_{31} h_{31}} \right) \tag{3.21}$$

Substitute the relations $e_{31} = d_{31} / s_{31}^D$ and $h_{31} = g_{31} / s_{31}^D$ into Eq. (3.21) and rearrange to obtain this form

$$\kappa_{31}^2 = \frac{d_{31}^2}{s_{11}^E \varepsilon_{33}^T} = \frac{d_{31}^2 \beta_{33}^S}{s_{11}^D} \left( \frac{s_{11}^D - g_{31} d_{31}}{s_{11}^D + g_{31} d_{31}} \right) \tag{3.22}$$

Now replace $h_{31}$ term with $\kappa_{31}$ in Eq. (3.20) and rearrange to form the electric field expression

$$E_3 = \beta_{33}^S D_3 \left( 1 - \kappa_{31}^2 \left( \frac{s_{11}^D + g_{31} d_{31}}{s_{11}^D - g_{31} d_{31}} \right) \frac{\cos \gamma x_1}{\cos \gamma \frac{L}{2}} \right) \tag{3.23}$$

The numerical value of the term in the small parenthesis in Eq. (3.23) for APC-850 piezoelectric material can be found as 1.396 and the value only changes with the material properties and does not depend on frequency. Upon substitution of Eq. (3.23) into Eq. (3.19)a, we can derive the voltage expression

$$V=\int_0^t \beta_{33}^S D_3 dx_3-\left(\frac{s_{11}^D+g_{31}d_{31}}{s_{11}^D-g_{31}d_{31}}\right)\frac{\kappa_{31}^2\beta_{33}^S D_3}{\cos\gamma\frac{L}{2}}\int_0^t \cos\gamma x_1 dx_3 \tag{3.24}$$

$$V=\beta_{33}^S D_3 t\left[1-\left(\frac{s_{11}^D+g_{31}d_{31}}{s_{11}^D-g_{31}d_{31}}\right)\frac{\kappa_{31}^2}{\cos\left(\gamma\frac{L}{2}\right)}\left(\cos\left(\gamma x_1\right)\right)\right] \tag{3.25}$$

Integrate Eq. (3.25) over $x_1$ direction again since it seems variable along direction 1.

$$V=\beta_{33}^S D_3 t\left[1-\left(\frac{s_{11}^D+g_{31}d_{31}}{s_{11}^D-g_{31}d_{31}}\right)\frac{\kappa_{31}^2}{\cos\left(\gamma\frac{L}{2}\right)}\int_{-L/2}^{L/2}\left(\cos\left(\gamma x_1\right)\right)\right] \tag{3.26}$$

$$V=\beta_{33}^S D_3 t\left[1-\left(\frac{s_{11}^D+g_{31}d_{31}}{s_{11}^D-g_{31}d_{31}}\right)\frac{\kappa_{31}^2}{\gamma L\cos\gamma\frac{L}{2}}\left(\sin\gamma x_1\Big|_{-L/2}^{L/2}\right)\right] \tag{3.27}$$

After rearrangement, we obtain the final expression of the voltage

$$V=\beta_{33}^S D_3 t\left[1-\kappa_{31}^2\left(\frac{s_{11}^D+g_{31}d_{31}}{s_{11}^D-g_{31}d_{31}}\right)\frac{\sin\gamma\frac{L}{2}}{\gamma\frac{L}{2}\cos\gamma\frac{L}{2}}\right] \tag{3.28}$$

Recall the current-charge relation, $I=\dot{Q}=\partial Q/\partial t$ and part b of Eq. (3.19)

$$I=i\omega D_3 bL \tag{3.29}$$

Substituting Eq. (3.29) into the impedance, $Z=V/I$, we can now derive the electromechanical impedance for in-plane mode under constant electric displacement assumption

$$Z = \frac{\beta_{33}^S t}{i\omega bL}\left[1-\kappa_{31}^2\left(\frac{s_{11}^D + g_{31}d_{31}}{s_{11}^D - g_{31}d_{31}}\right)\frac{1}{\gamma\frac{L}{2}\cot\gamma\frac{L}{2}}\right] \tag{3.30}$$

Introducing $\varphi = \frac{1}{2}\gamma L$ and substituting into Eq. (3.30) yields

$$Z = \frac{V}{I} = \frac{\beta_{33}^S t}{i\omega bL}\left[1-\kappa_{31}^2\left(\frac{s_{11}^D + g_{31}d_{31}}{s_{11}^D - g_{31}d_{31}}\right)\frac{1}{\varphi\cot\varphi}\right] \tag{3.31}$$

Recalling the capacitance of the material $C_0 = \frac{bL}{t\beta_{33}^S}$ and substituting into Eq. (3.31) also yields

$$Z = \frac{V}{I} = \frac{1}{i\omega C_0}\left[1-\kappa_{31}^2\left(\frac{s_{11}^D + g_{31}d_{31}}{s_{11}^D - g_{31}d_{31}}\right)\frac{1}{\varphi\cot\varphi}\right] \tag{3.32}$$

$$\left(\frac{s_{11}^D + g_{31}d_{31}}{s_{11}^D - g_{31}d_{31}}\right) \approx 1 \tag{3.33}$$

Since $g_{31}d_{31} = \left(-12.4x10^{-3}\right).\left(-175x10^{-12}\right) = 2170x10^{-15} \approx 0$ for PWAS denoted as APC 850. Then final form of the in-plane electromechanical impedance under constant electric displacement assumption can be expressed

$$Z = \frac{V}{I} = \frac{1}{i\omega C_0}\left[1-\kappa_{31}^2\frac{1}{\varphi\cot\varphi}\right] \tag{3.34}$$

### 3.2.3 EFFECT OF INTERNAL DAMPING

Table 3.1 Properties of APC 850 piezoelectric ceramic (www.americanpiezo.com).

| Property | $\rho$ (kg/m$^3$) | $d_{33}$ (m/V) | $d_{31}$ (m/V) | $g_{33}$ (Vm/N) | $g_{31}$ (Vm/N) | $s_{33}^E$ (m$^2$/N) | $s_{11}^E$ (m$^2$/N) | $\varepsilon_{33}^T/\varepsilon_0$ | $\kappa_p$ | $\kappa_{33}$ | $\kappa_{31}$ | $\nu$ |
|---|---|---|---|---|---|---|---|---|---|---|---|---|
| **APC 850** | 7700 | 400x10$^{-12}$ | -175x10$^{-12}$ | 26x10$^{-3}$ | -12.4x10$^{-3}$ | 17.3 x10$^{-12}$ | 15.3 x10$^{-12}$ | 1750 | 0.63 | 0.72 | 0.36 | 0.35 |

Piezoelectric material constants are given in Table 3.1 for APC 850 type PWAS and the PWAS EMIS models are based on these constants. The internal damping can be modeled analytically by complex compliance and dielectric constant

$$\begin{aligned}\bar{s}_{11} &= s_{11}(1-i\eta)\\ \bar{\varepsilon}_{33} &= \varepsilon_{33}(1-i\delta)\\ \bar{\beta}_{33} &= \beta_{33}(1-i\delta)\end{aligned} \tag{3.35}$$

The electromechanical resonance in in-plane, $d_{31}$, mode shows up at low frequency range. The internal damping is implied even in free PWAS case (whose boundaries are unbounded) of the in-plane mode in order to determine the impedance and admittance results assuming $\eta$ and $\delta$ are smaller than $5\%$. The admittance and impedance become complex expressions.

$$\bar{Z} = \frac{1}{i\omega\bar{C}_0}\left[1-\bar{\kappa}_{31}^2\left(\frac{\bar{s}_{11}+g_{31}d_{31}}{\bar{s}_{11}-g_{31}d_{31}}\right)\frac{1}{\bar{\varphi}\cot\bar{\varphi}}\right] \tag{3.36}$$

where $\bar{\kappa}_{31}^2 = \dfrac{d_{31}^2}{\bar{s}_{11}^E\bar{\varepsilon}_{33}} = \dfrac{d_{31}^2\bar{\beta}_{33}^S}{\bar{s}_{11}^D}\left(\dfrac{\bar{s}_{11}^D-g_{31}d_{31}}{\bar{s}_{11}^D+g_{31}d_{31}}\right)$ is the complex coupling factor, $\bar{C}_0 = (1-i\delta)C_0$, and $\bar{\varphi} = \varphi\sqrt{1-i\eta}$. As geometrical properties of the PWAS transducer, 7mm of length, 7mm of width, and 0.2mm of thickness are considered and the material properties are given in Table 3.1.

## 3.3 ANALYTICAL THICKNESS MODE EMIS MODEL UNDER CONSTANT $D_3$ ASSUMPTION

The general constitutive equations expressing the linear relation between stress-strain and stress-electric displacement in thickness mode are

$$\begin{aligned} &\text{(a)} \quad T_3 = c_{33}^D S_3 - h_{33} D_3 \\ &\text{(b)} \quad E_3 = -h_{33} S_3 + \beta_{33}^S D_3 \end{aligned} \tag{3.37}$$

The relations of the four piezoelectric constants to each other are in thickness mode as follows (Berlincourt et-al):

$$\begin{aligned} &\text{(a)} \quad d_{33} = \varepsilon_{33}^T g_{33} = e_{33} s_{33}^E \\ &\text{(b)} \quad g_{33} = \beta_{33}^T d_{33} = h_{33} s_{33}^D \\ &\text{(c)} \quad e_{33} = \varepsilon_{33}^S h_{33} = d_{33} c_{33}^E \\ &\text{(d)} \quad h_{33} = \beta_{33}^S e_{33} = g_{33} c_{33}^D \end{aligned} \tag{3.38}$$

### 3.3.1 MECHANICAL RESPONSE IN THICKNESS MODE

Under 1-D assumption, the out-of-plane (thickness) mode wave equation can be expressed

$$\frac{\partial^2 u_3}{\partial t^2} = \frac{c_{33}^D}{\rho} \frac{\partial^2 u_3}{\partial x_3^2} \tag{3.39}$$

Introducing the wave speed in direction of $x_3$ axis, $c_3 = \sqrt{\frac{c_{33}^D}{\rho}}$, and the wave number in thickness mode, $\gamma_t = \frac{\omega}{c_3}$ yields the particle displacement $u_3$ that is given by

$$u_3(x_3, t) = \hat{u}_3(x_3) e^{i\omega t} \tag{3.40}$$

where the general solution, i.e.

$$\hat{u}_3(x_3) = C_1 \sin\gamma_t x_3 + C_2 \cos\gamma_t x_3 \tag{3.41}$$

The coefficients $C_1$ and $C_2$ are to be determined from the boundary conditions to obtain the particular solution; the stress-free boundary conditions are

$$\begin{aligned} &\text{a-) } T_3(x_3 = t/2) = 0 \\ &\text{b-) } T_3(x_3 = -t/2) = 0 \end{aligned} \tag{3.42}$$

Note that $S_3 = \dfrac{\partial u_3}{\partial x_3} = u_3'$ and substitute Eq. (3.11) into Eq. (3.6)a to get

$$T_3 = c_{33}^D \gamma_t \left( C_1 \cos\gamma_t x_3 - C_2 \sin\gamma_t x_3 \right) - h_{33} D_3 \tag{3.43}$$

Imposing the stress-free boundary conditions yields the following equation system

$$T_3(x_3 = \frac{t}{2}) = c_{33}^D \gamma_t \left( C_1 \cos\frac{1}{2}\gamma_t t - C_2 \sin\frac{1}{2}\gamma_t t \right) - h_{33} D_3 = 0 \tag{3.44}$$

$$T_3(x_3 = -\frac{t}{2}) = c_{33}^D \gamma_t \left( C_1 \cos\frac{1}{2}\gamma_t t + C_2 \sin\frac{1}{2}\gamma_t t \right) - h_{33} D_3 = 0 \tag{3.45}$$

Addition of Eq. (3.14) and Eq. (3.15) will result in

$$C_1 = \frac{h_{33} D_3}{\gamma_t c_{33}^D \cos\frac{1}{2}\gamma_t t} \tag{3.46}$$

and $C_2 = 0$ since $\sin\frac{1}{2}\gamma_t t$ is assumed to be non-trivial term. Recall the particle displacement $u_3$

$$\hat{u}_3(x_3) = \frac{h_{33} D_3}{\gamma_t c_{33}^D \cos\gamma_t \frac{t}{2}} \sin\gamma_t x_3 \tag{3.47}$$

$$S_3 = \hat{u}_3{}' = \frac{h_{33} D_3}{c_{33}^D \cos\gamma_t \frac{t}{2}} \cos\gamma_t x_3 \tag{3.48}$$

### 3.3.2 ELECTRICAL RESPONSE UNDER CONSTANT ELECTRIC DISPLACEMENT ASSUMPTION

The electrical impedance can be expressed as division of the voltage by the current; $Z = \frac{V}{I}$ and the voltage and the current are respectively

$$\begin{aligned} &\text{a-) } V = \int_0^t E_3 dx_3 \\ &\text{b-) } I = \frac{d}{dt}\int_A D_3 dA = i\omega D_3 bl \end{aligned} \tag{3.49}$$

Recall the second constitutive equation and substitute Eq. (3.48) into Eq. (3.37)(b) to get the electric field expression

$$E_3 = -\frac{h_{33}^2 D_3}{c_{33}^D \cos\gamma_t \frac{t}{2}} \cos\gamma_t x_3 + \beta_{33}^s D_3 \tag{3.50}$$

Recalling the piezoelectric constant relations in Eq. (3.38). One can derive these relations $h_{33}{}^2 = \frac{e_{33}{}^2}{\varepsilon_{33}^{s\ 2}}$ using (3.7)(a); $\beta_{33}^s = \frac{1}{\varepsilon_{33}^s}$ using the combination of the part (d) and (c) of Eq. (3.38); and $e_{33} = \frac{d_{33}}{s_{33}^D}$ using part (a). Finally one can come up with the expression, $h_{33}{}^2 = \left(\frac{\beta_{33}^s d_{33}}{s_{33}^D}\right)^2$, and plug it into Eq. (3.20) noting that $c_{33}^D = 1/s_{33}^D$ and introduce the electro-mechanical coupling coefficient , $\kappa_{33}$, defined as $\kappa_{33}^2 = \frac{e_{33}^2}{c_{33}^D \varepsilon_{33}^S}$ (IEEE standard pg 39). Rearrange the Eq. (3.50) to obtain

$$E_3 = \beta_{33}^S D_3 \left( 1 - \kappa_{33}^2 \frac{\cos \gamma_t x_3}{\cos \gamma_t \frac{t}{2}} \right) \tag{3.51}$$

Upon substitution of Eq. (3.51) into Eq. (3.49)(a), we derive the voltage expression

$$V = \int_0^t \beta_{33}^S D_3 dx_3 - \frac{\kappa_{33}^2 \beta_{33}^S D_3}{\cos \gamma_t \frac{t}{2}} \int_0^t \cos \gamma_t x_3 dx_3 \tag{3.52}$$

$$V = \beta_{33}^S D_3 t \left[ 1 - \frac{\kappa_{33}^2}{\gamma_t t \cos \gamma_t \frac{t}{2}} \left( \sin \gamma_t x_3 \Big|_{-t/2}^{t/2} \right) \right] \tag{3.53}$$

After rearrangement, the voltage expression takes form

$$V = \beta_{33}^S D_3 t \left[ 1 - \kappa_{33}^2 \frac{1}{\frac{1}{2} \gamma_t t \cot \gamma_t \frac{t}{2}} \right] \tag{3.54}$$

Recall the electric current charge relation $I = \dot{Q} = \partial Q / \partial t$ and part (b) of Eq. (3.49) to have

$$I = i\omega D_3 bl \tag{3.55}$$

Substituting Eq. (3.54) into the impedance $Z = V / I$ yields

$$Z = \frac{\beta_{33}^S t}{i\omega bl} \left[ 1 - \kappa_{33}^2 \frac{1}{\frac{1}{2} \gamma_t t \cot \gamma_t \frac{t}{2}} \right] \tag{3.56}$$

Introduce $\varphi = \frac{1}{2} \gamma_t t$ and substitute to get

$$Z = \frac{V}{I} = \frac{\beta_{33}^S t}{i\omega bl} \left[ 1 - \kappa_{33}^2 \frac{1}{\varphi \cot \varphi} \right] \tag{3.57}$$

Recall the capacitance of the material $C_0 = \dfrac{bl}{t\beta_{33}^S}$ to eventually obtain the thickness mode electromechanical impedance equation under constant electric displacement assumption

$$Z = \frac{V}{I} = \frac{1}{i\omega C_0}\left[1 - \kappa_{33}^2 \frac{1}{\varphi \cot \varphi}\right] \tag{3.58}$$

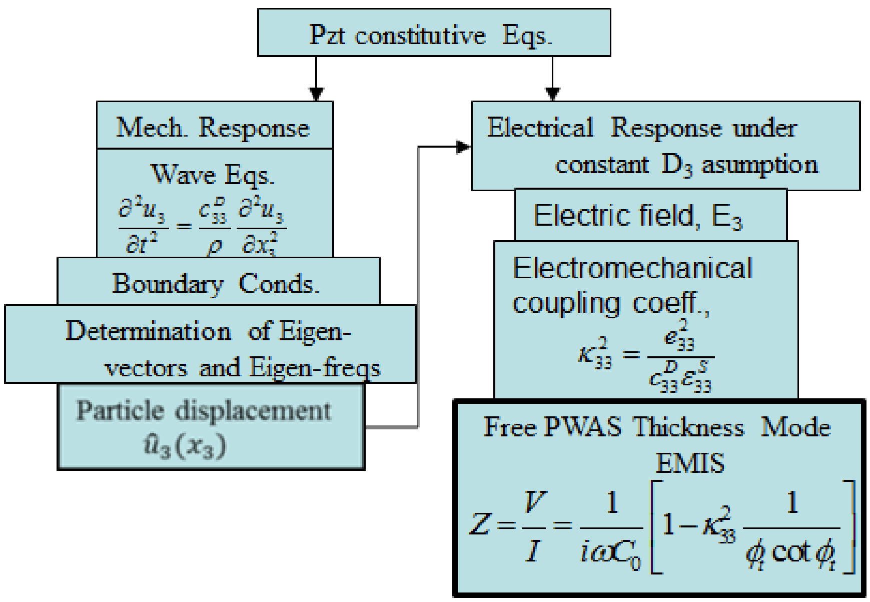


Figure 3.4 Flow chart of the 1-D analytical thickness mode EMIS for free PWAS.

As seen in the flow-chart (Figure 3.4), the analytical model begins with the piezoelectric constitutive equations, then the mechanical response is derived in terms of the particle displacement in PWAS implying traction-free boundary conditions to solve the wave equations. In the second part, the electrical response is derived under constant electrical displacement assumption to solve the second piezoelectric constitutive equation for the electrical field. Finally, implying the electromechanical coupling coefficient the close form solution for the free PWAS thickness mode E/M impedance can be expressed as a function of frequency. The real part of the thickness mode impedance and the admittance are presented in for 0.2mm thick and 7mm diameter PWAS are presented in Figure 3.5.

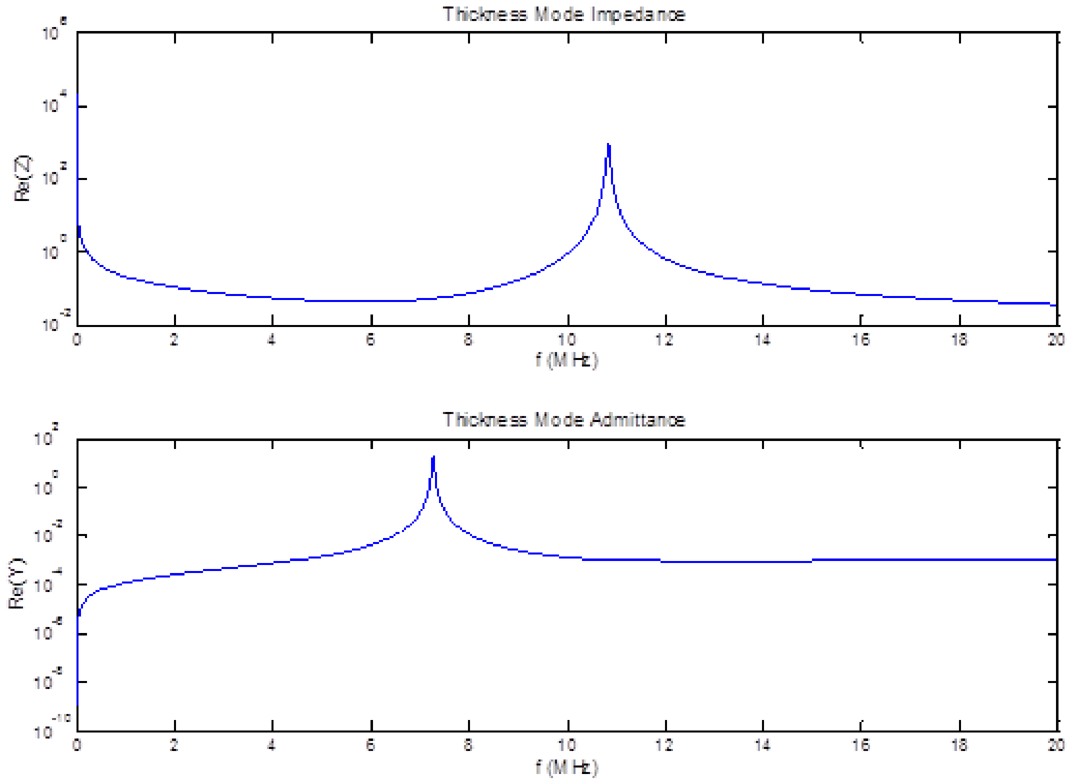


Figure 3.5 Real part of the impedance and the admittance for 0.2mm thick and 7mm diameter PWAS in out of plane (thickness) mode.

## 3.4 ANALYTICAL THICKNESS MODE EMIS MODEL UNDER CONSTANT $E_3$ ASSUMPTION

In this section, the behavior of a free PWAS in thickness mode will be addressed. The PWAS induced by the thickness polarization electric field, $E_3$ which is generated by harmonic voltage $V(t) = \hat{V}e^{i\omega t}$ between the top and bottom surface electrodes. $E_3$ is assumed to be uniform over the piezoelectric wafer as schematically illustrated in Figure 3.6. Thus, its derivative with respect to transversal axis is zero i.e. $\partial E_3 / \partial x_3 = 0$. The voltage excitation is harmonic so that the electric field $E_3 = \hat{E}_3 e^{i\omega t}$ and the mechanical response in terms of particle displacement are also harmonic, i.e. $u_3(x_3,t) = \hat{u}_3(x_3)e^{i\omega t}$ where $\hat{u}_3(x_3)$ is the complex amplitude that incorporates any phase difference between the excitation and response.

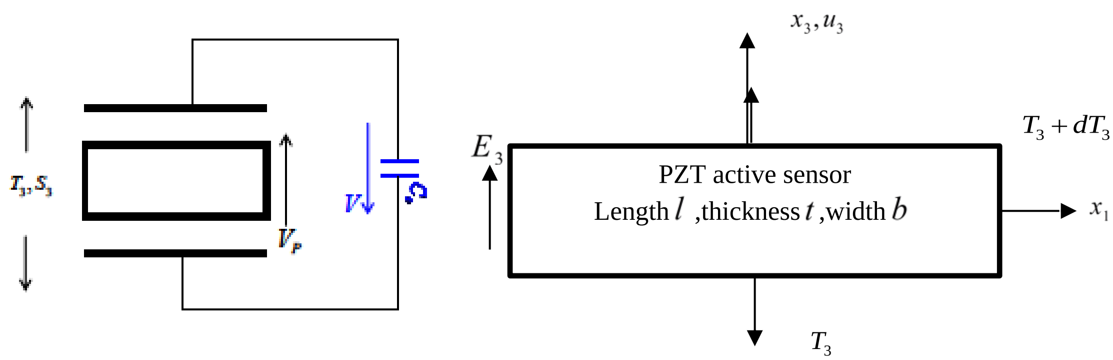


Figure 3.6 Schematic of thickness mode of a piezoelectric wafer active sensor and infinitesimal axial element.

The general constitutive equations expressing the linear relation between stress-strain and stress-electric displacement in thickness mode are

$$S_3 = s_{33}^E T_3 + d_{33} E_3 \tag{3.59}$$

$$D_3 = d_{33} T_3 + \varepsilon_{33}^T E_3 \tag{3.60}$$

where $S_3$ is the strain, $T_3$ is the stress, $D_3$ is the electrical displacement (charge per unit area), $s_{33}^E$ is the mechanical compliance at zero electric field, $\varepsilon_{33}^T$ is the dielectric constant at zero stress, $d_{33}$ is the induced strain coefficient (mechanical strain per unit electric field). Recalling Newton's law of motion, one can derive the differential equation(3.63).

$$\Sigma F = m.a \tag{3.61}$$

under 1-D assumption, use the transversal stresses on infinitesimal element of PWAS

$$(T_3 + dT_3 - T_3)Adx_3 = \rho Adx_3\ddot{u}(x_3, t) \tag{3.62}$$

$$T_3' = \rho\ddot{u}(x_3, t) \tag{3.63}$$

and recall the strain-displacement relation

$$S_3 = u_3' \tag{3.64}$$

Differentiate the Eq. (3.59) with respect to $x_3$ and since $\partial E_3 / \partial x_3 = 0$, the strain rate becomes

$$S_3{}' = s_{33}^E T_3{}' \tag{3.65}$$

Substituting the Eq. (3.63) and Eq. (3.64) into Eq. (3.65) yields

$$u_3'' = s_{33}^E \rho \ddot{u}_3 \tag{3.66}$$

Introduce the transversal wave speed of the material

$$c_3{}^2 = \frac{1}{\rho s_{33}^E} \tag{3.67}$$

and substitute into Eq. (3.66) thus, 1D wave equation can be written as

$$\ddot{u}_3 = c_3{}^2 u_3'' \tag{3.68}$$

The general solution of the wave equation is in harmonic wave form

$$u_3(x_3, t) = \hat{u}_3(x_3)e^{i\omega t} \tag{3.69}$$

where the general solution in terms of the displacement amplitude

$$\hat{u}_3(x_3) = C_1 \sin\gamma_t x_3 + C_2 \cos\gamma_t x_3 \tag{3.70}$$

and the wave number is introduced as the ratio between the angular frequency and the wave speed in thickness direction.

$$\gamma_t = \frac{\omega}{c_3} \tag{3.71}$$

### 3.4.1 MECHANICAL RESPONSE IN THICKNESS MODE

Starting from the constitutive equation under the 1-D assumption

$$S_3 = s_{33}^E T_3 + d_{33} E_3 \tag{3.72}$$

Electric field can be explicitly expressed for the thickness mode

$$E_3 = \frac{V}{t + \left( u_3\left(\frac{1}{2}t\right) - u_3\left(-\frac{1}{2}t\right)\right)} \tag{3.73}$$

where $u_3\left(\pm\frac{1}{2}t\right)$ is displacement oriented in thickness mode on top and bottom surfaces of PWAS resonator. For the free-PWAS, the stress-free boundary conditions ($T_3\left(\pm\frac{1}{2}t\right) = 0$) can apply to the strain equation. Substitution of Eq(3.73) into Eq(3.72) under stress-free boundary conditions yields

$$\hat{S}_3\left(-\frac{1}{2}t\right) = d_{33}\frac{\hat{V}}{t + \left( \hat{u}_3\left(\frac{1}{2}t\right) - \hat{u}_3\left(-\frac{1}{2}t\right)\right)} \tag{3.74}$$

The difference between the particle displacements on top and bottom surfaces is infinitesimally small the one can assume

$$u_3\left(\frac{1}{2}t\right) - u_3\left(-\frac{1}{2}t\right) \approx 0 \tag{3.75}$$

Then Eq. (3.74) takes form as

$$\hat{S}_3\left(-\frac{1}{2}t\right) = d_{33}\frac{\hat{V}}{t} \tag{3.76}$$

$$\hat{S}_3\left(-\frac{1}{2}t\right) = \hat{u}_3'\left(-\frac{1}{2}t\right) = \gamma_t\left(C_1\cos\gamma_t\frac{1}{2}t + C_2\sin\gamma_t\frac{1}{2}t\right) = d_{33}\frac{\hat{V}}{t} \tag{3.77}$$

$$\hat{S}_3\left(\frac{1}{2}t\right) = \hat{u}_3'\left(\frac{1}{2}t\right) = \gamma_t\left(C_1\cos\gamma_t\frac{1}{2}t - C_2\sin\gamma_t\frac{1}{2}t\right) = d_{33}\frac{\hat{V}}{t} \tag{3.78}$$

Summation of the Eq. (3.77) and Eq. (3.78) yields

$$\gamma_t C_1\cos\gamma_t\frac{1}{2}t = d_{33}\frac{\hat{V}}{t} \tag{3.79}$$

then

$$C_1 = \frac{d_{33}}{\gamma_t t}\frac{\hat{V}}{\cos\gamma_t\frac{1}{2}t} \tag{3.80}$$

$$\gamma_t C_1\sin\gamma_t\frac{1}{2}t = 0 \tag{3.81}$$

assuming $\sin\gamma_t\frac{1}{2}t \neq 0$, we obtain

$$C_2 = 0 \tag{3.82}$$

Substitution of Eq. (3.80) and Eq. (3.82) into Eq. (3.11) yields

$$\hat{u}_3(x_3) = \frac{d_{33}\hat{V}}{\gamma_t t}\frac{\sin\gamma_t x_3}{\cos\gamma_t\frac{1}{2}t} \tag{3.83}$$

or with substitution of the expression $\hat{E}_3 = \hat{V}/t$

$$\hat{u}_3(x_3) = \frac{d_{33}\hat{E}_3}{\gamma_t}\frac{\sin\gamma_t x_3}{\cos\gamma_t\frac{1}{2}t} \tag{3.84}$$

Recalling stress-displacement relation in Eq(3.64), we obtain

$$\hat{S}_3(x_3) = \hat{u}_3'(x_3) = d_{33}\hat{E}_3\frac{\cos\gamma_t x_3}{\cos\gamma_t\frac{1}{2}t} \tag{3.85}$$

### 3.4.2 ELECTRICAL RESPONSE UNDER CONSTANT ELECTRIC FIELD ASSUMPTION

$$D_3 = d_{33}T_3 + \varepsilon_{33}^T E_3 \tag{3.86}$$

Upon substitution of the strain-displacement relation of Eq. (3.64) into the first of the constitutive equations

$$u_3' = s_{33}^E T_3 + d_{33}E_3 \tag{3.87}$$

and solving Eq. (3.87) for $T_3$ yields

$$T_3 = \frac{u_3'}{s_{33}^E} - \frac{d_{33}E_3}{s_{33}^E} \tag{3.88}$$

Substituting Eq. (3.88) into Eq. (3.86) yields the electric displacement expression, i.e.

$$D_3 = \frac{d_{33}}{s_{33}^E}u_3' - \frac{{d_{33}}^2 E_3}{s_{33}^E} + \varepsilon_{33}^T E_3 \tag{3.89}$$

In another form

$$D_3 = \varepsilon_{33}^T E_3 \left[1 - \kappa_{33}^2\left(1 - \frac{u_3'(x_3)}{d_{33}E_3}\right)\right] \tag{3.90}$$

Recall Eq.(3.85) and substitute it into Eq.(3.90) to get

$$D_3 = \varepsilon_{33}^T E_3 \left[1 - \kappa_{33}^2\left(1 - \frac{\cos\gamma_t x_3}{\cos\gamma_t t/2}\right)\right] \tag{3.91}$$

where $\kappa_{33}^2 = \frac{d_{33}^2}{s_{33}^E \varepsilon_{33}^T}$ is the electromechanical coupling coefficient. Integration of Eq. (3.90) over the electrodes area $A = bl$ yields the total charge

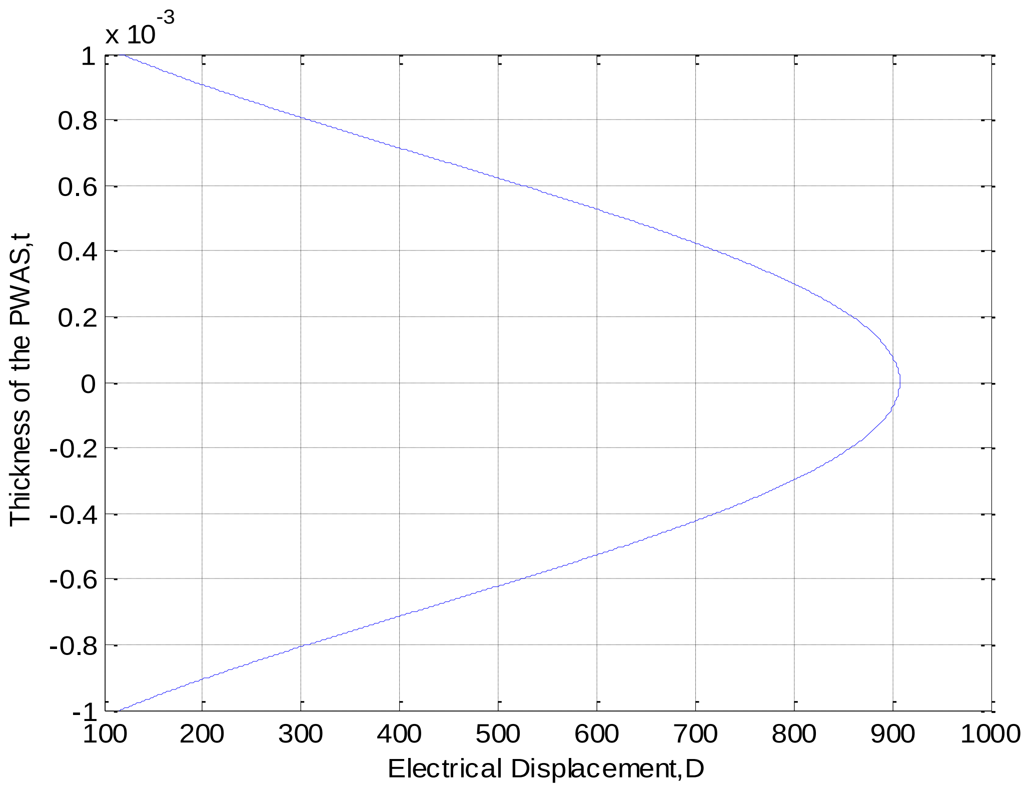


Figure 3.7 Electrical displacement change along the thickness of a square PWAS at frequency of 1 MHz.

The electrical displacement change along the thickness of a square PWAS at frequency of 1 MHz is presented in Figure 3.7. The varying electric displacement is determined under constant electric field assumption.

$$\hat{Q}(x_3) = \int_A D_3 dx_1 dx_2 = \int_{-l/2}^{l/2} \int_0^b D_3 dx_1 dx_2 = \varepsilon_{33}^T \hat{E}_3 bl \left[ 1 - \kappa_{33}^2 \left( 1 - \frac{\hat{u}_3'(x_3)}{d_{33}\hat{E}_3} \right) \right] \tag{3.92}$$

We introduce the equivalent charge expression by integrating the charge over thickness of the PWAS

$$\hat{Q}_{eq}(x_3) = \frac{1}{t} \int_{-t/2}^{t/2} \hat{Q}(x_3) dx_3 \tag{3.93}$$

Substituting Eq. (3.92) into the equivalent charge equation yields

$$\hat{Q}_{eq}(x_3) = \frac{1}{t}\int_{-t/2}^{t/2} \varepsilon_{33}^T \hat{E}_3 bl \left[1 - \kappa_{33}^2 \left(1 - \frac{\hat{u}_3'(x_3)}{d_{33}\hat{E}_3}\right)\right] dx_3 \tag{3.94}$$

Upon integration over thickness, we get

$$\hat{Q}_{eq}(x_3) = \frac{\varepsilon_{33}^T \hat{E}_3 bl}{t}\left[\left(1 - \kappa_{33}^2\right)t + \kappa_{33}^2 \frac{1}{d_{33}\hat{E}_3}\hat{u}_3(x_3)\Big|_{-\frac{1}{2}t}^{\frac{1}{2}t}\right] \tag{3.95}$$

$$\hat{Q}_{eq}(x_3) = \varepsilon_{33}^T \hat{E}_3 bl \left[1 - \kappa_{33}^2 + \kappa_{33}^2 \frac{\hat{u}_3(\frac{1}{2}t) - \hat{u}_3(-\frac{1}{2}t)}{d_{33}\hat{E}_3 t}\right] \tag{3.96}$$

Introduce the induced strain and induced displacement for the thickness mode

$$S_{ISA}^{(t)} = d_{33}\hat{E}_3 \tag{3.97}$$

$$u_{ISA}^{(t)} = S_{ISA}^{(t)} t = d_{33}\hat{E}_3 t \tag{3.98}$$

Upon substitution of Eq.(3.98) into Eq.(3.96), we obtain

$$\hat{Q}_{eq}(x_3) = \varepsilon_{33}^T \hat{E}_3 A \left[1 - \kappa_{33}^2 \left(1 - \frac{\hat{u}_3(\frac{1}{2}t) - \hat{u}_3(-\frac{1}{2}t)}{u_{ISA}^{(t)}}\right)\right] \tag{3.99}$$

where ISA denotes 'induced strain actuation' and the superscript $(t)$ denotes 'thickness mode'. Upon substitution of Eq.(3.84) into Eq.(3.99), we obtain

$$\hat{Q}_{eq}(x_3) = \varepsilon_{33}^T \hat{E}_3 A \left[1 - \kappa_{33}^2 \left(1 - \frac{\sin\frac{1}{2}\gamma_t t}{\frac{1}{2}\gamma_t t \cos\frac{1}{2}\gamma_t t}\right)\right] \tag{3.100}$$

Recall the capacitance of the material $C_0 = \dfrac{\varepsilon_{33}^T A}{t}$ and $\hat{E}_3 = \hat{V} / t$ then rearrange Eq.(3.100)

Then Eq.(3.100) takes the following form

$$\hat{Q}_{eq}(x_3) = C_0\hat{V}_3\left[1-\kappa_{33}^2+\kappa_{33}^2\frac{1}{\frac{1}{2}\gamma_t t\cot\frac{1}{2}\gamma_t t}\right] \tag{3.101}$$

The electric current is obtained as the time derivative of the electric charge i.e.

$$I = \dot{Q} = i\omega Q \tag{3.102}$$

Hence,

$$\hat{I} = i\omega C_0\hat{V}_3\left[1-\kappa_{33}^2+\kappa_{33}^2\frac{1}{\frac{1}{2}\gamma_t t\cot\frac{1}{2}\gamma_t t}\right] \tag{3.103}$$

The admittance, $Y$ , is defined as the fraction of current by voltage, i.e.

$$Y = \frac{I}{V} = i\omega C_0\left[1-\kappa_{33}^2+\kappa_{33}^2\frac{1}{\frac{1}{2}\gamma_t t\cot\gamma_t\frac{1}{2}t}\right] \tag{3.104}$$

Rearrange the admittance equation (3.104) introducing $\varphi = \frac{1}{2}\gamma_t t$

$$Y = i\omega C_0\left[1-\kappa_{33}^2\left(1-\frac{1}{\varphi\cot\varphi}\right)\right] \tag{3.105}$$

The impedance, $Z$ , is reciprocal of the admittance, i.e.,

$$Z = \frac{1}{i\omega C_0}\left[1-\kappa_{33}^2\left(1-\frac{1}{\varphi\cot\varphi}\right)\right]^{-1} \tag{3.106}$$

and the real part of the thickness mode impedance and admittance of free PWAS in size of 7mmx7mmx0.2mm are plotted in Figure 3.8.

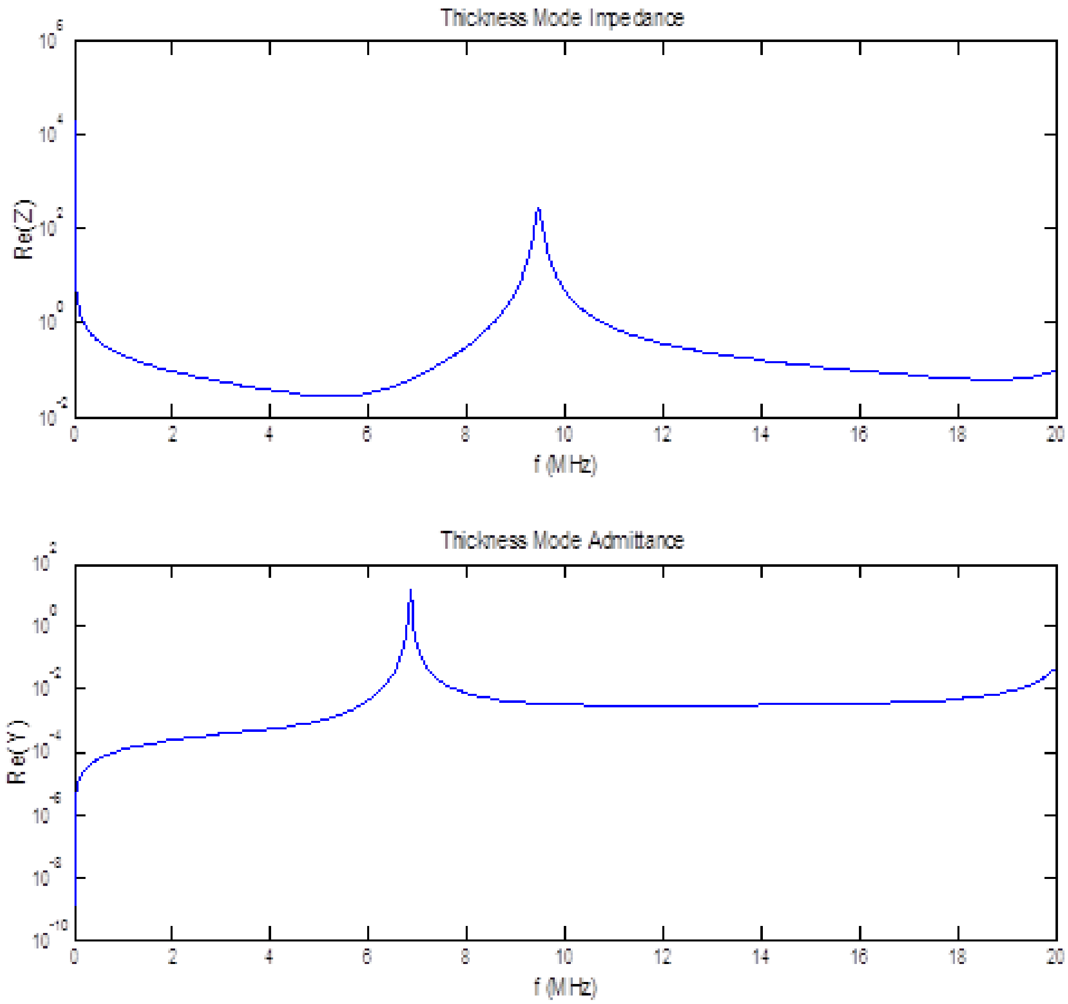


Figure 3.8 Real part of the impedance and the admittance for 0.2mm thick and 7mm diameter PWAS in out of plane (thickness) mode.

## 3.5 CASE STUDIES FOR FREE PWAS EMIS

This section includes the free PWAS experimental thickness mode impedance and admittance results and comparison with the analytical free PWAS thickness mode impedance results calculated under constant $D_3$ assumption by using the piezoelectric material properties. The thickness of the PWAS was measured to be 0.215 mm. The admittance measurement result for free square PWAS is illustrated in Figure 3.10 and focused on the thickness mode resonance peak at around 11.5 MHz.

The theoretically unexplained large peak also appears at around 3 MHz in admittance plot. This peak disappears as plotting the experimental impedance results. For free PWAS impedance results are relatively easy to be predicted by the analytical free PWAS thickness mode model with constant electrical displacement assumption. Therefore, one can see the perfect agreement between the experimental and analytical free PWAS-EMIS thickness mode results in Figure 3.9

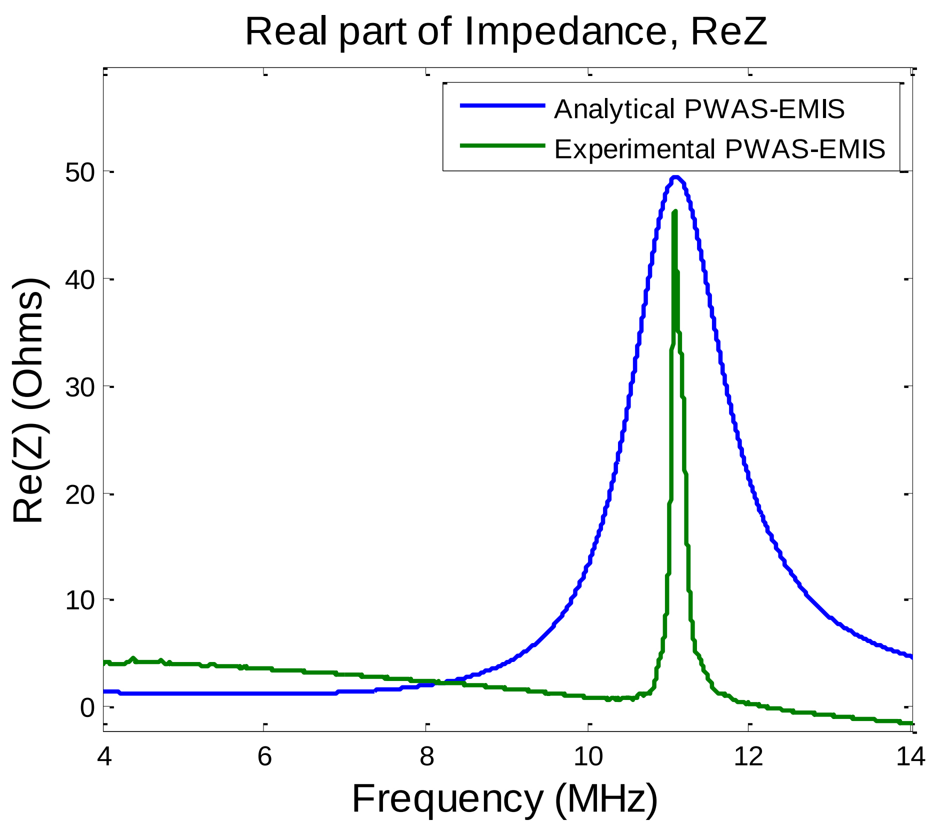


Figure 3.9 Comparison between analytical and experimental thickness mode impedance results.

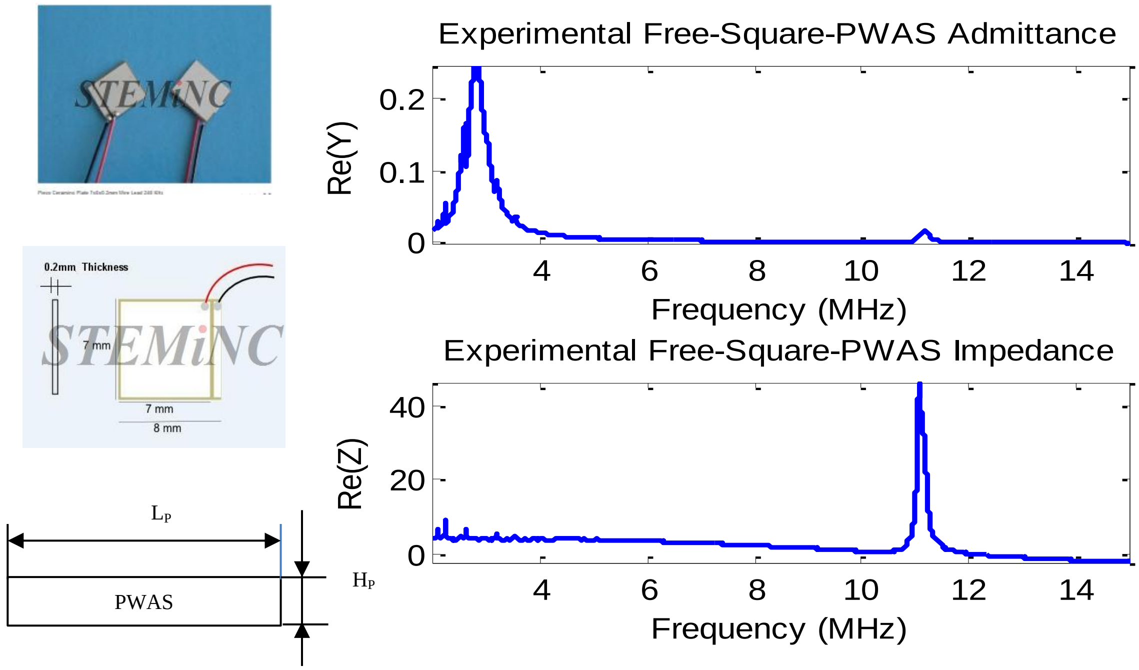


Figure 3.10 Illustration of schema and picture of square PWAS and admittance-impedance results for the free square PWAS.

Illustration of schema and picture of square PWAS and admittance/impedance measurements for the free square PWAS are presented in Figure 3.10. The trends which the admittance and impedance curves of free square PWAS follow are the same as those of circular PWAS. Admittance curve still has large mountain at around 2MHz and the thickness mode resonance frequency at around 11.5MHz. The thickness mode admittance is almost at the same frequency since the thickness of the square PWAS is almost same as that of circular PWAS.

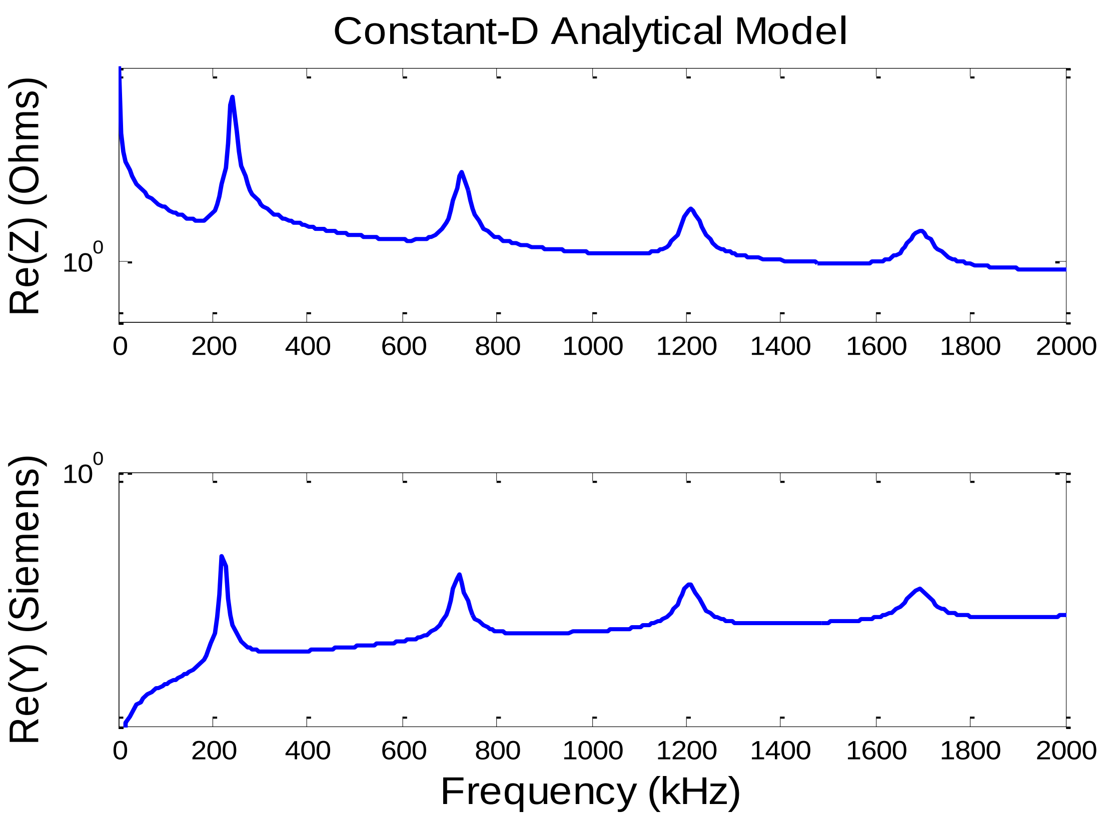


Figure 3.11 Analytical impedance and admittance simulation results for 7x7 mm$^2$ square 0.2 mm thick PWAS.

The results obtained from the analytical model of 1-D in-plane PWAS-EMIS under constant electrical displacement assumption are shown in terms of resonance (admittance) and anti-resonance (impedance) spectra in Figure 3.11.

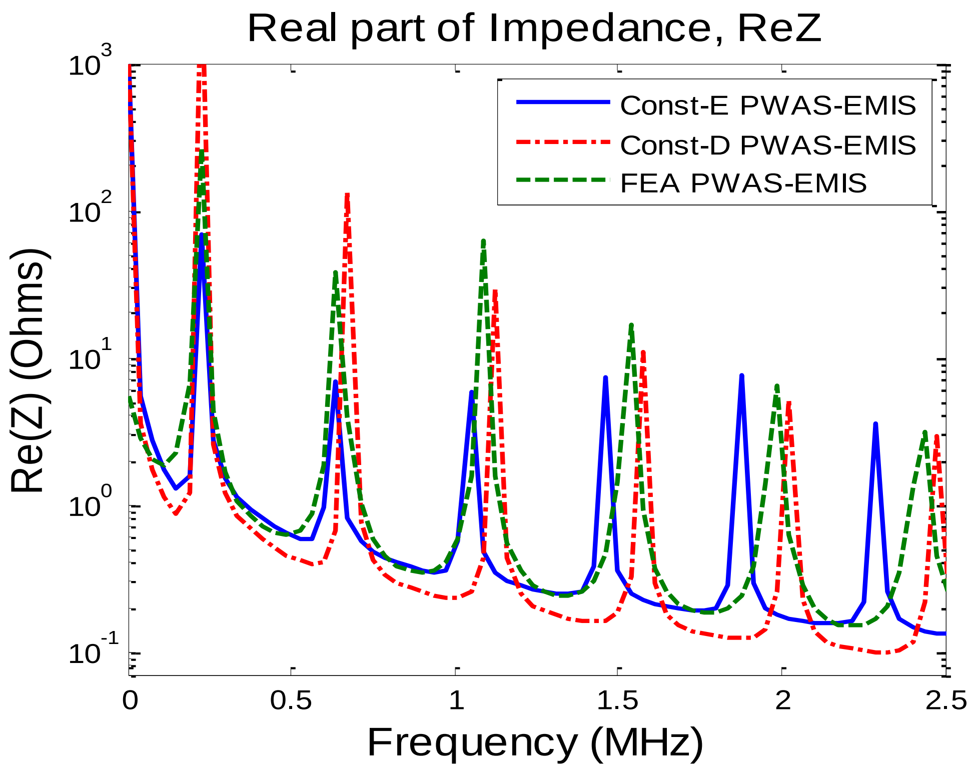


Figure 3.12 Impedance comparison for two 1-D analytical models regarding in-plane mode of PWAS resonator and 2-D finite element model for a 7 mm square 0.2 mm thick PWAS.

The analytical result from the in-plane EMIS model with the constant $D_3$ assumption is also compared with the corresponding analytical result for the constant $E_3$ assumption as well as the in-plane FEA PWAS-EMIS simulation results in Figure 3.12. The 1-D analytical and 2-D FEA in-plane PWAS-EMIS models collide at the first E/M impedance peak however discrepancies at higher overtone impedance peaks are observed as frequency increases. In this comparison, the impedance peaks from the model with constant D assumption, as frequency increases, has better agreement with the FEA simulation as opposed to the constant $E_3$ model in the frequency range of 2.5 MHz.

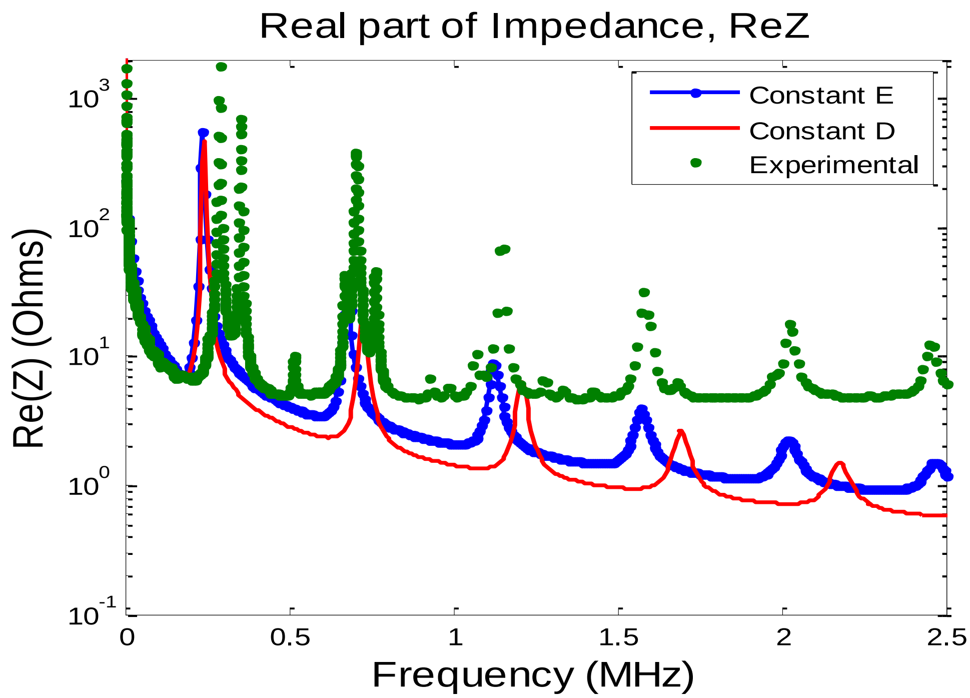


Figure 3.13 Impedance comparison for two models regarding in-plane mode of PWAS resonator and impedance measurement for a 7 mm square 0.2 mm thick PWAS under stress-free boundary condition.

The both in-plane 1-D PWAS-EMIS analytical simulation results from the in-plane EMIS model with the constant $D_3$ assumption with the corresponding analytical result for the constant $E_3$ assumption are validated by the experimental results in Figure 3.13. The both EMIS models collide at the first E/M impedance peak however a frequency shifts can be observed at the other peaks. In this comparison, the impedance peaks from the model with constant E assumption, as frequency increases, appears to be closer to the experimental E/M impedance measurement as opposed to the constant $D_3$ model in the frequency range of 2.5 MHz.

### 3.5.2 Comparison of Thickness Mode EMIS Models

This section compares two impedance results for two thickness mode models for a PWAS resonator. One model assumes that $E_3$ is uniform over the piezoelectric wafer whereas the other model assumes $D_3$ the electrical displacement (charge per unit area) as a constant value. The both results are shown in Figure 3.14.

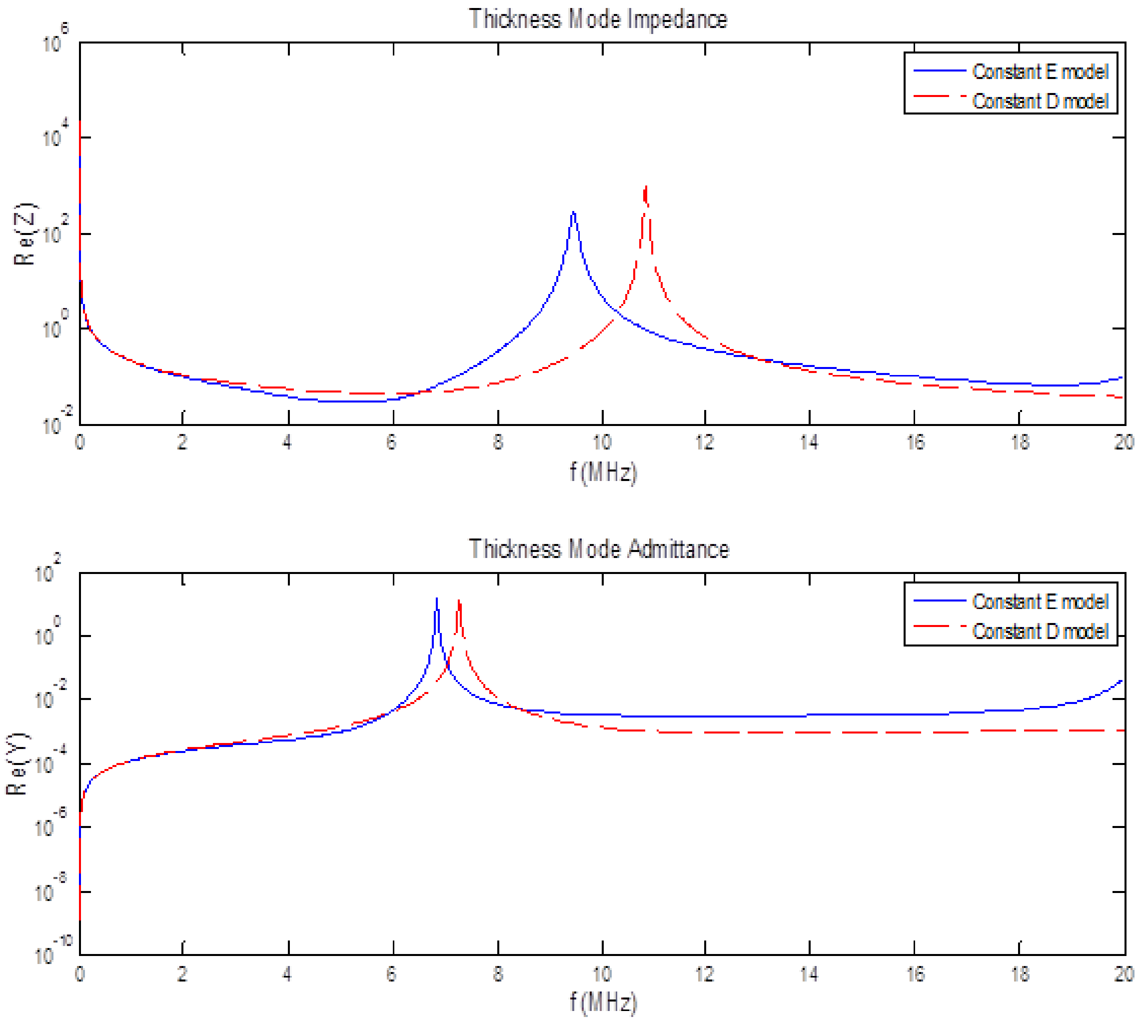


Figure 3.14 The comparison of the real part of the impedance and admittance results for both thickness mode analytical models for a 0.2 thick and 7 mm round PWAS resonator.

As seen some discrepancy occurs in impedance curves. The model which considers D constant has an anti-resonance peak at around 11 MHz while that of the other model is at a frequency lower than 10 MHz. From the experimental results for the 0.2 thick and 7mm round PWAS, we can conclude that the thickness mode impedance result for the constant D model has a better agreement with the experimental data than that for the other model as can be observed in Figure 3.15.

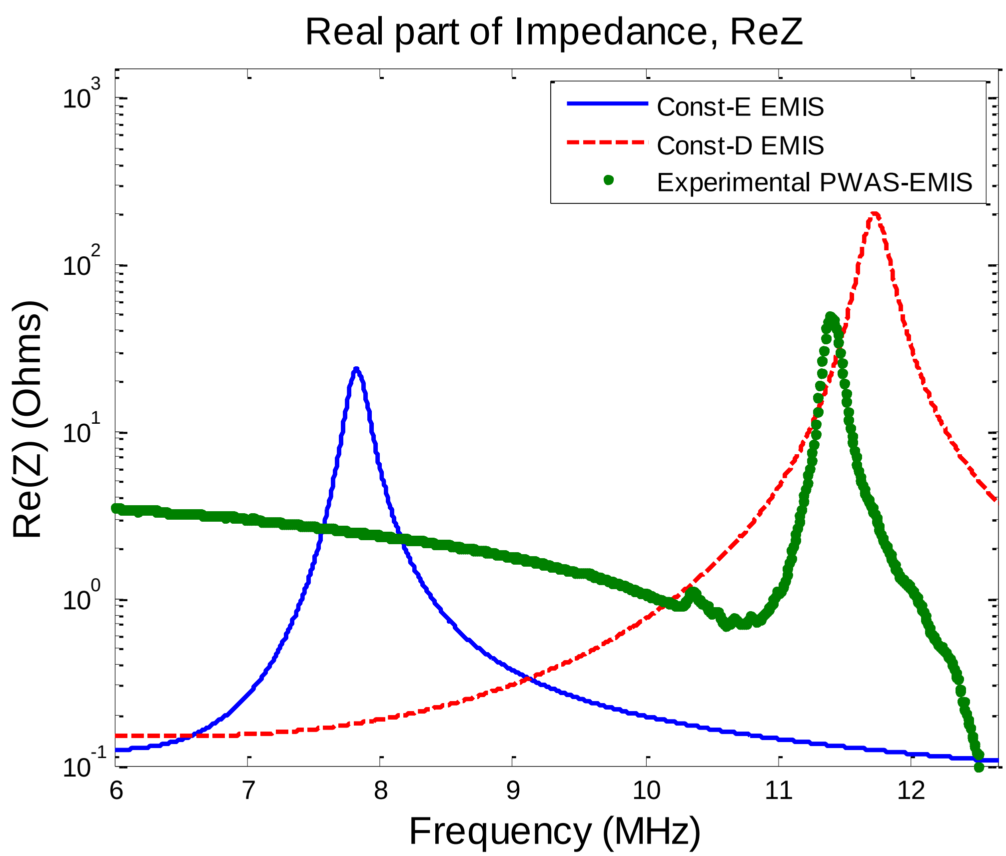


Figure 3.15 Experimental results of the impedance for 0.2 thick APC-850 PWAS resonator.

## 3.6 SUMMARY AND CONCLUSIONS

1-D analytical, 2-D finite element analyses are carried out for free PWAS-EMIS and the results obtained from the theoretical development are verified by comparison with the results from the corresponding measurements. Two main electrical assumptions in the electrical analyses are adopted to develop the in-plane and thickness modes of E/M impedance spectra.

To conclude, the constant electrical field assumption gives better results in in-plane EMIS prediction whereas the constant electrical displacement assumption brings better agreement in thickness mode with the experimental measurements.

# CHAPTER 4

# BEHAVIOR OF FREE PWAS AT ELEVATED TEMPERATURE

This chapter presents a literature survey to assess prior work the survivability of piezoelectric wafer active sensors (PWAS) at elevated temperature. Also, we could discover from the literature the extent of temperature dependence of the electric parameters, i.e. $d_{31}$ and $g_{31}$, and the elastic parameters, i.e. $s_{11}$ and Young's modulus ($c_{11}$), of different piezoelectric materials. Some preliminary results from parametric studies regarding PWAS-EMIS affected by changes in the piezoelectric wafer material properties were obtained by an analytical 1-D PWAS and 2-D circular PWAS impedance simulation. Then, the results from the experimental cycling of PWAS at gradually increasing temperatures are discussed. Trends of the results in terms of static capacitance, $C_0$ and electromechanical impedance spectroscopy (EMIS) are presented.

## 4.1 STATE OF THE ART

In Laboratory for Active Materials and Smart Structures (LAMSS), two researches regarding survivability of PWAS at extreme environments such as at cryogenic and high temperature had been conducted. Bottai & Giurgiutiu (2012) evaluated the structural health monitoring capability of PWAS on composite structures at cryogenic temperatures. They used EMIS method to qualify PWAS for cryogenic temperatures using PWAS instrumented composite specimens dipped in liquid nitrogen (Lin et-al., 2010). Then damage detection experiments were performed on laboratory-scale composite specimens with impact damage and built-in Teflon patches simulating delaminations. A comprehensive damage detection test was performed on a full-scale specimen subjected to pressure and cryogenic temperature cycles.

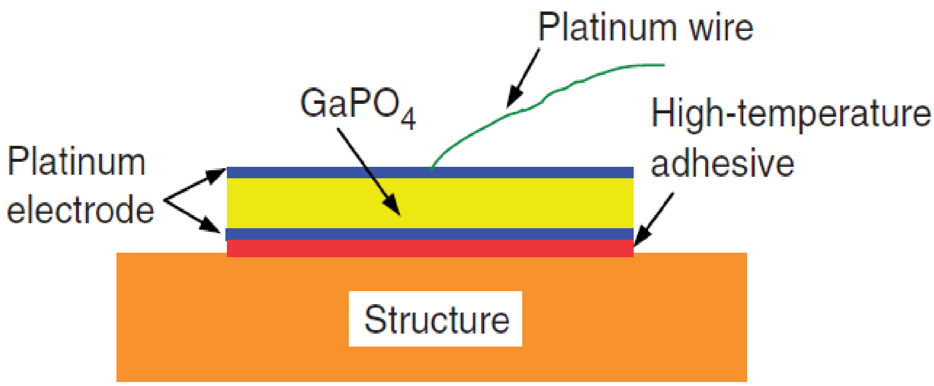


Figure 4.1 X-cut GaPO4 PWAS wafers comprised of a single crystal disks of 7mm diameter and 0.2mm thickness single crystal discs.

Another research aimed to develop and test a custom high-temperature PWAS (HT-PWAS) (Giurgiutiu, 2010). The HT-PWAS that they sought must have the Curie transition temperature well above the operating temperature; otherwise, Giurgiutiu reported that the piezoelectric material might depolarize under combined temperature and pressure conditions. The thermal energy causes large power dissipation and hysteretic behavior. Relatively high temperature variation produces pyroelectric charges, which interferes with the piezoelectric effect. In addition, many ferroelectrics become conductive at high temperatures, leading to the charge floats and partial loss of signal. The conductivity problem is aggravated during operation in atmosphere with low oxygen content, in which many oxygen-containing ferroelectrics may rapidly lose oxygen and become semi-conductive They chose Gallium orthophosphate ($GaPO_4$) material as piezoelectric wafer that shows remarkable thermal stability up to temperatures above 970ºC (1778F). Giurgiutiu noted that it displays no pyroelectric effect and no outgassing and also it has a high electric resistivity that guarantees high-precision piezoelectric measurements. The PZT wafers were X-cut $GaPO_4$ single crystal disks of 7mm diameter and 0.2mm thickness (Figure 4.1). They conducted EMIS, pitch-catch and material characterization tests (scanning electron microscopy, X-ray diffraction, energy dispersive spectrometry) (a) before and after exposure of HT-PWAS to high temperature (b) inside the oven. They reported that the GaPO4 HT-PWAS maintained their activity up to 1300F (705C). In comparison, conventional PZT sensors lose their activity at around 500 F (260C).

Regarding temperature dependence of the electric parameters, in (Wolf, 2004), lead zirconate titanate (PZT) thin films was measured between -55ºC and 85ºC to obtain the effective piezoelectric coefficient for different material composition. Films tend to have smaller dielectric, ferroelectric, and piezoelectric properties in comparison with their ceramic counterparts. PZT films were tested with 2, 4, and 6 mm thickness and 40/60, 52/48, and 60/40 Zr/Ti ratios. They reported that The effective transverse piezoelectric coefficient ($e_{31,f}$) that is defined in Eq.(4.1) increases with temperature. Average increases were 46%, 32%, and 12% for films with PZT 60/40, 52/48, and 40/60 compositions, respectively

$$e_{31,f} = \frac{d_{31}}{s_{11}^E + s_{12}^E} = e_{31} - \frac{c_{13}^E}{c_{33}^E} e_{33} \tag{4.1}$$

Poisson's ratios of pure PZT ceramics across much of the solid solution system at constant temperature $\nu = -s_{12} / s_{11}$. $e_{31,f}$ were consistent with the rapid rise in intrinsic $d_{31}$ as $T_c$ is approached (Figure 4.3).

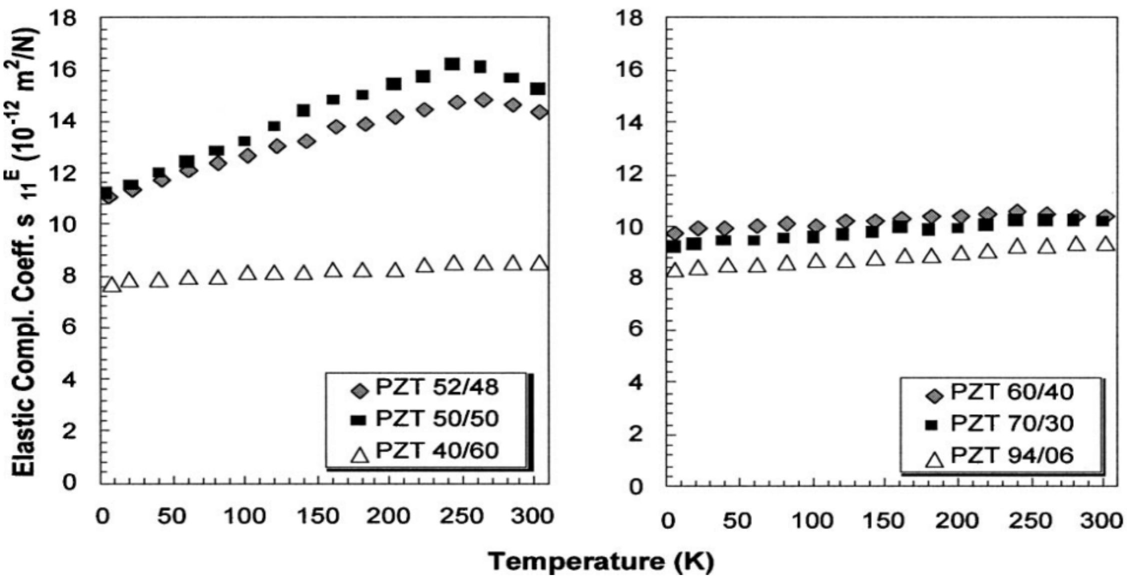


Figure 4.2 Low temperature elastic compliance coefficient ($s_{11}^{E}$) plotted as a function of temperature for several tetragonal and rhombohedral PZT compositions.

Wolf (2004) also reported increasing piezoelectric elastic compliance upto 250 K for PZT 52/48 and PZT 50/50 and their compliance values start decreasing after 250 K however other PZT material with different Zr/Ti compositions have monotonic increase until 300 K as seen in Figure 4.2.

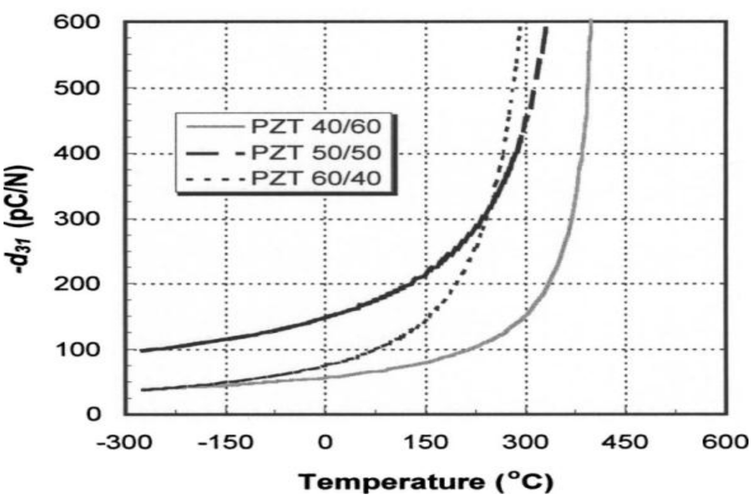


Figure 4.3 $-d_{31}$ of Pt/PZT/Pt stack plotted as a function of temperature for 2 µm Pt: Platinum electrode.

Raghavan & Cesnik in 2008 reported elastic and electric properties of a piezoelectric material, PZT-5A as a function of temperature raised up to 150 ºC as seen in Figure 4.4. The inverse of Young's modulus, Y, is the elastic compliance, i.e.

$$s = \frac{1}{Y} = \frac{\text{Strain}}{\text{Stress}} \left[ \text{m}^2/\text{N, 1/Pa} \right] \tag{4.2}$$

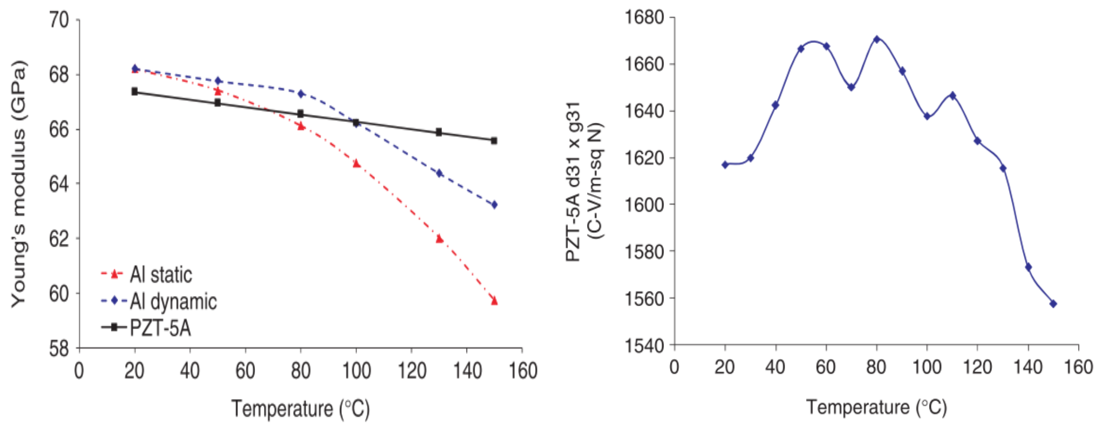


Figure 4.4 Variation of Young's modulus and $d_{31}xg_{31}$. Average thermal expansion for PZT-5A $\alpha_{\text{PZT-5A}}$=2.5µm/m-ºC.

Young's moduli of PZT-5A monotonically decreases as temperature increases between room temperature and 160ºC. The product of d31xg31 fluctuates along the temperature. It first monotonically inclines until 60 ºC, and it declines after 110 ºC and it goes lower than its original value at room temperature.

A NASA report by (Hooker, 1998) shows the temperature dependence of $d_{31}$ and $d_{33}$, the effective E/M coupling coefficient as well as the thermal expansion of three different piezoelectric materials. The effective E/M coupling coefficient is defined as a function of frequency

$$k_{eff} = \sqrt{\frac{f_n^2 - f_m^2}{f_n^2}} \tag{4.3}$$

where $f_m$ is the minimum impedance frequency and $f_n$ is the maximum impedance frequency

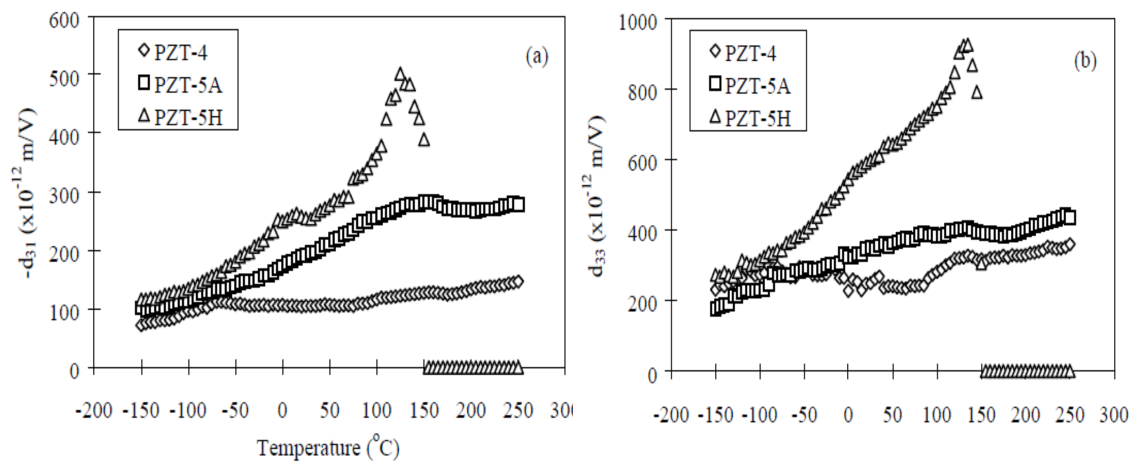


Figure 4.5 -$d_{31}$ and $d_{33}$ of three different PZT materials plotted as a function of temperature

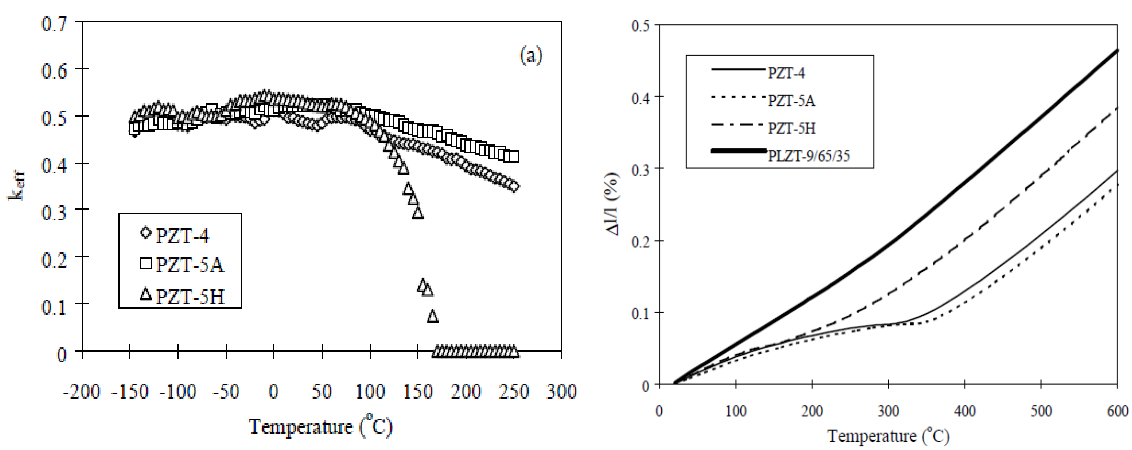


Figure 4.6 the effective E/M coupling coefficient and thermal expansion plotted as a function of temperature

(Freitas, 2006) reports ($x$)BiFeO3-($1$-$x$)PbTiO3 ceramics displaying piezoelectric, ferroelectric behaviors. A E4980 Agilent LCR bridge was used to determine resonance and anti-resonance frequencies that can be used for calculating piezoelectric coefficients.

With temperature increasing, the $g_{31}$ and $d_{31}$ coefficients present two distinct thermally stable regions. In temperatures ranging from 20 ºC to 100 ºC, and from 250 ºC to 300 ºC.. This thermal stability for piezoelectric coefficients at high temperatures attests the efficiency of 0.6BF-0.4PT ceramics for high temperature piezoelectric applications, as mechanical transducers and high power actuators. The piezoelectric voltage coefficient is defined by the relation and plotted in Figure 4.7.

$$g = \frac{\text{Strain developed}}{\text{Applied charge density}} = \frac{\text{Electric field developed}}{\text{Applied mechanical stress}} \tag{4.4}$$

$$g_{ij} = \frac{d_{ij}}{\varepsilon_{ii}^{T}} \tag{4.5}$$

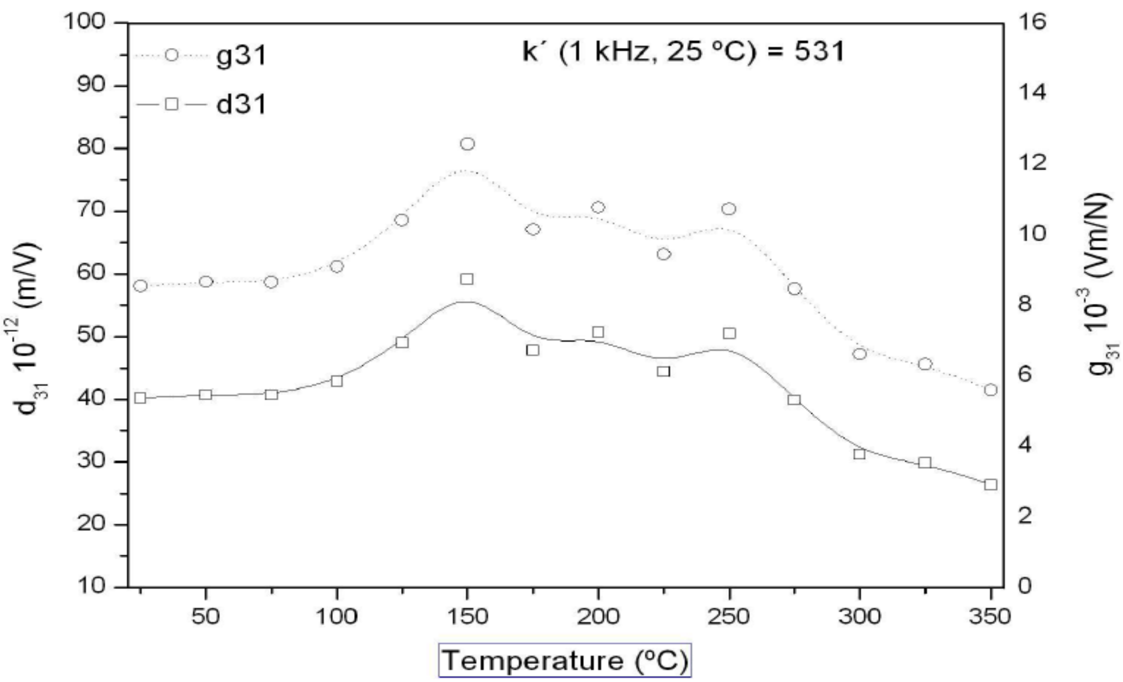


Figure 4.7 The piezoelectric voltage constant, $g_{31}$ and piezoelectric charge constant, $d_{31}$ with temperature increasing.

We have conducted a preliminary parametric study to understand the effects of the material properties on the impedance (anti-resonance) and admittance (resonance) spectra. We utilized the 1-D PWAS-EMIS model (Andrei Nikolaevitch Zagrai, 2002) for this analytical simulation.

$$Z = \frac{1}{i\omega C_0}\left[1 - \kappa_{31}^2\left(1 - \frac{1}{\varphi \cot \varphi}\right)\right]^{-1} \tag{4.6}$$

where $\varphi$ is a function of frequency and wave speed, i.e. $\varphi = \frac{1}{2}\omega l / c$ and the electro-mechanical coupling is denoted by $\kappa_{31}^2$ term. The material properties are given in Table 3.1.

## 4.2 1-D ANALYTICAL EMIS SIMULATIONS FOR PWAS AT ELEVATED TEMPERATURES

Herein, we first simulated the effects of the temperature increase via the stiffness coefficient change on impedance and admittance results through 1-D analytical in-plane EMIS model for free PWAS. Then, the piezoelectric coefficient was also taken into account to more precisely capture the degradation of the PWAS material due to the elevating temperature.

### 4.2.1 EFFECTS OF STIFFNESS COEFFICIENT $C_{11}$ CHANGE

We have varied the piezoelectric stiffness and the piezoelectric charge constant by 5% separately and together and plotted the admittance and impedance spectra as seen in Figure 4.8, Figure 4.9, and Figure 4.10.

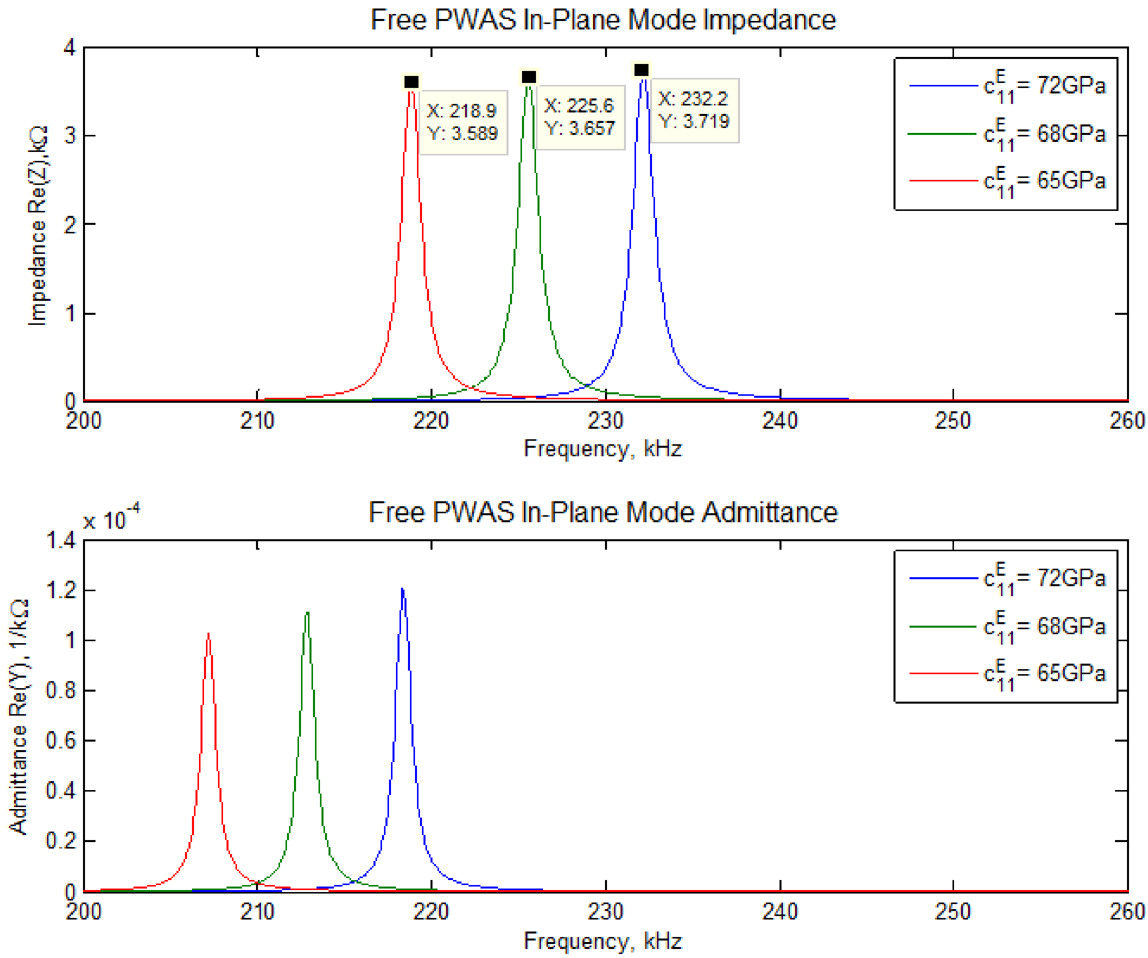


Figure 4.8 The stiffness change influence on both anti-resonance (impedance) and resonance frequency (admittance) in-plane EMIS of 7mmx0.2mm PWAS.

Apparently, the stiffness change has influence on both anti-resonance and resonance frequencies however not much influence on the amplitude of the impedance peaks whereas somewhat influence on the amplitude of the admittance.

### 4.2.2 Effect of Piezoelectric Coefficient $D_{31}$ Change

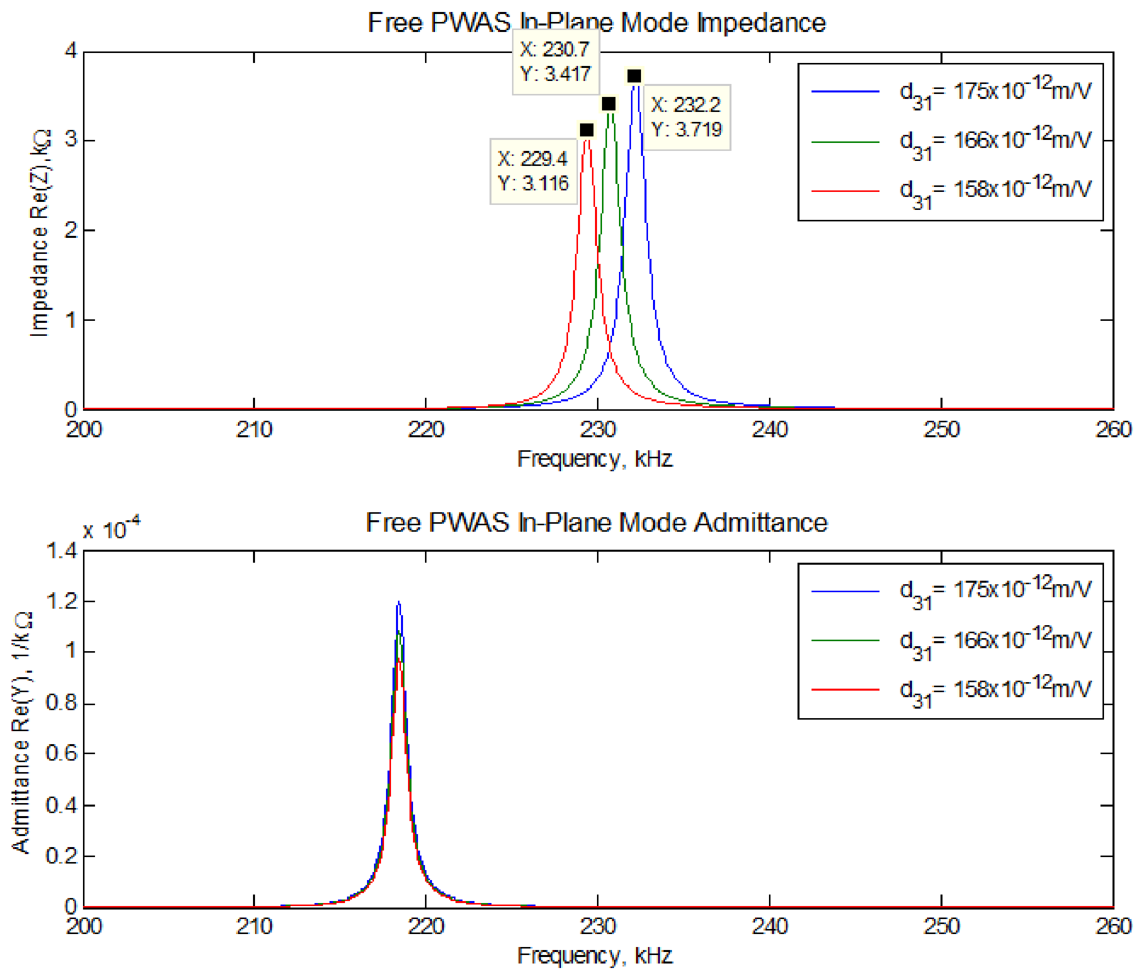


Figure 4.9 The piezoelectric charge constant $d_{31}$ change influence on both anti-resonance (impedance) and resonance frequency (admittance) in-plane EMIS of 7mmx0.2mm PWAS.

The piezoelectric charge constant change has influence on the first in-plane anti-resonance frequency however not any influence on the in-plane resonance frequency whereas has influence on both the amplitudes of the impedance and the admittance.

When we combined both the parameter changes and simulate the impedance and admittance of PWAS, we observe both the frequency and the amplitude shifts in both plots. We have phenomenological agreement in trends of the impedance spectra with the experimental results.

### 4.2.3 Effects of Stiffness Coefficient $C_{11}$, Piezoelectric Coefficient $D_{31}$ Changes

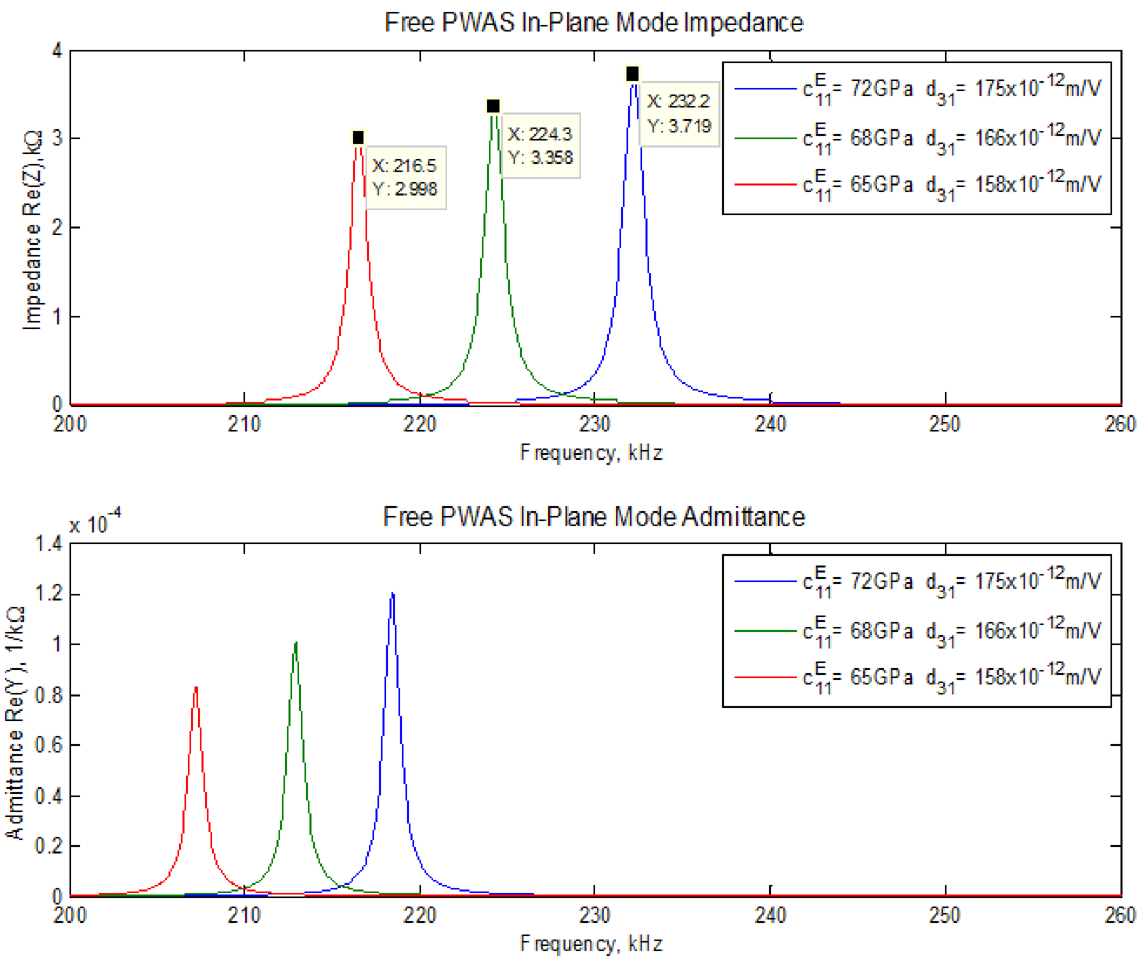


Figure 4.10 The stiffness and the piezoelectric charge constant $d_{31}$ change influence on both anti-resonance (impedance) and resonance frequency (admittance) in-plane EMIS of 7mmx0.2mm PWAS.

However, we still need to improve the agreement by using 2-D circular PWAS-EMIS analytical model and by including more parameter changes to reflect the temperature effects on the piezoelectric material degradation. The parameter changes need to be more linked to the temperature increase by using the experimental measurements in the literature. We also need to include in the model the capacitance change that is measured and found to be strongly dependent on the temperature increase.

## 4.3 2-D ANALYTICAL EMIS SIMULATIONS FOR PWAS AT ELEVATED TEMPERATURES

In this subsection, the temperature effects on free circular PWAS admittance and impedance are presented through the analytical model and the EMIS tests. The effects of the stiffness coefficient $c_{11}$, the piezoelectric coefficient $d_{31}$, and the static capacitance $C_0$ on impedance/admittance are taken into account.

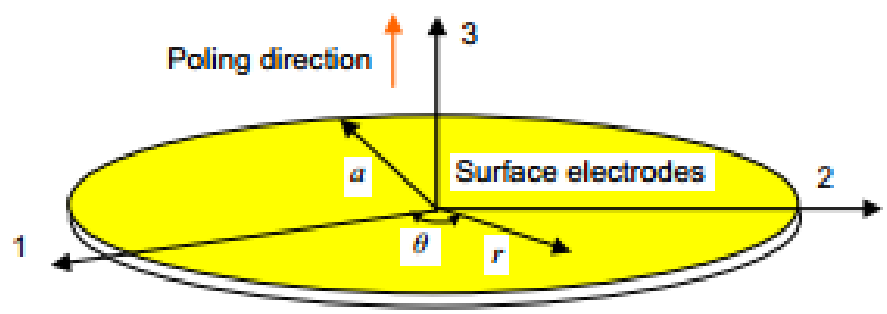


Figure 4.11 Schema of circular PWAS in cylindrical coordinate system.

Zagrai (2002) has developed 2-D EMIS for circular PWAS using the free circular PWAS model (Figure 4.11) and the derivation procedure shown in the flow-chart in Figure 4.12. In this section, we adopted herein his in-plane EMIS model to simulate the temperature effects on piezoelectric material degradation of free circular PWAS. The analytical simulation will be conducted by changing the stiffness coefficient, the piezoelectric coefficient, and the capacitance. The stiffness coefficient and the piezoelectric coefficient degradation have been discussed in the literature and plots for the material properties versus temperature increase have been provided. The capacitance dependence over temperature has been defined during our experimental studies. Therefore, the proportions of the elastic and piezoelectric material property degradations are attained from the literature and the capacitance proportion was obtained from the capacitance measurements over increasing temperature. The admittance and impedance simulations are presented respectively and compared with the experimental results.

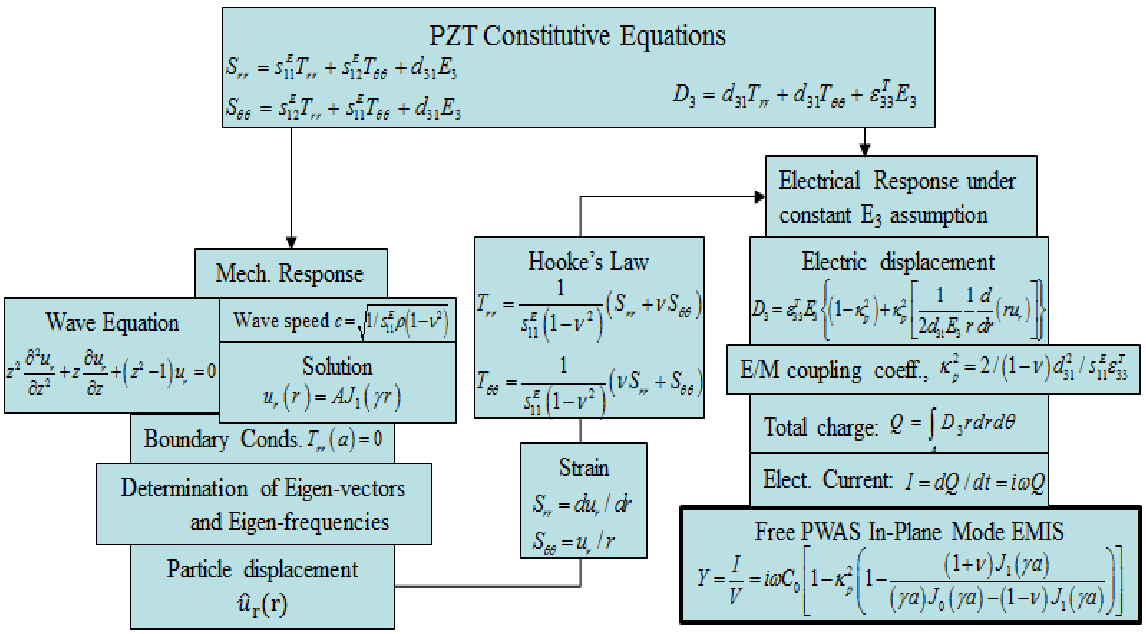


Figure 4.12 Flow-chart of the analytical modeling of 2-D in-plane EMIS of circular PWAS.

The EMIS tests are conducted for a PWAS in an oven at elevated temperature between 50˚C and 250˚C with the 50˚C step. During these tests, the piezoelectric material degradation has been observed. The affected material properties are defined via both the literature survey and the measurements. The degraded mechanical, electrical, and piezoelectric properties of PWAS were used to simulate the temperature effects on the first in-plane admittance and impedance peaks. For the analytical simulations, 2-D circular PWAS-EMIS model was utilized. The material properties used in this study are the stiffness coefficient $c_{11}$, the piezoelectric coefficient $d_{31}$ , and the capacitance $C_0$. The analytical and experimental results for admittance are shown in Figure 4.13 and the results for impedance are also shown in Figure 4.14.

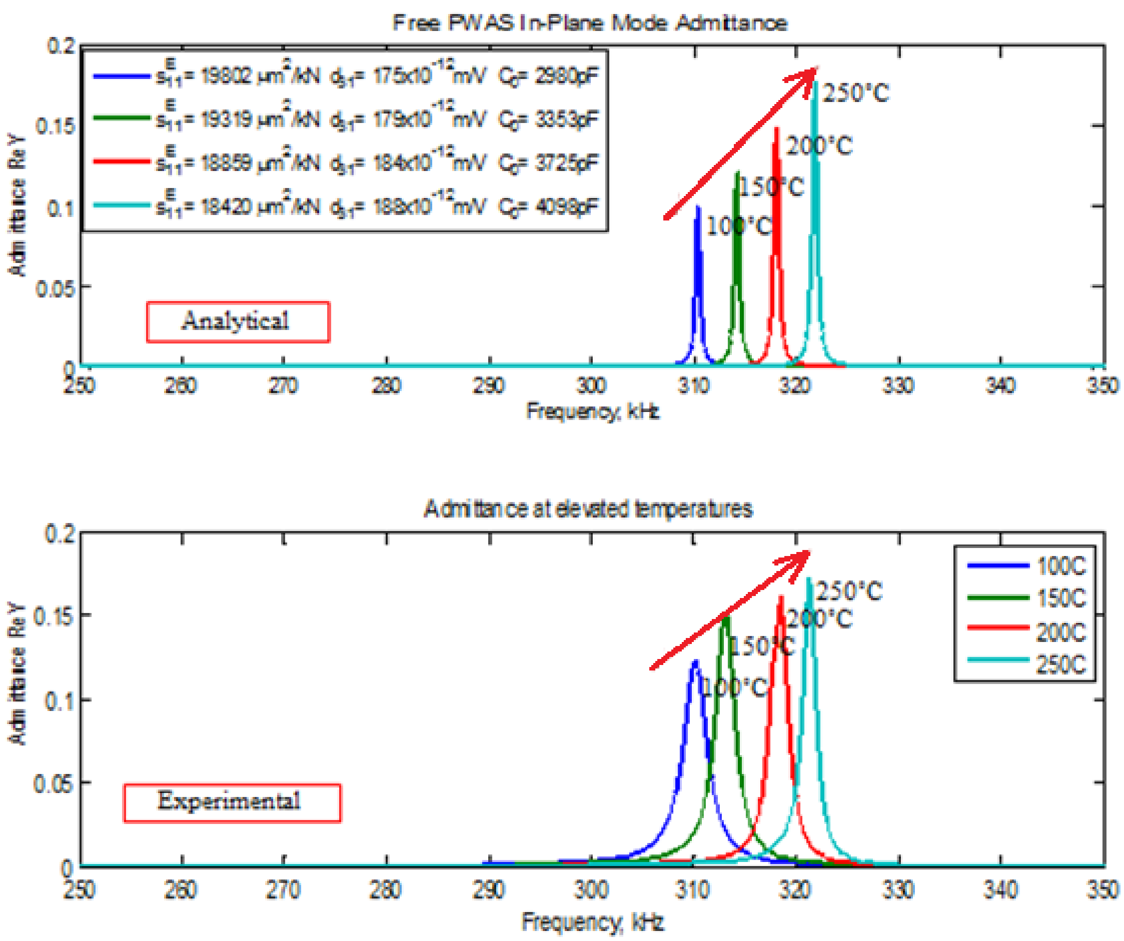


Figure 4.13 Stiffness coefficient $c_{11}$, piezoelectric coefficient $d_{31}$ , and capacitance $C_0$ influence on admittance.

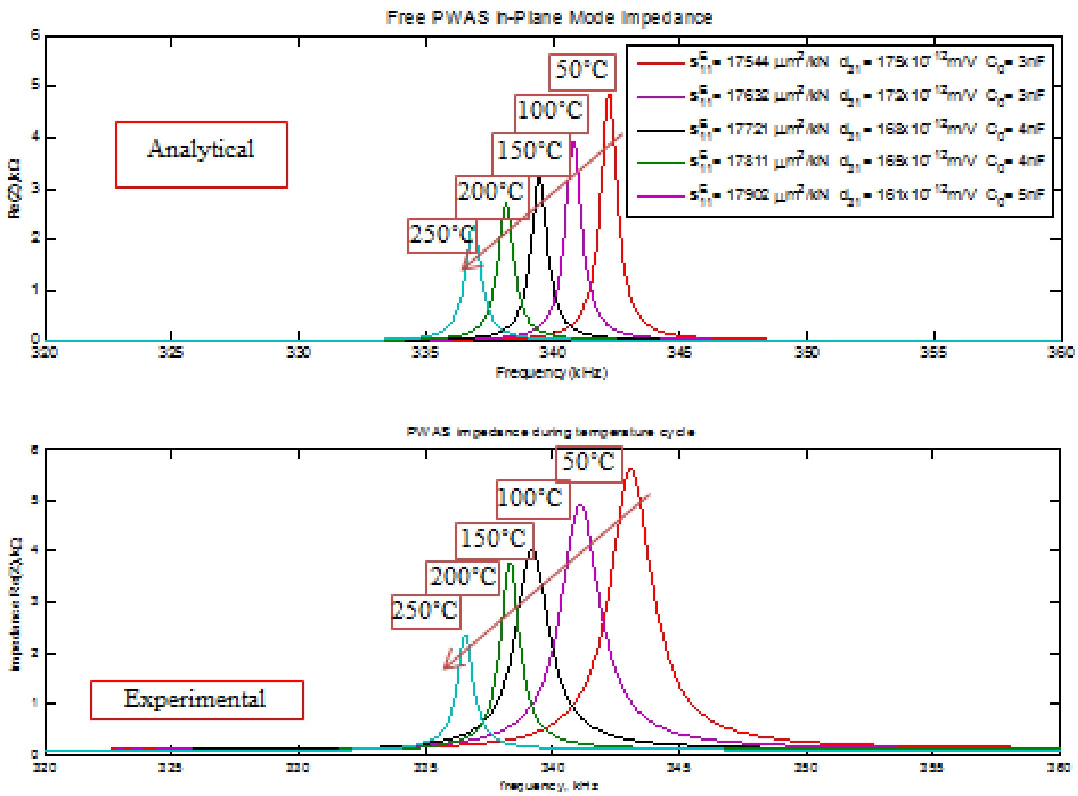


Figure 4.14 Stiffness coefficient $c_{11}$, piezoelectric coefficient $d_{31}$ , and capacitance $C_0$ influence on impedance.

## 4.4 EXPERIMENTAL WORK

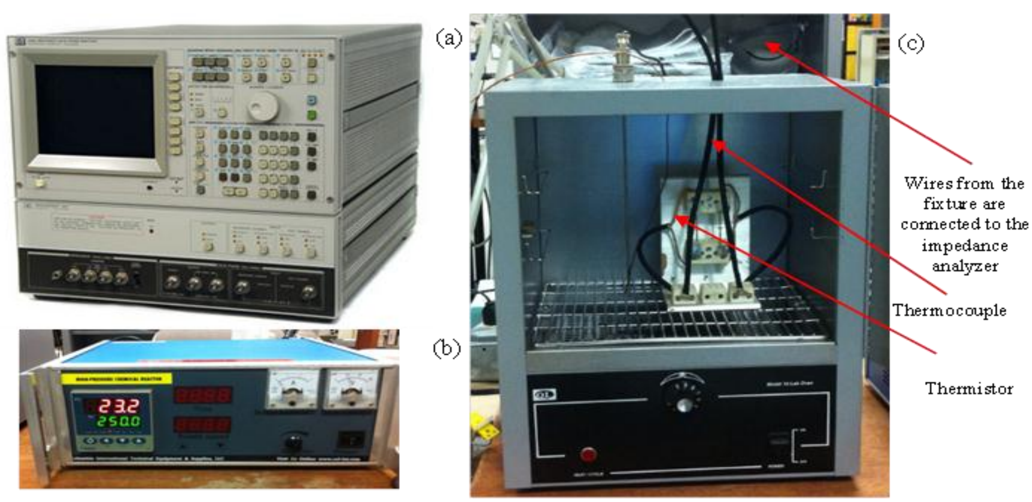


Figure 4.15 High temperature PWAS testing by (a) impedance analyzer, (b) PID temperature controller (c) oven.

The E/M impedance is used as a direct and convenient method to implement for PWAS impedance signature as a function of temperature up to relatively high temperature, the required equipment being an electrical impedance analyzer, such as HP 4194A impedance analyzer, PID temperature controller, and oven. An example of performing PWAS E/M impedance spectroscopy is presented for PWAS located in a fixture in the oven in Figure 4.15. PWAS has to have stress-free i.e. unconstrained boundary conditions so that it was fixed by pogo-pins that only apply low spring forces point-wise on the PWAS surfaces in the fixture. The fixture has wires that can be connected with the probes of the EMIS analyzer instrument. The impedance analyzer reads the E/M impedance of PWAS itself in the oven. It is applied by scanning a predetermined frequency range (300kHz-400kHz) and recording the complex impedance spectrum. A LabView data acquisition program was used to control the impedance analyzer and sweep the frequency range in steps (of 100Hz) that was predefined and to attain the data in a format that assists to data analysis. During the visualization of the frequency sweep, the real part of the E/M impedance, $\mathrm{Re}\left(Z\left(\omega\right)\right)$, follows up and down variation as the structural impedance goes through the peaks and valleys of the structural resonances and anti-resonances.

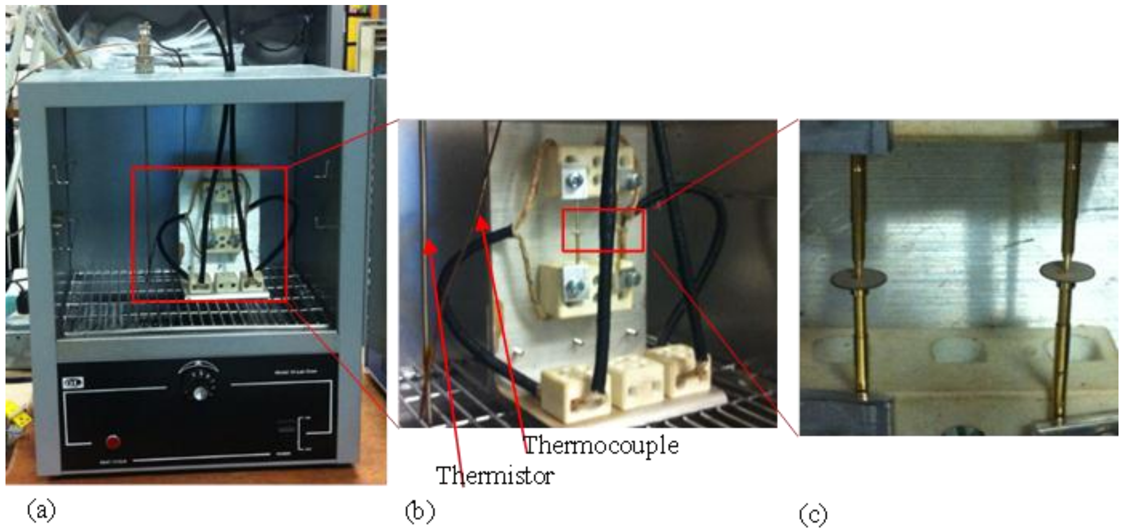


Figure 4.16 a) Fixture in the oven (b) fixture, thermistor, and thermocouple (c) PWAS in the fixture.

Our objective was to evaluate the extent of the temperature dependence of PWAS-capacitance and EMIS results and the degredation of PWAS material with respect to some electrical and elastical material properties. For the experimental study, we pursued the following protocol

- Measure baseline room temperature PWAS capacitance and electromagnetic impedance (EMI) spectrum.
- Elevate PWAS to 50 °C and hold it there for several minutes (e.g. 10-30 min)
- Measure PWAS capacitance and EMIS at the elevated temperature
- Drop PWAS temperature back to the room temperature
- Measure PWAS capacitance and EMI spectrum at room temperature
- Perform steps 2-5 for 100, 150, 200, and 250 °C

We have measured 6 PWAS at different temperatures starting from the room temperature. The capacitance and EMIS measurements have been performed for 50, 100, 150, 200, and 240ºC and the temperature was dropped to the room temperature after each step and obtained 5 temperature cycles and 5 more capacitance and EMIS reading at the room temperatures.

### 4.4.1 CAPACITANCE RESULTS

Figure 4.17 indicates the static capacitance results for only one of the PWAS at elevated temperatures as well as at the room temperatures in each temperature cycles whereas Figure 4.18 for all of the PWAS resonators at only elevated temperatures. Figure 4.19 also shows the averaged capacitance values over the static capacitance values that are obtained from 6 PWAS resonators. One can observe the monotonic increase in the capacitance values by increasing the temperature. The trend is linear up to 200 ºC however it is interesting to see that the temperature gradient of the capacitance increases after this temperature. The capacitance values at room temperatures after each cycling also vary for the PWAS 1R.

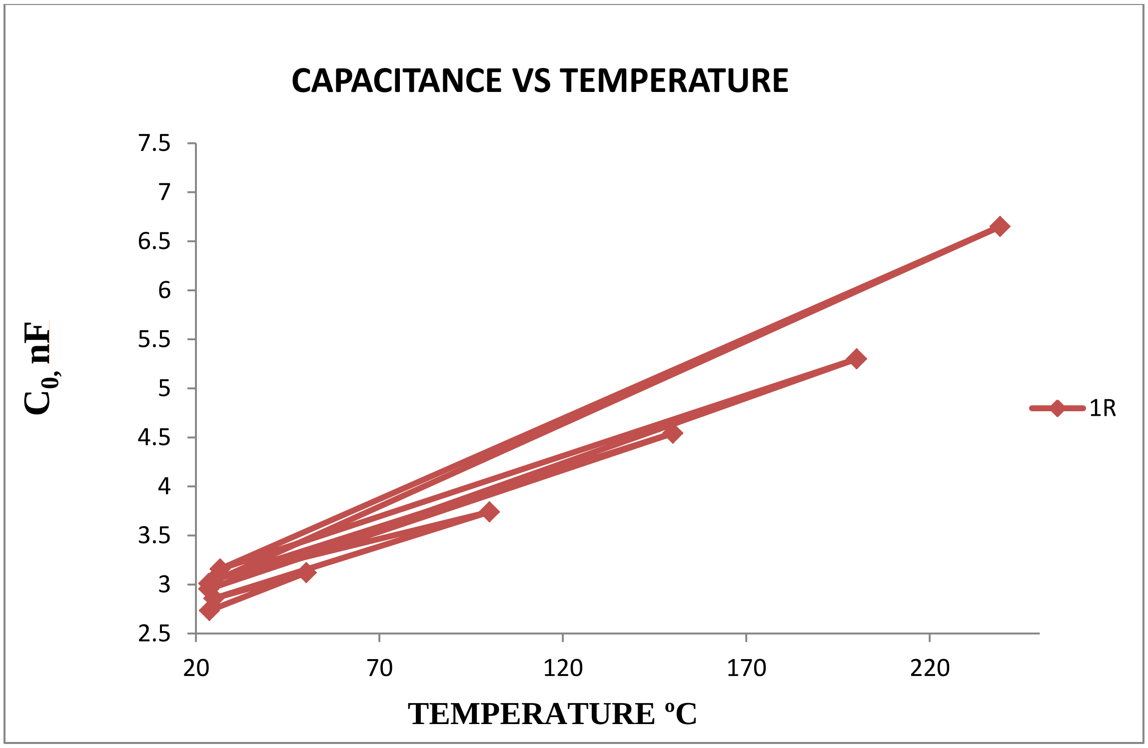


Figure 4.17 Static capacitance results for PWAS 1R (7mmx0.2mm PWAS) at elevated temperatures and room temperatures in each temperature cycle.

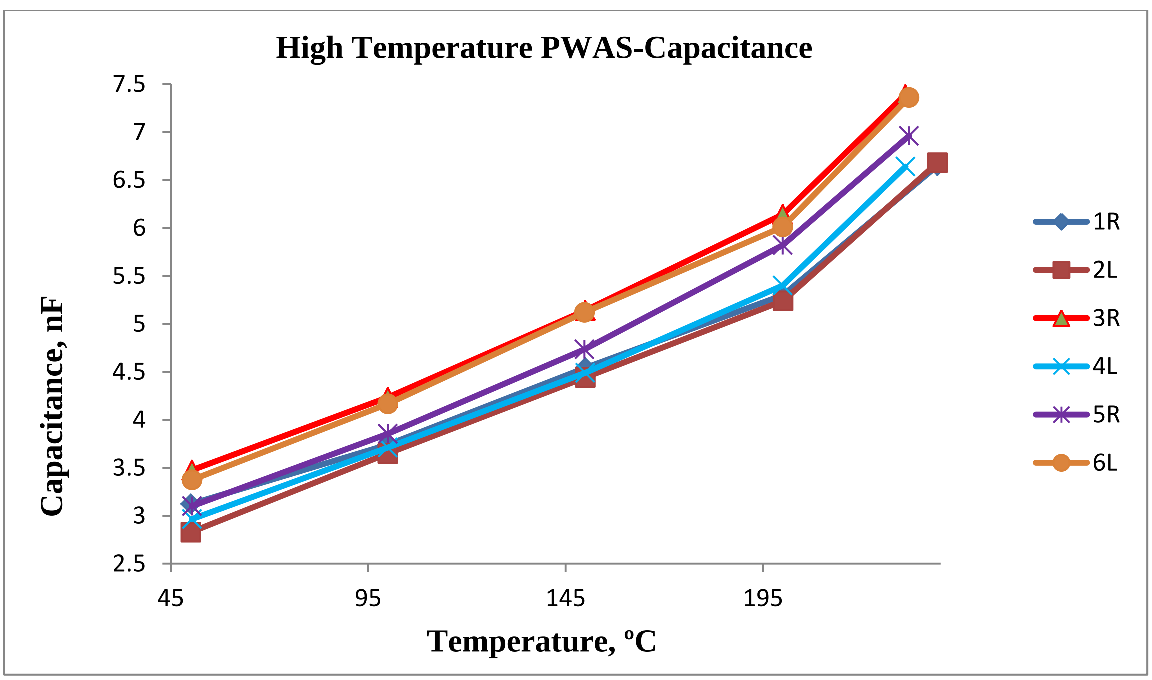


Figure 4.18 Static capacitance results for all of the circular PWAS resonators (7mmx0.2mm) at only elevated temperatures.

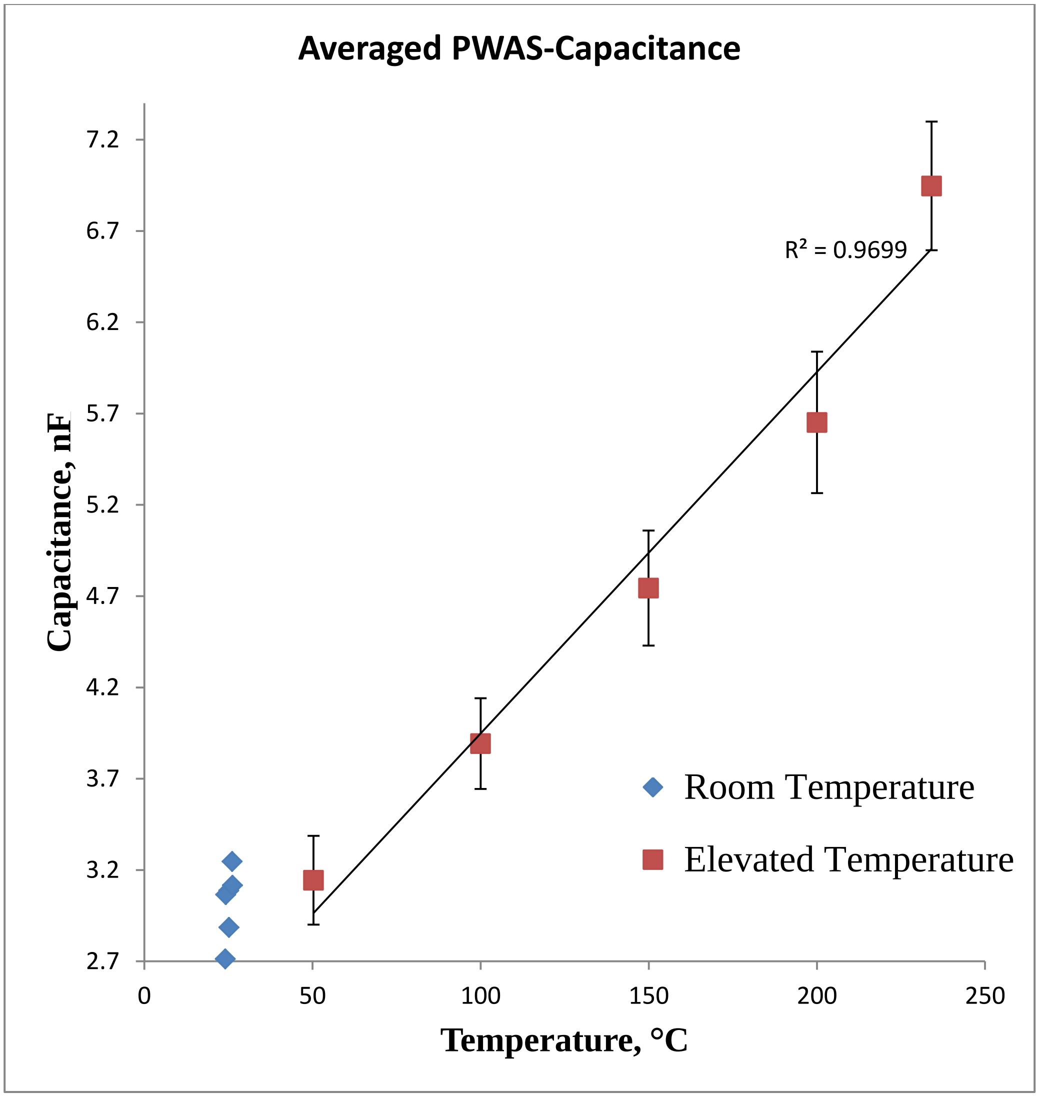


Figure 4.19 Averaged static capacitance results for all of the circular PWAS resonators (7mmx0.2mm) at room temperature and elevated temperatures.

### 4.4.2 EMIS RESULTS

We have measured 6 PWAS resonators in the high temperature EMIS test. We denoted them by their sequence number and a letter R or L that denotes right or left. Then PWAS 1R is the first PWAS located on right side of the fixture and 2L is the second PWAS on the left and so on. Moreover, the first room temperature in the cycle is denoted

RT1 as the second room temperature after cooling down from 50ºC is denoted RT2 so that the impedance signature for the first PWAS on the right at the first room temperature is represented by 1R_RT1 and the second PWAS on the left at the third room temperature after cooling from 100ºC is represented by 2L_RT3 and so on.

We will discuss the analyses of impedance results of each PWAS in sequential subsections. We will first plot all the impedance signatures at the first in-plane anti-resonance frequency for one PWAS at all elevated temperature-room temperature cycles with a time series plot that shows each time and date when the particular measurement was performed so one can observe how long the overall measurement has taken and how long a PWAS has been kept at a certain temperature. Next, we will separate the EMIS test results as the impedance plots at room temperatures and at elevated temperatures to see the trends of the frequency and amplitude shifts of the first impedance curves in both cases. Then, we will plot the impedance amplitude vs temperature including those at room temperatures in the same graph and also plot the impedance frequency vs temperature in the same way. Finally, we will present the amplitude and the frequency shifts separately at elevated temperatures and those at room temperatures were plotted by the order number of the room temperature.

PWAS 1R

PWAS impedance overlapped results during temperature cycle from room temperature up to 250ºC is illustrated in Figure 4.20. A time series plot also depicts the temperature against the time when a particular test was conducted. The overall tests has lasted 2 days because cooling down from high temperatures to the room temperature at each cycle has taken somewhat long time. No forced convection method was implied to quicken the cooling process.

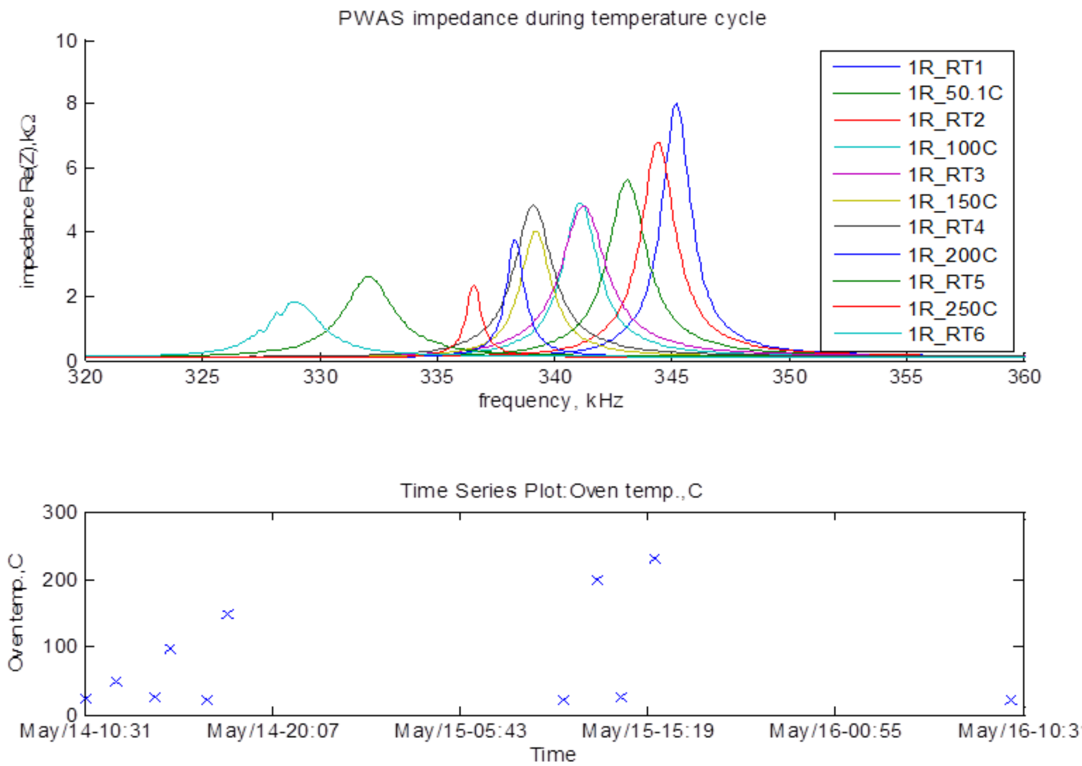


Figure 4.20 Impedance signature of PWAS-1R (7mmx0.2mm PWAS) at elevated temperatures and room temperatures in each temperature cycle.

The impedance peaks diminish in amplitude as the temperature increases and it keeps diminishing even PWAS is cooled down to the room temperature in each temperature cycle. Another phenomena is the frequency downshift as the temperature moves up however frequency upshift is also observed as PWAS cools down to the room temperature, the PWAS does not seem to recover completely and its impedance can not move up to its original anti-resonance frequency. One interesting phenomena is also the deformation on the impedance signature of PWAS-1R at RT6 after cooling it down from 250ºC as the other impedance signatures are smooth curves before.

Overall the trend seems by investigating the plot however it can be more clearly observed those at room temperatures and the elevated temperatures in separate plots as depicted in Figure 4.21. We utilized color codes for this two plots. For instance, the impedance curve at the second room temperature (1R_RT2) has the same color as the one at the temperature of 50ºC since it is the room temperature after cooling down from that temperature. The color codes are implied in such order to the other impedance curves.

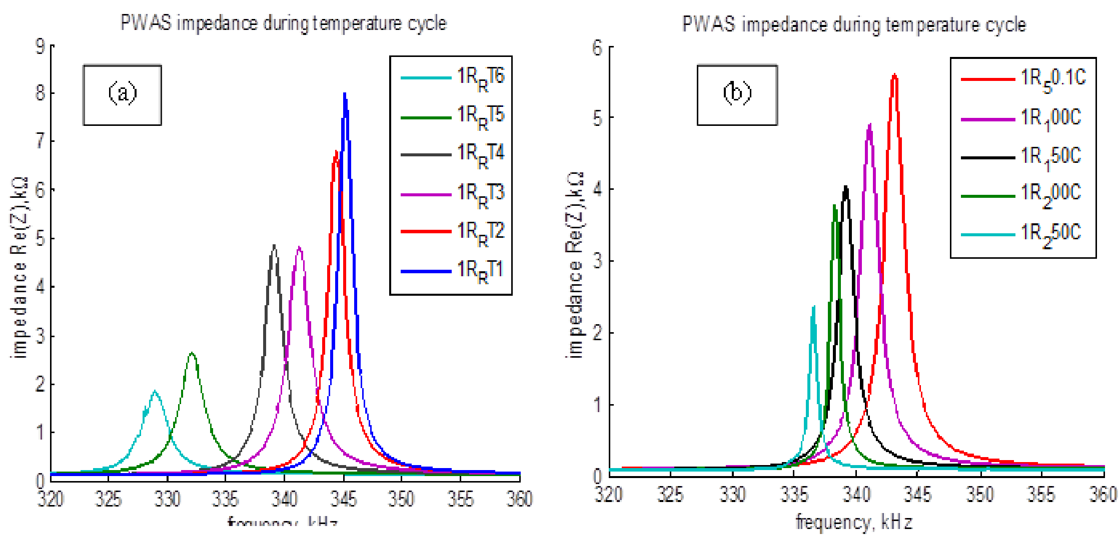


Figure 4.21 Impedance signature of PWAS-1R (7mmx0.2mm PWAS) at (a) elevated temperatures and (b) room temperatures in each temperature cycle.

Eventhough the trend in the amplitude and frequency shift during the temperature cycle seems more clearly now, we can further analyze the frequency shifts and the amplitude shifts separately as depicted in Figure 4.22 and Figure 4.23, respectively. In Figure 4.22, one can see that the frequency shifted all the way from 345.2 kHz to 328.9 kHz during the temperature cycle eventhough both anti-resonance frequencies were read at room temperatures. In the first cycle, from the room temperature to 50ºC and back to the room temperature, the impedance frequency first declines then inclines back to the close value although this does not occur in the next two cycles between the room temperature and the 100ºC and the 150ºC tests. In the test results from the temperature cycle between the room temperature and 100ºC, the impedance frequency remains the same as the PWAS cooled down to the room temperature, which also occurs in the cycle between the room temperature and the 150ºC. More significantly, in the results from the next two temperature cycles, the impedance frequency declines even further as the PWAS cools down back to the room temperature. The PWAS behaves in different manner after it has been heated up to 200ºC due to the material degradation as the temperature approaches to the Curie temperature of the piezoelectric material and due to the depolarization that may occur.

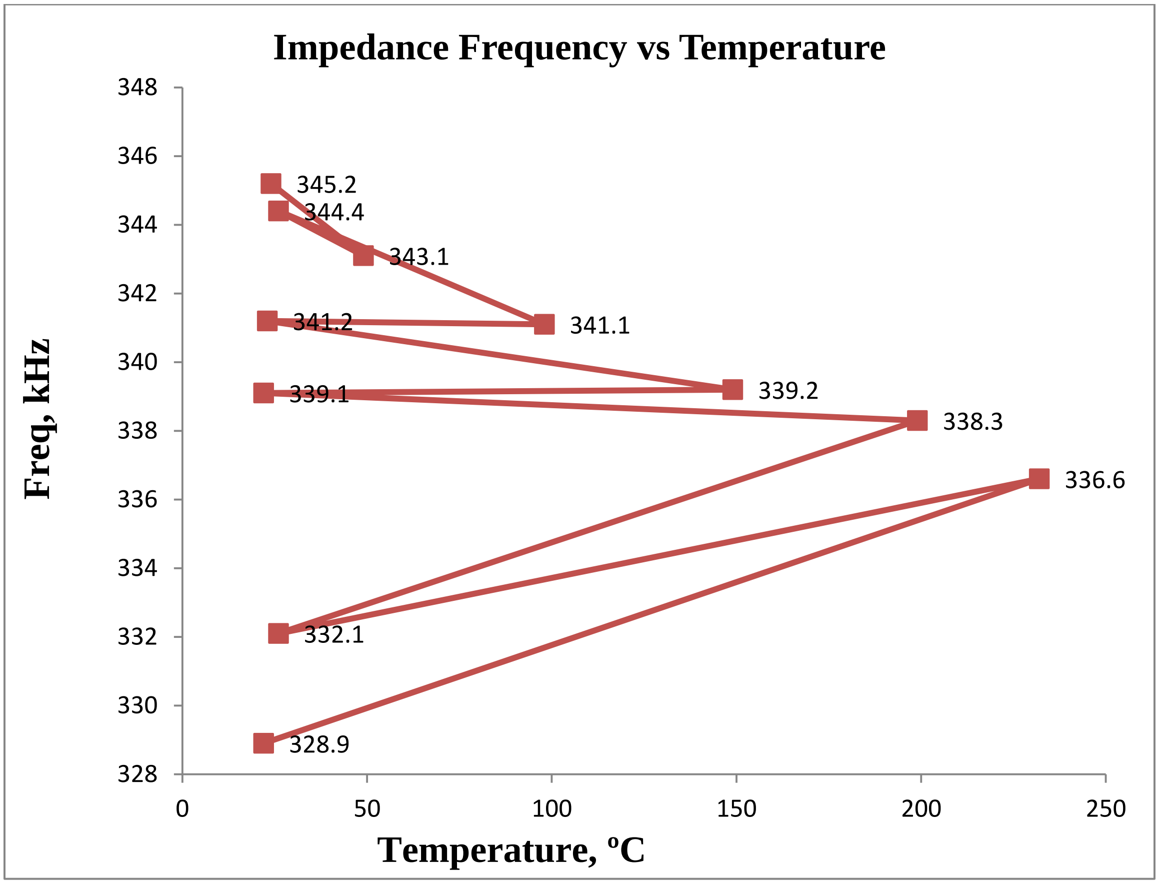


Figure 4.22 Impedance (anti-resonance) frequency of PWAS-1R (7mmx0.2mm PWAS) during temperature cycle.

In Figure 4.23, the amplitude also diminishes from ~8 kΩ down to ~1.8 kΩ. Eventhough, the PWAS impedance signature attempts to recover and move up in both frequency and amplitude at the room temperatures until the temperature of 200ºC, it no longer recovers after 200 ºC which is close enough to the Curie temperature for PWAS to possess distinct behavior.

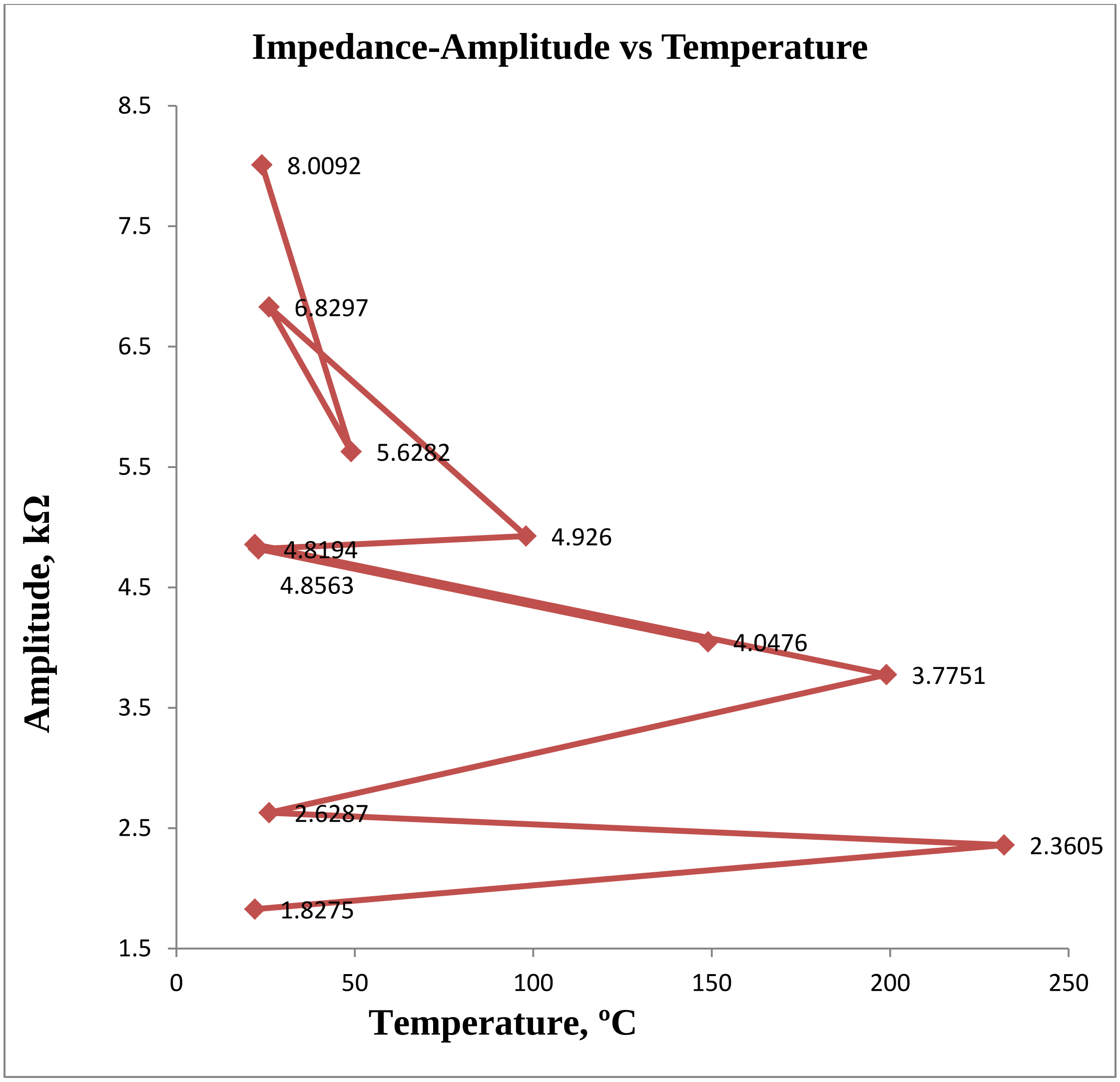


Figure 4.23 Impedance (anti-resonance) amplitude of PWAS-1R (7mmx0.2mm PWAS) during temperature cycle.

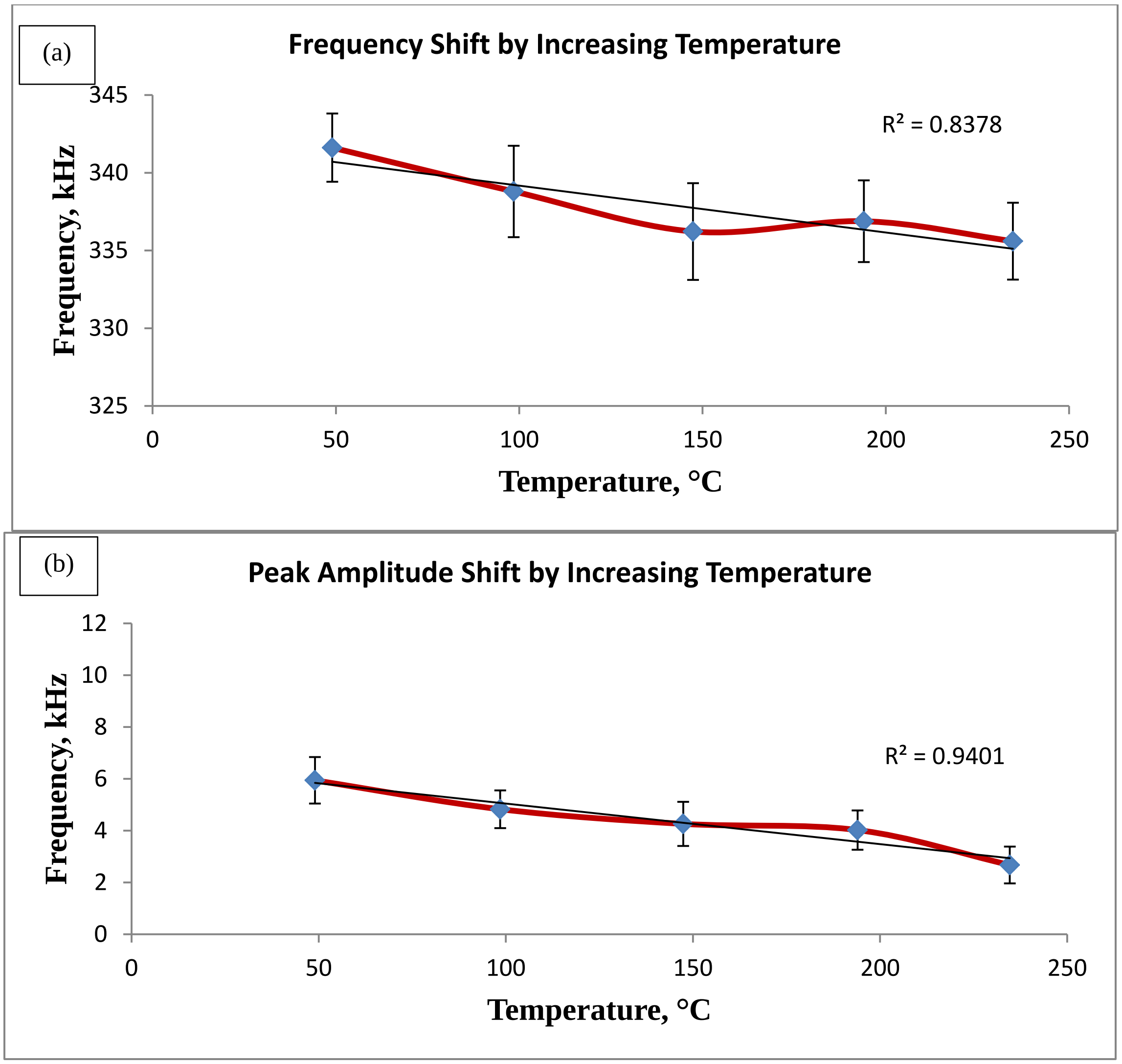


Figure 4.24 Averaged impedance (a) frequency and (b) ampllitde shift against elevated temperature.

The impedance peak amplitude and frequency against increasing temperature are plotted not including the room temperatures in Figure 4.24 to analyze the trend of the amplitude and the frequency shifts over elevated temperatures. The impedance peak amplitude and frequency at room temperatures are plotted against the room temperature number in Figure 4.25 to analyze the trend of the amplitude and frequency shifts at the room temperatures during the temperature cycle.

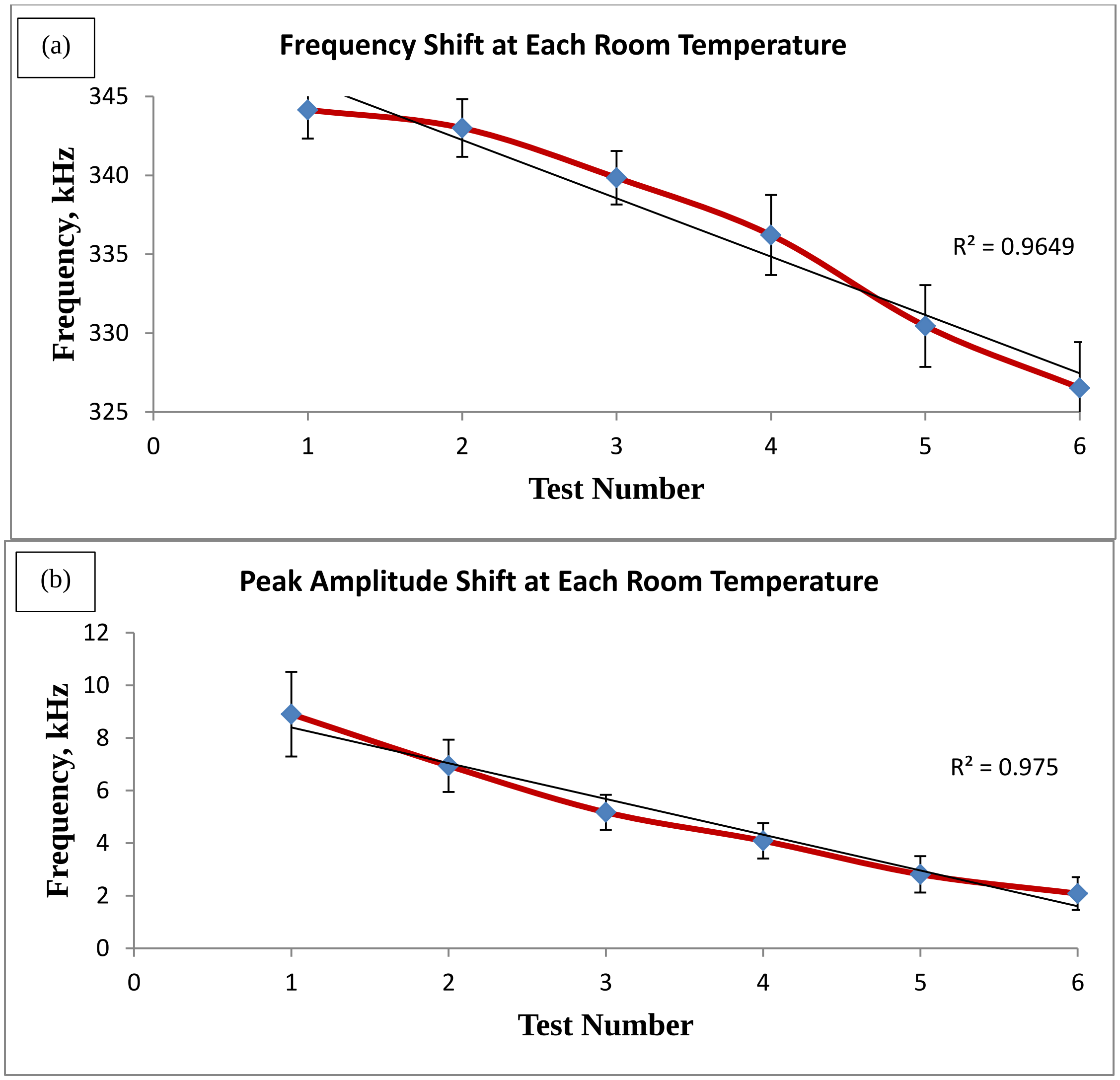


Figure 4.25 Averaged impedance (a) frequency and (b) ampllitde shift of PWAS-1R (7mmx0.2mm PWAS) at room temperature.

PWAS 2L:

We will seldom present the analyses of impedance amplitude and frequency shift during temperature cycle by depicting the representative plot since these two phenomena are dominating in the experimental study. Also, the trend can be observed clearly by analyzing the corresponding plots for the amplitude and the frequency shifts.

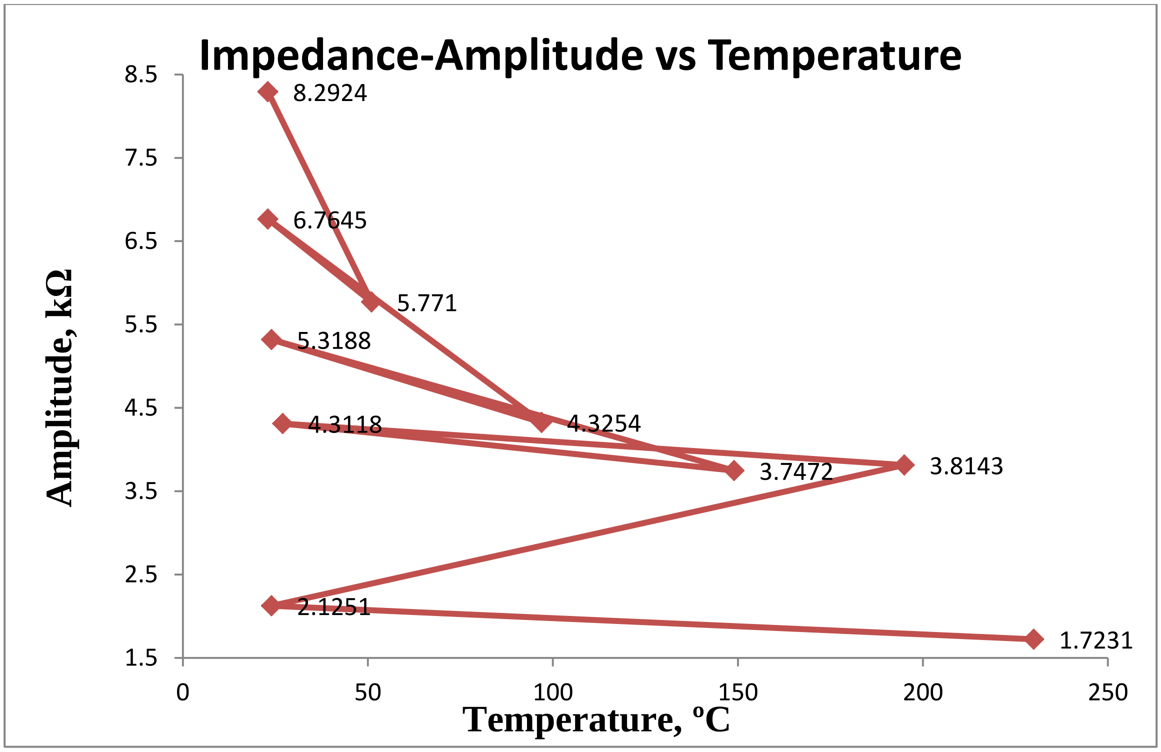


Figure 4.26 Impedance (anti-resonance) amplitude of PWAS-2L (7mmx0.2mm PWAS) during temperature cycle.

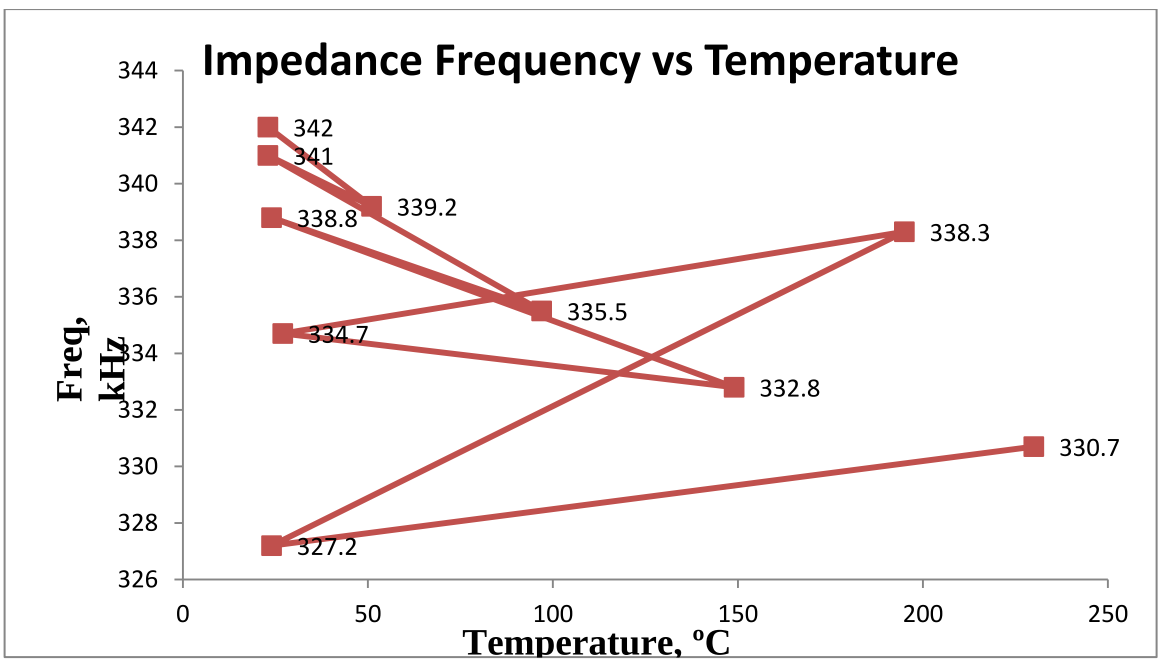


Figure 4.27 Impedance (anti-resonance) frequency of PWAS-2L (7mmx0.2mm PWAS) during temperature cycle.

### 4.4.3 ADMITTANCE SPECTRA AT ELEVATED TEMPERATURE

In this subsection, we present admittance results from free circular PWAS resonators at elevated temperatures using the same experimental setup. In Figure 4.28, 3-D plots of the admittance in frequency domain over time are illustrated for the measurements conducted at different temperatures. The temperature values for the each admittance measurement were kept constant by the closed loop temperature controller and monitored and recorded by the GUI software that was specifically designed and created by Jingjing (Jack) Bao and Bin Lin in LAMSS using LabVIEW for this admittance tests.

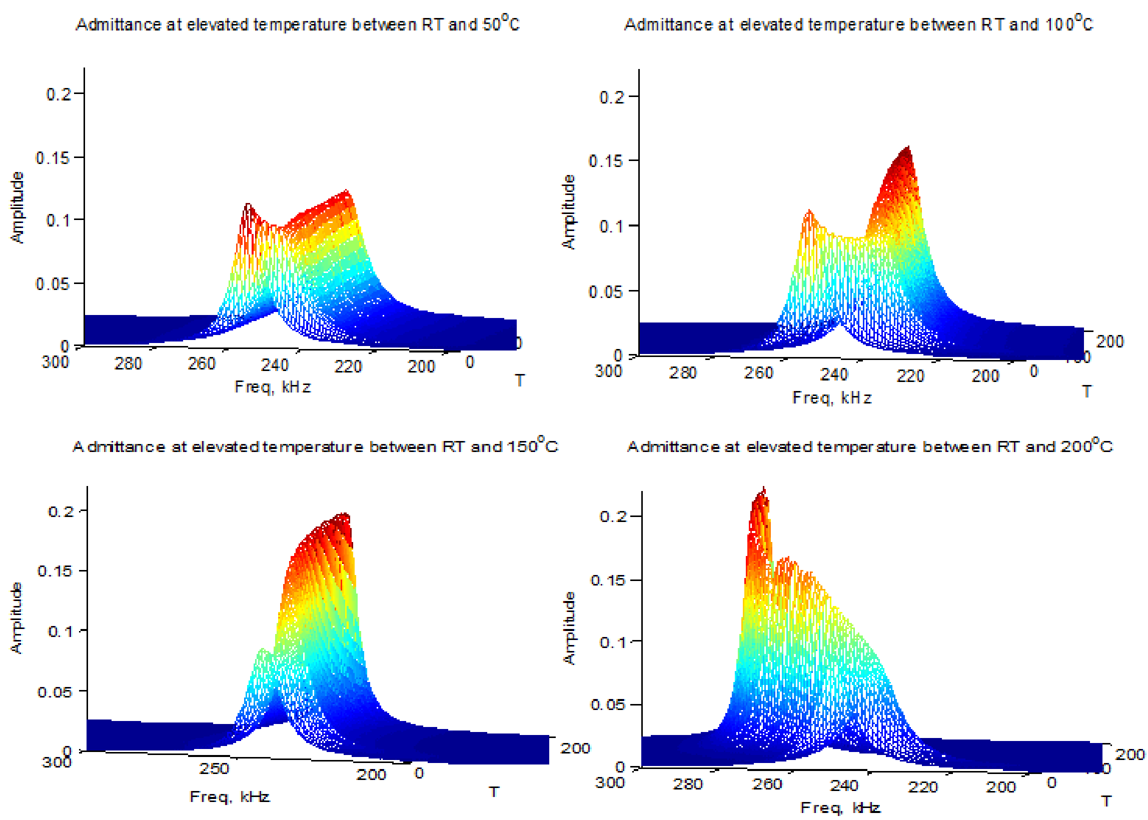


Figure 4.28 3D contour plots for admittance spectra at elevated temperatures.

Admittance amplitudes from a PWAS have been measured during the temperature increases from the room temperature to the elevated temperatures and the results were plotted and presented in Figure 4.29. The admittance amplitude also pursued the same track as reported in the preceding subsection regarding the impedance amplitude. It inclines as the temperature increases with the similar trend from the room temperature toward the elevated temperatures. Eventhough the admittance amplitude recovers after the PWAS cools down to the room temperature from the 50ºC, it cannot recover and drops down in the amplitude after the PWAS cools down from the higher temperatures. Another interesting behavior that can be observed in this test results is that the amplitude keeps increasing although the temperature remains the same at the elevated temperatures.

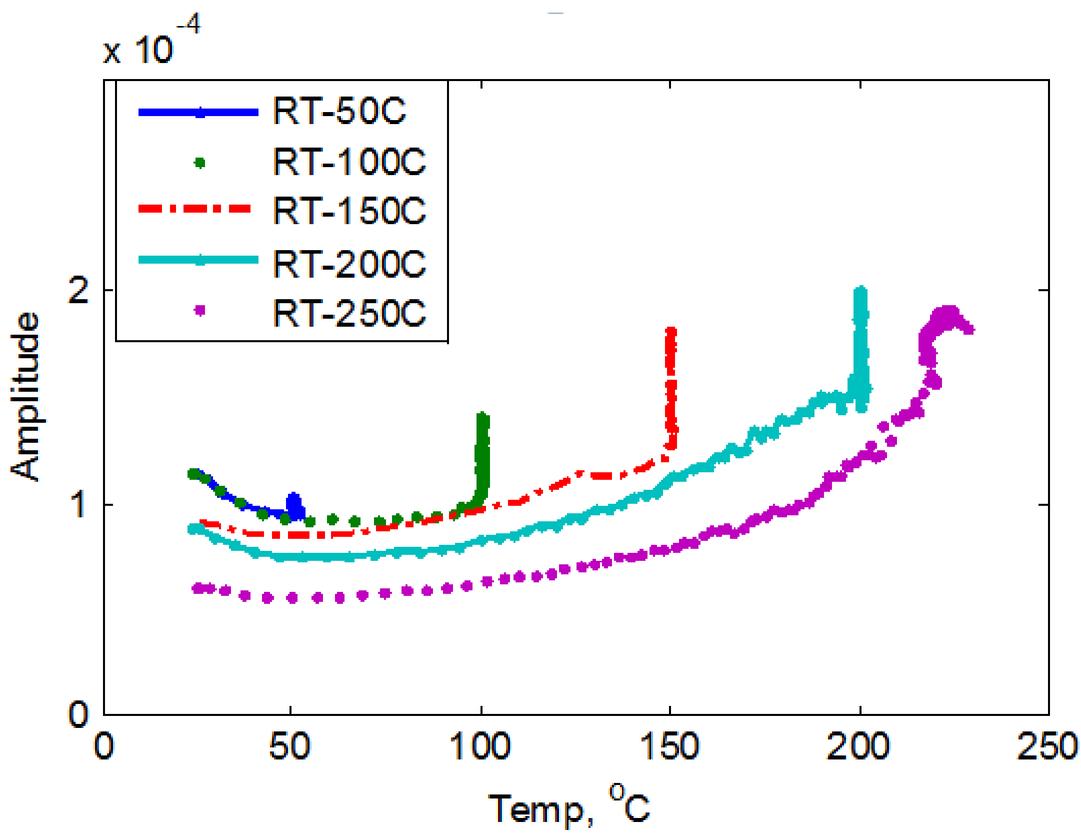


Figure 4.29 Admittance peak amplitude at the first in-plane resonance frequency of circular PWAS at elevated temperatures.

The first in-plane resonance frequency values of free PWAS in an oven as the temperature was increasing are plotted as shown in Figure 4.30. The similar phenomena can be observed in the frequency shifts as seen in the amplitude shifts.

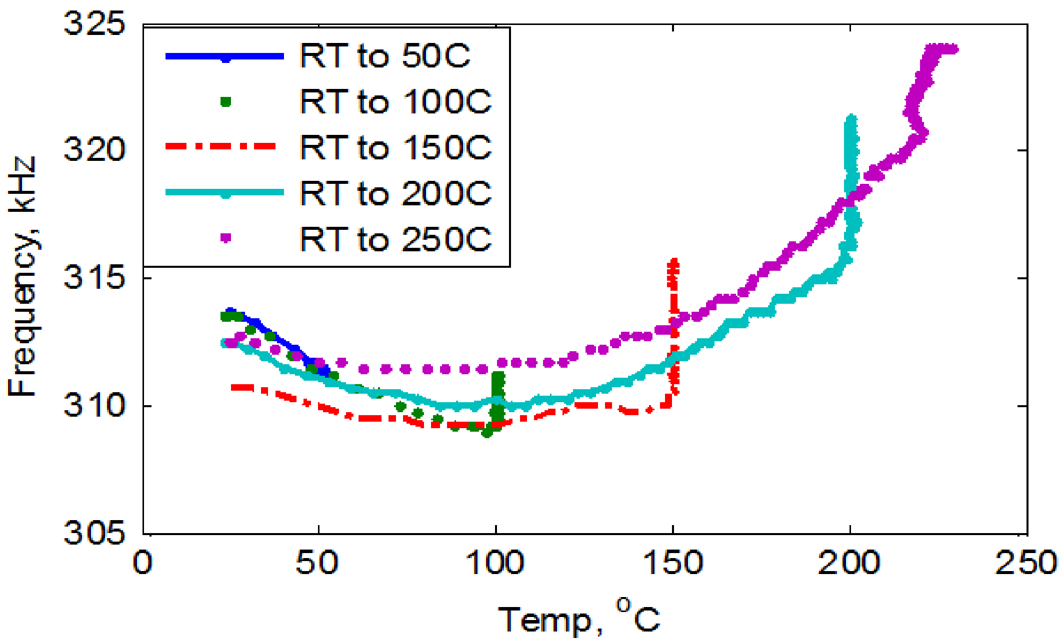


Figure 4.30 Admittance frequency at the first in-plane resonance frequency of circular PWAS at elevated temperatures.

## 4.5 SUMMARY AND CONCLUSIONS

Past researches were discussed to understand the survivability of piezoelectric wafer active sensors (PWAS) at extreme environments such as at very high temperature etc. Also, we could find out the extent of temperature dependence of the electric parameters, i.e. $d_{31}$ and $g_{31}$, and the elastic parameters, i.e. $s_{11}$ and Young's modulus ($c_{11}$), of different piezoelectric materials.

We have conducted a preliminary parametric study to understand the effects of the material properties on the impedance (anti-resonance) and admittance (resonance) spectra. We utilized the 1-D and 2-D PWAS-EMIS models for the analytical simulations.

We have varied the piezoelectric stiffness and the piezoelectric charge constant by 5%. When we combined both the parameter changes and simulate the impedance and admittance of PWAS, we observe both the frequency and the amplitude shifts in both plots. We have phenomenological agreement in trends of the impedance spectra with the experimental results. However, we still need to improve the agreement by using 2-D circular PWAS-EMIS analytical model and by including more parameter changes to reflect the temperature effects on the piezoelectric material degredation. The parameter changes need to be more linked to the temperature increase by using the experimental measurements in the literature. We also need to include in the model the capacitance change that is measured and found to be strongly dependent on the temperature increase.

From the experimental point of view, we observed a linear trend up to 200ºC then the behavior changes. In the first anti-resonance frequency peak during temperature cycle, we also observed PWAS impedance signature attempting to recover and move up in both frequency and amplitude at the room temperatures until the temperature of 200ºC, it no longer recovers after 200 ºC which is close enough to the Curie temperature for PWAS to possess distinct behavior. The degradation of peak shape after 200 ºC is consistent with the change in capacitance behavior. Downward trend in frequency is common among PWAS-EMIS over elevated temperatures eventhough the shapes of trend are not consistent among samples.

# CHAPTER 5

# IN PLANE EMIS OF CONSTRAINED PWAS USING GMM

This chapter addresses E/M impedance spectroscopy (EMIS) of piezoelectric wafer active sensor (PWAS) constrained on one surface and on both surfaces by isotropic elastic materials through analytical models. Theoretical work for EMIS of constrained piezoelectric actuator was performed.

In the first part of this study, analytical analyses begin with the piezoelectric wafer active sensor (PWAS) under constrained boundary conditions; a simplified two bar and three bar piezo-resonators are modeled using the resonator theory. Three bar resonator model includes a piezoelectric wafer active sensor (PWAS) in the center and two isotropic elastic bars bonded on both sides of the PWAS whereas in two-bar resonator model, PWAS is constrained on one side. The following assumptions are made for the models. First, the geometry and the cross-section area of all the bars are the same although they have different materials and different lengths. Second, the isotropic bars on the sides are assumed to be perfectly bonded to the PWAS at the interfaces. The two-bar and three-bar piezo-resonator models are used to obtain the resonance frequencies for the normal mode expansion method. Essentially, the models are used to build the basis for the proof-mass PWAS (PM-PWAS).

Global matrix method (GMM) is employed to carry all the information from each layer regarding the material properties, geometric properties as well as the boundary conditions into the eigenvalue problem. GMM is also utilized to solve the eigenvalue problem of the two and three-layered PM-PWAS models for the Eigen-vectors and the corresponding Eigen-frequencies.

## 5.1 STATE OF THE ART FOR CONSTRAINED PWAS-EMIS

The analytical in-plane impedance for piezoelectric ceramic transducers such as PWAS has been developed by Giurgiutiu and Zagrai (2000). One and two dimensional in-plane E/M impedance models for free PWAS and constrained PWAS were derived to model the dynamics of PWAS and substrate structure in terms of EMIS. They assumed the constant electric field to derive the in-plane EMIS. Another EMIS modeling of PZT actuator-driven active structures is carried out by Liang, Sun, and Rogers (1996) in low frequency range up to 650 Hz in in-plane mode. Park (2014) analytically investigated the EMIS of piezoelectric transducers bonded on a finite beam from the perspective of wave propagation. The analytic solutions of flexural waves are derived for coupled PWAS-infinite beam. Then the concept is used for finite beam in relatively low frequency range. Annamdas & Radhika (2013) also derived E/M admittance model for PWAS bonded on metallic and non-metallic host structures in relatively frequency range up to 500 kHz. Park et-al. uses impedance based health monitoring to interrogate a bolt jointed pipeline system (Park et al. 2003) in range up to 100 kHz and they also monitored the curing process of concrete structures un range between 100kHz-140kHz. Many other researchers have recently applied in-plane EMIS method for dynamically monitoring the smart structures in different materials and forms (Annamdas et-al 2013; Brus 2013; Liang and Sun 1994; Cheng and Wang, 2001; Park et al. 2012; Pavelko 2014; Peairs et al. 2003; Rugina et al. 2014). For high frequency-band in range of MHz, the analytical study for thickness mode of PWAS-EMIS was performed by Kamas, Lin, and Giurgiutiu 2013).

They aimed to extend the EMIS model of a constrained PWAS at high frequencies (up to 15MHz). The authors utilized the constant electric displacement assumption used in the literature (IEEE Ultrasonics 1987; Meeker 1972) and solved the piezoelectric constitutive equations for the thickness mode.

## 5.2 GLOBAL MATRIX METHOD (GMM) IN MULTILAYERED STRUCTURES

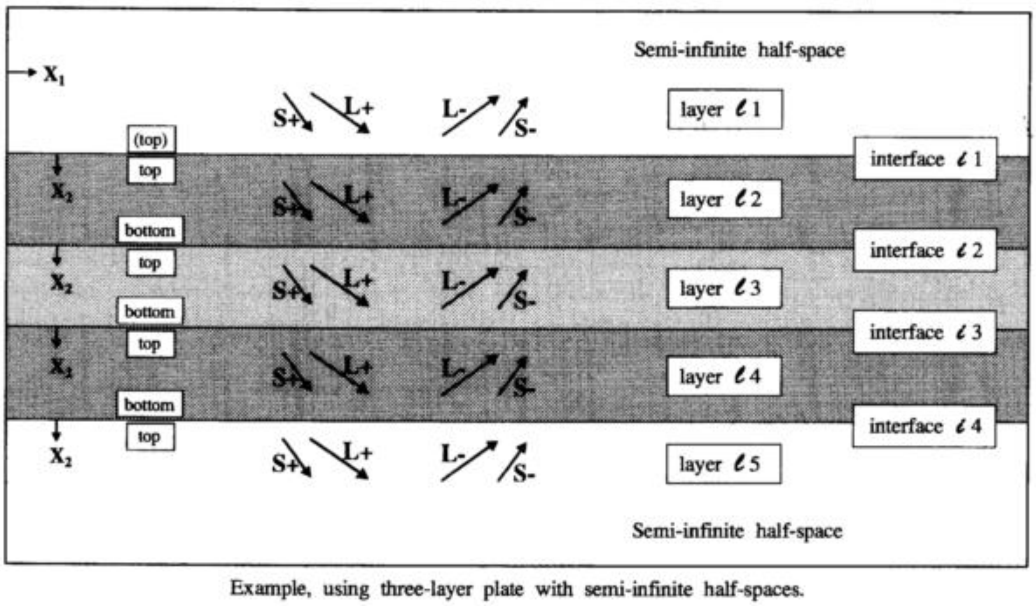


Figure 5.1 Schematic of a multi-layered structure for using Global Matrix Method (GMM) (Lowe, 1995).

Knopoff in 1964 introduced a matrix method for multilayered media which is alternative to the Transfer Matrix Methods (TMM). GMM may be used to avoid the large frequency-half thickness product problem since it is more robust at high frequencies. The same matrix may be used for all categories of solution whether response or modal, vacuum or solid-half spaces, real or complex plate wavenumber (Lowe, 1995). The drawback is largeness therefore the solution may be relatively slow. The system matrix consists of 4(n-1) equations where n is the total number of layers.

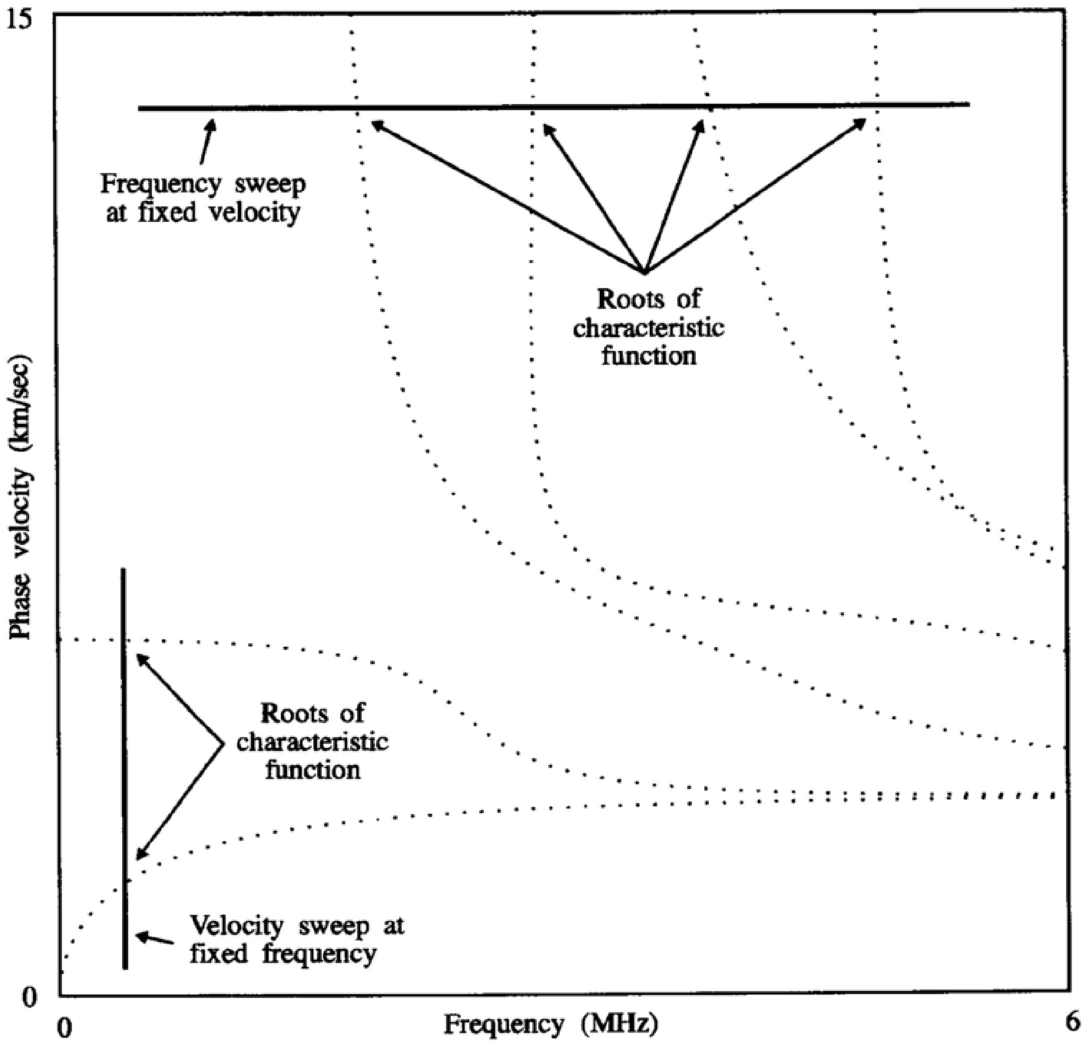


Figure 5.2 Generation of dispersion curves showing Lamb wave modes for 1mm thick sheet of titanium (Lowe, 1995).

The loci of roots of the characteristic function are the dispersion curves for the multilayer plate system. They are usually displayed as phase velocity against frequency but may also be plotted using the wavenumber. The roots are found by varying the phase velocity at fixed frequency or the frequency at fixed velocity (the “sweeps” in Figure 5.2). Each of these roots is the starting point for the calculation of a dispersion curve. To calculate a dispersion curve, the wavenumber is increased steadily (by fixed increments $\Delta k$ ) and a new solution is found at each step by iteration of the frequency. Clearly the speed of convergence and the stability of the iterations are improved by seeding the root-finding algorithm with a good initial guess of the frequency at each step.

## 5.3 IN-PLANE MODE OF PWAS CONSTRAINED FROM ONE SIDE

In this section, we analyze the in-plane mode two-bar resonator model including PWAS perfectly bonded from one side to an isotropic material as shown in Figure 5.3.

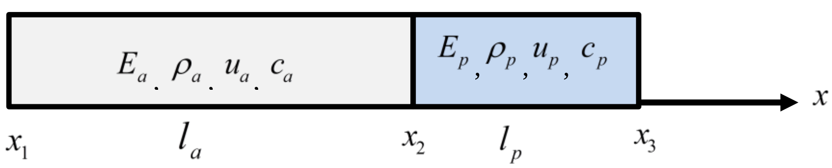


Figure 5.3 Illustration of a two bar resonator model with perfectly bonded PWAS on side of a bar.

### 5.3.1 MECHANICAL ANALYSIS FOR PWAS CONSTRAINED FROM ONE SIDE

The mechanical analysis is performed herein by using resonator theory to derive the resonance and anti-resonance frequencies as response to the electrical harmonic excitation in frequency domain. We obtain the wave equations for each division in the bar shown in Figure 5.3 from Newton's equation of motion as follows;

$$\begin{aligned} c^2 u'' &= \ddot{u} \\ c_a^2 u_a'' &= \ddot{u}_a \end{aligned} \tag{5.1}$$

The general wave equation solutions for each division can be also recalled as

$$\begin{aligned} u_a &= \left(C_1 e^{-i\gamma_a (x-x_1)} + C_2 e^{i\gamma_a (x-x_2)}\right) e^{i\omega t} = \hat{u}_a e^{i\omega t} \\ u_p &= \left(C_3 e^{-i\gamma_p (x-x_2)} + C_4 e^{i\gamma_p (x-x_3)}\right) e^{i\omega t} = \hat{u}_p e^{i\omega t} \end{aligned} \tag{5.2}$$

The strain-displacement relation is determined by

$$
\begin{aligned}
\hat{\varepsilon}_a &= \hat{u}'_a = i\gamma_a \left(-C_1 e^{-i\gamma_a (x-x_1)} + C_2 e^{i\gamma_a (x-x_2)}\right) e^{i\omega t} \\
\hat{\varepsilon}_p &= \hat{u}'_p = i\gamma_p \left(-C_3 e^{-i\gamma_p (x-x_2)} + C_4 e^{i\gamma_p (x-x_3)}\right) e^{i\omega t}
\end{aligned}
\tag{5.3}
$$

Linear Hooke's law applies to determine the stress-strain constitutive equation as follows

$$
\begin{aligned}
\sigma_a &= E_a \varepsilon_a = E_a \hat{u}'_a = iE_a \gamma_a \left(-C_1 e^{-i\gamma_a (x-x_1)} + C_2 e^{i\gamma_a (x-x_2)}\right) \\
\sigma_p &= E_p \varepsilon_p = E_p \hat{u}'_p = iE_p \gamma_p \left(-C_3 e^{-i\gamma_p (x-x_2)} + C_4 e^{i\gamma_p (x-x_3)}\right)
\end{aligned}
\tag{5.4}
$$

where $C_1, C_2, C_3, C_4$ denote the axial wave amplitudes as forward and backward directions respectively in x axis and $\gamma_a, \gamma_p$ denote the wave numbers for each material of the divisions and related to the wave speed in each material;

$$
\begin{aligned}
\gamma_a &= \frac{\omega}{c_a} \\
\gamma_p &= \frac{\omega}{c_p}
\end{aligned}
\tag{5.5}
$$

Four boundary conditions should be implied to the general wave solutions to obtain the four unknown coefficients. The stresses and displacement boundary conditions to be imposed are as follows;

$$
\begin{array}{lll}
@\, x = x_1 & N_a(x_1) = 0 \quad \rightarrow & \sigma_a(x_1) = 0 \rightarrow \varepsilon_a(x_1) = u'_a(x_1) = 0 \\
@\, x = x_2 & N_a(x_2) = N_p(x_2) & \\
 & u_a(x_2) = u_p(x_2) & \\
@\, x = x_3 & N_p(x_3) = 0 &
\end{array}
\tag{5.6}
$$

The first relation between two displacement amplitudes in the material on the left hand side is determined by the stress boundary condition on the left surface at $x = x_1 = 0$

$$
\begin{aligned}
& N_a(x_1) = 0 \\
& E_a \varepsilon_a(x_1) = E_a u'_a(x_1) = iE_a \gamma_a \left(-C_1 e^{-i\gamma_a (x_1-x_1)} + C_2 e^{i\gamma_a (x_1-x_2)}\right) = 0
\end{aligned}
\tag{5.7}
$$

Hence,

$$
-C_1 + C_2 e^{i\gamma_a (x_1-x_2)} = 0 \tag{5.8}
$$

The second relation is determined by the stress boundary condition on interface between the left and the middle bars.

$$\begin{aligned} N_a\left(x_2\right) &= N_p\left(x_2\right) \\ E_a\varepsilon_a\left(x_2\right) &= E_p\varepsilon_p\left(x_2\right) \\ E_a u_a'\left(x_2\right) &= E_p u_p'\left(x_2\right) \end{aligned} \tag{5.9}$$

$$iE_a\gamma_a\left(-C_1e^{-i\gamma_a(x_2-x_1)}+C_2e^{i\gamma_a(x_2-x_2)}\right)=iE_p\gamma_p\left(-C_3e^{-i\gamma_p(x_2-x_2)}+C_4e^{i\gamma_p(x_2-x_3)}\right) \tag{5.10}$$

$$iE_a\gamma_a\left(-C_1e^{-i\gamma_a(x_2-x_1)}+C_2\right)-iE_p\gamma_p\left(-C_3+C_4e^{i\gamma_p(x_2-x_3)}\right)=0 \tag{5.11}$$

$$iE_a\gamma_a\left(-C_1e^{-i\gamma_a(x_2-x_1)}+C_2\right)-iE_p\gamma_p\left(-C_3+C_4e^{i\gamma_p(x_2-x_3)}\right)=0 \tag{5.12}$$

Hence,

$$-C_1iE_a\gamma_ae^{-i\gamma_a(x_2-x_1)}+C_2iE_a\gamma_a+C_3iE_p\gamma_p-C_4iE_p\gamma_pe^{i\gamma_p(x_2-x_3)}=0 \tag{5.13}$$

The displacement boundary condition at $x=x_2$ determines the third relation

$$u_a\left(x_2\right)=u_p\left(x_2\right) \tag{5.14}$$

$$C_1e^{-i\gamma_a(x_2-x_1)}+C_2e^{i\gamma_a(x_2-x_2)}=C_3e^{-i\gamma_p(x_2-x_2)}+C_4e^{i\gamma_p(x_2-x_3)} \tag{5.15}$$

$$C_1e^{-i\gamma_a(x_2-x_1)}+C_2-C_3-C_4e^{i\gamma_p(x_2-x_3)}=0 \tag{5.16}$$

The stress boundary condition on the interface at $x=x_3$ determines the fourth relation between the displacement amplitudes

$$iE_p\gamma_p\left(-C_3e^{-i\gamma_p(x_3-x_2)}+C_4e^{i\gamma_p(x_3-x_3)}\right)=0 \tag{5.17}$$

$$-C_3e^{-i\gamma_p(x_3-x_2)}+C_4=0 \tag{5.18}$$

The equations determined in (5.8), (5.13), (5.16), and (5.18) are combined in a matrix to provide a solution of the Eigen-frequencies and to eventually obtain the Eigenvector (the displacement amplitudes). Therefore, this problem turns out to be an eigenvalue problem which requires a matrix that contains the material properties and wave-numbers as functions of frequency for all subsections in the bar and the matrix is to be multiplied by a tensor that contains the displacement amplitudes and the product of the two matrices will equal to zero as shown in Eq. (5.19).

$$\begin{bmatrix} -1 & e^{i\gamma_a(x_1-x_2)} & 0 & 0 \\ -e^{i\gamma_a(x_1-x_2)} & 1 & \dfrac{E_p}{E_a}\dfrac{\gamma_p}{\gamma_a} & -\dfrac{E_p}{E_a}\dfrac{\gamma_p}{\gamma_a}e^{i\gamma_p(x_2-x_3)} \\ e^{i\gamma_a(x_1-x_2)} & 1 & -1 & -e^{i\gamma_p(x_2-x_3)} \\ 0 & 0 & -e^{i\gamma_p(x_2-x_3)} & 1 \end{bmatrix} \begin{bmatrix} C_1 \\ C_2 \\ C_3 \\ C_4 \end{bmatrix} = 0 \qquad (5.19)$$

Substitute the wavenumbers in Eq. (5.5) into Eq.(5.19); we obtain the matrix in terms of frequency

$$\begin{bmatrix} -1 & e^{i\frac{\omega}{c_a}(x_1-x_2)} & 0 & 0 \\ -e^{i\frac{\omega}{c_a}(x_1-x_2)} & 1 & \dfrac{E_p}{E_a}\dfrac{c_a}{c_p} & -\dfrac{E_p}{E_a}\dfrac{c_a}{c_p}e^{i\frac{\omega}{c_p}(x_2-x_3)} \\ e^{i\frac{\omega}{c_a}(x_1-x_2)} & 1 & -1 & -e^{i\frac{\omega}{c_p}(x_2-x_3)} \\ 0 & 0 & -e^{i\frac{\omega}{c_p}(x_2-x_3)} & 1 \end{bmatrix} \begin{bmatrix} C_1 \\ C_2 \\ C_3 \\ C_4 \end{bmatrix} = 0 \qquad (5.20)$$

The determinant of the material property matrix must equal to zero to have non-trivial solution for the displacement amplitudes. However, the matrix is a singular matrix and requires to be converted to a non-singular or invertible matrix to obtain a solution of basis of the vector of unknown coefficients assuming one of them as 1. For example, let us assume $C_4 = 1$ in this problem and omit of one of the linearly dependent equation to solve the other linearly independent equations.

$$\begin{bmatrix} -1 & e^{i\frac{\omega}{c_a}(x_1-x_2)} & 0 \\ -e^{i\frac{\omega}{c_a}(x_1-x_2)} & 1 & \frac{E_p}{E_a}\frac{c_a}{c_p} \\ e^{i\frac{\omega}{c_a}(x_1-x_2)} & 1 & -1 \end{bmatrix} \begin{bmatrix} C_1 \\ C_2 \\ C_3 \end{bmatrix} = \begin{bmatrix} 0 \\ -\frac{E_p}{E_a}\frac{c_a}{c_p} e^{i\frac{\omega}{c_p}(x_2-x_3)} \\ -e^{i\frac{\omega}{c_p}(x_2-x_3)} \end{bmatrix} \tag{5.21}$$

### 5.3.2 MODE SHAPES

In this subsection, the in-plane mode shapes are derived and plotted by using the geometric sizes and the material properties of aluminum bar and PWAS that are indicated in Table 5.1. Then, the orthogonality of the mode shapes are verified and the normalized mode shapes are found and plotted.

Table 5.1 Geometric sizes and material properties of two-bar resonator.

| Geometric sizes | Material Properties | | |
|---|---|---|---|
| La=30 [mm] | | Aluminum | PWAS |
| Lp=40 [mm] | Elastic Modulus [Gpa] | 72.4 | 65.3 |
| Height=0.2 [mm] | Mass Density [kg/m3] | 2780 | 7700 |
| | Wave Speed [m/s] | 5103 | 2913 |
| | Compliance | | 1.53E-11 |
| | Permittivity | | 1.54E-08 |
| | Piezoelectric Constant | | -1.75E-10 |
| | Internal damping | | 0.05 |

Orthogonality of Mode Shapes

Recall mass-weighted integral to verify the orthogonality of the mode shapes and to find the modal participation factor, $m_i$ of each mode to scale the mode shape amplitudes.

$$\int_0^x \rho A U_i U_j dx = \begin{Bmatrix} 0 \ , \ if \ \ i \neq j \\ m_i \ \ , \ if \ \ i = j \end{Bmatrix} \tag{5.22}$$

For two bar problem, it takes the following form with side surface area, $A$, is omitted since it is equal for each bar in this problem;

$$\rho_a \int_{x_1}^{x_2} U_i^a U_j^a dx + \rho_b \int_{x_2}^{x_3} U_i^p U_j^p dx = \left\{ \begin{matrix} 0 \ , \ if \ \ i \neq j \\ m_i \ , \ if \ \ i = j \end{matrix} \right\} \tag{5.23}$$

Table 5.2 shows the orthogonality matrix that validates the mode shape solution and that gives the modal participation factors. The values off the diagonal should be nearly zero and the values on the diagonal of the matrix should be taken into account as modal mass factor to scale the mode shape down the have the normalized mode shapes.

Table 5.2 Orthogonality matrix that validates the mode shape solution and that gives the modal participation factors.

| | | | | |
|---|---|---|---|---|
| 908.344 + 0.000334i | 0.013 - 0.06i | 0.015 - 0.02i | 0.02 - 0.0001i | 0.02 + 0.0002i |
| 0.013 - 0.06130i | 992.529 - 0.026i | 0.007+ 0.0002i | 0.03 + 0.01i | 0.0017+ 0.007i |
| 0.015 - 0.02133i | 0.0076 + 0.00028i | 795.59- 0.058i | -0.02 | 0.02+ 0.01i |
| 0.02 - 0.00017i | 0.031 + 0.012i | -0.02 | 836.15 + 0.0002i | 0.005 + 0.0009i |
| 0.027 + 0.0002i | 0.0017 + 0.007i | 0.021 + 0.01i | 0.005 + 0.0009i | 1033.102+ 0.00015i |

Normalization of mode shapes: normal modes

After we obtained the modal participation factors (modal mass) which are the values on the diagonal of the orthogonality matrix, we can use the values to normalize the mode shapes by the following relation;

$$U^{new} = \frac{1}{\sqrt{m_i}} U \tag{5.24}$$

Then the mode shape amplitudes are scaled down to new mode shape amplitudes by the normalization. To analyze orthogonality with respect to stiffness, we consider the stiffness weighted integral for two bar resonator model.

$$E_a A \int_{x_1}^{x_2} U_i^{a\prime\prime} U_j^a dx + E_p A \int_{x_2}^{x_3} U_i^{p\prime\prime} U_j^p dx = \begin{Bmatrix} 0 \text{ , if } i \neq j \\ -k_i \text{ , if } i = j \end{Bmatrix} \tag{5.25}$$

We obtain the modal stiffness $k_i$ and considering $U_j = U_j^a + U_j^p$, we recall

$$\int_{x_1}^{x_3} EU_j'^2(x)\,dx = \omega_j^2 \int_{x_1}^{x_3} \rho U_j^2(x)\,dx \qquad j = 1, 2, 3, \ldots \tag{5.26}$$

Using Eq. (5.26), we can come up with

$$k_j = \omega_j^2 m_j \qquad j = 1, 2, 3, \ldots \tag{5.27}$$

We can now plot the normalized mode shapes $U^{new}(x)$ as seen in Table 5.3 at the resonant frequencies $f_r$.

Table 5.3 Normalized mode shapes and resonant frequencies.

| Mode # | Normalized Mode Shape | Resonant Frequency [kHz] |
| --- | --- | --- |
| 1 | 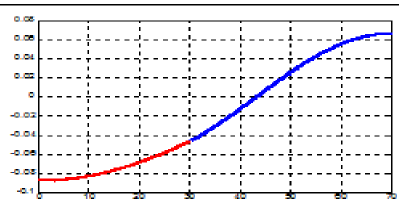 | 27.28 |
| 2 | 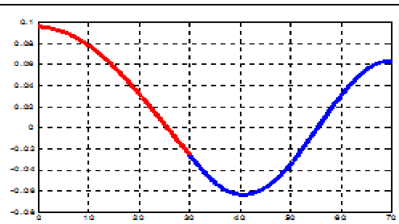 | 49. 83 |
| 3 | 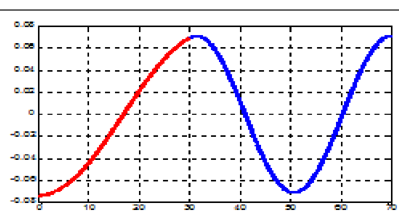 | 75.43 |

### 5.3.3 ELECTRO-MECHANICAL ANALYSIS UNDER CONSTANT ELECTRIC FIELD ASSUMPTION

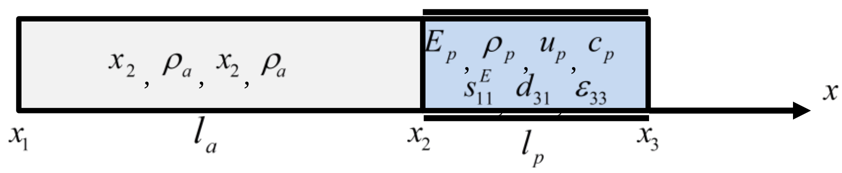


Figure 5.4 Schematic of two bar resonator excited by electrodes deposited on PWAS surfaces.

In-plane electromechanical analysis is conducted in this subsection for the PWAS constrained on one side as seen in Figure 5.4 under constant electric field assumption. Assume voltage applied to the piezoelectric bar, $E_3 = -V/t$, and corresponding induced strain

$$S_{ISA} = d_{31}E_3 = d_{31}\frac{-V}{t} \tag{5.28}$$

The wave speed depending on the piezoelectric material properties can be defined as

$$c^2 = \frac{1}{\rho s_{11}^E} \tag{5.29}$$

The constitutive equation for the strain, stress and the electrical field induced by the electrodes on top and bottom of the piezoelectric material located between two non-piezoelectric materials can be introduced as follows

$$S_1 = s_{11}T_1 + d_{31}E_3 \tag{5.30}$$

And the constitutive equations for the non-piezo materials can be introduced similar to the piezo-material however without the electrical fields;

$$S_1^a = s_{11}^a T_1^a \tag{5.31}$$

The boundary conditions change accordingly

$$@\,x = x_1 \qquad N_a(x_1)=0 \quad \rightarrow \quad \mathrm{T}_1^a(x_1)=0 \rightarrow S_1^a(x_1)=0$$
$$@\,x = x_2 \qquad N_a(x_2)=N_p(x_2) \quad \rightarrow \quad \mathrm{T}_1^a(x_2)=\mathrm{T}_1^p(x_2) \rightarrow \frac{S_1^a(x_2)}{s_{11}^a}=\frac{S_1^p(x_2)-d_{31}E_3}{s_{11}^p}$$
$$u_a(x_2)=u_p(x_2)$$
$$@\,x = x_3 \qquad N_p(x_3)=0 \quad \rightarrow \quad \mathrm{T}_1^p(x_3) \rightarrow S_1^p(x_3)-d_{31}E_3=0$$

(5.32)

$$@\,x = x_1 \qquad S_1^a(x_1)=u_a'(x_1)=0 \tag{5.33}$$

$$u_a=\left(C_1e^{-i\gamma_a(x-x_1)}+C_2e^{i\gamma_a(x-x_2)}\right)e^{i\omega t}=\hat{u}_ae^{i\omega t} \tag{5.34}$$

$$\hat{u}_a'(x_1)=-i\gamma_ae^{-i\gamma_a(x_1-x_1)}C_1+i\gamma_ae^{i\gamma_a(x_1-x_2)}C_2=0 \tag{5.35}$$

$$-C_1+e^{i\gamma_a(x_1-x_2)}C_2=0 \tag{5.36}$$

In matrix form

$$\begin{bmatrix}-1 & e^{i\gamma_a(x_1-x_2)} & 0 & 0\end{bmatrix}\begin{Bmatrix}C_1\\C_2\\C_3\\C_4\end{Bmatrix}=0 \tag{5.37}$$

$$@\,x = x_2 \qquad \frac{S_1^a(x_2)}{s_{11}^a}=\frac{S_1^p(x_2)-d_{31}E_3}{s_{11}^p} \tag{5.38}$$

The elastic modulus of the piezoelectric material is expressed in terms of the compliance

$$E_p=\frac{1}{s_{11}} \tag{5.39}$$

$$\begin{aligned}S_1^a&=u_a'\\S_1^p&=u_p'\end{aligned} \tag{5.40}$$

Upon substitution of Eq(5.39) and (5.40) into (5.38), we obtain

$$E_au_a'(x_2)=E_p\left(u_p'(x_2)-d_{31}E_3\right) \tag{5.41}$$

$$iE_a\gamma_a\left(-C_1e^{-i\gamma_a(x_2-x_1)}+C_2e^{i\gamma_a(x_2-x_2)}\right)=iE_p\gamma_p\left(-C_3e^{-i\gamma_p(x_2-x_2)}+C_4e^{i\gamma_p(x_2-x_3)}\right)-E_pd_{31}E_3$$

(5.42)

Upon rearrangement, Eq(5.42) takes the following form

$$-C_1iE_a\gamma_ae^{-i\gamma_a(x_2-x_1)}+C_2iE_a\gamma_a+C_3iE_p\gamma_p-C_4iE_p\gamma_pe^{i\gamma_p(x_2-x_3)}=-E_pd_{31}E_3 \tag{5.43}$$

In matrix form

$$\begin{bmatrix}-i\dfrac{E_a}{E_p}\gamma_ae^{-i\gamma_a(x_2-x_1)} & i\dfrac{E_a}{E_p}\gamma_a & i\gamma_p & -i\gamma_pe^{i\gamma_p(x_2-x_3)}\end{bmatrix}\begin{Bmatrix}C_1\\C_2\\C_3\\C_4\end{Bmatrix}=-d_{31}E_3 \tag{5.44}$$

$$@\,x=x_2 \qquad u_a(x_2)=u_p(x_2) \tag{5.45}$$

$$C_1e^{-i\gamma_a(x_2-x_1)}+C_2-C_3-C_4e^{i\gamma_p(x_2-x_3)}=0 \tag{5.46}$$

In matrix form

$$\begin{bmatrix}e^{-i\gamma_a(x_2-x_1)} & 1 & -1 & -e^{i\gamma_p(x_2-x_1)}\end{bmatrix}\begin{Bmatrix}C_1\\C_2\\C_3\\C_4\end{Bmatrix}=0 \tag{5.47}$$

$$@\,x=x_3 \qquad S_1^p(x_3)-d_{31}E_3=0 \tag{5.48}$$

$$-i\gamma_pC_3e^{-i\gamma_p(x_3-x_2)}+i\gamma_pC_4=d_{31}E_3 \tag{5.49}$$

In matrix form

$$\begin{bmatrix}0 & 0 & -i\gamma_pe^{-i\gamma(x_3-x_2)} & i\gamma_p\end{bmatrix}\begin{Bmatrix}C_1\\C_2\\C_3\\C_4\end{Bmatrix}=d_{31}E_3 \tag{5.50}$$

Combine the system of the equations derived from the boundary conditions into one matrix form

$$\begin{bmatrix} -1 & e^{i\gamma_a(x_1-x_2)} & 0 & 0 \\ -i\frac{E_a}{E_p}\gamma_a e^{-i\gamma_a(x_2-x_1)} & i\frac{E_a}{E_p}\gamma_a & i\gamma_p & -i\gamma_p e^{i\gamma_p(x_2-x_3)} \\ e^{-i\gamma_a(x_2-x_1)} & 1 & -1 & -e^{i\gamma_p(x_2-x_1)} \\ 0 & 0 & -i\gamma_p e^{-i\gamma(x_3-x_2)} & i\gamma_p \end{bmatrix} \begin{Bmatrix} C_1 \\ C_2 \\ C_3 \\ C_4 \end{Bmatrix} = \begin{Bmatrix} 0 \\ -d_{31}E_3 \\ 0 \\ d_{31}E_3 \end{Bmatrix} \quad (5.51)$$

where the normalized mode shape $U_j^{(new)}(x) = \frac{1}{\sqrt{m}} U_j(x)$. The frequency response function for the two bar resonator problem is

Recall the piezoelectric material constitutive equations under the constant electric field assumption.

$$S_1 = s_{11}^E T_1 + d_{31}E_3 \Rightarrow T_1 = \frac{1}{s_{11}^E} S_1 - \frac{d_{31}}{s_{11}^E} E_3 \quad (5.53)$$

$$D_3 = d_{31}T_1 + \varepsilon_{33}E_3 \quad (5.54)$$

Substitute Eq. (5.53) into Eq. (5.54)

$$D_3 = d_{31}\left(\frac{1}{s_{11}^E} S_1 - \frac{d_{31}}{s_{11}^E} E_3\right) + \varepsilon_{33}E_3 = \frac{d_{31}}{s_{11}^E} S_1 + \left(-\frac{d_{31}^2}{s_{11}^E} + \varepsilon_{33}\right) E_3 \quad (5.55)$$

Upon further rearrangement, the electrical displacement

$$D_3 = \frac{d_{31}}{s_{11}^E} S_1 + \varepsilon_{33}\left(1 - \kappa_{31}^2\right) E_3 \quad (5.56)$$

where $\kappa_{31}^2$ is the electro-mechanical coupling in longitudinal mode and defined as $\kappa_{31}^2 = \frac{d_{31}^2}{s_{11}^E \varepsilon_{33}}$. The electrical charge is given by integral of the electrical displacement over electrode surface area

$$Q_3 = \int_{A_p} D_3 dA = \frac{\varepsilon_{33} A_p}{h}\left(1 - \kappa_{31}^2\right) E_3 h + \frac{d_{31}}{s_{11}^E} \int_{A_p} S_1 dA \quad (5.57)$$

Recall the capacitance of the piezoelectric bar and the electrical potential

$$C_0 = \frac{\varepsilon_{33} A_p}{h} \tag{5.58}$$

$$V = E_3 h \tag{5.59}$$

where $h$ is the thickness of the piezoelectric bar. Upon substitution of Eq. (5.58) and Eq. (5.59) into Eq. (5.57), we have

$$Q_3 = C_0 \left(1 - \kappa_{31}^2\right) V + \frac{d_{31}}{s_{11}^E} b \int_{L_p} u' dx \tag{5.60}$$

$$Q_3 = C_0 \left(1 - \kappa_{31}^2\right) V + \frac{d_{31}}{s_{11}^E} b\, u \Big|_{x_2}^{x_3} \tag{5.61}$$

$$Q_3 = C_0 \left(1 - \kappa_{31}^2\right) V + \frac{d_{31}}{s_{11}^E} b \Delta u \tag{5.62}$$

Substitute Eq. (5.52) into Eq. (5.62)

$$\hat{Q}_3 = C_0 \left(1 - \kappa_{31}^2\right) V + \frac{d_{31}}{s_{11}^E} b \sum_{j=1}^{\infty} \left[ U_j^p \left(x_3\right) - U_j^p \left(x_2\right) \right]_{E/M} \tag{5.63}$$

or

$$\hat{Q}_3 = C_0 \hat{V} \left(1 - \kappa_{31}^2\right) + \frac{d_{31}}{s_{11}^E} b \hat{H}\left(x\right) \tag{5.64}$$

Recall the electrical current as a derivative of the electrical charge with respect to time.

$$I = i\omega Q_3 \tag{5.65}$$

and the electro-mechanical admittance is $Y = I / V$

$$Y = i\omega C_0 \left(1 - \kappa_{31}^2\right) + \frac{d_{31}}{s_{11}^E} \frac{b}{\hat{V}} \hat{H}\left(x\right) \tag{5.66}$$

In our case the frequency response function $\hat{H}\left(x\right)$ is the difference of the displacements at two ends of the piezoelectric electrodes.

$$\hat{H}(x) = \sum_{j=1}^{\infty} U_j^P(x_3) - U_j^P(x_2) \tag{5.67}$$

where

$$U_j^P(x) = C_3 e^{-j\gamma(x-x_2)} + C_4 e^{j\gamma(x-x_3)} \tag{5.68}$$

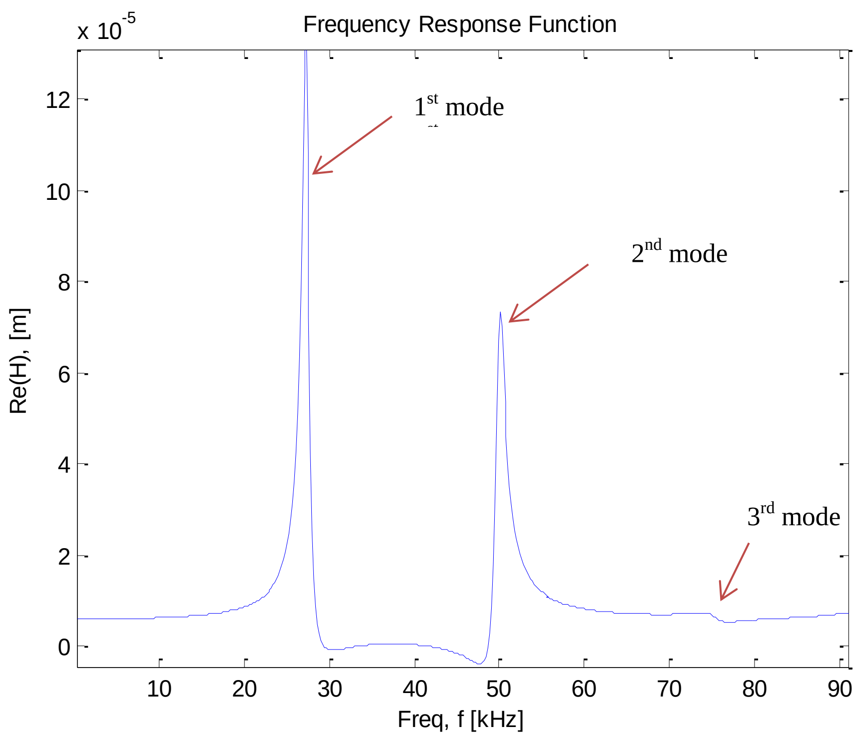


Figure 5.5 Frequency response function of two-bar PWAS resonator.

When we plot the frequency response function, we can see the displacement behavior at resonant frequencies. Now, we take a closer look at the first three resonant frequencies to explain the connection between the peak amplitudes and the mode shapes that were obtained from the mechanical analysis. It is presumed that the peak amplitude is larger when the difference of the amplitudes at two ends of the normalized mode shapes of the piezoelectric subsection $\Delta U^{(p)}$ is larger. However, this does not apply to the relation between the first and second modes as applying to the relation between the second and the third modes. As can be observed in the frequency response function plot in Figure 5.5 the third mode at 75.43 kHz can be barely seen since $\Delta U_3^{(p)}$ has small value. The results from the frequency response function for the two-bar resonator model is presented in Figure 5.6.

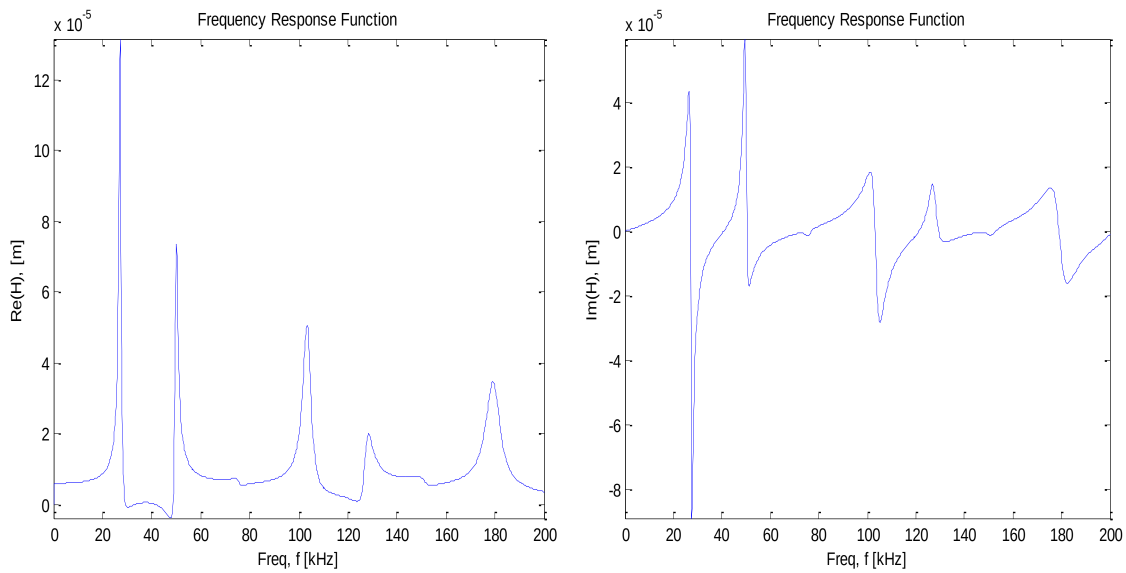


Figure 5.6 Frequency response function for two-bar resonator. Height is 0.2 mm and length of aluminum 30 mm and length of PWAS is 40 mm.

## 5.4 IN-PLANE MODE OF PWAS CONSTRAINED FROM BOTH SIDES

In this section, we analyze the in-plane mode three-bar resonator model including PWAS perfectly bonded from two sides to two isotropic materials as shown in Figure 5.7.

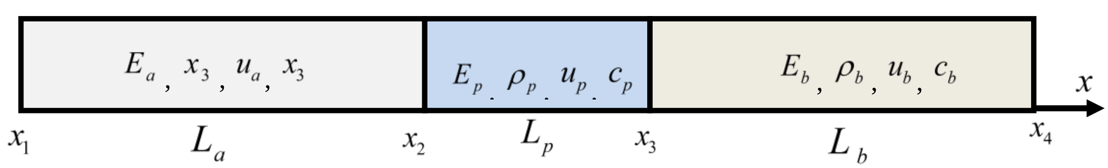


Figure 5.7 Illustration of a three bar resonator model with perfectly bonded PWAS on sides of two bars.

### 5.4.1 MECHANICAL ANALYSIS FOR PWAS CONSTRAINED FROM BOTH SIDES

The mechanical analysis is performed herein by using resonator theory to derive the resonance and anti-resonance frequencies as response to the electrical harmonic excitation in frequency domain. The 1-D wave equation is solved regarding harmonic standing waves. Then, the mode shapes at resonance frequencies are determined for in-plane mode and orthogonality of the mode shapes are verified and the normalized mode shapes are also determined using the modal mass factors that are determined as a diagonal values in the orthogonality matrix.

Harmonic Standing Waves

We obtain the wave equations for each division in the bar shown in Figure 5.3 from Newton's equation of motion as follows;

$$\begin{aligned} c^2 u'' &= \ddot{u} \\ c_a^2 u_a'' &= \ddot{u}_a \\ c_b^2 u_b'' &= \ddot{u}_b \end{aligned} \tag{5.69}$$

The general wave equation solutions for each division can be also recalled as

$$\begin{aligned} u_a &= \left( C_1 e^{-i\gamma_a (x-x_1)} + C_2 e^{i\gamma_a (x-x_2)} \right) e^{i\omega t} = \hat{u}_a e^{i\omega t} \\ u_p &= \left( C_3 e^{-i\gamma_p (x-x_2)} + C_4 e^{i\gamma_p (x-x_3)} \right) e^{i\omega t} = \hat{u}_p e^{i\omega t} \\ u_b &= \left( C_5 e^{-i\gamma_b (x-x_3)} + C_6 e^{i\gamma_b (x-x_4)} \right) e^{i\omega t} = \hat{u}_b e^{i\omega t} \end{aligned} \tag{5.70}$$

The strain-displacement relation is determined by

$$\begin{aligned} u_a' &= i\gamma_a \left( -C_1 e^{-i\gamma_a (x-x_1)} + C_2 e^{i\gamma_a (x-x_2)} \right) e^{i\omega t} \\ u_p' &= i\gamma_p \left( -C_3 e^{-i\gamma_p (x-x_2)} + C_4 e^{i\gamma_p (x-x_3)} \right) e^{i\omega t} \\ u_b' &= i\gamma_b \left( -C_5 e^{-i\gamma_b (x-x_3)} + C_6 e^{i\gamma_b (x-x_4)} \right) e^{i\omega t} \end{aligned} \tag{5.71}$$

Linear Hooke's law applies to determine the stress-strain constitutive equation as follows

$$\begin{aligned}
\sigma_a &= E_a\varepsilon_a = E_a u_a' = iE_a\gamma_a\left(-C_1 e^{-i\gamma_a(x-x_1)} + C_2 e^{i\gamma_a(x-x_2)}\right)e^{i\omega t} \\
\sigma_p &= E_p\varepsilon_p = E_p u_p' = iE_p\gamma_p\left(-C_3 e^{-i\gamma_p(x-x_2)} + C_4 e^{i\gamma_p(x-x_3)}\right)e^{i\omega t} \\
\sigma_b &= E_b\varepsilon_b = E_b u_b' = iE_b\gamma_b\left(-C_5 e^{-i\gamma_b(x-x_3)} + C_6 e^{i\gamma_b(x-x_4)}\right)e^{i\omega t}
\end{aligned} \tag{5.72}$$

where the capital coefficients denote the axial wave amplitudes as forward and backward directions respectively in x axis and $\gamma, \gamma_a, \gamma_b$ denote the wave numbers for each material of the divisions and related to the wave speed in each material;

$$\begin{aligned}
\gamma_a &= \frac{\omega}{c_a} \\
\gamma_p &= \frac{\omega}{c_p} \\
\gamma_b &= \frac{\omega}{c_b}
\end{aligned} \tag{5.73}$$

Six boundary conditions should be implied to the general wave solutions to obtain the six unknown coefficients. The stress and displacement boundary conditions to be imposed are as follows;

$$\begin{array}{ll}
@\,x = x_1 & N_a(x_1)=0 \quad \rightarrow \quad \sigma_a(x_1) = 0 \rightarrow \varepsilon_a(x_1) = u_a'(x_1) = 0 \\
@\,x = x_2 & N_a(x_2) = N_p(x_2) \\
 & u_a(x_2) = u_p(x_2) \\
@\,x = x_3 & N_p(x_3) = N_b(x_3) \\
 & u_p(x_3) = u_b(x_3) \\
@\,x = x_4 & N_b(x_4)=0
\end{array} \tag{5.74}$$

The first relation between two displacement amplitudes in the material on the left hand side is determined by the stress boundary condition on the left surface at $x = x_1$

$$\begin{aligned}
&N_a(x_1) = 0 \\
&E_a\varepsilon_a(x_1) = E_a u_a'(x_1) = 0 \\
&E_a i\gamma_a\left(-C_1 e^{-i\gamma_a(x_1-x_1)} + C_2 e^{i\gamma_a(x_1-x_2)}\right) = 0
\end{aligned} \tag{5.75}$$

Hence,

$$-C_1 + C_2 e^{i\gamma_a(x_1-x_2)} = 0 \tag{5.76}$$

The second relation is determined by the stress boundary condition on interface between the left and the middle bars.

$$\begin{aligned} N_a(x_2) &= N_p(x_2) \\ E_a\varepsilon_a(x_2) &= E_p\varepsilon_p(x_2) \\ E_a u_a'(x_2) &= E_p u_p'(x_2) \end{aligned} \tag{5.77}$$

$$E_a i\gamma_a\left(-C_1 e^{-i\gamma_a(x_2-x_1)} + C_2 e^{i\gamma_a(x_2-x_2)}\right) = E_p i\gamma_p\left(-C_3 e^{-i\gamma_p(x_2-x_2)} + C_4 e^{i\gamma_p(x_3-x_2)}\right) \tag{5.78}$$

$$-C_1 E_a i\gamma_a e^{-i\gamma_a(x_2-x_1)} + C_2 E_a i\gamma_a = -C_3 E_p i\gamma_p + C_4 E_p i\gamma_p e^{i\gamma_p(x_2-x_3)} \tag{5.79}$$

Hence,

$$-C_1 E_a i\gamma_a e^{-i\gamma_a(x_2-x_1)} + C_2 E_a i\gamma_a + C_3 E_p i\gamma_p - C_4 E_p i\gamma_p e^{i\gamma_p(x_2-x_3)} = 0 \tag{5.80}$$

The displacement boundary condition at $x = x_2$ determines the third relation

$$u_a(x_2) = u_p(x_2) \tag{5.81}$$

$$C_1 e^{-i\gamma_a(x_2-x_1)} + C_2 e^{i\gamma_a(x_2-x_2)} = C_3 e^{-i\gamma_p(x_2-x_2)} + C_4 e^{i\gamma_p(x_2-x_3)} \tag{5.82}$$

$$C_1 e^{-i\gamma_a(x_2-x_1)} + C_2 - C_3 - C_4 e^{i\gamma_p(x_2-x_3)} = 0 \tag{5.83}$$

The stress boundary condition on the interface at $x = x_3$ determines the fourth relation between the displacement amplitudes

$$E_p\gamma_p\left(-C_3 e^{-i\gamma_p(x_3-x_2)} + C_4 e^{i\gamma_p(x_3-x_3)}\right) = E_b\gamma_b\left(-C_5 e^{-i\gamma_b(x_3-x_3)} + C_6 e^{i\gamma_b(x_3-x_4)}\right) \tag{5.84}$$

$$-C_3 E_p\gamma_p e^{-i\gamma_p(x_3-x_2)} + C_4 E_p\gamma_p e^{i\gamma_p(x_3-x_3)} = -C_5 E_b\gamma_b e^{-i\gamma_b(x_3-x_3)} + C_6 E_b\gamma_b e^{i\gamma_b(x_3-x_4)} \tag{5.85}$$

$$-C_3 E_p\gamma_p e^{-i\gamma_p(x_3-x_2)} + C_4 E_p\gamma_p + C_5 E_b\gamma_b - C_6 E_b\gamma_b e^{i\gamma_b(x_3-x_4)} = 0 \tag{5.86}$$

as well as the displacement boundary conditions on the same interface determines the fifth relation

$$C_3 e^{-i\gamma_p(x_3-x_2)} + C_4 e^{i\gamma_p(x_3-x_3)} = C_5 e^{-i\gamma_b(x_3-x_3)} + C_6 e^{i\gamma_b(x_3-x_4)} \tag{5.87}$$

$$C_3 e^{-i\gamma_p(x_3-x_2)} + C_4 - C_5 - C_6 e^{i\gamma_b(x_3-x_4)} = 0 \tag{5.88}$$

The stress-free boundary condition on the free-surface at $x_4$ determines the sixth relation

$$E_b\left(-i\gamma_b C_5 e^{-i\gamma_b(x_4-x_3)} + i\gamma_b C_6 e^{i\gamma_b(x_4-x_4)}\right) = 0 \tag{5.89}$$

$$-C_5 e^{-i\gamma_b(x_4-x_3)} + C_6 = 0 \tag{5.90}$$

The linearly dependent equations determined in (5.76), (5.80), (5.83), (5.86), (5.88), and (5.90) by implying the stress and displacement boundary conditions and they are combined in a matrix form to provide a solution of the Eigen-frequencies and to eventually obtain the six Eigen-vectors (the displacement amplitudes). Therefore, this problem turns out to be an eigenvalue problem which requires a matrix that contains the material properties and wave-numbers as functions of frequency for all subsections in the bar and the matrix is to be multiplied by a tensor that contains the displacement amplitudes and the product of the two matrices will equal to zero as shown in Eq. (5.91)

$$\begin{pmatrix} 1 & -e^{i\gamma_a(x_1-x_2)} & 0 & 0 & 0 & 0 \\ -E_a\gamma_a e^{-i\gamma_a(x_2-x_1)} & E_a\gamma_a & E_p\gamma_p & -E_p\gamma_p e^{i\gamma_p(x_2-x_3)} & 0 & 0 \\ e^{-i\gamma_a(x_2-x_1)} & 1 & -1 & -e^{i\gamma_p(x_2-x_3)} & 0 & 0 \\ 0 & 0 & e^{-i\gamma_p(x_3-x_2)} & 1 & -1 & -e^{i\gamma_b(x_3-x_4)} \\ 0 & 0 & -E_p\gamma_p e^{-i\gamma_p(x_3-x_2)} & E_p\gamma_p & E_b\gamma_b & -E_b\gamma_b e^{i\gamma_b(x_3-x_4)} \\ 0 & 0 & 0 & 0 & -e^{-i\gamma_b(x_4-x_3)} & 1 \end{pmatrix} \begin{Bmatrix} C_1 \\ C_2 \\ C_3 \\ C_4 \\ C_5 \\ C_6 \end{Bmatrix} = 0 \qquad (5.91)$$

$$\begin{pmatrix} 1 & -e^{-i\gamma_a L_a} & 0 & 0 & 0 & 0 \\ -E_a\gamma_a e^{-i\gamma_a L_a} & E_a\gamma_a & E_p\gamma_p & -E_p\gamma_p e^{-i\gamma_p L_p} & 0 & 0 \\ e^{-i\gamma_a L_a} & 1 & -1 & -e^{-i\gamma_p L_p} & 0 & 0 \\ 0 & 0 & e^{-i\gamma_p L_b} & 1 & -1 & -e^{-i\gamma_b L_b} \\ 0 & 0 & -E_p\gamma_p e^{-i\gamma_p L_p} & E_p\gamma_p & E_b\gamma_b & -E_b\gamma_b e^{-i\gamma_b L_b} \\ 0 & 0 & 0 & 0 & -e^{-i\gamma_b L_b} & 1 \end{pmatrix} \begin{Bmatrix} C_1 \\ C_2 \\ C_3 \\ C_4 \\ C_5 \\ C_6 \end{Bmatrix} = 0 \qquad (5.92)$$

Each of the three divisions of the material property matrix represents each corresponding bar subsection. Upon rearrangement by substituting the wavenumbers in Eq. (5.5) into Eq.(5.91); we obtain the matrix in terms of frequency

$$\begin{pmatrix} 1 & -e^{-i\frac{\omega}{c_a}L_a} & 0 & 0 & 0 & 0 \\ -e^{-i\frac{\omega}{c_a}L_a} & 1 & \dfrac{E_p c_a}{E_a c_p} & -\dfrac{E_p c_a}{E_a c_p} e^{-i\frac{\omega}{c_p}L_p} & 0 & 0 \\ e^{-i\frac{\omega}{c_a}L_a} & 1 & -1 & -e^{-i\frac{\omega}{c_p}L_p} & 0 & 0 \\ 0 & 0 & e^{-i\frac{\omega}{c_p}L_p} & 1 & -1 & -e^{-i\frac{\omega}{c_b}L_b} \\ 0 & 0 & -\dfrac{E_p c_b}{E_b c_p} e^{-i\frac{\omega}{c_p}L_p} & \dfrac{E_p c_b}{E_b c_p} & 1 & -e^{-i\frac{\omega}{c_b}L_b} \\ 0 & 0 & 0 & 0 & -e^{-i\frac{\omega}{c_b}L_b} & 1 \end{pmatrix} \begin{Bmatrix} C_1 \\ C_2 \\ C_3 \\ C_4 \\ C_5 \\ C_6 \end{Bmatrix} = 0 \qquad (5.93)$$

The determinant of the material property matrix $A_{6x6}$ must equal to zero to have non-trivial solution for the displacement amplitudes.

$$\left| A_{6x6} \right| = 0 \qquad (5.94)$$

The material property matrix is a singular matrix and it does not have a unique solution. Therefore, we can find the basis of the eigenvector by assuming one of the unknowns is one i.e.

$$C_6 = 1 \qquad (5.95)$$

This assumption helps us obtain the following equation

$$
\begin{pmatrix}
1 & -e^{-i\frac{\omega}{c_a}L_a} & 0 & 0 & 0 \\
-e^{-i\frac{\omega}{c_a}L_a} & 1 & \dfrac{E_p c_a}{E_a c_p} & -\dfrac{E_p c_a}{E_a c_p} e^{-i\frac{\omega}{c_p}L_p} & 0 \\
e^{-i\frac{\omega}{c_a}L_a} & 1 & -1 & -e^{-i\frac{\omega}{c_p}L_p} & 0 \\
0 & 0 & -e^{-i\frac{\omega}{c_p}L_p} & 1 & -1 \\
0 & 0 & -\dfrac{E_p c_b}{E_b c_p} e^{-i\frac{\omega}{c_p}L_p} & \dfrac{E_p c_b}{E_b c_p} & 1
\end{pmatrix}
\begin{Bmatrix} C_1 \\ C_2 \\ C_3 \\ C_4 \\ C_5 \end{Bmatrix}
=
\begin{Bmatrix} 0 \\ 0 \\ 0 \\ e^{-i\gamma_b L_b} \\ e^{-i\frac{\omega}{c_b}L_b} \end{Bmatrix}
\tag{5.96}
$$

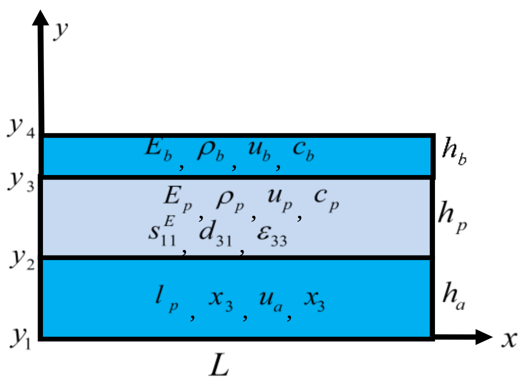


| Geometric sizes | Material Properties | | |
|---|---|---|---|
| ha=1 [mm] | | Aluminum | PWAS |
| hp=0.5 [mm] | Elastic Modulus [Gpa] | 72.4 | 65.3 |
| hb=0.5 [mm] | Mass Density [kg/m3] | 2780 | 7700 |
| Length=7 [mm] | Wave Speed [m/s] | 5103 | 2913 |
| | Compliance | | 1.53E-11 |
| | Permittivity | | 1.54E-08 |
| | Piezoelectric Constant | | -1.75E-10 |
| | Internal damping | | 0.05 |

Figure 5.8 Geometric sizes and material properties of proof-mass PWAS resonator.

<u>Normalization of mode shapes: normal modes</u>

After we obtained the modal participation factors (modal mass) which are the values on the diagonal of the orthogonality matrix, we can use the values to normalize the mode shapes by the following relation;

$$
U^{new} = \frac{1}{\sqrt{m_i}} U \tag{5.97}
$$

Then the mode shape amplitudes are scaled down to new mode shape amplitudes by the normalization. To analyze orthogonality with respect to stiffness, we consider the stiffness weighted integral for three bar resonator model.

$$E_a A\int_{x_1}^{x_2} U_i^{a\prime\prime} U_j^a dx + E_p A\int_{x_2}^{x_3} U_i^{p\prime\prime} U_j^p dx + E_b A\int_{x_3}^{x_4} U_i^{b\prime\prime} U_j^b dx = \begin{Bmatrix} 0 \text{ , if } i \neq j \\ -k_i \text{ , if } i = j \end{Bmatrix} \tag{5.98}$$

We obtain the modal stiffness $k_i$ and considering $U_j = U_j^a + U_j^p + U_j^b$, we recall

$$\int_{x_1}^{x_3} E U_j'^2 (x) dx = \omega_j^2 \int_{x_1}^{x_3} \rho U_j^2 (x) dx \qquad j = 1, 2, 3, \ldots \tag{5.99}$$

Using Eq. (5.26), we can come up with

$$k_j = \omega_j^2 m_j \qquad j = 1, 2, 3, \ldots \tag{5.100}$$

We can now plot the normalized mode shapes $U^{new}(x)$ at the resonant frequency $f_r$ for the three-bar resonator

Table 5.4 Mode numbers, normalized mode shapes, and resonant frequencies

| Mode # | Mode Shape | Resonant Frequency [kHz] |
|---|---|---|
| 1 | 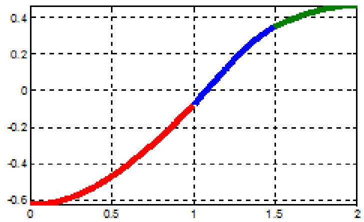 | 1.1718 |
| 2 | 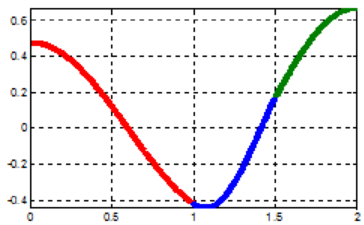 | 2.1358 |
| 3 | 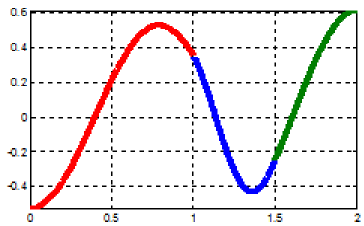 | 3.2321 |

### 5.4.2 ELECTRO-MECHANICAL ANALYSIS UNDER CONSTANT ELECTRIC FIELD ASSUMPTION

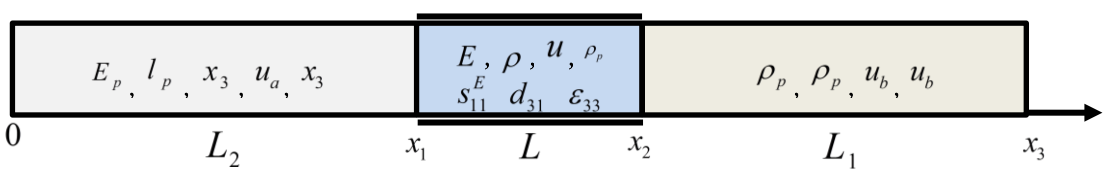


Figure 5.9 Schematic of three-bar resonator with excited PWAS through a harmonic electrical field induced by the elecrodes deposited on PWAS

In-plane electromechanical analysis is conducted in this subsection for the PWAS constrained on both sides as seen in Figure 5.9 under constant electric field assumption. The wave speed depending on the piezoelectric material properties can be defined as

$$c^2 = \frac{1}{\rho s_{11}^E} \tag{5.101}$$

The constitutive equation for the strain, stress and the electrical field induced by the electrodes on top and bottom of the piezoelectric material located between two non-piezoelectric materials can be introduced as follows

$$S_1 = s_{11}T_1 + d_{31}E_3 \tag{5.102}$$

and the constitutive equations for the non-piezo materials can be introduced similar to the piezo-material however without the electrical fields;

$$\begin{aligned} S_1^a &= s_{11}^a T_1^a \\ S_1^b &= s_{11}^b T_1^b \end{aligned} \tag{5.103}$$

The boundary conditions change accordingly

$$\begin{array}{lllll}
@\,x = x_1 & N_a(x_1) = 0 & \rightarrow & \mathrm{T}_1^a(x_1) = 0 \rightarrow S_1^a(x_1) = 0 & \\
@\,x = x_2 & N_a(x_2) = N_p(x_2) & \rightarrow & T_1^a(x_2) = T_1^p(x_2) & \rightarrow \dfrac{S_1^a(x_2)}{s_{11}^a} = \dfrac{S_1^p(x_2) - d_{31}E_3}{s_{11}^p} \\
 & u_a(x_2) = u_p(x_2) & & & \\
@\,x = x_3 & N_p(x_3) = N_b(x_3) & \rightarrow & T_1^P(x_3) = T_1^b(x_3) & \rightarrow \dfrac{S_1^p(x_3) - d_{31}E_3}{s_{11}^p} = \dfrac{S_1^b(x_3)}{s_{11}^b} \\
 & u_p(x_3) = u_b(x_3) & & & \\
@\,x = x_4 & N_b(x_4) = 0 & \rightarrow & \mathrm{T}_1^b(x_4) = 0 \rightarrow S_1^b(x_4) = 0 &
\end{array}$$

(5.104)

$$@\,x = x_1 \qquad S_1^a(x_1) = u_a'(x_1) = 0 \tag{5.105}$$

$$u_a = \left(C_1 e^{-i\gamma_a(x-x_1)} + C_2 e^{i\gamma_a(x-x_2)}\right)e^{i\omega t} = \hat{u}_a e^{i\omega t} \tag{5.106}$$

$$\hat{u}_a'(x_1) = -i\gamma_a e^{-i\gamma_a(x_1-x_1)}C_1 + i\gamma_a e^{i\gamma_a(x_1-x_2)}C_2 = 0 \tag{5.107}$$

$$-C_1 + e^{i\gamma_a(x_1-x_2)}C_2 = 0 \tag{5.108}$$

In matrix form

$$\begin{bmatrix} -1 & e^{i\gamma_a(x_1-x_2)} & 0 & 0 & 0 & 0 \end{bmatrix} \begin{Bmatrix} C_1 \\ C_2 \\ C_3 \\ C_4 \\ C_5 \\ C_6 \end{Bmatrix} = 0 \tag{5.109}$$

$$@\, x = x_2 \qquad \frac{S_1^a\left(x_2\right)}{s_{11}^a} = \frac{S_1^p\left(x_2\right) - d_{31}E_3}{s_{11}^p} \tag{5.110}$$

The elastic modulus of the piezoelectric material is expressed in terms of the compliance

$$\begin{aligned} E_a &= \frac{1}{s_{11}^a} \\ E_p &= \frac{1}{s_{11}^p} \end{aligned} \tag{5.111}$$

$$\begin{aligned} S_1^a &= u_a' \\ S_1^p &= u_p' \end{aligned} \tag{5.112}$$

Upon substitution of Eq(5.39) and (5.40) into (5.38), we obtain

$$E_a u_a'\left(x_2\right) = E_p\left(u_p'\left(x_2\right) - d_{31}E_3\right) \tag{5.113}$$

Upon rearrangement, Eq(5.42) takes the following form

$$-C_1 iE_a\gamma_a e^{-i\gamma_a(x_2-x_1)} + C_2 iE_a\gamma_a + C_3 iE_p\gamma_p - C_4 iE_p\gamma_p e^{i\gamma_p(x_2-x_3)} = -E_p d_{31}E_3 \tag{5.114}$$

In matrix form

$$\begin{bmatrix} -i\dfrac{E_a}{E_p}\gamma_a e^{-i\gamma_a(x_2-x_1)} & i\dfrac{E_a}{E_p}\gamma_a & i\gamma_p & -i\gamma_p e^{i\gamma_p(x_2-x_3)} & 0 & 0 \end{bmatrix} \begin{Bmatrix} C_1 \\ C_2 \\ C_3 \\ C_4 \\ C_5 \\ C_6 \end{Bmatrix} = -d_{31}E_3 \tag{5.115}$$

$$@\, x = x_2 \qquad u_a\left(x_2\right) = u_p\left(x_2\right) \tag{5.116}$$

$$C_1 e^{-i\gamma_a(x_2-x_1)} + C_2 - C_3 - C_4 e^{i\gamma_p(x_2-x_3)} = 0 \tag{5.117}$$

In matrix form

$$\begin{bmatrix} e^{-i\gamma_a(x_2-x_1)} & 1 & -1 & -e^{i\gamma_p(x_2-x_3)} & 0 & 0 \end{bmatrix} \begin{Bmatrix} C_1 \\ C_2 \\ C_3 \\ C_4 \\ C_5 \\ C_6 \end{Bmatrix} = 0 \tag{5.118}$$

The stress boundary condition on the interface at $x = x_3$ determines the fourth relation

$$@\, x = x_3 \qquad \frac{S_1^p(x_3) - d_{31}E_3}{s_{11}^p} = \frac{S_1^b(x_3)}{s_{11}^b} \tag{5.119}$$

$$E_p\left(u_p'(x_3) - d_{31}E_3\right) = E_b u_b'(x_3) \tag{5.120}$$

$$iE_p\gamma_p\left(-C_3 e^{-i\gamma_p(x_3-x_2)} + C_4 e^{i\gamma_p(x_3-x_3)}\right) - E_p d_{31}E_3 = iE_b\gamma_b\left(-C_5 e^{-i\gamma_b(x_3-x_3)} + C_6 e^{i\gamma_b(x_3-x_4)}\right)$$

(5.121)

Upon rearrangement

$$-C_3 i\gamma_p e^{-i\gamma_p(x_3-x_2)} + C_4 i\gamma_p + C_5 i\frac{E_b}{E_p}\gamma_b - C_6 i\frac{E_b}{E_p}\gamma_b e^{i\gamma_b(x_3-x_4)} = d_{31}E_3 \tag{5.122}$$

In a matrix form

$$\begin{bmatrix} 0 & 0 & -i\gamma_p e^{-i\gamma_p(x_3-x_2)} & i\gamma_p & i\frac{E_b}{E_p}\gamma_b & -i\frac{E_b}{E_p}\gamma_b e^{i\gamma_b(x_3-x_4)} \end{bmatrix} \begin{Bmatrix} C_1 \\ C_2 \\ C_3 \\ C_4 \\ C_5 \\ C_6 \end{Bmatrix} = d_{31}E_3 \tag{5.123}$$

The displacement boundary condition on the interface at $x = x_3$ determines the fifth relation

$$@\,x = x_3 \qquad u_p\left(x_3\right) = u_b\left(x_3\right) \tag{5.124}$$

$$C_3 e^{-i\gamma_p(x_3 - x_2)} + C_4 - C_5 - C_6 e^{i\gamma_p(x_3 - x_4)} = 0 \tag{5.125}$$

In a matrix form

$$\begin{bmatrix} 0 & 0 & e^{-i\gamma_p(x_3 - x_2)} & 1 & -1 & -e^{i\gamma_p(x_3 - x_4)} \end{bmatrix} \begin{Bmatrix} C_1 \\ C_2 \\ C_3 \\ C_4 \\ C_5 \\ C_6 \end{Bmatrix} = 0 \tag{5.126}$$

The stress boundary condition on the free surface at $x = x_4$ determines

$$@\,x = x_4 \qquad S_1^b\left(x_4\right) = u_b'\left(x_4\right) = 0 \tag{5.127}$$

$$u_b = \left(C_5 e^{-i\gamma_b(x - x_3)} + C_6 e^{i\gamma_b(x - x_4)}\right) e^{i\omega t} = \hat{u}_b e^{i\omega t} \tag{5.128}$$

$$\hat{u}_b'\left(x_4\right) = -i\gamma_b e^{-i\gamma_b\left(x_4 - x_3\right)} C_5 + i\gamma_b e^{i\gamma_b\left(x_4 - x_4\right)} C_6 = 0 \tag{5.129}$$

In matrix form

$$\begin{bmatrix} 0 & 0 & 0 & 0 & -i\gamma_b e^{-i\gamma_b\left(x_4 - x_3\right)} & 1 \end{bmatrix} \begin{Bmatrix} C_1 \\ C_2 \\ C_3 \\ C_4 \\ C_5 \\ C_6 \end{Bmatrix} = 0 \tag{5.130}$$

Combine the system of the equations derived from the boundary conditions into one matrix form

$$\begin{bmatrix} -1 & e^{i\gamma_a(x_1-x_2)} & 0 & 0 & 0 & 0 \\ -i\dfrac{E_a}{E_p}\gamma_a e^{-i\gamma_a(x_2-x_1)} & i\dfrac{E_a}{E_p}\gamma_a & i\gamma_p & -i\gamma_p e^{i\gamma_p(x_2-x_3)} & 0 & 0 \\ e^{-i\gamma_a(x_2-x_1)} & 1 & -1 & -e^{i\gamma_p(x_2-x_3)} & 0 & 0 \\ 0 & 0 & -i\gamma_p e^{-i\gamma_p(x_3-x_2)} & i\gamma_p & i\dfrac{E_b}{E_p}\gamma_b & -i\dfrac{E_b}{E_p}\gamma_b e^{i\gamma_b(x_3-x_4)} \\ 0 & 0 & e^{-i\gamma_p(x_3-x_2)} & 1 & -1 & -e^{i\gamma_p(x_3-x_4)} \\ 0 & 0 & 0 & 0 & -i\gamma_b e^{-i\gamma_b(x_4-x_3)} & 1 \end{bmatrix} \begin{Bmatrix} C_1 \\ C_2 \\ C_3 \\ C_4 \\ C_5 \\ C_6 \end{Bmatrix} = \begin{Bmatrix} 0 \\ -d_{31}E_3 \\ 0 \\ d_{31}E_3 \\ 0 \\ 0 \end{Bmatrix} \tag{5.131}$$

where the normalized mode shape $U_j^{(new)}(x) = \dfrac{1}{\sqrt{m}} U_j(x)$. The frequency response function for the three bar resonator problem is

$$H(x,t) = \Delta u(x,t) = \sum_{j=1}^{\infty} \left[ U_j^p(x_3) - U_j^p(x_2) \right] e^{i\omega t} \tag{5.132}$$

Recall the piezoelectric material constitutive equations under the constant electric field assumption.

$$S_1 = s_{11}^E T_1 + d_{31} E_3 \Rightarrow T_1 = \frac{1}{s_{11}^E} S_1 - \frac{d_{31}}{s_{11}^E} E_3 \tag{5.133}$$

$$D_3 = d_{31} T_1 + \varepsilon_{33} E_3 \tag{5.134}$$

Substitute Eq. (5.53) into Eq. (5.54)

$$D_3 = d_{31} \left( \frac{1}{s_{11}^E} S_1 - \frac{d_{31}}{s_{11}^E} E_3 \right) + \varepsilon_{33} E_3 = \frac{d_{31}}{s_{11}^E} S_1 + \left( -\frac{d_{31}^2}{s_{11}^E} + \varepsilon_{33} \right) E_3 \tag{5.135}$$

Upon further rearrangement, the electrical displacement

$$D_3 = \frac{d_{31}}{s_{11}^E} S_1 + \varepsilon_{33} \left( 1 - \kappa_{31}^2 \right) E_3 \tag{5.136}$$

where $\kappa_{31}^2$ is the electro-mechanical coupling in longitudinal mode and defined as $\kappa_{31}^2 = \frac{d_{31}^2}{s_{11}^E \varepsilon_{33}}$. The electrical charge is given by integral of the electrical displacement over electrode surface area

$$Q_3 = \int_{A_p} D_3 dA = \frac{\varepsilon_{33} A_p}{h} \left( 1 - \kappa_{31}^2 \right) E_3 h + \frac{d_{31}}{s_{11}^E} \int_{A_p} S_1 dA \tag{5.137}$$

Recall the capacitance of the piezoelectric bar and the electrical potential

$$C_0 = \frac{\varepsilon_{33} A_p}{h} \tag{5.138}$$

$$V = E_3 h \tag{5.139}$$

where $h$ is the thickness of the piezoelectric bar. Upon substitution of Eq. (5.58) and Eq. (5.59) into Eq. (5.57), we have

$$Q_3 = C_0\left(1-\kappa_{31}^2\right)V + \frac{d_{31}}{s_{11}^E} b \int_{L_p} u' dx \tag{5.140}$$

$$Q_3 = C_0\left(1-\kappa_{31}^2\right)V + \frac{d_{31}}{s_{11}^E} b \, u\Big|_{x_2}^{x_3} \tag{5.141}$$

$$Q_3 = C_0\left(1-\kappa_{31}^2\right)V + \frac{d_{31}}{s_{11}^E} b \Delta u \tag{5.142}$$

Substitute Eq. (5.132)into Eq. (5.62)

$$\hat{Q}_3 = C_0\left(1-\kappa_{31}^2\right)V + \frac{d_{31}}{s_{11}^E} b \sum_{j=1}^{\infty}\left[U_j^p\left(x_3\right) - U_j^p\left(x_2\right)\right]_{E/M} \tag{5.143}$$

or

$$\hat{Q}_3 = C_0 V\left(1-\kappa_{31}^2\right) + \frac{d_{31}}{s_{11}^E} b H\left(x\right) \tag{5.144}$$

Recall the electrical current as a derivative of the electrical charge with respect to time.

$$I = i\omega Q_3 \tag{5.145}$$

and the electro-mechanical admittance is $Y = I / V$

$$Y = i\omega C_0\left(1-\kappa_{31}^2\right) + \frac{d_{31}}{s_{11}^E} b \hat{H}\left(x\right) \tag{5.146}$$

In our case the frequency response function $\hat{H}\left(x\right)$ is the difference of the displacements at two ends of the piezoelectric electrodes.

$$\hat{H}\left(x\right) = \sum_{j=1}^{\infty} U_j^P\left(x_3\right) - U_j^P\left(x_2\right) \tag{5.147}$$

where

$$U_j^P\left(x\right) = C_3 e^{-j\gamma\left(x-x_2\right)} + C_4 e^{j\gamma\left(x-x_3\right)} \tag{5.148}$$

The frequency response function of a three three-bar resonator having the geometric and the material properties defined in Figure 5.8.

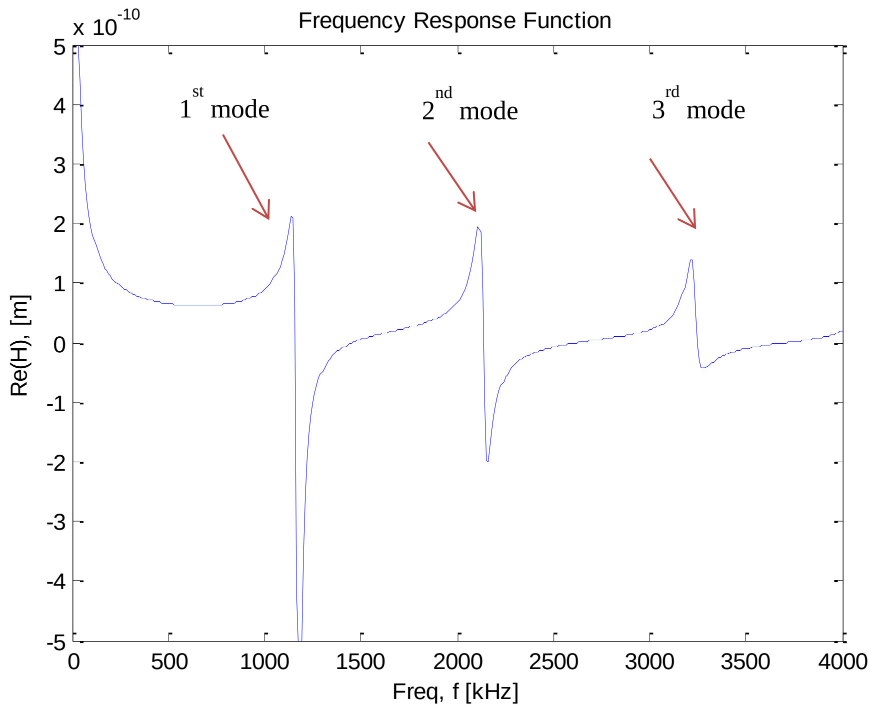


Figure 5.10 Frequency response function for three-bar PWAS resonator

When we plot the frequency response function, we can see the displacement behavior at resonant frequencies. Now, we take a closer look at the first three resonant frequencies to explain the connection between the frequency response function peak amplitudes and the mode shapes that were obtained from the mechanical analysis. It is presumed that the FRF peak amplitude and the difference of the amplitudes at two ends of the normalized mode shapes of the piezoelectric subsection $\Delta U^{(p)}$ follow the same trend.

Since the differences between the displacement amplitudes at two ends of the piezoelectric domain of the resonator are very close as can be seen in the normalized mode shapes in Table 5.4, this property in the mode shapes also reflects in the frequency response function. The amplitudes of the first three modes are in the same order of magnitudes.

# CHAPTER 6

# THICKNESS MODE EMIS OF CONSTRAINED PWAS

This chapter addresses theoretical framework for the thickness mode electromechanical impedance spectroscopy (TM-EMIS) of constrained piezoelectric wafer active sensor (PWAS). The analytical analyses were conducted by applying the resonator theory to derive the EMIS of PWAS constrained on one and both surfaces by isotropic elastic materials. The normalized thickness mode (Eigen-mode) shapes were obtained for the normal mode expansion (NME) method to predict the thickness mode impedance values of constrained PWAS using the correlation between a proof-mass-piezoelectric transducer and structural dynamic properties in the substrate structure. In another word, the normalized thickness mode shapes of the PM-PWAS-substrate structure at the resonance frequencies are obtained for the NME method.

## 6.1 THICKNESS MODE OF CONSTRAINED PWAS

The analytical model considers a PWAS of length $l_a$, thickness $t_a$, and width $b_a$, undergoing thickness expansion, $u_3$, induced by the thickness polarization electric field, $E_3$. The electric field is produced by the application of a harmonic voltage $V(t)=\hat{V}e^{i\omega t}$ between the top and bottom surface electrodes. The resulting electric field in the thickness mode, $E=V/t$, is assumed non-uniform with respect to $x_3\left(\partial E/\partial x_3 \neq 0\right)$ as opposed to the longitudinal mode; however, the electric displacement, $D$, is assumed uniform with respect to $x_3\left(\partial D/\partial x_3=0\right)$. The length, width, and thickness are assumed to have widely separated values $\left(t_a \ll b_a \ll l_a\right)$ such that the length, width, and thickness motions are practically uncoupled.

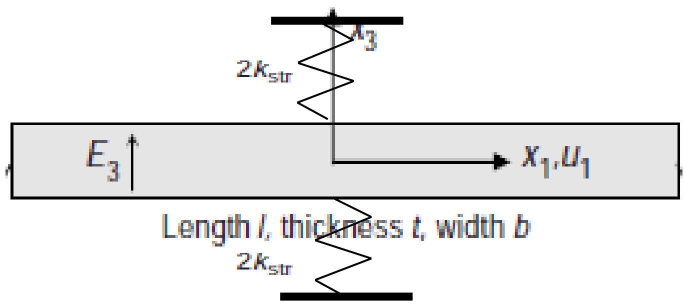


Figure 6.1 PWAS constrained by structural stiffness.

In this analytical model, PWAS is assumed to be constrained by structural stiffness on top and bottom surfaces as seen in Figure 6.1. The analytical analysis starts with the general piezoelectric constitutive equations expressing the linear relation between stress-strain and stress-electric displacement in thickness mode are

$$\begin{aligned}&\text{a-) } T_3 = c_{33}^D S_3 - h_{33} D_3\\&\text{b-) } E_3 = -h_{33} S_3 + \beta_{33}^S D_3\end{aligned} \tag{6.1}$$

The relations of the four piezoelectric constants to each other are in thickness mode (Berlincourt et al., 1958). IEEE Standard on Piezoelectricity (IEEE Ultrasonics, 1987) provides other relations to alternate the forms of the constitutive equations. In our model, the overall stiffness applied to the PWAS has been split into two equal components applied to the PWAS surfaces

$$\frac{1}{k_{total}} = \frac{1}{2k_{str}} + \frac{1}{2k_{str}} \;\; ; \; k_{total} = k_{str} \tag{6.2}$$

The boundary conditions applied at the PWAS ends balance the stress resultants, $T_3 bl$

$$T_3\left(x_3 = \pm\frac{t}{2}\right)bl = \mp 2k_{str}u_3\left(\pm\frac{t}{2}\right) \tag{6.3}$$

### 6.1.1 MECHANICAL RESPONSE FOR PWAS CONSTRAINED IN THICKNESS MODE

The resonance theory begins with the wave equation. Introducing the wave speed in direction of $x_3$ axis, $c_3 = \sqrt{c_{33}^D / \rho}$ , and the wave number in thickness mode, $\gamma_t = \omega / c_3$; the particle displacement $u_3$ is given by

$$\hat{u}_3(x_3) = C_1 \sin\gamma_t x_3 + C_2 \cos\gamma_t x_3 \tag{6.4}$$

$C_1$ and $C_2$ are to be determined from the boundary conditions. Note that $S_3 = \partial u_3 / \partial x_3 = u_3'$ and substitute Eq(6.4) into Eq. (6.3). Impose the boundary conditions on the PWAS surfaces that balance the stress resultant with the spring reaction force $2k_{str}u_3$. Introducing the quasi-static PWAS stiffness, $k_{PWAS} = Ac_{33}^D / t$ and the stiffness ratio $r = k_{str} / k_{PWAS}$. We can rearrange the equation using the ratio and it yields the following linear system in $C_1$ and $C_2$ by substitution of the general solution. Rearrange using $\phi_t = 0.5\gamma t$

$$\left(\phi_t \cos\phi_t + r\sin\phi_t\right)C_1 \mp \left(\phi_t \sin\phi_t - r\cos\phi_t\right)C_2 = \frac{t}{2}\frac{h_{33}D_3}{c_{33}^D} \tag{6.5}$$

Upon subtraction, we obtain $C_2 = 0$. Now add the two equations to obtain

$$C_1 = \frac{t}{2}\frac{h_{33}D_3}{c_{33}^D}\frac{1}{\left(\phi_t \cos\phi_t + r\sin\phi_t\right)} \tag{6.6}$$

Recall the strain $S_3 = \hat{u}_3{}'$

$$S_3 = \hat{u}_3{}' = \phi_t \frac{h_{33} D_3}{c_{33}^D \left( \phi_t \cos\phi_t + r \sin\phi_t \right)} \cos\gamma_t x_3 \tag{6.7}$$

### 6.1.2 ELECTRICAL RESPONSE UNDER CONSTANT ELECTRIC DISPLACEMENT ASSUMPTION

$$\begin{aligned} &\text{a-) } V = \int_{-t/2}^{t/2} E_3 dx_3 \\ &\text{b-) } I = \frac{d}{dt} \int_A D_3 dA = i\omega D_3 bl \end{aligned} \tag{6.8}$$

Recall the second constitutive equation and substitute Eq. (6.7) into the equation

$$E_3 = -\phi_t \frac{h_{33}{}^2 D_3}{c_{33}^D \left( \phi_t \cos\phi_t + r \sin\phi_t \right)} \cos\gamma_t x_3 + \beta_{33}^s D_3 \tag{6.9}$$

Recalling the piezoelectric constant relations, one can derive these relations $h_{33}{}^2 = e_{33}{}^2 / \varepsilon_{33}^{s\,2}$; $\beta_{33}^s = 1/\varepsilon_{33}^s$; and $e_{33} = d_{33} / s_{33}^D$; finally one can come up with the expression, $h_{33}{}^2 = \left( \beta_{33}^s d_{33} / s_{33}^D \right)^2$, and plug it into Eq(6.9) noting that $c_{33}^D = 1/s_{33}^D$ and introduce the electro-mechanical coupling coefficient $,\kappa_{33}$, defined as $\kappa_{33}^2 = e_{33}^2 / c_{33}^D \varepsilon_{33}^S$ (IEEE Ultrasonics, 1987)

$$E_3 = \beta_{33}^S D_3 \left( 1 - \kappa_{33}^2 \frac{\phi_t \cos\gamma_t x_3}{\phi_t \cos\phi_t + r \sin\phi_t} \right) \tag{6.10}$$

Upon substitution of Eq. (6.10) into Eq. (6.8)a, we obtain after rearrangement

$$V = \beta_{33}^S D_3 t \left[ 1 - \kappa_{33}^2 \frac{\sin\phi_t}{\left( \phi_t \cos\phi_t + r \sin\phi_t \right)} \right] \tag{6.11}$$

Recalling $I = \dot{Q} = \partial Q / \partial t$ and Eq. (6.8)b, we obtain $I = i\omega D_3 bl$. Substitute Eq. (6.11) and electrical current equation into the impedance $Z = V / I$ and recall the capacitance of the material $C_0 = bl / t\beta_{33}^S$

$$Z = \frac{V}{I} = \frac{1}{i\omega C_0}\left[1 - \kappa_{33}^2 \frac{1}{\phi_t \cot\phi_t + r}\right] \tag{6.12}$$

## 6.2 THICKNESS MODE OF PWAS CONSTRAINED FROM ONE SIDE

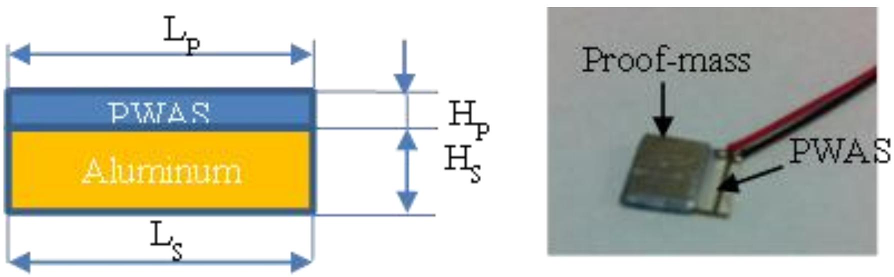


Figure 6.2 Illustration of a schema and picture of constrained PWAS.

This section introduces a theoretical framework for a two-layer resonator model including a PWAS and one isotropic elastic bar. The following assumptions were made for the two-bar piezo-resonator model.

First, the geometry and the cross-section area of the layers are the same although they have different materials and different thicknesses. Second, PWAS is assumed to be perfectly bonded to the isotropic elastic bar. The model shown in Figure 6.2can be used to develop an analytical solution to obtain the resonance frequencies essentially to build the basis for the PMPWAS actuator.

A procedure shown in Figure 6.4 can be pursued for the PMPWAS-EMIS. The global matrix is depicted in Eq(6.14) which is defined for the two layer model. The matrix elements are currently functions of the wave-speed and the frequency. They can be converted to the functions of the wave number by the wave number frequency relation, $\gamma_a = \omega / c_a$, $\gamma_p = \omega / c_p$. An eigenvalue problem with respect to the new PM-PWAS problem is solved in the similar manner regarding the Eigen-value problem of two-layered resonator in order to turn the singular matrix into a non-singular matrix. Therefore, the basis of the solution for the four eigenvectors can be found at each corresponding Eigen-modes.

The wave equations for each layer of the two bar resonator can be obtained from Newton's equation of motion; the general wave equation solution for the first layer can be determined as

$$u_a = \left( C_1 e^{-i\gamma_a (y-y_1)} + C_2 e^{i\gamma_a (y-y_2)} \right) e^{i\omega t} = \hat{u}_a e^{i\omega t} \tag{6.13}$$

where $u_a$ is the displacement for the isotropic elastic material on the left hand side, Similarly, the displacement, $u_p$, for PWAS can be determined. The capital coefficients denote the axial wave amplitudes as forward and backward directions respectively in y axis and $\gamma_a = \omega / c_a$ denote the wave numbers for each material of the divisions and related to the wave speed in the material-a. Linear Hooke's law applied to determine the stress-strain constitutive equations using the strain-displacement relation, $\varepsilon = \partial u / \partial x$, for each layer in 1-D two-bar resonator problem. The stress equations $\sigma_a, \sigma_p$ were determined in similar manner. Two unknown coefficients in each stress equation exist and four unknown coefficients in total therefore four boundary conditions should be implied to the general wave solutions to obtain the solutions of the wave equations in terms of the displacement mode shapes and the frequency responses at structural resonances for different modes.

### 6.2.1 EIGENVALUE PROBLEM

The stress and displacement boundary conditions to be imposed are; stress-free boundary condition at free ends, stress continuity condition and displacement continuity condition at the interface. The linearly dependent equation system was determined by implying the boundary conditions in a matrix form to provide a solution of the Eigen-frequencies and to eventually obtain the four Eigen-vectors (the displacement amplitudes). Therefore, this problem turned out to be an eigenvalue problem which requires a matrix as functions of frequency and the matrix to be multiplied by a tensor that contains the displacement amplitudes and the product of the two matrices was equal to zero as shown in Eq.(6.14).

$$\begin{pmatrix} -1 & e^{i\frac{\omega}{c_a}(y_1-y_2)} & 0 & 0 \\ -e^{i\frac{\omega}{c_a}(y_1-y_2)} & 1 & \frac{E_p}{E_a}\frac{c_a}{c_p} & -\frac{E_p}{E_a}\frac{c_a}{c_p}e^{i\frac{\omega}{c_p}(y_2-y_3)} \\ e^{i\frac{\omega}{c_a}(y_1-y_2)} & 1 & -1 & -e^{i\frac{\omega}{c_p}(y_2-y_3)} \\ 0 & 0 & -e^{i\frac{\omega}{c_p}(y_2-y_3)} & 1 \end{pmatrix} \begin{Bmatrix} C_1 \\ C_2 \\ C_3 \\ C_4 \end{Bmatrix} = 0 \tag{6.14}$$

The determinant of the global matrix $A_{4x4}$ must equal to zero to have non-trivial solution for the displacement amplitudes. Then one can say that the global matrix is apparently a singular matrix and it dos not have a unique solution. Therefore, we can find the basis of the eigenvector by assuming one of the unknowns is one i.e. $C_4 = 1$. This assumption helps us obtain $A_{3x3}$ non-singular matrix simply excluding 4$^{th}$ row that no longer represents an independent equation. The 4$^{th}$ column of the global matrix is moved to the right hand side of the equation to eventually obtain a non-trivial basis of the solution for the unknown constants.

### 6.2.2 MODAL EXPANSION THEOREM

For the forced axial vibration of two bars, we assume two bars undergoing axial vibration under the excitation of an externally applied time-dependent axial force per unit length, $f(x,t)$ as shown in Figure 6.3.

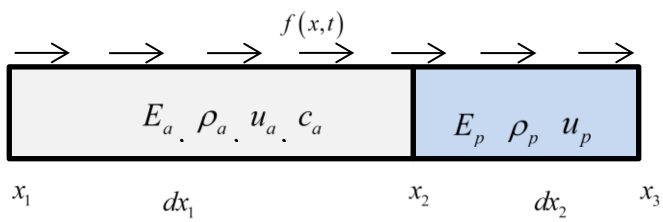


Figure 6.3 Constrained PWAS undergoing axial vibration under the excitation of an externally applied time-depen dent axial force per unit length.

The equation of motion for forced axial vibration;

$$\rho A\ddot{u}(x,t) - EAu''(x,t) = f(x,t) \tag{6.15}$$

without loss of generality, we assume the external excitation to be harmonic in the form

$$f(x,t) = \hat{f}(x)e^{i\omega t} \tag{6.16}$$

$$u(x,t) = \sum_{j=1}^{\infty}\eta_j U_j(x)e^{i\omega t} \tag{6.17}$$

where $U_j(x)$ are natural modes satisfying the free vibration equation of motion and the orthogonality conditions, whereas $\eta_j$ are the modal participation factors for the forced vibration modes. Substitution of Eq. (6.17) into Eq. (6.15) and division by $e^{i\omega t}$ yields

$$-\rho A\omega^2\sum_{i=1}^{\infty}\eta_i U_i\left(x\right)-EA\sum_{i=1}^{\infty}\eta_i U_i''\left(x\right)=\hat{f}\left(x\right) \tag{6.18}$$

Multiplication of Eq.(6.18) by $U_j\left(x\right)=U_j^a\left(x\right)+U_j^p\left(x\right)$ and integration over the total length of two bars

$$\begin{aligned}&-\omega^2\sum_{i=1}^{\infty}\eta_i\left[\int_{x_1}^{x_2}\rho_a U_i^a\left(x\right)U_j^a\left(x\right)dx_1+\int_{x_2}^{x_3}\rho_p U_i^p\left(x\right)U_j^p\left(x\right)dx_2\right]\\&-\sum_{i=1}^{\infty}\eta_p\left[\int_{x_1}^{x_2}E_a U_i^a\left(x\right)U_j^a\left(x\right)dx_1+\int_{x_2}^{x_3}E_p U_i^p\left(x\right)U_j^p\left(x\right)dx_2\right]=\int_{x_1}^{x_3}\hat{f}\left(x\right)U_j\left(x\right)dx\end{aligned} \tag{6.19}$$

where elastic moduli, $E_a$ and $E_p$, and mass densities, $\rho_a$ and $\rho_p$, are constant along corresponding bar's length therefore (6.19) is rearranged

$$\begin{aligned}&-\omega^2\sum_{i=1}^{\infty}\eta_i\left[\rho_a\int_{x_1}^{x_2}U_i^a\left(x\right)U_j^a\left(x\right)dx+\rho_p\int_{x_2}^{x_3}U_i^p\left(x\right)U_j^p\left(x\right)dx\right]\\&-\sum_{i=1}^{\infty}\eta_i\left[E_a\int_{x_1}^{x_2}U_i^a\left(x\right)U_j^a\left(x\right)dx+E_p\int_{x_2}^{x_3}U_i^p\left(x\right)U_j^p\left(x\right)dx\right]=\int_{x_1}^{x_3}\hat{f}\left(x\right)U_j\left(x\right)dx\end{aligned} \tag{6.20}$$

The expressions in the brackets represent the mass-weighted integral and the stiffness-weighted integral for orthogonality conditions.

$$\eta_j\left(-\omega^2 m_j+k_j\right)=f_j \qquad j=1,2,3,\ldots \tag{6.21}$$

where $f_j$ is the modal excitation given by

$$f_j=\int_{x_1}^{x_3}\hat{f}\left(x\right)U_j\left(x\right)dx \qquad j=1,2,3,\ldots \tag{6.22}$$

If the mode shapes are orthonormal (orthogonal+normalized), then substituting the orthonormality conditions (5.27) into (6.21)

$$\begin{aligned}&\eta_j\left(-\omega^2+k_j/m_j\right)=f_j \qquad j=1,2,3,\ldots\\&\eta_j\left(-\omega^2+\omega_j^2\right)=f_j\end{aligned} \tag{6.23}$$

The modal participation factors can be expressed in the form

$$\eta_j = \frac{f_j}{-\omega^2 + \omega_j^2} \qquad j = 1,2,3,\ldots \tag{6.24}$$

The modal participation factor for the forced vibration corresponds to the amplitude of undamped forced vibration of one degree of freedom (DOF) system.

$$u(x,t) = \sum_{j=1}^{\infty} \frac{f_j}{-\omega^2 + \omega_j^2} U_j(x) e^{i\omega t} \tag{6.25}$$

In reality, system has some damping $\zeta_i$. The modal participation factors for a damped system are given by

$$\eta_j = \frac{f_j}{-\omega^2 + 2i\zeta_j \omega_j \omega + \omega_j^2} \qquad j = 1,2,3,\ldots \tag{6.26}$$

Substitution of Eq. (6.26) into Eq. (6.17) yields

$$u(x,t) = \sum_{j=1}^{\infty} \frac{f_j}{-\omega^2 + 2i\zeta_j \omega_j \omega + \omega_j^2} U_j(x) e^{i\omega t} \tag{6.27}$$

Equation (6.27) represents a superposition of a number of terms, each term corresponding to a natural frequency and normal mode of vibration. It allows us to determine the response of the continuous structure to harmonic excitation of variable frequency. This leads to the frequency response function (FRF) concept.

### 6.2.3 NORMALIZED MODE SHAPES

The next step was the verification of orthogonality of the mode shapes The mass-weighted integral was used to verify the orthogonality of the mode shapes and to find the modal mass factor, $m_i$ of each mode to scale the mode shape amplitudes. For the two bar resonator problem, it takes the following form. The surface area, $A$, is omitted since it is equal for each layer in this problem;

$$\rho_a \int_{y_1}^{y_2} U_i^a U_j^a dy + \rho_p \int_{y_2}^{y_3} U_i^p U_j^p dy = \begin{Bmatrix} 0 \text{ , if } i \neq j \\ m_i \text{ , if } i = j \end{Bmatrix} \tag{6.28}$$

Table 6.1 Orthogonality matrix that validates the mode shape solution and that gives the modal participation factors.

| Modal factor | First mode | Second mode | Third mode | Fourth mode | Fifth mode |
|---|---|---|---|---|---|
| **First mode** | 908.344 + 0.000334i | 0.013 - 0.06i | 0.015 - 0.02i | 0.02 - 0.0001i | 0.02 + 0.0002i |
| **Second mode** | 0.013 - 0.06130i | 992.529 - 0.026i | 0.007+ 0.0002i | 0.03 + 0.01i | 0.0017+ 0.007i |
| **Third mode** | 0.015 - 0.02133i | 0.0076 +0.00028i | 795.59- 0.058i | -0.02 | 0.02+ 0.01i |
| **Fourth mode** | 0.02 - 0.00017i | 0.031 + 0.012i | -0.02 | 836.15 + 0.0002i | 0.005 + 0.0009i |
| **Fifth mode** | 0.027 + 0.0002i | 0.0017 + 0.007i | 0.021 + 0.01i | 0.005 + 0.0009i | 1033.102+ 0.00015i |

Then, the normalization of the mode shapes was carried out to find normal modes after the modal participation factors with respect to the modal mass values were obtained which are the values on the diagonal of the orthogonality matrix as given in Table 6.1. The values can be used to normalize the mode shapes by the following relation; $U^{new} = U / \sqrt{m_i}$

### 6.2.4 CALCULATION OF FREQUENCY RESPONSE FUNCTION THROUGH NORMAL MODE EXPANSION METHOD (NME)

The NME theorem combines the natural modes satisfying the free-vibration equation of motion and the orthogonality conditions with respect to mass and stiffness and factorizes the sum of the natural modes by the modal participation factors in terms of the modal mass or the modal stiffness factors.

The normalized mode shapes are substituted into the frequency response function (FRF) equation that was derived through the NME method to obtain the FRF to the single input single output excitation applied by the PWAS. The FRF of the damped axial vibration system in thickness mode is expressed as

$$\hat{u}_{PWAS} = \frac{1}{\rho A}\left\{\sum_{n_u} \frac{\left[U_{n_u}^{(3)}\left(y_a + t_p\right) - U_{n_u}^{(3)}\left(y_a\right)\right]^2}{\omega_{n_u}^2 + 2i\zeta\omega_{n_u}\omega - \omega^2}\right\} \tag{6.29}$$

The SISO FRF is the same as the dynamic structural compliance seen by the PWAS modal sensor placed on the structure. The dynamic structural stiffness is the reciprocal of the compliance

$$k_{str}(\omega) = \frac{1}{\hat{u}_{PWAS}} = \rho A\left\{\sum_{n_u} \frac{\left[U_{n_u}^{(3)}\left(y_a + t_p\right) - U_{n_u}^{(3)}\left(y_a\right)\right]^2}{\omega_{n_u}^2 + 2i\zeta\omega_{n_u}\omega - \omega^2}\right\}^{-1} \tag{6.30}$$

is defined to calculate the frequency dependent stiffness ratio, $r(\omega) = k_{str}(\omega)/k_{PWAS}$ where $k_{PWAS} = Ac_{33}^D/t$ the quasi-static PWAS stiffness, dependent on the area of the surface whose normal is on $y$ axis and the stiffness of PWAS in thickness direction and the thickness of the PWAS.

The impedance model shown in Eq. (6.12) for constrained PWAS in thickness mode is derived in section 6.1 by using the resonator theory under constrained boundary conditions and constant electrical displacement, $D_3$, assumption. The coefficients defined in the procedure can be adjusted by the GMM that conveys the new boundary conditions into the FRF through NME method and then substituted into the thickness mode EMIS equation for constrained PWAS by the stiffness ratio.

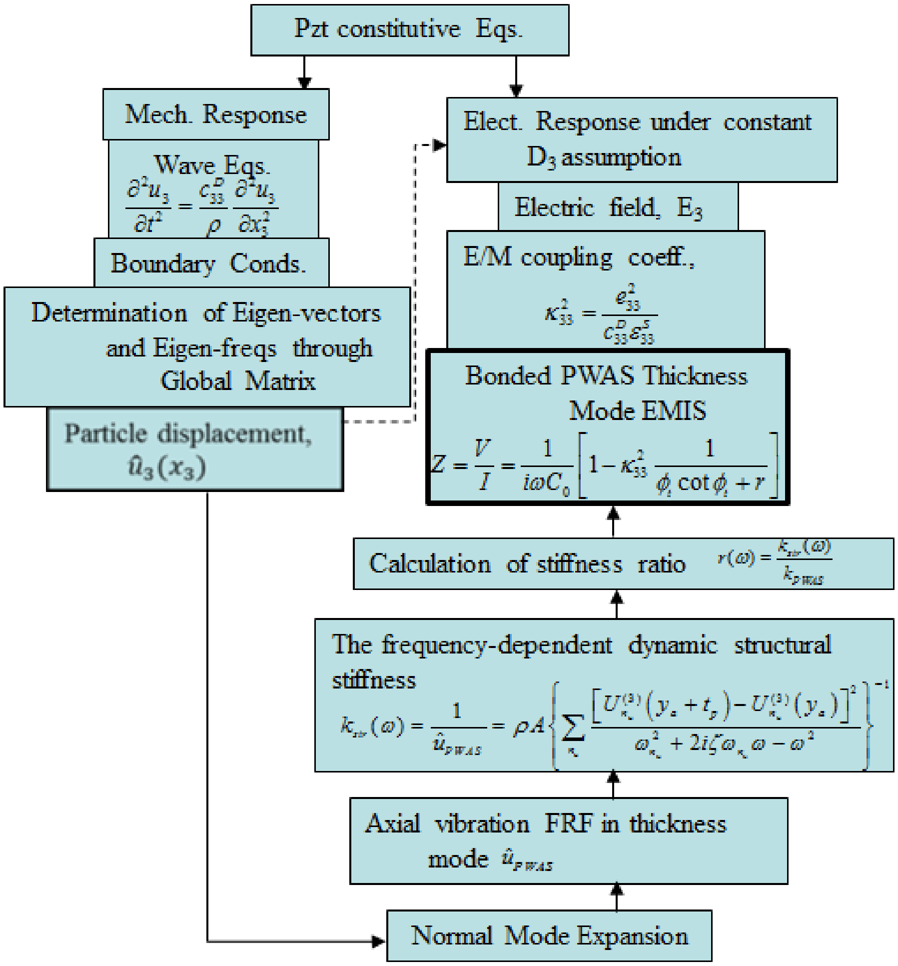


Figure 6.4 Flow chart of the one dimensional analytical thickness mode EMIS for constrained PWAS.

A procedure shown in Figure 6.4 can be pursued for the constrained PWAS EMIS. The global matrix is depicted in Eq.(6.31) which is defined for the two layer model. The matrix elements are currently functions of the wave-speed and the frequency. They can be converted to functions of wave number by the wave number frequency relation, $\gamma_a = \omega / c_a$, $\gamma_p = \omega / c_p$, $\gamma_b = \omega / c_b$ . An eigenvalue problem with respect to the new constrained PWAS problem is solved in the similar manner described in the previous section regarding the Eigenvalue problem of two-bar resonator in order to turn the singular matrix into non-singular matrix. Therefore, the basis of the solution for the four eigenvectors can be found at each corresponding Eigenmodes.

$$\begin{bmatrix} -1 & e^{i\frac{\omega}{c_a}(y_1-y_2)} & 0 & 0 \\ -e^{i\frac{\omega}{c_a}(y_1-y_2)} & 1 & \dfrac{E_p}{E_a}\dfrac{c_a}{c_p} & -\dfrac{E_p}{E_a}\dfrac{c_a}{c_p}e^{i\frac{\omega}{c_p}(y_2-y_3)} \\ e^{i\frac{\omega}{c_a}(y_1-y_2)} & 1 & -1 & -e^{i\frac{\omega}{c_p}(y_2-y_3)} \\ 0 & 0 & -e^{i\frac{\omega}{c_p}(y_2-y_3)} & 1 \end{bmatrix} \begin{bmatrix} C_1 \\ C_2 \\ C_3 \\ C_4 \end{bmatrix} = 0 \tag{6.31}$$

### 6.2.5 NUMERICAL EXAMPLES

In this subsection, the normalized mode shapes and the frequency response functions are determined and presented for the constrained PWAS in thickness mode as seen in the model presented in Figure 6.5. The geometric sizes and material properties of the PWAS and the substrate material are also presented. The solutions are determined for PWAS in different thicknesses. The resonance responses in terms of mode shapes and the frequency response functions for both PWAS in thickness of 0.5mm and of 0.2mm are presented as followings.

<u>For PWAS thickness of 0.5mm</u>

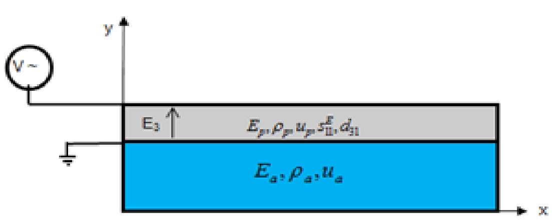


| Geometric sizes | Material Properties | | |
|---|---|---|---|
| ha=1 [mm] | | Aluminum | PWAS |
| hp=0.5 [mm] | Elastic Modulus [Gpa] | 72.4 | 65.3 |
| Length=7 [mm] | Mass Density [kg/m3] | 2780 | 7700 |
| | Wave Speed [m/s] | 5103 | 2913 |
| | Compliance | | 1.53E-11 |
| | Permittivity | | 1.54E-08 |
| | Piezoelectric Constant | | -1.75E-10 |
| | Internal damping | | 0.05 |

Figure 6.5 Schematic of PWAS bonded on bar and geometric and material properties.

When we plot the frequency response function in thickness mode for the system seen in Figure 6.5, we can see the displacement behavior at resonant frequencies.

In this example, one can observe at the first two resonant frequencies in thickness mode to explain the connection between the peak amplitudes and the mode shapes that were obtained from the mechanical analysis. It is presumed that the peak amplitude is larger when the difference of the amplitudes at two ends of the normalized mode shapes of the piezoelectric subsection $\Delta U^{(p)}$ is larger. The relation applies between the first and second modes. As one can observe in the frequency response function plot in Figure 6.6, the first mode at 1.34 MHz smaller amplitude than the second mode at 2.76 MHz since $\Delta U_1^{(p)}$ has smaller value than $\Delta U_2^{(p)}$.

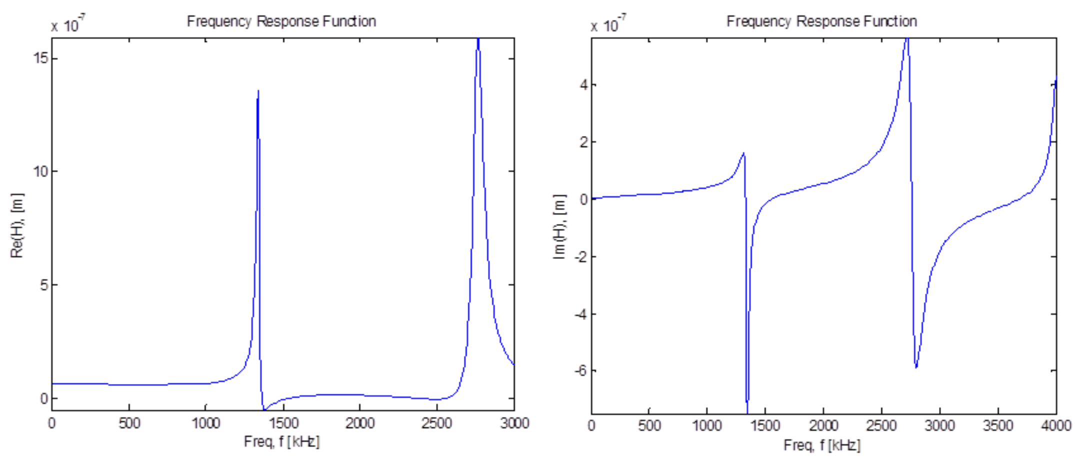


Figure 6.6 Frequency response function for two-bar resonator. Height of aluminum is 1mm and height of PWAS is 0.5mm and length is 7mm.

Table 6.2 shows the normalized mode shapes for the first two thickness modes PWAS in height of 0.5 mm and length of 7 mm.

Table 6.2 Normalized mode shapes for the first two modes PWAS at the height of 0.5 mm and length of 7 mm.

| Mode # | Mode Shape | Resonant Frequency [kHz] | Amplitude Difference [mm] |
|---|---|---|---|
| 1 | 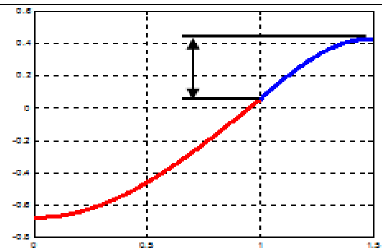 | 27.28 | $\Delta U_1^{(p)} = \left\|U_1^{(p)}(x_3)\right\| - \left\|U_1^{(p)}(x_2)\right\| = 0.378$ |
| 2 | 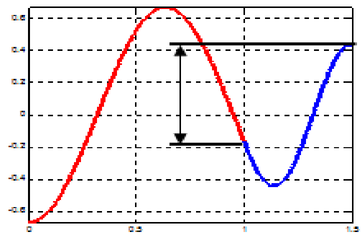 | 49. 83 | $\Delta U_2^{(p)} = \left\|U_2^{(p)}(x_3)\right\| - \left\|U_2^{(p)}(x_2)\right\| = 0.605$ |

For PWAS thickness of 0.2mm

The same relation between the peak amplitudes and the mode shapes $\Delta U^{(p)}$ also applies in this numerical example when we plot the frequency response function in thickness mode. Now let us look at the first two resonant frequencies in thickness mode in Table 6.3 to explain the connection. As can be observed in the frequency response function plot in Figure 6.7 the first mode at 1.76 MHz smaller amplitude than the second mode at 3.79 MHz since $\Delta U_1^{(p)}$ has smaller value than $\Delta U_2^{(p)}$.

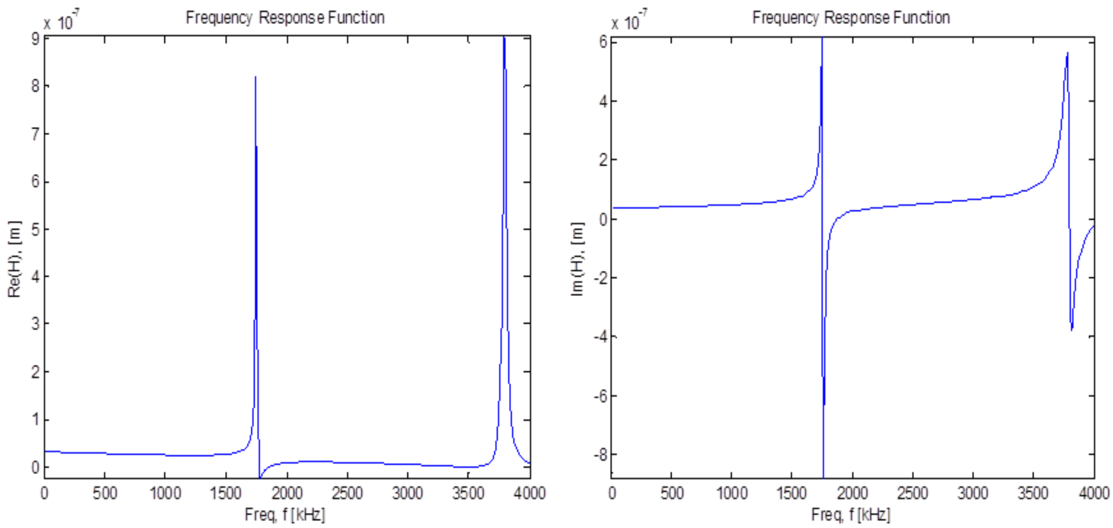


Figure 6.7 Frequency response function for two-bar resonator. Height of aluminum is 1 mm and height of PWAS is 0.2 mm and length is 7 mm.

Table 6.3 Normalized mode shapes for the first two modes PWAS at the height of 0.2 mm and length of 7 mm.

| Mode # | Mode Shape | Resonant Frequency [kHz] | Amplitude Difference [mm] |
|---|---|---|---|
| 1 | 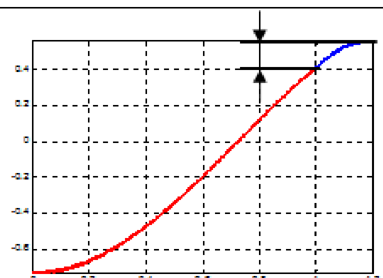 | 27.28 | $\Delta U_1^{(p)} = \left\|U_1^{(p)}(x_3)\right\| - \left\|U_1^{(p)}(x_2)\right\| = 0.151$ |
| 2 | 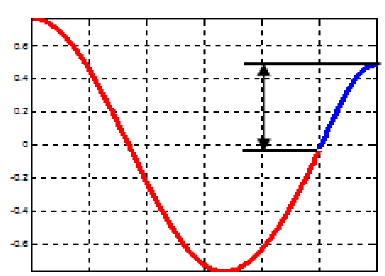 | 49. 83 | $\Delta U_2^{(p)} = \left\|U_2^{(p)}(x_3)\right\| - \left\|U_2^{(p)}(x_2)\right\| = 0.518$ |

## 6.3 THICKNESS MODE OF PWAS CONSTRAINED FROM BOTH SIDES

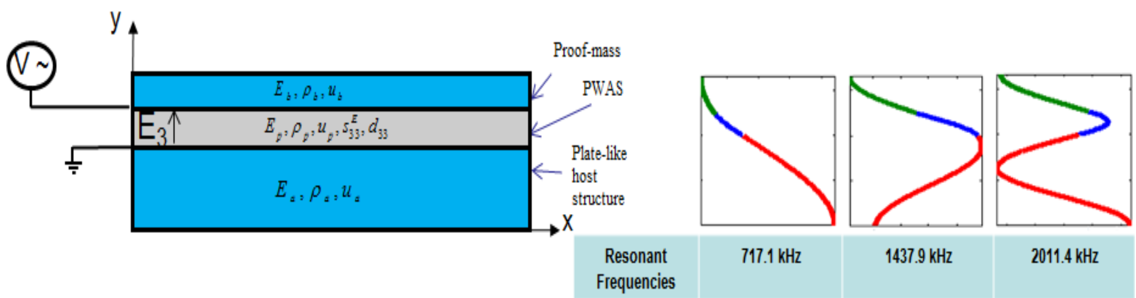


Figure 6.8 Illustration of a PM-PWAS transducer bonded on a substrate material and its mode shapes at fundamental and overtone resonant frequencies.

A similar procedure as shown in the flow-chart (Figure 6.4) to the constrained PWAS-EMIS can be pursued for the constrained PM-PWAS EMIS. Only difference is the global matrix as seen in Eq. (6.32) that was defined for the three-bar resonator model additionally including proof-mass bonded on PWAS. The elements of the matrix discretized in each box correspond to one of the three layers. The elements in the left box are from the substrate material, in the middle box are from the PWAS layer, and in the right are from the proof-mass layer. The matrix elements are currently functions of the wave-number. They can be converted to functions of frequency by the wave number frequency relation, $\gamma_a = \omega / c_a$, $\gamma_p = \omega / c_p$, $\gamma_b = \omega / c_b$ . An eigenvalue problem with respect to the new three-bar resonator problem is solved in the similar manner described in the previous Eigenvalue problem subsection in order to turn the singular matrix into non-singular matrix. Therefore, the basis of the solution for the six eigenvectors can be found at each corresponding Eigenmodes. Then, the modal participation factor is obtained through the verification of the orthogonality of the mode shapes by the mass weighted integral method. The normalized mode shapes are determined by the calculated participation factor for each modes.

$$\begin{bmatrix} 1 & -e^{-i\gamma_a H_a} & 0 & 0 & 0 & 0 \\ -E_a\gamma_a e^{-i\gamma_a H_a} & E_a\gamma_a & E_p\gamma_p & -E_p\gamma_p e^{-i\gamma_p H_p} & 0 & 0 \\ e^{-i\gamma_a H_a} & 1 & -1 & -e^{-i\gamma_p H_p} & 0 & 0 \\ 0 & 0 & e^{-i\gamma_p H_p} & 1 & -1 & -e^{-i\gamma_b H_b} \\ 0 & 0 & -E_p\gamma_p e^{-i\gamma_p H_p} & E_p\gamma_p & E_b\gamma_b & -E_b\gamma_b e^{-i\gamma_b H_b} \\ 0 & 0 & 0 & 0 & -e^{-i\gamma_b H_b} & 1 \end{bmatrix} \begin{Bmatrix} C_1 \\ C_2 \\ C_3 \\ C_4 \\ C_5 \\ C_6 \end{Bmatrix} = 0 \qquad (6.32)$$

The frequency response function (FRF) $\hat{H}(x)$ for the three bar resonator problem is the summation of the differences between displacements at two ends of the piezoelectric electrodes.

$$H(x,t) = \Delta u(x,t) = \sum_{j=1}^{\infty}\left[U_j^{p(New)}(x_3) - U_j^{p(New)}(x_2)\right]e^{i\omega t} \qquad (6.33)$$

The frequency response function was plotted as illustrated in Figure 6.9. Both the PM and the host structure are aluminum in this study. The PM-PWAS was assumed to be perfectly bonded on a 2 mm thick plate-like structure in the same length as PM-PWAS. The displacement response in frequency domain reached the highest values at resonant frequencies in various modes where the system with PM-PWAS actuator resonated as well as the displacement mode shapes shown in Figure 6.8 were defined.

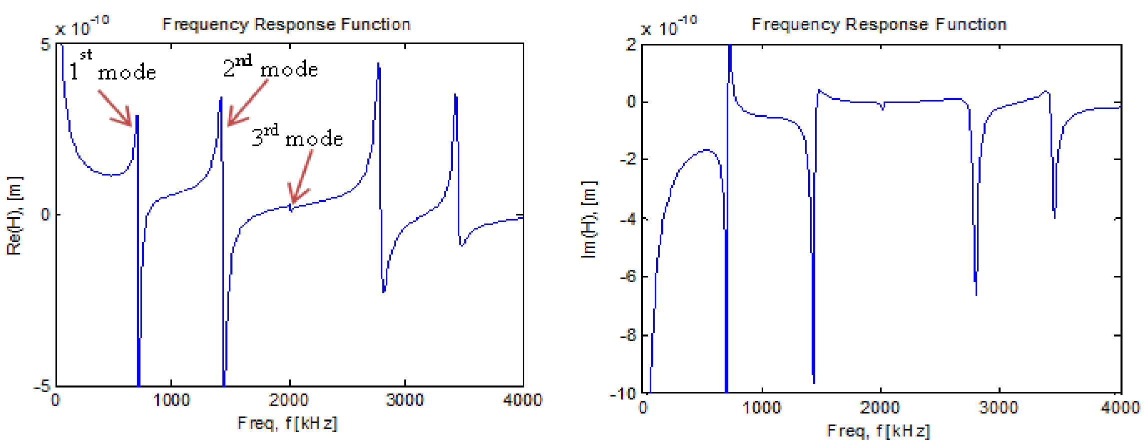


Figure 6.9 Illustration of the real and imaginary parts of the Frequency Response Function (FRF).

Table 6.4 Three bar resonator mode shapes, resonant frequencies and amplitude differences at different modes.

| Mode Number | Mode Shape | Resonant Frequency [kHz] | Amplitude Difference [mm] |
|---|---|---|---|
| 1 | 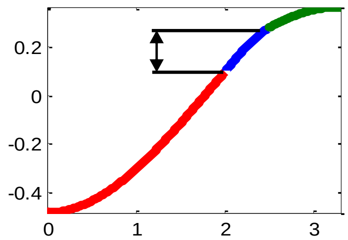 | 717.1 | $\Delta U_1^{(p)} = U_1^{(p)}(x_3) - U_1^{(p)}(x_2) = 0.184$ |
| 2 | 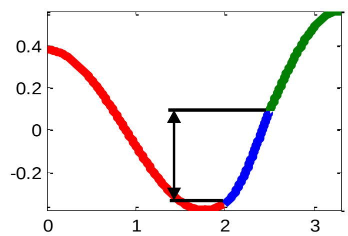 | 1437.9 | $\Delta U_2^{(p)} = U_2^{(p)}(x_3) - U_2^{(p)}(x_2) = 0.4352$ |
| 3 | 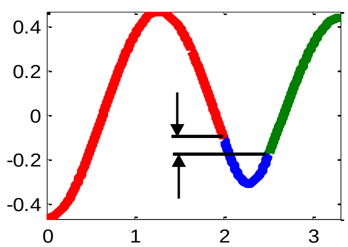 | 2011.4 | $\Delta U_3^{(p)} = U_3^{(p)}(x_3) - U_3^{(p)}(x_2) = 0.063$ |
| 4 | 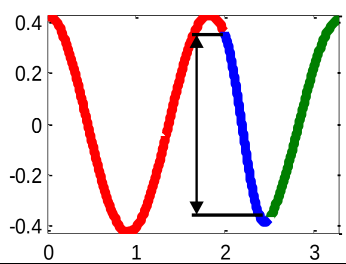 | 2787.2 | $\Delta U_4^{(p)} = U_4^{(p)}(x_3) - U_4^{(p)}(x_2) = 0.7396$ |

Table 6.4 depicts the PM-PWAS-substrate structure mode shape, resonant frequency and amplitude difference at different modes. The mode shapes represent the displacement amplitudes along the bars at resonant frequencies (Eigen-frequencies). The motion in the PM-PWAS and plate structure system occurred solely due to the electrical excitation generated in harmonic manner by the electrodes deposited on top and bottom of PWAS actuator. This is called the induced strain actuation (ISA) that was expressed as

$$S_{ISA} = d_{31}E_3 \tag{6.34}$$

The displacement amplitude difference at two ends of the electrodes was substantial and was shown in each mode shape at resonant frequencies in the defined frequency range (up to 4 MHz).

$$\Delta\hat{U}_j^p = U_j^p\left(x_3\right) - U_j^p\left(x_2\right) \tag{6.35}$$

As paying a closer attention to the first four resonant frequencies to explain the connection between peak amplitudes in the frequency response and the mode shapes that were obtained from the mechanical analysis. It is indicated that the FRF peak amplitude and the difference of the amplitudes at two ends of the normalized mode shapes of the piezoelectric subsection $\Delta U_i^{(p)}$ follow similar trend against the proof-mass size change at the first four modes in Figure 6.11.

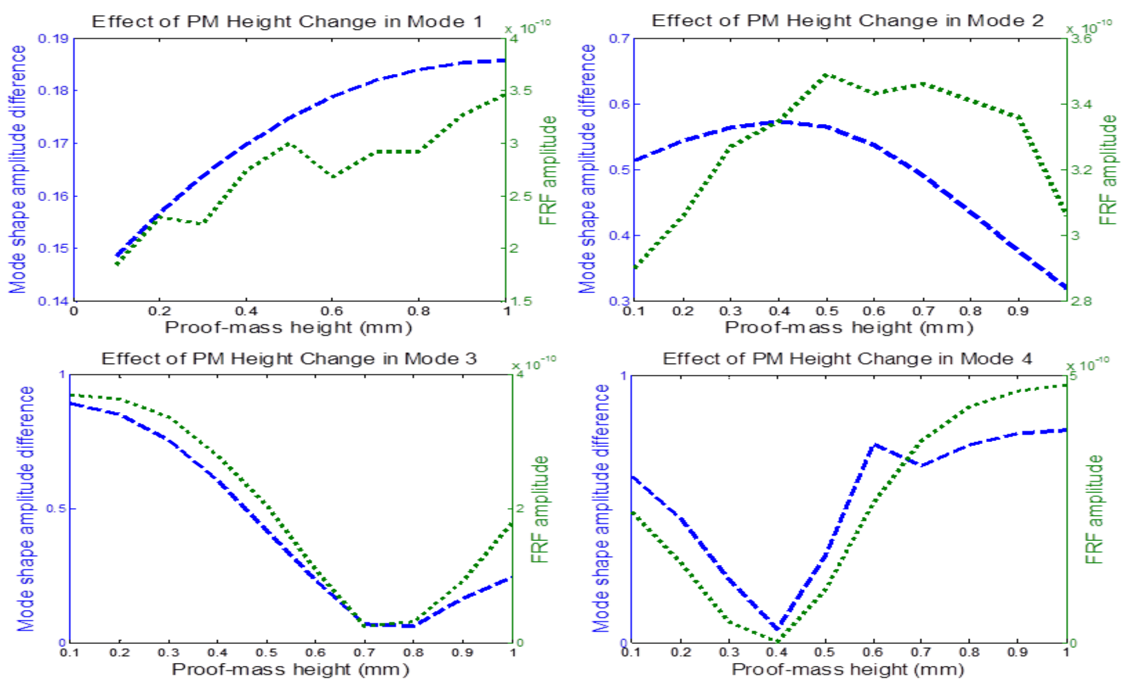


Figure 6.10 Illustration of the effect of Proof-Mass size change on mode shapes in relation with frequency response function amplitudes at resonance frequencies (Kamas, Giurgiutiu, & Lin, 2013).

The dashed-line curve represents the FRF amplitude at resonance frequencies and the dotted line curve represents the mode shape amplitude difference. The both curves in mode 1 inclines along the PM height. The second mode, FRF and $\Delta U_j^{(P)}$ curves rise up to the PM height of 0.4-0.5 mm and lowers in both manner as the PM height more increases. The third and fourth modes have similar pattern by being mitigated at certain PM height and then they both climb up along the increasing height. The resonance frequency of the PM transducer system slightly shifts downward as the height of PM increases at each mode as expected.

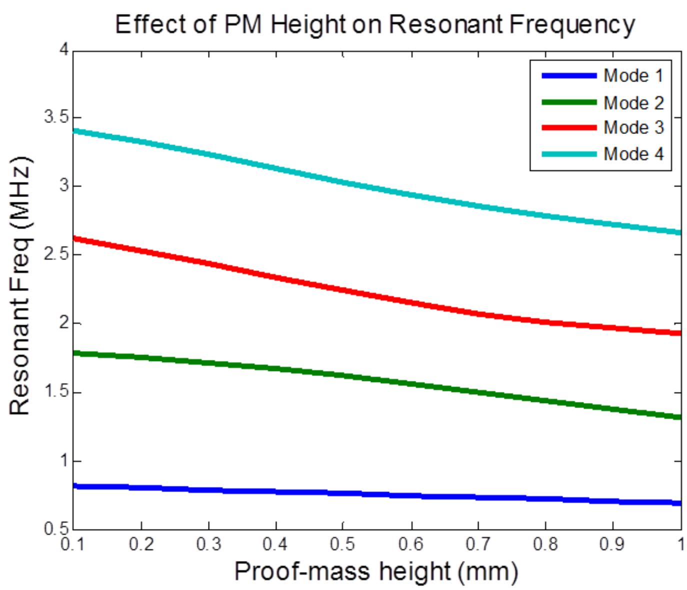


Figure 6.11 Effect of proof-mass height on resonance frequencies at multiple modes.

The resonance frequency of the PM-PWAS slightly shifts downward as the height of PM increases at each mode as expected.

To conclude this part of the PM-PWAS parametric study, the three bar piezo-resonator model was used to obtain the resonance frequencies for the normal mode expansion method. The resonator theory is used to build the basis for the proof-mass

PWAS (PM-PWAS) transducer configured with a PWAS actuator and proof-mass on top. The study was followed by proof-mass analysis to investigate tuning of specific modes using the correlation between a proof-mass transducer and structural dynamic properties in the host plate-like structure. It was found that proof masses could shift system resonance towards optimal frequency point. A parametric study was conducted to indicate the mitigation of certain modes is possible by varying geometric size of proof mass.

# CHAPTER 7

# PROOF-MASS PIEZOELECTRIC WAFER ACTIVE SENSOR

This chapter presents theoretical and experimental work on thickness mode electromechanical impedance spectroscopy (EMIS) of proof-mass piezoelectric actuator for tuning the Lamb wave modes in high frequency-band. Proof masses shift system resonance towards optimal frequency point. A new type of PM transducer has been designed to generate the desired wave mode through the PM tuning method in a substrate plate-like structure. Analytical analysis begins with the piezoelectric wafer active sensor (PWAS) under constrained boundary conditions and it is carried out by using the resonator theory considering the simplified one-dimensional three layered and five layered models. In the first part of this study, a simplified proof-mass piezo-resonator with three layers was modeled using the resonator theory. The resonator model includes a piezoelectric wafer active sensor (PWAS) and the PWAS is bonded on one isotropic elastic bar by an adhesive bonding layer. The following assumption was made for the proof-mass PWAS resonator model; the geometry and the cross-section area of PWAS and the elastic bar were the same although they have different materials and different thicknesses. The model was used to obtain the resonance frequencies for the normal mode expansion method. Essentially, this model was to build the basis for the EMIS of the proof-mass PWAS (PM-PWAS). Next, the model was extended to a five layered model including a PWAS resonator in the middle and two isotropic elastic bars constraining the PWAS from both surfaces by two adhesive bonding layers. Global matrix method (GMM) is employed to solve the eigenvalue problems of the PM-PWAS models for the Eigen-vectors and the corresponding Eigen-frequencies. Eigen-modes are determined for the normal mode expansion (NME) method to predict the thickness mode impedance values of PM-PWAS using the correlation between a proof-mass-piezoelectric transducer and structural dynamic properties in the substrate structure. The study was followed by proof-mass analysis to investigate desired control objectives (such as tuning of axial wave modes). PM-PWAS transducer can be used for better high frequency local modal sensing at a desired excitation frequency utilizing the proof masses affixed on PWAS in different sizes and materials to tune system resonance towards optimal frequency point. A parametric study is conducted to indicate effect of the proof-mass size change on mode shapes in relation with frequency response function amplitudes at resonance frequencies. The bonded PWAS and PM-PWAS models are also numerically generated in a commercial multi-physics finite element analysis (MP-FEA) software, ANSYS®. The thickness mode EMIS results from analytical, numerical, and experimental analyses are presented. The analytical PM-PWAS and constrained PM-PWAS models are verified by MP-FEA computational results and experimental measurement results in terms of the thickness mode EMIS of PM-PWAS bonded on a plate-like host structures.

## 7.1 STATE OF THE ART FOR PROOF-MASS PWAS

Since the 1980’s, the proof-mass (PM) concept has received considerable attention especially regarding vibration suppression control by (Griffin et al. 2013; Zimmerman & Inman 1990). PM actuators have been provided for structural vibration control problems with respect to a broad range of applications. The PM actuator has been modeled as a mass bonded to a structure with dynamic stiffness and internal damping. The effectiveness of the PM actuator depends strongly on how precisely it is tuned. However, in the literature, the PM actuators have been developed mostly for flexible structures vibrating in a relatively low frequency band at a magnitude of 100-1000 Hz whereas PWAS needs to work at high frequency range at magnitude of MHz. Kamas, Giurgiutiu, & Lin (2013) first adopted the proof-mass concept to develop the theoretical basis of proof-mass PWAS (PMPWAS) resonator. The authors derived the frequency response function of PMPWAS resonator and conducted an analytical parametric study for the effect of the proof-mass height on the frequency response function and the displacement amplitude prediction. The effect of the thickness variation in the proof-mass on the thickness mode resonance frequency was noticed. Further study was conducted to develop the thickness mode EMIS for PMPWAS and finite element/experimental validation in their work (Kamas, Lin, & Giurgiutiu, 2014).

However, the analytical thickness mode EMIS of PMPWAS has not been yet developed by using normal mode expansion (NME) method. In the current study, the further development of analytical EMIS model for PMPWAS has been performed by using the NME method. The NME was utilized to derive the frequency response function and the dynamic structural stiffness ratio for the 1-D thickness mode EMIS model of PMPWAS. The analytical analyses began with PWAS under constrained boundary conditions; a simplified two layered and three layered piezo-resonators are modeled using the resonator theory. Three-layered resonator model included a PWAS in the center and two isotropic elastic bars bonded on both surfaces of the PWAS; whereas in two-layered resonator model, PWAS was only constrained on one surface. These two-layered and three-layered piezo-resonator models are used to obtain the resonance frequencies for the NME method. Global matrix method (GMM) was employed to carry all the information from each layer regarding the material properties, geometric properties as well as the boundary conditions into the eigenvalue problem (Kamas, Giurgiutiu, & Lin, 2014). GMM was also utilized to solve the eigenvalue problem of the two and three-layered PMPWAS models for the Eigen-vectors and the corresponding Eigen-frequencies. Eigen-modes were determined for the NME method to predict the thickness mode impedance values of PMPWAS using the correlation between a proof-mass-piezoelectric transducer and structural dynamic properties in the substrate structure. Essentially, the models were used to build the basis for the PMPWAS tuning concept.

In order to explain the PM thickness change effects on the thickness mode impedance, the study is then followed by proof-mass analysis to investigate desired control objectives (such as tuning of wave modes) using the correlation between a PMPWAS transducer and structural dynamic properties in the substrate structure. Proof masses shift system resonance towards optimal frequency point. The coupled-field models for the PMPWAS and bonded PMPWAS on a substrate structure are also numerically generated in commercial multi-physics finite element analysis software, ANSYS®. The thickness mode EMIS results from analytical, numerical, and experimental analyses are presented. The analytical models are verified by the computational and experimental results.

## 7.2 ANALYTICAL EMIS ANALYSIS FOR PM-PWAS

This section first presents PM-PWAS analytical model including the bonding layer. The mechanical analysis is conducted regarding the harmonic standing waves. Secondly, an analytical model for PM-PWAS constrained on a plate-like substrate including the two bonding layers is proceeded. Eventually, the comparisons of the analytical impedance results with the corresponding experimental measurements are presented for validation.

### 7.2.1 PM-PWAS INCLUDING BONDING LAYER

This section presents a three layer analytical model including an adhesive layer between PWAS and an isotropic elastic material layer. The boundary conditions and accordingly the global matrix will be redefined however the global matrix element order will differ solely due to the material order and overall feature of the global matrix will remain the same as the global matrix of the three bar resonator.

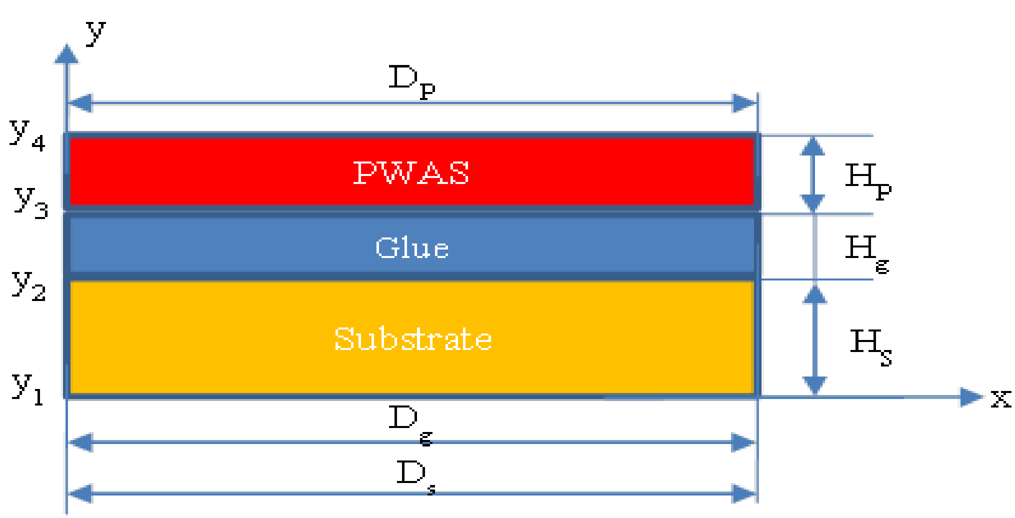


Figure 7.1 Illustration of constrained PWAS model including adhesive bonding layer.

Mechanical Analysis: Harmonic Standing Waves

We obtain the wave equations for each division in the model shown in Figure 7.1 from Newton's equation of motion as follows;

$$\begin{aligned} c_s^{\,2} u_s'' &= \ddot{u}_s \\ c_g^2 u_g'' &= \ddot{u}_g \\ c_p^2 u_p'' &= \ddot{u}_p \end{aligned} \tag{7.1}$$

The subscripts $s$, $g$, and $p$ denote for substrate layer, adhesive bonding (glue) layer, and piezoelectric layer respectively. The general wave equation solutions for substrate layer can be recalled as

$$u_s = \left( C_1 e^{-i\gamma_s (y-y_1)} + C_2 e^{i\gamma_s (y-y_2)} \right) e^{i\omega t} = \hat{u}_s e^{i\omega t} \tag{7.2}$$

where $u_s$ is the displacement for the isotropic elastic material of the substrate layer, Similarly, the displacement, $u_g$, for the adhesive bonding layer and, $u_p$, for PWAS layer, can be determined. The capital coefficients denote the axial wave amplitudes as forward and backward directions respectively in x axis and $\gamma_p = \omega / c_p$, $\gamma_a = \omega / c_a$, $\gamma_b = \omega / c_b$ denote the wave numbers for each material of the divisions and related to the wave speed in each material.

Linear Hooke's law applies to determine the stress-strain constitutive equation using the strain-displacement relation, $\varepsilon = \partial u / \partial x$, for each subsection in 1-D three-bar resonator problem as follows;

$$\sigma_s = E_s \varepsilon_s = E_s u_s' = iE_s \gamma_s \left( -C_1 e^{-i\gamma_s (y-y_1)} + C_2 e^{i\gamma_s (y-y_2)} \right) e^{i\omega t} \tag{7.3}$$

The stress equations $\sigma_p$ and $\sigma_b$ were determined in similar manner. Two unknown coefficients in each stress equation exist and six unknown coefficients in total therefore six boundary conditions should be implied to the general wave solutions to obtain the solutions of the wave equations in terms of the displacement mode shapes and the frequency responses at structural resonances for different modes. The stress and displacement boundary conditions to be imposed are; stress-free boundary condition at free ends, stress continuity condition and displacement continuity condition at two interfaces.

$$\begin{array}{ll} @\, y = y_1 & N_s(y_1)=0 \quad \rightarrow \quad \sigma_s(y_1)=0 \rightarrow \varepsilon_s(y_1)=u_s'(y_1)=0 \\ @\, y = y_2 & N_s(y_2)=N_g(y_2) \\ & u_s(y_2)=u_g(y_2) \\ @\, y = y_3 & N_g(y_3)=N_p(y_3) \\ & u_g(y_3)=u_p(y_3) \\ @\, y = y_4 & N_p(y_4)=0 \end{array} \tag{7.4}$$

The first relation between two displacement amplitudes in the material on the left hand side is determined by the stress boundary condition on the left surface at $y = y_1$

$$\begin{aligned} & N_s(y_1)=0 \\ & E_s\varepsilon_s(y_1)=E_s u_s'(y_1)=0 \\ & E_s i\gamma_s\left(-C_1 e^{-i\gamma_s(y_1-y_1)}+C_2 e^{i\gamma_s(y_1-y_2)}\right)=0 \end{aligned} \tag{7.5}$$

Hence,

$$-C_1+C_2 e^{i\gamma_s(y_1-y_2)}=0 \tag{7.6}$$

The second relation is determined by the stress boundary condition on interface between the left and the middle bars.

$$\begin{aligned} & N_s(y_2)=N_g(y_2) \\ & E_s\varepsilon_s(y_2)=E_g\varepsilon_g(y_2) \\ & E_s u_s'(y_2)=E_g u_g'(y_2) \end{aligned} \tag{7.7}$$

$$E_s i\gamma_s\left(-C_1 e^{-i\gamma_s(y_2-y_1)}+C_2 e^{i\gamma_s(y_2-y_2)}\right)=E_g i\gamma_g\left(-C_3 e^{-i\gamma_g(y_2-y_2)}+C_4 e^{i\gamma_g(y_3-y_2)}\right) \tag{7.8}$$

Hence,

$$-C_1E_si\gamma_se^{-i\gamma_s(y_2-y_1)}+C_2E_si\gamma_s+C_3E_gi\gamma_g-C_4E_gi\gamma_ge^{i\gamma_g(y_2-y_3)}=0 \tag{7.9}$$

The displacement boundary condition at $y=y_2$ determines the third relation

$$u_s(y_2)=u_g(y_2) \tag{7.10}$$

$$C_1e^{-i\gamma_s(y_2-y_1)}+C_2e^{i\gamma_s(y_2-y_2)}=C_3e^{-i\gamma_g(y_2-y_2)}+C_4e^{i\gamma_g(y_2-y_3)} \tag{7.11}$$

$$C_1e^{-i\gamma_s(y_2-y_1)}+C_2-C_3-C_4e^{i\gamma_g(y_2-y_3)}=0 \tag{7.12}$$

The stress boundary condition on the interface at $y=y_3$ determines the fourth relation between the displacement amplitudes

$$E_g\gamma_g\left(-C_3e^{-i\gamma_g(y_3-y_2)}+C_4e^{i\gamma_g(y_3-y_3)}\right)=E_p\gamma_p\left(-C_5e^{-i\gamma_p(y_3-y_3)}+C_6e^{i\gamma_p(y_3-y_4)}\right) \tag{7.13}$$

$$-C_3E_g\gamma_ge^{-i\gamma_g(y_3-y_2)}+C_4E_g\gamma_ge^{i\gamma_g(y_3-y_3)}=-C_5E_p\gamma_pe^{-i\gamma_p(y_3-y_3)}+C_6E_p\gamma_pe^{i\gamma_p(y_3-y_4)} \tag{7.14}$$

$$-C_3E_g\gamma_ge^{-i\gamma_g(y_3-y_2)}+C_4E_g\gamma_g+C_5E_p\gamma_p-C_6E_p\gamma_pe^{i\gamma_p(y_3-y_4)}=0 \tag{7.15}$$

as well as the displacement boundary conditions on the same interface determines the fifth relation

$$C_3e^{-i\gamma_g(y_3-y_2)}+C_4e^{i\gamma_g(y_3-y_3)}=C_5e^{-i\gamma_p(y_3-y_3)}+C_6e^{i\gamma_p(y_3-y_4)} \tag{7.16}$$

$$C_3e^{-i\gamma_g(y_3-y_2)}+C_4-C_5-C_6e^{i\gamma_p(y_3-y_4)}=0 \tag{7.17}$$

The stress-free boundary condition on the free-surface at $y_4$ determines the sixth relation

$$E_p\left(-i\gamma_pC_5e^{-i\gamma_p(y_4-y_3)}+i\gamma_pC_pe^{i\gamma_p(y_4-y_4)}\right)=0 \tag{7.18}$$

$$-C_5e^{-i\gamma_p(y_4-y_3)}+C_6=0 \tag{7.19}$$

The linearly dependent equations determined in (7.6), (7.9), (7.12), (7.15), (7.17), and (7.19) by implying the stress and displacement boundary conditions and they are combined in a matrix form to provide a solution of the Eigen-frequencies and to eventually obtain the six Eigen-vectors (the displacement amplitudes). Therefore, this problem turns out to be an eigenvalue problem which requires a matrix that contains the material properties and wave-numbers as functions of frequency for all subsections in the bar and the matrix is to be multiplied by a tensor that contains the displacement amplitudes and the product of the two matrices will equal to zero as shown in Eq. (7.20)

$$\begin{pmatrix} 1 & -e^{-i\gamma_s H_s} & 0 & 0 & 0 & 0 \\ -e^{-i\gamma_s H_s} & 1 & \dfrac{E_g\gamma_g}{E_s c_s} & -\dfrac{E_g\gamma_g}{E_s\gamma_s} e^{-i\gamma_g H_g} & 0 & 0 \\ e^{-i\gamma_s H_s} & 1 & -1 & -e^{-i\gamma_g H_g} & 0 & 0 \\ 0 & 0 & -\dfrac{E_g\gamma_g}{E_p\gamma_p} e^{-i\frac{\omega}{c_p}L_p} & \dfrac{E_g\gamma_g}{E_p\gamma_p} & 1 & -e^{-i\gamma_p H_p} \\ 0 & 0 & e^{-i\gamma_g H_g} & 1 & -1 & -e^{-i\gamma_p H_p} \\ 0 & 0 & 0 & 0 & -e^{-i\gamma_p H_p} & 1 \end{pmatrix} \begin{Bmatrix} C_1 \\ C_2 \\ C_3 \\ C_4 \\ C_5 \\ C_6 \end{Bmatrix} = 0 \qquad (7.20)$$

The determinant of the global matrix $A_{6x6}$ must equal to zero to have non-trivial solution for the displacement amplitudes. Then one can say that the global matrix is apparently a singular matrix and it does not have a unique solution. Therefore, we can find the basis of the eigenvector by assuming one of the unknowns is one i.e. $C_6 = 1$. This assumption helps us obtain $A_{5x5}$ non-singular matrix simply excluding 6th row that no longer represents an independent equation. The 6th column of the global matrix is moved to the right hand side of the equation to eventually obtain a non-trivial basis of the solution for the unknown constants. The basis of the coefficient solutions i.e. eigenvectors are used to obtain the basis of the mode shape solutions at the resonance frequencies i.e. eigenvalues or Eigen-frequencies. The modal participation factor (modal mass) is found by the mass weighted integral method and the modal mass that differs at each mode is used to normalize and scale down each mode shape amplitude. The normal mode shapes are utilized for the normal mode expansion method to obtain the frequency response function is plotted as illustrated in Figure 7.2a. The dynamic structural stiffness is found taking the inverse of the FRF and multiplying by the mass density and the surface area of PWAS and the stiffness ratio is found by the relation $r(\omega) = k_{str}(\omega)/k_{PWAS}$, where $k_{PWAS} = Ac_{33}^{D}/t$ is the PWAS stiffness in thickness mode that contains; $A$ is the PWAS surface area, $c_{33}^{D}$ is the stiffness if the piezoelectric material in thickness direction under the constant electric displacement assumption, and $t$ is the PWAS thickness. The stiffness ratio can then be plugged into the thickness mode impedance equation that can be adopted for the PWAS-glue-substrate model. The real part of the impedance prediction is plotted as illustrated in Figure 7.2b. More precise agreement is captured between the experimental and analytical results.

Comparison of the analytical impedance results with the experimental results

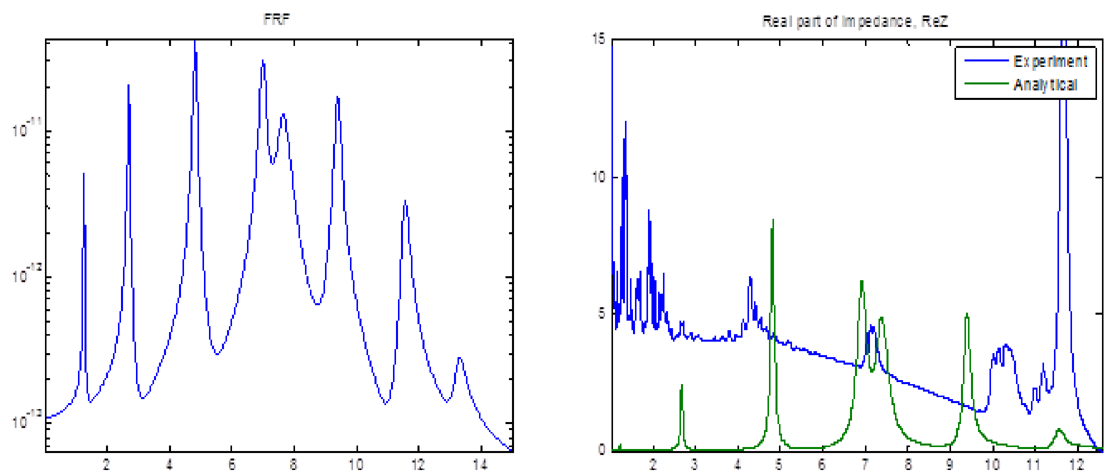


(a) (b)

Figure 7.2 (a) Frequency response function whose amplitude is plotted in logarithmic scale; (b) experimental and analytical real part of the E/M impedance results for PWAS installed on 1mm thick aluminum 7mm x 7mm square plate-like aluminum substrate.

The frequency response function whose amplitude is plotted in logarithmic scale and one-dimensional analytical E/M impedance model results are presented in Figure 7.2 for square PWAS size is 7x7x0.2 $mm^3$ , bonding layer is modeled in 80 μm thickness with 8GPa elastic modulus and 1500 $kg/m^3$ mass density. Experimental and analytical real part of the E/M impedance results are compared by superimposing in the same plot herein for PWAS installed on 1mm thick aluminum square plate-like aluminum substrate. Internal damping of PWAS is assumed to be 5% whereas the structural damping is 1% and thickness mode electro-mechanical coupling coefficient $k_{33}$ is 0.42.

### 7.2.2 PM-PWAS ON SUBSTRATE INCLUDING THE BONDING LAYERS

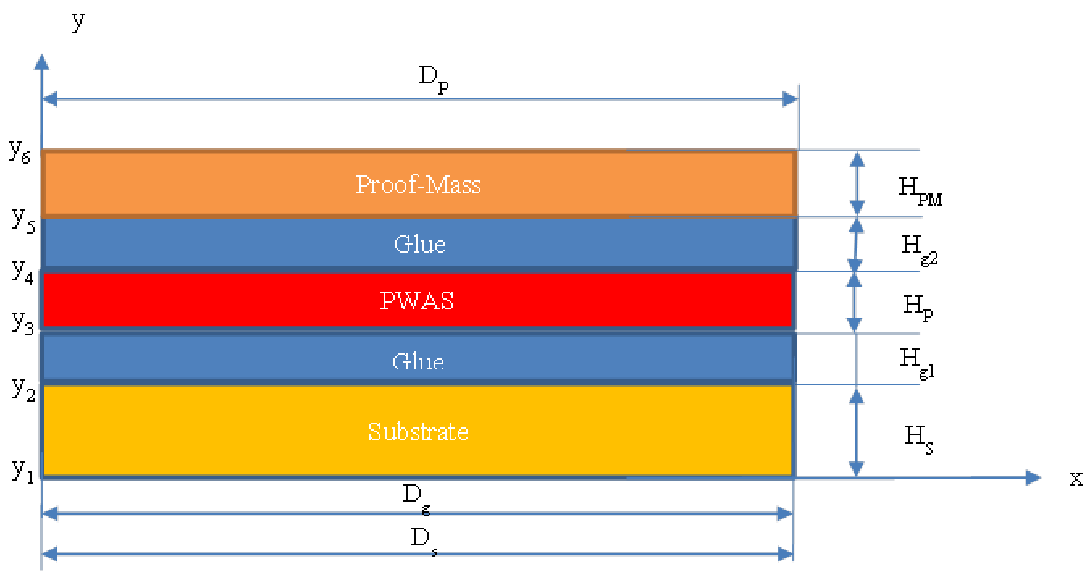


Figure 7.3 Illustration of constrained PM-PWAS model including two adhesive bonding layers.

The resonator theory was also adopted as in three-layer structures and the two-layer for the similar procedure of the analytical modeling of EMIS of the five layer structure including proof-mass, one adhesive layer between proof-mass and PWAS, another adhesive layer between the PWAS and the substrate, one can come up with the 10x10 global matrix $[A]$ in (7.21). The global matrix $[A]$ carries the material and geometrical aspects of all the five layers as a function of wave number. The wave number-frequency relations as similarly defined in Eq.(5.5) for each layer are substituted into the matrix to obtain the frequency dependency. The eigenvalue problem can be set by using the matrix $[A]\{C_i\}=0$ where $C$ vector includes the mode shape amplitudes i.e. coefficients with subscript of $i=1,2,3,...,10$

$$
[A]=\begin{bmatrix}
1 & -e^{-i\gamma_s H_s} & 0 & 0 & 0 & 0 & 0 & 0 & 0 & 0 \\
-e^{-i\gamma_s H_s} & 1 & \dfrac{E_{g1}\gamma_{g1}}{E_s\gamma_s} & -\dfrac{E_{g1}\gamma_{g1}}{E_s\gamma_s}e^{-i\gamma_{g1}H_{g1}} & 0 & 0 & 0 & 0 & 0 & 0 \\
e^{-i\gamma_s H_s} & 1 & -1 & -e^{-i\gamma_{g1}H_{g1}} & 0 & 0 & 0 & 0 & 0 & 0 \\
0 & 0 & -e^{-i\gamma_{g1}H_{g1}} & 1 & \dfrac{E_p\gamma_p}{E_{g1}\gamma_{g1}} & -\dfrac{E_p\gamma_p}{E_{g1}\gamma_{g1}}e^{-i\gamma_p H_p} & 0 & 0 & 0 & 0 \\
0 & 0 & e^{-i\gamma_{g1}H_{g1}} & 1 & -1 & -e^{-i\gamma_p H_p} & 0 & 0 & 0 & 0 \\
0 & 0 & 0 & 0 & -e^{-i\gamma_p H_p} & -1 & 1 & -e^{-i\gamma_{g2}H_{g2}} & 0 & 0 \\
0 & 0 & 0 & 0 & -\dfrac{E_p\gamma_p}{E_{g2}\gamma_{g2}}e^{-i\gamma_p H_p} & \dfrac{E_p\gamma_p}{E_{g2}\gamma_{g2}} & 1 & e^{-i\gamma_{g2}H_{g2}} & 0 & 0 \\
0 & 0 & 0 & 0 & 0 & 0 & -e^{-i\gamma_{g2}H_{g2}} & -1 & 1 & e^{-i\gamma_{PM}H_{PM}} \\
0 & 0 & 0 & 0 & 0 & 0 & -\dfrac{E_{g2}\gamma_{g2}}{E_{PM}\gamma_{PM}}e^{-i\gamma_{g2}H_{g2}} & \dfrac{E_{g2}\gamma_{g2}}{E_{PM}\gamma_{PM}} & 1 & -e^{-i\gamma_{PM}H_{PM}} \\
0 & 0 & 0 & 0 & 0 & 0 & 0 & 0 & -e^{-i\gamma_{PM}H_{PM}} & 1
\end{bmatrix} \quad (7.21)
$$

Once the eigenvalue problem is solved for the eigenvectors (mode-shape amplitudes) and eigen-frequencies (resonance frequencies), the mode shapes at each resonance frequency can be defined to use for normal model expansion (NME) method. Eventually, the FRF and dynamic structural stiffness can be obtained from NME method. The stiffness ratio is calculated and substituted into the constrained thickness mode PWAS-EMIS Eq.(6.12). After the internal damping effects are included, one can plot the EMIS calculation for the regarding constrained PM-PWAS model including two adhesive bonding layers.

The theoretical calculation of real part of impedance (ReZ) is compared with experimental measurement of ReZ in Figure 7.4. EMIS of PM-PWAS on aluminum substrate assuming perfect bonding without adhesive layers is illustrated on the left and EMIS of PM-PWAS on aluminum substrate including two adhesive bonding layers on the right. Both results are for PM height of 1.5mm and lateral sizes are in $7 \times 7mm^2$ for both aluminum PM and 1mm thick host-structure.

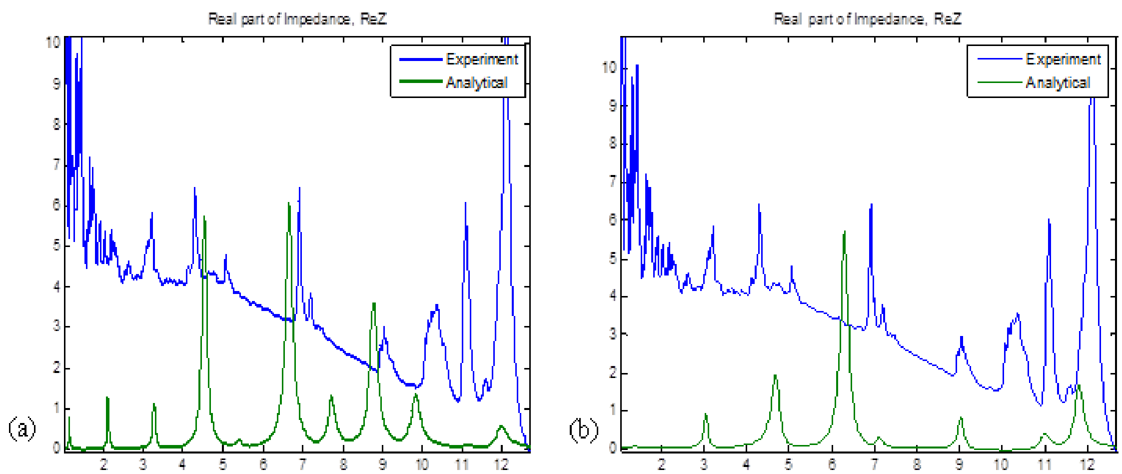


Figure 7.4 Comparison of analytical and experimental (a) EMIS of PM-PWAS on aluminum substrate neglecting adhesive bonding layers (b) EMIS of PM-PWAS on aluminum substrate including two adhesive bonding layers

## 7.3 COUPLED FIELD FINITE ELEMENT ANALYSIS OF PMPWAS EMIS

In CF-FEA approach, the mechanical coupling between the structure and the sensor is implemented by specifying boundary conditions of the sensor, while the electromechanical coupling is modeled by multi-physics equations for the piezoelectric material. The first coupling allows the mechanical response sensed by the piezoelectric element to be reflected in its impedance signature. The aluminum beam was modeled as a homogeneous isotropic material with assumed density $\rho = 2780\ \text{kg/m}^3$ and elastic modulus $E = 72.4\ \text{GPa}$.

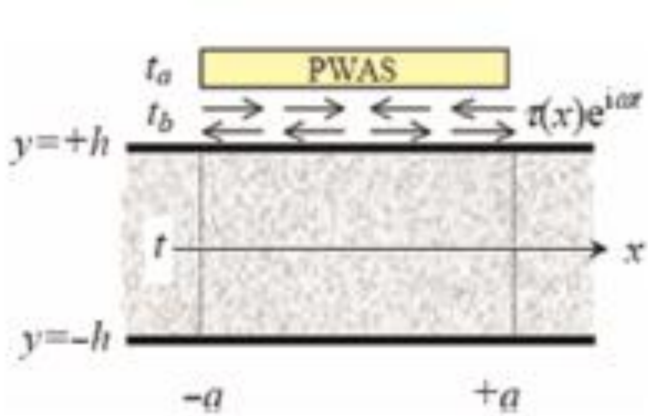


Figure 7.5 Interaction between PWAS and structure

The coupled field FEM matrix element can be expressed as follows

$$\begin{bmatrix} [M] & [0] \\ [0] & [0] \end{bmatrix} \begin{Bmatrix} \{\ddot{u}\} \\ \{\ddot{V}\} \end{Bmatrix} + \begin{bmatrix} [C] & [0] \\ [0] & [0] \end{bmatrix} \begin{Bmatrix} \{\dot{u}\} \\ \{\dot{V}\} \end{Bmatrix} + \begin{bmatrix} [K] & [K^Z] \\ [K^Z]^T & [K^d] \end{bmatrix} \begin{Bmatrix} \{u\} \\ \{V\} \end{Bmatrix} = \begin{Bmatrix} \{F\} \\ \{L\} \end{Bmatrix} \quad (7.22)$$

where $[M]$, $[C]$, and $[K]$ are the structural mass, damping, and stiffness matrices, respectively; $\{u\}$ and $\{V\}$ are the vectors of nodal displacement and electric potential, respectively, with dot above variables denoting time derivative; $\{F\}$ is the force vector; $\{L\}$ is the vector of nodal, surface, and body charges; $\{K^Z\}$ is the piezoelectric coupling matrix; and $\{K^d\}$ is the dielectric conductivity.

This CF-FEA method is very convenient for evaluating the impedance signatures as it is measured by the impedance analyzer. PWAS dimensions are $7 \times 0.2\ \text{mm}^2$. For a plane strain analysis, only a longitudinal section of the specimen and PWAS were analyzed; hence 2-D meshed CF-FEA model was generated which reduced considerably the computational time. The 2D plane element PLANE42 is used for the aluminum beam; this element has 4 nodes and 2 DOF at each node. The 2D plane element PLANE13 is used to model the PWAS using the coupled field formulation presented in Eq.(7.22). Then, the impedance spectrum up to 15 MHz was calculated.

### 7.3.1 CF-FEA VALIDATION OF PM-PWAS MODEL

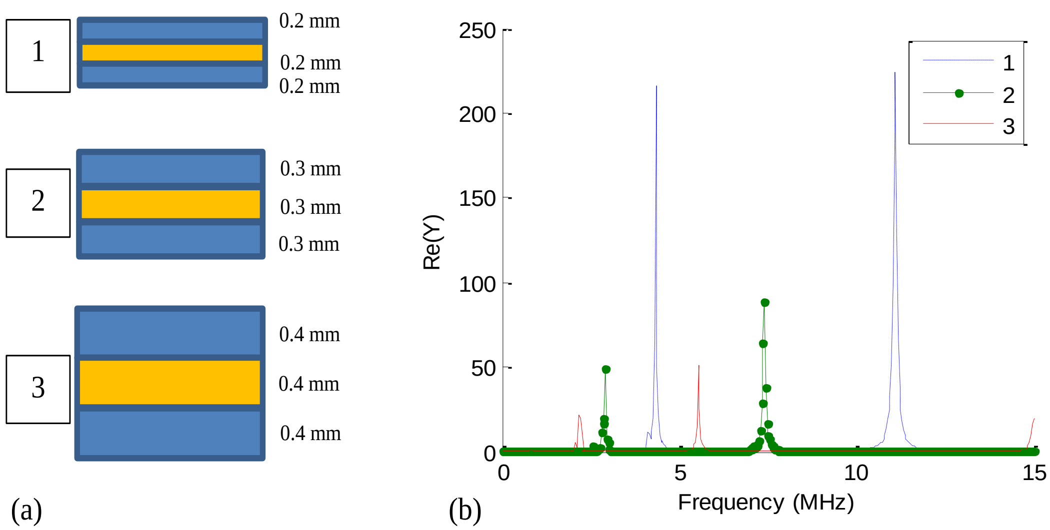


Figure 7.6 (a) three configurations of PM-PWAS in different thickness; (b) real part of the admittance spectra in regards with the corresponding configurations of PM-PWAS system

The coupled field finite element analysis (CF-FEA) is conducted for PM-PWAS E/M admittance spectroscopy to visualize the resonance frequency shifting phenomena due to the thickness variation in the PM-PWAS-substrate structure in thickness mode. This message is obviously delivered in Figure 7.6(b). The admittance peaks that represent the thickness mode resonance frequencies shift further down as the thickness of the PM-PWAS configuration increases. The first model thickness is 0.6mm in total whereas the third model thickness is 1.2mm that is as twice thick as the first one so one should expect the same thickness mode resonance frequency of the first model in should be as twice as that of the third model. For example, the second admittance peak of the first PM-PWAS model in Figure 7.6(b) appears nearly at 11MHz where the second peak of the third PM-PWAS model is at around 5.5MHz. The numerical resonance frequency results are also extracted from FEA and corresponding analytical prediction and shown in

Table 7.1 where one can see the exact frequency shift in what mode due to the thickness change.

Table 7.1 Analytical and finite element analysis results for the thickness mode resonance frequencies of three configuration of PM-PWAS system

| Configuration | 1 | | 2 | | 3 | |
|---|---|---|---|---|---|---|
| Thickness mode [MHz] | Analytical | FEA | Analytical | FEA | Analytical | FEA |
| First resonance frequency | 3.889 | 4.32 | 2.593 | 2.974 | 1.944 | 2.017 |
| Second resonance frequency | 6.702 | 6.756 | 4.468 | 4.378 | 3.351 | 3.432 |
| Third resonance frequency | 9.732 | 9.688 | 6.488 | 7.325 | 4.866 | 4.119 |
| Fourth resonance frequency | 13.803 | 11.008 | 9.202 | 9.237 | 6.901 | 5.470 |
| Fifth resonance frequency | | | 11.617 | 11.577 | 8.713 | 8.718 |
| Sixth resonance frequency | | | 13.415 | 13.824 | 10.061 | 10.374 |
| Seventh resonance frequency | | | | | 11.718 | 11.795 |
| Eighth resonance frequency | | | | | 13.786 | 13.726 |

The information regarding the mode numbers can be more explicitly received in the tabular numerical presentation. The first PM-PWAS configurations seem to have four thickness modes whereas the second configuration has six and third one has eight thickness modes however they are all not visible in the graphical presentation only three admittance peaks show up for each configuration.

<u>CF-FEA models for PM-PWAS with different PM height</u>

One more example shall be presented in this case study regarding the resonance frequency shifting. In this example, only the thickness of the proof-mass is varied and CF-FEA is carried out for six different configurations and results for the real part of the E/M admittance spectra are illustrated in Figure 7.7. The first configuration is free PWAS in thickness of 0.2mm, second one is PWAS constrained on bottom surface by an aluminum substrate in thickness of 0.2mm.From third to sixth configuration aluminum proof-mass is attached on top surface of PWAS in gradually increasing thickness from 0.2mm to 0.8mm so that the thickness mode admittance peaks can be clearly distinguished for each configuration in the frequency range of 100Hz-15MHz.

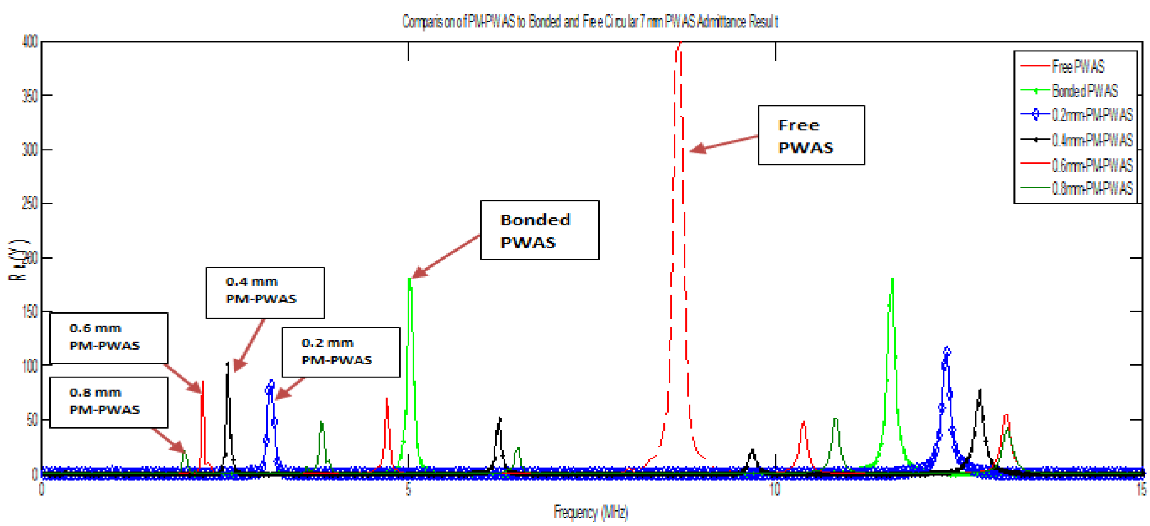


Figure 7.7 Illustration of proof-mass effect on PWAS-EMIS results

A particular thickness mode resonance frequency shift is depicted in the admittance spectra. The admittance peak shifts further downward to lower frequency as the proof-mass thickness increases (Figure 7.7). Also a considerable shift appears between the admittance peak of the free PWAS and that of the PWAS bonded on 0.2mm thick aluminum substrate. All models have the same length of 7mm.

Three different smaller PM length increment by 0.05 mm is analyzed by the analytical and numerical EMIS results. This study also verifies the analytical EMIS model by CF-FEA model depicting the same trends as well as very close agreement in Figure 7.8. The first anti-resonance frequency shifts all the way down to 5.175 MHz as the PM length increased up to 0.15mm in the analytical impedance plot whereas the frequency shifts downward to 6.135 MHz in the numerical model. The agreement between the analytical and the numerical models become closer at larger length of PM. The first anti-resonance frequency shifts down to 5.85 MHz as the PM length is 0.05mm in the analytical impedance plot whereas the frequency shifts downward to 7.7 MHz in the same length of PM-PWAS in the CF-FEA model.

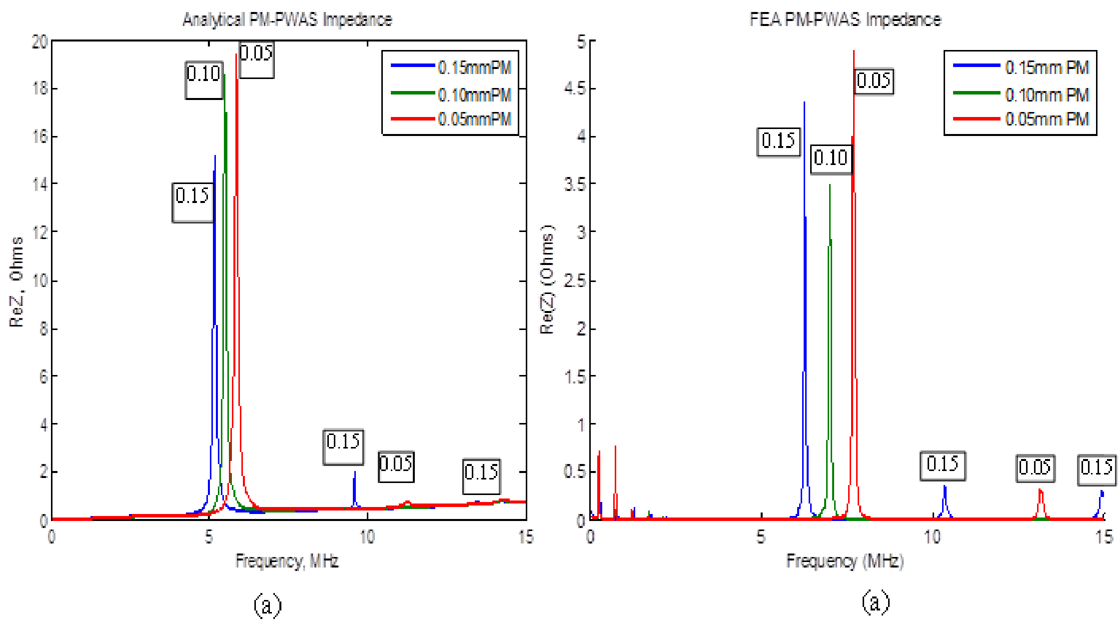


Figure 7.8 Thickness mode PM-PWAS EMIS simulations by 1-D analytical and 2-D FEA-models.

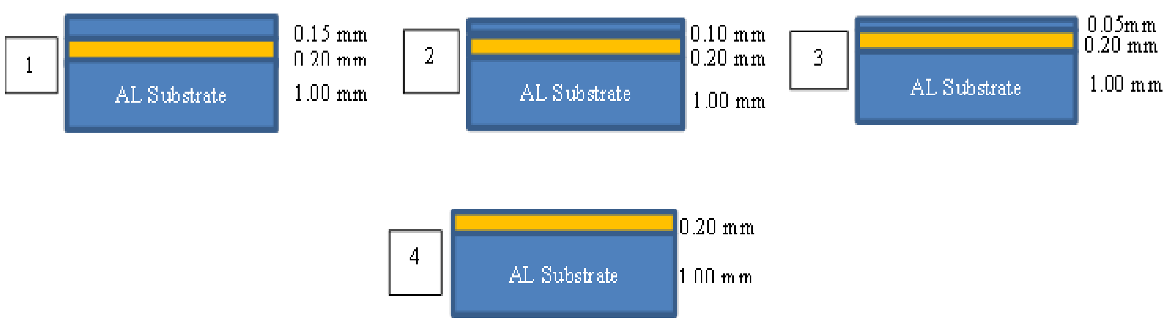


Figure 7.9 Four different configurations designed for CF-FEA to analyze the effect of proof-mass length on PWAS resonator

To experimentally realize the model with 0.1mm thick aluminum substrate would be challenging therefore the analytical analyses for the model with 1mm thick substrate were carried out with the same step sizes of the proof-masses and the same PWAS height of 0.2mm. The downward shifts were also clearly seen at the first frequency as well as the overtone anti-frequencies in the Figure 7.10.

Table 7.2 E/M impedance frequencies as the proof-masses incline from no mass up to 0.15mm PM height

| | Analytical EMIS | | | | |
|---|---|---|---|---|---|
| | PM Height | 0.15 | 0.1 | 0.05 | 0 |
| Resonance F | First res. Freq. | 1.935 | 1.964 | 1.994 | 2.028 |
| | Second res. Freq. | 4.26 | 4.359 | 4.423 | 4.487 |
| | Third res. Freq. | 6.004 | 6.23 | 6.422 | 6.608 |
| | Fourth res. Freq. | 7.927 | 8.131 | 8.293 | 8.456 |
| | | | | | |
| | CF-FEA EMIS | | | | |
| Resonance F | First res. Freq. | 1.801 | 1.83 | 1.865 | 1.9 |
| | Second res. Freq. | 4.072 | 4.113 | 4.154 | 4.194 |
| | Third res. Freq. | 6.28 | 6.46 | 6.565 | 6.64 |
| | Fourth res. Freq. | 7.756 | 8.412 | 8.749 | 8.964 |

E/M impedance plots as the proof-masses incline from no mass up to 0.15mm PM height as can be seen in Table 7.2. Each overtone frequencies are analyzed one by one and each obviously confirmed the monotonic frequency shift.

Similar EMIS results are obtained from CF-FEA to verify the analytical model in this example. The same four configurations are employed in the FEA model (Kamas, Giurgiutiu & Lin, 2014). We came up with the impedance peaks harmonically increasing as overtones and the overtones appearing at nearly the same anti-resonance frequencies. The shifting downward in both analytical and FEA results is depicted as the PM height increases for each overtone peak in Figure 7.10.

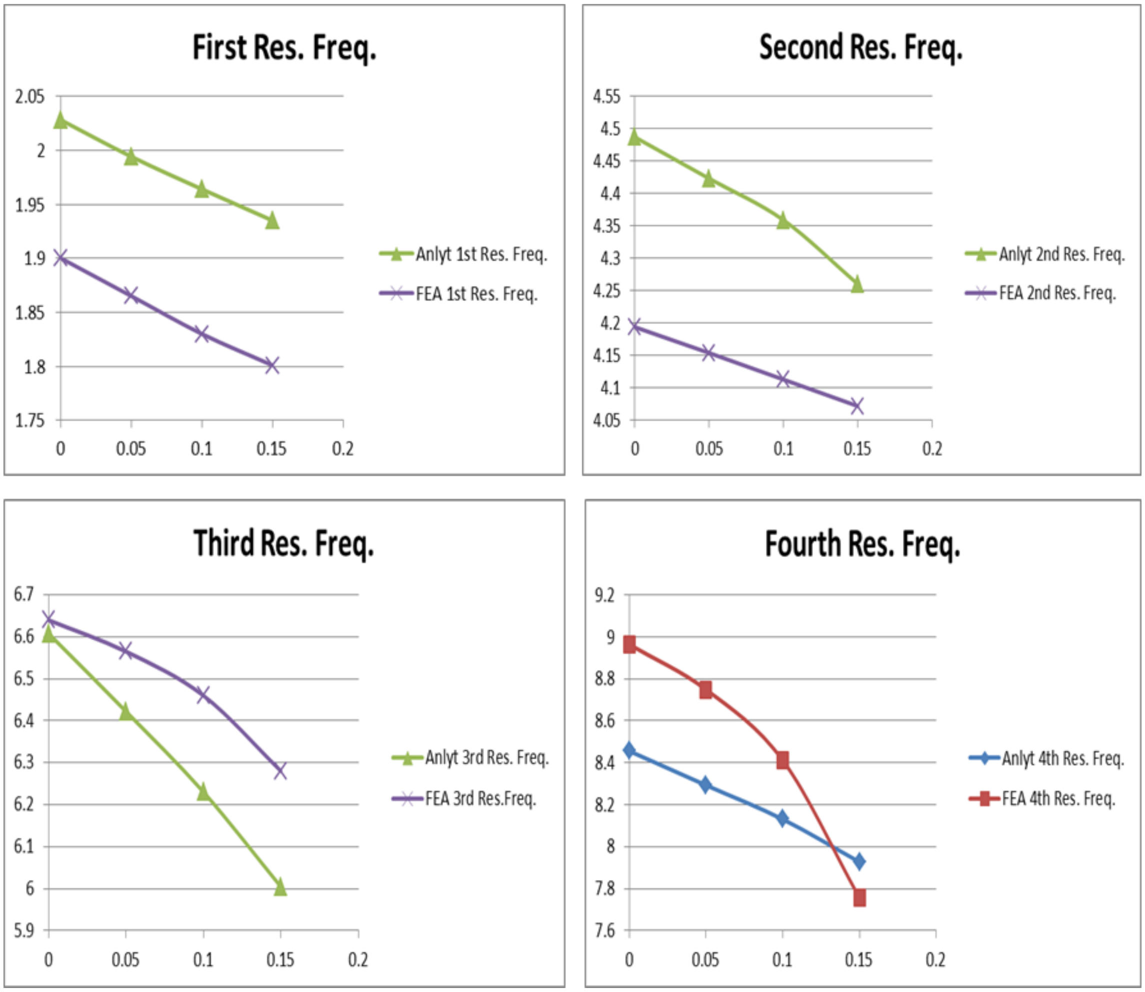


Figure 7.10 Resonance frequency changes as proof-mass height increases calculated by 1-D analytical and 2-D FEA models

<u>Plane strain assumption</u>

It is noticed that the aspect ratio H:7 where H is the height and at least 6 times smaller than the width in the FEA model i.e. the aspect ratio is at least 1:6. Therefore, CF-FEA processor should perform the multi-physics PM-PWAS analysis under the plane strain analysis. In the plane strain analysis, the constitutive relation between stress and strain includes the square of the Poisson ratio, $\nu$ , as seen in Eq.(7.23).

$$
\begin{Bmatrix} \sigma_x \\ \sigma_y \\ \sigma_{xy} \end{Bmatrix} = \frac{E}{1-\nu^2} \begin{bmatrix} 1 & \nu & 0 \\ \nu & 1 & 0 \\ 0 & 0 & 0.5(1-\nu) \end{bmatrix} \begin{Bmatrix} \varepsilon_x \\ \varepsilon_y \\ \varepsilon_{xy} \end{Bmatrix} \tag{7.23}
$$

Thus, we added the plane strain constitutive relation in x axis into our 1-D analytical EMIS model as a correction factor, i.e. we multiplied the elastic modulus by $1/1-\nu^2$. We obtained the analytical EMIS results for PM-PWAS problem in better agreement with the CF-FEA EMIS results as can be seen in tabulated resonance frequencies at first four modes of PM-PWAS EMIS in Table 7.3, and in graphical illustration in Figure 7.11. We also plotted the tabulated resonance frequency values for different height of PM in Figure 7.12. One can observe the nearly 10% downshift of the analytical results after the Poisson ratio of 0.33 is involved as presumed since

$$
\frac{E}{1-\nu^2} = \frac{E}{1-0.33^2} = \frac{E}{0.8911} = 1.12E \tag{7.24}
$$

Table 7.3 E/M impedance frequencies as the proof-masses incline from no mass up to 0.15mm PM height

| | | | | | |
|---|---|---|---|---|---|
| | Analytical EMIS | | | | |
| | PM Height | 0.15 | 0.1 | 0.05 | 0 |
| Resonance F | First res. Freq. | 1.79 | 1.825 | 1.866 | 1.901 |
| | Second res. Freq. | 3.842 | 3.935 | 4.01 | 4.086 |
| | Third res. Freq. | 5.521 | 5.759 | 5.957 | 6.12 |
| | Fourth res. Freq. | 7.224 | 7.456 | 7.683 | 7.887 |
| | | | | | |
| | CF-FEA EMIS | | | | |
| Resonance F | First res. Freq. | 1.801 | 1.83 | 1.865 | 1.9 |
| | Second res. Freq. | 4.072 | 4.113 | 4.154 | 4.194 |
| | Third res. Freq. | 6.28 | 6.46 | 6.565 | 6.64 |
| | Fourth res. Freq. | 7.756 | 8.412 | 8.749 | 8.964 |

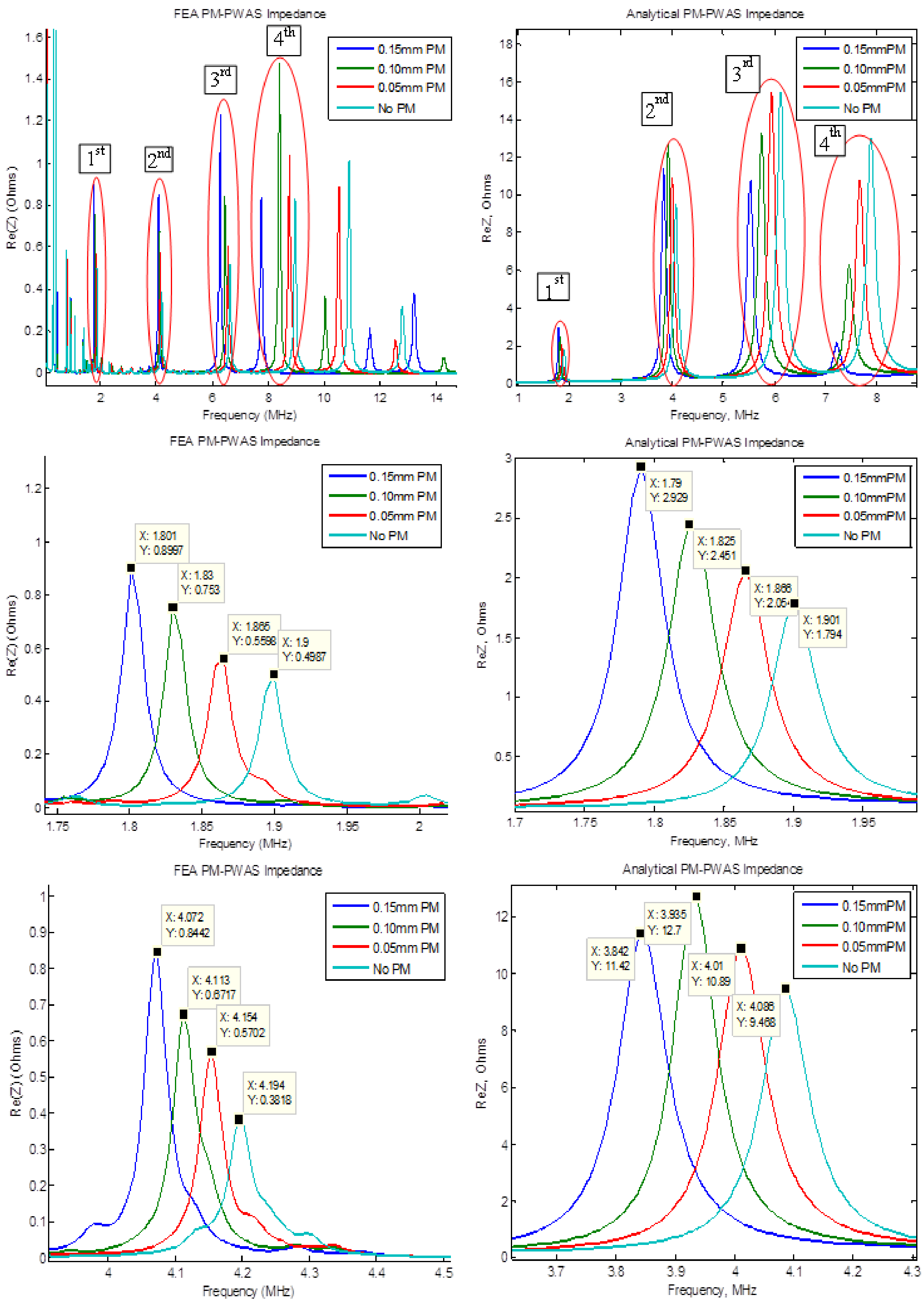
FEA PM-PWAS Impedance
1st
2nd
3rd
4th
0.15mm PM
0.10mm PM
0.05mm PM
No PM
Re(Z) (Ohms)
Frequency (MHz)
Analytical PM-PWAS Impedance
0.15mmPM
0.10mmPM
0.05mmPM
No PM
ReZ, Ohms
Frequency, MHz
X: 1.801
Y: 0.8997
X: 1.83
Y: 0.753
X: 1.866
Y: 0.5568
X: 1.9
Y: 0.4987
X: 1.79
Y: 2.929
X: 1.825
Y: 2.451
X: 1.866
X: 1.901
Y: 1.794
X: 4.072
Y: 0.8442
X: 4.113
Y: 0.6717
X: 4.154
Y: 0.5702
X: 4.194
Y: 0.3818
X: 3.842
Y: 11.42
X: 3.935
Y: 12.7
X: 4.01
Y: 10.89
X: 4.086
Y: 9.468

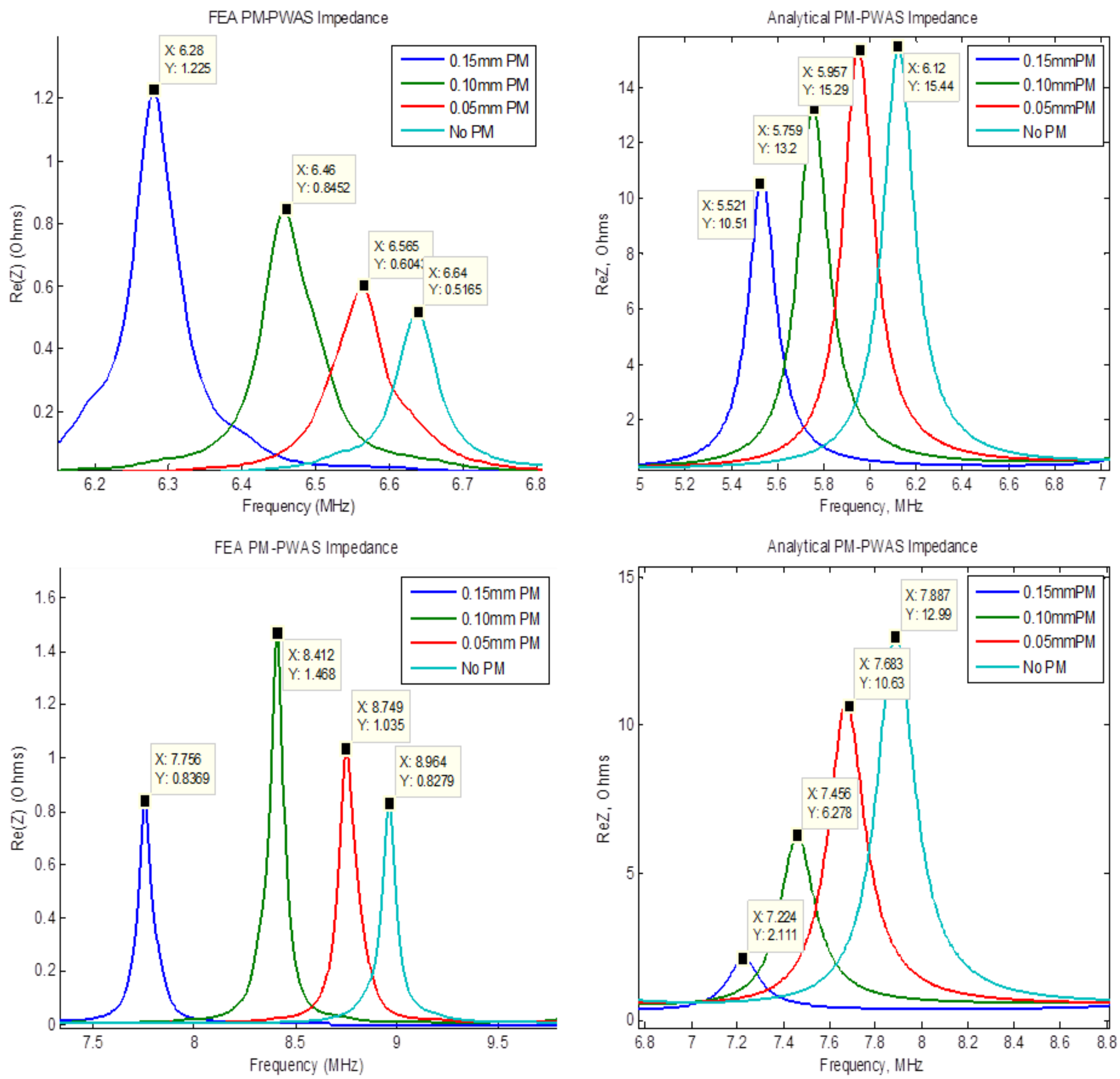


Figure 7.11 FEA and analytical PM-PWAS impedance spectra at first four thickness modes

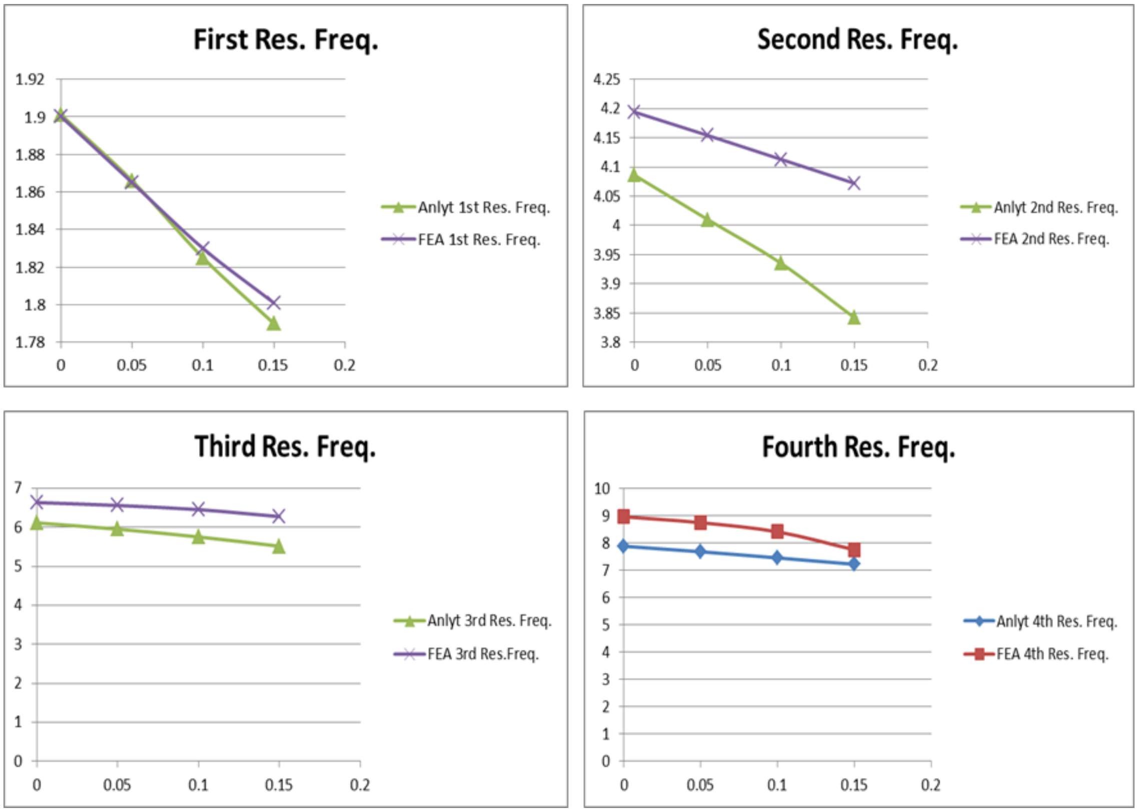


Figure 7.12 Resonance frequency changes as proof-mass height increases calculated by 1-D analytical and 2-D FEA models

EMIS results are obtained from CF-FEA for 2-D PWAS perfectly bonded in the center of an aluminum plate with 100mm length and 1.0mm thickness to verify the corresponding analytical model in this example. The same four configurations are employed in the FEA model as in the analytical models. We came up with the impedance peaks harmonically increasing as overtones and the overtones appearing at nearly the same anti-resonance frequencies. The downward shift phenomena were also clearly seen at the first frequency as well as the overtone anti-frequencies in the E/M impedance plots (Fig. 7) as the proof-masses incline from no mass up to 0.15mm PM height. Each overtone frequencies are analyzed one by one and each obviously confirmed frequency shift as shown for the first four thickness impedance modes in Figure 7.12. The stiffer the material is the further down shift in resonance frequency occurs. Thus, the analytical first E/M impedance peak obviously shifts down as much.

## 7.4 EXPERIMENTAL EMIS STUDY FOR PM-PWAS

This section presents the experimental study that has been conducted regarding electro-mechanical impedance spectroscopy (EMIS) of the proof-mass piezoelectric wafer active sensor (PM-PWAS). Various geometries and materials were used as proof-masses which were attached onto PWAS to validate the corresponding analytical multi-layer structure harmonic analysis. For these EMIS measurements, five different sets of experiment have been designed. The results of these experiments shall be presented and discussed in the following sections. Eventually those experimental results that agree with the analytical PM-PWAS impedance and admittance results will be investigated by comparison in the corresponding geometric sizes and material properties. The experimental work will be presented in the following layout.

1. EMIS results from washer PM-PWAS on AL plate
2. Steel PM-PWAS on Steel substrate
3. Steel PM-PWAS on AL plate
4. Experimental and analytical EMIS results for aluminum PM-PWAS on AL plate
5. Aluminum PM-PWAS on AL substrate

### 7.4.1 EXPERIMENTAL SETUP

The E/M impedance based SHM method is direct and convenient to implement, the only required equipment being an electrical impedance analyzer, such as HP 4194A impedance analyzer. A HP 4194A impedance analyzer was used for the experimental analysis. The impedance analyzer reads the E/M impedance of PWAS itself as well as the in-situ E/M impedance of PWAS attached to a specimen. It is applied by scanning a predetermined frequency range in high frequency band (up to 15MHz) and recording the complex impedance spectrum. A LabView data acquisition program was used to control the impedance analyzer and sweep the frequency range in steps that was predefined and to attain the data in a format that assists to data analysis. During the visualization of the frequency sweep, the real part of the E/M impedance, $\mathrm{Re}\left(Z\left(\omega\right)\right)$, follows up and down variation as the structural impedance goes through the peaks and valleys of the structural resonances and anti-resonances.

### 7.4.2 EXPERIMENTAL AND CF-FEA VALIDATION OF CONSTRAINED PWAS MODEL

The two bar resonator model solution can be used to be a basis of the solution for the PWAS bonded on plate-like structure. The global matrix -that consists of the piezoelectric material properties can be oriented into thickness mode and corresponding eigenvalue problem can be solved for the mode shape at thickness mode resonance frequencies. Then the thickness mode shapes can be substituted into frequency response function and eventually the dynamic structural stiffness and the stiffness ratio, $r\left(\omega\right)=k_{str}\left(\omega\right)/k_{PWAS}$, can be found where $k_{PWAS}=Ac_{33}^{D}/t$ is the PWAS stiffness in thickness mode that contains; $A$ is the PWAS surface area, $c_{33}^{D}$ is the stiffness if the piezoelectric material in thickness direction under the constant electric displacement assumption, and $t$ is the PWAS thickness. The stiffness ratio can then be plugged into the thickness mode impedance equation for one side constrained PWAS.

In the one side constrained model, the following assumptions were made. First, the geometry and the cross-section area of the two layers were the same although they have different materials and different thicknesses. Second, the isotropic bar was assumed to be perfectly bonded to the PWAS on the interfaces. A bonding layer was not considered in this two layer model.

### 7.4.3 COMPARISON OF EXPERIMENTAL AND ANALYTICAL EMIS RESULTS

The results obtained from the analytical prediction in terms of the frequency response function (FRF) and the E/M impedance is presented in Figure 7.13. The theoretical EMIS prediction is compared by the results from the corresponding experimental setup shown in Figure 7.14a for the PWAS bonded on a 1mm thick aluminum substrate.

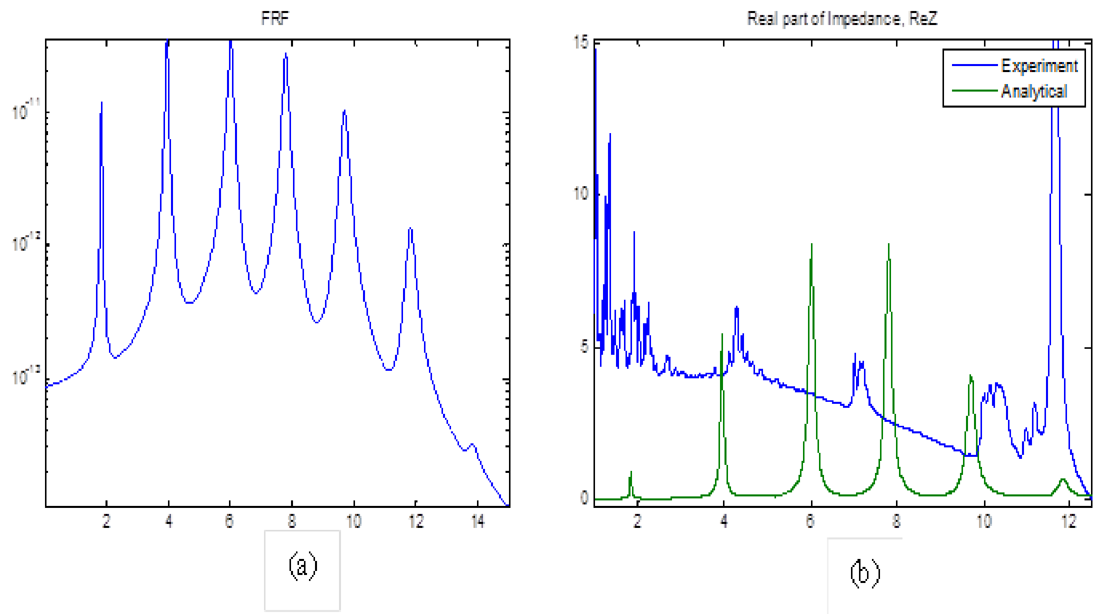


Figure 7.13 (a) Frequency response function; (b) experimental and analytical real part of the E/M impedance results for PWAS installed on 1mm thick aluminum square plate-like aluminum substrate.

On the comparison by superimposing the plots of the real parts of E/M impedance from both analytical calculation and experimental readings, one can see that the agreement is somewhat acceptable except for some discrepancy on the third and fourth impedance spectra. The main impedance spectra that rise from the PWAS domain that appears right below 12 MHz are in very good agreement in terms of the frequency. The first thickness mode impedance spectrum measurement is difficult to distinguish from the in-plane mode impedance spectra therefore it is hardly possible to compare the first thickness mode impedance spectrum prediction with the experimental reading. However, the second and fifth E/M impedance spectra predictions are in also in good agreement with the experimental EMIS measurements.

To have less discrepancy and closer agreement, it turned out that more physical conditions that the experimental setup possesses need to be acquired in the theoretical prediction. Hence, the adhesive bonding layer being neglected was decided to be added into the analytical model to have more precise approach to the EMIS measurements.

A few square PWAS were installed on aluminum rectangular 5x7x1 $mm^3$ substrate and impedance and admittance measurements for the constrained PWAS specimens were conducted and the results were plotted. The admittance plot of one specimen can be seen in Figure 7.14.

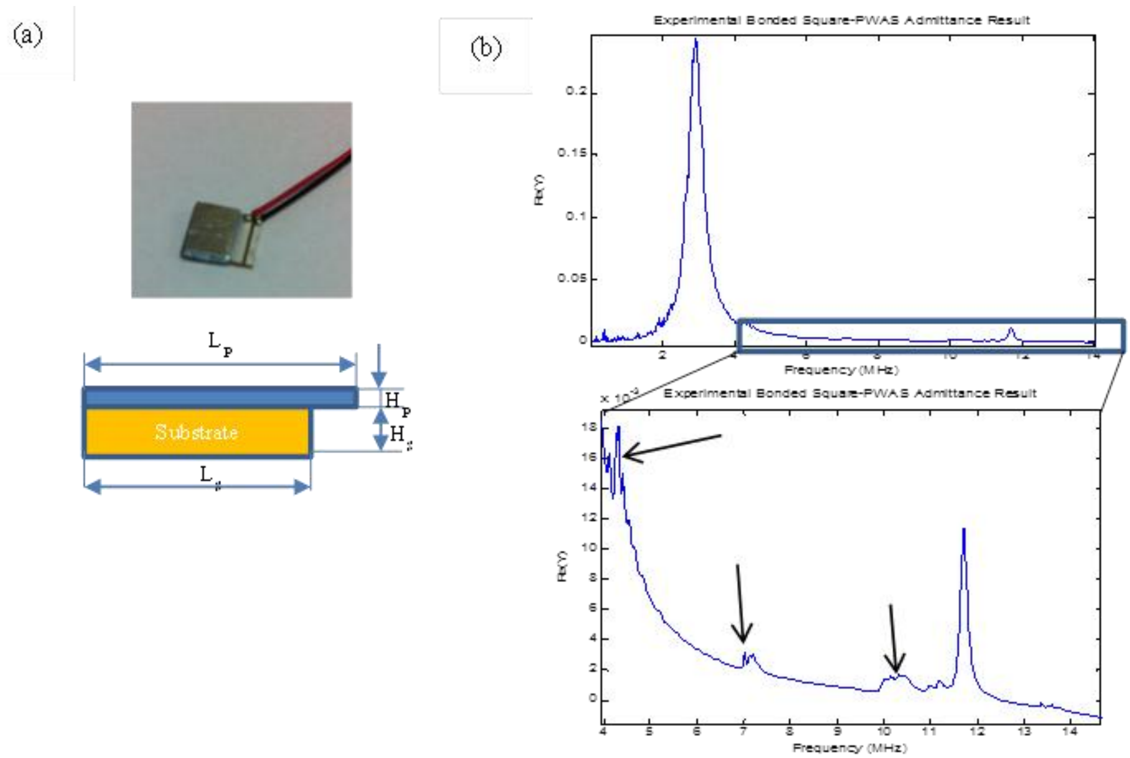


Figure 7.14 (a) Illustration of a schema and picture of constrained PWAS and (b) experimental admittance result of one of the constrained PWAS specimens

The focal interest is in the thickness mode so the results were focused in the relatively high frequency range; between 4-14.5 MHz in this case to see the thickness resonance peaks that come from the substrate material at around 4.2 MHz, 7.2 MHz, and 10.2 MHz beside the resonance peak that comes from the PWAS itself at around 11.8 MHz. The experimental measurement from one of the constrained PWAS specimen was also compared with the corresponding analytical thickness model in terms of impedance in Figure 7.15.

| Mode number | Analytical Resonance Freq MHz | Experimental Resonance Freq MHz |
|---|---|---|
| 1 | 1.834 | 1.9 |
| 2 | 3.976 | 4.32 |
| 3 | 6.011 | |
| 4 | 7.744 | 7.15 |
| 5 | 9.743 | 10.2 |
| 6 | 11.89 | 11.7 |
| 7 | 13.749 | 13.5 |

a

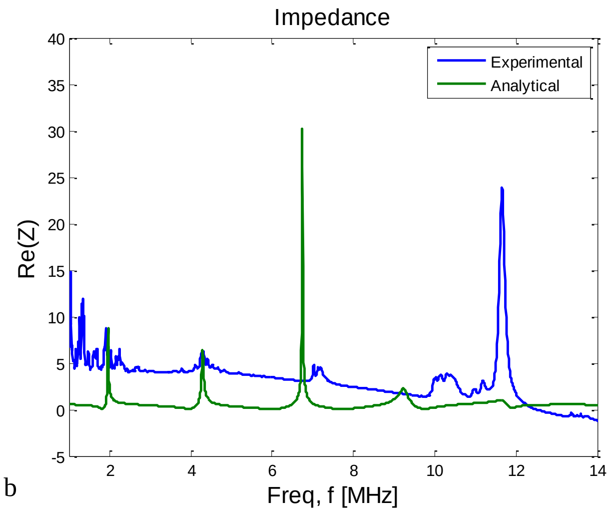


b

Figure 7.15 Comparison between analytical and experimental a-) resonance frequency b-) impedance results of a constrained PWAS on an aluminum substrate in thickness of 1mm and in length of 7mm and in width of 5mm

The number of the thickness mode resonance peaks was predicted correctly by the analytical thickness mode impedance model for the constrained PWAS. The resonance frequency values were also predicted in good agreement. Only the fifth thickness mode has nearly 0.5 MHz discrepancy in frequency.

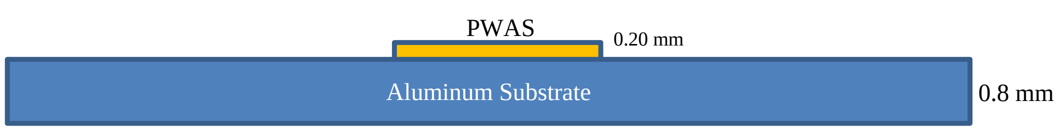


Figure 7.16 Schematic illustration of bonded PWAS on an aluminum substrate

Table 7.4 E/M impedance frequencies in the first four thickness modes as the proof-masses incline from no mass up to 0.15mm PM height

| | Analytical EMIS | | | | |
|---|---|---|---|---|---|
| | PM Height | 0.15 | 0.1 | 0.05 | 0 |
| Resonance F | First res. Freq. | 1.79 | 1.825 | 1.866 | 1.901 |
| | Second res. Freq. | 3.842 | 3.935 | 4.01 | 4.086 |
| | Third res. Freq. | 5.521 | 5.759 | 5.957 | 6.12 |
| | Fourth res. Freq. | 7.224 | 7.456 | 7.683 | 7.887 |
| | | | | | |
| | CF-FEA EMIS | | | | |
| Resonance F | First res. Freq. | 1.801 | 1.83 | 1.865 | 1.9 |
| | Second res. Freq. | 4.072 | 4.113 | 4.154 | 4.194 |
| | Third res. Freq. | 6.28 | 6.46 | 6.565 | 6.64 |
| | Fourth res. Freq. | 7.756 | 8.412 | 8.749 | 8.964 |

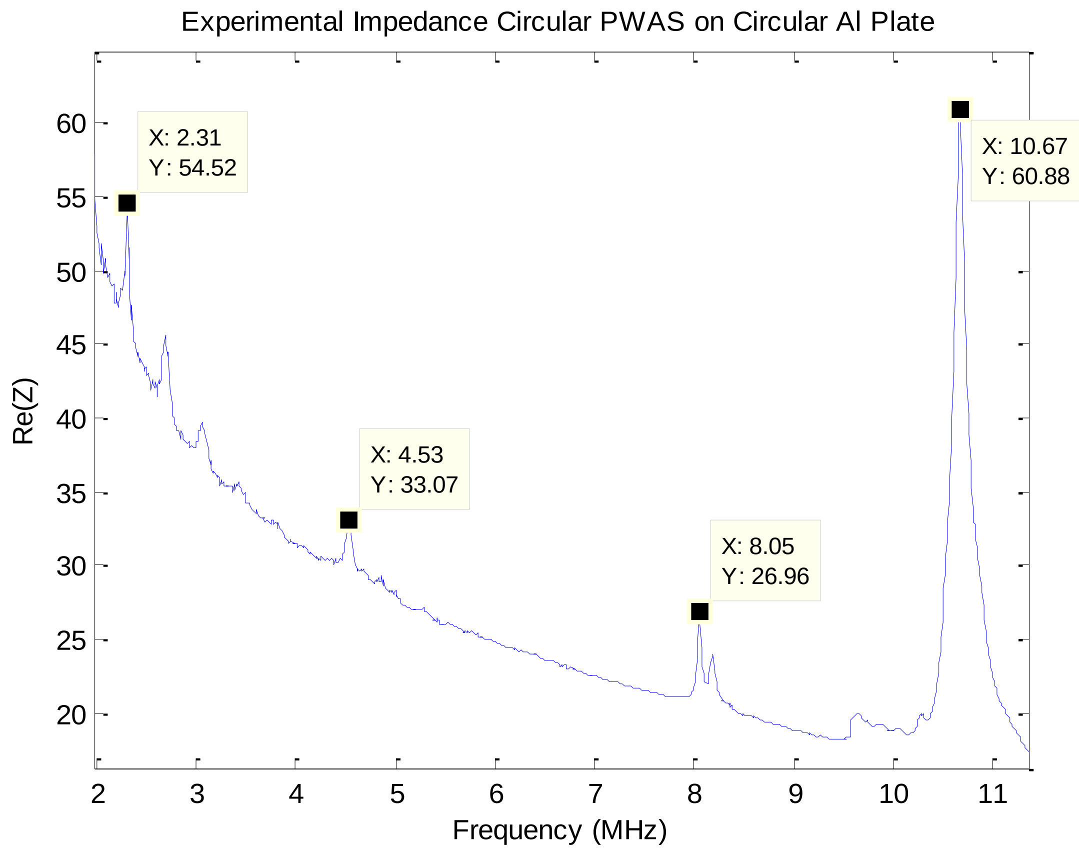


Figure 7.17 EMIS measurement result for a circular PWAS in diameter of 7mm and in thickness of 0.2mm is bonded on a circular aluminum plate in diameter of 100mm and in thickness of 0.8mm

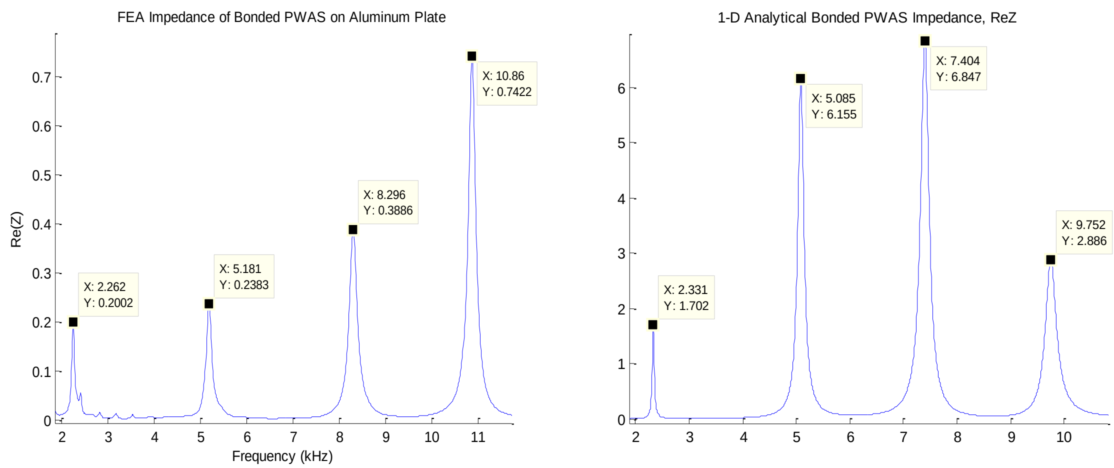


Figure 7.18 EMIS results from a) 2-D CF-FEA b) 1-D analytical models for PWAS perfectly bonded in the center of an aluminum plate with 100mm length and 0.8mm thickness

Spectra from anaytical, numerical simulation and experiment of the constrained-PWAS are obtained for out-of-plane EMIS in high frequency range. Constrained PWAS-EMIS measurement results is seen in Figure 7.17 for 0.2mm thick PWAS on 0.8mm aluminum plate. Globally good matching is observed as compared to verify the analytical constrained PWAS-EMIS model. Also 2-D CF-FEA model is used to validate the corresponding analytical model however some discrepancies between the analytical PWAS-EMIS and CF-FEA PWAS-EMIS are visible for the thickness mode peak as can be seen in Figure 7.18. Small differences at high frequencies are expected between the analytical and the numerical responses due to the simplifying assumptions made in the one-dimensional analytical analysis. The first impedance peak is predicted by using the thickness mode analytical and numerical models and found to be at 2.31 MHz that has good agreement with the predictions. 2-D CF-FEA model results seem to match better in comparison with the 1-D analytical two-bar resonator model results. It is also noticable that in higher thickness modes, the impedance results agree reasonably well in comparing the analytical thickness mode EMIS model of PWAS with the corresponding CF-FEA and experimental results.

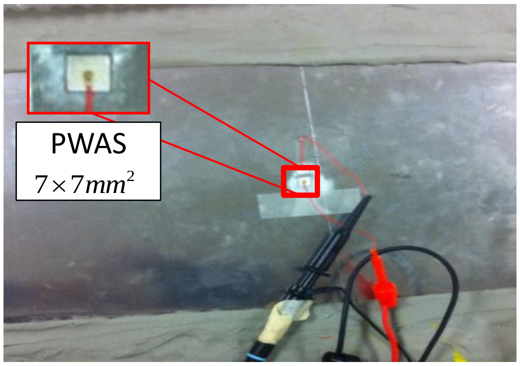


Figure 7.19 Second experimental setup for constrained PWAS-EMIS measurement: large aluminum plate in thickness of 2.1mm and PWAS in 7x7mm$^2$

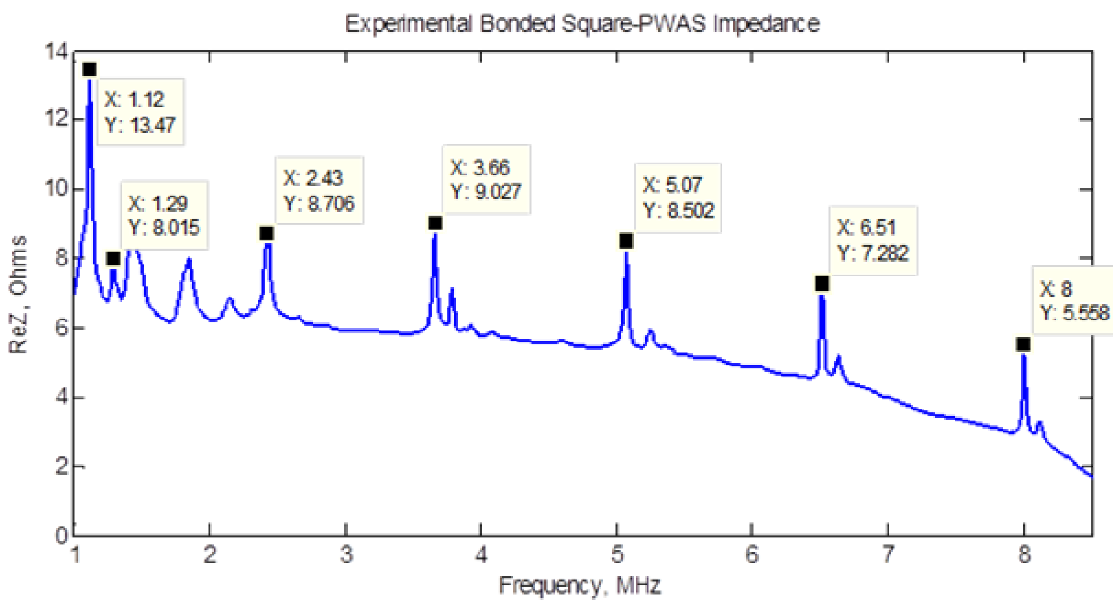


Figure 7.20 Constrained PWAS-EMIS measurement to indicate thickness mode impedance spectra.

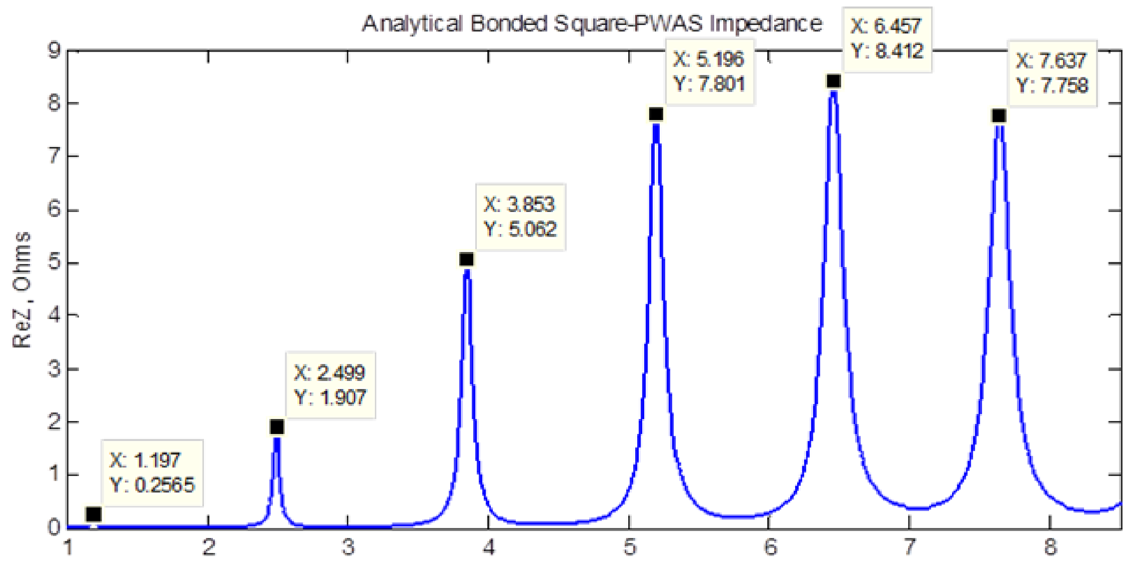


Figure 7.21 1-D analytical constrained PWAS-EMIS prediction to indicate thickness mode impedance spectra.

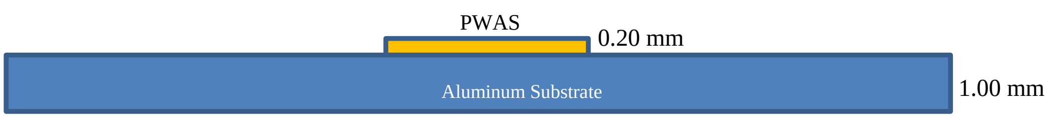


Figure 7.22 Schematic illustration of bonded PWAS on an aluminum substrate

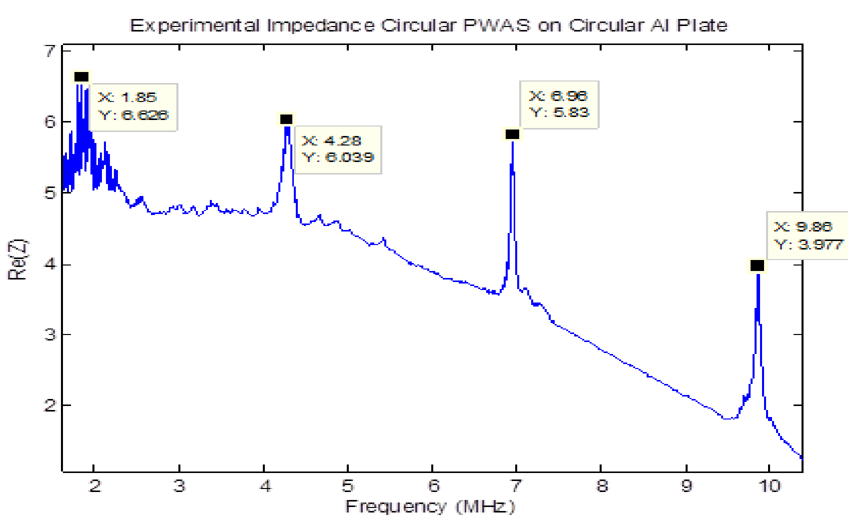


Figure 7.23 EMIS measurement result for a circular PWAS in diameter of 7mm and in thickness of 0.2mm is bonded on a circular aluminum plate in diameter of 100mm and in thickness of 1mm

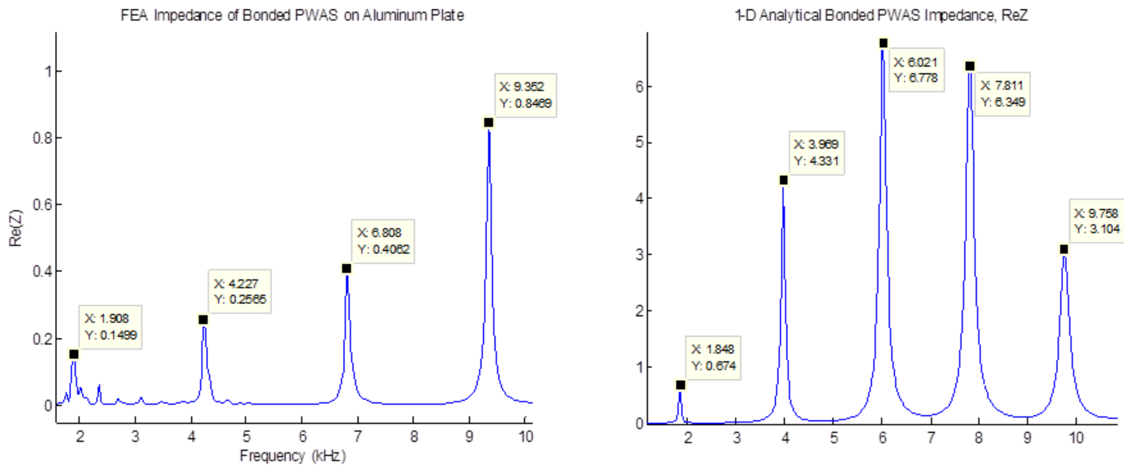


Figure 7.24 EMIS results from a) 2-D CF-FEA b) 1-D analytical models for PWAS perfectly bonded in the center of an aluminum plate with 100mm length and 0.8mm thickness

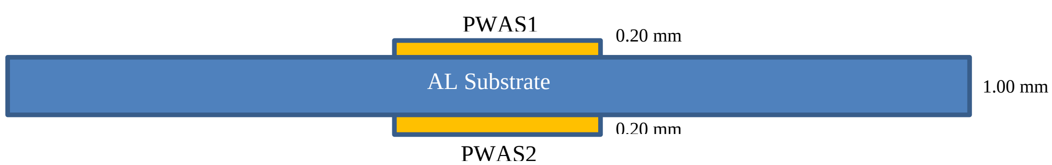


Figure 7.25 Schematic illustration of bonded two PWAS on two surfaces of aluminum substrate

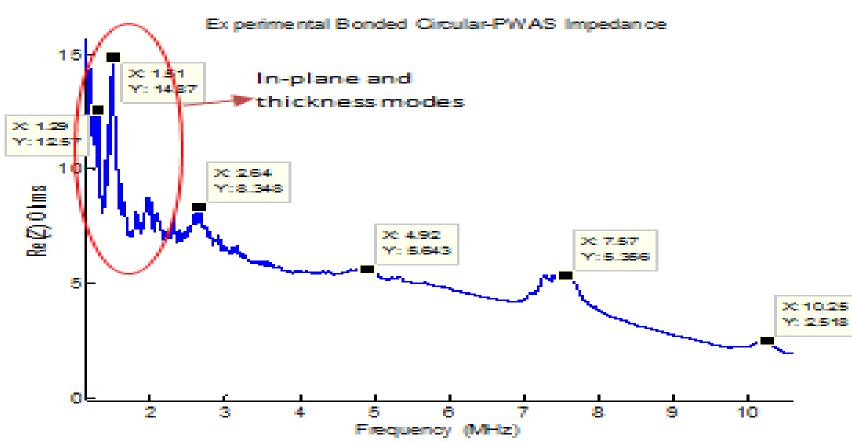


Figure 7.26 EMIS measurement result for a circular PWAS in diameter of 7mm and in thickness of 0.2mm is bonded on a circular aluminum plate in diameter of 100mm and in thickness of 1mm

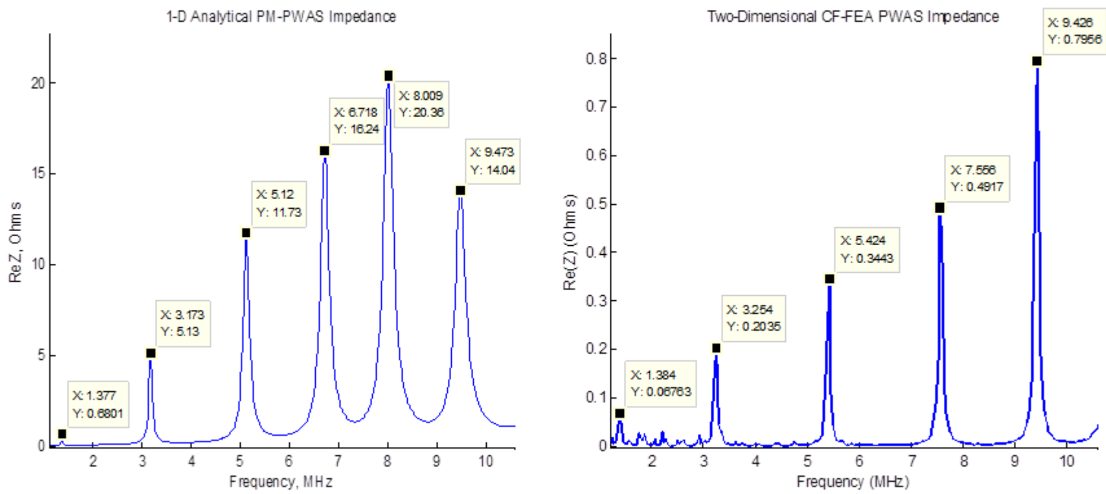


Figure 7.27 EMIS results from a) 2-D CF-FEA b) 1-D analytical models for PWAS perfectly bonded in the center of an aluminum plate with 100mm length and 0.8mm thickness

Spectra from anaytical, numerical simulation and experiment of the constrained-PWAS are obtained for out-of-plane EMIS in high frequency range. Constrained PWAS-EMIS measurement results are seen in Figure 7.23 and Figure 7.26 for 0.2mm thick PWAS on 1mm aluminum plate. Globally good matching is observed as compared to verify the analytical constrained PWAS-EMIS model. Also 2-D CF-FEA model is used to validate the corresponding analytical model however some discrepancies between the analytical PWAS-EMIS and CF-FEA PWAS-EMIS are visible for the thickness mode peak as can be seen in Figure 7.24 and Figure 7.27. Small differences at high frequencies are expected between the analytical and the numerical responses due to the simplifying assumptions made in the one-dimensional analytical analysis. The first impedance peak is predicted by using the thickness mode analytical and numerical models and found to be at 1.37 MHz that has good agreement with the predictions. 2-D CF-FEA model results seem to match better in comparison with the 1-D analytical two-bar resonator model results. It is also noticable that in higher thickness modes, the impedance results agree reasonably well in comparing the analytical thickness mode EMIS model of PWAS with the corresponding CF-FEA and experimental results.

### 7.4.4 SPECIAL CASE STUDIES

EMIS results from washer PM-PWAS on aluminum plate

For this set of experiment, three specimens were measured. The specimens were designed by using circular PWAS resonators in diameter of 25mm and in thickness of 0.2mm, aluminum plates in diameter of 100mm and in thickness of 1mm. Also three washers were used for each specimen.

First geometric sizes and capacitance of the free PWAS resonators were measured. Then EMIS readings of the free PWAS were conducted.

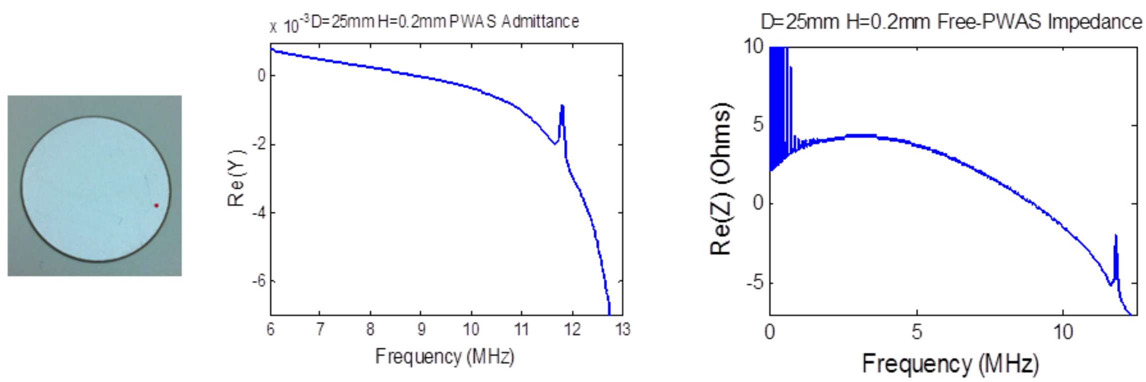


Figure 7.28 Illustration of free circular PWAS in diameter of 25mm and in thickness of 0.2mm and admittance and impedance plots

The thickness mode resonance frequency was the focal interest therefore the impedance readings were converted into admittance by the relation, $Y = 1/Z$ where $Y$ is admittance which represents the resonance frequency spectra and $Z$ is impedance which represents the anti-resonance frequency. To focus on the thickness resonance peak in the admittance spectrum, we adjusted the range of frequency between 6MHz-13 MHz so that the resonance peak appears at around 12 MHz. The anti-resonance frequency in thickness mode of the free PWAS also shows up at around 12 MHz in the impedance spectrum. In-plane mode peaks appear in large number in low frequency range since the lateral size of PWAS (diameter) is much larger than the transversal (thickness) size. Since the resonance of a system occurs harmonically as a harmonic function of the size of the system, the resonance frequency and its overtones repeat periodically depending on the largeness of the size. The resonance modes are classified in names of the sizes, i.e. longitudinal mode, width mode, thickness mode. The smaller the size of the structure is the larger frequency the resonance peak and its overtones in that mode show up at.

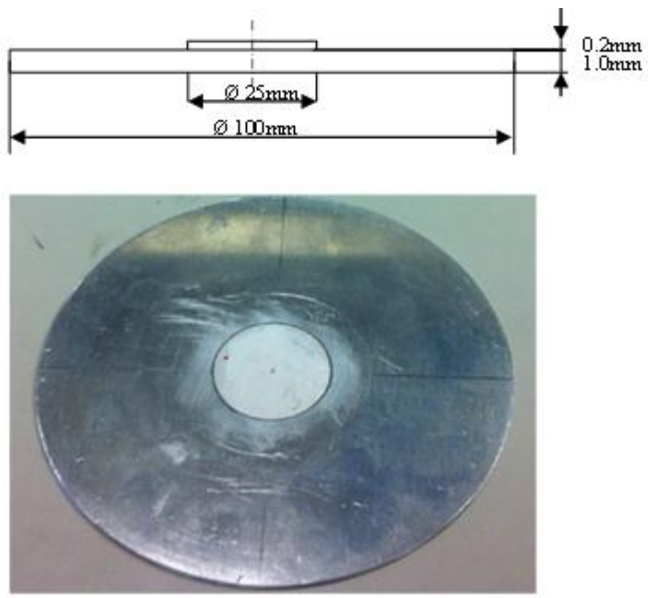


Figure 7.29 Illustration of the schema and picture of
the bonded PWAS on an aluminum plate

In the second step of the experiment, the PWAS resonators were installed in the center of the circular aluminum plate as seen in Figure 7.29 by adhesive bond. The EMIS measurement was taken and also converted to the admittance result and both were plotted as seen in Figure 7.30.

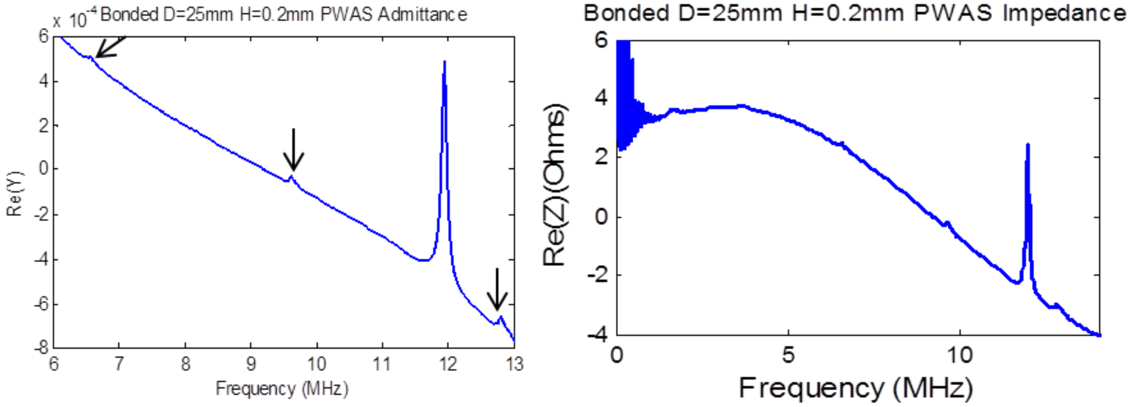


Figure 7.30 Illustration of admittance and impedance results of the bonded PWAS in 25mm diameter on Al plate in 100 mm diameter

In admittance plot, the additional resonance peaks which are resulted from the substrate structure can be noticed at around 6.5MHz, 9.5MHz, and 12.5 MHz. The main thickness mode resonance peak that is resulted from PWAS is still seen little below 12 MHz. The longitudinal mode anti-resonance peaks in the impedance plot of the bonded PWAS look more intense in comparison with the free PWAS longitudinal impedance results because of the additional peaks come from the substrate plate.

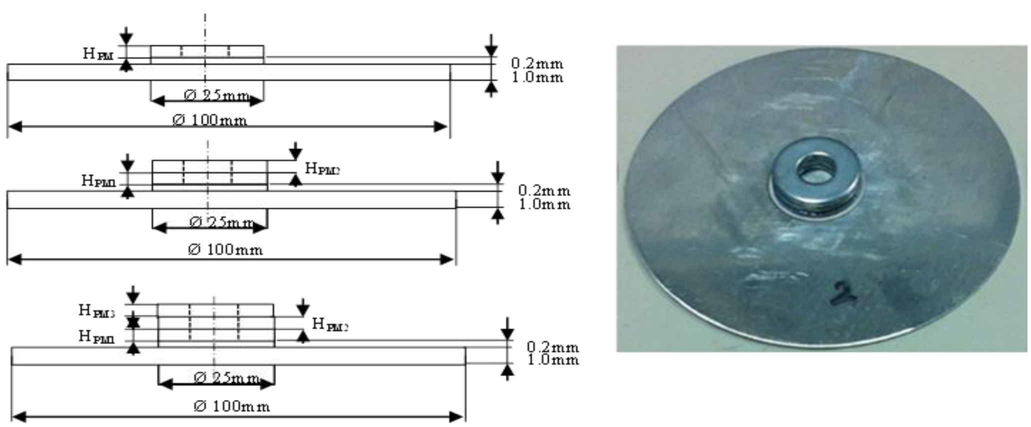


Figure 7.31 Illustration of schema and picture of the washer proof-mass PWAS

In the third step of the experiment set, the washers were installed on the PWAS-aluminum plate system one by one. The first washer was installed on bonded PWAS, the second washer was bonded onto the 1st washer, and eventually the 3rd washer was bonded onto the 2nd washer Figure 7.31. The sizes of the three washers installed on the first specimen are presented in Table 7.5.

Table 7.5 Geometrical sizes of the washers bonded on the first specimen

| PM-PWAS | Thickness mm | Outer diameter mm | Inner diameter mm |
|---|---|---|---|
| Washer 1 | 1.85 | 22.36 | 9.51 |
| Washer 2 | 2 | 22.27 | 9.63 |
| Washer 3 | 2.52 | 22.32 | 9.54 |

The EMIS of the specimen with 1 washer, 2 washers, and 3 washers were measured by the impedance analyzer instrument. For the impedance readings, the probe was touched on the PWAS surface through the hole of the washers installed on the PWAS. The impedance and admittance results were plotted after installation of each washer. The impedance and admittance plots shown in Figure 7.32 are for PM-PWAS with three washers.

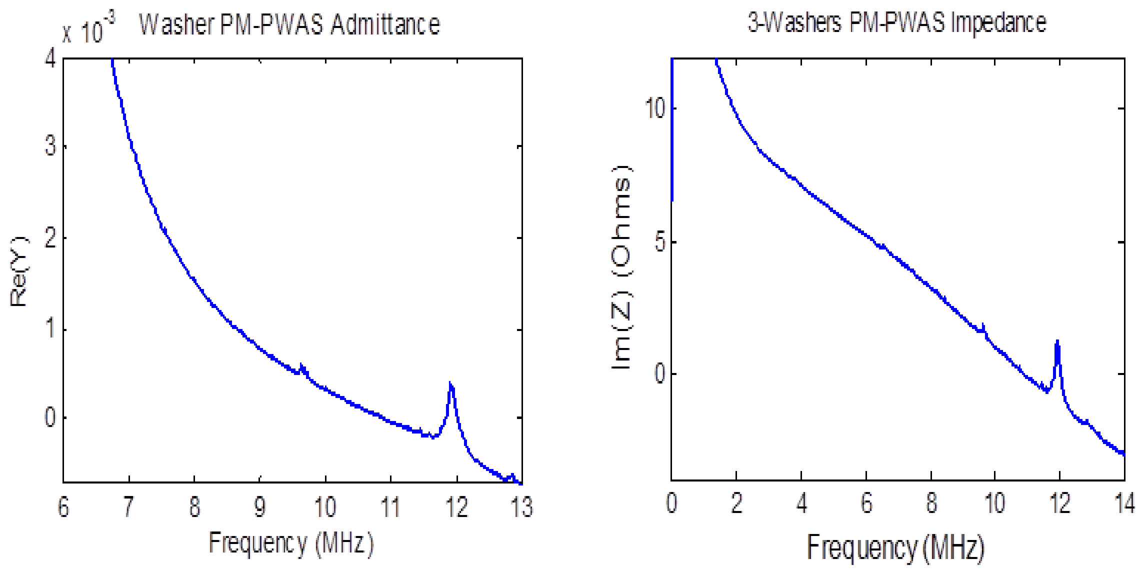


Figure 7.32 Admittance and impedance results for the PM-PWAS with three washers

As can be noticed, the results do not have much difference than the PWAS bonded on aluminum plate without any washers (Figure 7.30). The addition of the proof-masses might not have reflected due to the two reasons: improper acquisition of the data or improper installation of the washers. The first reason may be the probe should have been touched on the top washer, not on the PWAS, which do not reflect the change in the total structure. EMIS measurement can reflect only the local dynamic structural changes. The second reason may be the adhesive bonding thickness should have been thinner. The adhesive layer thickness might have been higher than necessary because of the surface roughness of the steel washer. The surface of the washer surface should have been finer for the adhesive to be thinner for the standing waves to go through the adhesive layer and sense the near field structural change.

The admittance results are shown for the three specimens Figure 7.33. Each corresponding plot has at least three color coded curves with respect to the 1 washer, 2 washers, and 3 washers installed. PM-PWAS1 curve shows PWAS with 1 washer, PM-

PWAS2 shows PWAS with 2 washers, PM-PWAS3 shows PWAS with 3 washers, additionally Bonded PWAS curve shows thickness mode admittance peak at around 12 MHz for the PWAS bonded aluminum that does not have any proof-mass (washer) installed.

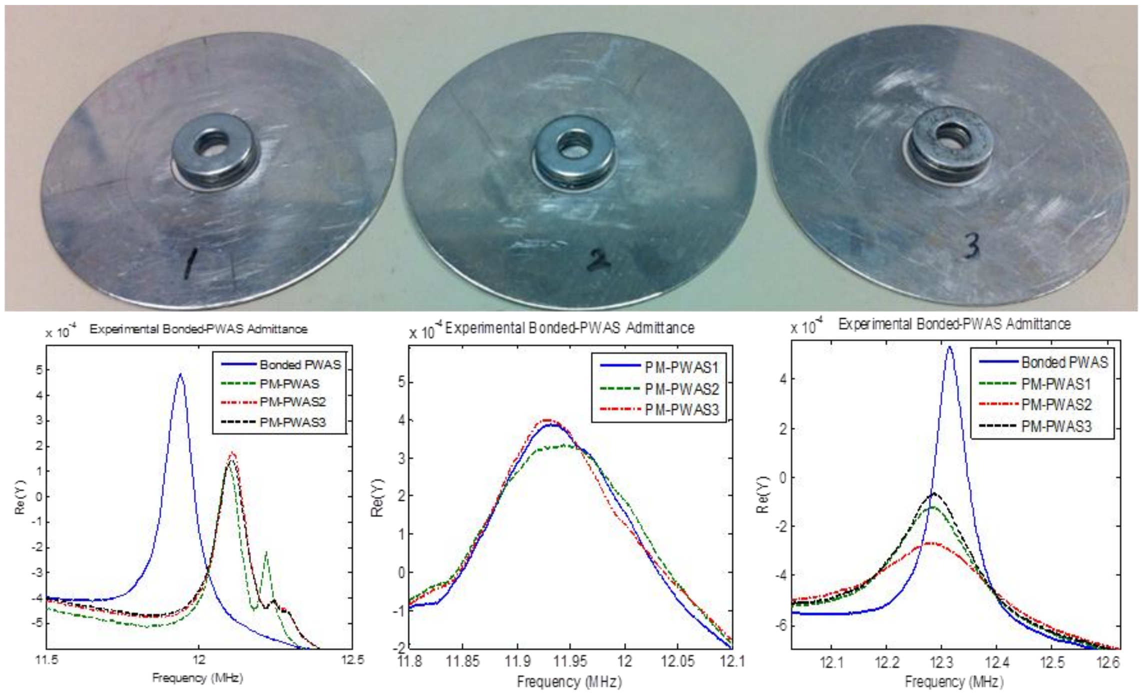


Figure 7.33 Experimental admittance peak illustration PM PWAS with no washer, one, two, and three washers installed

Steel PM-PWAS installed on steel substrate

Twenty free circular PWAS in thickness of $2.00 + 0.03mm$ in diameter of $7.00mm$ were chosen for this set of experiment. Static capacitance of each PWAS was also measured and the capacitances vary between 2.81-3.06 pF.

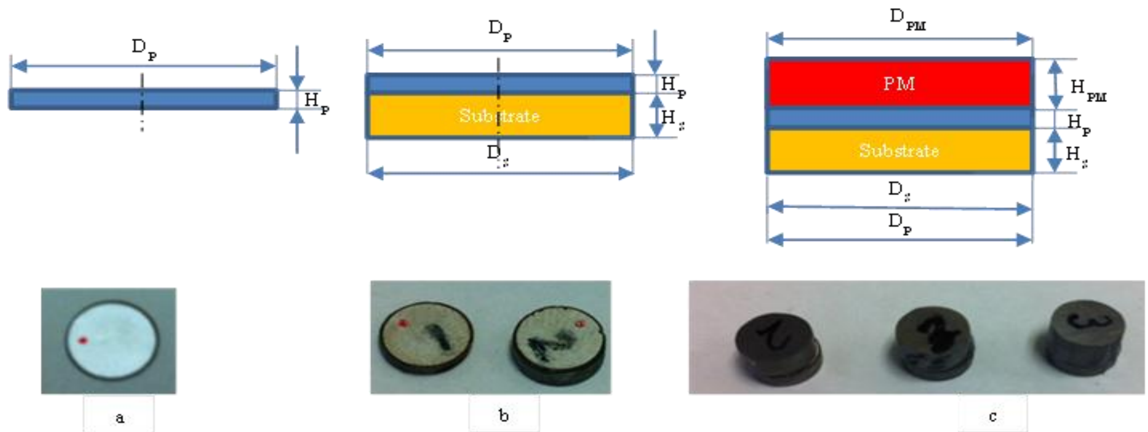


Figure 7.34 Illustration of schema and pictures of a-) free PWAS b-) constrained PWAS on steel substrate c-) steel proof-mass PWAS constrained on steel disc

In this set of experiment, instead of bonding more than one proof-mass on a PWAS to obtain PM-PWAS with different height, we fabricated steel discs in different height with a certain step size to use them as proof-masses so that we could have seen effects of the change in the size of the proof-mass in resonance frequencies. Steel discs were manufactured in diameter of 7mm and in thicknesses between 1mm and 4mm with a step size of 0.5mm to use as proof-masses on PWAS. Also steel discs in diameter of 7mm in thickness of 2mm were manufactured to utilize as substrate structure. The free circular PWAS EMIS was measured as well as PM-PWAS EMIS with proof-masses in different height. The admittance results for free PWAS and the comparison of admittance of PM-PWAS in different height can be seen in

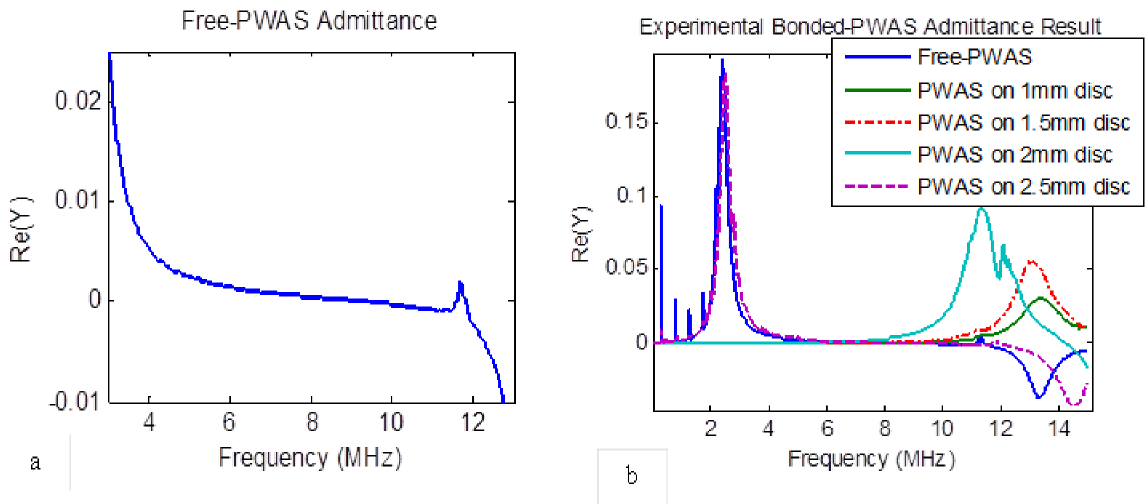


Figure 7.35 Experimental admittance results for a-) free PWAS b-) constrained PWAS on steel discs with different height

Figure 7.35 as well as impedance results in Figure 7.36. The results are all not consistent as seen in impedance and admittance plots. The only graphical result that looks reasonable from 2.5mm PM-PWAS was focused. The purple cut-line shows the thickness mode overtones from the proof-mass in the impedance plot as well as the right shift of the main thickness mode impedance peak that is from the PWAS with respect to the free PWAS thickness mode impedance peak.

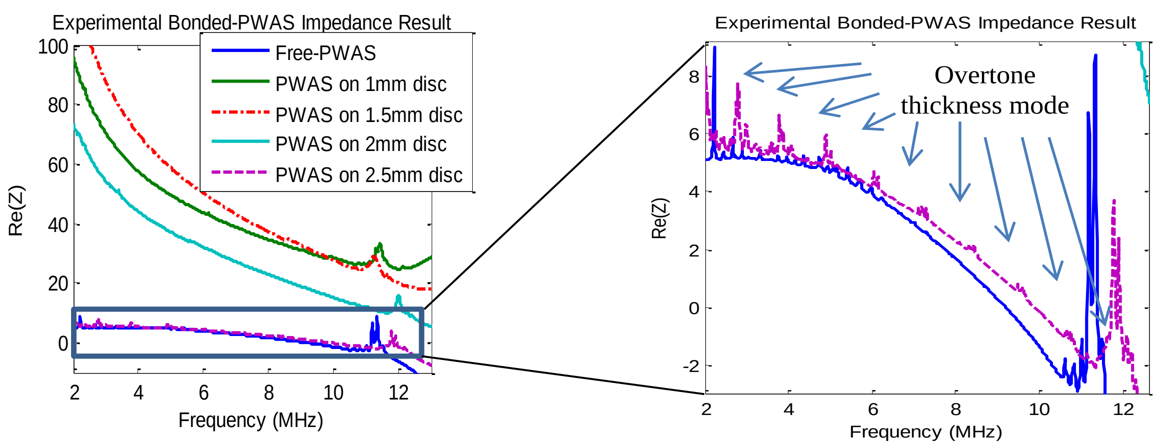


Figure 7.36 Experimental impedance results for constrained PWAS on steel discs with different height

The PM-PWAS with proof-mass in thickness of 3mm, 3.5mm, 4mm were installed on steel discs in thickness of 2mm and in diameter of 7mm. The capacitance and EMIS of each PM-PWAS-steel substrate system were measured and EMIS results were compared in one plot as seen in Figure 7.37.

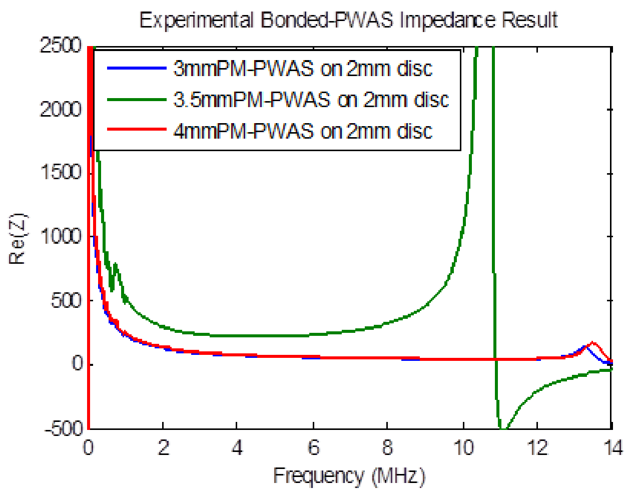


Figure 7.37 Experimental impedance results for constrained PM-PWAS

On the PM-PWAS impedance results, one can see that the impedance curves do not seem to follow a consistent trend. The impedance curves for 3mm PM-PWAS and 4mm PM-PWAS only capture the thickness mode impedance peak at around 13MHz and show the shift of the main peak to the right as the proof-mass height increases from 3mm to 4mm.

## Steel PM-PWAS on aluminum plate

In the experiment with the steel substrate, the results were not convenient due to the steel surface roughness, therefore as a substrate structure using aluminum plate that has finer surface finish seemed to change the results to better. The PWAS size and proof-mass size and material were kept the same and the previous measurements were repeated with only substrates changed in the specimens.

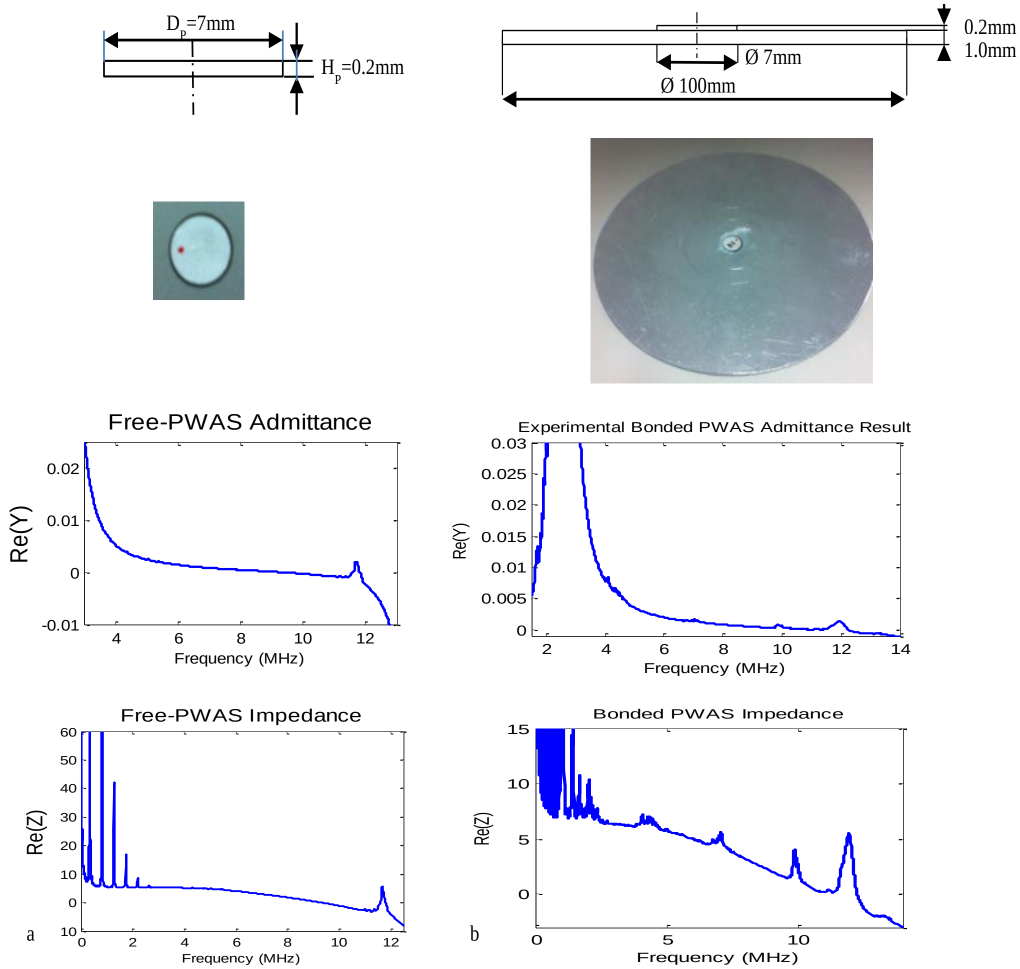


Figure 7.38 Experimental admittance and impedance results for a-) free PWAS and b-) constrained PWAS on an aluminum plate in thickness of 1mm and diameter of 100mm

The corresponding results for free PWAS was basically the same; the EMIS of PWAS bonded on aluminum plate was measured. The results for free and bonded PWAS in terms of admittance and impedance are shown in Figure 7.38.

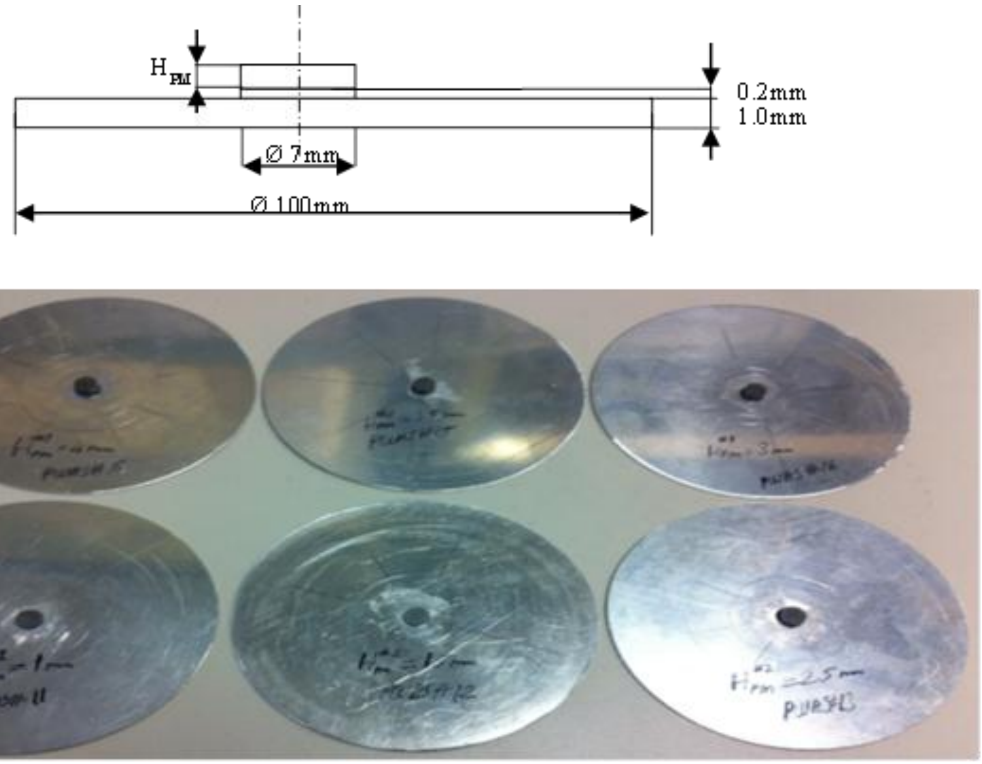


Figure 7.39 Illustration of schema and pictures of PM-PWAS resonators with different height which are constrained on aluminum plate

We could consistently obtain the EMIS readings from PWAS bonded on Al plate for 6 specimens. However, after we installed the steel proof-masses in different height to each PWAS and measured capacitance and impedance, we could only obtain consistent and meaningful results from two of the specimens which have proof masses in height of 1mm and 3mm.

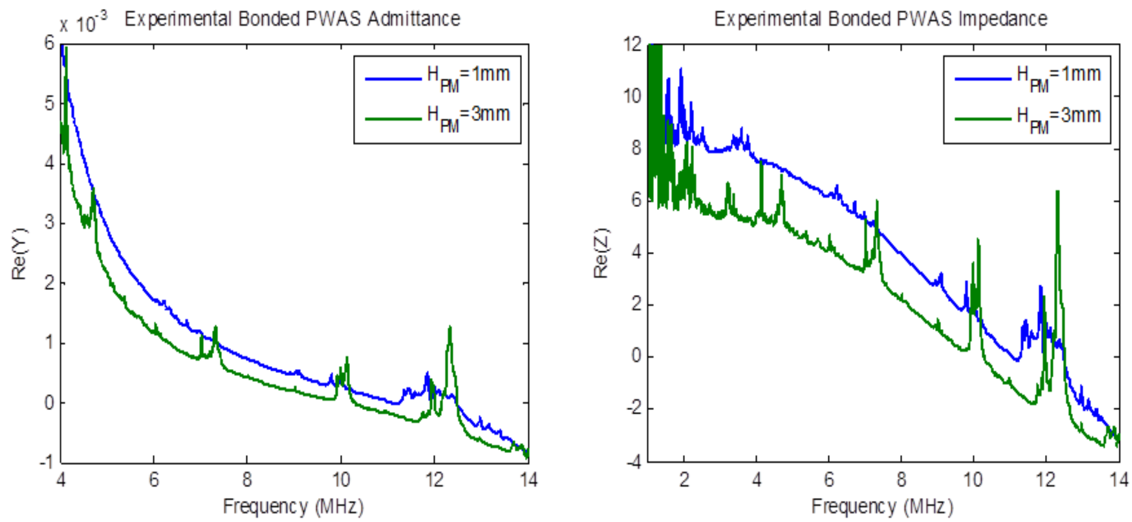


Figure 7.40 Experimental admittance and impedance results for PM-PWAS with different PM height.

Aluminum PM-PWAS on aluminum plate

To have closer geometrically to the analytical multilayer thickness mode impedance model, in this experiment, square PWAS was chosen as well as rectangular proof-mass. The static electric and dynamic electro-mechanical properties of the free PWAS such as capacitance and E/M impedance were measured. The geometry, sizes and the admittance and impedance results of the free square PWAS.

The aluminum plate-like substrate was only circular and different than the size and the geometry of the substrate geometry in the analytical model however, the substrate geometry difference did not cause much change as compared with the admittance and impedance results of the latter experiment with aluminum 5x7 rectangular substrate. The measurements for impedance and admittance of the square PWAS bonded on aluminum plate were taken for four specimens. The admittance and impedance of one of the specimen are shown in Figure 7.41. The similar phenomenon of additional overtone admittance and impedance peaks from the host structure also seems in the bonded PWAS results beside the main peak that is from PWAS itself.

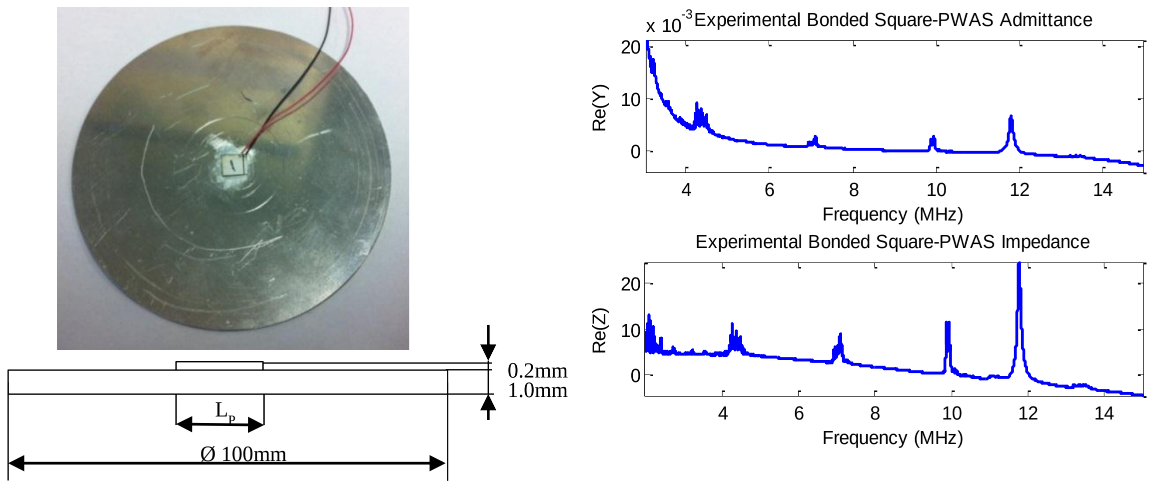


Figure 7.41 Illustration of the schema and picture of a constrained square PWAS and admittance/impedance results for the constrained PWAS

The constrained PWAS impedance results are used to validate the analytical model for the constrained PWAS on an aluminum host structure as can be seen in Figure 7.42. The experimental overtone impedance peaks can be almost captured by the analytical impedance results at close frequencies. The only issue in the results from the analytical model seems to be the main impedance peak that comes from the PWAS itself. The impedance peak that shows up at around 12MHz is always the highest amplitude peak eventhough this behavior of the 12MHz peak cannot be captured by the analytical model impedance result.

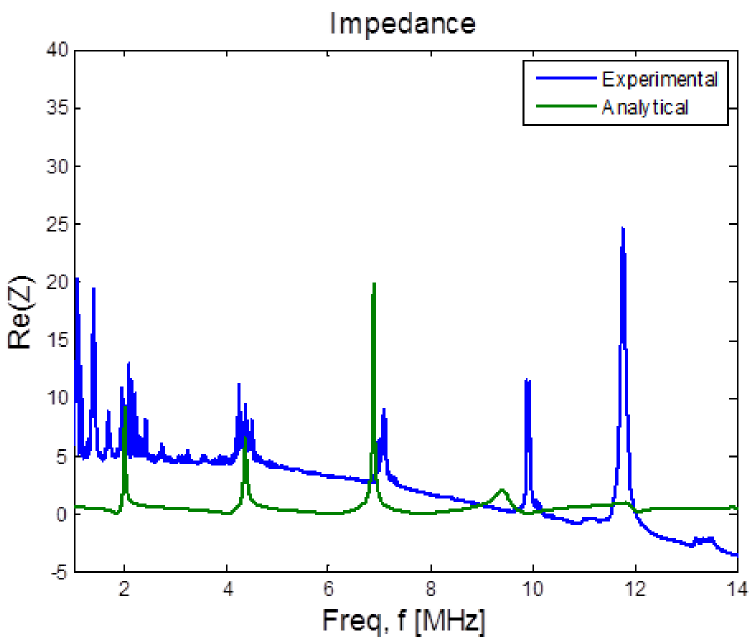


Figure 7.42 Comparison between the analytical model and the experimental results for impedance of constrained PWAS

In this part of the section, a comparison of experimental admittance and impedance results for PM-PWAS resonators -which have proof masses in height of 1mm and 2mm respectively- is presented. The experimental resonance frequencies of PM-PWAS systems are extracted from the admittance results and tabulated in comparison with the corresponding analytical resonance frequencies.

As can be noticed in Figure 7.43 as well as in Table 7.6 and in Table 7.7, increase in the number of the resonance (admittance) and anti-resonance (impedance) peaks and shifts of the resonance frequencies occur toward lower frequencies as the PM-PWAS height increases.

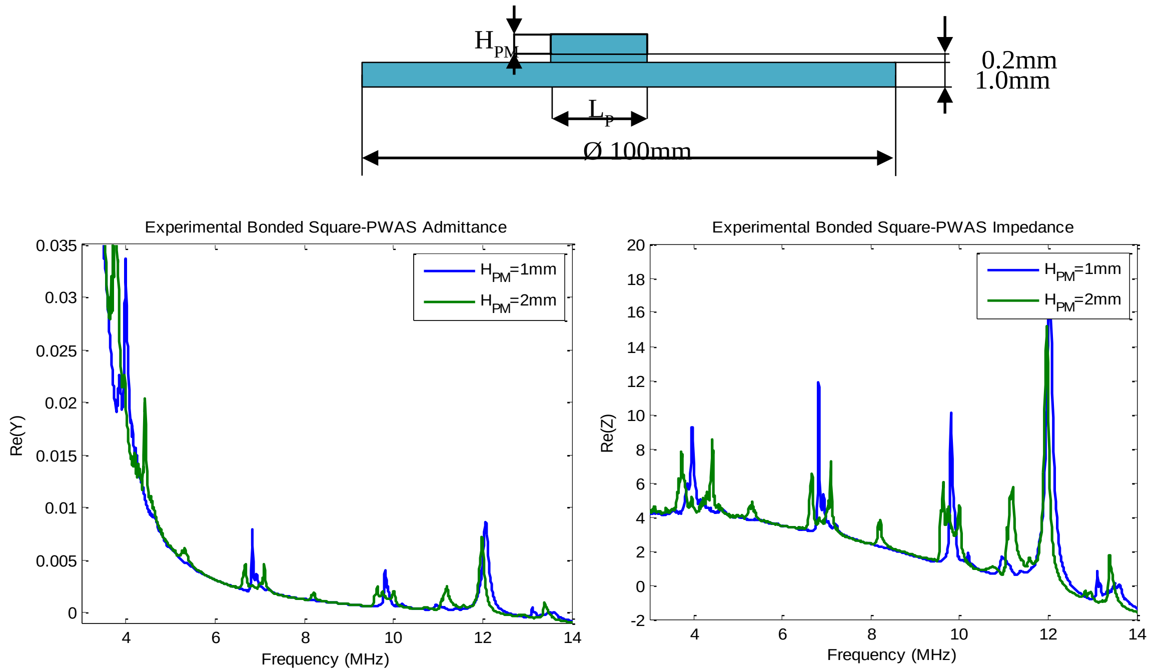


Figure 7.43 Schematic illustration of PM-PWAS constrained on an aluminum plate and experimental admittance and impedance results for PM-PWAS different steel proof-mass height

In the same range of the frequency, PM-PWAS whose proof mass height is 1mm has 10 resonance frequencies in thickness mode whereas that with 2mm proof-mass height has 15 resonance frequencies. The experimental thickness mode resonance frequencies in relatively low frequency range could not be extracted due to the conflict with the in-plane resonance frequencies. Also at some thickness mode resonance frequencies, the experimental admittance peaks do not show up due to the mode shape.

Table 7.6 Anayltical and experimental resonance frequencies of steel PM-PWAS constrained on an aluminum plate with the proof-mass in height of 1mm

Proof-Mass Height = 1mm

| Mode # | Analytical Res. Fr. MHz | Exp. Res. Fr. MHz | Mode # | Analytical Res. Fr. MHz | Exp. Res. Fr. MHz |
|---|---|---|---|---|---|
| 1 | 1.442 | | 6 | 7.938 | |
| 2 | 2.341 | | 7 | 8.933 | 9.8 |
| 3 | 4.225 | 3.95 | 8 | 10.767 | 10.95 |
| 4 | 5.061 | | 9 | 11.572 | 12.05 |
| 5 | 6.66 | 6.8 | 10 | 13.3 | 13.1 |

Table 7.7 Anayltical and experimental resonance frequencies of steel PM-PWAS constrained on an aluminum plate with the proof-mass in height of 2mm

Proof-Mass Height = 2mm

| Mode # | Analytical Res. Fr. MHz | Exp. Res. Fr. MHz | Mode # | Analytical Res. Fr. MHz | Exp. Res. Fr. MHz |
|---|---|---|---|---|---|
| 1 | 0.921 | | 9 | 8.165 | 8.2 |
| 2 | 1.828 | 1.8 | 10 | 8.856 | |
| 3 | 2.523 | | 11 | 9.932 | 10 |
| 4 | 3.721 | 3.7 | 12 | 10.977 | 11.2 |
| 5 | 4.577 | 4.4 | 13 | 11.564 | 11.9 |
| 6 | 5.316 | 5.3 | 14 | 12.703 | 12.8 |
| 7 | 6.396 | 6.7 | 15 | 13.6 | 13.4 |
| 8 | 7.216 | 7.1 | 16 | | |

The analytical electro-mechanical impedance model is validated by comparing with the experimental EMIS results. The comparison in terms of the real part of impedance of the PM-PWAS system with 1mm PM height can be seen in Figure 7.44. Eventhough the discrepancy between the analytical impedance peaks and experimental impedance peaks occurs and increases at high frequency range, the analytical results can reflect the structural local dynamic behavior well.

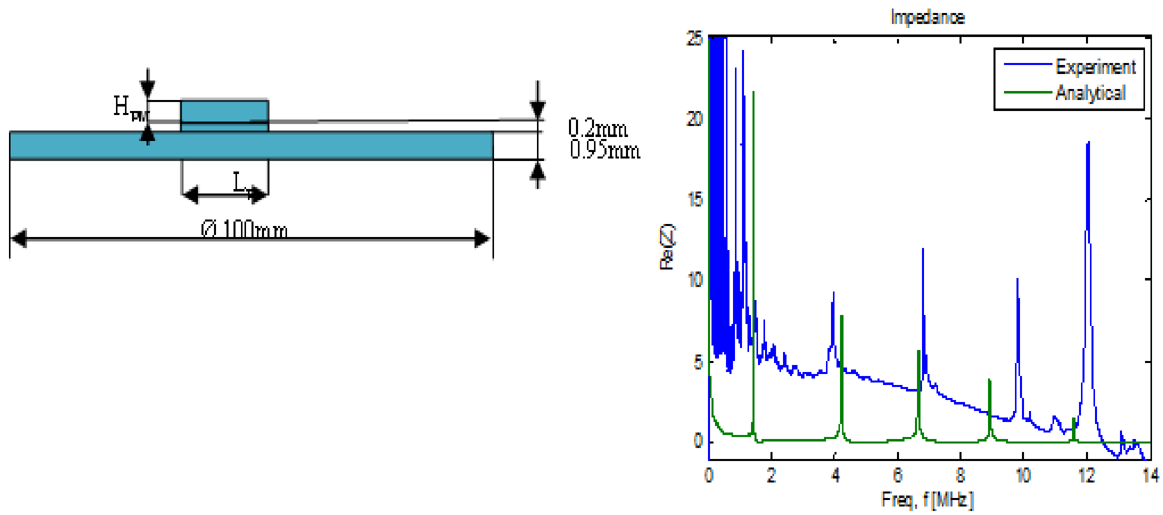


Figure 7.44 Illustration of the experimental setup and the impedance results for the geometric parameters; $H_{sub} = 0.95mm, H_{PWAS} = 0.2mm, H_{PM} = 0.95mm$ and for the material properties $E_{AL} = 60GPa,\ \rho_{AL} = 1800kg/m^3$

The comparisons between analytical and experimental results were held with other PM-PWAS resonators with different PM height such as 2mm, 2.5mm, 3mm as they can be seen respectively in tabular and graphical forms in Figure 7.45.

**Proof-Mass Height = 2mm**

| Mode # | Analytical Res. Fr. MHz | Exp. Res. Fr. MHz | Mode # | Analytical Res. Fr. MHz | Exp. Res. Fr. MHz |
|---|---|---|---|---|---|
| 1 | 0.921 | | 9 | 8.165 | 8.2 |
| 2 | 1.828 | 1.8 | 10 | 8.856 | |
| 3 | 2.523 | | 11 | 9.932 | 10 |
| 4 | 3.721 | 3.7 | 12 | 10.977 | 11.2 |
| 5 | 4.577 | 4.4 | 13 | 11.564 | 11.9 |
| 6 | 5.316 | 5.3 | 14 | 12.703 | 12.8 |
| 7 | 6.396 | 6.7 | 15 | 13.6 | 13.4 |
| 8 | 7.216 | 7.1 | 16 | | |

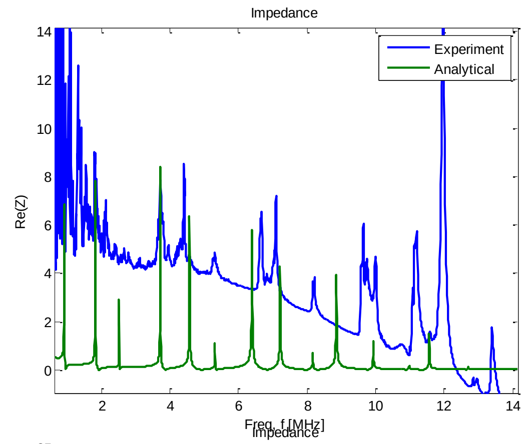


**Proof-Mass Height = 2.5mm**

| Mode # | Analytical Res. Fr. MHz | Exp. Res. Fr. MHz | Mode # | Analytical Res. Fr. MHz | Exp. Res. Fr. MHz |
|---|---|---|---|---|---|
| 1 | 0.775 | | 10 | 7.81 | 7.46 |
| 2 | 1.627 | | 11 | 8.469 | 8.45 |
| 3 | 2.174 | 2.4 | 12 | 9.179 | 9.5 |
| 4 | 3.054 | 3.5 | 13 | 10.177 | 9.85 |
| 5 | 4.041 | 4.15 | 14 | 10.961 | 10.55 |
| 6 | 4.642 | 4.65 | 15 | 11.519 | 11.6 |
| 7 | 5.372 | 5.43 | 16 | 12.448 | 12.2 |
| 8 | 6.257 | 6.45 | 17 | 13.237 | 13.2 |
| 9 | 6.974 | 6.85 | 18 | 13.971 | 13.68 |

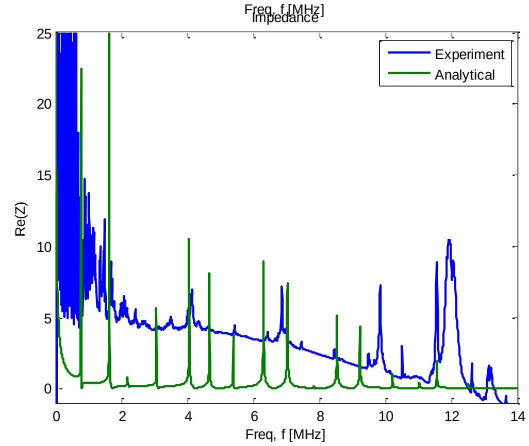


**Proof-Mass Height = 3mm**

| Mode # | Analytical Res. Fr. MHz | Exp. Res. Fr. MHz | Mode # | Analytical Res. Fr. MHz | Exp. Res. Fr. MHz |
|---|---|---|---|---|---|
| 1 | 0.67 | | 11 | 7.54 | 7.15 |
| 2 | 1.44 | | 12 | 8.23 | 8.05 |
| 3 | 1.98 | | 13 | 8.75 | 9.3 |
| 4 | 2.61 | | 14 | 9.52 | 10 |
| 5 | 3.46 | 3.1 | 15 | 10.37 | 10.6 |
| 6 | 4.25 | 4.2 | 16 | 11 | |
| 7 | 4.73 | | 17 | 11.52 | 11.85 |
| 8 | 5.43 | 5.5 | 18 | 12.32 | 12.35 |
| 9 | 6.2 | | 19 | 13.05 | |
| 10 | 6.84 | 6.74 | 20 | 13.68 | 13.7 |

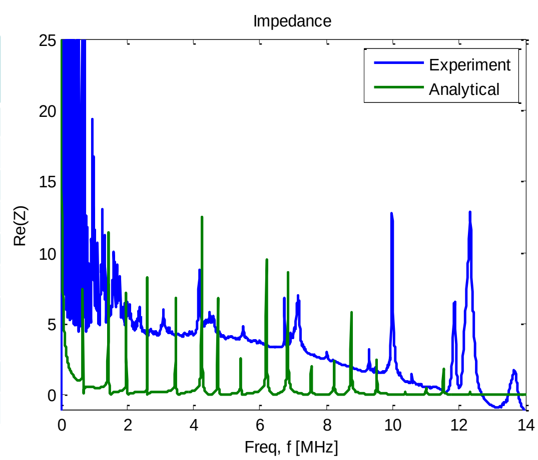


a

Figure 7.45 a-) Comparison between experimental and analytical resonance frequencies and b-) impedance results

Aluminum PM-PWAS on AL substrate

The similar experimental protocol was followed as the previous sets of experiments with different geometry and size of PWAS, proof-masses and substrates. First the EMIS measurements were taken from the free PWAS; then the PWAS resonators were attached on $7 \times 5 \times 1\ \mathrm{mm}^3$ aluminum substrate and the EMIS measurements were taken for the bonded PWAS. Eventually, $7 \times 5 \times H_{PM}\ \mathrm{mm}^3$ aluminum proof-masses were attached on each specimen of bonded PWAS with varying thickness, $H_{PM}$, from 1.0 mm to 3.00 mm by 0.5 mm step size. Impedance and admittance results were analyzed by graphical illustration and comparison with the corresponding analytical results from the two-bar and three-bar resonator models as seen in Figure 7.46.

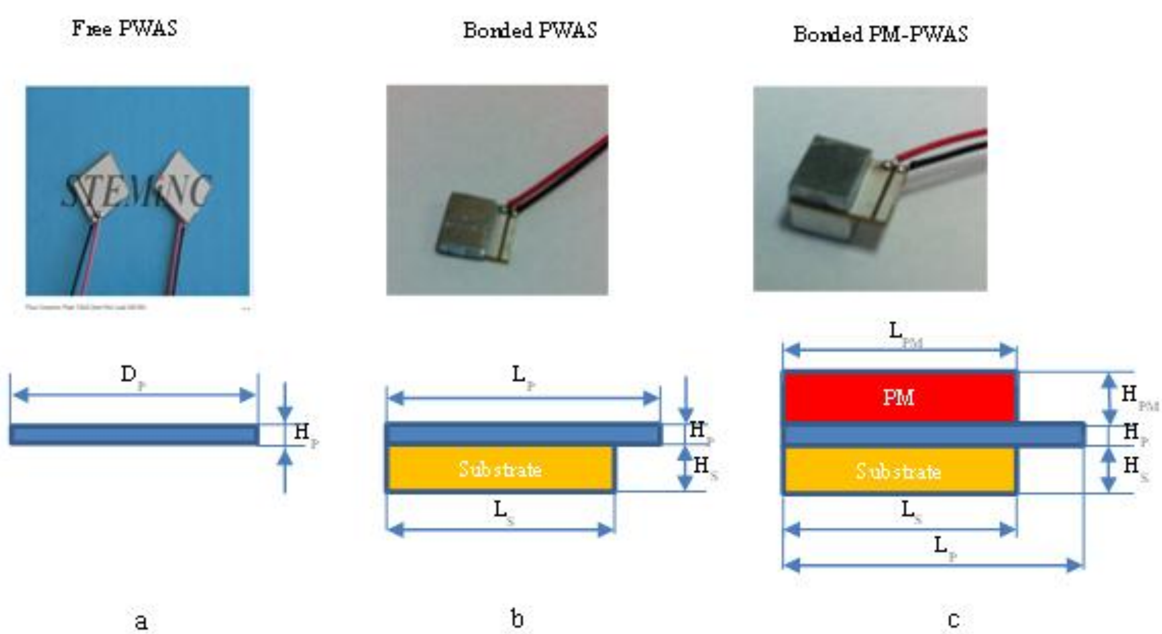


Figure 7.46 Illustration of a-) free PWAS, b-) one-side constrained PWAS c-)two-side constrained PWAS by proof-mass and substrate materials

Eventually, $7 \times 5 \times H_{PM}$ $mm^3$ aluminum proof-masses were attached on each specimen of bonded PWAS with varying thickness, $H_{PM}$, from 1.0 mm to 3.00 mm by 0.5 mm step size. Impedance and admittance results of one specimen which has 1.5mm thick proof-mass was analyzed by tabular and graphical illustration and comparison with the corresponding analytical results from the three-bar resonator model as seen in Table 7.8 and Figure 7.47 respectively.

Table 7.8 Comparison between analytical and experimental resonance frequencies for aluminum square PM-PWAS with proof-mass height of 1.5mm

| | Mode # | Analytical Res. Fr. MHz | Exp. Res. Fr. MHz | Mode # | Analytical Res. Fr. MHz | Exp. Res. Fr. MHz |
|---|---|---|---|---|---|---|
| Proof-Mass Height = 1.5 mm | 1 | 1.07 | | 8 | 8.02 | |
| | 2 | 1.9 | | 9 | 9.07 | 9.07 |
| | 3 | 3.02 | 3.2 | 10 | 10.23 | 10.95 |
| | 4 | 4.18 | 4.3 | 11 | 10.97 | 10.4 |
| | 5 | 4.95 | 5.1 | 12 | 12.34 | 12.1 |
| | 6 | 6.19 | | 13 | 13.1 | 13.6 |
| | 7 | 7.1 | 6.85 | 14 | 14.16 | |

The first two thickness mode impedance peaks could not be distinguished among the in-plane modes.

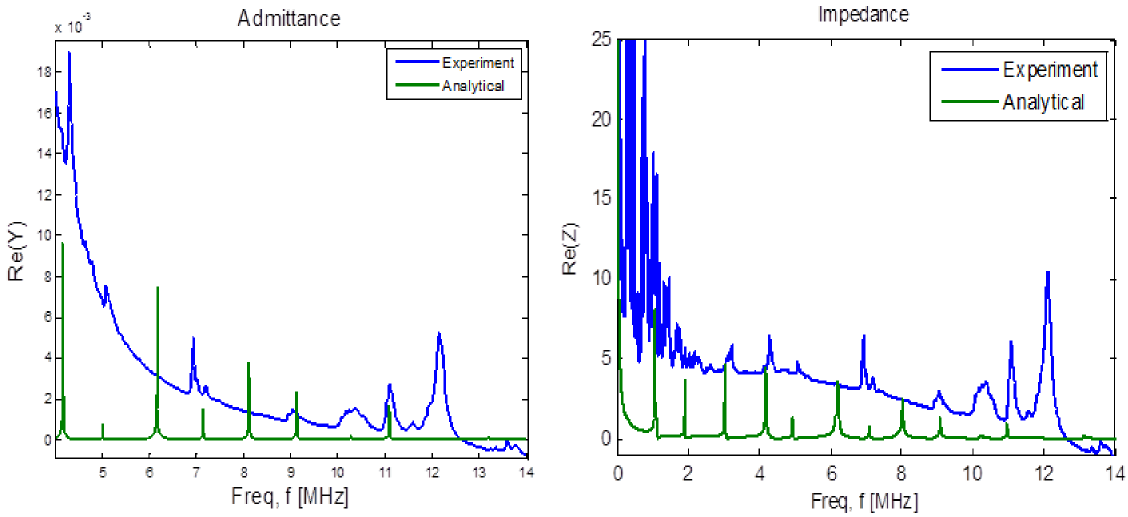


Figure 7.47 Comparison between analytical and experimental admittance and impedance results for aluminum square PM-PWAS with proof-mass height of 1.5mm

Additionally, the analytical models with proof-mass height of 2mm, 2.5mm, and 3mm were also validated by comparison with the corresponding experimental anti-resonance results graphically and the resonance frequency results numerically in tables, which can be seen in Figure 7.48.

**Proof-Mass Height = 2 mm**

| Mode # | Analytical Res. Fr. MHz | Exp. Res. Fr. MHz | Mode # | Analytical Res. Fr. MHz | Exp. Res. Fr. MHz |
|---|---|---|---|---|---|
| 1 | 0.9 | | 9 | 8.06 | 8.22 |
| 2 | 1.8 | | 10 | 8.77 | |
| 3 | 2.51 | | 11 | 9.9 | 9.7 |
| 4 | 3.7 | 3.6 | 12 | 10.8 | 10.85 |
| 5 | 4.49 | | 13 | 11.5 | 11.2 |
| 6 | 5.28 | 5.32 | 14 | 12.6 | 12.1 |
| 7 | 6.35 | 6.55 | 15 | 13.4 | 13.15 |
| 8 | 7.15 | | 16 | | |

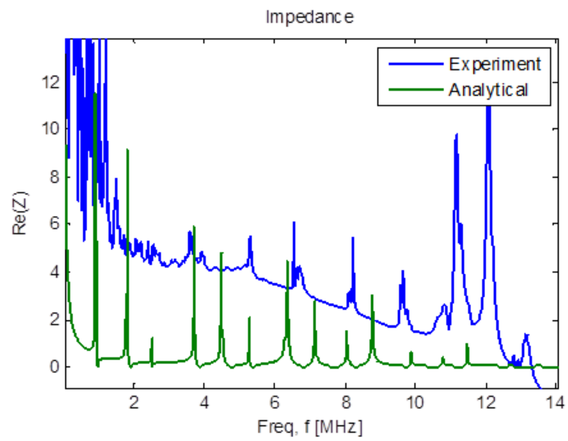


**Proof-Mass Height = 2.5mm**

| Mode # | Analytical Res. Fr. MHz | Exp. Res. Fr. MHz | Mode # | Analytical Res. Fr. MHz | Exp. Res. Fr. MHz |
|---|---|---|---|---|---|
| 1 | 0.756 | | 10 | 7.6 | 7.46 |
| 2 | 1.577 | | 11 | 8.2 | 8.05 |
| 3 | 2.113 | 2.4 | 12 | 8.97 | 9.3 |
| 4 | 2.98 | 3.5 | 13 | 9.94 | 9.85 |
| 5 | 3.94 | 4.15 | 14 | 10.58 | 10.55 |
| 6 | 4.48 | 4.65 | 15 | 11.22 | 11.6 |
| 7 | 5.24 | 5.43 | 16 | 12.17 | 12.2 |
| 8 | 6.11 | 6.45 | 17 | 12.9 | 13.2 |
| 9 | 6.8 | 6.85 | 18 | 13.6 | 13.68 |

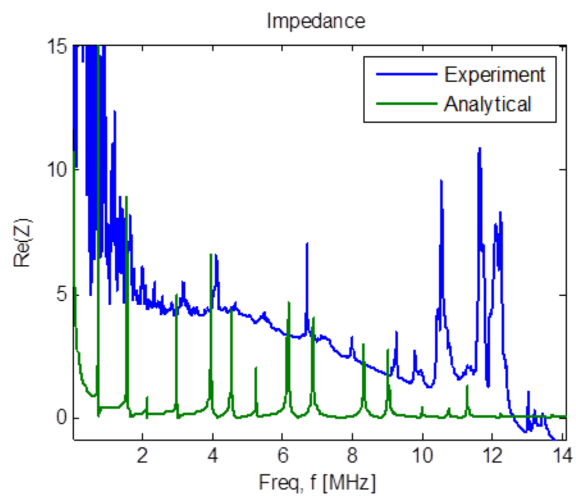


**Proof-Mass Height = 3mm**

| Mode # | Analytical Res. Fr. MHz | Exp. Res. Fr. MHz | Mode # | Analytical Res. Fr. MHz | Exp. Res. Fr. MHz |
|---|---|---|---|---|---|
| 1 | 0.67 | | 11 | 7.54 | 7.15 |
| 2 | 1.44 | | 12 | 8.23 | 8.05 |
| 3 | 1.98 | | 13 | 8.75 | 9.3 |
| 4 | 2.61 | | 14 | 9.52 | 10 |
| 5 | 3.46 | 3.1 | 15 | 10.37 | 10.6 |
| 6 | 4.25 | 4.2 | 16 | 11 | |
| 7 | 4.73 | | 17 | 11.52 | 11.85 |
| 8 | 5.43 | 5.5 | 18 | 12.32 | 12.35 |
| 9 | 6.2 | | 19 | 13.05 | |
| 10 | 6.84 | 6.74 | 20 | 13.68 | 13.7 |

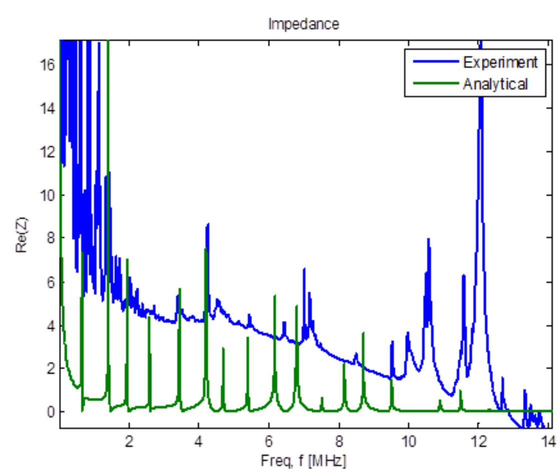


Figure 7.48 Comparison between analytical and experimental a-) resonance frequencies b-) impedance results for aluminum square PM-PWAS with proof-mass height of 2mm, 2.5mm, and 3mm

Comparison of chirp signal test to EMIS test for PWAS on aluminum plate

The basic theory of the chirp signal is explained to have understanding of the experimental results. In a linear chirp, the instantaneous frequency $f(t)$ varies linearly with time:

$$f(t) = f_0 + kt \tag{1.25}$$

where $f_0$ is the starting frequency (at time $t = 0$), and $k$ is the rate of frequency increase or chirp rate.

$$k = \frac{f_1 - f_0}{t_1} \tag{1.26}$$

where $f_1$ is the final frequency and $f_0$ is the starting frequency. The corresponding time-domain function for a sinusoidal linear chirp is the sine of the phase in radians:

$$x(t) = \sin\left[\phi_0 + 2\pi\left(f_0 t + \frac{k}{2}t^2\right)\right] \tag{1.27}$$

After the review of the chirp (sweep) signal theory, we could use the pitch-catch test configuration with two PWAS transducer bonded on 2.1 mm thick large aluminum plate. The modeling clays are applied on the edges of the plate to avoid the reflection signals from the edges. Two PWAS are employed as actuator and receiver; the actuator was excited by sweep signal with the start frequency, $f_0 = 500kHz$ and the stop frequency, $f_1 = 1MHz$ and the receiver PWAS was monitored by the oscilloscope to observe the received signal. Thus, the sweep (chirp) signal is transmitted through 0.2mm thick 7x7 mm$^2$ square PWAS and received by PWAS in the same sizes as seen in Figure 7.49.

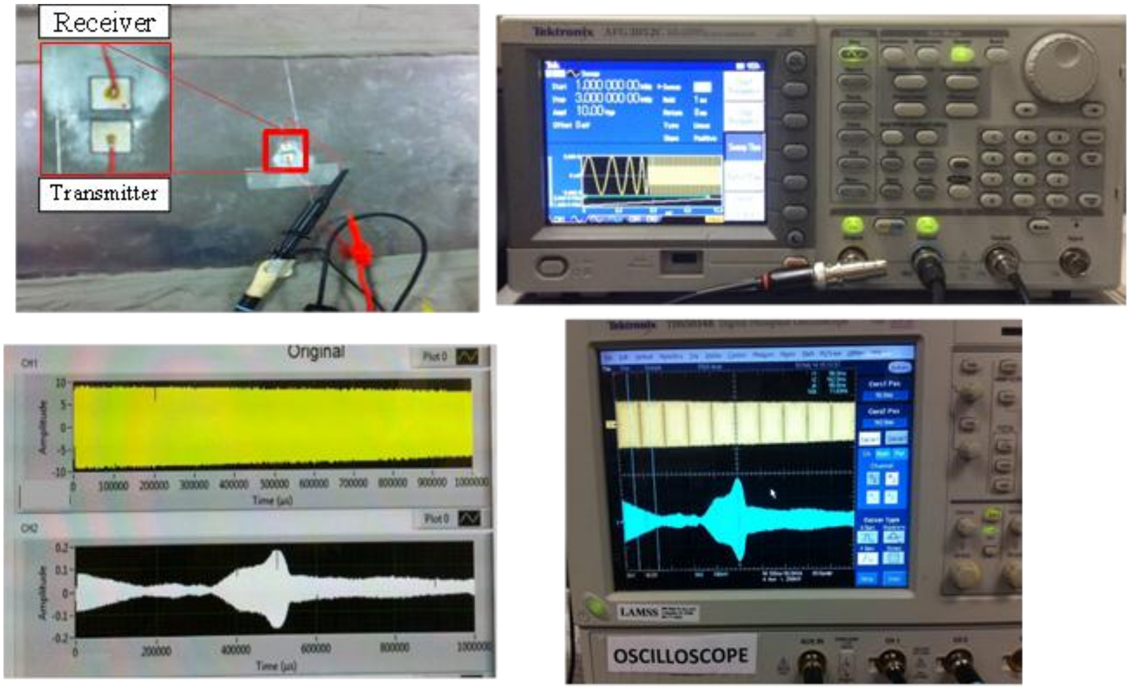


Figure 7.49 Sweep (chirp) signal is transmitted through 0.2mm thick 7x7 mm$^2$ square PWAS and received by PWAS in the same sizes on an 2.1mm thick aluminum plate. The start frequency, $f_0 = 500kHz$ and the stop frequency, $f_1 = 1MHz$.

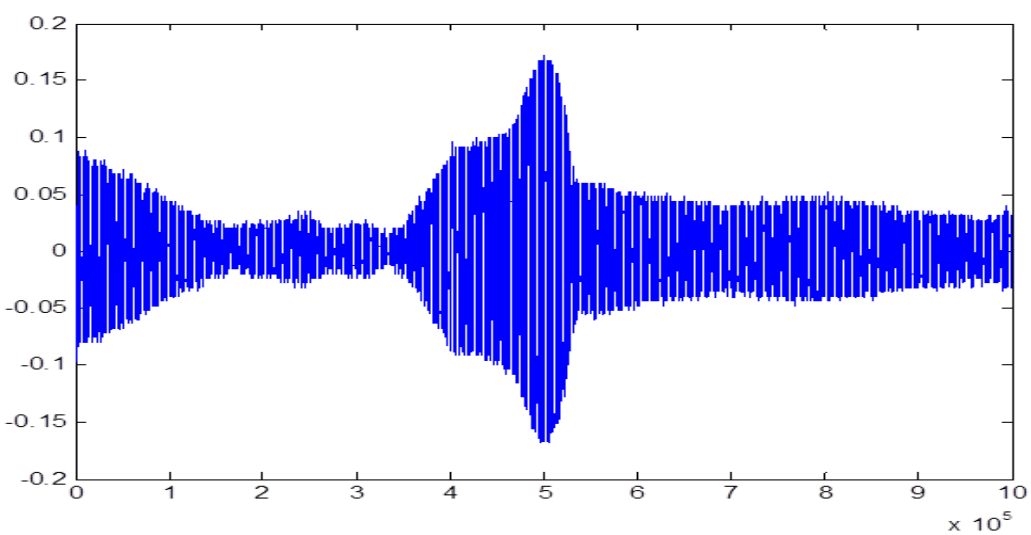


Figure 7.50 Illustration of the signal received by 0.2mm thick 7x7 mm$^2$ square receiver PWAS and the signal transmitted as a chirp signal through 0.2mm thick 7x7 mm$^2$ square PWAS in the same sizes on an 2.1mm thick aluminum plate. The start frequency $f_0 = 500kHz$ and the stop frequency, $f_1 = 1MHz$.

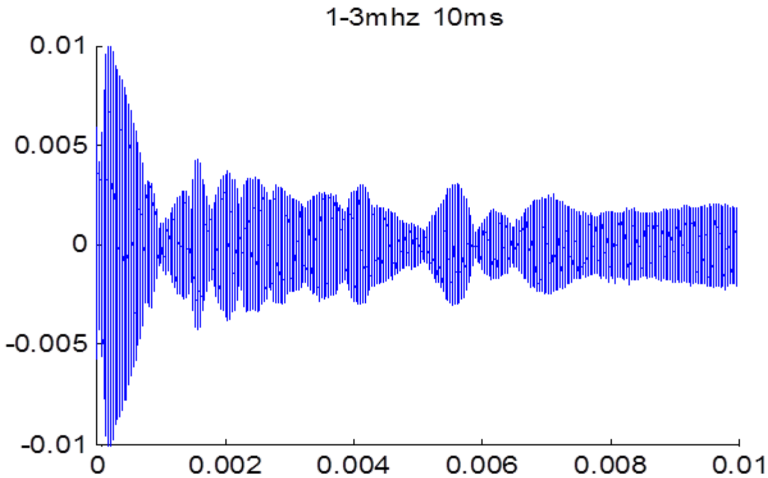


Figure 7.51 Illustration of the signal received by 0.2mm thick 7x7 mm$^2$ square receiver PWAS and the signal transmitted as a chirp signal through the same size PWAS in 10mm distance on 2.1mm thick aluminum plate. The start frequency is 1MHz and the stop frequency is 3MHz

The received signal in time domain is illustrated in Figure 7.50. As seen in the signal, a spike exists right in the middle that depicts the resonance at the location of the structure where the measurement was taken; in the same way that an EMIS measurement would show. Since the start frequency $f_0$ is $500kHz$ and the stop frequency $f_1$ is $1MHz$ the spike at the received chirp signal appears at around $750kHz$. We can see the impedance peak in frequency spectra (Figure 7.52) at the similar frequency $768kHz$. Another received signal in time domain is illustrated in Figure 7.51. As seen in the signal, the first spike at 1.1 MHz at the location of the structure where the measurement was taken; in the same way that an EMIS measurement would show as a second impedance peak. Since the start frequency $f_0$ is 1MHz and the stop frequency $f_1$ is 3MHz, the first spike at the received chirp signal appears at around 1.1MHz. We can see the impedance peak in frequency spectra (Figure 7.52) at the similar frequency of 1.12MHz.

To conclude, the chirp (sweep) signal method employs a wave propagation technique and pitch-catch experimental setup however the wave is not excited at a constant center frequency; instead, it is excited as sweeping the frequency at certain range so that, this method can capture the local resonance frequency of the structure alike EMIS method.

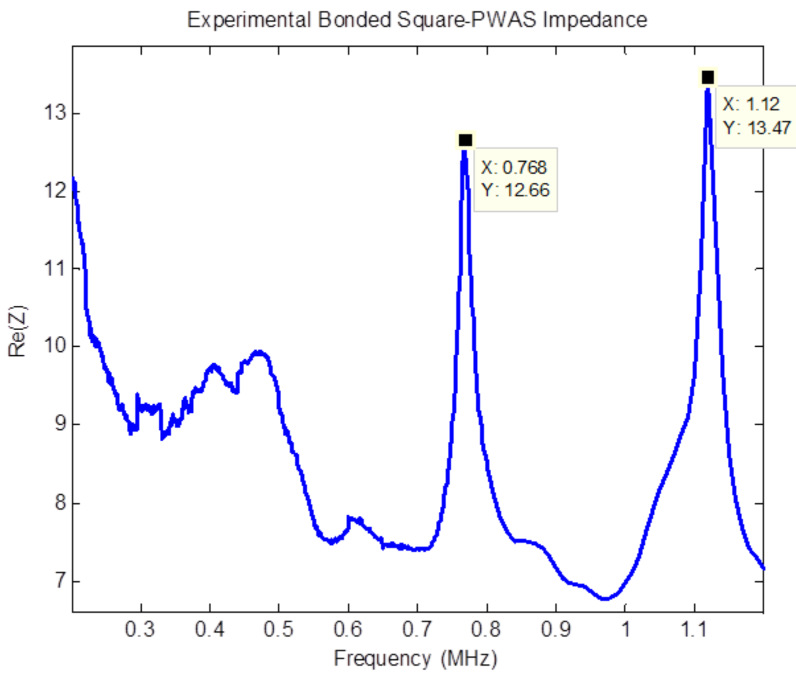


Figure 7.52 Measurement results of the real part of *in-plane* mode impedance for a 0.2mm thick 7x7 mm2 square PWAS on a 2.1 mm thick aluminum plate

# CHAPTER 8

# BEHAVIOR OF PWAS IN FLUID MEDIUM

## 8.1 STATE OF THE ART FOR HEALTH MONITORING WITH BIOMEDICAL SENSOR

SHM has been adopted so that pathologies associated with changes in mechanical behavior have been shown to be detectable i.e. the mechanical changes in a biological tissue due to a complication -such as fibrous encapsulation, inflammation, and tissue necrosis- can be detected employing SHM techniques to provide continuous in-situ detection via biomedical sensors (Bender et al., 2006).

The objective is to develop a scientific and engineering basis for the analysis of PWAS performance on a fluid-loaded structure in SHM. From the applications point of view, this study can indicate that PWAS transducers can be used for viscosity measurement such that these transducers can be utilized for bio-sensing in an environment of varying viscosity and stiffness of a texture of an animal tissue. We aim at development of a new methodology to predict the behavior of biomedical-sensor embedded in various biological tissues. We developed an analytical model of piezoelectric wafer active sensor (PWAS) in contact with a soft medium to establish the theoretical basis that enables interrogation of dynamic characteristics of a biological component. The overall purpose of the research is to develop theoretical models under simplifying assumptions to perform wide-parameter simulation of response of a bio-PWAS implanted into a biological medium.

The novel coupled field analytical models of bio-PWAS embedded into different bio-media enable a wide-parameter analysis having precise control over the model, enabling fast and accurate predictions under a variety of different scenarios and operating conditions. Thus, the complications associated with biomedical implants can be quantitatively studied due to the mechanical changes in the tissue that can be detected by bio-PWAS. The in-situ health monitoring of biomedical implants via bio-PWAS and SHM techniques has potential benefits over other medical imaging systems (e.g. magnetic resonance imaging that requires large and expensive MRI scanner) SHM techniques are continuous, easy to visualize and interpret the data, able to investigate months after sensor implantation, using of ultrasonic sound waves, and having long-life cycle

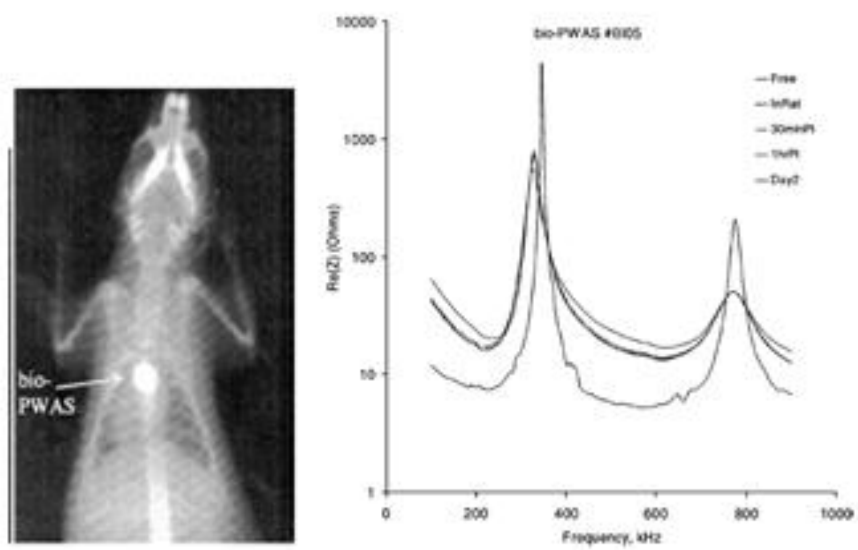


Figure 8.1 X-ray of bio-PWAS implanted in  a rat and the impedance reading from bio-PWAS after implementation and 2 days later

The theoretical approaches of shear waves of bio-PWAS excited in different embedding biological soft media shall be developed analytically via EMIS method. GMM method has been used to calculate the dispersion (wave speed in frequency domain) curves of traveling ultrasonic surface waves in multi-layered structures(Demcenko & Mažeika, 2002). Bio-PWAS will be considered embedded into viscous liquid medium (blood). Groups of parametric studies will be carried out with the significant parameters such as viscosity and density.

## 8.2 1-D ANALYSIS PIEZO-WAFER RESONATOR IN CONTACT WITH LIQUID LAYER

In this section, the response of a piezo-resonator coupled with liquid layer is derived first in terms of resonance frequency. Then, the shear horizontal waves and the corresponding piezoelectric constitutive equations will be taken into account to derive the E/M impedance response of a PWAS resonator in contact with liquid layer.

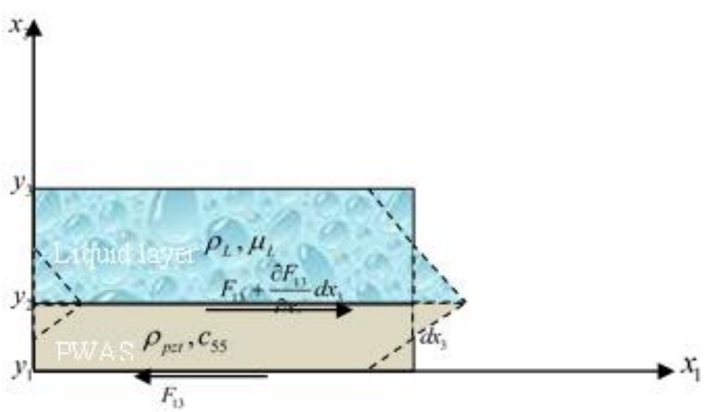


Figure 8.2 Schema of piezo-wafer resonator deformed in shear horizontal $d_{13}$ mode by induced $T_5 = T_{13}$ shear stress

### 8.2.1 SHEAR STRESS IN SOLID PART

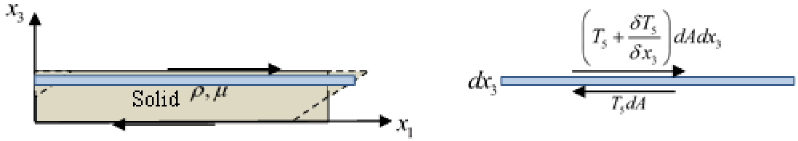


Figure 8.3 Schema of infinitesimal chunk of solid in which the shear stress is induced

Shear stress in solid medium is defined as

$$T_5 = \mu \frac{\partial u_1(x_3, t)}{\partial x_3} \tag{8.1}$$

where $\mu$ is the shear modulus of the solid material and $u_1$ is the elastic displacement along $x_1$ axis. From Newton's law of motion, the net force acting across the thickness $dx_3$ equals to the acceleration of a particle for a region of area, $dA$

$$\sum F_{x_1} = \rho dA dy \frac{\partial^2 u_1(x_3, t)}{\partial t^2} \tag{8.2}$$

Substituting the net shear force along $x_1$ axis $\partial T_5 / \partial x_3 dA dy$, we obtain

$$\frac{\partial F_{x_1}(x_3, t)}{\partial x_3} = \rho dA \frac{\partial^2 u_1(x_3, t)}{\partial t^2} \tag{8.3}$$

where $\rho$ is the density of the material. Now, recall shear stress-elastic displacement relation in Eq.(8.1).

$$\frac{\partial^2 u_1(x_3, t)}{\partial {x_3}^2} = \left(\frac{\rho}{\mu}\right) \frac{\partial^2 u_1(x_3, t)}{\partial t^2} \tag{8.4}$$

This is the Helmholtz wave equation having as a general steady-state solution

$$u_1(x_3, t) = \left[C_1 e^{-i\gamma(x_3 - y_1)} + C_2 e^{i\gamma(x_3 - y_2)}\right] e^{i\omega t} \tag{8.5}$$

where $\gamma = \omega\sqrt{\rho / \mu}$. This solution describes shear waves traveling in $+x_3$ direction with the amplitude $C_1$ and $-x_3$ direction with the amplitude $C_2$. The bottom surface $(x_3 = y_1)$ is free-boundary or traction-free.

$$T_5(y_1,t) = \mu \frac{\partial u_1(y_1,t)}{\partial x_3} = 0 \tag{8.6}$$

The free boundary conditions implies that $C_1 = C_2 = C_0$, a real constant. The general solution for strain can be obtained by taking spatial derivative of the elastic displacement with respect to $x_3$

$$u_1'(x_3,t) = \left[-i\gamma C_1 e^{-i\gamma(x_3-y_1)} + i\gamma C_2 e^{i\gamma(x_3-y_2)}\right]e^{i\omega t} \tag{8.7}$$

Since $\partial u_1(y_1,t)/\partial x_3 = 0$ and $\partial u_1(y_2,t)/\partial x_3 = 0$ for free PWAS case as one can conclude from Eq. (8.6) where free bottom and top surfaces of PWAS are at $x_3 = y_1$ and $x_3 = y_2$, respectively

$$u_1'(y_1,t) = i\gamma\left[-C_1 e^{-i\gamma(y_1-y_1)} + C_2 e^{i\gamma(y_1-y_2)}\right]e^{i\omega t} = 0 \tag{8.8}$$

$$u_1'(y_2,t) = i\gamma\left[-C_1 e^{-i\gamma(y_2-y_1)} + C_2 e^{i\gamma(y_2-y_2)}\right]e^{i\omega t} = 0 \tag{8.9}$$

Rearrange to simplify

$$C_1 - C_2 e^{-i\gamma h_p} = 0 \tag{8.10}$$

$$C_1 e^{-i\gamma h_p} - C_2 = 0 \tag{8.11}$$

Eq. (8.10) and Eq. (8.11) shows that $C_1 = C_2 = C_0$ to have non-trivial solution, the free PWAS resonator case has this requirement $\gamma h_p = n\pi$. For the fundamental resonance mode, $n = 1$, the resonance frequency equation resulted from free PWAS as followings

$$\omega\sqrt{\frac{\rho}{\mu}}h_p = \pi \quad \rightarrow \quad \omega_r = \sqrt{\frac{\mu}{\rho}}\frac{\pi}{h_p} \quad , \quad f_r = \frac{1}{2h_p}\sqrt{\frac{\mu}{\rho}} \tag{8.12}$$

The general solution for the strain simplifies to

$$u_1'\left(x_3,t\right) = i\gamma C_0\left[-e^{-i\gamma\left(x_3-y_1\right)} + e^{i\gamma\left(x_3-y_2\right)}\right]e^{i\omega t} \tag{8.13}$$

and the solution for the particle displacement becomes

$$u_1\left(x_3,t\right) = C_0\left[e^{-i\gamma\left(x_3-y_1\right)} + e^{i\gamma\left(x_3-y_2\right)}\right]e^{i\omega t} \tag{8.14}$$

### 8.2.2 SHEAR STRESS IN LIQUID MEDIUM

The upper surface is not traction-free however rather is connected with a liquid layer. The stress relation for the liquid is

$$\frac{F_x\left(x_3,t\right)}{dA} = \eta_L \frac{\partial v_x\left(x_3,t\right)}{\partial x_3} \tag{8.15}$$

where $\eta_L$ is the absolute viscosity and $v_x$ the fluid particle velocity in the $x_1$ direction. Again from Newton's law of motion, the net force gives rise to acceleration

$$\frac{\partial F_x\left(x_3,t\right)}{\partial x_3}\cancel{dx_3} = \rho_L dA\cancel{dx_3}\frac{\partial v_x\left(x_3,t\right)}{\partial t} \tag{8.16}$$

where $\rho_L$ is the fluid density. Combine (8.15) and (8.16) to get the diffusion equation which is identical to simplified steady state Navier Stokes' equations.

$$\frac{\partial^2 v_x\left(x_3,t\right)}{\partial {x_3}^2} = \frac{\rho_L}{\eta_L}\frac{\partial v_x\left(x_3,t\right)}{\partial t} \tag{8.17}$$

The solution to the Eq. (8.17) is

$$v_x\left(x_3,t\right) = \left[C_3 e^{i\gamma_L\left(x_3-y_2\right)} + C_4 e^{-i\gamma_L\left(x_3-y_3\right)}\right]e^{i\omega t} \tag{8.18}$$

where $\gamma_L = \sqrt{\omega\rho_L / 2\eta_L}\left(1-i\right)$

### 8.2.3 BOUNDARY CONDITIONS: THE RADIATION CONDITION AND THE VELOCITY CONTINUITY

Impose the radiation condition for $v_x\left(x_3,t\right)$ to remain finite as liquid thickness goes to infinitive, then to bind the liquid particle velocity we assume $C_4 = 0$. The solution further simplifies to

$$v_x\left(x_3,t\right) = C_3 e^{-i\gamma_L\left(x_3-y_2\right)} e^{i\omega t} \tag{8.19}$$

Therefore the amplitude of liquid particle velocity must match the amplitude of the velocity of PWAS particles. At $x_3 = y_2$ interface, the liquid particle velocity amplitude becomes

$$\hat{v}_x\left(y_2\right) = C_3 = \hat{V}_0 \tag{8.20}$$

At $x_3 = y_2$ interface, the PWAS particle velocity amplitude becomes

$$\hat{u}_1\left(y_2\right) = i\omega C_0\left(e^{-i\gamma h_p} + 1\right) \tag{8.21}$$

So that eventually we obtain from the velocity continuity

$$\hat{V}_0 = i\omega C_0\left(e^{-i\gamma h_p} + 1\right) \tag{8.22}$$

Then, the solution for the liquid particle velocity becomes

$$v_x\left(x_3,t\right) = \left[i\omega C_0\left(e^{-i\gamma h_p} + 1\right) e^{i\gamma_L\left(x_3-y_2\right)}\right] e^{i\omega t} \tag{8.23}$$

The shear stress continuity

The shear stress component on the liquid side of the interface must be equal and opposite to the shear stress on the PWAS side, as required by Newton's law, using Eqs. (8.1) and (8.15), we obtain the resonance condition,

$$T_5^{(Pzt)}\left(y_2,t\right) = -T_5^{(L)}\left(y_2,t\right) \tag{8.24}$$

$$\mu \frac{\partial u_1\left(y_2,t\right)}{\partial x_3} = -\eta_L \frac{\partial v_x\left(y_2,t\right)}{\partial x_3} \tag{8.25}$$

Recall the solution for PWAS shear strain $S_5 = \partial u_1\left(x_3,t\right)/\partial x_3$ in Eq. (8.13),

$$\frac{\partial u_1\left(y_2,t\right)}{\partial x_3} = i\gamma C_0\left[-e^{-i\gamma\left(y_2-y_1\right)} + e^{i\gamma\left(y_2-y_2\right)}\right]e^{i\omega t} \tag{8.26}$$

$$\frac{\partial u_1\left(y_2,t\right)}{\partial x_3} = i\gamma C_0\left(-e^{-i\gamma h_p}+1\right)e^{i\omega t} \tag{8.27}$$

The particle velocity continuity

Now, recall the solution for the liquid particle velocity in Eq. (8.23) and take its spatial derivative with respect to $x_3$ to obtain

$$\frac{\partial v_x\left(x_3,t\right)}{\partial x_3} = \omega\gamma_L C_0\left[\left(e^{-i\gamma h_p}+1\right)e^{-i\gamma_L\left(x_3-y_2\right)}\right]e^{i\omega t} \tag{8.28}$$

at $x_3 = y_2$, Eq.(8.28) becomes

$$\frac{\partial v_x\left(y_2,t\right)}{\partial x_3} = \omega\gamma_L C_0\left(e^{-i\gamma h_p}+1\right)e^{i\omega t} \tag{8.29}$$

Substitute Eqs. (8.27) and (8.29) into (8.25) to get

$$i\mu\gamma\left(-e^{-i\gamma h_p}+1\right) = -\eta_L\omega\gamma_L\left(e^{-i\gamma h_p}+1\right) \tag{8.30}$$

Recall wave numbers for PWAS and liquid, respectively

$$\gamma = \omega\sqrt{\rho / \mu} \tag{8.31}$$

$$\gamma_L = \sqrt{\omega\rho_L / 2\eta_L}\left(i-1\right) \tag{8.32}$$

and substitute them into Eq. (8.30)

$$\frac{\sqrt{\omega}\left(e^{-i\omega\sqrt{\rho/\mu}h_p}+1\right)}{\left(-e^{-i\omega\sqrt{\rho/\mu}h_p}+1\right)} = \frac{\sqrt{\rho/\mu^3}}{\eta_L\sqrt{\rho_L/2\eta_L}\left(i-1\right)} \tag{8.33}$$

$$\eta_L\sqrt{\omega\rho_L/2\eta_L}\left(i-1\right)\left(e^{-i\omega\sqrt{\rho/\mu}h_p}+1\right) - \sqrt{\rho/\mu^3}\left(-e^{-i\omega\sqrt{\rho/\mu}h_p}+1\right) = 0 \tag{8.34}$$

Solve Eq. (8.34) for the resonance frequency $\omega$

## 8.3 MECHANICAL RESPONSE:

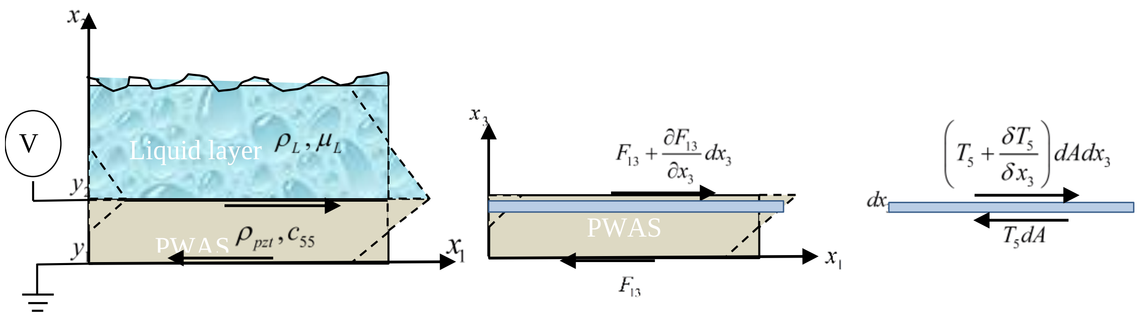


Figure 8.4 Schema of piezo-wafer resonator in contact with a liquid layer and both PWAS and liquid layer deformed in shear horizontal $d_{13}$ mode by induced $T_5 = T_{13}$ shear stress

Piezoelectric constitutive equations

$$\begin{aligned} S_{ij} &= s_{ijkl}^E T_{kl} + d_{kij} E_k \\ D_j &= d_{jkl} T_{kl} + \varepsilon_{jk}^T E_k \end{aligned} \tag{8.35}$$

Simplify the piezoelectric constitutive equations under constant electric field assumption for shear horizontal stress and strain in $d_{35}$ mode

$$2S_5 = u_1'(x_3,t) = s_{55}^E T_5 + d_{35}E_3 \tag{8.36}$$

$$D_3 = d_{35}T_5 + \varepsilon_{33}E_3 \tag{8.37}$$

### 8.3.1 SHEAR STRESS IN PWAS

In general, the relation between the shear stress and the particle displacement is defined by

$$T_5 = \mu\left(\frac{\partial u_1}{\partial x_3} + \frac{\partial u_3}{\partial x_1}\right) \tag{8.38}$$

However, we assume that the particle displacement in $x_1$ direction is constant so that the gradient of the displacement with respect to $x_1$ is zero then Eq. (8.38) becomes

$$T_5 = \mu\frac{\partial u_1}{\partial x_3} \tag{8.39}$$

where $\mu = 1/s_{55}^E$ is the shear modulus of piezoelectric material and $T_5 = T_{13}$ is the shear stress in $x_3$ direction and normal to $x_1$ plane. Recall the Helmholtz wave equation having derived as in Eq. (8.4) in prior section

$$\frac{\partial^2 u_1(x_3,t)}{\partial {x_3}^2} = \left(\frac{\rho}{\mu}\right)\frac{\partial^2 u_1(x_3,t)}{\partial t^2} \tag{8.40}$$

and its general steady-state solution

$$u_1(x_3,t) = \left[C_1 e^{-i\gamma(x_3-y_1)} + C_2 e^{i\gamma(x_3-y_2)}\right]e^{i\omega t} \tag{8.41}$$

where $\gamma = \dfrac{\omega}{c_s}$ ; $c_s = \sqrt{\dfrac{\mu}{\rho}} = \sqrt{\dfrac{1}{\rho s_{55}^E}}$ and $\omega = 2\pi f$ rad/sec

### 8.3.2 BOUNDARY CONDITIONS

Stress-free boundary condition at lower surface of PWAS as well as the shear stress continuity and particle velocity continuity at the interface between PWAS and liquid are defined as

$$\begin{aligned} &T_5^{(P)}\left(x_3 = y_1, t\right) = 0 \\ &T_5^{(P)}\left(x_3 = y_2, t\right) = -T_5^{(L)}\left(x_3 = y_2, t\right) \\ &\frac{\partial \hat{u}_1\left(x_3 = y_2, t\right)}{\partial t} = \hat{v}_L\left(x_3 = y_2\right) \end{aligned} \tag{8.42}$$

Recall the actuation constitutive equation (8.36) and impose the stress-free boundary condition at lower PWAS surface $y_1$

$$u_1'\left(y_1, t\right) = d_{35} E_3 \tag{8.43}$$

Recall the solution for displacement in Eq. (8.7)

$$\frac{\partial u_1\left(y_1, t\right)}{\partial x_3} = i\gamma\left[-C_1 e^{-i\gamma\left(x_3 - y_1\right)} + C_2 e^{i\gamma\left(x_3 - y_2\right)}\right] e^{i\omega t} \tag{8.44}$$

Substitute Eq. (8.44) into (8.43) to get the amplitude of the PWAS particle displacement

$$C_1 = C_2 e^{-i\gamma h_p} - \frac{d_{35}\hat{E}_3}{i\gamma} \tag{8.45}$$

Therefore, the solution for PWAS particle displacement in Eq. (8.14) takes this form

$$u_1\left(x_3, t\right) = \left[C_2\left(e^{-i\gamma\left(x_3 - y_1 + h_p\right)} + e^{i\gamma\left(x_3 - y_2\right)}\right) - \frac{d_{35}\hat{E}_3}{i\gamma} e^{-i\gamma\left(x_3 - y_1\right)}\right] e^{i\omega t} \tag{8.46}$$

and the PWAS strain is defined by using the strain-displacement constitutive relation $S_5 = \partial u_1(x_3,t)/\partial x_3$

$$S_5(x_3,t) = \left[ i\gamma C_2 \left( -e^{-i\gamma\left(x_3 - y_1 + h_p\right)} + e^{i\gamma\left(x_3 - y_2\right)} \right) + d_{35}\hat{E}_3 e^{-i\gamma\left(x_3 - y_1\right)} \right] e^{i\omega t} \tag{8.47}$$

where $E_3 = \hat{E}_3 e^{i\omega t}$ is the harmonic steady electric field polarized in thickness direction

Recall the shear stress equation for PWAS side substituting the general solution for PWAS particle displacement into the equation. Eq. (8.36) yields the stress as function of strain and electric field, i.e.

$$T_5^{(P)} = \frac{1}{s_{55}^E}\left(u_1' - d_{35}E_3\right) \tag{8.48}$$

$$T_5^{(P)}(x_3,t) = \frac{1}{s_{55}^E}\left\{ \left[ i\gamma C_2 \left( -e^{-i\gamma\left(x_3 - y_1 + h_p\right)} + e^{i\gamma\left(x_3 - y_2\right)} \right) + d_{35}\hat{E}_3 e^{-i\gamma\left(x_3 - y_1\right)} \right] - d_{35}\hat{E}_3 \right\} e^{i\omega t} \tag{8.49}$$

Recall the shear stress equation for liquid layer side substituting Eq. (8.28) which is spatial derivative of the liquid particle velocity

$$T_5^{(L)}(x_3,t) = \eta_L \frac{\partial v_x(x_3,t)}{\partial x_3} \tag{8.50}$$

Recall liquid particle velocity

$$v_L(x_3,t) = C_3 e^{i\gamma_L\left(x_3 - y_2\right)} e^{i\omega t} \tag{8.51}$$

From non-slip boundary condition, one can assume that the amplitude of the liquid particle velocity is equal to the amplitude of the PWAS particle velocity at the interface $y_2$

$$C_3 = \hat{V}_0 = \hat{\dot{u}}_1(y_2) = C_2 i\omega\left(e^{-2i\gamma h_p} + 1\right) - \frac{d_{35}\hat{E}_3}{i\gamma} i\omega e^{-i\gamma h_p} \tag{8.52}$$

Substitute Eq. (8.52) into (8.51)

$$v_x\left(x_3,t\right)=\left[C_2 i\omega\left(e^{-i2\gamma h_p}+1\right)-\frac{d_{35}\hat{E}_3}{\gamma}\omega e^{-i\gamma h_p}\right]e^{i\gamma_L\left(x_3-y_2\right)}e^{i\omega t} \tag{8.53}$$

Thus Eq. (8.50) takes this form

$$T_5^{(L)}\left(x_3,t\right)=\eta_L\gamma_L\omega\left[C_2\left(e^{-i2\gamma h_p}+1\right)-\frac{d_{35}\hat{E}_3}{i\gamma}e^{-i\gamma h_p}\right]e^{i\gamma_L\left(x_3-y_2\right)}e^{i\omega t} \tag{8.54}$$

From the shear stress continuity at interface $y_2$

$$T_5^{(P)}\left(y_2,t\right)=-T_5^{(L)}\left(y_2,t\right) \tag{8.55}$$

$$C_2=\frac{\left[s_{55}^E\eta_L\gamma_L\omega e^{-i\gamma h_p}-i\gamma\left(e^{-i\gamma h_p}-1\right)\right]}{\left[i\gamma\left(-e^{-2i\gamma h_p}+1\right)+s_{55}^E\eta_L\gamma_L\omega\left(e^{-i2\gamma h_p}+1\right)\right]}\frac{d_{35}\hat{E}_3}{i\gamma} \tag{8.56}$$

Recall Eq. (8.45)

$$C_1=\left\{\frac{\left[s_{55}^E\eta_L\gamma_L\omega e^{-i\gamma h_p}-i\gamma\left(e^{-i\gamma h_p}-1\right)\right]}{\left[i\gamma\left(-e^{-2i\gamma h_p}+1\right)+s_{55}^E\eta_L\gamma_L\omega\left(e^{-i2\gamma h_p}+1\right)\right]}e^{-i\gamma h_p}-1\right\}\frac{d_{35}\hat{E}_3}{i\gamma} \tag{8.57}$$

Recall Eq. (8.52)

$$C_3=\hat{V}_0=\left\{\frac{\left[s_{55}^E\eta_L\gamma_L\omega e^{-i\gamma h_p}-i\gamma\left(e^{-i\gamma h_p}-1\right)\right]}{\left[i\gamma\left(-e^{-2i\gamma h_p}+1\right)+s_{55}^E\eta_L\gamma_L\omega\left(e^{-i2\gamma h_p}+1\right)\right]}i\omega\left(e^{-2i\gamma h_p}+1\right)-i\omega e^{-i\gamma h_p}\right\}\frac{d_{35}\hat{E}_3}{i\gamma} \tag{8.58}$$

and the liquid particle velocity can be defined by recalling Eq. (8.51) substituting Eq. (8.58) into it

$$v_L\left(x_3,t\right)=\left\{\frac{\left[s_{55}^E\eta_L\gamma_L\omega e^{-i\gamma h_p}-i\gamma\left(e^{-i\gamma h_p}-1\right)\right]}{\left[i\gamma\left(-e^{-2i\gamma h_p}+1\right)+s_{55}^E\eta_L\gamma_L\omega\left(e^{-i2\gamma h_p}+1\right)\right]}i\omega\left(e^{-2i\gamma h_p}+1\right)-i\omega e^{-i\gamma h_p}\right\}\frac{d_{35}E_3}{i\gamma}e^{i\gamma_L\left(x_3-y_2\right)} \tag{8.59}$$

PWAS particle displacement is

$$u_1\left(x_3,t\right)=\left\{\frac{\left[s_{55}^{E}\eta_L\gamma_L\omega e^{-i\gamma h_p}-i\gamma\left(e^{-i\gamma h_p}-1\right)\right]}{\left[i\gamma\left(-e^{-2i\gamma h_p}+1\right)+s_{55}^{E}\eta_L\gamma_L\omega\left(e^{-i2\gamma h_p}+1\right)\right]}\left(e^{-i\gamma\left(x_3-y_1+h_p\right)}+e^{i\gamma\left(x_3-y_2\right)}\right)-e^{-i\gamma\left(x_3-y_1\right)}\right\}\frac{d_{35}E_3}{i\gamma} \tag{8.60}$$

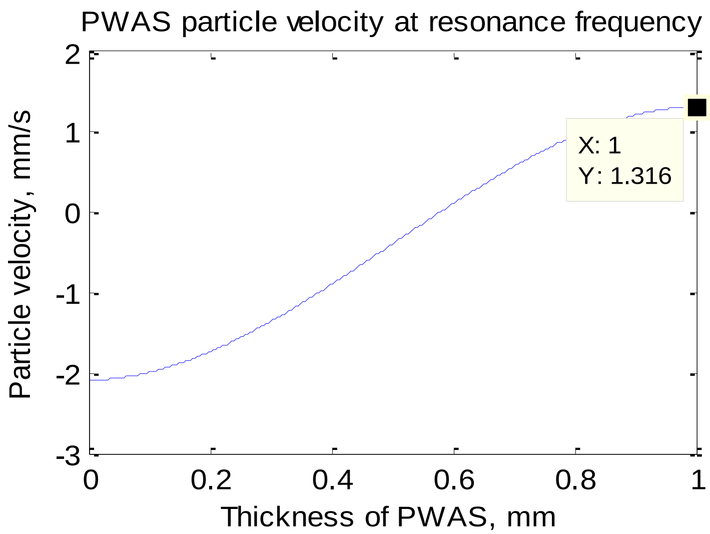


Figure 8.5 Particle velocity of PWAS along its thickness in contact with water, the particle velocity at the interface is 1315 µm/sec at electric field amplitude of 20 kV/m PWAS sizes 15mmx15mmx1mm.

The particle velocity of PWAS along its thickness in contact with water can be seen in Figure 8.5, the particle velocity at the interface is 1315 µm/sec at electric field amplitude of 20 kV/m PWAS sizes 15mmx15mmx1mm. The particle velocity of PWAS along its thickness in contact with honey can be seen in Figure 8.6, the particle velocity at the interface is 1672 µm/sec at electric field amplitude of 20 kV/m PWAS sizes 15mmx15mmx1mm.

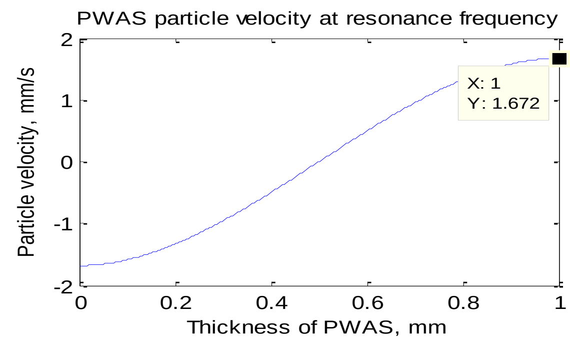


Figure 8.6 Particle velocity of PWAS along its thickness in contact with honey, PWAS sizes 15mmx15mmx1mm

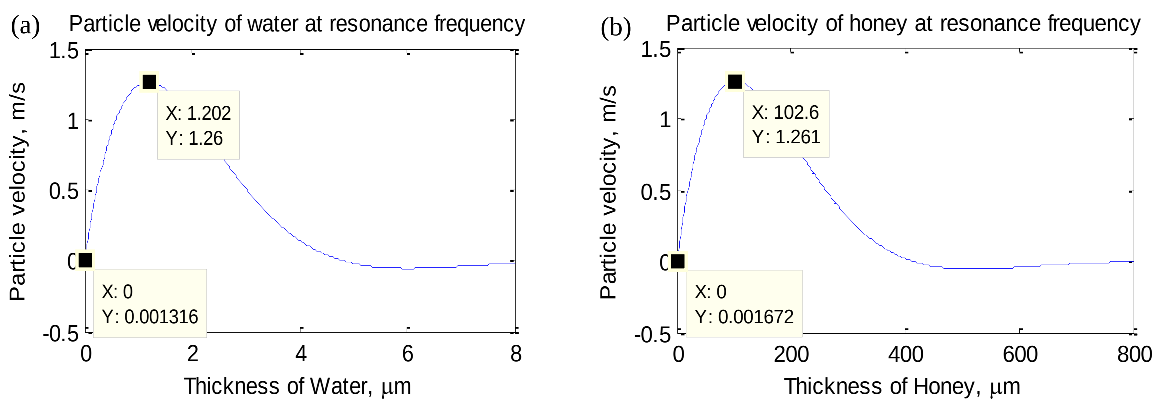


Figure 8.7 Liquid particle velocity change in the vicinity of PWAS-liquid interface at the first resonance frequency of 850.4kHz (a) for water with the density of 1000kg/m and the dynamic viscosity of 0.001 Pa.s (b) for honey with the density of 1350kg/m and the dynamic viscosity of 10 Pa.s. PWAS sizes 15mmx15mmx1mm

Liquid particle velocity change in the vicinity of PWAS-liquid interface at the first resonance frequency of 850.4kHz is illustrated in Figure 8.7(a) for water with the density of 1000kg/m and the dynamic viscosity of 0.001 Pa.s and in Figure 8.7 (b) for honey with the density of 1350kg/m and the dynamic viscosity of 10 Pa.s. PWAS sizes are 15mmx15mmx1mm. PWAS strain is

$$S_5\left(x_3,t\right)=\left\{\frac{\left[s_{55}^{E}\eta_L\gamma_L\omega e^{-i\gamma h_p}-i\gamma\left(e^{-i\gamma h_p}-1\right)\right]}{\left[i\gamma\left(-e^{-2i\gamma h_p}+1\right)+s_{55}^{E}\eta_L\gamma_L\omega\left(e^{-i2\gamma h_p}+1\right)\right]}\left(-e^{-i\gamma\left(x_3-y_1+h_p\right)}+e^{i\gamma\left(x_3-y_2\right)}\right)+e^{-i\gamma\left(x_3-y_1\right)}\right\}d_{35}E_3 \qquad (8.61)$$

## 8.4 ELECTRICAL RESPONSE:

Consider PWAS in contact with liquid under harmonic electric excitation as shown in Figure 8.4. Recall Eq. (8.37) representing electrical displacement

$$D_3 = d_{35}T_5 + \varepsilon_{33}E_3 \tag{8.62}$$

Eq. (8.36) yields the stress as function of strain and electric field, i.e.

$$T_5 = \frac{1}{s_{55}^E}\left(2S_5 - d_{35}E_3\right) \tag{8.63}$$

Hence, the electric displacement can be expressed as

$$D_3 = \frac{d_{35}}{s_{55}^E}\left(2S_5 - d_{35}E_3\right) + \varepsilon_{33}E_3 \tag{8.64}$$

$$D_3 = \frac{d_{35}}{s_{55}^E}\left(u_1'\left(x_3,t\right) - d_{35}E_3\right) + \varepsilon_{33}E_3 \tag{8.65}$$

Introduce the E/M coupling coefficient

$$\kappa_{35}^2 = \frac{d_{35}^2}{\varepsilon_{33}^T s_{55}^E} \tag{8.66}$$

and substitute into the electric displacement equation and rearrange

$$D_3 = \varepsilon_{33}^T E_3\left[1 - \kappa_{35}^2\left(1 - \frac{u_1'\left(x_3,t\right)}{d_{35}E_3}\right)\right] \tag{8.67}$$

Upon substitution of Eq. (8.61) into Eq.(8.67), we get

$$D_3 = \varepsilon_{33}^T E_3\left[1 - \kappa_{35}^2\left(1 - \left\{\frac{\left[s_{55}^E\eta_L\gamma_L\omega e^{-i\gamma h_p} - i\gamma\left(e^{-i\gamma h_p} - 1\right)\right]}{\left[i\gamma\left(-e^{-2i\gamma h_p} + 1\right) + s_{55}^E\eta_L\gamma_L\omega\left(e^{-i2\gamma h_p} + 1\right)\right]}\left(-e^{-i\gamma\left(x_3 - y_1 + h_p\right)} + e^{i\gamma\left(x_3 - y_2\right)}\right) + e^{-i\gamma\left(x_3 - y_1\right)}\right\}\right)\right]$$

(8.68)

Integration of Eq. (8.67) over the area of the piezoelectric wafer yields the total charge

$$\hat{Q}(x_3) = \int_A D_3 dx_1 dx_2 = \int_{-\frac{l}{2}}^{+\frac{l}{2}} \int_0^b D_3 dx_1 dx_2 \tag{8.69}$$

Assuming harmonic time dependence $Q(x_3, t) = \hat{Q}(x_3)e^{i\omega t}$

$$\hat{Q}(x_3) = \int_A D_3 dx_1 dx_2 = \int_{-l/2}^{l/2} \int_0^b D_3 dx_1 dx_2 = \varepsilon_{33}^T \hat{E}_3 bl \left[ 1 - \kappa_{35}^2 \left( 1 - \frac{\hat{u}_1'(x_3)}{d_{35}\hat{E}_3} \right) \right] \tag{8.70}$$

$$\hat{Q}_{eq}(x_3) = \frac{1}{t} \int_{y_1}^{y_2} \hat{Q}(x_3) dx_3 \tag{8.71}$$

$$\hat{Q}_{eq}(x_3) = \frac{1}{t} \int_{y_1}^{y_2} \varepsilon_{33}^T \hat{E}_3 bl \left[ 1 - \kappa_{35}^2 \left( 1 - \frac{\hat{u}_1'(x_3)}{d_{35}\hat{E}_3} \right) \right] dx_3 \tag{8.72}$$

$$\hat{Q}_{eq}(x_3) = \frac{\varepsilon_{33}^T \hat{E}_3 bl}{h_p} \left[ \left( 1 - \kappa_{35}^2 \right) h_p + \kappa_{35}^2 \frac{1}{d_{35}\hat{E}_3} \hat{u}_1(x_3) \Big|_{y_1}^{y_2} \right] \tag{8.73}$$

$$\hat{Q}_{eq}(x_3) = \varepsilon_{33}^T \hat{E}_3 bl \left[ 1 - \kappa_{35}^2 + \kappa_{35}^2 \left( \frac{\hat{u}_1(y_2) - \hat{u}_1(y_1)}{d_{35}\hat{E}_3 h_p} \right) \right] \tag{8.74}$$

Introduce the induced strain and induced displacement for the thickness mode

$$S_{ISA}^{(SH)} = d_{35}\hat{E}_3 \tag{8.75}$$

$$u_{ISA}^{(SH)} = S_{ISA}^{(SH)} h_p = d_{35}\hat{E}_3 h_p \tag{8.76}$$

Upon substitution of Eq. (8.76) into Eq. (8.74), we obtain

$$\hat{Q}_{eq}(x_3) = \varepsilon_{33}^T \hat{E}_3 A \left[ 1 - \kappa_{35}^2 \left( 1 - \frac{\hat{u}_1(y_2) - \hat{u}_1(y_1)}{u_{ISA}^{(SH)}} \right) \right] \tag{8.77}$$

where ISA denotes ‘induced strain actuation’ and the superscript $(SH)$ denotes ‘shear horizontal mode’.

Recall the capacitance of the material $C_0 = \frac{\varepsilon_{33}^T A}{t}$ and $\hat{E}_3 = \hat{V} / t$ then rearrange Eq. (8.77)

$$\hat{Q}_{eq}(x_3) = C_0 \hat{V}_3 \left[ 1 - \kappa_{35}^2 \left( 1 - \frac{\hat{u}_1(y_2) - \hat{u}_1(y_1)}{u_{ISA}^{(SH)}} \right) \right] \tag{8.78}$$

The electric current is obtained as the time derivative of the electric charge i.e.

$$I = \dot{Q} = i\omega Q \tag{8.79}$$

Hence,

$$\hat{I} = i\omega C_0 \hat{V}_3 \left[ 1 - \kappa_{35}^2 + \kappa_{35}^2 \left( \frac{\hat{u}_1(y_2) - \hat{u}_1(y_1)}{u_{ISA}^{(SH)}} \right) \right] \tag{8.80}$$

The admittance, $Y$ , is defined as the fraction of current by voltage, i.e.

$$Y = \frac{I}{V} == i\omega C_0 \left[ 1 - \kappa_{35}^2 + \kappa_{35}^2 \left( \frac{\hat{u}_1(y_2) - \hat{u}_1(y_1)}{u_{ISA}^{(SH)}} \right) \right] \tag{8.81}$$

Recall Eq. (8.60)

$$u_1(x_3, t) = \left\{ \frac{\left[ s_{55}^E \eta_L \gamma_L \omega e^{-i\gamma h_p} - i\gamma \left( e^{-i\gamma h_p} - 1 \right) \right]}{\left[ i\gamma \left( -e^{-2i\gamma h_p} + 1 \right) + s_{55}^E \eta_L \gamma_L \omega \left( e^{-i2\gamma h_p} + 1 \right) \right]} \left( e^{-i\gamma(x_3 - y_1 + h_p)} + e^{i\gamma(x_3 - y_2)} \right) - e^{-i\gamma(x_3 - y_1)} \right\} \frac{d_{35} E_3}{i\gamma}$$
(8.82)

At $x_3 = y_1$, the amplitude of the displacement is

$$\hat{u}_1(y_1) = \left\{ \frac{2\left[ s_{55}^E \eta_L \gamma_L \omega e^{-i\gamma h_p} - i\gamma \left( e^{-i\gamma h_p} - 1 \right) \right] e^{-i\gamma h_p}}{\left[ i\gamma \left( -e^{-2i\gamma h_p} + 1 \right) + s_{55}^E \eta_L \gamma_L \omega \left( e^{-i2\gamma h_p} + 1 \right) \right]} - 1 \right\} \frac{u_{ISA}^{(SH)}}{i\gamma h_p} \tag{8.83}$$

At $x_3 = y_2$, the amplitude of the displacement is

$$u_1\left(y_2\right)=\left\{\frac{\left[s_{55}^E\eta_L\gamma_L\omega e^{-i\gamma h_p}-i\gamma\left(e^{-i\gamma h_p}-1\right)\right]\left(e^{-2i\gamma h_p}+1\right)}{\left[i\gamma\left(-e^{-2i\gamma h_p}+1\right)+s_{55}^E\eta_L\gamma_L\omega\left(e^{-i2\gamma h_p}+1\right)\right]}-e^{-i\gamma h_p}\right\}\frac{u_{ISA}^{(SH)}}{i\gamma h_p} \tag{8.84}$$

Introduce the notation $\phi_{SH}=i\gamma h_p$

$$\hat{u}_1\left(y_1\right)=\left\{\frac{2\left[s_{55}^E\eta_L\gamma_L\omega e^{-\phi_{SH}}-i\gamma\left(e^{-\phi_{SH}}-1\right)\right]e^{-\phi_{SH}}}{\left[i\gamma\left(-e^{-2\phi_{SH}}+1\right)+s_{55}^E\eta_L\gamma_L\omega\left(e^{-2\phi_{SH}}+1\right)\right]}-1\right\}\frac{u_{ISA}^{(SH)}}{\phi_{SH}} \tag{8.85}$$

$$u_1\left(y_2\right)=\left\{\frac{\left[s_{55}^E\eta_L\gamma_L\omega e^{-\phi_{SH}}-i\gamma\left(e^{-\phi_{SH}}-1\right)\right]\left(e^{-2\phi_{SH}}+1\right)}{\left[i\gamma\left(-e^{-2\phi_{SH}}+1\right)+s_{55}^E\eta_L\gamma_L\omega\left(e^{-i\phi_{SH}}+1\right)\right]}-e^{-\phi_{SH}}\right\}\frac{u_{ISA}^{(SH)}}{\phi_{SH}} \tag{8.86}$$

Upon substitution of Eqs. (8.85)and (8.86) into Eq. (8.81), one can obtain the admittance for PWAS in contact with liquid in $d_{35}$ shear horizontal mode

$$Y=i\omega C_0\left[1-\kappa_{35}^2+\frac{\kappa_{35}^2}{\phi_{SH}}\left\{\begin{array}{l}\left\{\dfrac{\left[s_{55}^E\eta_L\gamma_L\omega h_p e^{-\phi_{SH}}-\phi_{SH}\left(e^{-\phi_{SH}}-1\right)\right]\left(e^{-2\phi_{SH}}+1\right)}{\left[\phi_{SH}\left(-e^{-2\phi_{SH}}+1\right)+s_{55}^E\eta_L\gamma_L\omega h_p\left(e^{-\phi_{SH}}+1\right)\right]}-e^{-\phi_{SH}}\right\}\\ -\left\{\dfrac{2\left[s_{55}^E\eta_L\gamma_L\omega h_p e^{-\phi_{SH}}-\phi_{SH}\left(e^{-\phi_{SH}}-1\right)\right]e^{-\phi_{SH}}}{\left[\phi_{SH}\left(-e^{-2\phi_{SH}}+1\right)+s_{55}^E\eta_L\gamma_L\omega h_p\left(e^{-2\phi_{SH}}+1\right)\right]}-1\right\}\end{array}\right\}\right] \tag{8.87}$$

As geometrical properties of the PWAS transducer, 7mm of length, 7mm of width, and 0.2mm of thickness are considered and the material properties are given in Table 1. The liquid side is water whose density is 1000 kg/m$^3$ and dynamic viscosity is 1.002x10$^{-3}$ Pa.sec at temperature of 20˚C. The admittance of PWAS resonator is shown in Figure 8.8 for PWAS in 7mm of length, 7mm of width, and 0.2mm of thickness in contact with water in density is 1000 kg/m3 and dynamic viscosity is 1.002x10-3 Pa.sec at temperature of 20˚C. The impedance of PWAS resonator is shown in Figure 8.9 for PWAS in 7mm of length, 7mm of width, and 0.2mm of thickness in contact with water in density is 1000 kg/m$^3$ and dynamic viscosity is 1.002x10$^{-3}$ Pa.sec at temperature of 20˚C

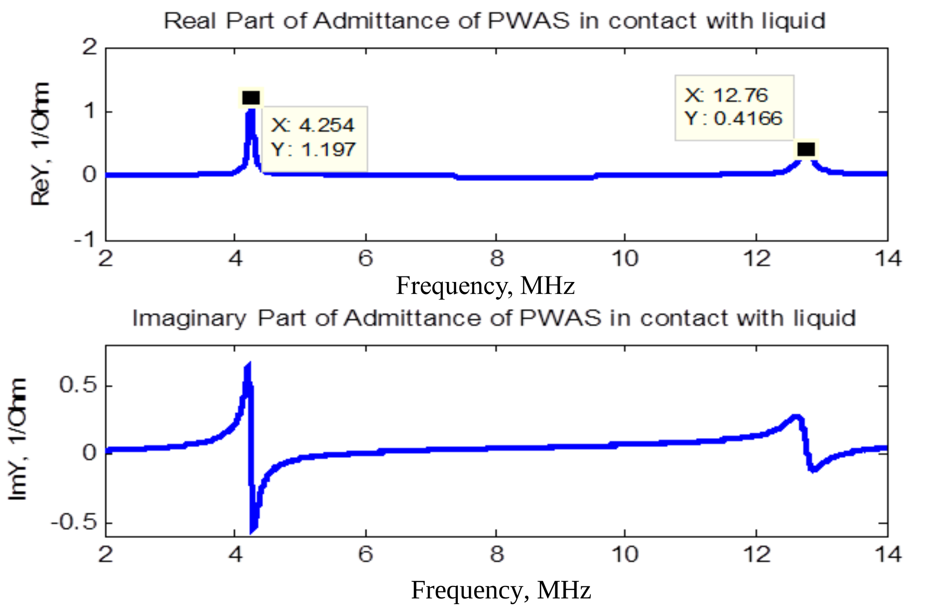


Figure 8.8 Admittance of PWAS resonator in 7mm of length, 7mm of width, and 0.2mm of thickness in contact with water in density is 1000 kg/m3 and dynamic viscosity is 1.002x10-3 Pa.sec at temperature of 20˚C

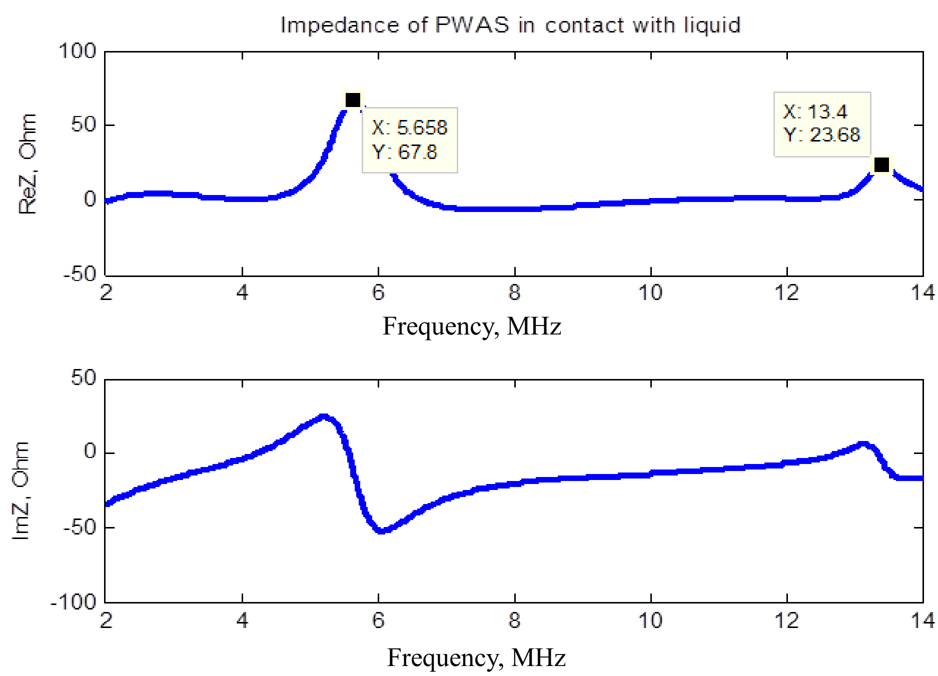


Figure 8.9 Impedance of PWAS resonator in 7mm of length, 7mm of width, and 0.2mm of thickness in contact with water in density is 1000 kg/$m^3$ and dynamic viscosity is $1.002 \times 10^{-3}$ Pa.sec at temperature of 20˚C

Figure 8.10 shows the admittance of PWAS resonator in 7mm of length, 7mm of width, and 0.2mm of thickness in free condition; in contact with water in density of 1000 kg/m$^3$ and dynamic viscosity of 1.002x10$^{-3}$ Pa.sec; and in contact with honey in density of 1000 kg/m$^3$ and dynamic viscosity is 10x10$^{-3}$ Pa.sec at temperature of 20˚C. Figure 8.11 depicts the impedance of PWAS resonator in 7mm of length, 7mm of width, and 0.2mm of thickness in free condition; in contact with water in density of 1000 kg/m$^3$ and dynamic viscosity of 1.002x10$^{-3}$ Pa.sec; and in contact with another liquid in density of 1000 kg/m$^3$ and dynamic viscosity is 10x10$^{-3}$ Pa.sec.

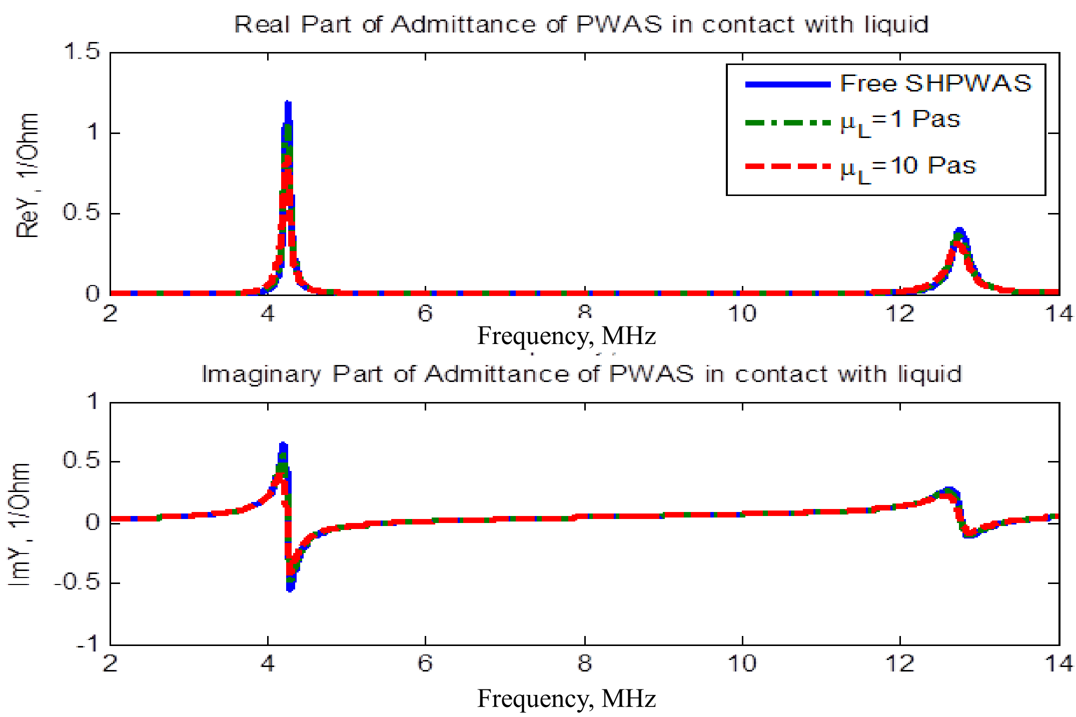


Figure 8.10 Admittance of PWAS resonator in 7mm of length, 7mm of width, and 0.2mm of thickness in free condition; in contact with water in density of 1000 kg/m$^3$ and dynamic viscosity of 1.002x10$^{-3}$ Pa.sec; and in contact with honey in density of 1000 kg/m$^3$ and dynamic viscosity is 10x10$^{-3}$ Pa.sec at temperature of 20˚C

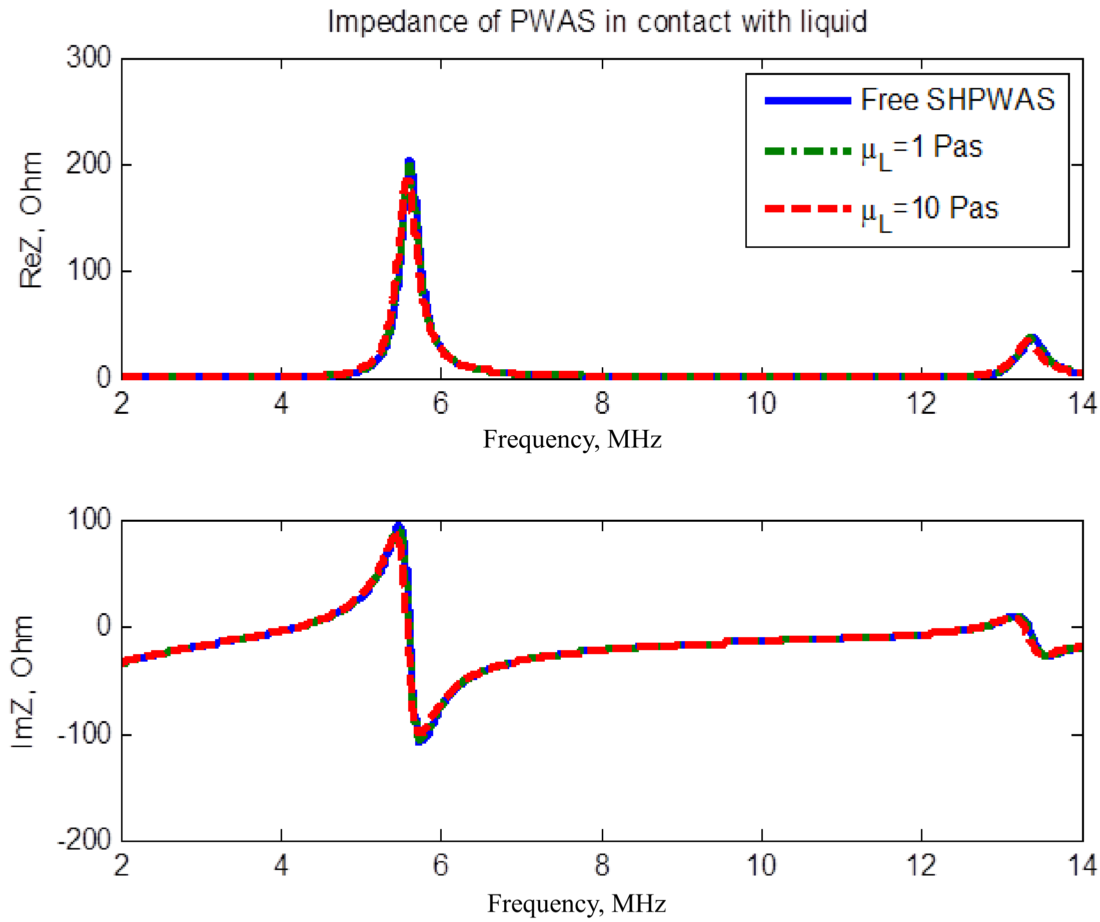


Figure 8.11 Impedance of PWAS resonator in 7mm of length, 7mm of width, and 0.2mm of thickness in free condition; in contact with water in density of 1000 kg/m$^3$ and dynamic viscosity of 1.002x10$^{-3}$ Pa.sec; and in contact with another liquid in density of 1000 kg/m$^3$ and dynamic viscosity is 10x10$^{-3}$ Pa.sec

The first admittance peak of PWAS resonator is depicted in Figure 8.12 for PWAS in 7mm of length, 7mm of width, and 0.2mm of thickness in free condition and in contact with liquids in different density and same dynamic viscosity is 1.0 Pa.sec. The first impedance peak of PWAS resonator is shown in Figure 8.13 for PWAS in 7mm of length, 7mm of width, and 0.2mm of thickness in free condition and in contact with liquids in different density and same dynamic viscosity is 1.0 Pa.sec.

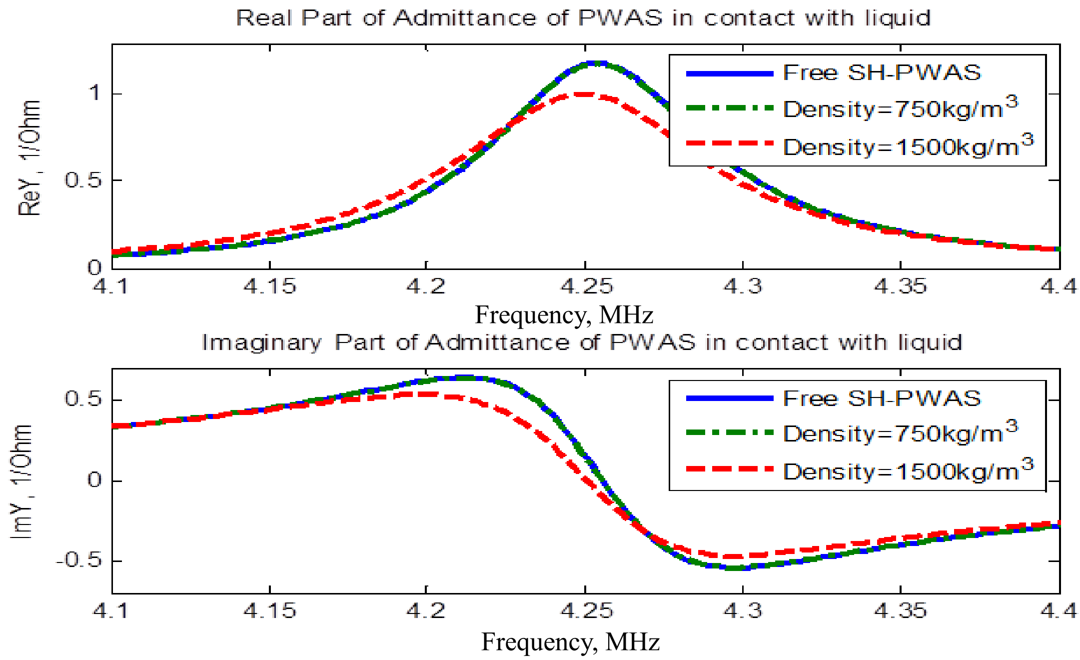


Figure 8.12 First admittance peak of PWAS resonator in 7mm of length, 7mm of width, and 0.2mm of thickness in free condition and in contact with liquids in different density and same dynamic viscosity is 1.0 Pa.sec

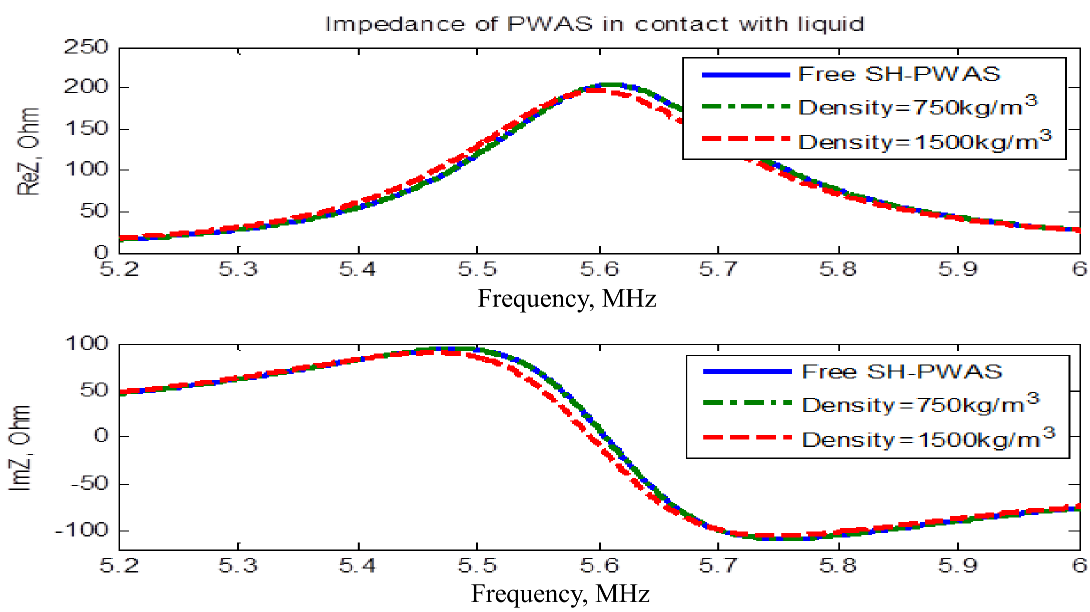


Figure 8.13 First impedance peak of PWAS resonator in 7mm of length, 7mm of width, and 0.2mm of thickness in free condition and in contact with liquids in different density and same dynamic viscosity is 1.0 Pa.sec

In order to show the effect of the different viscosity, the first admittance peaks of PWAS resonator are plotted in Figure 8.14 for PWAS in 7mm of length, 7mm of width, and 0.2mm of thickness in free condition; in contact with water in density of 1000 kg/m$^3$ and dynamic viscosity of 1.002x10$^{-3}$ Pa.sec; and in contact with another liquid in density of 1000 kg/m$^3$ and dynamic viscosity is 10x10$^{-3}$ Pa.sec. Also, the first impedance peaks of PWAS resonator is shown in Figure 8.15 for PWAS in 7mm of length, 7mm of width, and 0.2mm of thickness in free condition; in contact with water in density of 1000 kg/m$^3$ and dynamic viscosity of 1.002x10$^{-3}$ Pa.sec; and in contact with another liquid in density of 1000 kg/m$^3$ and dynamic viscosity is 10x10$^{-3}$ Pa.sec.

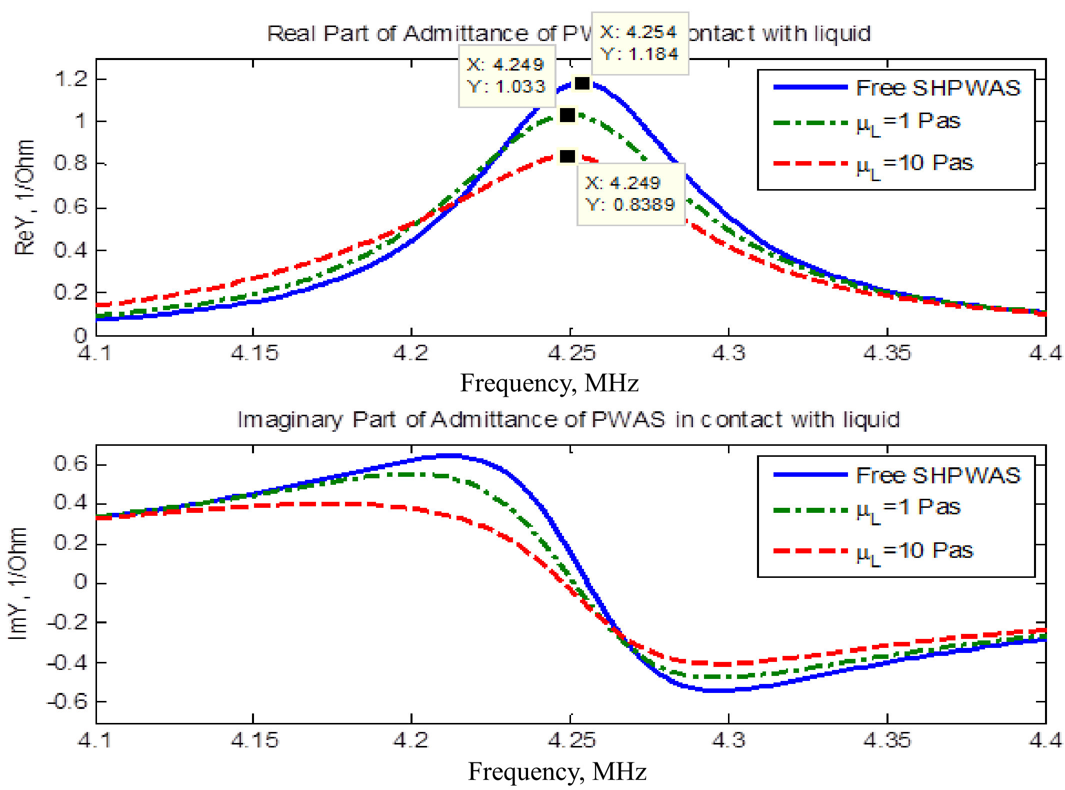


Figure 8.14 First admittance of the admittance spectra of PWAS resonator in 7mm of length, 7mm of width, and 0.2mm of thickness in free condition; in contact with water in density of 1000 kg/m$^3$ and dynamic viscosity of 1.002x10$^{-3}$ Pa.sec; and in contact with another liquid in density of 1000 kg/m$^3$ and dynamic viscosity is 10x10$^{-3}$ Pa.sec

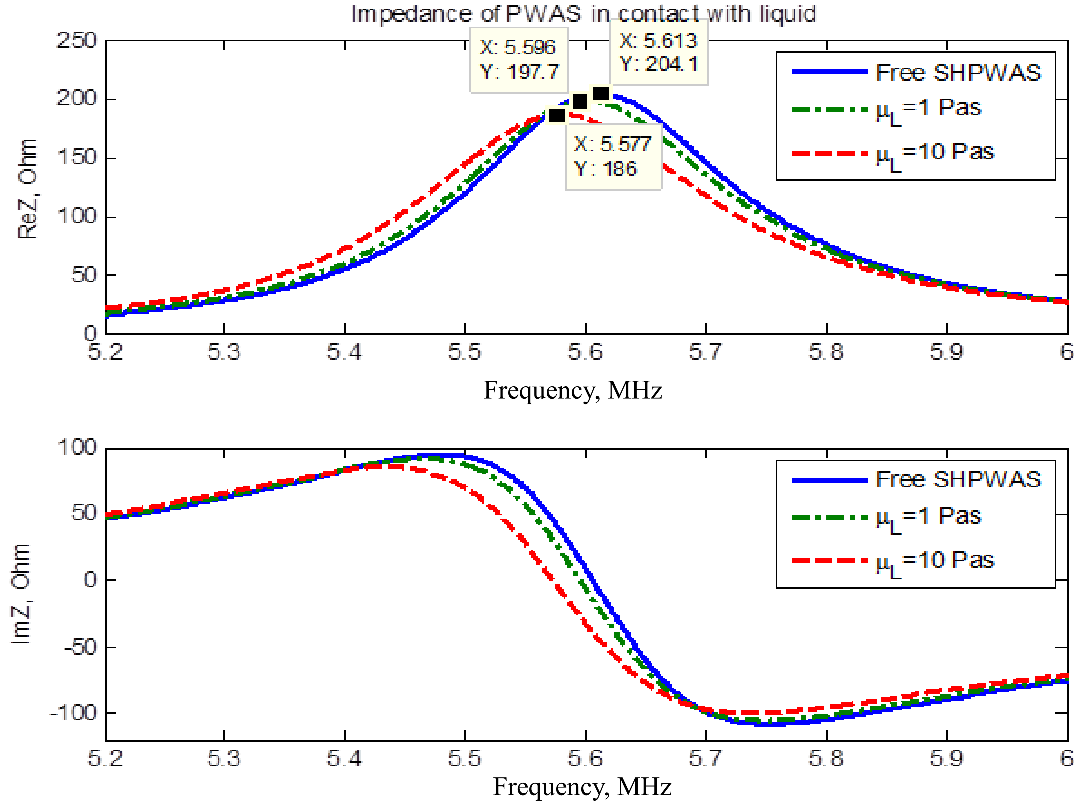


Figure 8.15 First impedance peak of the impedance spectra of PWAS resonator in 7mm of length, 7mm of width, and 0.2mm of thickness in free condition; in contact with water in density of 1000 kg/m$^3$ and dynamic viscosity of 1.002x10$^{-3}$ Pa.sec; and in contact with another liquid in density of 1000 kg/m$^3$ and dynamic viscosity is 10x10$^{-3}$ Pa.sec

As geometrical properties of the PWAS transducer, 15mm of length, 15mm of width, and 1mm of thickness are considered. In order to show the effect of the different density of the liquid media, the real part of admittance spectra of PWAS resonator is shown in Figure 8.16 for PWAS in 15mm of length, 15mm of width, and 1mm of thickness in free condition and in contact with liquids in different density and same dynamic viscosity is 1.0 Pa.sec. Also, the real part of impedance spectra of PWAS resonator is also indicated in Figure 8.17 for PWAS in 15mm of length, 15mm of width, and 1mm of thickness in free condition and in contact with liquids in different density and same dynamic viscosity is 1.0 Pa.sec.

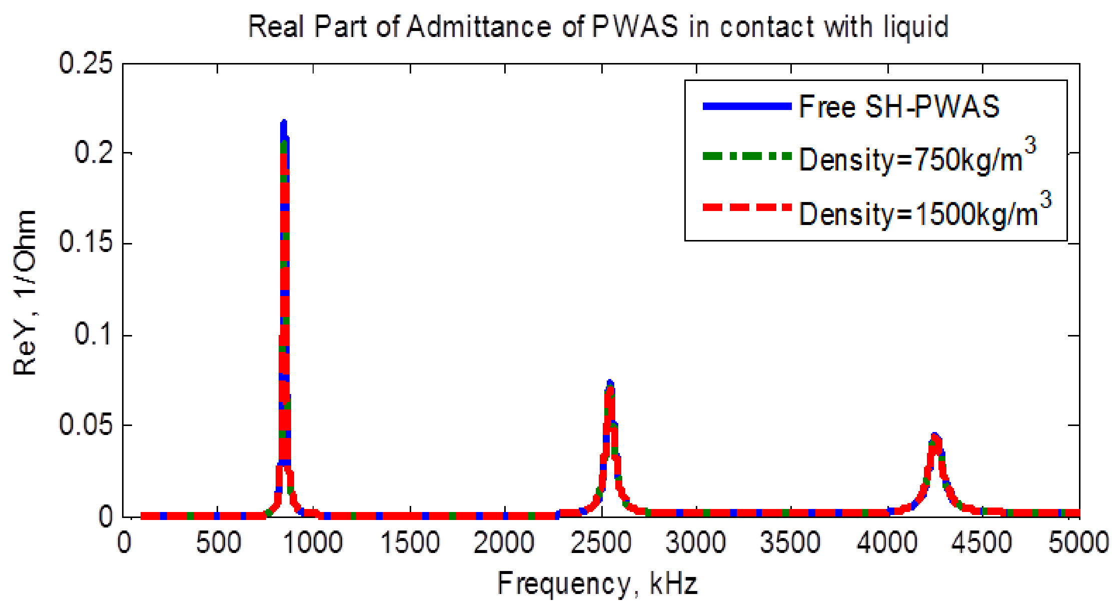


Figure 8.16 Real part of admittance spectra of PWAS resonator in 15mm of length, 15mm of width, and 1mm of thickness in free condition and in contact with liquids in different density and same dynamic viscosity is 1.0 Pa.sec

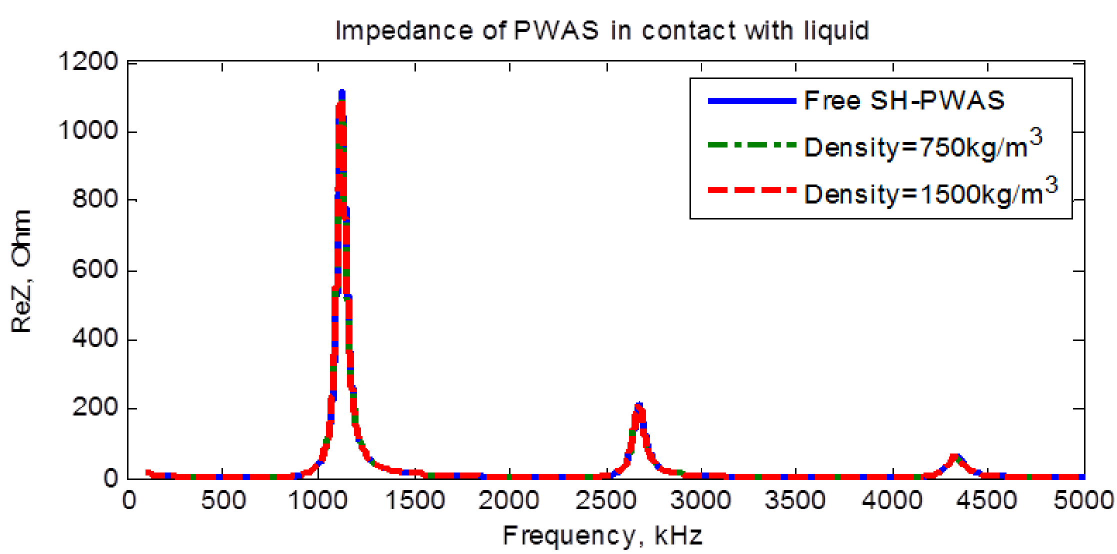


Figure 8.17 Real part of impedance spectra of PWAS resonator in 15mm of length, 15mm of width, and 1mm of thickness in free condition and in contact with liquids in different density and same dynamic viscosity is 1.0 Pa.sec

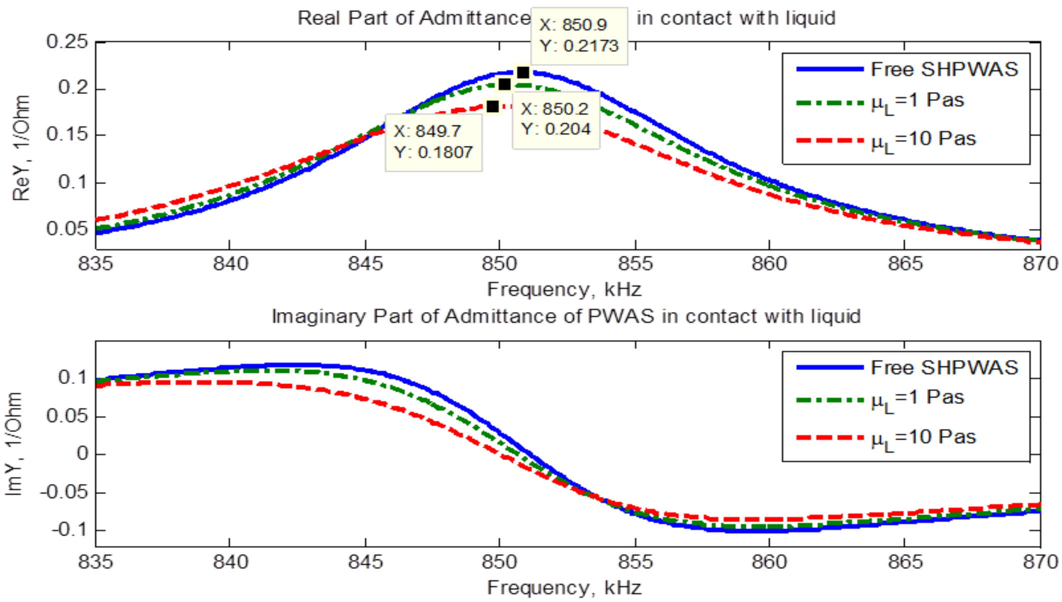


Figure 8.18 First admittance peak of admittance spectra for PWAS resonator in 15mm of length, 15mm of width, and 1mm of thickness in free condition and in contact with liquid with different dynamic viscosities and both densities are assumed to be 1000 kg/m$^3$

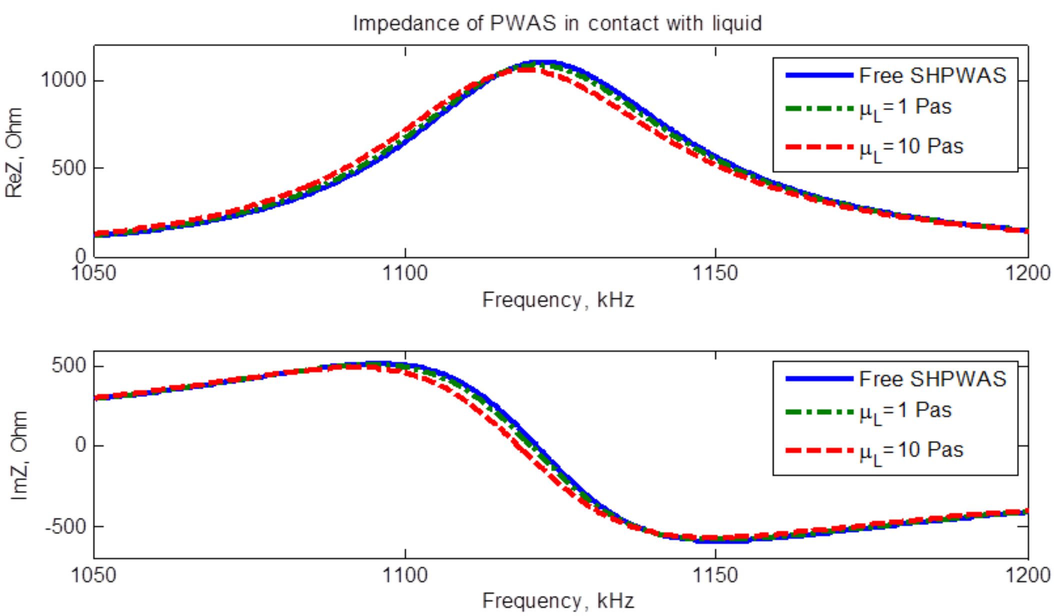


Figure 8.19 First impedance peak of impedance spectra for PWAS resonator in 15mm of length, 15mm of width, and 1mm of thickness in free condition and in contact with liquid with different dynamic viscosities and both densities are assumed to be 1000 kg/m$^3$

In order to show the effect of the different viscosity of the liquid media, Figure 8.18 shows the first peak of admittance for PWAS resonator in 15mm of length, 15mm of width, and 1mm of thickness in free condition and in contact with liquid with different dynamic viscosities and both densities are assumed to be 1000 kg/m$^3$ whereas Figure 8.19 shows the first peak of impedance for PWAS resonator in 15mm of length, 15mm of width, and 1mm of thickness in free condition and in contact with liquid with different dynamic viscosities and both densities are assumed to be 1000 kg/m$^3$.

In order to understand the effect of the different density of the liquid media, Figure 8.20 depicts the first peak of admittance for PWAS resonator in 15mm of length, 15mm of width, and 1mm of thickness in free condition and in contact with liquid with different densities and both liquid viscosities are assumed to be 1.0 Pa.s. Also, Figure 8.21 shows the first peak of impedance for PWAS resonator in 15mm of length, 15mm of width, and 1mm of thickness in free condition and in contact with liquid with different densities and both liquid viscosities are assumed to be 1.0 Pa.s.

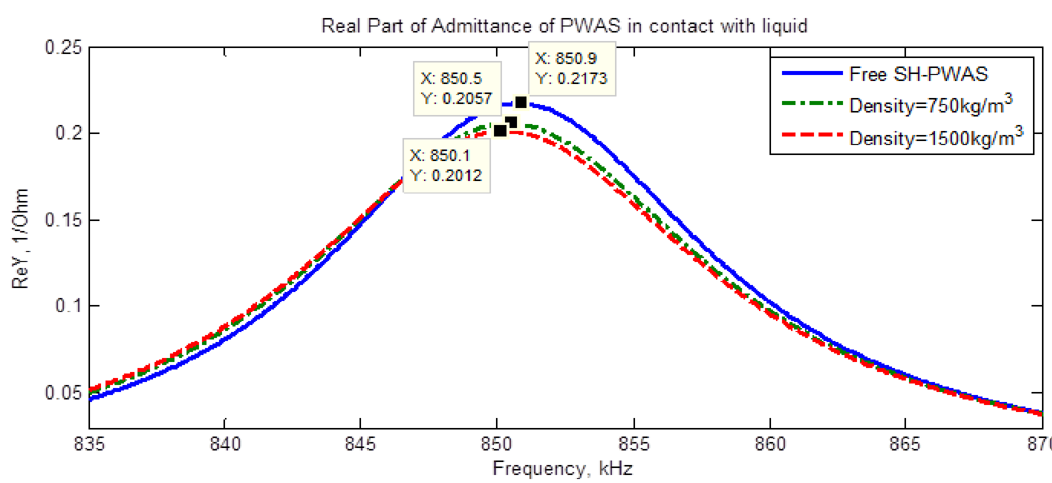


Figure 8.20 First peak of admittance for PWAS resonator in 15mm of length, 15mm of width, and 1mm of thickness in free condition and in contact with liquid with different densities and both liquid viscosities are assumed to be 1.0 Pa.s

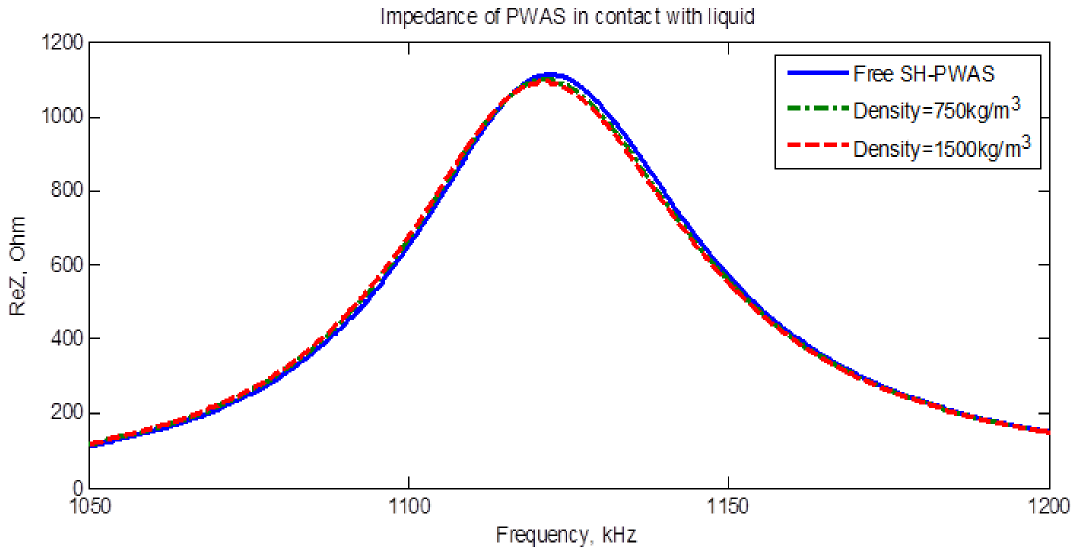


Figure 8.21 First peak of impedance for PWAS resonator in 15mm of length, 15mm of width, and 1mm of thickness in free condition and in contact with liquid with different densities and both liquid viscosities are assumed to be 1.0 Pa.s

## 8.5 EXPERIMENTAL ANALYSIS OF A PWAS INTERACTING WITH VISCOUS LIQUID

Electro-mechanical impedance measurements have been conducted for free PWAS and PWAS in different liquid media such as silicone oil and honey as seen in Figure 8.22. The real and imaginary E/M impedance and admittance results were compared based on amplitude and frequency shifts in in-plane and out-of-plane (thickness) modes. The objective is to relate the immitance results to the material property change of the liquid media to utilize EMIS to capture any change that occurs in liquid media such as density, conductivity or viscosity change.

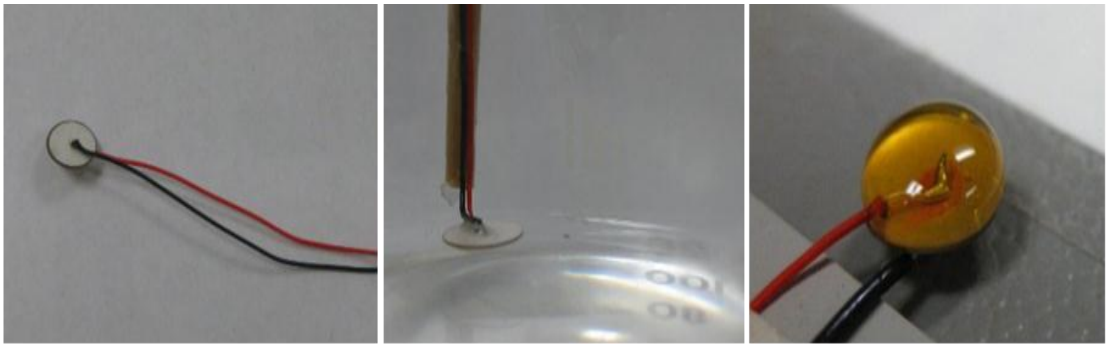

Figure 8.22 Free PWAS, PWAS with silicone oil and PWAS with honey

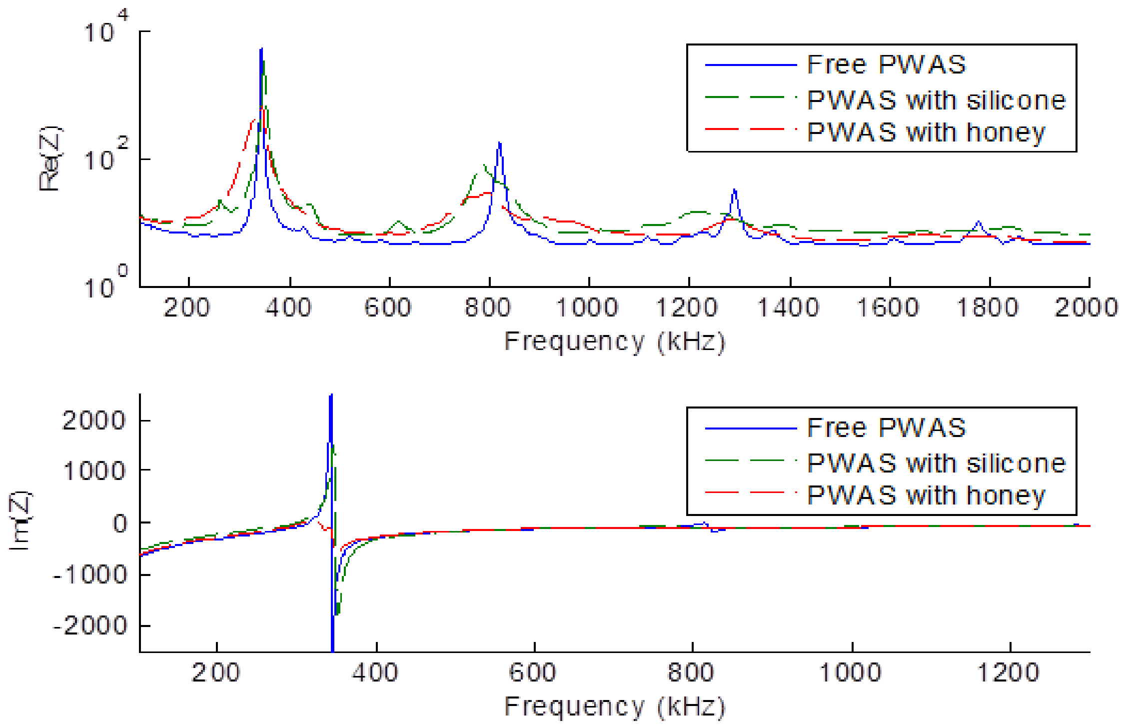


Figure 8.23 Real and imaginary impedance measurements for free PWAS; PWAS with silicone; and PWAS with honey

Nevertheless, developing the new method for sensing liquid domain requires more insightful investigation by conducting more experiments as well as analytical and numerical analyses to capture the trend in EMIS plots. The plots that are shown in Figure 8.23 and Figure 8.24 indicate some preliminary results.

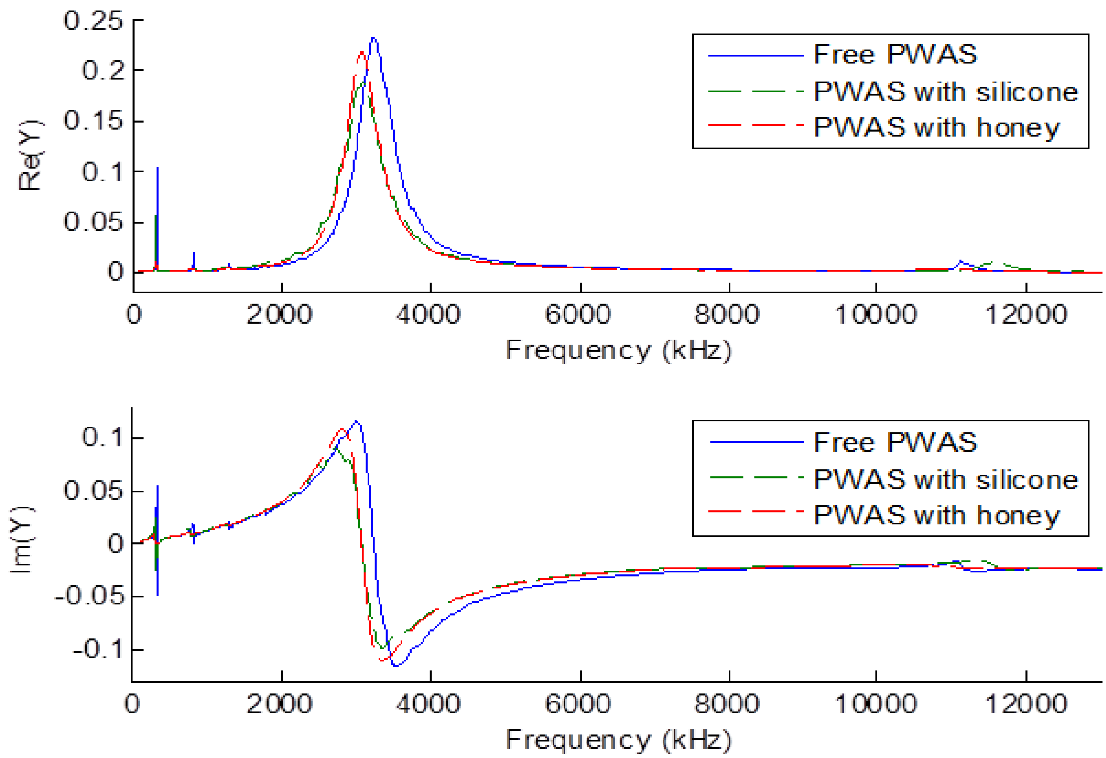


Figure 8.24 Real and imaginary admittance measurements for free PWAS; PWAS with silicone; and PWAS with honey

Presumably, the thickness mode of the EMIS results is more significant for the current PWAS-liquid configuration than the in-plane mode. Figure 8.25 illustrates significant shifts in frequency as well as amplitude as compared for PWAS in vacuum and PWAS in silicone oil and honey.

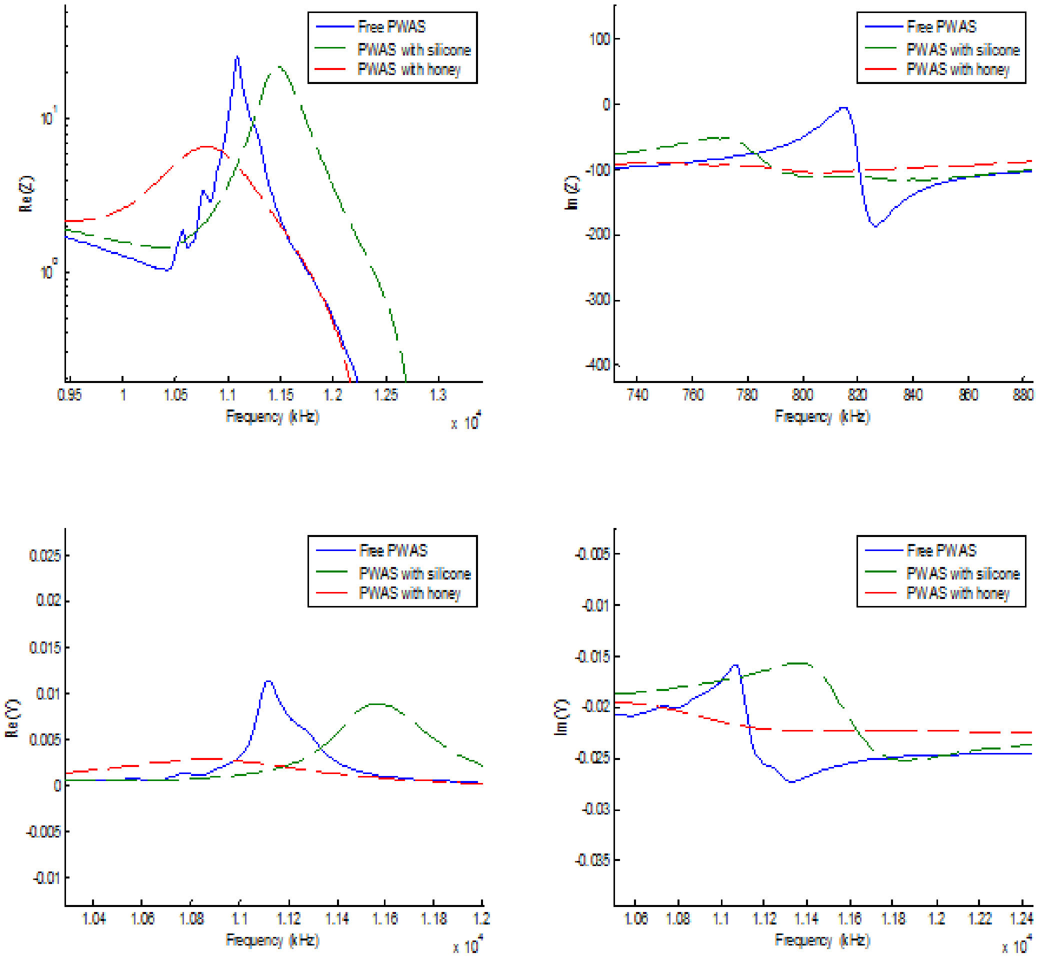


Figure 8.25 Thickness mode E/M impedance/admittance measurements

# CHAPTER 9

# PWAS GENERATED ULTRASONIC WAVES IN SOLID MEDIA

## 9.1 INTRODUCTION

Exploring and inventing new structural health monitoring (SHM) technologies enables the industry to reduce the maintenance cost, shorten the service down time, and improve the safety and reliability of engineering structures. SHM methods have improved the management in both the health monitoring of aging structures by predicting the remaining life of the structure and the development of novel self-sensing smart structures by inclusion of sensors. Ultrasonic techniques are commonly used for validation of welded structures in many in-situ monitoring applications: in nuclear industry, in pressure vessel industry, in pipelines, and in a range of naval applications. The tuned quasi-Rayleigh wave mode is essential for the applications in the in-situ inspection of relatively thick structures with butt weld such as naval offshore structures.

The SHM sensors that are capable of active interrogation are called piezo-ceramic wafer active sensors (PWAS). They are widely employed as in-situ ultrasonic health monitoring active sensors in wide frequency band. They can also be used as transmitters that produce traveling waves in a structure so that SHM active and passive sensing can be conducted for interrogation of the structure through wide-band PWAS that generates propagating guided ultrasonic waves in substrate structure to detect damages e.g. crack or corrosion by interrogating the structure with certain tuned wave modes (Giurgiutiu, 2008).

This chapter deals with a basic aspect of the interaction between PWAS and structure during the active SHM process, i.e., the tuning between the PWAS and the Lamb waves traveling in the structure. The PWAS devices are strain-coupled transducers that are small, lightweight, and relatively low-cost. Upon electric excitation, the PWAS transducers can generate Lamb waves in the structural material by converting the electrical energy into the acoustic energy of ultrasonic wave propagation (Yu et-al, 2008). In the same time, the PWAS transducers are able to convert acoustic energy of the ultrasonic waves back into an electric signal. Under electric excitation, the PWAS undergo oscillatory contractions and expansions, which are transferred to the structure through the bonding layer to excite Lamb waves into the structure. In this process, several factors influence the behavior of the excited wave: PWAS length, excitation frequency, wavelength of the guided wave, etc. We will show that tuning opportunities exist through matching between the characteristic direction of PWAS expansion and contraction (Lin et-al., 2012). The tuning is especially beneficial when dealing with multimode waves, such as the Lamb waves.

Lamb waves are a type of ultrasonic waves that are guided between two parallel free surfaces, such as the upper and lower surfaces of a plate. Lamb waves can exist in two basic types, symmetric and antisymmetric (Lin & Giurgiutiu, 2011). The Lamb wave motion has asymptotic behavior at low frequency and high frequency. At low frequency, the symmetric mode resembles axial waves, while the antisymmetric mode resembles flexural waves. At high frequency, both symmetric and antisymmetric wave approaches

Rayleigh waves, because the particle motion is strong at the surfaces and decays rapidly across the thickness. The axial wave and flexural wave, by their nature, are only low frequency approximations of Lamb waves. The plate structure cannot really sustain pure axial and flexural motion at large frequency-thickness product values.

Rayleigh wave that resembles to axial wave mode is an elastic wave that propagates close to free surface with as low penetration into the medium as of the order of its wavelength. Rayleigh wave in an isotropic elastic medium are in many cases an appropriate tool for ultrasonic inspection by utilizing the useful property of Rayleigh waves, the propagation speed is independent of frequency (12). Rayleigh wave, the high frequency guided wave mode in isotropic plates, was interpreted as the convergence of the first anti-symmetric $A_0$ and symmetric $S_0$ Lamb wave modes by Chew & Fromme (2014). It can be seen in dispersion curves of Lamb wave modes that for large frequency-thickness products, the wave speeds of $A_0$ and $S_0$ Lamb wave modes coalesce at the wave speed of a Rayleigh wave. In the literature, the Rayleigh wave a.k.a surface acoustic wave or surface guided wave has been utilized for in-situ monitoring of many types of defects in a medium. Chew & Fromme, 2014; Fromme, 2013; Masserey & Fromme, 2014 used Rayleigh waves for detection of fatigue crack growth and corrosion through wall thickness with theoretical predictions for the thickness loss.

Experimental study of PWAS Lamb-wave tuning concept is presented. PWAS transducers in different sizes are investigated. A sweet spot for the excitation of $S_0$ Lamb wave mode, which is preferred for certain SHM applications, is illustrated.

## 9.2 TUNING CURVES FOR LAMB WAVE MODES IN THIN PLATE

PWAS pitch-catch setup in 1-D model is shown in Figure 9.1. PWAS transmitter A with length $l_A$ locates at location $x_A$ , PWAS receiver B with length $l_B$ locates at location $x_B$. For pitch-catch setup, we have two forces at PWAS A and B. For the comparison, each PWAS need to be used as an actuator and a receiver.

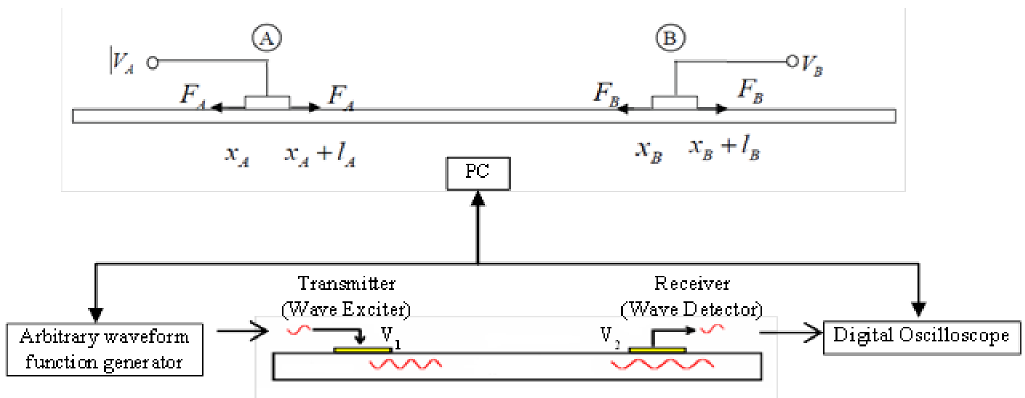


Figure 9.1 Schematic of a PWAS pitch-catch setup on a bar.

The consistence of PWAS bond is essential to the correct damage detection. We first checked the capacitance of each sensor on the aluminum plate and compared with theoretical free capacitance.

Table 9.1 Free Capacitance for 7mm round PWAS with 0.2mm and 0.5mm thickness

| | Thickness mm | Diameter mm | $\varepsilon_{33}^T / \varepsilon_0$ | Theoretical Capacitance nF | Measured mean Capacitance nF |
|---|---|---|---|---|---|
| SM-412 | 0.5 | 8.7 | 1350 | 1.4205 | 1.49456 |
| APC-850 | 0.2 | 7 | 1350 | 2.299 | 2.38 |
| | $\varepsilon_0 = 8.85e-12$ | | | | |

We also monitored the receiver voltage output. It is clear that S0 and A0 wave are separated. S0 is not dispersive and A0 is dispersive. The wave propagation is best illustrated through the study of the propagation of single frequency wave packets (tone bursts). A tone burst consists of a single-frequency carrier wave of frequency, whose amplitude is modulated such as to generate a burst-like behavior. The excitation signal used in this application is 3-count 10V amplitude 50 kHz Hanning windowed tone burst. The excitation voltage signal is shown in Figure 9.2-a. The receiver output voltage is shown in Figure 9.2-b. The first wave pack is axial wave that is not dispersive. The second wave pack is flexural wave that shows the dispersive nature. The third wave pack is the axial wave reflected from the boundary and received by the receiver.

Table 9.2 Material properties of SM 412 piezo-electric wafer active sensor

| PROPERTY | UNIT | SYMBOL | SM412 |
|---|---|---|---|
| EQUIVALENCE | | | PZT-5A |
| | | | Navy Type II |
| Electromechanical Coupling Coefficient | | $K_p$ | 0.63 |
| | | $K_t$ | 0.42 |
| | | $K_{31}$ | 0.35 |
| Frequency Constant | Hz.m | $N_p$ | 2080 |
| | | Nt | 2080 |
| | | $N_{31}$ | 1560 |
| Piezoelectric Constant | $x10^{-12}$ m/V | $d_{33}$ | 450 |
| | | $d_{31}$ | -190 |
| | $x10^{-3}$ Vm/N | $g_{33}$ | 25.6 |
| | | $g_{31}$ | -12.6 |
| Elastic Constant | $x10^{10}$ N/m$^2$ | $Y_{33}$ | 5.6 |
| | | $Y_{11}$ | 7.6 |
| Mechanical Quality Factor | ------- | $Q_m$ | 100 |
| Dielectric Constant | @1KHz | $\varepsilon_{T33}/ \varepsilon_0$ | 1850 |
| Dissipation Factor | %@1KHz | $\tan\delta$ | 1.2 |
| Curie Temperature | $^0$C | $T_c$ | 320 |
| Density | g/cm$^3$ | $\rho$ | 7.8 |

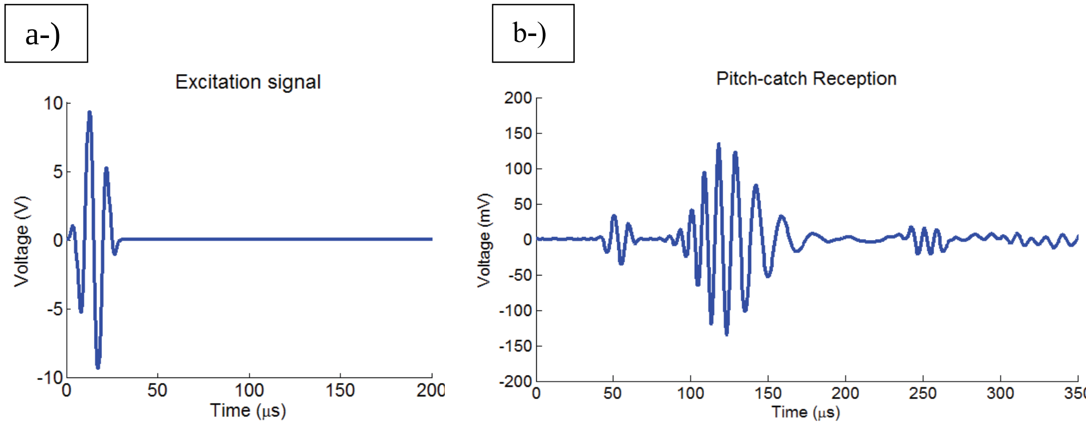


Figure 9.2 a-) Transmitter non-harmonic excitation signal b-) Receiver voltage response under a 3-count 100 kHz tone-burst excitation.

In 3-D model, the PZT polarization is along the z-axis. The free-free aluminum alloy 2024 beam dimension is 1220 mm long, 1220 mm wide, and 1 mm thick. The diameters of the PZT active sensors are 7 mm and thickness dimensions are 0.2 mm and 0.5 mm respectively. The distances between PWAS locations are as shown in Figure 9.3. An experimental setup is shown in Figure 9.4.

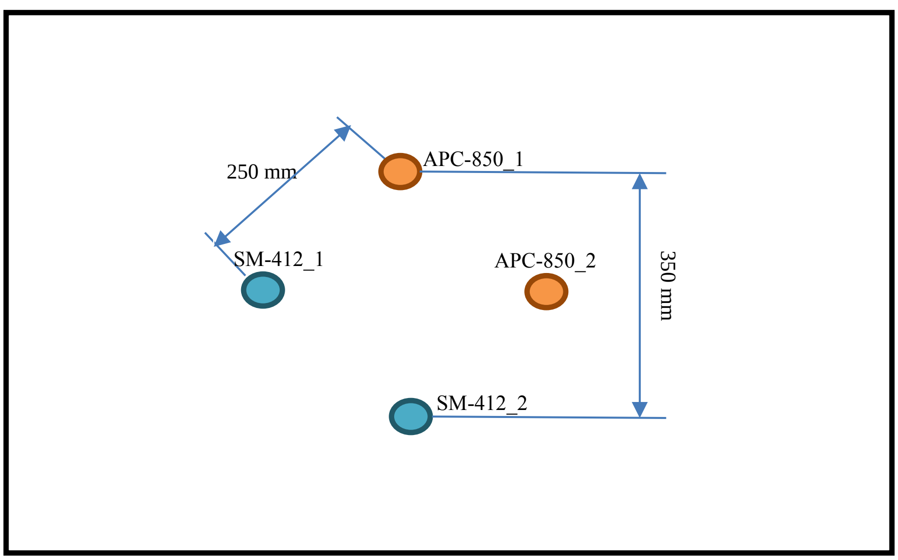


Figure 9.3 Schematic of the panel specimen and PWAS configuration

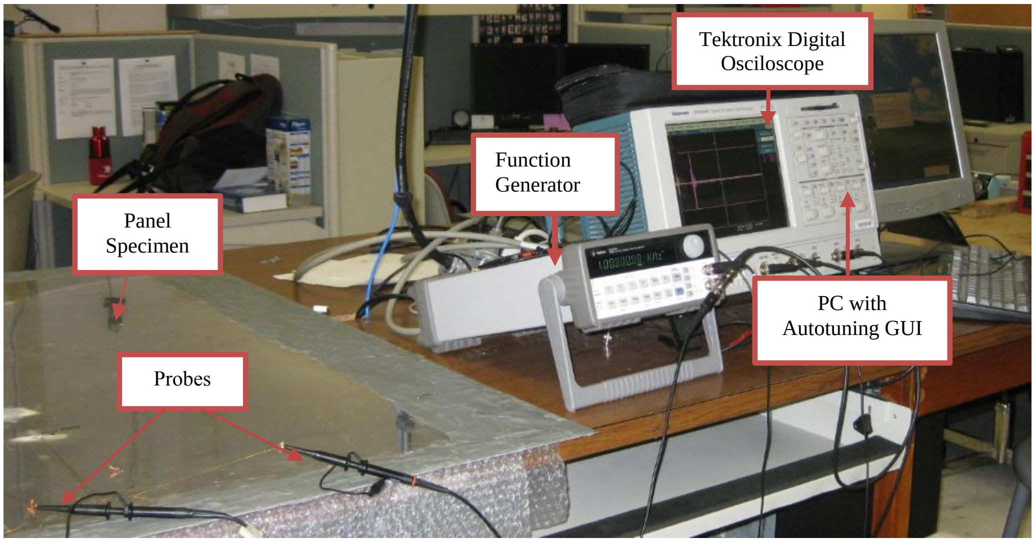


Figure 9.4 Experimental setup for assessing the difference between new (thicker) PWAS and conventional PWAS

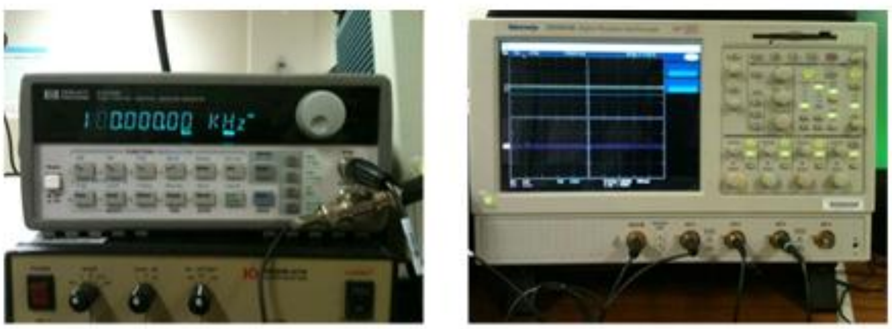

(a) (b)

Figure 9.5 The wave propagation experiment instruments a-) Function generator (Hewlett Packard 33120 A 15 MHz function/ arbitrary waveform generator) b-) Digital oscilloscope (Tektronix TDS5034B Digital Phosphor Oscilloscope 350 MHz 5GS/s)

Lamb waves signals received by PZT active sensor which was employed as a receiver were recorded by using Autotuning Graphical User Interface (GUI) developed by Patrick Pollock in LAMSS (Laboratory for Active Materials and Smart Structures) utilizing National Instruments LABVIEW software. The received data were composed in tdms format by the Autotuning GUI.

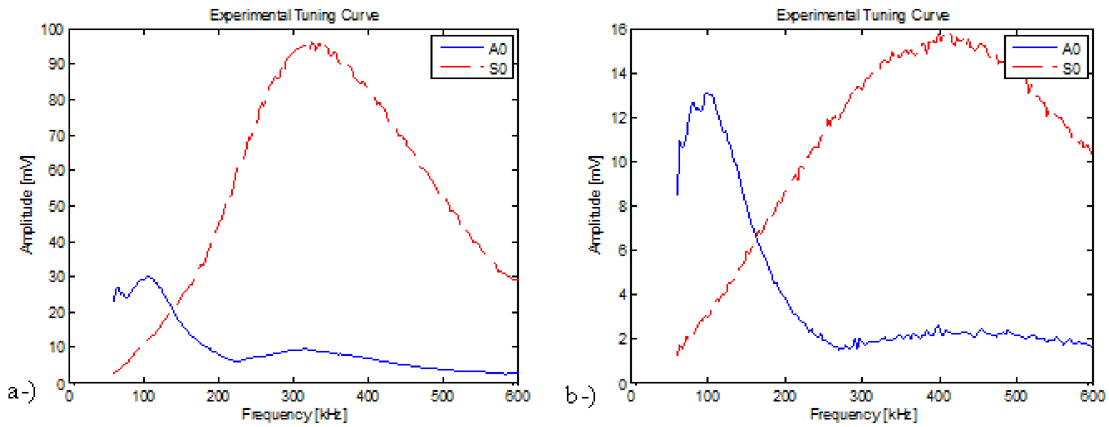


Figure 9.6 Tuning curves obtained by using pitch-catch method generating and sensing Lamb wave propagation with a-) a transmitter and a receiver both having the same diameter of 8.7mm and thickness of 0.5mm b-) a transmitter and a receiver whose diameter 7mm and thickness 0.2mm

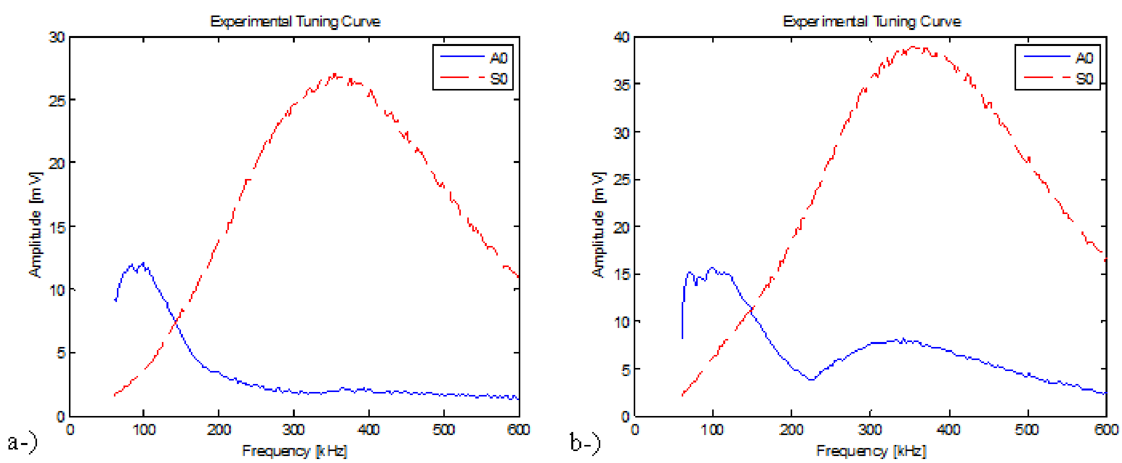


Figure 9.7 Tuning curves obtained by using pitch-catch method generating and sensing Lamb wave propagation with a-) a transmitter having the diameter of 8.7mm and thickness of 0.5mm a receiver having the diameter of 7mm and thickness of 0.2mm b-) a transmitter having the diameter of 7mm and thickness of 0.2mm a receiver having the diameter of 8.7mm and thickness of 0.5m

The data has been manually imported into Microsoft Excel files. A MATLAB program was also developed to postprocess the data listed on the Excel files and the

MATLAB program has generated the plots indicating tuning curves and anti-symmetry and symmetry modes as shown in Figure 9.6 and Figure 9.7. The data taken using the experimental setup shown in Figure 9.4 are corresponding to four different cases. In the first case, both transmitter and receiver are PWAS having thickness of 0.5 mm which were denoted as APC-850_1 and APC-850_2 respectively. In the second case, both PWAS are conventional ones having thickness of 0.2 mm and being referred as APC-850_1  and APC-850_2. In the third case, the SM-412_1 was assigned to be a transmitter and APC-850_2 a receiver. For the fourth case, APC-850_1 was connected to the probe – which was also connected to the function generator - as a transmitter, and SM-412_2 was connected to the other probe as a receiver.

In the first case, as expected, the thicker PWAS generated somewhat higher response in amplitude for both anti-symmetry and symmetry mode in comparison to those in the other PWAS configurations. A0 wave pack shows up at lower frequency and reaches the peak amplitude at around 100 kHz in all four transmitter-receiver configurations. S0 wave pack amplitude appears to be increasing up to 300 kHz for three configurations whereas only for the APC-850_1-APC-850_2 configuration, the amplitude of S0 mode increases up to 400 kHz. The tuning curves for A0 and S0 wave packages intersects at 145 kHz in all PWAS configurations, which means that A0 and S0 amplitudes become equal at that frequency. And the other significant outcome from the comparison is the fact that the peak amplitude value of A0 tuning curve (13.5 mV) is very close to the peak amplitude value of S0 tuning curve (15.5 mV) while the peak amplitude of A0 mode is much lower than that of S0 wave package where the thicker PWAS was used either as a transmitter or as a receiver or as both (in the first config.).

## 9.3 TUNING CURVES FOR QUASI-RAYLEIGH WAVE IN THICK STRUCTURES

Rayleigh waves i.e. surface acoustic waves (SAW) are a high frequency approximation of the fundamental symmetric (S0) and anti-symmetric (A0) Lamb wave modes as the frequency becomes relatively high as seen in Figure 9.8. S0 and A0 wave speeds converges into the same value and become constant i.e. non-dispersive which is exactly the Rayleigh wave speed. Eventhough the condition for Rayleigh wave is that it can only travel along a flat surface of a semi-infinite medium, which is hardly possible to generate in reality, when the plate thickness is larger than the Rayleigh wavelength at that frequency, $d \gg \lambda_{R,}$ the measurements should be acceptable. The wave mode is then called quasi-Rayleigh wave having Rayleigh wave speed.

### 9.3.1 QUASI-RAYLEIGH WAVE TUNING THEORY

Rayleigh wave speed depends on the shear wave speed and the Poisson ratio. A common approximation of the wave speed of the Rayleigh wave is given in the form

$$
\begin{aligned}
c_S &= \sqrt{\frac{E}{2(1+\nu)\rho}} \\
c_R &= c_S \frac{(0.87+1.12\nu)}{1+\nu}
\end{aligned}
\tag{9.1}
$$

For more detailed derivation, the readers are suggested to read through chapter 6 of the reference by Giurgiutiu (2014).

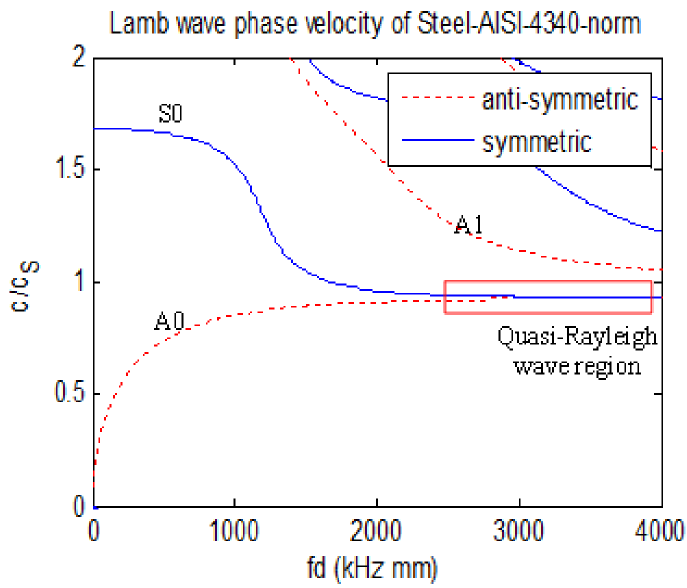


Figure 9.8. Phase velocity dispersion curves of Lamb wave modes in a steel plate where $c_s$=3062.9 m/s indicating the quasi-Rayleigh wave approximation of fundamental Lamb wave modes in high f.d product

The dispersion curves, the displacement vectors, and the mode shapes through thickness are calculated using a MATLAB® graphical user interface (GUI) named 'Modeshape_v2e'(Bao & Giurgiutiu, 2003) generated in Laboratory for Active Materials and Smart Structures (LAMSS). In Figure 9.9, the displacement vectors for S0 mode on the left and the S0 mode shape on the right are given as well as in Figure 9.10, the displacement vectors for A0 mode on the left and the A0 mode shape on the right are given. In mode shape across thickness plots shows both the in-plane and out-of-plane displacement changes, the continuous lines depict the in-plane displacement $u_x$ and the dotted lines depict the out-of-plane displacement $u_y$ (Bao, 2003).

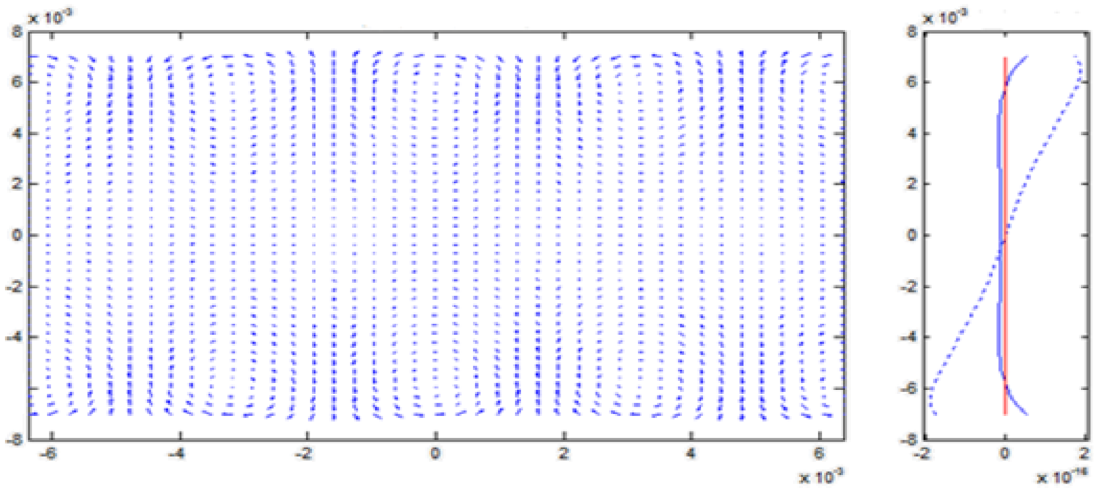

Figure 9.9. (a) Displacement vectors in 14 mm thick steel plate at central frequency of 450 kHz in the form of the first symmetric Lamb wave mode and (b) the mode shape through thickness

At $fd = 3150$ kHz.mm, the $u_x$ displacement is almost zero over the inner 80% part of the thickness, while most of the activity happens in the upper and lower 20% parts; the $u_y$ displacement on the surface is almost twice as large as that on the mid-surface Figure 9.10(b).

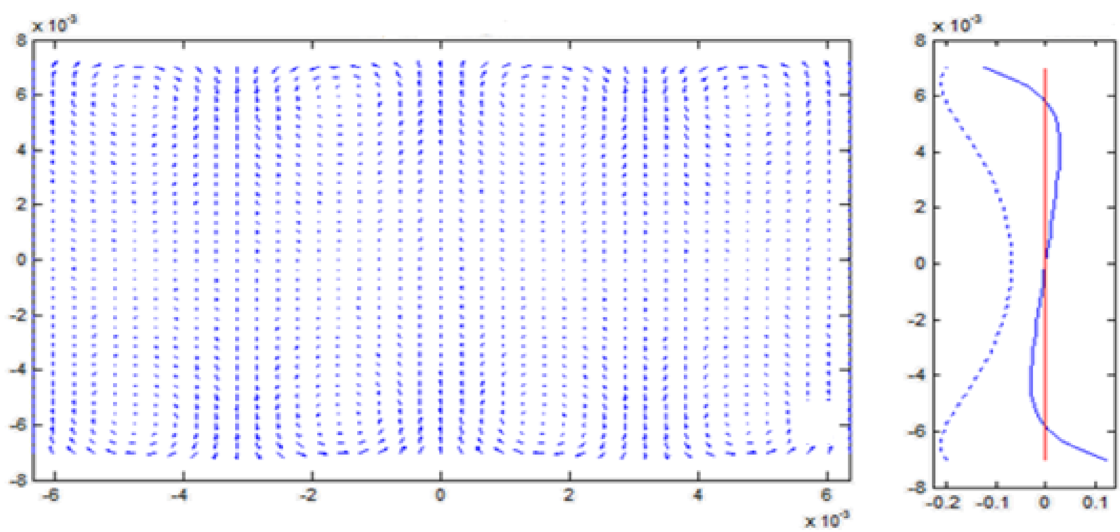

Figure 9.10. (a) Displacement vectors in 14 mm thick steel plate at central frequency of 450 kHz in the form of the first antisymmetric Lamb wave mode and (b) the mode shape through thickness

The tuning curve of quasi-Rayleigh strain wave (Figure 9.11) is calculated using the strain function which depends on the distance between the transmitter and the receiver PWAS and the expression is shown in Eq(9.2).

$$\varepsilon(x) = i\varepsilon_a(\sin\xi_0 a)e^{i(\xi_0 x - \omega t)} \tag{9.2}$$

where $\xi_0 = \omega^2 / c_R^{\ 2}$ is the wavenumber of Rayleigh waves in the 1-D medium $\varepsilon_a = d_{31}E_3$ is the induced strain and assumed to be uniform over the PWAS length(Victor Giurgiutiu, 2008d). The distance between PWAS transducers is measured to be 460 mm. The elastic modulus of steel is assigned to be 190 GPa, the density is 7850 kg/m$^3$, the Poisson ratio is 0.29. The electrical parameter such as the induced voltage is 80V and the piezoelectric parameter $d_{31}$ is -175x10$^{-12}$ m/V. The analytical tuning curve agrees well with the experimental tuning curves plots in Figure 10.12.

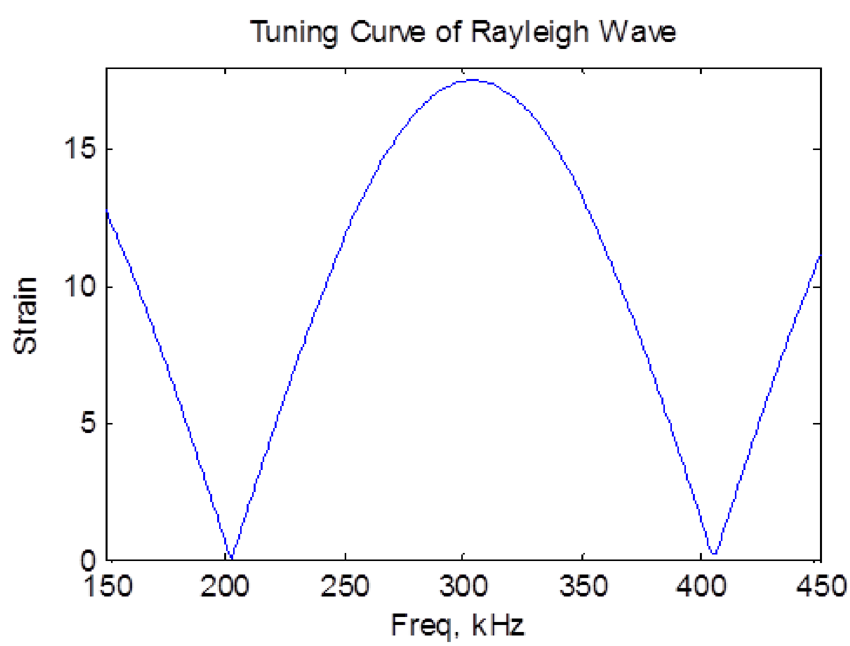


Figure 9.11. Analytical tuning curve of Rayleigh wave in steel plate

### Mode-Shape Analysis

The mode shape analysis is conducted in order to depict the resemblance between mode shapes obtained from the standing wave analysis and the mode shapes acquired from the propagating guided Lamb wave analysis. The mode shapes begin to have this similarity as approaching to the QRW region shown in the phase velocity dispersion curve.

In both standing and guided wave mode shape analyses, the material properties used for PWAS are shown in Table 3.1. The density of aluminium substrate is assumed to be 2780 kg/m$^3$ and the elastic modulus is 72 GPa. The plate thickness is 2.1 mm and the PWAS thickness is 0.2mm. The mode shapes from both analyses are presented at the same resonance frequencies in this study. The thickness mode resonance frequencies are respectively 1.19 MHz, 2.49 MHz, and 3.85 MHz.

### Standing wave mode shape analysis

The standing wave analysis uses the axial wave approximation across the thickness of PWAS and the aluminium plate-like structure that hosts the PWAS. The mode shapes at certain thickness mode resonance frequencies are shown in Figure 9.12.

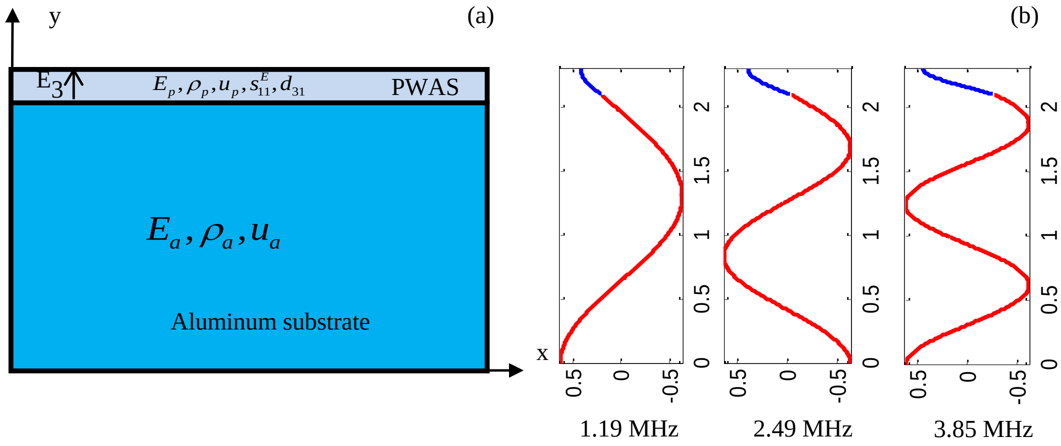


Figure 9.12 (a) Schema of PWAS transducer ideally bonded on aluminum plate and (b) high frequency modal analysis results considering the standing waves in thickness mode for PWAS bonded on aluminum plate: plate thickness=2.1 mm, PWAS thickness=0.2mm.

Guided wave mode shape analysis

The guided wave analysis uses the Lamb wave (superposition of axial and flexural wave approximation) propagating in a plate. The mode shapes across the thickness of the aluminium plate structure are simulated. The mode shapes at certain thickness mode resonance frequencies are shown in Figure 9.14

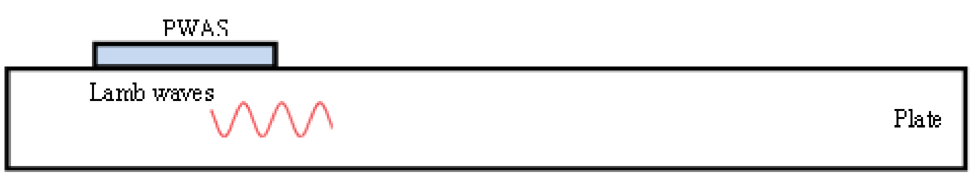


Figure 9.13 Schema of PWAS transducer ideally bonded on aluminum plate

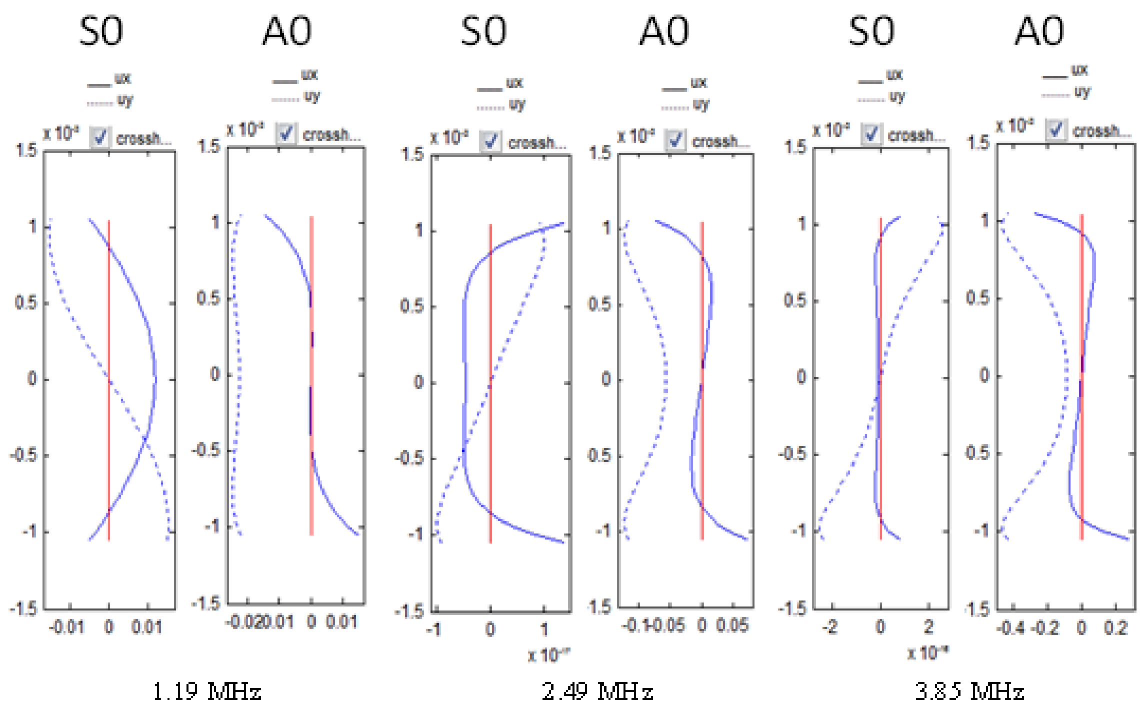


Figure 9.14 High frequency modal analysis results considering the guided waves in thickness mode for PWAS bonded on aluminum plate: plate thickness = 2.1 mm, PWAS-thickness=0.2mm.

As considering the mode shapes from both standing and guided wave analysis, the similarity between the first standing axial wave mode shape and the S0 mode shape is obvious because the S0 mode is non-dispersive alike axial wave at 1.19 MHz. However, the similarity occurs between the second thickness mode shape and the A0 mode at 2.49 MHz. since A0 mode is predominant having much higher displacement amplitude than that of S0 mode. A0 mode also becomes non-dispersive as the structure is excited at the second resonance frequency. At the third thickness mode, since A0 is predominant and non-dispersive, the resemblance still occurs between the third thickness mode shape and the A0 mode shape. The structure is actually excited in the QRW region as the excitation frequencies are at the second and third thickness mode resonance frequencies.

### 9.3.2 EXPERIMENTAL STUDY FOR QUASI-RAYLEIGH WAVE TUNING

In this experimental setup, PWAS transducers serve as high-bandwidth strain sensors for active sensing of far-field. Transmitter PWAS bonded on a substrate structure excites the structure by induced voltage in tone-burst sine wave form with three-counts through the function generator. Then, receiver PWAS senses the wave signals traveling in certain modes along the structure and the received signals as output voltage are read by the oscilloscope in time domain and recorded for post-processing the data.

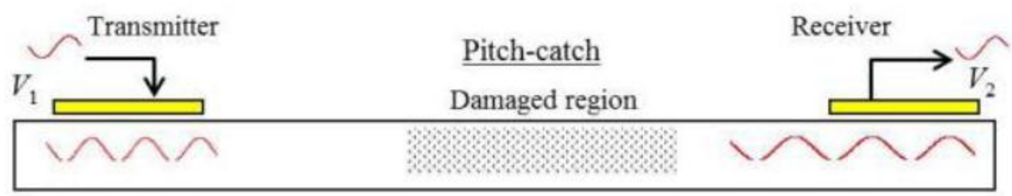


Figure 9.15 Schema of pitch-catch sensing method (Giurgiutiu, 2008)

In the both EMIS and GWP experimental setup, pristine aluminum and steel specimens are used. PWAS transducers are bonded on the short edges and clay is applied on both long edges to avoid reflections and obtain more clear signals.

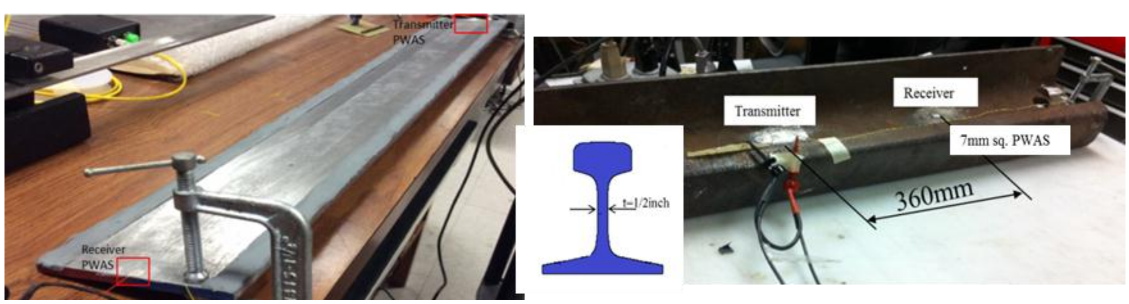


Figure 9.16 (a) ¼" thick, 4" width, 3' length high strength 2024 aluminum plate (b) A pristine steel rail I-beam ½" thick

A steel rail beam which is adequate wave guidance is also used for GWP test as another specimen. 7mm x 7mm x 0.2mm PWAS transducers are bonded on both specimens.

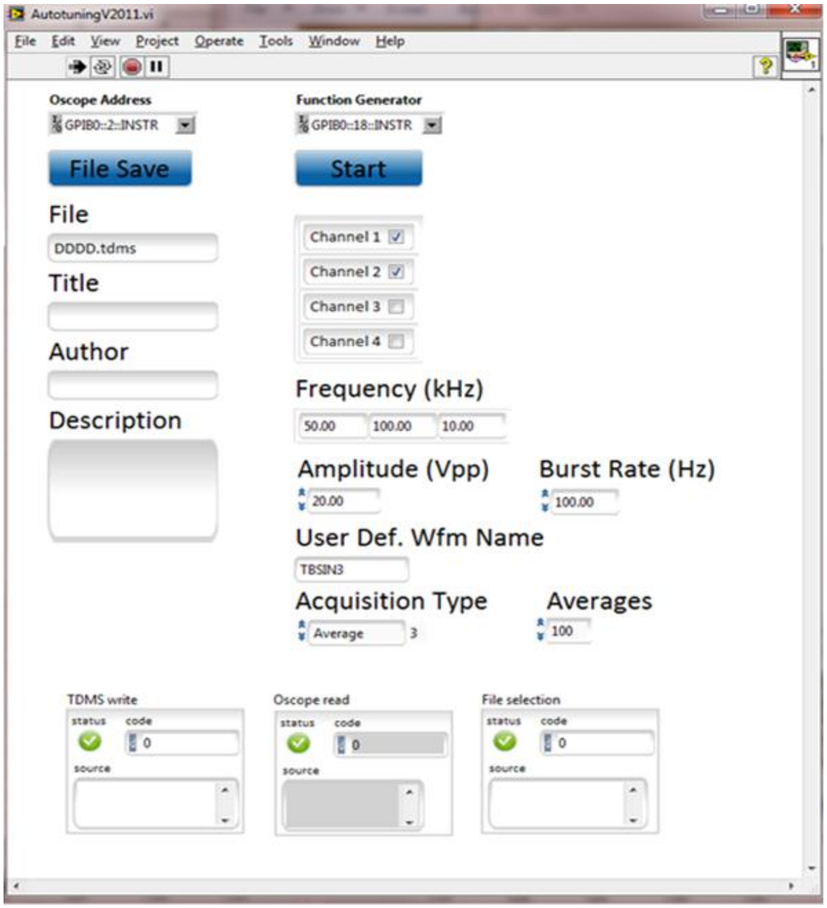


Figure 9.17 Autotuning2011 Graphical user interface (GUI),Laboratory for Active Materials and Smart Structures (LAMSS)

Autotuning GUI (Figure 9.17) -developed in LAMSS using LabView software- is utilized to control the function generator and automatically sweep the predefined frequency band and record the data for each frequency step in an excel file then eventually post-process the data to generate the tuning curve for certain wave packets in the received signals.

A square PWAS in 7mm x 0.2mm dimensions is modeled as a layer on a homogeneous isotropic material (aluminum) substrate layer. The density of the aluminum substrate is 2780 kg/m$^3$ and the elastic modulus is 72.4 GPa. Electromechanical material properties of the piezoelectric transducer are defined in Table 9.2.

Two SM412 PWAS are bonded by the two ends of the aluminum specimen (Figure 9.16) in distance of 910mm to each other. GWP test has been conducted on the specimen using the PWAS transducers as transmitter in this task. Tone-burst sine wave with 3 counts is generated through the function generator to excite the transmitter PWAS and generate a strain wave into the host aluminum plate. The guided wave information travels in the material in different modes and at various wave speeds depending on the excitation frequency-thickness product. In this particular study, we are interested in Rayleigh wave mode, therefore we selected relatively high excitation frequency band to receive the signal dominated by Rayleigh wave modes as can be seen in a few examples of received Rayleigh wave signals (Figure 9.18) that travels at constant wave speed i.e. independent from frequency change. The all received wave signals show that Rayleigh wave packet appears distinguishably dominating among other wave packets at the same time window eventhough the frequency increases in the range between 300 kHz and 600 kHz. The Rayleigh wave packets appear at even as low frequency as 180 kHz up to 1.8MHz however the amplitude dramatically decreases after 1MHz as realized by studying the tuning curve compiled from the experimental data. The tuning curve in the frequency band between 150-600 kHz is illustrated in Figure 9.19. The upper plot shows the analytical calculation of Rayleigh wave tuning curve whereas the lower plot shows the experimental reading of the tuning curve. The trend the analytical and experimental tuning curves agree somewhat closely. They possess the valleys and hills appear in the same frequency bands.

The smooth trends that Rayleigh wave packet draws over frequency and distinguishability of dominating wave packet are promising features that eases predictability and signal processing. As the thicker specimens are analyzed, it's realized that the frequency band where Rayleigh wave packets appear becomes higher. Therefore, it gives the advantage of having the Rayleigh wave mode in also local thickness mode modal sensing because thickness mode EMIS is also for relatively high frequency range in order of MHz. Since Rayleigh wave resembles to the axial wave which has constant wave speed with respect to frequency as seen in the dispersion plot, prediction of the E/M impedance signature of the local structure in thickness mode becomes easier. One can use the proof-mass concept by increasing the thickness or density of the substrate analyzed to attain Rayleigh wave mode and downshift the local resonance frequency of PWAS-substrate structure so that the thickness mode constrained PWAS-EMIS signature becomes easily predictable by using the standing Rayleigh waves in local structural dynamic sensing

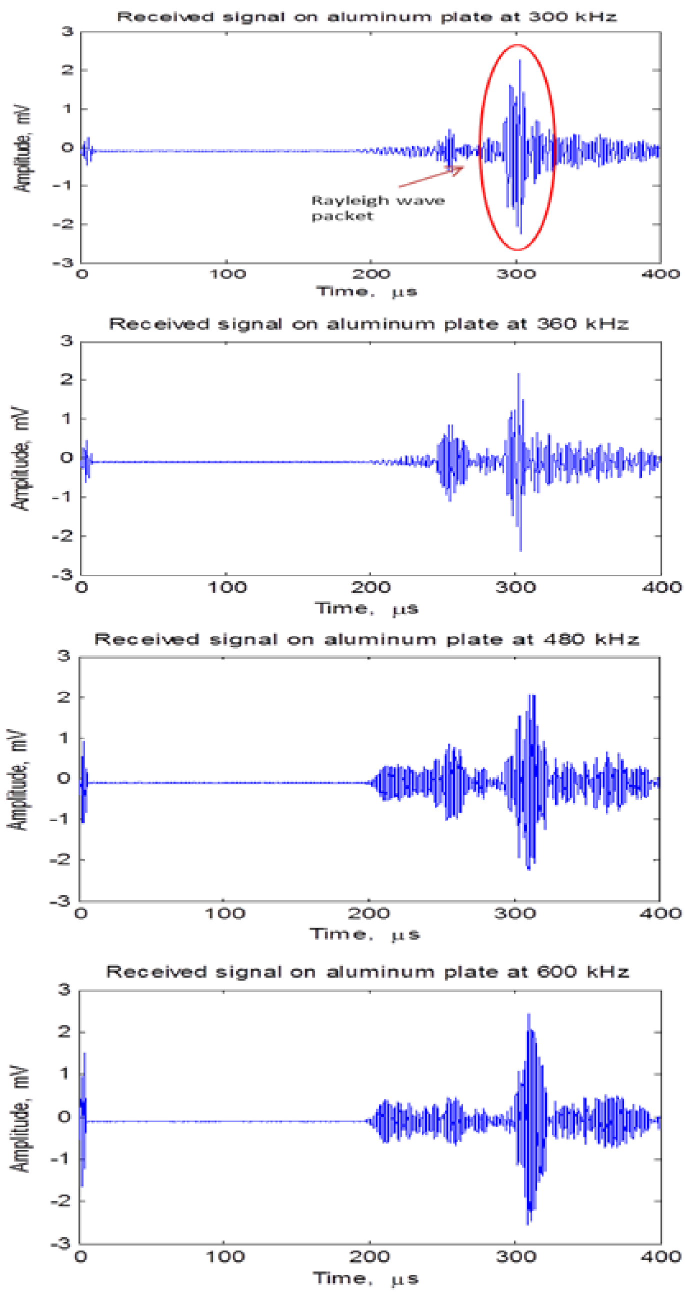


Figure 9.18 Received signals from 7x7 mm2 PWAS on
¼" thick aluminum plate at different frequencies

In Figure 9.20, Rayleigh wave phase velocity and time of flight are measured and compared with the calculation. The distance between the trasmitter-PWAS and the receiver-PWAS is 910mm. The material of the specimen is Aluminum 2024 with the elastic modulus of 72.4GPa, the density of 2780kg/m$^3$ and the Poisson's ratio of 0.33. The QRW tuning curve was predicted using these information regarding the material properties and pitch-catch configuration. The decent agreement between the analytical and the experimental tuning curves can be seen in Figure 9.19.

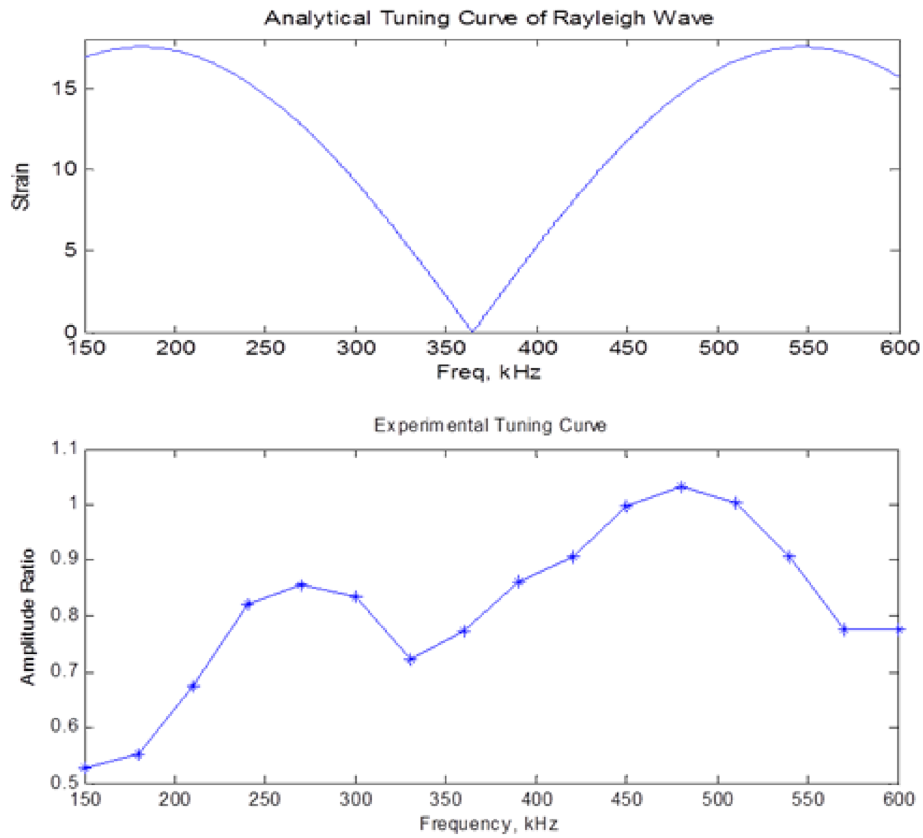


Figure 9.19 Analytical and experimental Rayleigh wave tuning curves for $7\text{mm}\times7\text{mm}\times0.2\text{mm}$ SM412 PWAS on 6.35 mm thick Aluminum-2024 plate with the elastic modulus of 72.4GPa, the density of 2780kg/m$^3$ and the Poisson's ratio of 0.33

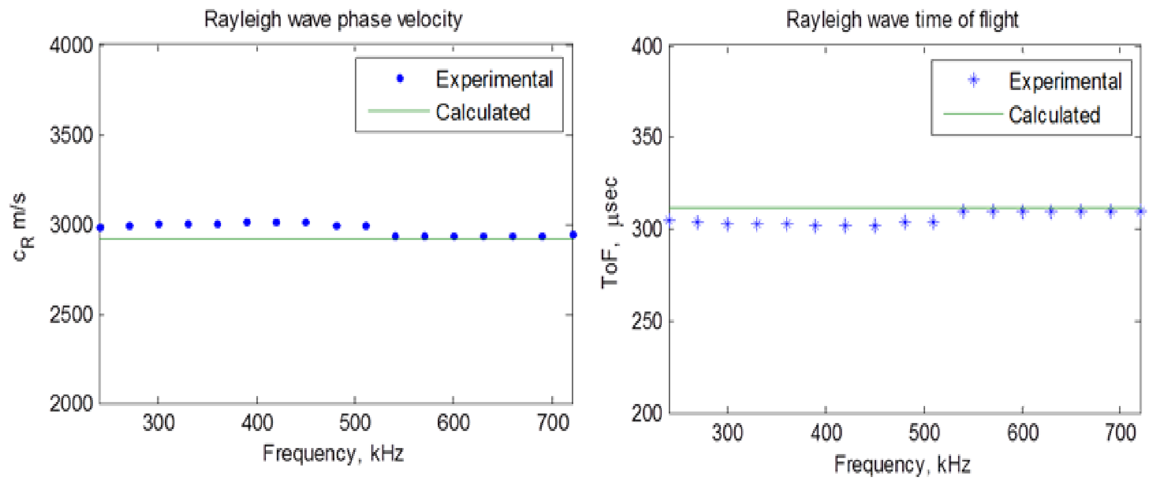


Figure 9.20 Rayleigh wave phase velocity and time of flight analytical and experimental results for the distance of 910mm between T-PWAS and R-PWAS on ¼" thick aluminum plate

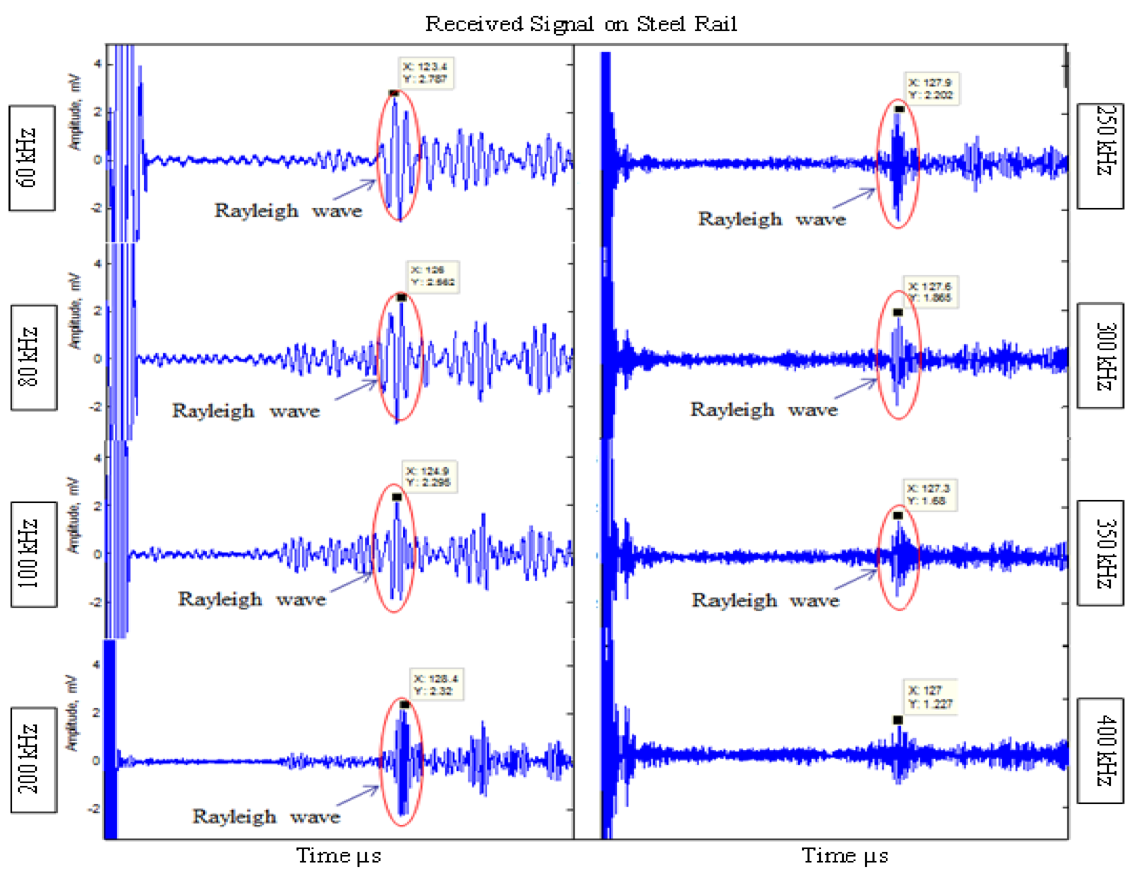


Figure 9.21 Received signals from 7x7 mm$^2$ PWAS on 1/2" thick steel rail I-beam at different frequencies

Another GWP test is presented on the rail I-beam using the PWAS transducers as transmitter and receiver in distance of 360mm. Tone-burst sine wave with 3 counts is generated for this test also to excite the transmitter PWAS and generate a strain wave into the host steel rail-beam. Rayleigh wave modes can be seen in a few examples of received Rayleigh wave signals (Figure 9.21) that travels at constant wave speed. The all received wave signals show that Rayleigh wave packet appears distinguishably dominating among other wave packets at the same time window eventhough the frequency increases in the range between 60 kHz and 400 kHz. The tuning curve in the frequency band between 150-600 kHz is illustrated in Figure 9.22. The upper plot shows the analytical calculation of the tuning curve whereas the lower plot shows the experimental reading of the tuning curve. The trends of the analytical and experimental tuning curves agree somewhat closely. They possess the valleys and hills appear in the same frequency bands.

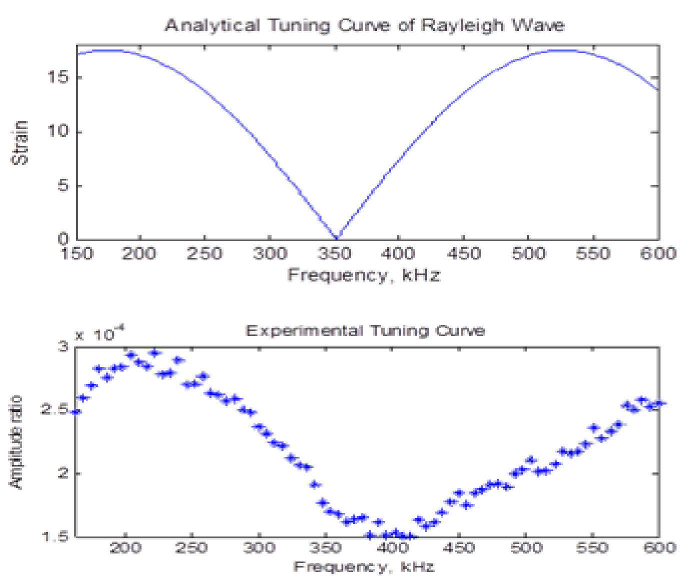


Figure 9.22 Analytical and experimental Rayleigh wave tuning curves for $7\text{mm}\times 7\text{mm}\times 0.2\text{mm}$ SM412 PWAS on 12.7 mm thick steel rail I-beam with the elastic modulus of 200GPa, the density of 7850kg/m$^3$ and the Poisson's ratio of 0.29

In Figure 9.23, Rayleigh wave phase velocity and time of flight are measured and compared with the calculation  by using Eqs. (9.1) and  respectively. The distance between the trasmitter-PWAS and the receiver-PWAS is 360mm. The material of the specimen is Steel-AISI-4340-400F with the elastic modulus of 190GPa, the density of 7850kg/m$^3$ and the Poisson's ratio of 0.29.

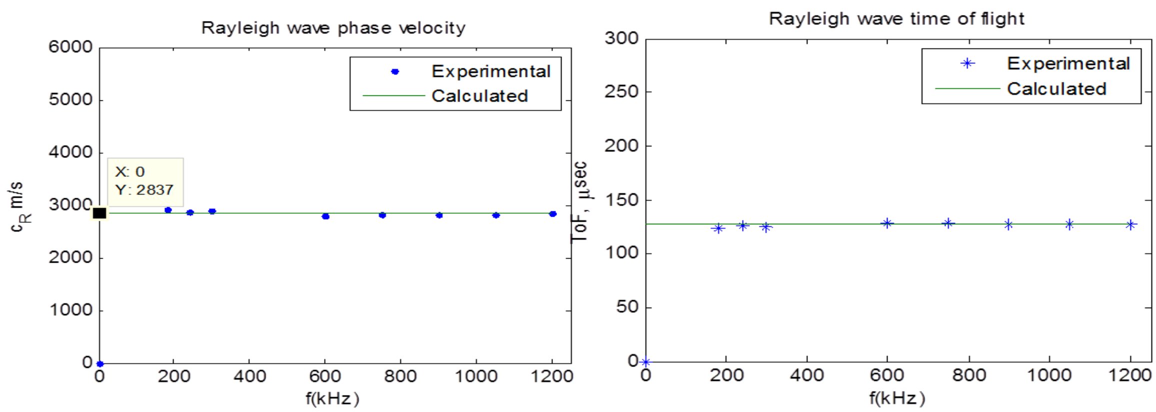


Figure 9.23 Rayleigh wave phase velocity and time of flight analytical and experimental results for the distance of 910mm between T-PWAS and R-PWAS on 12.7 mm thick steel rail I-beam

The steel specimen is 13.75 mm thick high temperature steel that has V-groove butt weld bead lying along the centre of the plate. The weld bead is around 1mm thicker than the steel plate. The welded thick steel plate specimen is produced using metal inert gas (MIG) welding and donated by Savannah River Nuclear Plant. In this particular study, we were interested in QRW mode, therefore we selected relatively high excitation frequency band to receive the signal dominated by QRW modes.

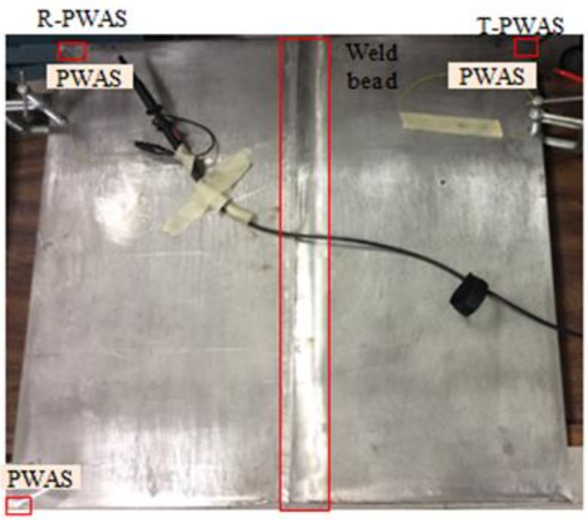


Figure 9.24 A pristine steel 13.75mm thick

The QRW tuning curve is predicted (Figure 9.25) by using the model defined in subsection-9.3.1 for the distance of 460 mm between the transmitter-PWAS and receiver-PWAS installed on a steel plate in thickness of 13.75 mm.

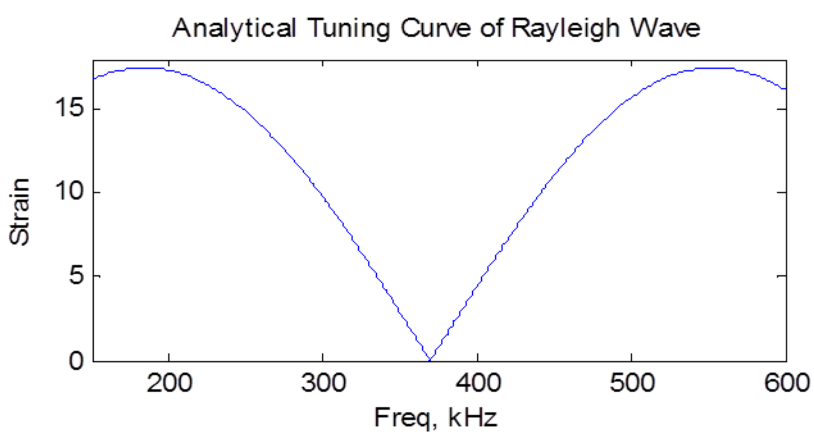


Figure 9.25 Quasi-Rayleigh wave tuning curve prediction for propagating wave in a distance of 460 mm in a thick steel plate in thickness of 13.75 mm

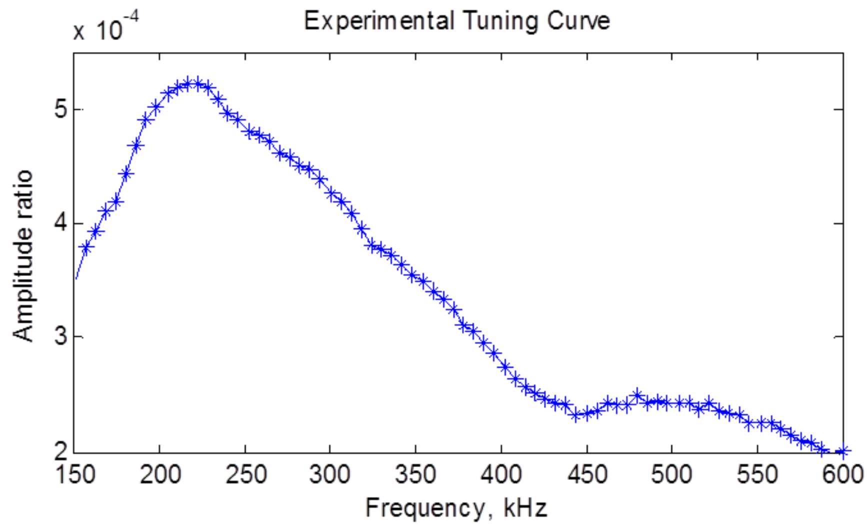


Figure 9.26 Quasi-Rayleigh wave tuning curve from pitch-catch test across the weld bead on a thick steel plate in thickness of 13.75 mm

The guided quasi-Rayleigh wave packets are determined in the received signals in time domain by using the time of flight information from the analytical quasi-Rayleigh wave speed prediction. Since QRW mode is non-dispersive i.e. constant speed at high excitation frequency-band, the location of the wave packet in time domain, time of flight, is also constant. Therefore, the time where the QRW packets are located was easily defined. Thus, the maximum amplitude of the non-dispersive wave QRW packets are captured as sweeping through the high excitation frequency-band between 150 kHz and 600 kHz where the QRW shows up in the thick steel plate. The maximum amplitudes of the wave packet in terms of the ratio between input voltage and output voltage are used to obtain the experimental tuning curve of the QRW mode that can be excited at relatively high frequency band and in thick structures. The two experimental QRW tuning curves are shown in Figure 9.26 and Figure 9.27. The first tuning curve (Figure 9.26) was obtained from the pitch-catch test conducted using two square PWAS situated on the edge of the steel plate that lie across the weld bead whereas the second tuning curve

(Figure 9.27) was from the pitch-catch test instrumented by PWAS transducers bonded on the plate edge along the weld bead as demonstrated in Figure 9.24.

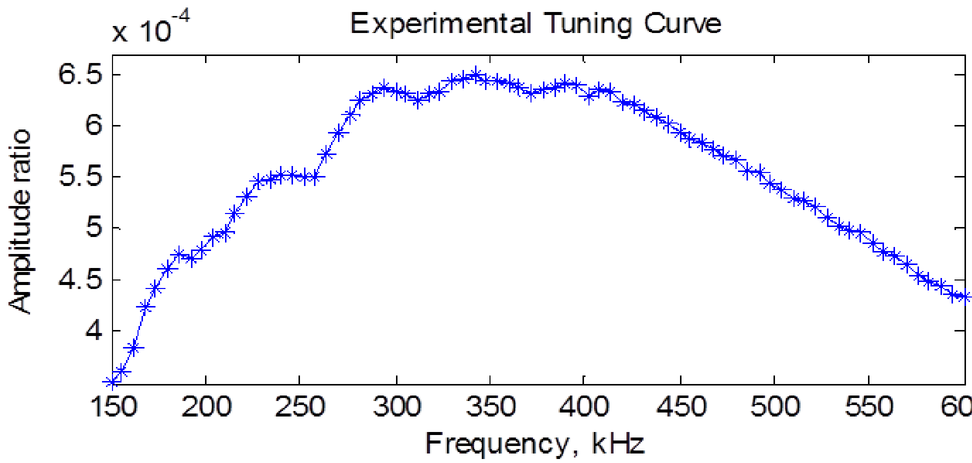


Figure 9.27 Quasi-Rayleigh wave tuning curve from pitch-catch test in direction of the weld bead on a thick steel plate in thickness of 13.75 mm

The agreement between the analytical tuning curve and the first experimental tuning curve is better in comparison with that of the second experimental tuning curve. This evidence depicts the effect of the weld bead on the tuning of the QRW mode. The higher amplitude of the second tuning curve that was obtained from the pitch-catch test along the weld bead was noticed as compared to that of the first tuning curve at corresponding excitation frequencies.

# CHAPTER 10

# WELD GUIDED WAVES IN THICK STRUCTURES

## 10.1 INTRODUCTION

Rayleigh waves are widely used in non-destructive testing (NDT) and SHM applications as well as in seismology. Rayleigh waves i.e. surface acoustic waves (SAW) are a high frequency approximation of the S0 and A0 Lamb waves as the frequency becomes relatively high, S0 and the A0 wave speeds coalesce and both have the same value. This value is exactly Rayleigh wave speed. They become non-dispersive wave, i.e. constant wave-speed along the frequency. Rayleigh wave can only travel along a flat surface of a semi-infinite medium, which is hardly possible to generate in reality however for the plate thickness $d >> \lambda_{R,}$ the measurements should be acceptable(Brook, 2012). The wave mode is then called quasi-Rayleigh wave having Rayleigh wave speed. (Tuncay Kamas, Giurgiutiu, et al., 2014) discussed the tuning effect of the thickness change and geometry of the substrate material on standing wave modes in local sensing and guided wave modes regarding especially tuned and guided quasi-Rayleigh wave mode propagating in the structure in various geometry and thickness.

In literature regarding weld guided waves, the weld guided compression (S0) mode was first experimentally investigated by (Sargent, 2006) in butt welded steel plate in 6 mm thickness for corrosion detection. (Juluri, Lowe, & Cawley, 2007) also studied the weld guided S0 and SH0 wave modes using semi-analytical finite element (SAFE) method. They simply simulated the butt-weld bead with thicker region in thickness of

18mm and in the width of 16mm lying between two steel plate in thickness of 6 mm. The compression mode leaks the SH0 wave in the plates when the velocity of the guided mode in the weld bead is higher than that of SH0 wave in the plate. (Fan & Lowe, 2009) carried out an elaborate study and discussed in general the feature guided waves in relatively low frequency range and the physical phenomena of feature guided wave modes.

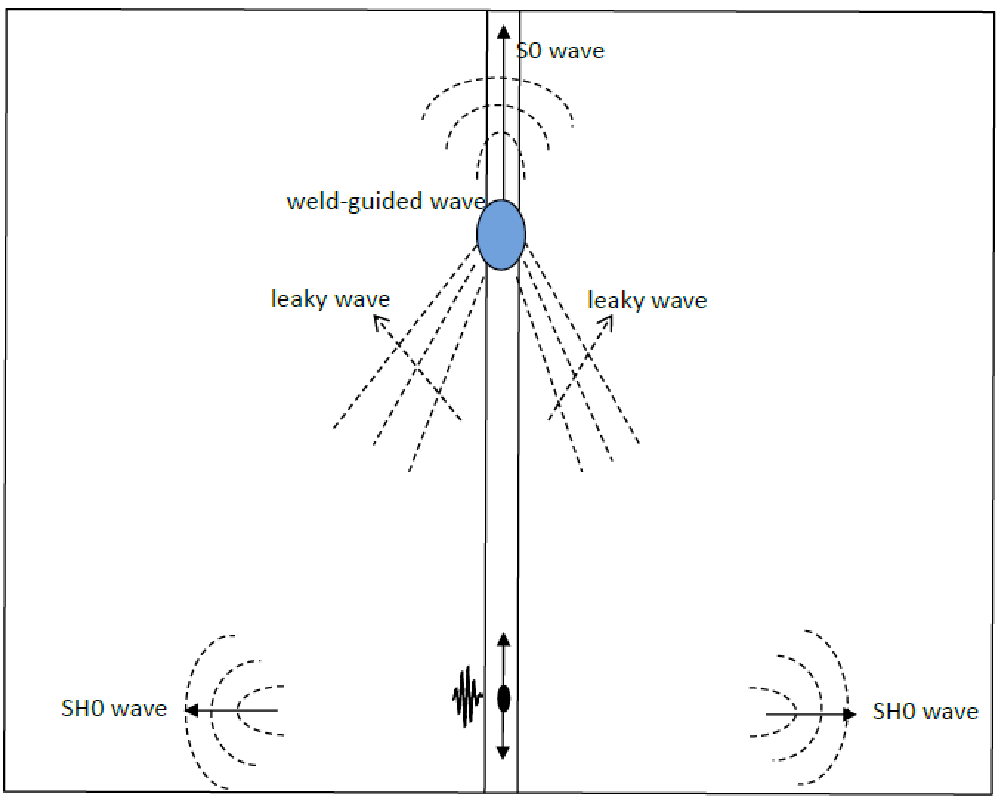


Figure 10.1. Schematic of feature-guided wave propagation on a welded plate

The main objective of this research is to show whether quasi-Rayleigh waves are trapped along a butt weld bead that joints two thick steel plates through the tuning curves from pitch-catch method to investigate the strength of the wave mode in weld. The quasi-Rayleigh wave is expected to be received by a receiver sensor that is bonded on lower surface. The quasi-Rayleigh wave-damage interaction is also investigated through finite element models. One eventually can use this SAW method to examine quasi-Rayleigh wave interaction with damages at inaccessible locations in a welded thick plate-like structure.

## 10.2 WELD GUIDED QUASI-RAYLEIGH WAVES (QRW)

This section discusses theoretical and experimental analyses of weld guided surface acoustic waves (SAW) through the guided wave propagation (GWP) analyses. The GWP analyses have been carried out by utilizing piezoelectric wafer active sensors (PWAS) for in situ structural inspection of a thick steel plate with butt weld as the weld bead is ground flush. Ultrasonic techniques are commonly used for validation of welded structures in many in-situ monitoring applications, e.g. in off-shore structures, in nuclear and pressure vessel industries and in a range of naval applications. PWAS is recently employed in such ultrasonic applications as a resonator as well as a transducer. Quasi-Rayleigh waves a.k.a. SAW can be generated in relatively thick isotropic elastic plate having the same phase velocity as Rayleigh waves whereas Rayleigh waves are a high frequency approximation of the first symmetric ($S_0$) and anti-symmetric ($A_0$) Lamb wave modes. As the frequency becomes very high the $S_0$ and the $A_0$ wave speeds coalesce, and both have the same value. This value is exactly the Rayleigh wave speed and becomes constant along the frequency i.e. Rayleigh waves are non-dispersive guided surface acoustic waves. The study is followed with weld-GWP tests through the pitch-catch method along the butt weld line. The tuning curves of quasi-Rayleigh wave are determined to show the tuning and trapping effect of the weld bead that has higher thickness than the adjacent plates on producing a dominant quasi-Rayleigh wave mode. The significant usage of the weld tuned and guided quasi-Rayleigh wave mode is essentially discussed for the applications in the in-situ inspection of relatively thick structures with butt weld such as naval offshore structures.

## 10.3 FINITE ELEMENT MODEL OF BUTT-WELDED THICK STEEL PLATE

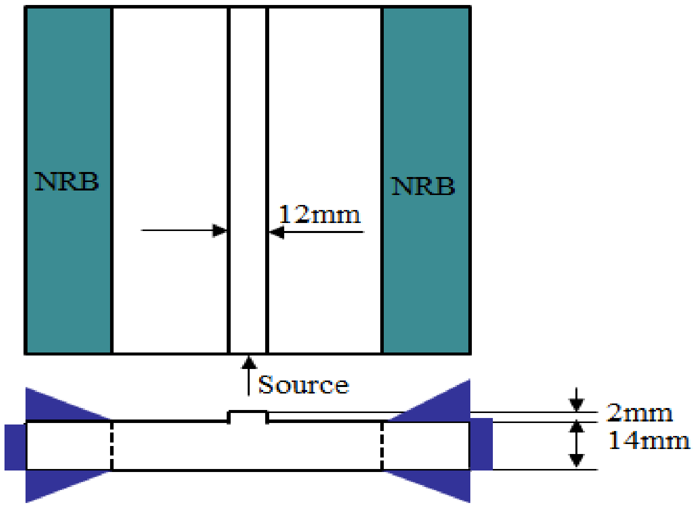


Figure 10.2. Finite element model of butt-welded plate including non-reflecting boundaries on two sides of the steel plate

A square steel plate is modeled in sizes of 400mm x 400mm x 14mm meshed with MESH200 3-D quadrilateral with 8 nodes and SOLID185 3-D 8-node structural solid element. The plate is excited by a pin-point force ($F_Z$) for full-transient analysis on commercial finite element software, ANSYS®. 400mm x 12mm x 16mm idealized rectangular butt-weld bead lay out between the adjacent side plates and is meshed with the same solid elements. The material of the weld is assumed to be the same as the plate materials. In addition, non-reflected boundaries (COMBIN14 spring-damper element) were defined with 100 mm length on two sides as seen in Figure 10.2. The reader is recommended to read through related chapters of the PhD dissertation by Shen in 2014 to obtain more detailed information about the non-reflected boundaries.

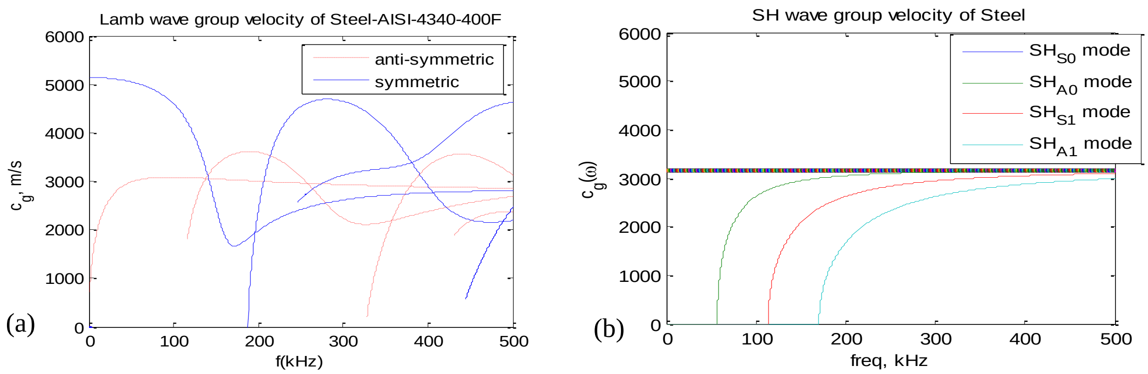


Figure 10.3. Group velocity dispersion curves of (a) Lamb wave modes and (b) shear horizontal (SH) wave modes in steel plate

In Figure 10.3, the group velocities for symmetric and anti-symmetric modes of Lamb waves on the left and of shear horizontal (SH) waves on the right are shown to have track on the weld guided wave modes simulated by the finite element model. Also, the snapshots of animation of the weld guided wave propagation at 67.6 μsec are illustrated for the pristine and damaged welded plates in Figure 10.4.

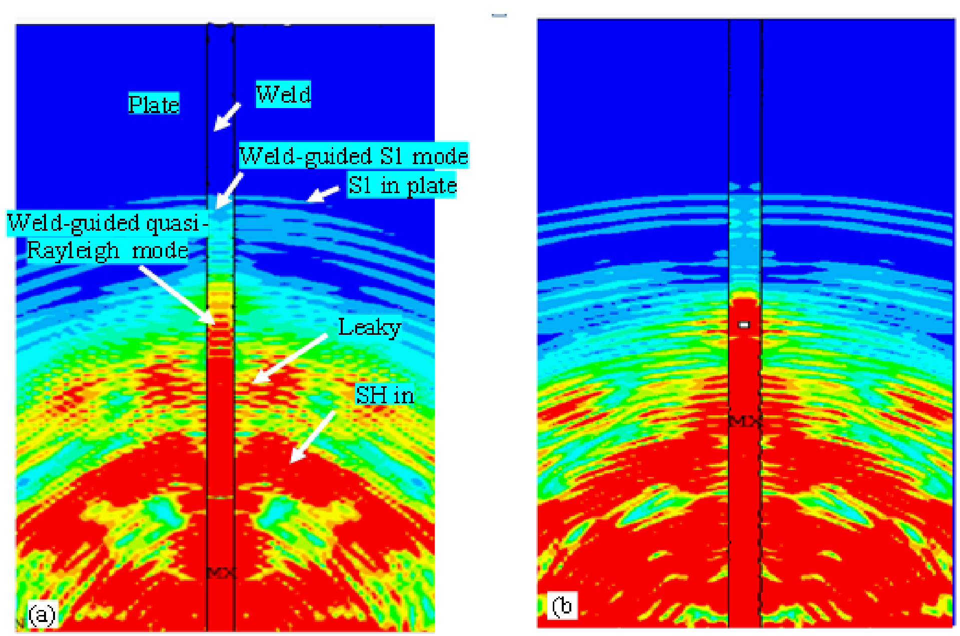


Figure 10.4. Snapshots of weld guided wave simulations on (a) pristine and (b) damaged thick plates. The pin-point force is excited at 300 kHz

It is observed from the Lamb wave group velocity dispersion curves that S1 mode is almost one and half time faster than the Rayleigh wave mode in steel plate so that the S1 mode is the leading mode with small amplitude as depicted in the snapshot. The weld guided quasi Rayleigh wave mode follows the S1 mode and leads the leaky SH modes propagating in the wake of the weld guided surface acoustic wave mode toward into the adjacent steel plates. The weld guided wave modes pursue almost the same template in the pristine and damaged plates where the damage is simulated as a hole across the thickness that is introduced in the center of the weld bead. The simulated weld guided wave forms at 300 kHz are demonstrated in Figure 10.5 for the plain (not welded) case as seen on the left and the welded plate case on the right. The results obtained from pristine and damaged plate models are overlapped to understand the response from the weld guided wave-damage interaction on welded thick plate. The same analysis is conducted for the plain plate case so that one can compare the effect of the existence of the weld bead.

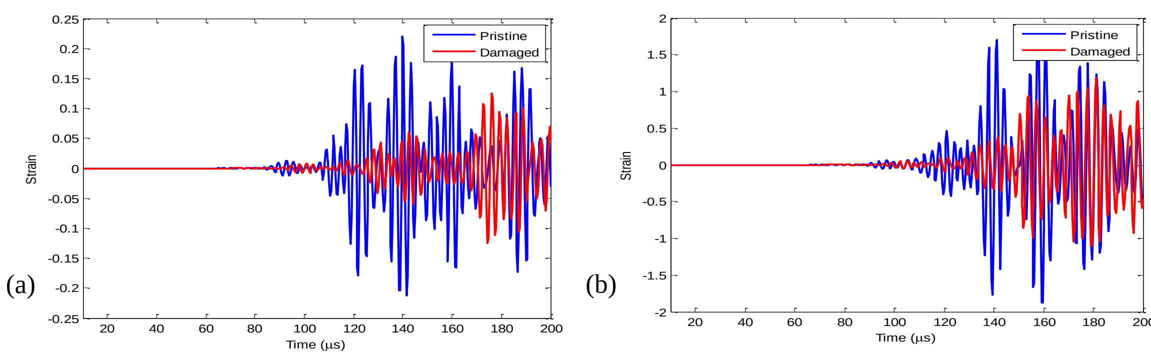


Figure 10.5. Overlapped plots of the received signals from pristine and damaged (a) plain plate and (b) welded plate

As one can clearly observe from the results seen in the plots (Figure 10.5), both weld guided waves and the guided waves in plate reduced in amplitude after they interacted with the damage. However the speed of the waves in weld did not reduce whereas those in the plate reduced.

## 10.4 EXPERIMENTAL ANALYSIS FOR TUNING OF WELD GUIDED QRW

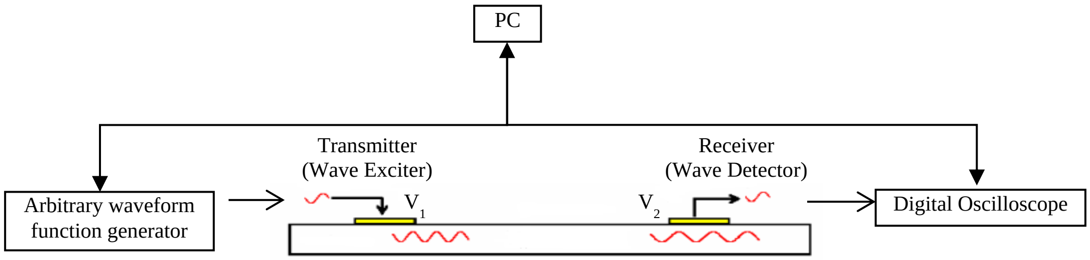


Figure 10.6 Schematic illustration of the experimental setup for the pitch-catch tests.

In this experimental setup (Figure 10.6), transmitter PWAS bonded on a substrate structure excites the structure by induced voltage in tone-burst sine wave form with three-counts through the function generator. Then, receiver PWAS senses the wave signals traveling in certain modes along the structure and the received signals as output voltage are read by the oscilloscope in time domain and recorded for post-processing the data.

In the experiments, 7mm x 7mm x 0.2mm PWAS transducers are bonded on the specimens. PWAS transducers served as high-bandwidth strain sensors for active sensing of local and far-field in the substrate structures. EMIS and GWP tests have been conducted on thick isotropic elastic specimens such as aluminum and steel plates by using SM412 PWAS transducers on each substrate material. In order to discuss the tuning effect of the thickness of the thick plate-like structures in relatively high frequency region, and the tuning effect of a feature on the structures, the EMIS tests and the experimental tuning curve measurements have been conducted. The results from the analytical models and the tests are compared to discuss the tuning of QRW mode that can be excited in thick structures and at high frequencies. Clear and smooth trend observed in the spectra in frequency domain as the QRW is locally excited and distinguishability of the dominating the QRW packet in time domain. These features of the QRW are promising features that ease the predictability and the signal post-processing.

In the EMIS experimental setup, two pristine aluminum specimens shown in Figure 10.7 and Figure 10.8 are used. PWAS transducers are bonded on the short edges and clays are applied on long edges of the both aluminum specimens to avoid reflections and obtain more clear signals. PWAS is bonded at center location of 2.1 mm thick plate whereas other two PWAS transducers are bonded on the two ends of the 6.35 mm (1/4 in.) thick plate in order to avoid the possible reflections from the non-clayed edges. The two PWAS transducers are employed as resonators for EMIS measurements; and transmitter PWAS (T-PWAS) and receiver PWAS (R-PWAS) for pitch-catch tests later on.

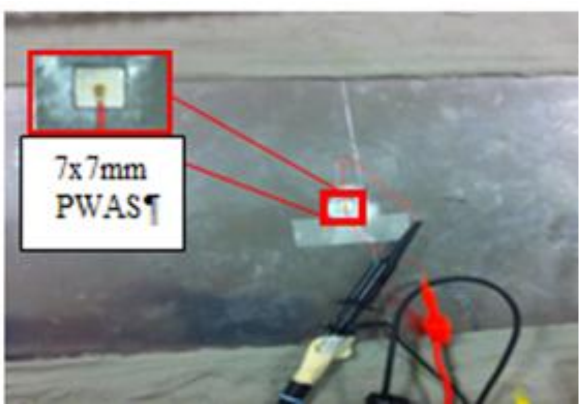


Figure 10.7 Square PWAS in 0.2mm thickness bonded on a pristine aluminum plate in 2.1mm thickness.


Figure 10.8 Two square PWAS transducers in 0.2mm thickness are bonded on a pristine aluminum plate in ¼” thickness.

The steel specimen is 13.75 mm thick high temperature steel that has V-groove butt weld bead lying along the center of the plate as seen in Figure 10.9(c). The weld bead is around 1mm thicker than the steel plate. The welded thick steel plate specimen is produced using metal inert gas (MIG) welding and donated by Savannah River Nuclear Plant. In this particular study, we were interested in QRW mode, therefore we selected relatively high excitation frequency band to receive the signal dominated by QRW modes.

Auto-tuning graphical user interface (GUI) -developed in LAMSS using LabView program- is utilized to control the function generator and automatically sweep the predefined frequency band and record the data for each frequency step in an excel file then eventually post-process the data to generate the tuning curve for certain wave packets in the received signals.

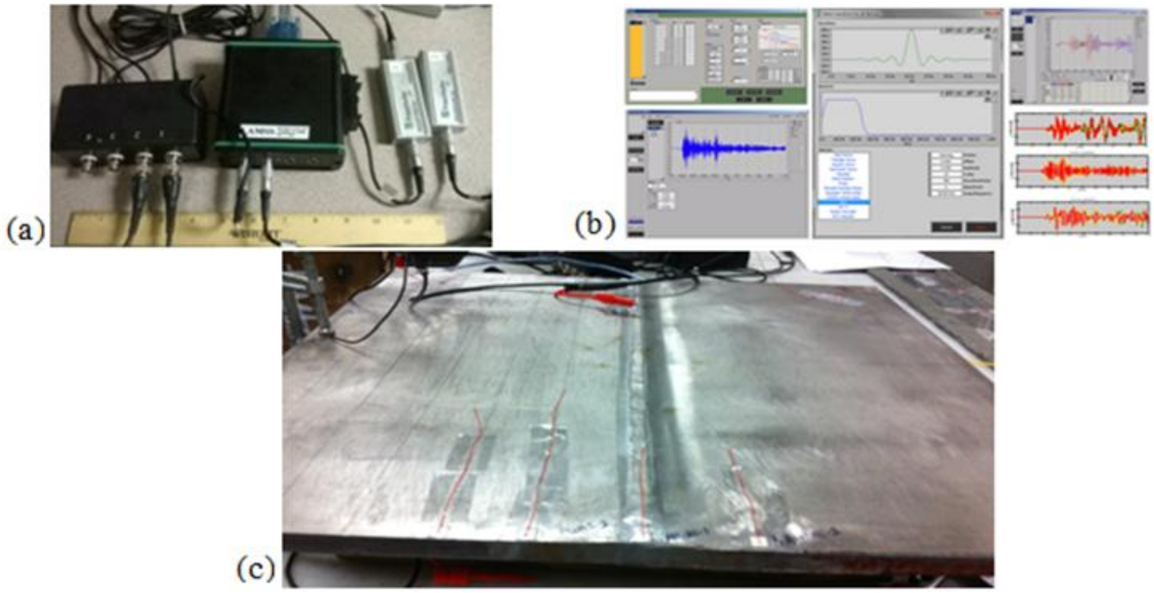

Figure 10.9. (a) Multi-channel Acoustic Measurement System (MAS) (b) a LabVIEW graphical user interface, CANWare (c) stainless steel plates in thickness of 14mm jointed with butt weld instrumented by 7mm x 7mm x 0.2mm PWAS

Figure 10.9(c) indicates the specimen employed for the experimental setup. The steel plates were jointed with butt weld and were instrumented by 7mm x 7mm x 0.2mm PWAS on and off the weld bead on two ends as the layout can also be seen in Figure 10.10. The excitation signal is selected to be Hanning windowed tone-burst with 5 counts in amplitude of 80V. For exciting the waves in the substrate structure at transducer terminal and receive the propagating wave signals at the reception terminal, a compact size instrument as seen in Figure 10.9(a) is utilized. The ultrasonic instrument called multi-channel Acoustic Measurement System (MAS) is composed of function generator oscilloscope and preamplifier and designed by Fraunhofer IKTS-MD, Germany. Also a LabVIEW graphical user interface, CANWare as shown in Figure 10.9(b), provided general sensor signal acquisition and basic signal processing for the MAS device.

The layout for the first experimental setup is illustrated in Figure 10.10. We conducted pitch-catch wave propagation technique to acquire the data. The welded steel plate is instrumented by 7mm square PWAS transducers on two ends. The first pitch-catch measurement is carried out on the butt-weld and the second one on one of the adjacent steel plates. The path where the wave is generated and received on the weld is called Path-1 and the other is called Path-2.

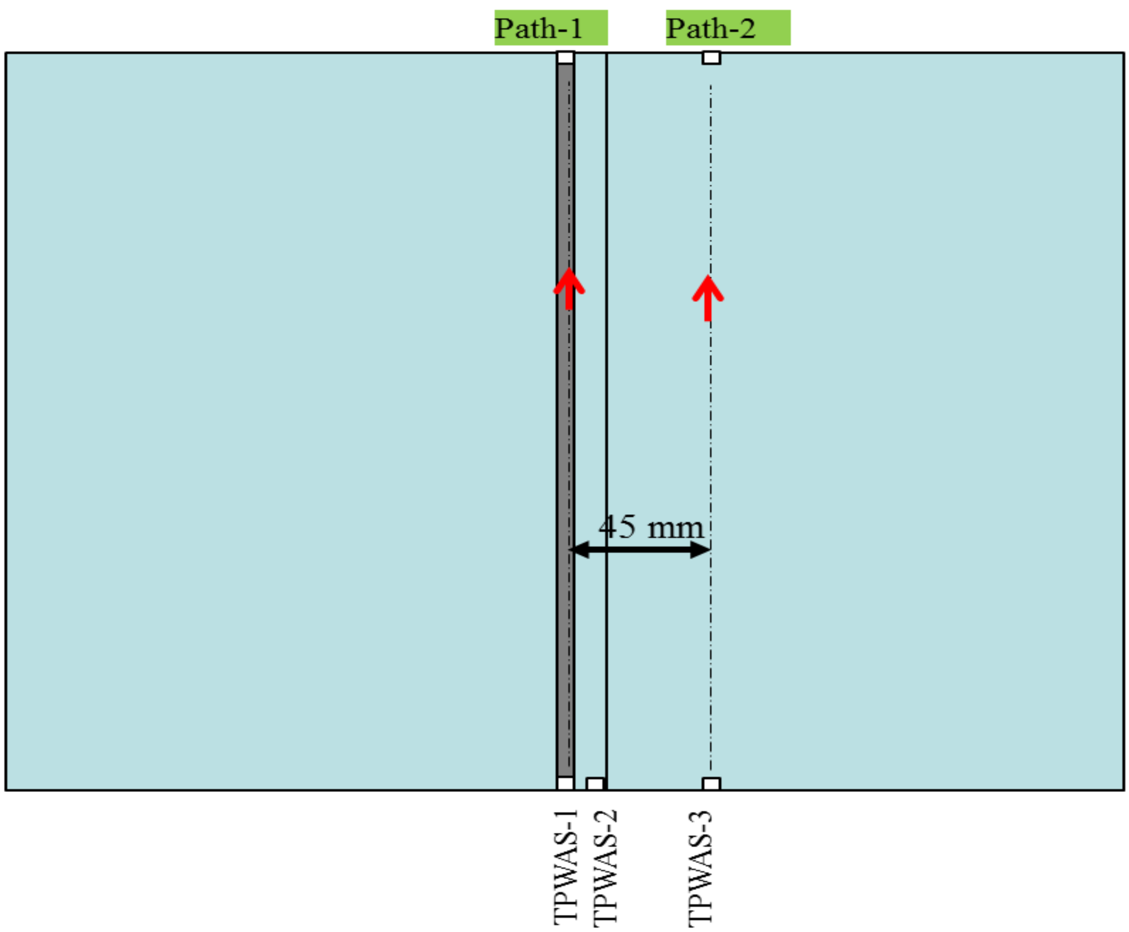


Figure 10.10. Experimental setup layout as stainless steel plates in thickness of 14mm jointed with butt weld instrumented by 7mm x 7mm x 0.2mm PWAS on and off the weld bead on two ends

The data are acquired for various excitation frequencies in the range between 150 kHz and 450 kHz from both Path. The waveforms for certain frequencies are illustrated in

Figure 10.11 to understand when the non-dispersive Rayleigh wave packets (depicted in red boxes) are captured and how large their amplitudes are. Therefore, one can observe and compare the difference of the quasi-Rayleigh wave amplitude acquired from Path-1 and Path-2.

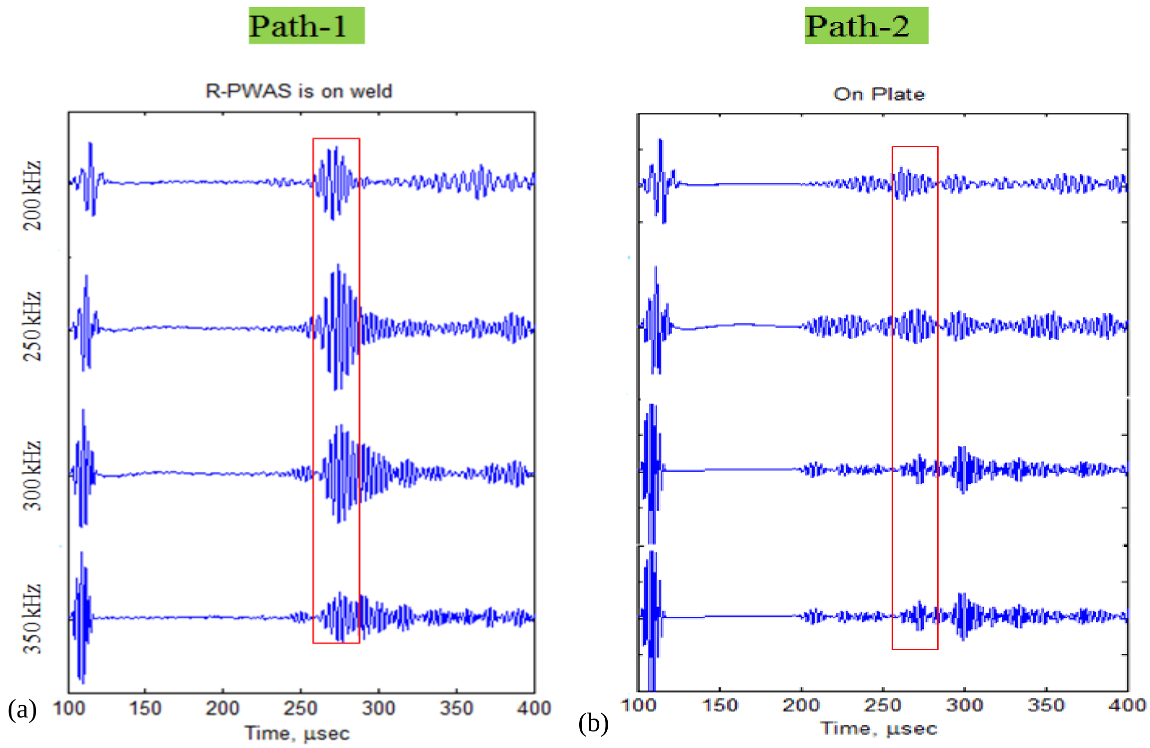


Figure 10.11. Experimental received wave signals at different central frequency from (a) path 1 on weld and (b) path 2 on plate

The amplitude difference is also clearly seen in the experimental tuning curves shown in Figure 10.12. The amplitude of the received quasi-Rayleigh wave packet reaches at its maximum value at around 300kHz central frequency as predicted by the analytical calculation of the Rayleigh wave tuning curve (Figure 9.11) .As seen in experimental tuning curves, the quasi-Rayleigh wave amplitude reaches up to 3800 mV at the excitation frequency of 270 kHz on Path-1 (on-weld) whereas it is only 2500 mV at the same frequency on Path-2 (off-weld). Hence, the results show that the quasi-Rayleigh wave packet is trapped and guided across the butt-weld bead. Then the quasi-Rayleigh wave mode can be used as weld-guided wave mode for future applications.

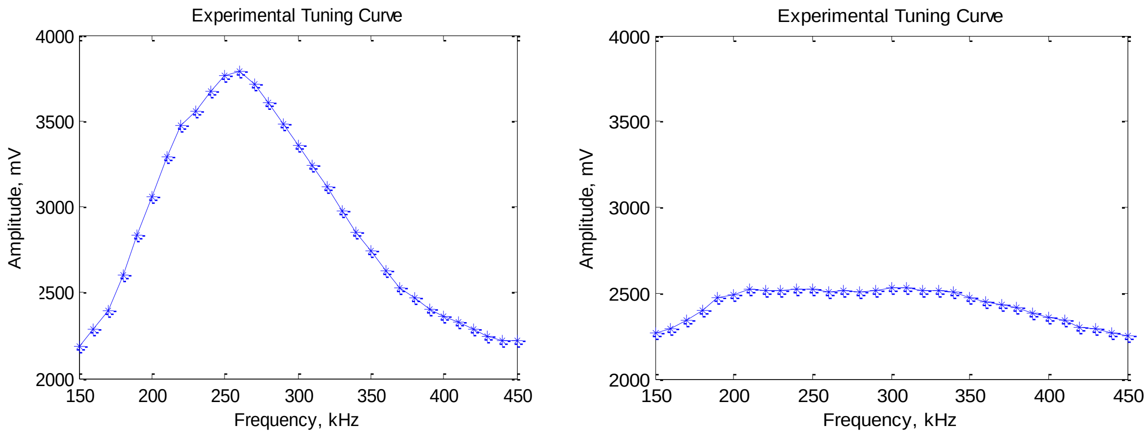


Figure 10.12. Experimental tuning curves of quasi-Rayleigh waves obtained from (a) path 1 on weld and from (b) path2 on plate

The layout for the second set of experiment is illustrated in Figure 10.13. The same butt-welded thick sectioned steel plate is utilized for this experimental setup. As seen, the difference is that the receiver PWAS is attached on the lower surface of the welded thick steel plate whereas the transmitter PWAS is bonded on the upper surface. This GWP pitch-catch technique is conducted to understand how the weld guides the quasi-Rayleigh wave mode. As expected, the wave mode is received with the high amplitude as strong as it was received on the same surface. The mode shape analysis in the previous section (Figure 9.9 and Figure 9.10) also showed the similar perturbation on the lower surface of a plate as the same activity occurs on upper surface at high frequency-thickness product. Thus, this technique can be used to detect a damage that may occur at inaccessible locations on thick plate-like structures.

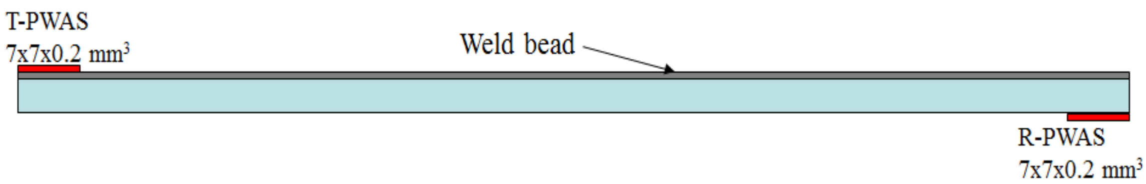


Figure 10.13. Outline of the transmitter and receiver PWAS on the butt-welded stainless steel plate specimen

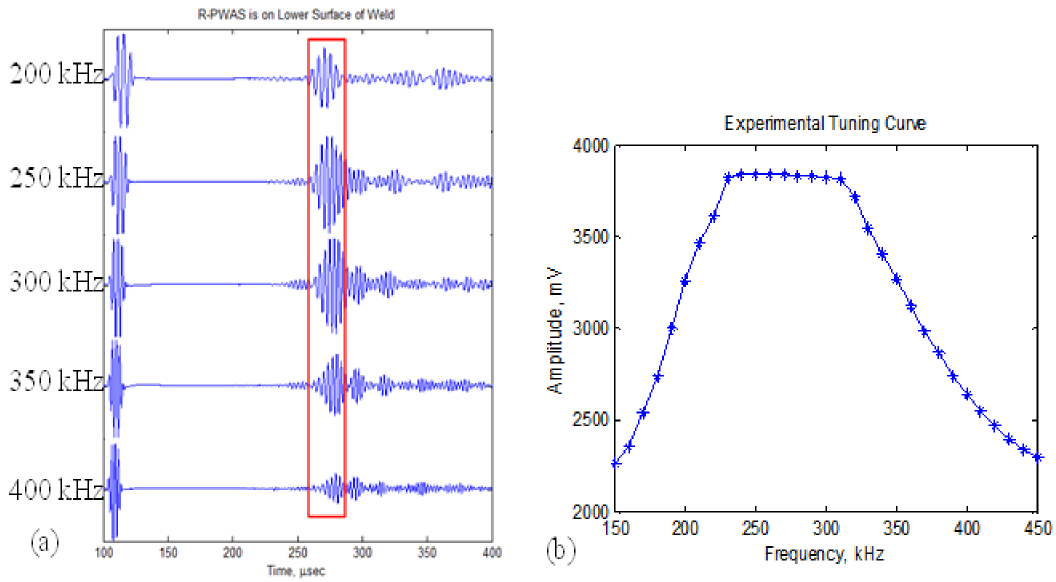


Figure 10.14. (a) Experimental received wave signals at different central frequency (b) Experimental tuning curves of quasi-Rayleigh waves obtained

## 10.5 SUMMARY AND CONCLUSIONS

Experimental and theoretical studies were conducted for in situ structural inspection of a thick steel plate with butt weld. Both experimental and FEA results verified our hypothesis which is the fact that the quasi-Rayleigh wave is guided and tuned by butt-weld having higher amplitude compared to that in the thick plain-plate. We investigated the quasi-Rayleigh wave behavior in pristine structure as well as damaged structure. Experimental and analytical tuning curves agreed. The wave signals and tuning curves showed that quasi-Rayleigh wave traveling in weld can also be received from the opposite surface of a thick plate structure. We theoretically investigated quasi-Rayleigh wave damage interaction by simulated damage modeled as 4mm x 4mm square hole. Both weld guided waves and waves in plate reduced in amplitude after they interacted with the damage. However the speed of the wave in weld did not reduce whereas that in the plate reduced.

As suggested future work, one can repeat the experiments on thick walled welded pipes to understand how the quasi-Rayleigh wave is captured by R-PWAS installed both on outer and inner surfaces. Eventually, one can investigate the quasi-Rayleigh wave interaction with damages at inaccessible locations in a pipe.

# CHAPTER 11

# SUMMARY AND CONCLUSIONS

The chapter presents summary and conclusions to the overall dissertation manuscript by addressing the development and contribution of conducting the research, discussing each research topic of the dissertation.

This dissertation has presented the developments in impedance based and propagating wave based structural health monitoring (SHM) using ultrasonic guided waves, with a focus on the development of accurate, efficient, and versatile modeling for guided wave based active sensing procedures.

The dissertation started with an introduction to SHM concepts, guided waves, and piezoelectric wafer active sensors (PWAS). Accurate and efficient theoretical models for standing and propagating waves and tuning of certain wave modes have been developed and presented in the dissertation. The research covered some work on the analytical modeling, finite element simulation, and experiments for the development of SHM concepts. The modeling techniques were advanced in both near-field and far-field interrogation. A 1-D analytical framework which can describe standing harmonic wave in thickness mode has been constructed including the frequency response function, the electromechanical admittance and impedance and linear higher harmonic overtones in relatively high frequency range of MHz. The concept developed in the thickness mode free PWAS case was extended to the thickness mode constrained PWAS from its one surface and both surfaces. A proof-mass PWAS actuator was designed to tune the standing wave mode by shifting the resonance frequency of the system by adding a proof-mass and changing the size or material of a proof-mass on the piezo-ceramic actuator. An analytical model of the electromechanical response of PWAS with various liquids with different material properties was developed. An analytical simulation of 2-D circular PWAS-EMIS at elevated temperature was carried out in order to study the piezoelectric material degradation and compensation at high temperature environment. Theoretical and experimental study on tuning guided waves in thin and thick structures was performed. A concept of weld guided waves was adopted to develop and SHM technique using the weld guided waves in welded thick structures and to study their interaction with damages in thick structures in high frequency range. The PWAS pitch-catch method were conducted and compared with FEM simulations. A review of the main results of this research is given next.

PWAS itself demands an understanding of its electromechanical characteristic before its interaction with a medium. The intrinsic electromechanical impedance/admittance of PWAS is a significant indicator in frequency spectra. The frequency response of a sensor to the electrical excitation defines its dynamic properties. Free PWAS-EMIS can be defined using resonator theory in various vibration modes such as in longitudinal (in-plane), in thickness (out-of-plane), and in shear horizontal (thickness shear, length shear) modes etc.

As the PWAS resonator is embedded into a medium, the electromechanical impedance spectroscopy (EMIS) method applies standing waves generated by piezoelectric wafer resonator so that E/M impedance/admittance spectra indicates the local resonance response of the coupled medium-resonator in frequency domain at anti-resonance and resonance frequencies that are slightly different. It is substantial to extend the theoretical development to accurately and quantitatively predict the local dynamic characteristics of PWAS in different environmental conditions and in various embedding media. The development of analytical and numerical models under simplifying assumptions is paramount importance to perform simulation of response of PWAS-EMIS and constrained PWAS-EMIS in wide range of applications.

For selection of desired ultrasonic wave modes to avoid complexity in post processing of the received and recorded signals and for the sake of easiness of the interpretation, the sizes of PWAS transducers, size of the structure and the excitation frequency of the input waveform should be tuned. The proof-mass concept has received considerable attention recently. Proof-masses shift the system resonance toward optimal frequency points. Therefore, proof-mass concept has been adopted to develop a new method for tuning ultrasonic wave modes. The theoretical framework on proof mass actuator has been developed as a mass bonded to the piezoelectric actuator. The model is used to build the basis for a proof-mass piezoelectric wafer active sensor (PM-PWAS). Then, the sets of parametric studies with the PM-PWAS transducer model has been carried out by PM analysis to investigate desired control objectives using the correlation between a PM-PWAS and structural dynamic properties in the substrate structure. Analytical and numerical models have been implemented for the PM-PWAS transducer attached to an isotropic elastic plate. The models have been verified and validated by the serious of experiments.

Piezoelectric transducer and liquid domain interaction has been commonly investigated through theoretical analysis of resonance spectra in frequency domain using certain types of standing wave modes; shear horizontal waves and thickness shear waves by using different techniques. The fact that the electrical excitation of a PWAS could be converted into the mechanical vibration as regards to the stress and the strain waves have been utilized to develop a micro-acoustic sensor to measure chemical, physical, and biological properties of a liquid medium located in the vicinity or possessing an interface with the sensor. An analytical EMIS model has been developed to predict the mechanical properties of the liquid medium such as the viscosity and the density which affect the energy transduction of sensor as well as the electrical properties of the medium concerning the sensitivity of the wave mode. Thus, the detection of changes in mechanical properties and electrical conductivity of the biomedical implants by bio-PWAS enables to capture the protein or solution concentration (pH) changes that influence the conductivity, the ultrasonic wave modes and electro-mechanical impedance readings.

In second part of the dissertation, the tuning of the propagating waves by using different techniques was presented. First, the study regarding the tuning effect of the PWAS was performed using PWAS transducers in different sizes on thin plate. Tuning of the fundamental Lamb wave modes was discussed. Then, tuning effect of the size of the substrate structure was experimentally studied using relatively thick structures and the quasi-Rayleigh waves i.e surface acoustic waves (SAW) were captured in high frequency range. Rayleigh waves have been widely used in non-destructive testing (NDT), SHM applications as well as in seismology. Rayleigh waves are a high frequency approximation of the first symmetric (S0) and anti-symmetric (A0) modes of Lamb waves as the frequency-thickness product becomes relatively high. They become non-dispersive wave, i.e. constant wave speed along the frequency. Rayleigh wave can only travel along a flat surface of a semi-infinite medium, which is hardly possible to generate in reality however for the plate thickness d >> $\lambda_R$ , the measurements should be acceptable. The wave mode is then called quasi-Rayleigh wave having Rayleigh wave speed. We tuned the quasi-Rayleigh wave modes by using the structure thickness and high excitation frequency in order to take advantage of quasi-Rayleigh wave's promising features on ultrasonic inspections. Finally, we adopted the weld guided wave techniques for the thick welded structures and tuned weld guided quasi-Rayleigh wave mode, which is essential for the applications in the in-situ inspection of relatively thick structures with butt weld such as naval offshore structures or pipelines.

## 11.1 RESEARCH CONCLUSIONS

### 11.1.1 FREE AND CONSTRAINED PWAS-EMIS

An analytical framework has been developed for prediction of in-plane and out-of-plane (thickness) modes of E/M impedance spectroscopy (EMIS) of free PWAS. Two main electrical assumptions were applied for both PWAS-EMIS modes. These assumptions are 1- constant electrical field assumption and 2- constant electrical displacement assumption. The analytical simulations under these two assumptions were carried out and verified by corresponding finite element simulations as well as experimental measurements. To conclude, the constant electrical field assumption gives better results in in-plane EMIS prediction whereas the constant electrical displacement assumption brings better agreement in thickness mode with the experimental measurements.

We have conducted a preliminary parametric study to understand the effects of the material properties on the impedance (anti-resonance) and admittance (resonance) spectra. We utilized the 1-D and 2-D PWAS-EMIS models for the analytical simulations. We have varied the piezoelectric stiffness, the piezoelectric charge constant and the static capacitance of free PWAS. We had phenomenological agreement in trends of the impedance spectra with the experimental results reflecting the temperature effects on the piezoelectric material degradation.

The theoretical frameworks for the in-plane mode and thickness mode electromechanical impedance spectroscopy (TM-EMIS) of constrained piezoelectric wafer active sensor (PWAS) have been developed. The analytical analyses were conducted by applying the resonator theory to derive the EMIS of PWAS constrained on one and both surfaces by isotropic elastic materials. The normalized thickness mode (Eigen-mode) shapes were obtained for the normal mode expansion (NME) method to predict the thickness mode impedance values of constrained PWAS using the correlation between a proof-mass-piezoelectric transducer and structural dynamic properties in the substrate structure. In another word, the normalized thickness mode shapes of the PM-PWAS-substrate structure at the resonance frequencies are obtained for the NME method. GMM was utilized to solve the eigenvalue problem of the constrained PWAS models for the Eigen-vectors and the corresponding Eigen-frequencies.

### 11.1.2 DEVELOPMENT OF PM-PWAS TRANSDUCER FOR TUNING OF ULTRASONIC WAVES

The constrained PWAS-EMIS models having been developed in the preceding chapters were used to build the basis for the EMIS of the proof-mass PWAS (PM-PWAS). The model was extended to a five layered model including a PWAS resonator in the middle and two isotropic elastic bars constraining the PWAS from both surfaces by two adhesive bonding layers. Global matrix method (GMM) was employed to solve the eigenvalue problems of the PM-PWAS models for the Eigen-vectors and the corresponding Eigen-frequencies. Eigen-modes are determined for the normal mode expansion (NME) method to predict the thickness mode impedance values of PM-PWAS using the correlation between a proof-mass-piezoelectric transducer and structural dynamic properties in the substrate structure. The study was followed by proof-mass analysis to investigate desired control objectives (such as tuning of axial wave modes). PM-PWAS transducer can be used for better high frequency local modal sensing at a desired excitation frequency utilizing the proof masses affixed on PWAS in different sizes and materials to tune system resonance towards optimal frequency point. A parametric study is conducted to indicate effect of the proof-mass size change on mode shapes in relation with frequency response function amplitudes at resonance frequencies. The bonded PWAS and PM-PWAS models are also numerically generated in a commercial multi-physics finite element analysis (MP-FEA) software, ANSYS®. The thickness mode EMIS results from analytical, numerical, and experimental analyses are presented. The analytical PM-PWAS and constrained PM-PWAS models are verified by

MP-FEA computational results and experimental measurement results in terms of the thickness mode EMIS of PM-PWAS bonded on a plate-like host structures.

### 11.1.3 EMIS OF PWAS IN CONTACT WITH LIQUID MEDIA

The overall purpose of the research was to develop theoretical models under simplifying assumptions to perform wide-parameter simulation of response of a bio-PWAS implanted into a biological medium. A scientific and engineering basis for the analysis of PWAS performance in contact with fluid for health monitoring has been developed. From the applications point of view, this study can indicate that PWAS transducers can be used for viscosity measurement such that these transducers can be utilized for bio-sensing in an environment of varying viscosity and stiffness of a texture of a soft tissue. We developed an analytical model for shear horizontal mode EMIS of piezoelectric wafer active sensor (PWAS) in contact with a liquid medium to establish the theoretical basis that enables interrogation of dynamic characteristics of a biological component.

### 11.1.4 GUIDED LAMB WAVE TUNING

We aimed at analyzing the different features of coupled PWAS-substrate for tuning the guided ultrasonic waves. In tuning process, several factors influence the behavior of the excited wave: PWAS length, excitation frequency, wavelength of the guided wave, etc. We have shown that tuning opportunities exist through change in size of PWAS, in size of substrate structure especially thickness, and the features on the structure such as weld bead. The tuning is especially beneficial when dealing with multimode waves, such as the Lamb waves.

#### 11.1.5 WELD GUIDED QUASI-RAYLEIGH WAVE TUNING

Finite element and experimental analyses were conducted for in situ structural inspection of a thick steel plate with butt weld. Both experimental and FEA results verified our hypothesis which was the fact that the quasi-Rayleigh wave is guided and tuned by butt-weld having higher amplitude compared to that in the thick plain-plate. We investigated the quasi-Rayleigh wave behavior in pristine structure as well as damaged structure (Kamas, Giurgiutiu & Lin, 2014). Experimental and analytical tuning curves agreed. The wave signals and tuning curves showed that quasi-Rayleigh wave traveling in weld can also be received from the opposite surface of a thick plate structure. We theoretically investigated quasi-Rayleigh wave damage interaction by simulated damage modeled as 4mm x 4mm square hole. Both weld guided waves and waves in plate reduced in amplitude after they interacted with the damage. However the speed of the wave in weld did not reduce whereas that in the plate reduced.

## 11.2 MAJOR CONTRIBUTIONS

This dissertation has contributed to the SHM community in a variety of ways. The major contributions of this dissertation to the state of the art are listed below:

- We constructed analytical framework which can describe standing harmonic wave in thickness mode that are generated by PWAS resonators, The electromechanical admittance and impedance spectra are modeled along with linear higher harmonic overtones in relatively high frequency range of MHz.

- We carried out an analytical simulation of circular PWAS-EMIS at elevated temperature in order to study the piezoelectric material degradation and compensation at high temperature environment.
- We extended the concept developed in the thickness mode free PWAS case to the thickness mode constrained PWAS on its one surface and both surfaces i.e. two-layers and three layers.
- A novel methodology was proposed by constructing a proof-mass PWAS actuator to tune the wave modes by shifting the resonance frequency of the system by adding a proof-mass and changing the size or material of a proof-mass on the piezo-ceramic actuator. Some case studies with experimental analyses have been conducted for depicting the effects of the proof-mass size change especially in thickness.
- We developed an analytical model of the shear horizontal mode EMIS of PWAS with various liquids with different material properties.
- We performed theoretical and experimental study on weld guided waves and the weld guided wave interaction with damages in thick structures in high frequency range and found out and used the promising features of the quasi-Rayleigh wave mode in welded thick structures such as plates and pipes.

## 11.3 RECOMMENDATION FOR FUTURE WORK

This dissertation has presented various analytical and FEA models for the simulation of EMIS through standing waves and pitch-catch through guided wave propagation. This work has laid the foundation for future investigations to extend the methodologies to more complicated structures. The suggestions for future work are listed below:

1. The analytical model of the thickness mode EMIS of free PWAS should be extended to two-dimensional for more accurate prediction of circular PWAS impedance signature at high frequency range of MHz.
2. EMIS model of PM-PWAS should include the flexural wave approximation to predict the tuning effects of the proof-masses on the non-dispersive Lamb wave modes.
3. The inclusion of the bonding layers in the multi-layer analytical model may involve the shear lag approach as considered in the literature for the effective impedance prediction.
4. The free PWAS-EMIS simulations at increasing temperature should be reconsidered by using the piezoelectric constitutive equations including thermal term for both 1-D and 2-D PWAS-EMIS analytical modeling.
5. The shear horizontal EMIS model of PWAS in contact to liquid layer can be extended to different scenario such as PWAS in contact with semi-infinite liquid medium, PWAS fully embedded into liquid medium etc. by considering for both 1-D and 2-D circular PWAS models.

6. The weld guided quasi-Rayleigh wave experiments should be conducted on pipes. Interaction of the weld guided waves with various defects in welded thick structures should be inspected through FEA models and experiments

# REFERENCES


Alleyne, D.N., Pavlakovic B., Lowe, M.J.S., Cawley, P. (2000). Rapid long range inspection of chemical plant pipework using guided waves. *Roma 2000 15th WCNDT.*

Annamdas, V. G., Pang, J. H., Zhou, K., & Song, B. (2013). Efficiency of electromechanical impedance for load and damage assessment along the thickness of lead zirconate titanate transducers in structural monitoring. *Journal of Intelligent Material Systems and Structures*, *24*(16), 2008–2022. doi:10.1177/1045389X13488252

Annamdas, V. G., & Radhika, M. a. (2013). Electromechanical impedance of piezoelectric transducers for monitoring metallic and non-metallic structures: A review of wired, wireless and energy-harvesting methods. *Journal of Intelligent Material Systems and Structures*, *24*(9), 1021–1042. doi:10.1177/1045389X13481254

Auld, B. A. (1973). *Acoustic Fields and Waves in Solids Volume I* (Volume I., pp. 211–213). John Wiley&Sons.

Ballato, A. (2001). Modeling piezoelectric and piezomagnetic devices and structures via equivalent networks. *IEEE transactions on ultrasonics, ferroelectrics, and frequency control*, *48*(5), 1189–1240.

Ballato, Arthur. (1977). Doubly Rotated Thickness Mode Plate Vibrators. *Physical Acuoustics Vol XIII* (Vol. XIII, pp. 115–181).

Ballato, Arthur. (2000). Extended Christoffel-Bechmann elastic wave formalism for piezoelectric, dielectric media. *Frequency Control Symposium and Exhibition, 2000. Proceedings of the 2000 IEEE/EIA International* (pp. 340–344). Kansas City, MO.

Bandey, H. L., Martin, S. J., Cernosek, R. W., & Hillman, A. R. (1999). Modeling the Responses of Thickness-Shear Mode Resonators under Various Loading Conditions. *Analytical Chemistry*, *17*(11), 2205–2214.

Bao, J. (2003). *Lamb Wave Generation and Detection with Piezoelectric Wafer Active Sensors*. University of South Carolina. Bao, J., & Giurgiutiu, V. (2003). Modeshape_v2e. Retrieved from http://www.me.sc.edu/research/lamss/html/software.html

Basic Technology of Quartz Crystal Resonators. (2012). Retrieved from http://www.4timing.com/techcrystal.htm

Bender, J. W., Friedman, H. I., Giurgiutiu, V., Watson, C., Fitzmaurice, M., & Yost, M. L. (2006). The Use of Biomedical Sensors to Monitor Capsule Formation Around SoftTissue Implants. *Annals of Plastic Surgery*, *56*(1), 72–77. doi:10.1097/01.sap.0000189620.45708.5f

Berlincourt, D. A., Curran, D. R., & Jaffe, H. (1958). Piezoelectric and Piezomagnetic Materials and Their Function in Transducers. In W. P. Mason (Ed.), *Physical Acoustics and The Properties of Solids* (pp. 169–188). Van Nostrand: Van Nostrand Company Inc.

Bleustein, J. L. (1968). A New Surface Wave in Piezoelectric Materials, *13*(12), 412–413.

Brook, M. V. (2012). *Ultrasonic Inspection Technology Development and Search Unit Design: Examples of Pratical Applications* (p. 216). New Jersey: Wiley Publishers IEEE press.

Brus, V. V. (2013). The effect of interface state continuum on the impedance spectroscopy of semiconductor heterojunctions. *Semiconductor Science and Technology*, *28*(2), 025013. doi:10.1088/0268-1242/28/2/025013

Bund, A., & Schwitzgebel, G. (1998). Viscoelastic Properties of Low-Viscosity Liquids Studied with Thickness-Shear Mode Resonators. *Analytical Chemistry*, *70*(13), 2584–2588.

C. Liang, F. P. Sun, C. A. R. (1994). An impedance method for dynamic analysis of active material systems. *Journal of Vibration and Acoustics*, *116*(1), 120–128. Retrieved from http://vibrationacoustics.asmedigitalcollection.asme.org/article.aspx?articleid=1469365&TokenID=wnOfoYHMIYjHr28oNxcKd8pcGbVO27Dm6u2QrcJm6j1x55aLUrwGAeDpSSK3oy9g

Cao, W., Zhu, S., Jiang, B., & Introduction, I. (1998). Analysis of shear modes in a piezoelectric vibrator, *83*(8), 4415–4420.

Cassiède, M., Daridon, J.-L., Paillol, J. H., & Pauly, J. (2011). Characterization of the behaviour of a quartz crystal resonator fully immersed in a Newtonian liquid by impedance analysis. *Sensors and Actuators A: Physical*, *167*(2), 317–326. doi:10.1016/j.sna.2011.03.002

Cegla, F. B., Cawley, P., & Lowe, S. M. J. (2005). Material property measurement using quasi-Scholte mode-A waveguide sensor. *Journal of Acoustical Society of America*, *117*(3), 1098–1107.

Chen, J., Wang, W., Wang, J., Yang, Z., & Yang, J. (2008). A Thickness Mode Acoustic Wave Sensor for Measuring Interface Stiffness Between Two Elastic Materials. *IEEE Transactions on Ultrasonics, Ferroelectrics, and Frequency Control*, *55*(8), 1678–81. doi:10.1109/TUFFC.2008.852

Chen, Z., Han, T., Ji, X., Guo, H., & Shi, W. (2006). Lamb wave sensors array for nonviscous liquid sensing. *Science in China Series G: Physics, Mechanics and Astronomy*, *49*(4), 461–472. doi:10.1007/s11433-006-0461-0

Cheng, C C, & Wang, J. K. (1998). Structural Acoustic Response Reduction of a Fluid-loaded Beam Using Unequally-spaced Concentrated Masses, *54*(4).

Cheng, C. C., & Wang, P. W. (2001). Applications of the Impedance Method on Multiple Piezoelectric Actuators Driven Structures. *Journal of Vibration and Acoustics*, *123*(2), 262. doi:10.1115/1.1362322

Chew, D., & Fromme, P. (2014). Monitoring of corrosion damage using high-frequency guided ultrasonic waves. (T. Kundu, Ed.), *9064*, 90642F. doi:10.1117/12.2046301

Cook, D. A., & Berthelot, Y. H. (2001). Detection of small surface-breaking fatigue cracks in steel using scattering of Rayleigh waves, *34*, 483–492.

Demcenko, A., & Mažeika, L. (2002). Calculation of Lamb waves Dispersion Curves in Multi-Layered Planar Structures. *Ultragarsas*, *3*(3), 15–17. Retrieved from http://www.ktu.lt/ultra/journal/pdf_44_3/44-2002-Vol.3_03-A.Demcenko.pdf

Divisions, M., Structures, A., & Symposium, M. S. (1999). MODELING OF THE ELECTRO-MECHANICAL ( E / M ) IMPEDANCE RESPONSE OF A DAMAGED COMPOSITE BEAM, *59*, 39–46.

Emeterio, J. L. S., & Ramos, A. (2008). 4 Models for Piezoelectric Transducers Used in Broadband Ultrasonic Applications. In A. A. Vives (Ed.), *Piezoelectric Transducers and Applications* (Second Edi., pp. 97–115). Valencia, Spain: Springer-Verlag. doi:10.1007/978-3-540-77508-9

Fan, Z., & Lowe, M. J. S. (2009). Elastic waves guided by a welded joint in a plate. *Proceedings of the Royal Society A: Mathematical, Physical and Engineering Sciences*, *465*(2107), 2053–2068. doi:10.1098/rspa.2009.0010

Feijter, J. A. D. (1979). The propagation of surface shear waves.pdf. *Journal of Colloid and Interface Science*, *69*(3), 375–383.

Freitas, V. F. (2006). Piezoelectric Characterization of BiFeO 3 – PbTiO 3 Multiferroic Ceramics, *128*(1), 122911.

Fromme, P. (2013). Noncontact measurement of guided ultrasonic wave scattering for fatigue crack characterization. (J. P. Lynch, C.-B. Yun, & K.-W. Wang, Eds.), *8692*, 86921N. doi:10.1117/12.2009460

Gazis, D. C. (1959). Three-Dimensional Investigation of the Propagation of Waves in Hollow Circular Cylinders. I. Analytical Foundation. *The Journal of the Acoustical Society of America*, *31*(5), 568. doi:10.1121/1.1907753

Giurgiutiu, V. (2005). Damage Detection in Thin Plates and Aerospace Structures with the Electro-Mechanical Impedance Method. *Structural Health Monitoring*, *4*(2), 99–118. doi:10.1177/1475921705049752

Giurgiutiu, V. (2010). Development and Testing of High-temperature Piezoelectric Wafer Active Sensors for Extreme Environments. *Structural Health Monitoring*, *9*(6), 513–525. doi:10.1177/1475921710365389

Giurgiutiu, Victor. (2008a). *Structural Health Monitoring with Piezoelectric Wafer Active Sensors* (First edit.). Columbia, SC, USA: Elsevier Inc.

Giurgiutiu, Victor. (2008b). *Structural Health Monitoring with Piezoelectric Wafer Active Sensors*. *Chemistry & …*. Retrieved from http://onlinelibrary.wiley.com/doi/10.1002/cbdv.200490137/abstract

Giurgiutiu, Victor. (2008c). Piezoelectric Wafer Active Sensors. *Structural Health Monitoring with Piezoelectric Wafer Active Sensors* (pp. 239–247). Columbia, SC, USA.

Giurgiutiu, Victor. (2008d). *Structural Health Monitoring with Piezoelectric Wafer Active Sensors*. Columbia, SC, USA.

Giurgiutiu, Victor. (2014). *Structural Health Monitoring with Piezoelectric Wafer Active Sensors* (Second Edi.). Columbia, SC, USA: Elsevier Academic Press.

Giurgiutiu, Victor, Friedman, H., Bender, J., Borg, T., Yost, M., Newcomb, W., Black, A., et al. (n.d.). Electromechanical impedance sensor for in vivo monitoring the body reaction to implants. *Journal of Investigative Surgery : The Official Journal of The Academy of Surgical Research*, *17*(5), 257–70. doi:10.1080/08941930490502835

Giurgiutiu, Victor, & Zagrai, A. (2000a). Damage Detection in Simulated Aging-Aircraft Panels Using The Electro-Mechanical Impedance Technique. *Adaptive Structures and Material Systems Symposium, ASME Winter Annual Meeting* (pp. 1–10). Orlando, FL.

Giurgiutiu, Victor, & Zagrai, A. N. (2000b). Characterization of Piezoelectric Wafer Active Sensors, *11*(December), 959–975.

Griffin, S., Lane, S. A., Hansen, C., & Cazzolato, B. (2013). Active Structural Acoustic Control of a Rocket Fairing Using Proof Mass Actuators. *Journal of Spacecraft and Rockets*, *38*(2), 219–225.

Guo, F. L., & Sun, R. (2008). Propagation of Bleustein–Gulyaev wave in 6mm piezoelectric materials loaded with viscous liquid. *International Journal of Solids and Structures*, *45*(13), 3699–3710. doi:10.1016/j.ijsolstr.2007.09.018

Guo, F.-L., Song, Y., & Wang, G.-Q. (2006). The Bleustein Gulyaev wave in piezoelectric 6 mm crystals for liquid sensing applications. *Piezoelectricity, acoustic waves and device applications proceedings of the 2006 Symposium, Zheijang University* (pp. 205–209).

Hooker, M. W. (1998). Properties of PZT-Based Piezoelectric Ceramics Between – 150 and 250 o C, (September).

IEEE Ultrasonics. (1987). IEEE Standard on Piezoelectricity. New York, New York, USA: The institute of Electrical and Electronics Engineers, Inc.

J. P. Sargent. (2006). Corrosion detection in welds and heat zone affected zones using ultrasonic Lamb waves. *Insight*, *48*(3), 160–167.

Josse, F., & Shana, Z. (1988). Analysis of shear horizontal surface waves at the boundary between a pieazoelectric crystal and a viscous fluid medium. *Journal of Acoustical Society of America*, 978–984.

Juluri, N., Lowe, M., & Cawley, P. (2007). The Guiding of Ultrasound by a Welded Joint in a Plate. *AIP Conference Proceedings*, *894*(2007), 1079–1086. doi:10.1063/1.2718087

Kamas, T., Giurgiutiu, V., & Lin, B. (2013). Analytical Modeling of Proof-Mass Piezoelectric Wafer Active Sensor for Symmetric Lamb Waves Tuning. *International workshop of Structural Health Monitoring, IWSHM*. San Francisco, CA.

Kamas, T, Giurgiutiu, V., & Lin, B. (2013). Analytical Modeling of Proof-Mass Piezoelectric Wafer Active Sensor for Symmetric Lamb Waves Tuning. *International workshop of Structural Health Monitoring, IWSHM*.

Kamas, T., Giurgiutiu, V., & Lin, B. (2014). Modeling and Experimentation of Thickness Mode E/M Impedance and Rayleigh wave Propagation for Piezoelectric Wafer Active Sensors on Thick Plates. *ASME-SMASIS* (pp. 1–9).

Kamas, T., & Lin, B. (2014). Quasi-Rayleigh Waves in Butt-Welded Thick Steel Plate. *AIP Conference Proceedings: Quantitative Nondestructive Evaluation*.

Kamas, T., Lin, B., & Giurgiutiu, V. (2013). Analytical modeling of PWAS in-plane and out-of-plane electromechanical impedance spectroscopy (EMIS). In J. P. Lynch, C.-B. Yun, & K.-W. Wang (Eds.), *SPIE Smart Structure and Materials + Nondestructive Evaluation and Health Monitoring 2013, Sensors and Smart Structures Technologies for Civil, Mechanical, and Aerospace Systems* (Vol. 8692, p. 869227). doi:10.1117/12.2009249

Kamas, T., Lin, B., & Giurgiutiu, V. (2014). Modeling and Experimentation of Proof-Mass Piezoelectric Wafer Active Sensor Thickness Mode E/M Impedance Spectroscopy. *AIAA Region II Student Conference* (pp. 1–12). Memphis, TN.

Kanazawa, K. K., & Gordon, J. G. (1985). The oscillation frequency of a quartz resonator in contact with a liquid. *Analytica Chemica Acta*, *175*, 99–105.

Krimholtz, R., Leedom, D. A., & Matthaei, G. L. (1970). New Equivalent Circuits for Elementary Piezoelectric Transducers.pdf.

Lamb, H. (1917). On Waves in an Elastic Plate. *Proceedings of the Royal Society A: Mathematical, Physical and Engineering Sciences*, *93*(648), 114–128. doi:10.1098/rspa.1917.0008

Lawson, A. W. (1942). The Vibration of Piezoelectric Plates. *Physical Review*, *62*, 71–76. Retrieved from http://prola.aps.org/pdf/PR/v62/i1-2/p71_1

Lee, P. C. Y., Liu, N., & Ballato, A. (2004). Thickness Vibrations of a Piezoelectric Plate with Dissipation, *51*(1), 52–62.

Lee, Y.-C., & Kuo, S. H. (2006). Leaky Lamb wave of a piezoelectric plate subjected to conductive fluid loading: Theoretical analysis and numerical calculation. *Journal of Applied Physics*, *100*(7), 073519. doi:10.1063/1.2357648

Liang, C., Sun, F. P., & Rogers, C. a. (1994). Coupled Electro-Mechanical Analysis of Adaptive Material Systems -- Determination of the Actuator Power Consumption and System Energy Transfer. *Journal of Intelligent Material Systems and Structures*, *5*(1), 12–20. doi:10.1177/1045389X9400500102

Liang, Chen, Sun, F., & Rogers, C. a. (1996). Electro-mechanical impedance modeling of active material systems. *Smart Materials and Structures*, *5*(2), 171–186. doi:10.1088/0964-1726/5/2/006

Lin, B., & Giurgiutiu, V. (2011). Simplified 2D modeling of power and energy transduction of piezoelectric wafer active sensors for structural health monitoring. *SPIE 2011 Sensors and Smart Structures Technologies for Civil, Mechanical, and Aerospace Systems*, *7981*, 79812R–79812R–12. doi:10.1117/12.880120

Lin, B., Giurgiutiu, V., Pollock, P., Xu, B., & Doane, J. (2010). Durability and Survivability of Piezoelectric Wafer Active Sensors on Metallic Structure. *AIAA Journal*, *48*(3), 635–643. doi:10.2514/1.44776

Lin, B., Kamal, A., Giurgiutiu, V., & Kamas, T. (2012). Multimodal Lamb Waves Power and Transfer Function Analysis of Structurally-Bonded PWAS. *The ASME 2012 Conference on Smart Materials, Adaptive Structures and Intelligent Systems* (pp. 1–7). Stone Mountain, Georgia.

Love, A. E. H. (1944). *A Treatise on the Mathematical Theory of Elasticity*. *Zhurnal Eksperimental'noi i Teoreticheskoi Fiziki* (Fourth Edi.). Cambridge University Press. Retrieved from http://scholar.google.com/scholar?hl=en&btnG=Search&q=intitle:No+Title#0

Lowe, M. J. S. (1995). Matrix techniques for modeling ultrasonic waves in multilayered media. *IEEE Transactions on Ultrasonics, Ferroelectrics and Frequency Control*, *42*(4), 525–542. doi:10.1109/58.393096

Martin, S. J., Bandey, H. L., Cernosek, R. W., Hillman, A. R., Brown, M. J., & Le, L. (2000). Equivalent-Circuit Model for the Thickness-Shear Mode Resonator with a Viscoelastic Film Near Film Resonance, *II*(1), 141–149.

Mason, Warren P. (1948). *Electromechanical Transducers and Wave Filters* (Second.). D. Van Nostrand Company, Inc.

Masserey, B., & Fromme, P. (2014). Noncontact monitoring of fatigue crack growth using high frequency guided waves. (J. P. Lynch, K.-W. Wang, & H. Sohn, Eds.), *9061*, 90611D. doi:10.1117/12.2046312

Meeker, T. R. (1972). Thickness mode piezoelectric transducers. *Ultrasonics*, *10*(1), 26–36.

Meitzler, A. H. (1961). Mode Coupling Occurring in the Propagation of Elastic Pulses in Wires. *The Journal of the Acoustical Society of America*, *33*(4), 435. doi:10.1121/1.1908685

Mindlin, R. D., & Deresiewicz, H. (1953). *Thickness Shear And Flexural Vibrations of a Circular Disk*.

Nayfeh, A. H., & Nagy, P. B. (1997). Excess attenuation of leaky Lamb waves due to viscous fluid loading. *The Journal of the Acoustical Society of America*, *101*(5), 2649–58.

Nwankwo, E., & Durning, C. J. (1998a). Mechanical response of thickness-shear mode quartz-crystal resonators to linear viscoelastic fluids. *Sensors and Actuators A: Physical*, *64*, 119–124.

Nwankwo, E., & Durning, C. J. (1998b). Impedance analysis of thickness-shear mode quartz crystal resonators in contact with linear viscoelastic media. *Review of Scientific Instruments*, *69*(6), 2375. doi:10.1063/1.1148963

Nwankwo, E., & Durning, C. J. (1999). Fluid property investigation by impedance characterization of quartz crystal resonators: Part I: Methodology, crystal screening, and Newtonian fluids. *Sensors and Actuators A: Physical*, 99–109. Retrieved from http://www.sciencedirect.com/science/article/pii/S0924424798002167

Park, G., Sohn, H., Farrar, C. R., & Inman, D. J. (2003). Overview of Piezoelectric Impedance-Based Health Monitoring and Path Forward. *The Shock and Vibration Digest*, *35*(6), 451–463. doi:10.1177/05831024030356001

Park, H. W. (2014). Understanding the electromechanical admittance of piezoelectric transducers collocated on a finite beam from the perspective of wave propagation. *Journal of Intelligent Material Systems and Structures*. doi:10.1177/1045389X14549874

Park, H.-J., Sohn, H., Yun, C.-B., Chung, J., & Lee, M. M. S. (2012). Wireless guided wave and impedance measurement using laser and piezoelectric transducers. *Smart Materials and Structures*, *21*(3), 035029. doi:10.1088/0964-1726/21/3/035029

Pavelko, V. (2014). New applications of a model of electromechanical impedance for SHM. In T. Kundu (Ed.), *SPIE Health Monitoring of Structural and Biological Systems* (Vol. 9064, p. 90640Y). doi:10.1117/12.2044260

Peairs, D. M., Grisso, B., Inman, D. J., Page, K. R., Athman, R., & Margasahayam, R. N. (2003). Proof-of-Concept Application of Impedance Based Health Monitoring on Space Shuttle Ground Structures. National Aeronautics and Space Administration.

Puttmer, A., Hauptmann, P., Lucklum, R., Krause, O., & Henning, B. (1997). SPICE Model for Lossy Piezoceramic Transducers. *IEEE Transactions on Ultrasonics, Ferroelectrics and Frequency Control*, *44*(1), 60–66.

R. D. Mindlin. (1951). Thickness shear and flexural vibrations of crystal plates. *Journal of applied physics*, *22*(3), 316–323.

R. D. Mindlin. (1960). Waves and vibrations in isotropic elastic plates. *Structural Mechanics; proceedings of the first symposium on naval structural mechanics held at Stanford University* (pp. 199–232).

Raghavan, a., & Cesnik, C. E. S. (2008). Effects of Elevated Temperature on Guided-wave Structural Health Monitoring. *Journal of Intelligent Material Systems and Structures*, *19*(12), 1383–1398. doi:10.1177/1045389X07086691

Redwood, M. (1961). Transient performance of a piezoelectric transducer. *Acoustical Society of America*, *33*(4), 527–536.

Roman, C. (2012). *Structural Health Monitoring of Composite Laminates using Piezoelectric and Fiber Optics Sensors*.

Rose, J. L., Ditri, J. J., Pilarski, A., Rajana, K., & Carr, F. (1994). A guided wave inspection technique for nuclear steam generator tubing. *NDT & E International*, *27*(6), 307–310. doi:10.1016/0963-8695(94)90211-9

Rugina, C., Giurgiutiu, V., Toader, A., & Ursu, I. (2014). The electromechanical impedance method on thin plates.

Santoni-Bottai, G., & Giurgiutiu, V. (2012). Damage detection at cryogenic temperatures in composites using piezoelectric wafer active sensors. *Structural Health Monitoring*, *11*(5), 510–525. doi:10.1177/1475921712442441

Schneider, T. W., & Martin, S. J. (1995). Influence of Compressional Wave Generation on Thickness-Shear Mode Resonator Response in a Fluid, *67*(78), 3324–3335.

Shen, Y. (2014). *Structural Health Monitoring Using Linear and Nonlinear Ultrasonic Guided Waves*. University of South Carolina.

Sherrit, S., Leary, S. P., Dolgin, B. P., & Bar-Cohen, Y. (1999). Comparison of the Mason and KLM equivalent circuits for piezoelectric resonators in the thickness mode. *1999 IEEE Ultrasonics Symposium. Proceedings. International Symposium (Cat. No.99CH37027)*, *2*, 921–926. doi:10.1109/ULTSYM.1999.849139

Silk, M. G., & Bainton, K. F. (1979). The propagation in metal tubing of ultrasonic wave modes equivalent to Lamb waves. *Ultrasonics*, *17*(1), 11–19. doi:10.1016/0041-624X(79)90006-4

Suh, Y. K., & Kim, Y. H. (2010). Effect of Overlayer Viscoelasticity on Resonant Characteristics of a Quartz Crystal Resonator. *Japanese Journal of Applied Physics*, *49*(6), 065801. doi:10.1143/JJAP.49.065801

Sun, F. P., Liang, C., & Rogers, C. A. (1994a). Structural modal analysis using collocated piezoelectric actuator/sensors: an electromechanical approach. *Proc. SPIE 2190, Smart Structures and Materials 1994: Smart Structures and Intelligent Systems, 238*. Orlando, FL.

Sun, F. P., Liang, C., & Rogers, C. A. (1994b). Structural modal analysis using collocated piezoelectric actuator/sensors: an electromechanical approach. *SPIE Smart Structures and Materials 1994: Smart Structures and Intelligent systems*.

Tiersten, H. F. (1963). Thickness Vibrations of Piezoelectric Plates. *J. Acoustic Society of America*, *35*(1), 53–58.

Wolf, R. a. (2004). Temperature dependence of the piezoelectric response in lead zirconate titanate films. *Journal of Applied Physics*, *95*(3), 1397. doi:10.1063/1.1636530

Wu, J. R., & Zhu, Z. M. (1992, March). The propagation of Lamb waves in a plate bordered with layers of a liquid. *The Journal of the Acoustical Society of America*. Retrieved from http://www.ncbi.nlm.nih.gov/pubmed/1556318

Xu, B., Giurgiutiu, V., & Crachiolo, G. (2006). Development of Piezoelectric Oscillator Sensor for In-Vivo Monitoring of Capsule Formation around Soft Tissue Implants. *SPIE 2006 Smart Structure/NDE, Health Monitoring and Smart NDE of Structural and Biological Systems V* (pp. 1–11). San Diego, California.

Yamada, T., & Niizeki, N. (1970). Admittance of piezoelectric plates vibrating under the perpendicular field excitation. *Proceedings of the IEEE* (pp. 941 – 942).

Yamada, Tomoaki. (1970). Formulation of Admittance for Parallel Field Excitation of Piezoelectric Plates. *Journal of Applied Physics*, *41*(9), 3604. doi:10.1063/1.1659478

Yu, L. (Lucy). (2006). *In-Situ Structural Health Monitoring With Piezoelectric Wafer Active Sensor Guided Wave Phased Arrays*.

Yu, L., Santoni-Bottai, G., Xu, B., Liu, W., & Giurgiutiu, V. (2008). Piezoelectric wafer active sensors for in situ ultrasonic-guided wave SHM. *Fatigue & Fracture of Engineering Materials & Structures*, *31*(8), 611–628. doi:10.1111/j.1460-2695.2008.01256.x

Zagrai, A., & Giurgiutiu, V. (2001). Electro-Mechanical Impedance Method for Crack Detection in Thin Plates. *Journal of Intelligent Material Systems and Structures*, *12*(October 2001). Retrieved from http://jim.sagepub.com/content/12/10/709.short

Zagrai, Andrei N, & Giurgiutiu, V. (2001). Electro-Mechanical Impedance Method for Damage Identification in Circular Plates, *40*.

Zagrai, Andrei Nikolaevitch. (2002). *Piezoelectric Wafer Active Sensor Electro-Mechanical Impedance Structural Health Monitoring*. University of South Carolina. Retrieved from http://onlinelibrary.wiley.com/doi/10.1002/cbdv.200490137/abstract

Zemanek, J. (1972). An Experimental and Theoretical Investigation of Elastic Wave Propagation in a Cylinder. *The Journal of the Acoustical Society of America*, *51*(1B), 265. doi:10.1121/1.1912838

Zhang, C., Caron, J. J., & Vetelino, J. F. (2001). The Bleustein ± Gulyaev wave for liquid sensing applications, *76*, 64–68.

Zhang, W., Wang, A., Vlahopoulos, N., & Wu, K. (2003). High-frequency vibration analysis of thin elastic plates under heavy fluid loading by an energy finite element formulation. *Journal of Sound and Vibration*, *263*(1), 21–46. doi:10.1016/S0022-460X(02)01096-9

Zhu, Z., & Wu, J. (1995). The propagation of Lamb waves in a plate bordered with a viscous liquid. *The Journal of the Acoustical Society of America*, *98*(2), 1057–64.

Zimmerman, D. C., & Inman, D. J. (1990). On the nature of the interaction between structures and proof-mass actuators. *Journal of guidance, control, and dynamics*, *13*(1), 82–88.